

Nano Studies

8

2013

NANO STUDIES

8

2013

Nano Studies, 2013, 8

UDG [53 + 54 + 620.22] (051.2)
N – 21

Nano Studies is a biannual scientific journal published in Georgia.

Nano Studies' topics of interest include Nanoscience and related problems of Physics, Chemistry and Materials Science.

Nano Studies publish following categories of scientific articles: research papers, communications, reviews and discussions.

Nano Studies publish scientific articles in English and also in Georgian and in Russian.

Summaries of all the articles of **Nano Studies** are referred in **Georgian Abstracts Journal** and are accessible in **Tech Inform** (Georgia's Central Institute for Scientific and Technical Information) database: <http://www.tech.caucasus.net>

Full-texts of articles published in **Nano Studies** are free-accessible in **Nano Archive** database: <http://www.nanoarchive.org> and journal's web-site: www.NanoStudies.org

Editor & Publisher: **Levan Chkhartishvili**

Editorial Assistant: **Tamar Berberashvili**

Address of Editorial Office: **Department of Physics
Georgian Technical University
Campus 4, Room 307
77 Merab Kostava Avenue
Tbilisi, 0175, Georgia
www.NanoStudies.org**

E-mail: **chkharti2003@yahoo.com**

Phone: **995 322 37 19 42**

Mobile: **995 599 34 07 36**

© Authors of articles, 2013

Publishing House **Nekeri**

ISSN 1987 – 8826

CONTENTS

Proceedings of the International Conference & Exhibition on Advanced
& Nano Materials (August 12 – 14, 2013, Quebec-City, Canada)

Studies on thermal properties of silicone–acrylic nanopowders and of organic polymer coatings modified with such nanopowders J. Trzaskowska, J. Kozakiewicz	7-16
Electromagnetic shielding and mechanical properties of knitted fabric reinforced composites E. Sancak, M. Akalın, M. Yüksek, N. Demirel, İ. Usta, E. İsgören	17-28
Research on water-repellant nanofiber spun by electro bubble spinning method M. Iwamoto, H. Ino, T. Kimura, Y. Kishimoto	29-34
Heterogeneous nano cerium chromate as a new and selective oxidant for selective conversion of alcohols to corresponding carbonyl compounds S. Oftadehgan, N. Goudarzian	35-44
Porous Si substrate: A high-quality and cheap substrate for advanced RF applications Y. Belaroussi, M. T. Belaroussi, G. Scheen, K. Ben Ali, J.-P. Raskin	45-52
Nanocrystalline nickel cobalt ferrite ($\text{Ni}_{1/2}\text{Co}_{1/2}\text{Fe}_2\text{O}_4$) for electromagnetic interference (EMI) shielding applications D. K. Tiwari, A. K. Thakur, S. E. Borjas–García, L. M. Villaseñor Cendejas, N. Dasgupta–Schubert	53-62
Characterization of AlN thin films annealed by CO ₂ laser J.-Sh. Chen, J.-Y. Wang, Y.-J. Yao, Ch.-T. Chiang	63-68
Analysis of dielectric resonator antennas (DRA) based on complex perovskite CNBTOX – $\text{Ca}(\text{Nb}_{1/2}\text{Bi}_{1/2})_x\text{Ti}_{1-x}\text{O}_3$ A. D. S. Bruno Costa, R. C. S. Costa, F. W. de O. Amarante, A. S. B. Sombra	69-76
Fast set-up of classical molecular dynamics simulations of nanomaterials using Wolffia J. O. Sotero–Esteve, F. Matrnéz, R. Quiñones, W. Cuadrado, A. de Jesús	77-84
Apparent Hall mobility of charge carriers in silicon with nano-sized “metallic” inclusions L. Chkhartishvili, T. Pagava	85-94

Contents.

Phase transition of nanoparticles of organic pigments M. Kakuichi, K. Kasatani, Y. Morita	95-102
Investigation of the mechanical properties of polyamide 6 / chitosan / hydroxyapatite based electrospun nanofibrous biocomposites R. Erdem, E. Sancak, S. S. Pazarlioglu, M. Akalin, O. Atak	103-110
Mechanical properties of nanostructured copper coatings made by cold gas dynamic spray R. Maev, V. Leshchynsky, E. Strumban, D. Dzhurinskiy, J. Kocimski, E. Maeva	111-120
Structural and dielectric studies of Cr ³⁺ doped ZnFe ₂ O ₄ nanoparticles R. M. Sebastian, K. Maniammal, Sh. Xavier, E. M. Mohammed	121-130
Compact low-pass filter using complementary rose curve resonators (CRCRs) I. Sassi, L. Talbi, K. Hettak	131-138
Formation and evolution of nickel silicides in silicon nanowires A. Katsman, M. Beregovsky, Y. E. Yaish	139-152
Separation of nanoparticles from nanoparticle enhanced phase change material M. H. Sheikh, M. A. R. Sharif, P. A. Rupar	153-164
Comparative studies of TiO ₂ nanomaterial with its photo-catalytic applications Y. H. Ng, Y. H. Leung, M. T. Wong, A. B. Djurišić, F. C. C. Leung, W. K. Chan	165-170
Nano-sphere of metal carbonates: Synthesis and characterization as energy storage materials Y. Sharma, A. Kumar, P. Chaturvedi	171-182
Study of ion beam mixing of Te / In and Se / In systems by cascade collisional mixing model B. A. M. Ibrahim	183-190

Regular Papers

Model of NMR spectroscopic analysis of azide containing organic molecules T. Chachibaia	191-200
Non-wetting of cavity walls of zeolites by metals – <i>in Russian</i> A. A. Kapanadze, G. V. Rtveliashvili, G. D. Tabatadze	201-202

Boreholes water level and earthquake's daily monitoring A. Sborshchikovi, G. Kobzev, S. Ch. Mavrodiev, G. Melikadze	203-212
Accumulation of cadmium by basil (<i>Ocimum basilicum</i>), coriander (<i>Coriandrum sativum</i>) and saffron (<i>Crocus sativus</i> L) from cadmium-enriched soil – <i>in Georgian</i> A. Rcheulishvili, O. Rcheulishvili, N. Rcheulishvil, E. Ginturi, L. Tugushi, E. Gelagutashvili	213-216
Properties of boron nitride synthesized under the effect of concentrated light radiation – <i>in Russian</i> L. L. Sartinska, Eu. V. Voynich, A. F. Andreeva, A. M. Kasumov, I. I. Timofeeva, A. Yu. Koval, G. A. Frolov, T. Eren, E. Altay	217-222
Investigation the influence of absorption of mercury on the structure and morphology of the gold thin films N. I. Khachidze, T. I. Khachidze	223-226
Tomographical model of inhomogeneous structure of Earth crust for Georgia and nearest territories developed by data of surface seismic Rayleigh waves T. Gegechkori, V. Gotciridze, N. Zhukova, A. Sborshchikovi, I. Shengelia	227-230
Short dictionary (glossary) on nanochemistry and nanotechnology. Part III Ts. Ramishvili, V. Tsitsishvili	231-252
Modeling of the quasi-dielectric state in PbSnTe and PbSnSe nanolayers with high concentration of nonstoichiometric defects A. M. Pashaev, O. I. Davarashvili, M. I. Erukashvili, Z. G. Akhvlediani, L. P. Bychkova, V. P. Zlomanov	253-258
Attenuation of gamma-radiation concomitant neutron- absorption in boron–tungsten composite shields G. Nabakhtiani, L. Chkhartishvili, A. Gigineishvili, O. Tsagareishvili, D. Gabunia, Z. Rostomashvili, Sh. Dekanosidze	259-266
Once more on effective electrical charge of atomic nuclei L. Chkhartishvili, T. Berberashvili	267-272
Bioindication and biotesting in the scope of environment protection – <i>in Georgian</i> T. Pavliashvili, T. Kalabegishvili	273-282
Acoustic spectrometer – <i>in Russian</i> D. G. Driaev, K. O. Kakhiani, F. Kh. Akopov, S. J. Tsakadze	283-288

Contents.

The theory of polaron low temperature mobility B. Kotia, D. Khutsishvili	289-304
Composite ceramics based on boron carbide enriched in isotope ¹¹ B as a promising radiation resistant structural material – <i>in Russian</i> I. A. Bairamashvili, M. V. Galustashvili, J. Sh. Jobava, V. G. Kvatchadze, Z. Z. Mestvirishvili	305-310
Investigation of optical transmission spectrum of TiN thin films obtained by HF-reactive sputtering method – <i>in Russian</i> A. P. Bibilashvili, Z. V. Jibuti, N. D. Dolidze	311-314
Some issues of ultradispersive α -aluminum oxide powders of low temperature synthesis – <i>in Georgian</i> T. V. Kuchukhidze, T. N. Archuadze, V. G. Gabunia, M. A. Kadaria, O. I. Lekashvili, R. V. Chedia	315-326
New mechanism for materials indentation on nanometer and submicron levels – <i>in Russian</i> A. B. Gerasimov, G. D. Chiradze, T. K. Ratiani, M. T. Vepkhvadze	327-332

Science History Pages

The beginnings of the aluminum industry F. Habashi	333-344
--------------------------------------------------------------------	---------

Books & Media Reviews

Radiation synthesis of nanomaterials – <i>in Georgian</i> T. Berberashvili	345-346
--------------------------------------------------------------------------------------------	---------

Chronicle

Powder Metallurgy – 2012 – <i>in Georgian</i> A. Gachechiladze	347-352
2013 International Conference & Exhibition on Advanced & Nano Materials – <i>in Georgian</i> L. Chkhartishvili	353-358

STUDIES ON THERMAL PROPERTIES OF SILICONE–ACRYLIC NANOPOWDERS AND OF ORGANIC POLYMER COATINGS MODIFIED WITH SUCH NANOPOWDERS

J. Trzaskowska, J. Kozakiewicz

Industrial Chemistry Research Institute
Warsaw, Poland
joanna.trzaskowska@ichp.pl

Accepted September 19, 2013

1. Introduction

Thermal analysis is widely used to characterize nanoparticles with hybrid structure [1, 2]. Thermal analysis is also considered as excellent technique to evaluate powder coatings [3, 4].

Due to their environmental and economical advantages powder coatings (PC) constitute quite important and constantly growing sub-sector in the paint industry [5, 6]. Many studies have confirmed that impact strength of PC can be improved through the introduction of appropriately structured nanoparticles because more energy could be consumed by the interfacial surface between polymer and nanoparticles when the polymer matrix is impacted or tensed [7]. Furthermore, if such nanoparticles contain polysiloxanes it provides excellent transparency and thermal stability to the nanocomposites. High thermal stability of polysiloxanes [8] is directly attributable to the considerably higher energy and ionic character of the Si–O bond relative to the C–C bond, so higher temperatures of degradation onset could be expected [9, 10].

The results of earlier investigations carried out in the Industrial Chemistry Research Institute (ICRI) in Poland proved that significant increase in coating impact resistance and elasticity could be achieved at very low (only 3 %) content of silicone-acrylic nanopowders in the PC [11]. Nanopowders were obtained in a form of agglomerates of silicone-acrylic core-shell nanoparticles and were prepared in a three-step process developed in ICRI [12]. The first step of that process was synthesis of silicone resin aqueous dispersion, the second step was emulsion polymerization of methacrylic monomer in that dispersion resulting in obtaining of a hybrid dispersion of core-shell nanoparticles of ca 100 nm size (see **Figure 1**), and the third step was spray-drying of that dispersion which led to nanopowder particles (see **Figure 2**) of few micron size, structured as agglomerates of the said core-shell nanoparticles.

The results of our recent studies confirmed that chemical composition of silicone core of such nanoparticles affected the properties of dispersions, nanopowders and coatings properties modified with such nanopowders. It was found that the increased share of trifunctional monomers (methyltrimethoxysilane–METM and methacryloyltrimethoxysilane–MATMS) in silicone monomers mixture applied in synthesis of silicone resin which constituted the core of the nanoparticles led to increased crosslinking density of the resin and consequently resulted in the increase in its T_g value [13].

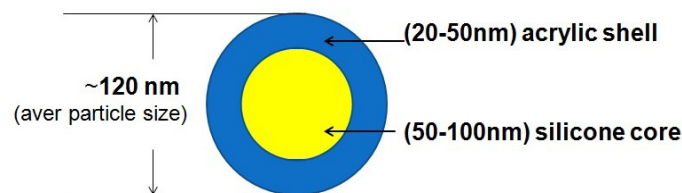


Figure 1. The structure of silicone–acrylic core–shell nanoparticle.

In the study presented in this paper the effect of chemical structure of silicone core of the core–shell nanoparticles which constituted the nanopowders on the thermal properties of the nanopowders and of epoxy–polyester and polyester PC, both unmodified and modified with 3 % of such nanopowders, was investigated using differential scanning calorimetry (DSC) and thermogravimetric analysis (TGA). Since in our earlier studies [11] where the effect of the nanopowder content in the PC on coating properties was studied we found that using 3% of nanopowders distinct improvement of substantial coating properties (impact resistance, elasticity) could be achieved while not deteriorating the other coating properties (hardness, abrasion resistance) we decided to study thermal properties of the PC containing only that specific optimum amount of nanopowders.

2. Experimental

2.1. Materials

The materials used to obtain the PC were: epoxy resin (Epidian 012) from Chemical Company Organika–Sarzyna Poland, carboxylated polyester resin (Policen 300 T) from PPG Polifarb Cieszyn Poland, hardener (acid value 33) for epoxy–polyester and polyester coatings, hydroxyalkylamide crosslinker (Primid XL 552) for PC from EMS–Chemie AG, pigment (TiO₂ rutile) from Chemical Company Police Poland, standard additives for PC (benzoin from DSM and resiflow PV 88 supplied by Worlee Chemie GmbH), The nanopowders (NP) (see **Figure 2**) of different chemical composition (**Table 1**) were obtained in our laboratory.

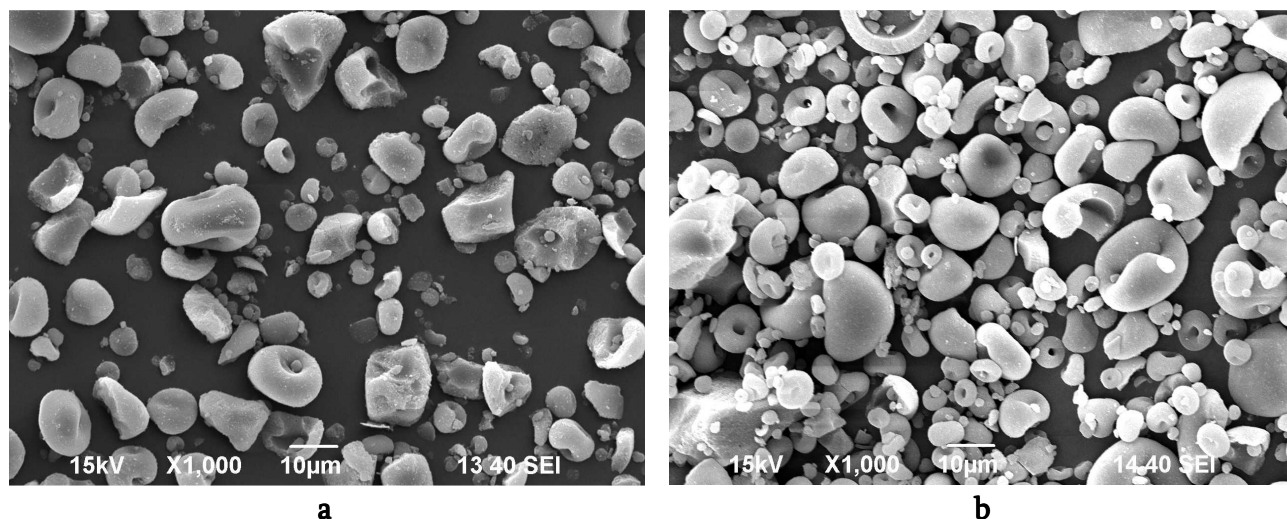


Figure 2. SEM images of nanopowder particles: (a) NPA nanopowder and (b) NPB nanopowder.

Table 1. Chemical and physicochemical properties of the nanopowders.

Sample designation	Share of trifunctional monomers (MATMS and METMS) in silicone monomers mixture, wt. %	Volatile substances content, wt. %	Bulk density, g / cm ³	Size of nanopowder particles, μm	Range of individual core-shell nanoparticle size, nm
NPA	7.93	3.82	0.253	1 – 15 (lesser share of smaller particles)	101.8 – 147.6
NPB	24.12	1.77	0.302	1 – 15 (greater share of smaller particles)	72.5 – 98.1

Results shown in **Figure 2** and **Table 1** revealed differences in physicochemical properties of both nanopowders. NPA nanopowder particles (agglomerates of core-shell nanoparticles) were bigger than those of NPB (see **Figure 2**) and also individual core-shell nanoparticles contained inside agglomerates were bigger in case of NPA nanopowder. Furthermore, both nanopowders differed in the values of bulk density and volatile substances content.

2.2. Preparation of nanostructured PC

The epoxy-polyester and polyester PC modified with NPA and NPB nanopowders were prepared from the physical mixture of the ingredients which were given in **Table 2**.

Table 2. Composition of PC.

Ingredient	P-E-0, parts	P-E-A, parts	P-E-B, parts	P-0, Parts	P-A, parts	P-B, parts
Epoxy resin	30	30	30	–	–	–
Polyester resin	–	–	–	56.05	56.05	56.05
Hardener	70	70	70	2.95	2.95	2.95
TiO ₂	30	30	30	37	37	37
Standard additives	1	1	1	1	1	1
NPA	–	3 % per coating mass	–	–	3% per coating mass	–
NPB	–	–	3 % per coating mass	–	–	3 % per coating mass

All PC components were well-mixed in a grinder at 1000 rpm for 3 min and extruded in a Buss Ko–Knether PR–46 extruder (temperature of the screw – 82 °C and adapter – 102 °C, screw rotational speed 3.5 rpm.). The extrudate was crushed and pulverized to fine powder into particle size of less than 85 μm, and next curing properties were characterized by DSC and thermal stability by TGA.

The resulting powder was sprayed on both sides of steel plates using electrostatic spraying and then cured in an oven at 180 °C for 15 min. to yield coats of thickness 60 – 90 μm. The obtained cured PC were removed from the plates and then examined by DSC.

2.3. DSC measurements

DSC studies were carried out using a DSCQ 2000 apparatus from TA Instruments. The system was calibrated with indium (mp = 156.63 °C; $\Delta H = 29.21$ J / g) and with adamantane (mp = –65.23 °C; $\Delta H = 19.82$ J / g). About 6 – 7 mg of the nanopowders or of the uncured or cured PC samples were placed and closed in aluminum pans. Experiments were carried out under dynamic helium atmosphere (25 mL / min) at heating and cooling rate of 20 °C / min, at the temperature interval from – 150 to 150 °C for nanopowders, from 20 to 300 °C for uncured PC samples and from – 150 to 300 °C for cured PC samples, using heat–cool–heat cycle regime.

2.4. TGA measurements

Thermogravimetric curves were obtained in a thermobalance (Q50 model from TA Instruments) under conditions of dynamic nitrogen atmosphere. The samples about 15 – 20 mg were heated in an alumina crucible at a heating rate of 10 °C / min within the temperature range from 25 to 700 °C.

3. Results and discussion

3.1. Differential scanning calorimetry (DSC) analysis

Results of the DSC investigations of the nanopowders are presented in **Figure 3**.

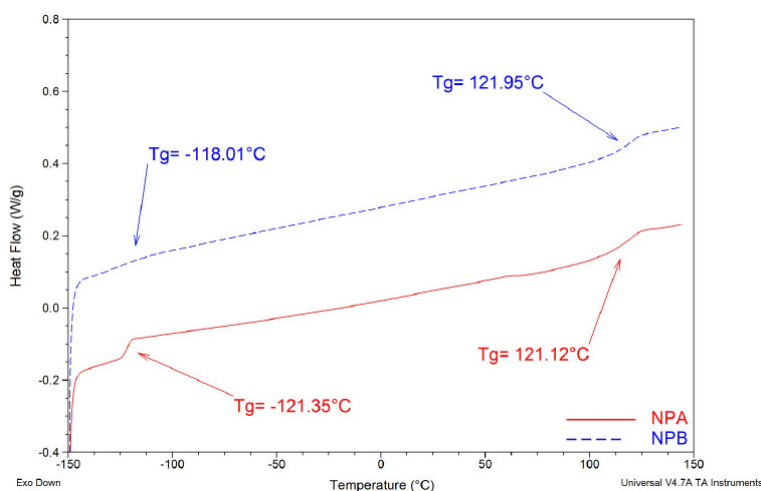


Figure 3. DSC curves obtained for nanopowders in the second heating at a rate of 20 °C / min.

Based on the results shown in **Figure 3** it can be noted that the T_g values of the silicone part of the core-shell nanoparticles contained in the two different nanopowders investigated in this study were different whereas the T_g values of acrylic part remained unchanged. For NPB nanopowder T_g value of silicone part was about three degrees Celsius higher what can be explained by the higher share of trifunctional monomers in the silicone monomers composition applied for synthesis of silicone resin core of nanoparticles. It can be anticipated that the increase in cross-linking density of silicone resin resulted in restriction of the rotational motion of the silicone polymer chain segments and thus led to an increase in T_g value.

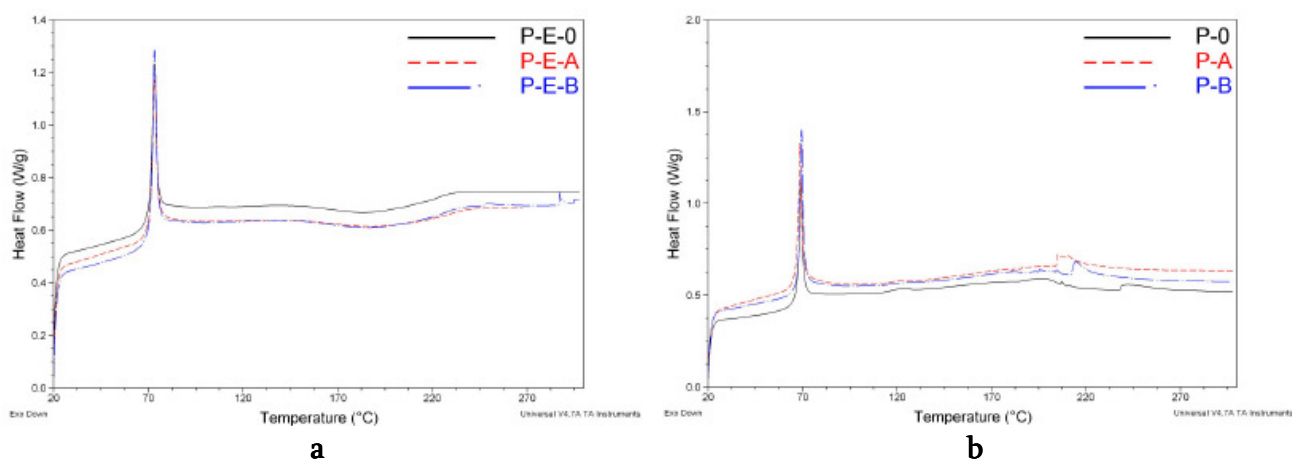


Figure 4: DSC diagram of uncured PC: (a) epoxy-polyester PC and (b) polyester PC, obtained in first heating with 20 °C / min scanning rate.

As it can be seen in the **Figure 4** and in **Table 3** the addition of NPB nanopowder to epoxy-polyester and polyester powder coatings led to a slight delay in start of their melting. The reason for that could be weaker interaction between bigger nanoparticles of NPA and matrix resin than that of smaller NPB nanoparticles – compare results shown in **Table 1**. It has been reported earlier that better dispersing and more suitable size of nanoparticles in PC favors the formation of a nanocomposite system, in which nanoparticles can delay the starting of melting process [14].

Table 3. Characteristic points obtained from DSC scan of epoxy-polyester and polyester PC.

Sample designation	Onset of melting T_{m0} , °C	Melting peak temperature T_m , °C
P-E-0	70.97	73.19
P-E-A	70.97	73.39
P-E-B	71.36	73.26
P-0	67.32	69.05
P-A	66.91	68.60
P-B	68.03	69.42

Figure 5 shows DSC curves of cured PC both unmodified and modified with NPA and NPB nanopowders.

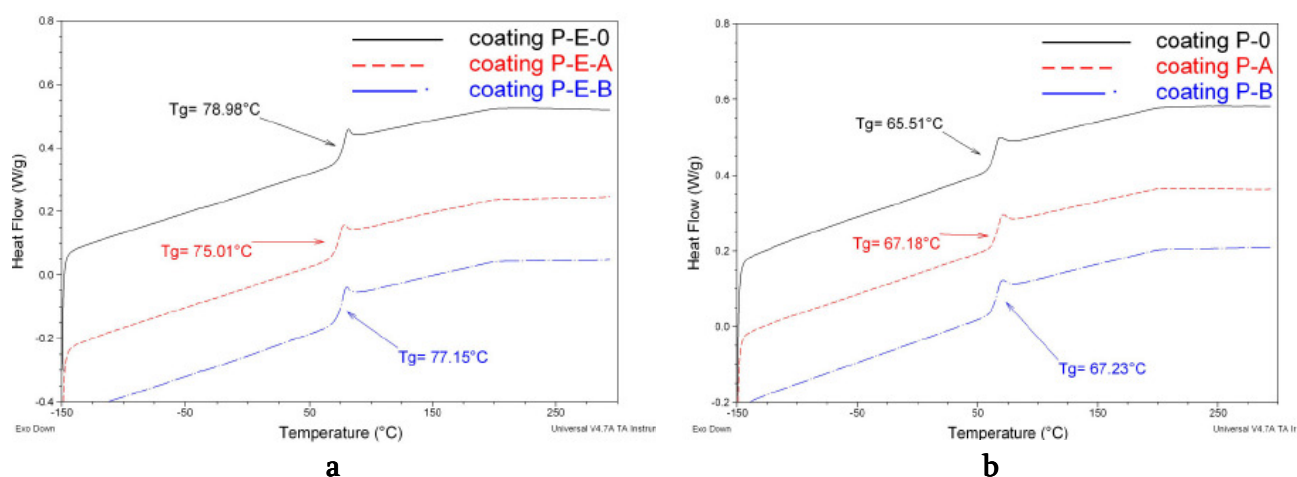


Figure 5. DSC spectra of cured PC: (a) epoxy–polyester PC and (b) polyester PC, obtained in second heating with 20 °C / min scanning rate.

Results shown in **Figure 5a** confirm that the addition of polysiloxane-containing nanoparticles to the epoxy–polyester PC resulted in a decrease in T_g value of the modified cured PC (P–E–A and P–E–B). As it could be expected, the P–E–A coating modified with nanoparticles of lower share of crosslinked polysiloxane chains in the silicone resin (NPA) showed lower T_g in comparison to the P–E–B coating.

Based on the results presented in **Figure 5b** it can be noted that in the case of cured polyester PC the addition of nanopowders led to increase in T_g values regardless of the silicone resin structure. This phenomenon can be explained by higher cross-linking density of polyester coatings as compared to epoxy–polyester ones and by the ability of the nanopowders to reduce void content in the matrix resin [15, 16] regardless of chemical structure of the nano-modifier.

3.2. Thermogravimetric analysis

Table 4 and **Figure 6** show the results of TGA measurements obtained in nitrogen atmosphere for nanopowder (NPA–NPB) samples with various contents of crosslinked polysiloxanes in the core of core–shell nanoparticles. The characteristic values of mass loss temperature and residue at 700 °C are presented in **Table 4**. As it can be noted from the results presented in **Table 4** thermal stability of the nanopowder NPB increased with the increasing share of crosslinked polysiloxanes – compare the results obtained for NPA and NPB nanopowder. At 483.22 °C the mass loss observed for NPA nanopowder was complete, whereas for NPB the end of degradation occurred only at 528.52 °C. Not only the temperature of degradation onset or characteristic mass loss, but also the DTG maxima were shifted to higher temperature – see **Figure 6b** and **Table 4**.

Table 4. TGA results obtained for nanopowders within the range of 25 – 700 °C at N₂ atmosphere.

Sample designation	Temperature for mass loss, °C			Temperature for maximal rate of mass loss (DTG maxima), °C	Residual mass $\Delta m_{res.}$ at 700 °C, %
	1 % (onset)	5 %	50 %		
NPA	117.60	214.37	378.12	120.73; 370.20; 456.59	0.91
NPB	122.41	254.57	382.71	119.05; 360.69; 473.89	1.70

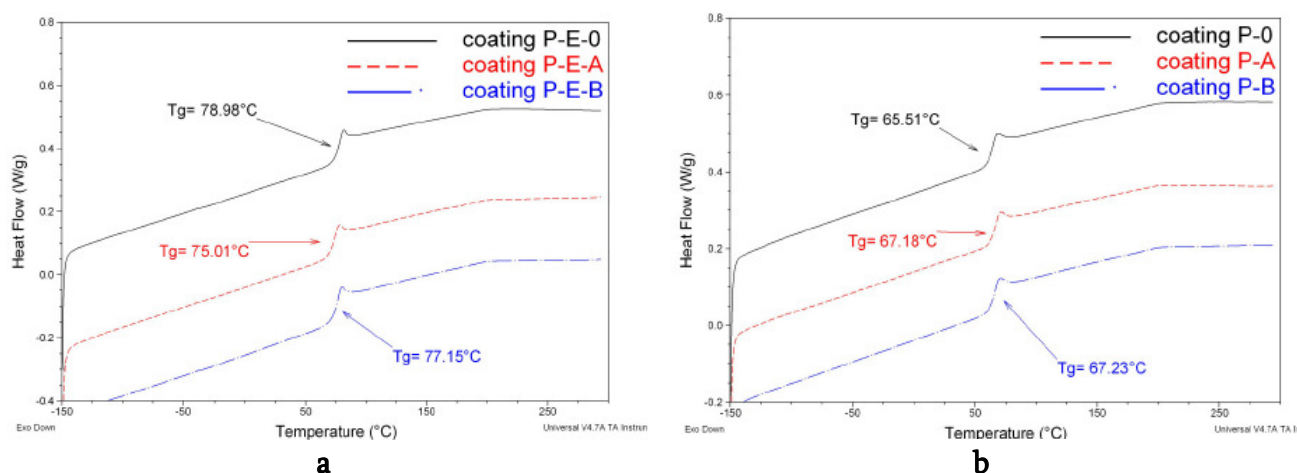


Figure 6. TGA (a) and DTG (b) curves obtained for nanopowders, nitrogen atmosphere, heating rate 10 °C / min.

The DTG curves of both nanopowders shown on **Figure 6b** are characterized by several maxima what can be related to multistage degradation process. The temperatures of onset degradation for polysiloxanes are low (NPA = 117.60; NPB = 122.41) and can be attributed to depolymerization starting from end groups in polymer chains. Degradation residues are quite different: in case of NPA the residue represents only 0.91 % of the initial mass, whereas in case NPB it is significantly higher – 1.70 %. The amount of solid residue (NPA = 0.123 mg; NPB = 1.69 mg) increases with decrease of crosslinked polysiloxane content. General conclusion from TGA studies is then that the increase in cross-linking density of silicone resin which constitutes the core of core-shell particle leads to increase in thermal stability of related nanopowders.

Table 5. The TG data of PC obtained within range of 25 – 700 °C at a nitrogen atmosphere.

Sample designation	First event			Second event		
	Temperature onset of weight loss T_{ons} , °C	Temperature final of event T_f , °C	Δm , %	Temperature onset of weight loss T_{ons} , °C	Temperature final of event T_f , °C	Δm , %
P-E-0	401.37	425.01	45.62	480.37	511.27	5.49
P-E-A	402.88	423.67	47.41	477.26	513.68	5.23
P-E-B	404.89	426.04	52.21	481.81	512.31	5.91
P-0	390.33	409.96	52.93	494.71	583.20	9.24
P-A	403.45	411.08	54.37	517.65	612.63	7.27
P-B	396.12	413.75	57.67	602.33	666.49	4.34

As it can be seen in **Table 5** and in **Figure 7**, epoxy-polyester and polyester PC investigated in our study had thermal decomposition proceeding in two events under nitrogen atmosphere and clear two weight losses can be observed. It is important to note that the first weight loss occurred in the inert atmosphere whereas the second weight loss proceeded in the artificial atmosphere of synthetic air created by addition of O₂ as a result of first degradation

step, what apparently led to acceleration of the degradation process [17]. The temperatures of degradation onset for both PC investigated in our study were above the 390 °C what could be associated with degradation of the polymer matrix. The second event observed above 470 °C could be associated with strong interaction between all additives and the epoxy–polyester or polyester resin restricting the molecular mobility and finally increasing the thermal stability of PC.

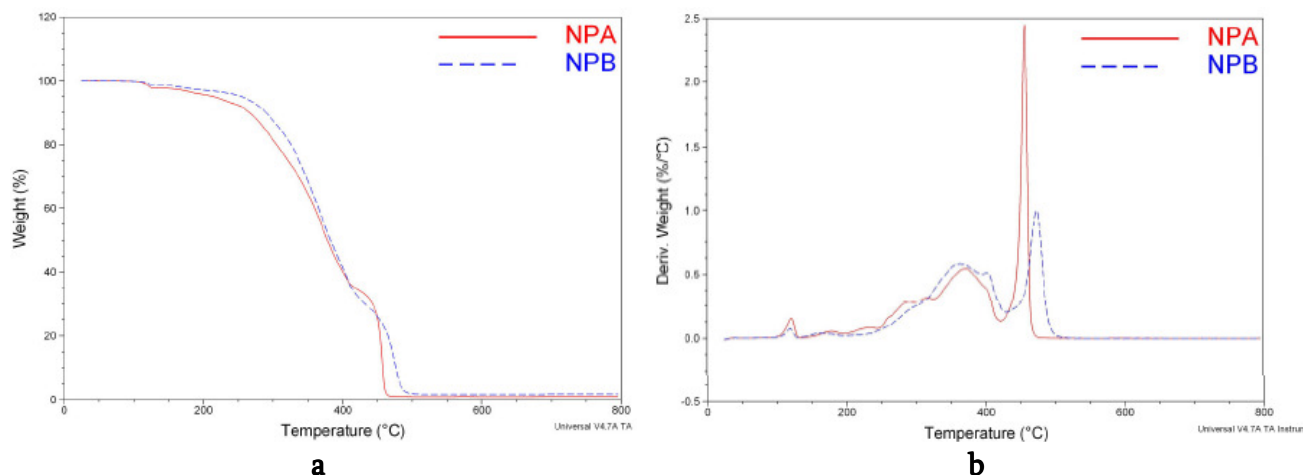


Figure 7. The TGA curves of (a) epoxy–polyester PC and (b) polyester PC obtained in N₂ atmosphere; within range of 25 – 700 °C.

Based on the results of TG analysis shown in **Table 5** and in **Figure 7** it may be noted that the values of temperature onset of weight loss in both first and second events were shifted to higher temperatures for PC modified with NPA and NPB nanopowders. This phenomenon can be explained by the presence of silicone-containing nanoparticles which are very flexible and can well dissipate heat. Therefore additional portion of energy to offset this heat dissipation will be needed to achieve increased thermal stability [16]. Based on the results shown in **Table 5**, it can be concluded that the modification of epoxy–polyester and polyester PC with NPB nanopowder as compared to PC modified with NPA nanopowder led to increase in the values of temperature onset of weight loss and temperature of final event, especially in case of second event of degradation process.

4. Conclusions

In this paper thermal properties of both silicone–acrylic core–shell nanoparticles – containing nanopowders and epoxy–polyester and polyester powder coatings modified with such nanopowders were investigated. DCS analysis revealed that T_g values of nanopowders depended on the chemical structure of the silicone core and were lower when less crosslinked polysiloxanes constituted the core. Results of DSC analysis showed that T_g values of polyester powder coatings increased when nanopowders were added which indicated the increase in cross-linking density of coatings resulting from **Figure 5b** whereas the T_g values of epoxy–polyester powder coatings decreased with NP addition, especially in the case of nanopowder with higher share of linear polysiloxanes in the core of nanoparticles due to increased mobility of polymer chains.

TGA analysis confirmed that the increase in the share of trifunctional monomers (methyltrimethoxysilane–METM and methacryloyltrimethoxysilane–MATMS) in silicone monomers mixture resulted in the increase in maximum degradation temperature and finally in the increase in thermal stability of nanoparticles. TGA has also proved that thermal stability of powder coatings can be more significantly improved by addition of nanopowders containing more crosslinked polysiloxanes in the core of core-shell nanoparticles.

In general, based on the results of DSC and TGA studies it can be concluded that the chemical structure of the silicone core of core-shell nanoparticles contained in the agglomerated form in nanopowder particles used as impact modifiers for powder coatings influenced Tg values and thermal stability of both the nanopowders and powder coatings modified with such nanopowders.

Acknowledgements

The authors wish to thank The Polish National Centre for Research and Development for providing financial support for the studies described in this paper that were conducted under the project N R08–0004 10.

The authors wish to acknowledge the assistance of Ms H. Kuczynska in preparation of powder coatings, of Ms A. Kowiecznikow in conducting the TGA measurements, of Ms S. Kowalska and Ms A. Lukomska in SEM investigations and of Ms I. Ofat in preparation of nanopowders samples.

References

1. W. D. Hergeth, U.-J. Steinau, H.-J. Bittrich, H. Tanneberger. A DSC study of PVAC–PMMA two-stage emulsion polymers. *Colloid Polymer Sci.* 268 (1990) 991-994.
2. M. Lu, H. Keskkula, D. R. Paul. Thermodynamics of solubilization of functional copolymers in the grafted shell of core-shell impact modifiers: 2. Experimental. *Polymer* 37 (1996) 125-135.
3. L. Gherlone, T. Rossini, V. Stula. Powder coatings and differential scanning calorimetry: The perfect fit. *Prog. Org. Coat.* 34 (1998) 57-63.
4. D. F. Parra, L. P. Mercuri, J. R. Matos, H. F. Brito, R. R. Romano. Thermal behavior of the epoxy and polyester powder coatings using thermogravimetry / differential thermal analysis coupled gas chromatography / mass spectrometry (TG / DTA–GC / MS) technique: Identification of the degradation products. *Thermochim. Acta.* 386 (2002) 143-151.
5. R. Mafi, S. M. Mirabedini, M. M. Attar, S. Moradian . Cure characterization of epoxy and polyester clear powder coatings using differential scanning calorimetry (DSC) and dynamic mechanical thermal analysis (DMTA). *Prog. Org. Coat.* 54 (2005)164-169.
6. Q. Shi, W. Huang, Y. Zhang, Y. Zhang, Y. Xu, G. Guo. Curing of polyester powder coating modified with rutile nano-sized titanium dioxide studied by DSC and real-time FT–IR. *J. Thermal Anal. & Calorim.* 108 (2012) 1243-1249.

7. H. J. Yu, L. Wang, Q. Shi, G. H. Jiang, Z. R. Zhao, X. C. Dong. Study on nano-CaCO₃ modified epoxy powder coatings. *Prog. Org. Coat.* 55 (2006) 296-300.
8. W. Zhou, H. Yang, X. Guo, J. Lu. Thermal degradation behaviors of some branched and linear polysiloxanes. *Polym. Degrad. & Stab.* 91 (2006) 1471-1475.
9. T. C. Chang, C. L. Liao, K. H. Wu, G. P. Wang, Y. S. Chiu. Characterization and degradation of the poly(methyl phenylsiloxane)-poly(methyl methacrylate) graft copolymer. *J. Polymer Sci. A* 36 (1998) 2521-2530.
10. J. D. Jovanovic, M. N. Govedarica, P. R. Dvornic, I. G. Popovic. The thermogravimetric analysis of some polysiloxanes. *Polymer Degrad. & Stab.* 61 (1998) 87-93.
11. J. Kozakiewicz, H. Kuczyńska, T. Jesionowski, R. Nowakowski, J. W. Sobczak, A. Koncka–Foland. Application of nanoparticles of designed structure as modifiers for powder coatings. *Inżynieria Materiałowa* 6 (2007) 863-866.
12. J. Kozakiewicz, J. Skarżyński, W. Domanowski, A. Koncka–Foland, A. Grott. Sposób wytwarzania wodnych dyspersji polimerycznych nanocząstek typu “rdzeń–otoczka”. Polish Patent # 210583 (2011).
13. J. Kozakiewicz. Silicone–acrylic hybrid aqueous dispersions of core–shell particle structure and corresponding silicone–acrylic nanopowders designed for modification of powder coatings and plastics. *Prog. Org. Coat.* – in press.
14. D. Y. Perera. Effect of pigmentation on organic coating characteristics. *Prog. Org. Coat.* 50 (2004) 247-262.
15. N. Chisholm, H. Mahfuz, V. K. Rangari, A. Ashfaq, Sh. Jeelani. Fabrication and mechanical characterization of carbon / SiC–epoxy nanocomposites. *Composite Str.* 67 (2005) 115-124.
16. Y. Liu, W. Liu, D. Yu. Thermal properties and flame retardancy of epoxy resins modified with polysiloxane containing epoxy groups and redistributed poly(2,6-dimethyl-1,4-phenylene) chains. *Iranian Polymer J.* 18 (2009) 445-452.
17. D. Piazza, N. P. Lorandi, Ch. I. Pasqual, L. C. Scienza, A. J. Zattera. Influence of a microcomposite and a nanocomposites on the properties of an epoxy-based powder coating. *Mater. Sci. & Eng. A.* 528 (2011) 6769-6775.

ELECTROMAGNETIC SHIELDING AND MECHANICAL PROPERTIES OF KNITTED FABRIC REINFORCED COMPOSITES

E. Sancak, M. Akalın, M. Yüksek, N. Demirel, İ. Usta, E. İşgören

Marmara University
Istanbul, Turkey
esancak@marmara.edu.tr

Accepted September 19, 2013

1. Introduction

Human needs increasing day by day are the most important and effective factors for developing scientific and technological improvements. Innovative research in different scientific disciplines generates new application fields for textile materials. Smart textiles, which use smart materials, can perceive signals from environment and respond to these stimuli and also adapt themselves to the new conditions. Recently, there have been many studies about smart textiles, and a part of them found commercial applications. Smart materials such as photovoltaic materials, shape memory materials, or phase change materials are used for manufacturing smart textiles (fiber, yarn, fabric, and garment) [1, 2].

Electrically conductive textiles can meet the demands for smart textiles and can be produced by easy and common manufacturing techniques. Electrically conductive textile structures are utilized in a broad area including industry, military, space, and medicine for purposes of defense, protection, health, communication, or automation. Today, conductive yarns, which used to be used for electromagnetic protection and heating in the beginning, are utilized to fulfill different requirements in warning controllers, power transfer, sensors, transmitters, and microcontrollers. In military garments, conductive textile products are utilized to provide various functions such as electrical conductivity and communication. Nowadays, there are very smart or intelligent textiles, which can perceive and then respond to external stimuli such as light, pH, pressure, heat, electricity, and which possess a lot of functional designs [1, 3, 4].

With the rapid growth of the electrical and electronic devices and accessories, which emit electromagnetic energy in the different frequency bands used in the markets, it becomes essential to limit and shield electronic equipment against all sources of interference due to all these electromagnetic energies. There is a growing need for setting limits on the electromagnetic emissions from these devices in order to minimize the possibilities of interfering with radio and wire communications [1]. Among the various solutions offered, textile products and textile-based composite materials have caught the attention of researchers for the versatility and conformability these textile structures provide. Increased awareness of EMI has led to the formulation of new regulations around the globe for the manufacturers of electrical and electronic equipment to comply with the electromagnetic compatibility requirements [5]. Many countries legislating new regulations so that the manufacturers of

electrical and electronic equipment comply with the electromagnetic compatible (EMC) requirement. In USA the Federal Communications Commission (FCC) is entrusted with the responsibility of controlling the interference from and to wire and radio communications [6].

Many devices contribute to such exposure such as cell phones with frequencies of 900 and 1800MHz, microwave ovens of 2450 MHz, radar signal communication systems extending from 1 to 10 000 MHz, and FM / AM radio broadcasts of 30 – 300 MHz and 300 – 3000 KHz, respectively. Cell phone use is particularly widespread [7].

Several methods are available for shielding the electromagnetic radiations such as ionic plating, electroless plating, cathode sputtering, conductive paints, vacuum metallization, zinc paints, zinc flame spraying, zinc arc spraying, and conductive fillers such as copper, stainless steel, and aluminum. The above methods can be categorized under two headings, such as surface treatments and fillers. Surface treatments are often time consuming, labor intensive, and costly. Conductive fillers in the form of particulates, filament, and woven fabrics are increasingly being used for shielding electromagnetic radiations. Attempts by researchers using woven fabric indicate that the shielding effectiveness of the fabrics depends on the conductive filler content. Various conductive fillers are selected based on their electromagnetic shielding effectiveness (EMSE) values at different electromagnetic frequencies [5].

Woven metal cloth along with base textile material is being increasingly utilized in shielding EMI and in anti-electrostatic purposes in various applications such as the defence, electrical, and electronic industries. This is mainly due to their desirable properties in terms of flexibility, good formability, mechanical properties, electrostatic discharge, EMI protection, and radio frequency interference protection [5].

If an electromagnetic wave gets into an organism, it vibrates molecules to give out heat. In the same way, when an electromagnetic wave enters the human body, it will obstruct a cell's regeneration of DNA and RNA. Furthermore, it brings on abnormal chemical activities to produce cancer cells, and increases the possibility of leukemia and other cancers. Injuries by electromagnetic waves to the human body are the top priority of professionals and scholars, and we are most concerned with solving this problem [7, 8].

1.1. Shielding effectiveness

Shielding can be specified in the terms of reduction in magnetic (and electric) field or plane-wave strength caused by shielding (Figure 1).

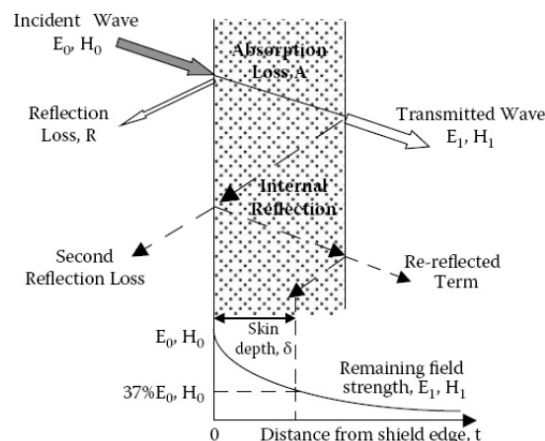


Figure 1. Graphical representation of EMI shielding.

The effectiveness of a shield and its resulting EMI attenuation are based on the frequency, the distance of the shield from the source, the thickness of the shield, and the shield material. Shielding effectiveness (SE) is normally expressed in decibels (dB) as a function of the logarithm of the ratio of the incident and exit electric (E), magnetic (H), or plane-wave field intensities $SE (dB) = 20 \log (E_0 / E_i)$, $SE (dB) = 20 \log (H_0 / H_i)$, and $SE (dB) = 20 \log (F_0 / F_i)$, respectively [9].

2. Experimental

2.1. Materials

Fabrication of core-spun yarns

The yarns were produced with same thicknesses of stainless steel, copper and silver coated copper wires. The same thicknesses of stainless steel, copper and silver coated copper wires covered same amount cotton fibers in same yarn group. Yarns were produced in the ring machine by core-spun method. Core-spun yarns have two components, which are core component and covering component. In this our study, the covering component is cotton fibers and core components are stainless steel, copper and silver coated copper wires. Properties of materials are given in **Tables 1** and **2**.

Table 1. Characteristic of metal filaments.

Metal fibers	Stainles steel (SS)	Copper (Cu)	Silver coated Copper (Ag)
Linear density, μm	50	50	50
Density, kg / dm^3	9.0	8.9	7.9





Table 2. Characteristic of core-spun yarns.

Yarn counts	Structure
Ne 9/1	Cotton / 0.050 mm SS
Ne 9/1	Cotton / 0.050 mm Cu
Ne 9/1	Cotton / 0.050 mm Ag

Fabrication of space knitting fabrics

Produced yarns were formed into weft-knitted fabrics using 7G automatic flat knitting machine whose model is Stoll CMS 420. Kind of knit structure is namely called spacer knitting fabric. Four different kinds of spacer fabrics were determined for producing knitting fabrics. Properties of knitting fabrics are given in **Table 3**.

Table 3. Characteristic of spacer knitted fabrics.

Fabric code	Structure	Course density, courses / cm	Wale density, wale / cm	Thickness, mm
Sample – A		4	5	4.2
Sample – B		4	5	4
Sample – C		4	5	3.4
Sample – D		4	5	3

Manufacturing of composite structures

Matrix resin which is thermoset polyester (Polipol 351) manufactured by Poliya (TURKEY) were used to fabricate composite structures. Thermoset polyester resin was chosen to fabricate composite because of its low price.

Table 4. Properties of reinforced composites.

Composites Codes	Structure of fabric	Fabric weight, g / m ²	Total weight, g / m ²	Thickness, mm
A-Cu	Surface yarn = Cotton The joining yarn = Copper	654	1683	2.5
A-SS	Surface yarn = Cotton The joining yarn = Stainless steel	695	1975	2.5
A-Ag	Surface yarn = Cotton The joining yarn = Silver coated copper	667	1858	2.5
B-Cu	Surface yarn = Cotton The joining yarn = Copper	582	1376	2.3
B-SS	Surface yarn = Cotton The joining yarn = Stainless steel	610	1598	2.3
B-Ag	Surface yarn = Cotton The joining yarn = Silver coated copper	591	1464	2.3
C-Cu	Surface yarn = Cotton The joining yarn = Copper	552	1426	2.1
C-SS	Surface yarn = Cotton The joining yarn = Stainless steel	589	1727	2.1
C-Ag	Surface yarn = Cotton The joining yarn = Silver coated copper	565	1660	2.1
D-Cu	Surface yarn = Cotton The joining yarn = Copper	544	1397	2
D-SS	Surface yarn = Cotton The joining yarn = Stainless steel	599	1627	2
D-Ag	Surface yarn = Cotton The joining yarn = Silver coated copper	556	1455	2

Thermosetting polyester was applied as a resin. There are several major manufacturing methods in fiber-reinforced polymer industry. Thermosetting polyester laminates were manufactured via vacuum infusion. In order to remove air bubbles created at the initial resin-hardener mixing stage, the mixture was subjected to vacuum (0.91 bars) for 10 – 15 min. Properties of reinforced composites are given in **Table 4**.

2.2. Methods

EM shielding effectiveness (EMSE) measurement

A coaxial transmission line method specified in ASTM D4935–10 was used to test the EMSE of the conductive textile composites (**Tables 5** and **6**). The specimen is prepared with the standard test size of various thicknesses as shown in **Figure 2**. The specimen dimension is 133 mm in diameter of the outer ring. It's needed to prepared two specimens for test, one for reference and another for load testing. Various researchers have described the detailed set-up and testing procedure using a plane-wave electromagnetic field in the frequency range of 15 MHz – 3 GHz. The spectrum analyzer and shielding effectiveness test fixture (Electro-Metrics, Inc., EM-2107A) were used to measure the EMSE (**Figure 3**), which is measured in decibels (dB) in this investigation [10, 11].

Table 5. Professional use.

Grade	5 Excellent	4 Very good	3 Good	2 Moderate	1 Fair
Percentage of electromagnetic shielding	ES > 99.99999 %	99.9999 % ≥ ES > 99.999 %	99.999 % ≥ ES > 99.99 %	99.99 % ≥ ES > 99.9 %	99.9 % ≥ ES > 99.0 %
Shielding Effectiveness	SE ≥ 60 dB	60 dB ≥ SE > 50 dB	50 dB ≥ SE > 40 dB	40 dB ≥ SE > 30dB	30 dB ≥ SE > 20 dB

SE: shielding effectiveness (dB);
ES: percentage of electromagnetic shielding (%) [12].

Table 5. General use.

Grade	5 Excellent	4 Very good	3 good	2 Moderate	1 Fair
Percentage of electromagnetic shielding	ES > 99.9 %	99.9 % ≥ ES > 99.0 %	99.0 % ≥ ES > 90 %	90 % ≥ ES > 80 %	80 % ≥ ES > 70 %
Shielding effectiveness	SE ≥ 30 dB	30 dB ≥ SE > 20 dB	20 dB ≥ SE > 10 dB	10 dB ≥ SE > 7 dB	7 dB ≥ SE > 5 dB

SE: shielding effectiveness (dB);
ES: percentage of electromagnetic shielding (%) [12].

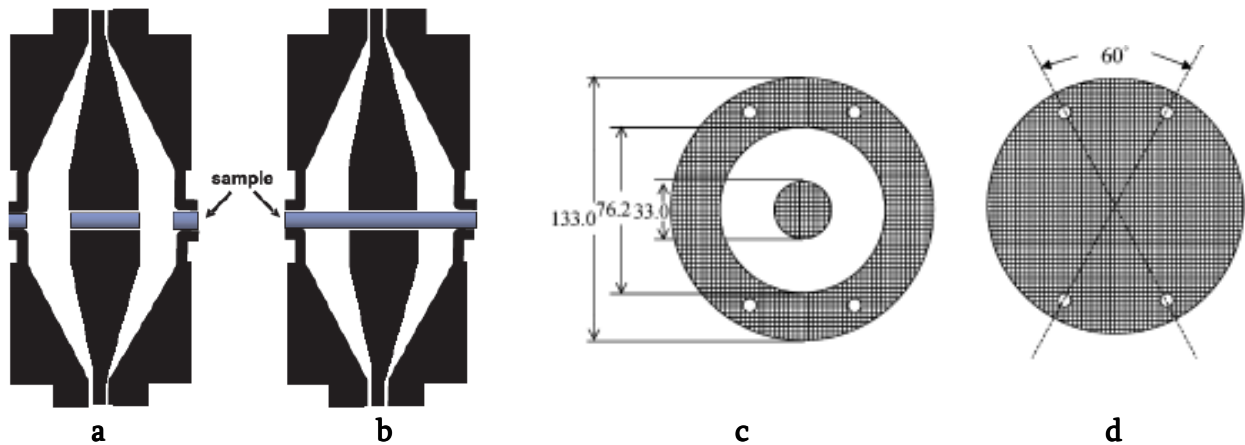


Figure 2. A cross-section of the shielding effectiveness test fixture: (a) reference sample in the jig, (b) load sample in the jig, (c) reference sample, and (d) load sample.

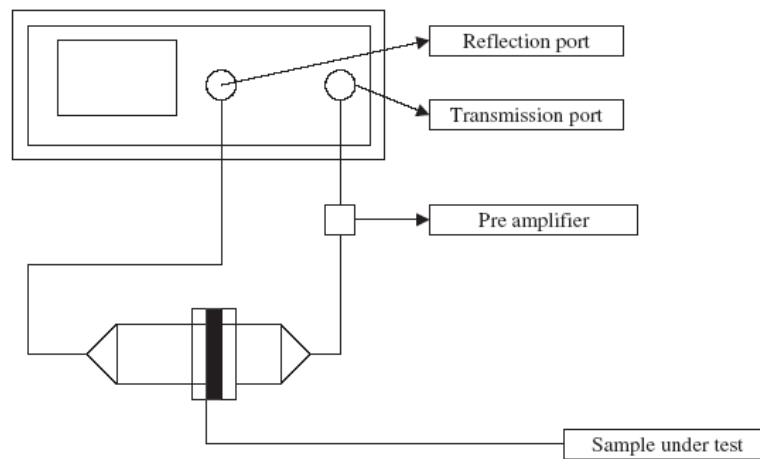


Figure 3.A Typical coaxial transmitter for EMSE testing.

Mechanical property characterization

Tensile test technique, ASTM D3039/ 3039M-07 was used to determine the tensile strength of the composite laminates. The specimens were tested using Devotrans Universal test machine at a crosshead speed of 10 mm/min. At least five specimens for each composition were tested. Impact strength was checked by means of CHEAST charpy impact resistance based on ISO 179-1 standard[13, 14] [Bozkurt E., et al., Wu Du G. and Ko F.].

3. Results and discussions

3.1. Electromagnetic shielding effectiveness of knitted fabric composites

The knitting fabric reinforced composites were scanned with electromagnetic frequencies ranging from 15 to 3000 MHz and the EMSE values were recorded. The values obtained using measurement techniques in above have been graphically investigated in below. In these investigations, EMSE of the composite structures have been considered in terms of kind of conductive wires and the knitting fabric patterns.

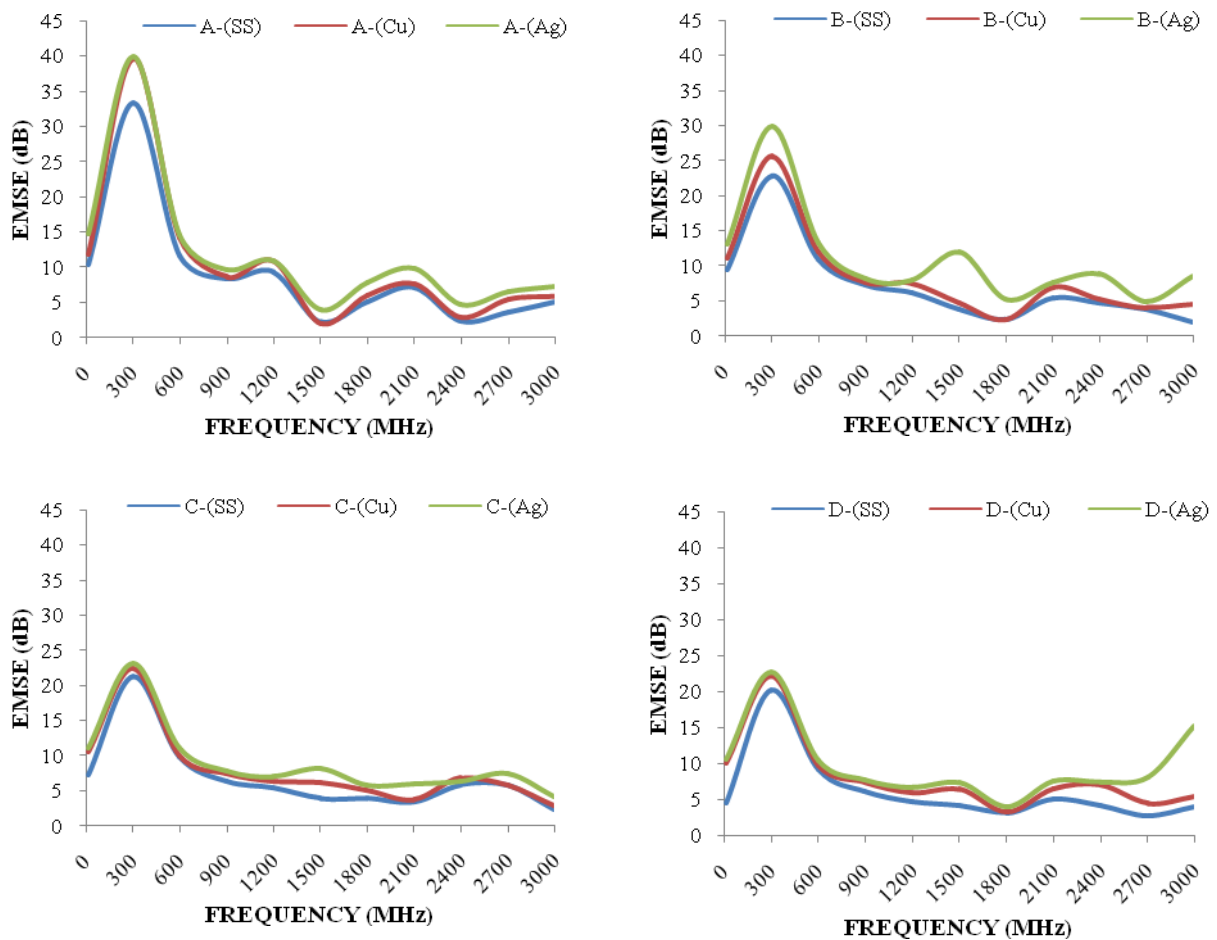


Figure 4. The effect of kind of conductive materials on electromagnetic shielding effectiveness (EMSE).

The four images in **Figure 4** show the variation of EMSE of all knitted fabric composites with the incident frequency in the range from 15 to 3000 MHz. The EMSE of the composites increased until 300 MHz and decreased between 300 and 3000 MHz. Among all the composites, the A-(Ag) composite displayed the highest EMSE whereas the D-(SS) composite displayed lowest EMSE. All composites exhibit the best Electromagnetic Shielding Effectiveness (EMSE) between 0 and 450 MHz. Although electromagnetic shielding effectiveness (EMSE) is low between 600 and 1800 MHz, it becomes stable throughout this frequency range. It is reasonably decreasing after 1800 MHz. Electromagnetic shielding effectiveness is not remarkable after 2400 MHz. The composite reinforced with knitted fabric, which includes silver coated copper wire shows higher electromagnetic shielding effectiveness than the others in for four kind of knitted fabric patterns. This can be explained due to conductivity properties of conductive material. By controlling the kind of conductive materials, the EMSE of knitted fabric reinforced composites can be adjusted.

The three images in Figure 5 show the variation of EMSE of all knitted fabric composites with the incident frequency in the range from 15 to 3000 MHz. The EMSE of the composites increased until 300 MHz and decreased between 300 and 3000 MHz. Among all the composites, the A-(Ag) composite displayed the highest EMSE whereas the D-(SS) composite displayed lowest EMSE.

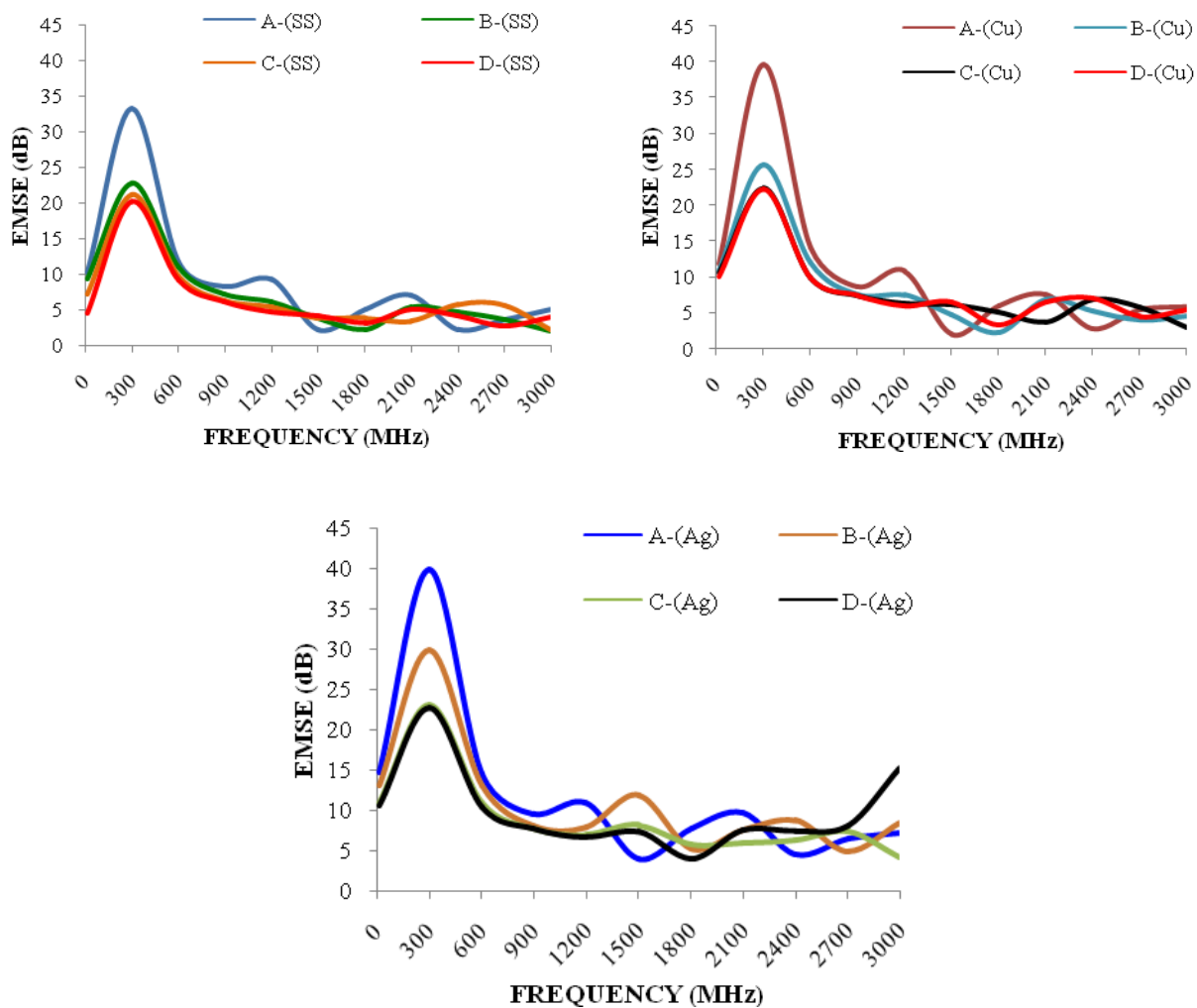


Figure 5. The effect of kind of knitting fabric pattern on electromagnetic shielding effectiveness (EMSE).

All composites exhibit the best electromagnetic shielding effectiveness (EMSE) between 0 and 450 MHz. Although electromagnetic shielding effectiveness (EMSE) is low between 600 and 1800 MHz, it becomes stable throughout this frequency range. It is reasonably decreasing after 1800 MHz. Electromagnetic shielding effectiveness is not remarkable after 2400 MHz.

When the effect of kind of knitting fabric pattern on electromagnetic shielding effectiveness (EMSE) of composite structures examine, among the four knitting patterns, the pattern–A displayed the highest EMSE whereas the pattern–D displayed lowest EMSE. This can be explained due to knitting patterns. By controlling the kind of knitting patters, the EMSE of knitted fabric reinforced composites can be adjusted.

3.2. Mechanical properties of composite structures

Mechanical tests were conducted for each sample in one direction and experiments were repeated as specified in the standards. Tensile strength, three-point flexural and impact strength tests were applied to the composite materials. Results of the mechanical tests were compared in the graphics.

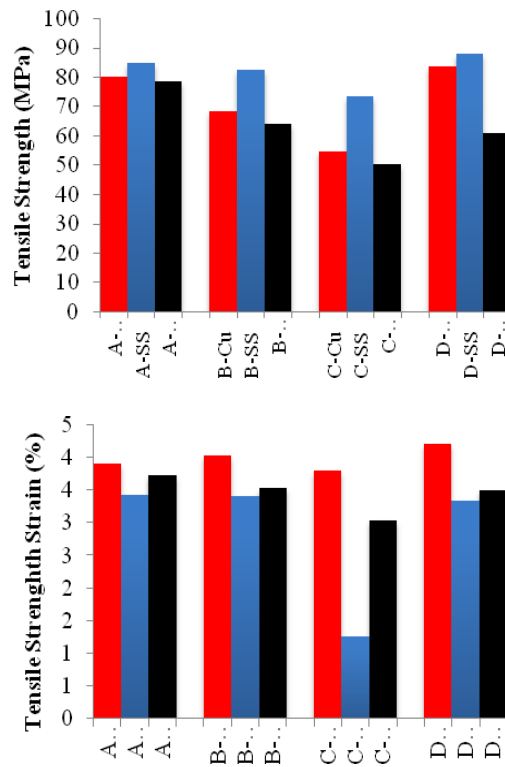


Figure 6. Tensile strength (MPa) and strain (%) of knitted fabric reinforced composites.

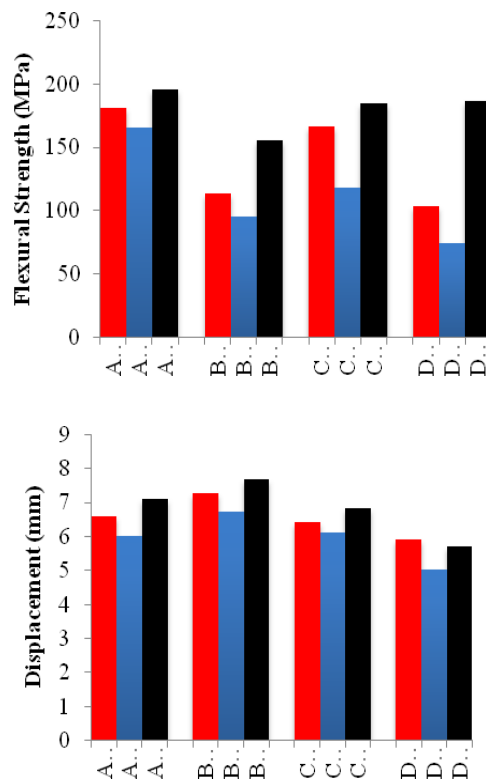


Figure 7. Three point flexural strength (MPa) and displacement (mm) of knitted fabric reinforced composites.

Tensile strength and strain of composites were evaluated in the **Figure 6**. When graphics are examined, it is observed that, when considering the type of conductive materials, the knitted fabric reinforced composite (D–SS) displays higher tensile strength than the others and the knitted fabric reinforced composite (D–Cu) displays higher tensile strength strain than the others as well. Among all the composites, when comparing the kind of knitting pattern, the knitted fabric reinforced composite that is composed of sample–A displays higher tensile strength and tensile strength strain than the others.

Three point flexural strength and displacements of composites were evaluated in the **Figure 7**. When graphics are examined, it is observed that, when considering the type of conductive materials, the knitted fabric reinforced composite (A–Ag) displays Three point flexural strength than the others and the knitted fabric reinforced composite (B–Ag) displays Three point flexural strength displacement than the others as well. Among all the composites, when comparing the kind of knitting pattern, the knitted fabric reinforced composite that is composed of sample–A displays higher three point flexural strength and sample–B higher three point flexural strength displacement than the others.

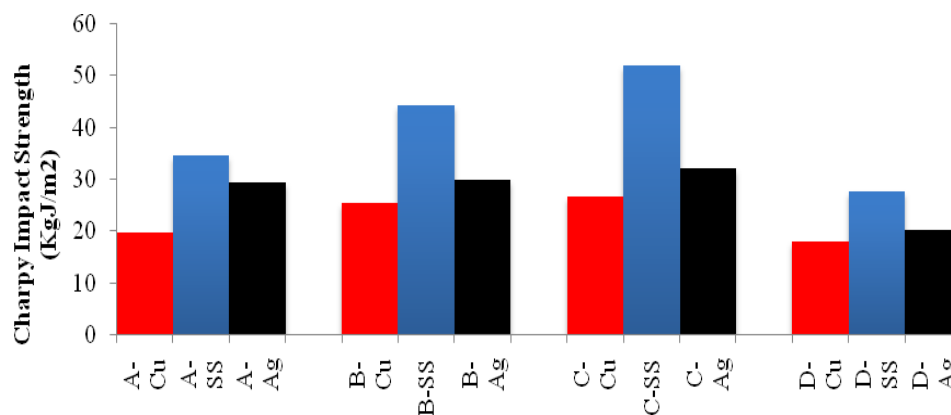


Figure 8. Charpy impact strength (kg J / m²) of knitted fabric reinforced composites.

Charpy impact strength of composites was evaluated in the **Figure 8**. When graphic is examined, it is observed that, when considering the type of conductive materials, the knitted fabric reinforced composite (C–SS) displays charpy impact strength than the others. Among all the composites, when comparing the kind of knitting pattern, the knitted fabric reinforced composite that is composed of sample–C displays higher charpy impact strength than the others.

4. Conclusions

In this study, stainless steel, copper and silver coated copper wires are used. Stainless steel wire is more widely used because it is cheap. Conductive materials are necessary for electromagnetic shielding. At the same time, conductive materials improve the mechanical properties of composites. EMSE properties of knitted fabric reinforced composites that are produced with conductive wires are measured. Based on the present results, it is concluded that

different knitting fabric pattern and conductive materials in composite have different effects on its EMSE characteristics. From the experiments, it can be clearly seen that the best electromagnetic shielding effectiveness become between 0 and 600 MHz. These composites protect about 90.0 – 99.9 % against electromagnetic wave in this frequency range. Protection is about 80 % in the other frequency range. The knitted fabric reinforced composite (C–SS) displays the best Charpy impact strength. The knitted fabric reinforced composite (A–Ag) displays the best three point flexural strength. The knitted fabric reinforced composite (D–SS) displays the best tensile strength. One of the most important factors affecting the mechanical properties of the composites is conductive wire properties and the other important factor is the knitting fabric types.

Acknowledgements

This work was supported by SANKO HOLDİNG A.Ş. We thank to their manager and engineers of the Department of Research for their help with the experiments. This work was supported by the Scientific Research Project Unit (BAPKO) of the Marmara University (Project number FEN–D–100713–0338).

References

1. A. Bedeloglu, N. Sunter, Y. Bozkurt. Manufacturing and properties of yarns containing metal wires. *Mater. & Manuf. Proc.*, 2011, 26, 11, 1378-1382.
2. F. Salaün, E. Devaux, S. Bourbigot, P. Rumeau. Development of phase change materials in clothing. Part I: Formulation of microencapsulated phase change. *Textile Res. J.*, 2010, 80, 3, 195-205.
3. R. Perumalraj, B. S. Dasaradan. Electromagnetic shielding effectiveness of copper core yarn knitted fabrics. *Ind. J. Fibre & Textile Res.*, 2009, 34, 2, 149-154.
4. J. F. Gu, S. Gorgutsa, M. Skorobogatiy. Soft capacitor fibers using conductive polymers for electronic textiles. *Smart Mater. Str.*, 2010, 19, 115006, 1-13.
5. K. B. Cheng, T. W. Cheng, R. N. Nadaraj, V. R. Giri Dev, R. Neelakandan. Electromagnetic shielding effectiveness of the twill copper woven fabrics. *J. Reinforced Plastics & Composites*, 2006, 25, 7, 699-709.
6. K. B. Cheng. Production and electromagnetic shielding effectiveness of the knitted stainless steel / polyester fabrics. *J. Textile Eng.*, 2000, 46, 2, 42-52.
7. Ch.-I. Su, J.-Ts. Chern. Effect of stainless steel-containing fabrics on electromagnetic shielding effectiveness. *Textile Res. J.*, 2010, 74, 51, 51-54.
8. S. Şeker, O. Çerezci. *Çevremizdeki Radyasyon ve Korunma Yöntemleri*. 1997, İstanbul: Boğaziçi Üniversitesi Yayınları, 44-45.
9. X. C. Tong. *Advanced materials and design for electromagnetic interference shielding*. 2009, New York: CRC Press – Taylor & Francis Group, 44-45.
10. H. C. Chen, K. C. Lee, J. H. Lin, M. Koch. Comparison of electromagnetic shielding effectiveness properties of diverse conductive textiles via various measurement techniques. *J. Mater. & Proc. Technol.*, 2007, 192-193, 0, 549-554.

11. D4935–10: Standard Test Method for Measuring the Electromagnetic Shielding Effectiveness of Planar Materials. 2010, ASTM.
12. FTTS–FA–003: Test Method of Specified Requirements of Electromagnetic Shielding Textiles. 2003, 1-4.
13. D. G. Wu, F. Ko. Analysis of multiaxial warp-knit performs for composite reinforcement. *Composites Sci. & Technol.*, 1996, 56, 3, 253-260.
14. E. Bozkurt, E. Kaya, M. Tanoğlu. Mechanical and thermal behavior of non-crimp glass fiber reinforced layered clay / epoxy nanocomposites. *Composites Sci. & Technol.*, 2007, 67, 15-16, 3394-3403.

**RESEARCH ON WATER-REPELLANT NANOFIBER
SPUN BY ELECTRO BUBBLE SPINNING METHOD**

M. Iwamoto¹, H. Ino¹, T. Kimura¹, Y. Kishimoto²

¹Kyoto Institute of Technology
Kyoto, Japan
m2651003@edu.kit.ac.jp
²Hirose Paper Mfg Co., Ltd
Kochi, Japan

Accepted September 19, 2013

1. Introduction

In recent years, board and sheet material that have high water repellency and permeability attract much attention. These materials are in demand in various fields, such as moisture permeable and waterproof sheet. However, such material is not used widely in commercialat present. It is because the material that has both high water repellency and high permeability is difficult to produce. There is only insufficient one or the production cost is very high even if producible. Especially moisture permeable and waterproof sheet is used in the interior part of construction materials, and it is playing an important role which prevents rain water soaking from the outer wall and holding the permeability which wicks away moisture from indoors, in order to maintain the interiorof room at comfortable environment. Although moisture permeable and water proof sheet is tried to manufacture from the nonwoven fabric, in many cases the water repellency is insufficient. In this research, the development of sheet material that has both high water repellency and high permeability was attempted paying attention to the fine structure characteristic of nanofiber nonwoven fabric. In the nanofiber nonwoven fabric, there are a lot of interstices between nanofibers. Moreover, since the slip flow effect occurs from nano size structure of fiber, higher permeability material may be obtained, in comparison with a conventional nonwoven fabric. In addition, it is known that the contact angle of waterdrop on a smooth surface will not exceed 130 degrees according to the current theory. However, it is known that bulk contact angle can be improved by building a fine structure on the material surface. Therefore, the water-repellent material was tried to obtain by using the fine structure of a nanofiber nonwoven fabric in this study. Furthermore, it the aim of controlling water repellency of material, building more fine structure on nonwoven fabric surface by adhering fine particles on the nanofiber nonwoven was tried. As the materials of nanofiber, polyvinyl alcohol (PVA), which has solubility against hot water, easiness for handling low cost and environmentally friendliness, was used. If fine particles were adhered to nanofiber nonwoven fabric afterwards, it is probable that the fine particles drop out or binder material interfere the formation of fine structure. Therefore, direct electrospinning from PVA solution containing fine particles was performed. However in that case, usual nozzle based electrospinning method is not so suitable because of the possibility of nozzle sticking by the added fine particles. So, in this research, the electrospinning method from bubbling solution

(electro bubble spinning method, described later in detail) was adopted. By using the electro bubble spinning method, since bubbles always agitate the polymer solution the separation of solid-liquid heterogeneous system can be suppressed. In consideration of affinity with nanofiber, same PVA was also selected as the materials of fine particles. In order to form fine particle, emulsion method was applied. Moreover, since PVA is highly hydrophilic, nanofiber nonwoven fabric cannot be served as a water-repellent material without modification. So, the nanofiber surface was converted to water repellent by treating with a fluorocarbon-based reagent. Since the reagent reacts only with the surface of nanofibers, it is more preferable at the point of production cost compared with the material made of entire fluororesin material.

2. Materials

2.1. Material for nanofiber

As a source material of nanofiber, PVA polymer powder (JF-17, Japan Vam & Poval Co, Ltd., polymerization degree = 1700, saponification degree = 98.0 ~ 99.0 %) was used.

2.2. Materials for fine particle

As a source material of fine particle, the PVA polymer JF-17, which is the same with the source of nanofiber, was used. As a medium of emulsion, 2,2,4-trimethyl pentane (Nacalai Tesque Co, Ltd.) and distilled water were used. As a surfactant, AOT (1,4-bis(2-ethylhexyl) sodium sulfosuccinate) (Nacalai Tesque Co., Ltd.) was used.

2.3. Fluorocarbon-based water repellent reagent

As a fluorocarbon based water repellent reagent, nonafluorohexyltriethoxysilane (Gelest Inc.) was used.

3. Experiment

3.1. Preparation of PVA solution

PVA powder was weighted and was put into distilled water so that the concentration of PVA solution becomes to be 8 wt. %, then it was dissolved on heating for 24 h. After that, PVA solution was cooled to be 25 °C and it was used for fine particle formation. By the similar manner, 9 wt. % PVA aqueous solution was obtained for the source of electrospinning.

3.2. Preparation of fine particle

Fine particle was obtained from W/O emulsion of PVA. At first, AOT was dissolved in 2,2,4-trimethyl pentane with the concentration of 50 100 and 150 mmol / l and then 8 wt. % PVA solution was added with the volume ratio of 8 vol. %. Then the mixture was stirred with homogenizer (ULTRA-TURRAX T-25, IKA Japan Co, Ltd.) for 10 min at the revolving speed of 10 000, 15 000, 20 000 and 25 000 rpm. For the sample of observation, a drop of obtained

emulsion was placed on a glass plate and dried. Then, the shape and average diameter of PVA particle were observed with the microscope (VHX-100, Keyence Co.). Moreover, the obtained emulsion was heated and concentrated by a factor of ten.

3.3. Electrospinning of nanofiber

As the spinning method of nanofiber, electro bubble spinning method was selected. The pattern diagram of electro bubble spinning method used in this study is shown in **Figure 1**. Firstly, the PVA emulsion was mixed with 9 wt. % PVA solution with the mixing volume ratio of 5 vol. %. Then the polymer mixture was poured into stainless container that has porous board on the bottom. In the next step, the bubbles were generated and burst by passing compressed air from the bottom of container. 10 kV voltage was applied between electrode plate and container, so the polymer jets are blasted off from the burst bubble on the surface of solution. Finally polymer jet diverged repeatedly to make a number of nanofibers, and the nanofibers adhered directly to the nonwoven fabrics attached to the electrode plate. By generating these bubbles from whole surface of solution, a lot of nanofibers were simultaneously electrospun.

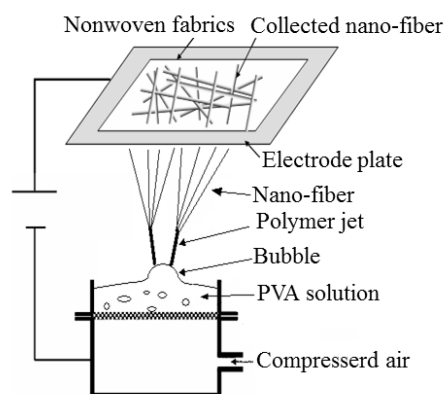


Figure 1. Diagram of electro bubble spinning method.

The electrode distance was varied from 200 to 350 mm. And the surface of PVA nanofiber nonwoven fabric was observed with the scanning electron microscope (S-3000, Hitachi Ltd.), and the average particle size was calculated.

3.4. Water repellent property test

The nanofiber nonwoven fabric was dipped in *n*-hexane with 3[wt%] of nonafluorohexyltriethoxysilane for 24 h. After that, the nonwoven fabric was removed from the solution and dried in an oven at 100 °C for 1 h. Thus, water repellent nonwoven fabric was obtained.

The contact angle of sample was measured according to Japanese Industrial standard (JIS) R 3257. A drop of distilled water was placed on the surface of the nanofiber nonwoven fabric and the waterdrop was observed with a microscope (VHX-100, Keyence Co.). The contact angle was calculated by measuring the height and contact radius of waterdrop. The contact angle was measured for five points as each sample. In addition, in order to keep the waterdrop spherical, the volume of waterdrop was set to be below 4 ml.

4. Result and consideration

4.1. The average particle size of PVA contained in emulsion

Figure 2 shows the relationship between the AOT concentration contained in emulsion and the average diameter of PVA particles. When AOT concentration increases, the average particle size becomes small. If the concentration of AOT increases, it can cover larger area of interface between water and oil. Therefore, the average size of PVA particles can be smaller.

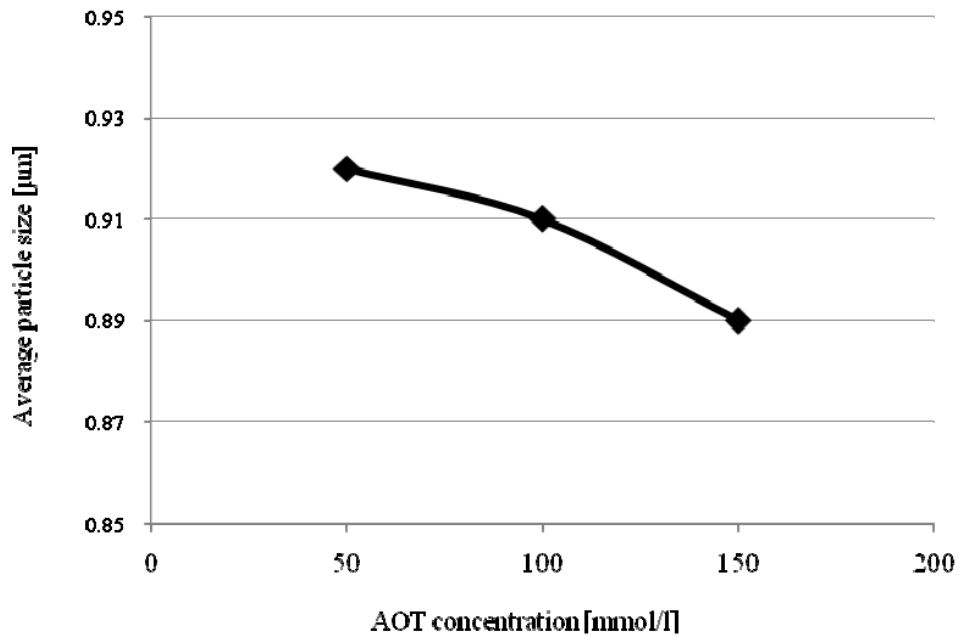


Figure 2. Relationship between AOT concentration and average particle.

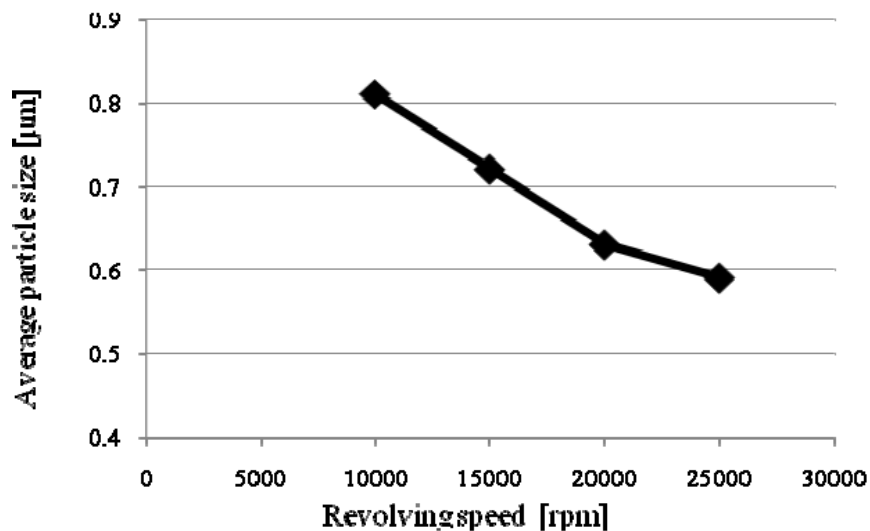


Figure 3. Relationship between revolving speed and average particle size.

Figure 3 shows the relationship between the revolving speed and the average particle size of PVA. As is shown in this figure, when the revolving speed becomes larger, the average particle size of PVA becomes smaller.

4.2. The average particle size contained in the nanofiber nonwoven fabric

Figure 4 is an SEM image of nanofiber nonwoven fabric spun with PVA particles. As is shown in figure, there are PVA particles in nonwoven. **Figure 5** shows the relationship between the electrode distance and the average particle size contained in the nanofiber nonwoven fabric after electro bubble spinning. This figure shows that, when the electrode distance becomes longer, the average particle size in nonwoven becomes smaller. As this reason, when electrode distance becomes longer at constant voltage, the intensity of electric field becomes weaker and therefore large and heavy particles seem to be difficult to pass through the electric field against the force of gravity.

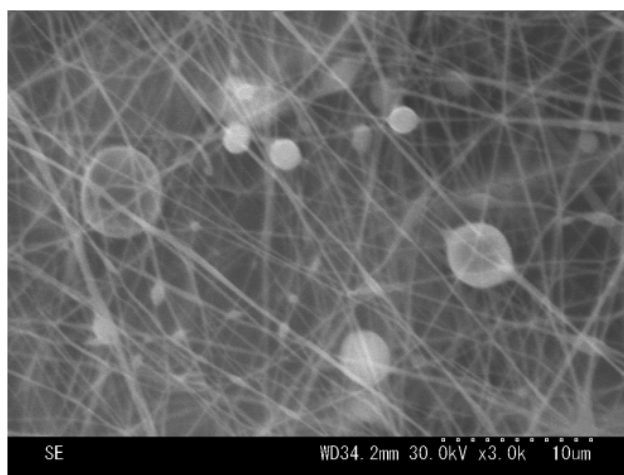


Figure 4. Nanofiber nonwoven fabric surface PVA particles adhered.

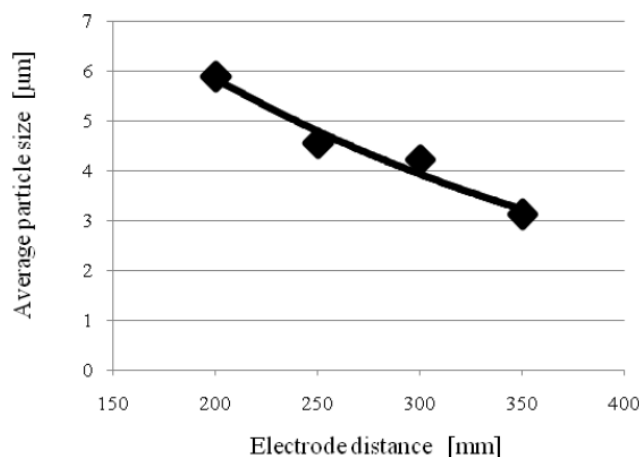


Figure 5. Relationship between electrode distance and average particle size in nonwoven.

4.3. Water repellency

Figure 6 is a photograph of waterdrop on the nanofiber nonwoven fabric containing PVA particles. Contact angle θ was calculated from the equation $\theta = 2 \arctan(h / r)$, where h is the height of waterdrop and r is contact radius. **Figure 7** shows the relationship between the average particle size of PVA contained in the nonwoven fabric and the contact angle. The point on vertical axis indicates the contact angle of the nanofiber nonwoven fabric without PVA

particle. From this figure, it can be concluded that the contact angle of the nonwoven fabrics with PVA particles are larger than the one without particles. Moreover, it is clarified that when the average particle size becomes smaller, the contact angle becomes larger and water repellency improves.

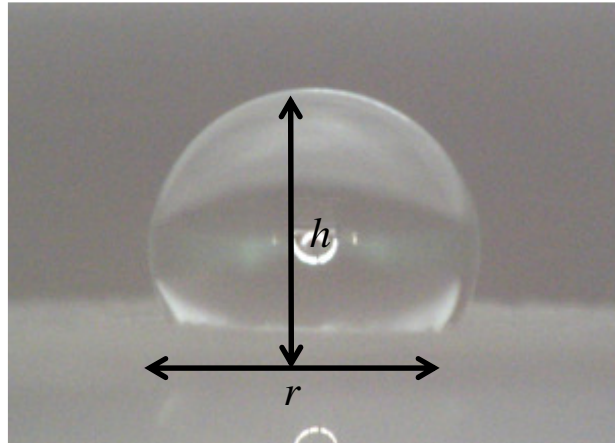


Figure 6. Microscope image of waterdrop on nonwoven fabric.

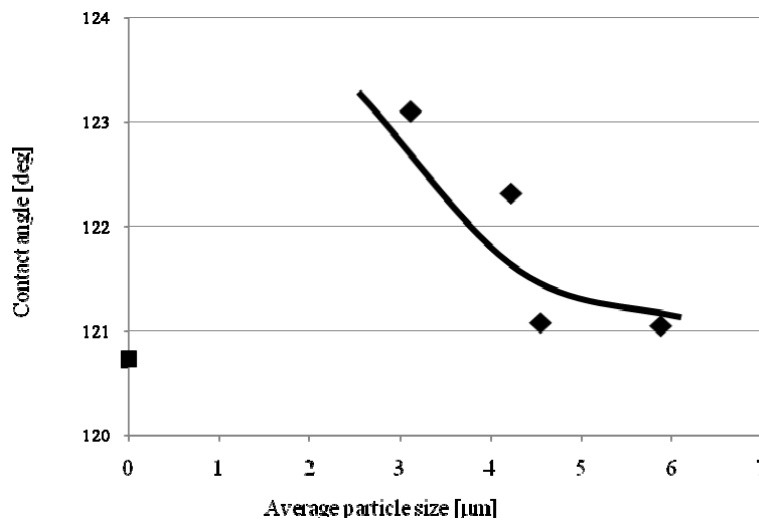


Figure 7. Relationship between a contact angle and an average particle size.

5. Conclusions

In the aim of obtaining water repellent material, PVA fine particles were prepared by emulsion method and the PVA nanofiber nonwoven fabric containing PVA fine particles was spun by electro bubble spinning method. As the result, the following things were clarified.

For the fine particle preparation by emulsion method, when the concentration of AOT increases and the revolving speed increases, the diameter of particle decreases.

When the electrode distance increases the average particle size in nanofiber nonwoven fabric decreases. The contact angle of water on the nonwoven improves when fine particles exist in the nanofiber nonwoven. In addition, the contact angle increases when the average diameter of fine particles decreases.

**HETEROGENEOUS NANO CERIUM CHROMATE AS A NEW
AND SELECTIVE OXIDANT FOR SELECTIVE CONVERSION OF
ALCOHOLS TO CORRESPONDING CARBONYL COMPOUNDS**

S. Oftadehgan, N. Goudarzian

Islamic Azad University
Shiraz, Iran
Somayeh.oftadegan@gmail.com

Accepted September 19, 2013

Introduction

In recent years, the efficient use of non-toxic and more selective supported solid acidic catalyst has received more attention in different areas of organic synthesis because of their environmentally compatibility, reusability, high selectivity, simple operation and ease of isolation of the products [1 – 5]. The study of polymer supported catalyst is motivated by the major advantages of the physical separation of the supported catalyst from the substrates and products, thereby allowing the recycling of expensive or toxic catalyst and thus releases less waste material to the environment [4 – 6]. The potential use of polymer supported catalysts as heterogeneous and recyclable catalysts in organic transformation make reaction methods more convenient, economic and environmentally benign. The reactions can be performed under mild conditions and product purification is simple due to easy separation of insoluble polymer support from the reaction medium.

Many reactions can be carried out cleanly, rapidly and in high yields. In the past two decades, several papers have been published on the preparation and applications of different kinds of polymeric reagents, such as polymeric condensing reagents [6], polymeric redox reagents [7] and polymeric alkylating reagents [8]. The greatest advantage in using a polymer-supported reagent in an organic reaction, compared with the monomeric form, is the simplification of the reaction work-up, that is product separation and isolation. In the case of an insoluble polymeric reagent, filtration and repeated washings with suitable solvents can be used at the end of the reaction to isolate the pure product. Supported reagents may also be used more conveniently in excess to drive reactions to completion, without incurring a penalty in the work-up procedure. Ever-increasing environmental concerns have resulted in much attention being recently directed toward the development of new protocols for the oxidation of alcohols using transition-metal dichromate catalysts [9]. Among them, cerium based catalyst show very interesting and promising catalytic activity, and different types of cerium-based homogenous and heterogeneous catalysts [10, 11] in the form of metal complexes or nanoparticles [12] have been developed for this purpose. Accordingly, the application of cerium based catalysts has also been well documented for the oxidation reactions [13, 14]. Although, significant progress has been achieved in improving catalytic activity, selectivity and substrate scope, there is still the

major problem that cerium agglomeration and the formation of cerium black can cause catalyst deactivation in many cases.

Although a large number of reagents are known in the literature for such transformation of alcohol to aldehyde, there is still need either to improve the existing oxidation method or to introduce new reagents to obtain better selectivity under milder conditions [15, 16].

In synthetic organic chemistry, oxidation under phase transfer catalysis finds wide application, but using polymer supported oxidizing agents for kinetic and mechanistic studies are limited [15 – 17]. The polymer supported oxidizing agent can be used and be reused without loss of capacity, and also very easy work up and safety is the major factors of interest for the present study. By use of polymer supported oxidizing agent the side reaction decreases and the oxidation process stops at the product aldehyde step only.

In continuing of our studies on the development of application of polymer supported reagents in organic synthesis [15, 16, 18, 19], herein we report synthesis and application of polyethyleneimine supported nano cerium chromate, [PEI-NCeCrO₄⁻] as a green, clean, and stable polymer supported cerium chromate for conversion of primary and secondary benzylic or allylic alcohols to their aldehydes and ketones under aprotic, and heterogeneous conditions.

By using this polymeric oxidizing reagent, many problems associated with metal chromate oxidizing agent, such as the necessity of having an acidic solution, and instability of metal chromate [20] has been overcome.

For chemical and mechanical stability, highly branched polyethyleneimine is used nowadays and also because the polymer swells strongly in several solvents. The reactions carried out using such highly branched polymer result in high yield transformation. Considering all these advantages the title reaction, in which polymer supported nano cerium chromate is used as an oxidant, was investigated and the results are given below.

Experimental

Chemicals

All chemical substrates were either prepared in our laboratory or were purchased from Fluka, Sigma Aldrich chemical Co., Merck chemical Co. Progress of the reaction was followed by TLC using silica gel Poly Gram SIL G/UV 254 plates or gas chromatography (GC). All products were characterized by comparison of their FT-IR, ¹H-NMR spectra, TLC, and physical data with pure compounds.

FT-IR spectra were run on a Perkin Elmer RXI spectrophotometer. ¹H-NMR spectra were recorded on a Bruker Avance DPX instrument (250 MHz). The Ce analyses and the leaching test were carried out by ICP-OES analyzer (Warian, Vista – Pro), TEM analyses were performed on an EM 912 Omega electron microscope with an acceleration voltage of 120 kV instrument. Scanning electron micrographs were obtained by SEM, Hitachi S-4700 microscope operated at an acceleration voltage of 10 kV. Melting points were determined in open capillaries with an Electro thermal 9100 melting point apparatus and were not corrected all yields refer to the isolated yield unless reported as GC yield.

Preparation of polyethyleneimine supported nanoceriumtrichloride

Polyethyleneimine (PEI) (1 g, 23.2 mmol) in dioxane was added drop wise to nano CeCl₃ (1 g, 4.05 mmol) solution in 20 ml methanol. Precipitation occurred immediately. The mixture

was stirred and kept warm for 30 min and then stored in refrigerator for 24 h. The precipitate was filtered and washed several times with methanol, then dried in vacuum overnight.

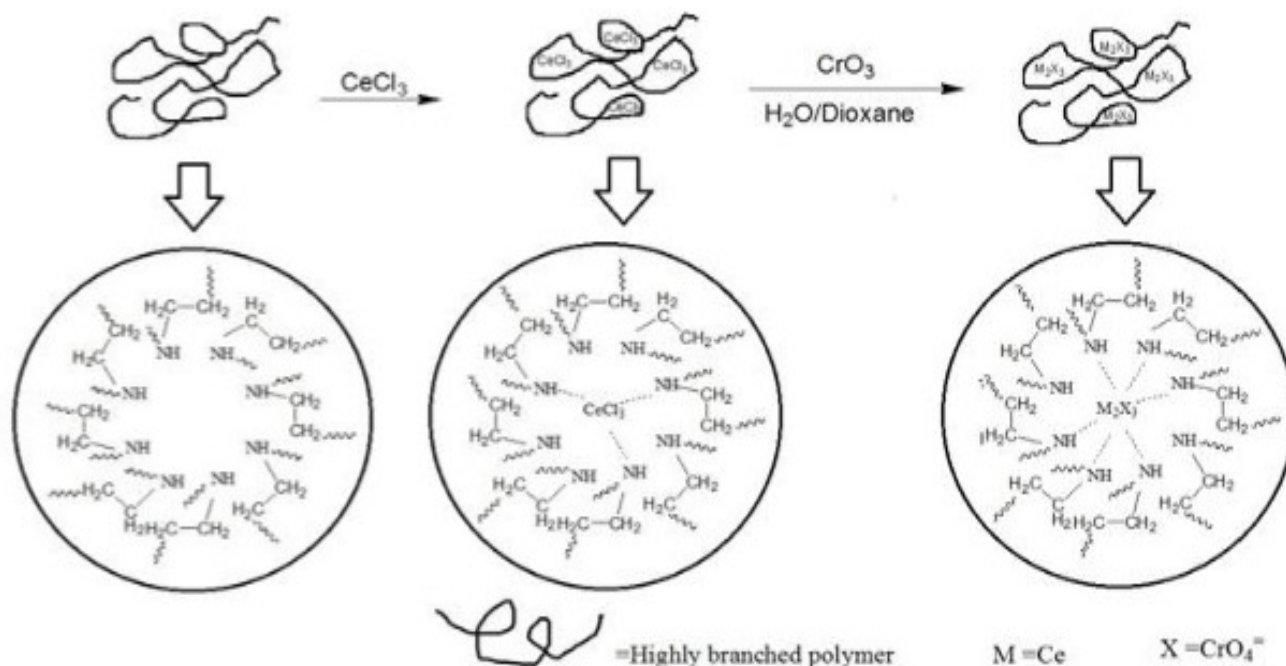
The ratio of polyethyleneimine units to the metal ion as determined, by gravimetric and atomic absorption technique was about 6 : 1, m.p.: 200 – 205 °C (decomposed).

FT-IR (KBr) ν (cm^{-1}): 3400 – 3500 (N-H), 1570 – 1620 (C-H ben.), 1354 (C-N).

Preparation of polyethyleneimine supported nano cerium chromate (PEI-NCeCrO₄⁻)

Polyethyleneimine supported nanoceriumtrichloride (1 g, 4.05 mmol) was suspended in dioxane and added to a cold solution of chromiumtrioxide (2 g, 10 mmol) in water / dioxane (10 ml / 20 ml). The mixture was stirred magnetically at room temperature for 10 h. The resulting resin was separated and washed several times with deionized water and diethyl ether and then dried in vacuum overnight to produce reddish, stable and non-hygroscopic powder (**Scheme 1**). The FT-IR spectrum showed bonds at 852, 858, 889, 942, and 1722 cm^{-1} characteristics of chromate ion. Capacities of the reagent determined by titration method, atomic absorption and ICP technique in terms of mmol CrO_4^- per gram reagent was 2 mmol CrO_4^- / g. m.p.: 218 °C (decomposed).

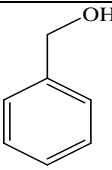
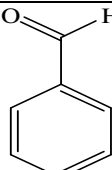
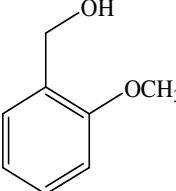
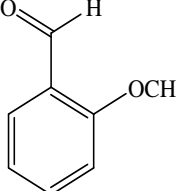
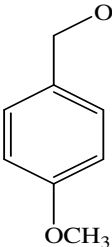
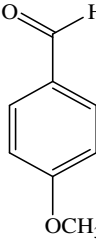
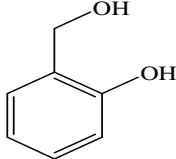
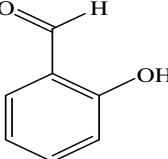
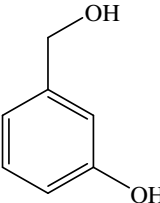
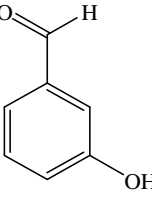
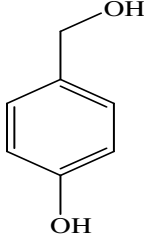
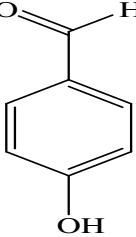
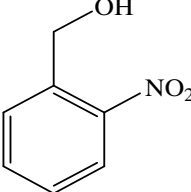
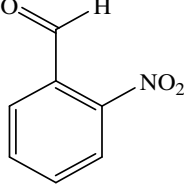
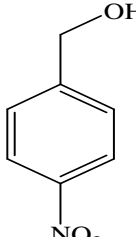
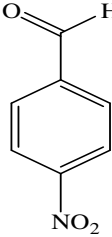
Scheme 1. Scheme of the synthesis of the polymer metal complexes on the base of PEI prearranged for nano cerium chromate.

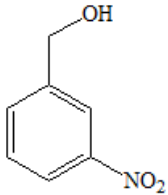
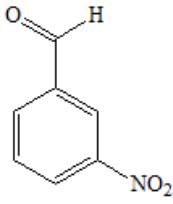
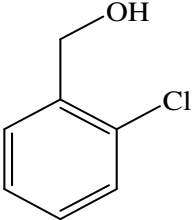
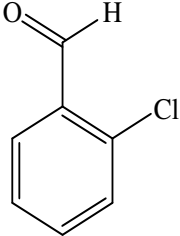
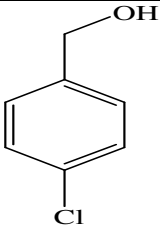
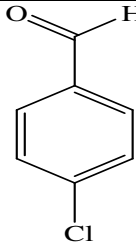
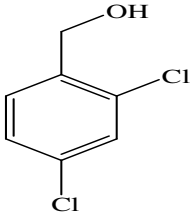
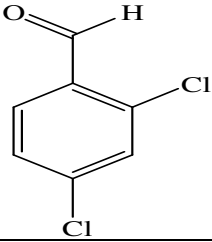
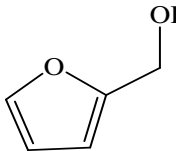
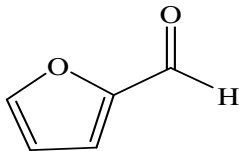
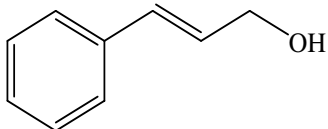
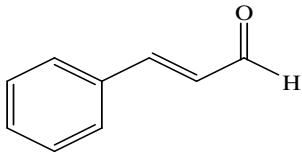
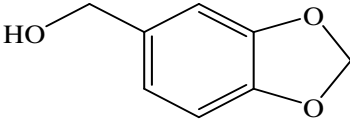
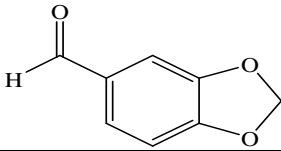
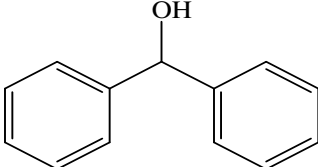
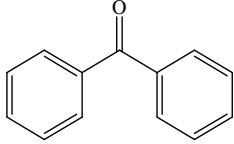
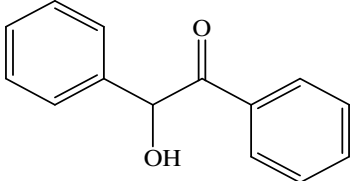
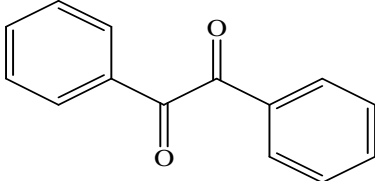


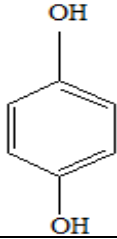
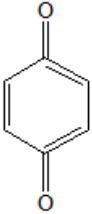
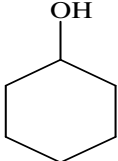
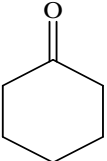
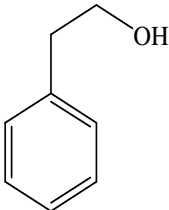
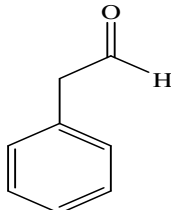
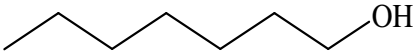
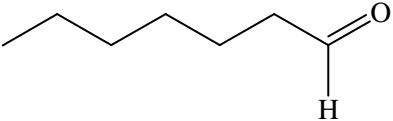
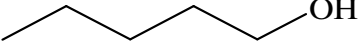
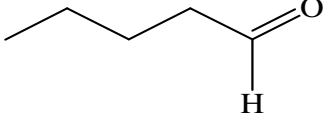
General procedure for oxidation of primary or secondary alcohols using (PEI-NCeCrO₄⁻) (representative procedure)

To a mixture of primary or secondary alcohol (1 mmol) and dioxane (10 mL) in a round-bottomed flask (25 mL), 0.5 g of (PEI-NCeCrO₄⁻) was added, and the mixture was stirred under reflux conditions for the time specified in **Table 1**. The progress of the reaction was monitored by TLC (ethyl acetate: n-hexane) (2 : 10). On completion of reaction, the mixture was filtered, and the solvent was evaporated to obtain pure aldehydes or ketones in high yields (80 – 95 %) (**Table 1**). The spent polymer was stored for regeneration.

Table 1. Oxidation of various alcohols using (PEI-NCeCrO₄⁻) in dioxane under reflux conditions.

Entry	Substrate	Product	Time, h	Yield, %
1			5	90
2			4	95
3			4.5	95
4			6	95
5			6	90
6			6	93
7			9	85
8			10	85

9			7	85
10			8	87
11			7	85
12			10	80
13			5	85
14			10	90
15			10	87
16			12	65
17			12	70

18			10	75
19			24 24 ^a	15 50
20			10	70
21			24 24 ^a	0 35
22			24 24 ^a	0 37

^a The molar ratio of the oxidant to substrate were near 3.

Preparation of piperonal from piperonol: A typical procedure

To a mixture of piperonol (152.15 mg, 1 mmol) and dioxane (10 mL) in a round-bottomed flask (25 mL), ~ 0.5 g of (PEI-NCeCrO₄[±]) was added, and the mixture was stirred under reflux conditions for 10 h. The progress of the reaction was monitored by TLC (ethyl acetate: n-hexane) (2 : 10). On completion of reaction, the mixture was filtered, and the solvent was evaporated to obtain pure piperonal (10.57 mg, 87 % yield).

The melting point: 35 – 34 °C, (37 °C lit.)

FT-IR (KBr): 1687 (C=O), 1488 – 1602 (C=C Ar), 1038 – 1366 (C-O), 2716 – 2846 (C-H aldehyde).

¹H-NMR: δ (ppm): 6.08 (2H, s), 6.94 (1H, d), 7.34 (1H, d), 7.42 (1H, dd), 9.82 (1H, s).

Determination of the capacity of (PEI-NCeCrO₄[±])

To determine the Ce content of the catalyst (PEI-NCeCrO₄[±]), it was treated successively with 25 cm³ mixture of concentrated H₂SO₄, HNO₃ and HCl, and filtered.

The filtrate was diluted to 30 cm³ with distilled water and subjected to ICP determination using calibration curve method. Ce content equal 1.6 mmol g⁻¹, and for determined the capacity we used atomic absorption technique by the same method used for ICP determination. The results showed Cr content equal 2 mmol g⁻¹ reagent that showed the amounts of mmol g⁻¹ CrO₄[±] (the capacity of (PEI-NCeCrO₄[±])). The gravimetric method and iodometric titration confirm this result.

General procedure for regeneration (PEI–NCeCrO₄)

10 g of the reddish spent reagent (originally prepared from highly branched PEI (0.40 g), was treated with (2N) hydrochloric acid (50 ml). The obtained suspension was dropped into excess aqueous sodium hydroxide (5N), when a cream precipitate was formed. After filtration and successive washings with distilled water the precipitate was dried in vacuum at 40 °C for 12 h to give PEI as a fine precipitate 0.38 g. The filtrate showed positive test for presence of chromium by atomic absorption method. The precipitate was slightly darker than original PEI. The weight loss of the obtained polymer compared to the starting PEI was only 5 %.

Result and discussion

Highly branched Polyethyleneimine-supported nano cerium chromate was prepared by complexation of the polymer with nanoceriumchloride and then exchanging the chloride anions with chromates.

Dioxane was the solvent of choice, and all of the oxidation reactions were carried out in this medium. The nano cerium and chromium ions remained firmly bound to the insoluble polymer support after the oxidation reactions, in fact which makes this reagent preferable to most monomeric reagents. The product isolation and purification were easy, simply by filtration of the reaction mixture, evaporation of the solvent and, if necessary, further separation of the unreacted starting material by column or plate chromatography shown in **Table 1**, this reagent is effective in the oxidation of various types of hydroxy compounds, such as primary and secondary benzylic and allylic alcohols and acyloins, to their corresponding carbonyl compounds and no product of over-oxidation was detected in the reaction mixtures at the end of the oxidation reactions.

In comparison with the already reported chromium (VI)-based polymeric oxidants used for oxidation of alcohols [21 – 24] this reagent can be used in equimolar amounts with respect to the substrates. It is non-acidic and useful for oxidation of acid-sensitive compounds, a fact which was reported essential in the use of some other polymeric reagents [16]. This makes it suitable for oxidation of water-sensitive compounds.

An excess of the reagent can be used, separation of the product is very easy, and can be obtained by simple filtration and evaporation of the solvent, no waste or by-products are formed; and the method can be used for selective oxidation of various alcohols. Also, based on our observation during the study, the polymeric reagent is stable and can be stored for months without losing its activity, to demonstrate the stability of polymeric reagent we used th (PEI–NCeCrO₄[−]) that stored in our laboratory for 6 month, for oxidation of the same alcohols the results are the same as freshly prepared (PEI–NCeCrO₄[−]).

(PEI–NCeCrO₄[−]) does not irritate mucous membrane and skin and also this reagent is nonvolatile and seems to be a nontoxic and non-pollutant oxidizing reagent. The morphology of the polymeric reagent studied by transmission electron microscopy (TEM) and scanning electron microscopy (SEM). By SEM images some information about the morphology particles was obtained as presented in **Figure 1**. The same image shows particles with good dispersion and dissociation in the polymer bed. TEM image clearly shows that Ce nanoparticles were formed and well-defined spherical particles dispersed homogenous in the polymer matrix (**Figure 2**).

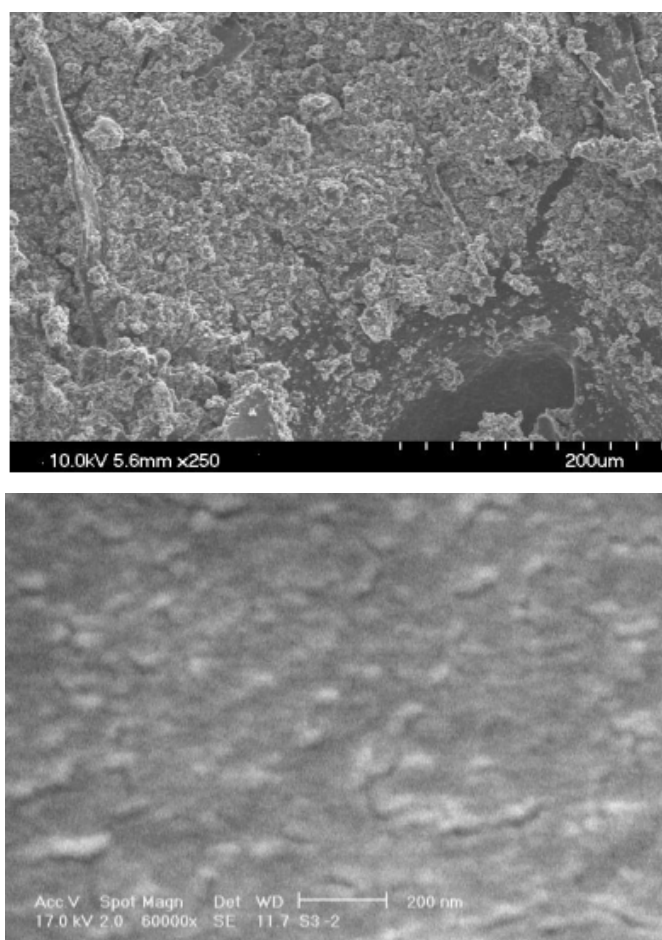


Figure 1. Scanning electron microscopy images of (PEI-NCeCrO₄⁼).

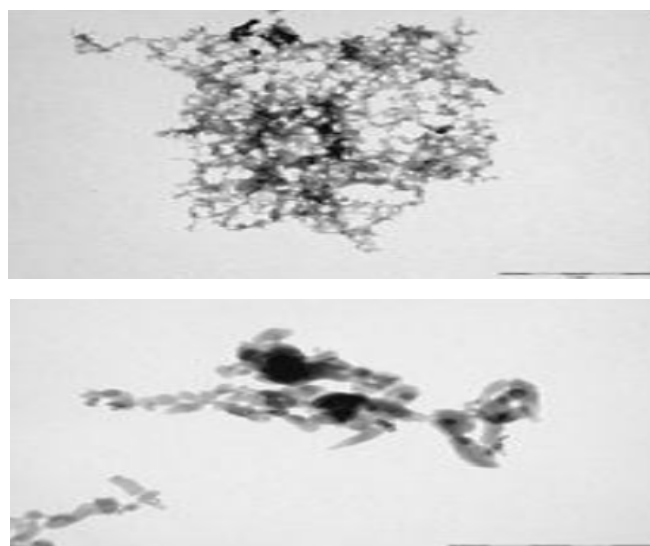


Figure 2. Transmission electron microscopy images of (PEI-NCeCrO₄⁼).

The structure of the products was confirmed by comparing their boiling point, melting point, FT-IR and ¹H-NMR spectra with pure compounds.

Optimization of the reaction conditions showed that for most of the reactions, dioxane at reflux conditions give the best results and the best molar ratio of the oxidant to substrate is 1 / 1. All the reactions were performed under reflux conditions **Table 1**.

The scope and generality of this process is illustrated with several examples of primary and secondary saturated, benzylic alcohols, and the representative results are summarized in **Table 1**. This polymeric reagent is effective mild and selective oxidizing reagent and can oxidize the primary and secondary benzylic alcohols, to corresponding carbonyl compounds in high yields and short time but primary or secondary saturated alcohols remained intact in the reaction mixture after 24 h, this reagents oxidized in hard conditions for example they oxidized with the molar ratio of the oxidant to substrate near 3 after 24 h. To demonstrate the selectivity of this method, a competitive reaction was performed between *p*-nitrobenzyl alcohol and pentanol with the molar ratio of the oxidant to substrate 1 / 1. It was observed that *p*-nitrobenzaldehyde is only product in 98 % yield, and pentanol no reacted after 24 h, the results are shown in Table I.

The oxidizing reagent is able to oxidize primary benzylic alcohols to corresponding aldehydes and secondary benzylic alcohols to corresponding ketones. As seen in **Table 1**, the presence of an electron acceptor group on the ring of benzyl alcohols increases the reaction time, and the presence of electron realizing group or substituted group on ortho, meta and para positions of the ring decreases the reaction time (**Table 1**).

Selected ¹H NMR, FT-IR spectra and physical data of the compounds

Para nitrobenzaldehyde – mp = 103 – 105 °C (lit. [25 – 27], mp: 106 °C); FT-IR (KBr) ν (cm⁻¹): 1706 (C=O), 1347 and 1543 (NO₂), 1608 (C=C Ar), 2827 (C-H aldehyde), ¹H NMR (250 MHz, CDCl₃) δ (ppm): 8.105 (d), 8.414 (d), 10.186 (s).

2-nitrobenzaldehyde – mp = 41 – 45 °C (lit. [25 – 27], mp: 43.5 °C); FT-IR (KBr) ν (cm⁻¹): 1736 (C=O), 134716, and 1532 (NO₂), 1346 (C=C Ar), 2887 (C-H aldehyde), ¹H NMR (250 MHz, CDCl₃) δ (ppm): 7.75 – 7.83 (m), 7.96 (dd), 8.13 (dd), 10.43 (s).

Para chlorobenzaldehyde – mp = 42 – 48 °C (lit. [25 – 27], mp: 44 °C); FT-IR (KBr) ν (cm⁻¹): 1699 (C=O), 617 – 841 (Cl), 1486 – 1597 (C=C Ar), 2835 (C – H aldehyde), ¹H NMR (250 MHz, CDCl₃) δ (ppm): 7.52 (d), 7.82 (d), 9.99 (s).

Para methoxybenzaldehyde – bp = 247 – 252 °C (lit. [25 – 27], bp: 248 °C); FT-IR (KBr) ν (cm⁻¹): 1698 (C=O), 1025 – 1302 (C–O), 1394 – 1443 (CH₃ bending), 1461 – 1601 (C=C Ar), ¹H NMR (250 MHz, CDCl₃) δ (ppm): 3.86 (s), 6.98 (d), 7.81 (d), 9.86 (s).

2-methoxybenzaldehyde – mp = 33.5 – 41 °C (lit. [25 – 27], mp: 38°C); FT-IR (KBr) ν (cm⁻¹): 1689 (C=O), 1023 – 1305 (C–O), 1396 – 1440 (CH₃ ben.), 1485 – 1601 (C=C Ar), ¹H NMR (250 MHz, CDCl₃) δ (ppm): 3.93 (s), 6.98 – 7.05 (m), 7.56 (d), 7.83 (d), 10.48 (s).

Cinnamaldehyde – bp = 249 – 253 °C (lit. [25 – 27], mp: 248 °C); FT-IR (KBr) ν (cm⁻¹): 1727 (C=O), 1605 – 1678 (C=C), 1496 (C=C Ar), 2743 – 2814 (C-H aldehyde), ¹H NMR (250 MHz, CDCl₃) δ (ppm): 9.7 (d), 7.4 (m), 6.6 (q).

Benzophenone – mp = 43 – 50°C (lit. [25 – 27], mp: 47.9°C); FT-IR(KBr) ν (cm⁻¹): 1656 (C=O), 1461 – 1601 (C=C Ar), ¹H NMR (250 MHz, CDCl₃) δ (ppm): 7.9 (d), 7.7 (d), 7.5 (m).

Benzaldehyde – bp = 176 – 180 °C (lit. [25 – 27], bp:179°C); FT-IR(KBr) ν (cm⁻¹): 1703 (C=O), 2696 – 2820 (C-H aldehyde), 1456 – 1584 (C=C Ar), ¹H NMR (250 MHz, CDCl₃) δ (ppm): 7.51 – 7.67 (m), 7.87 – 7.91 (m), 10.03 (s).

Piperonal – mp = 35 – 44°C (lit. [25 – 27], mp: 37 °C); FT-IR(KBr) ν (cm⁻¹): 1687 (C=O), 1488 – 1602 (C=C Ar), 1038 – 1366 (C–O), 2716 – 2846 (C–H aldehyde), ¹H NMR (250 MHz, CDCl₃) δ (ppm): 6.08 (s), 6.94 (d), 7.34 (d), 7.42 (dd), 9.82 (s).

Conclusion

In conclusion, the reagent used has been regenerated several times without noticeable change in its activity. Thus, high stability and regeneration of the polymeric bed makes this reagent economically suitable for medium to large-scale operations and is a useful addition to present methodologies.

Acknowledgment

We would like to appreciate the Islamic Azad University, Shiraz branch and Iran Nanotechnology Initiative Council for partial support of this work.

References

1. A. Akelah, D. C. Sherrington, *Chem. Rev.*, 1981, 81, 557.
2. A. Akelah, D. C. Sherrington, *Polymer*, 1983, 24, 1369.
3. A. mc Killop, D. W. Young. *Synthesis*, 1979, 11, 401.
4. H. B. Friedrich. *Platinum Metals Rev.*, 1999, 43, 94.
5. M. H. Heravi, D. Ajami, K. Aghapoor, M. Chassemzadeh. *Chem Commun.*, 1999, 9, 833.
6. N. M. Weinshenker, C. M. Shen. *Tetrahedron Lett.*, 1972, 13, 3281.
7. M. L. Hallens. *J. Polym. Sci. C*, 1974, 41, 7.
8. G. R. Marshall, E. Liener. *J. Org. Chem.*, 1970, 35, 867.
9. B. Hinzen, S. V. Ley. *J. Chem. Soc. Perkin Trans.*, 1997, 1, 1907.
10. O. Mitsuhiro, S. Yoko, Y. Ichiro. *Cryst. Growth*, 2011, 11, 2540.
11. J.-Y. Luo, M. Meng, Y.-Q. Zha, L.-H. Guo. *J. Phys. Chem. C*, 2008, 112, 8694.
12. B. Chanteau, J. Fresnais, J. F. Berret. *Langmuir*, 2009, 25, 9064.
13. B. Tamami, N. Iranpoor, M. A. Karimi Zarchi. *Polymer*, 1993, 34, 2011.
14. C. Parmeggiani, F. Cardona. *Green Chem.*, 2012, 14, 547.
15. B. Tamami, M. Hatam, D. Mohadjer. *Polym Bull.*, 1989, 21, 531.
16. J. M. J. Frechet, P. Darling, M. J. Farrall. *J. Org. Chem.*, 1981, 46, 1728.
17. B. F. Holger, S. Nirad. *Tetrahedron Lett.*, 2000, 41, 3971.
18. N. Goudarzian, M. Gholinejad, P. Ghahramani. *J. Chem. Sci.*, 2011, 123, 485.
19. N. Goudarzian, P. Ghahramani. *J. Chem. Soc.*, 2012, 34, 5.
20. V. Y. Sonawane. *Res. J. Chem. Sci.*, 2011, 1, 25.
21. G. Cainelli, G. Cardillo, G. Osen, S. Andri. *J. Am. Chem. Soc.*, 1976, 98, 6737.
22. G. Cardillo, M. Orena, S. Sandri. *Tetrahedron Lett.*, 1976, 17, 3985.
23. J. M. J. Frechet, J. Warnock, M. J. Farrall. *J. Org. Chem.*, 1978, 43, 2618.
24. V. K. Sharma, S. K. Mishra, N. Nesnas. *Environ Sci Technol.*, 2006, 40, 7222.
25. Z. Rappoport. *Hand Book of Tables for Organic Compounds Identification*. 1966, CRC Press.
26. J. Workman Jr. *The Academic Press Handbook of Organic Compounds: NIR, IR, Raman, and UV-VIS Spectra Featuring Polymers, and Surfactants*. 2000, Boston: Academic Press.
27. M. Reinhard, A. Drefahl. *Toolkit for Estimating Physicochemical Properties of Organic Compounds*. 1999, Weinheim: John Wiley & Sons.

POROUS Si SUBSTRATE: A HIGH-QUALITY AND CHEAP SUBSTRATE FOR ADVANCED RF APPLICATIONS

Y. Belaroussi¹, M. T. Belaroussi¹, G. Scheen², K. Ben Ali², J.-P. Raskin²

¹ Centre for Development of Advanced Technologies (CDTA)

Algiers, Algeria

ybelaroussi@cdta.dz

² Université catholique de Louvain

Louvain-la-Neuve, Belgium

Accepted September 19, 2013

1. Introduction

Porous silicon is a well-known material produced by anodization of silicon in hydrofluoric acid (HF)-based electrolyte. A number of factors, such as the doping type and level in silicon substrate and the electrochemical parameters determine the pore morphology. Porous structures are typically sorted into three categories by the size of the pores, i.e. micropores (diameters < 10 nm), mesopores (diameters between 10 and 50 nm) and macropores (diameters > 50 nm). All three kinds of pore structures have found their own applications. Though each of the three types of pores (micro, meso, and macropores) has been extensively investigated and can be produced under a variety of conditions [1 – 3], much less work has been performed on the multilayer structures with completely different pore morphologies. Other technological solutions have also been proposed using silicon nano-pillar arrays to create a vertically oriented field effect transistor for the decoupling of device density from channel length [4].

The ability to insert a thick porous silicon layer on a low resistivity Si wafer, on which the RF devices can be integrated, enabled the elaboration of insulating / semiconductor mixed substrates [5]. In fact, this material exhibits low permittivity, whose value depends on the porosity between those of air ($\epsilon_r = 1$) and silicon ($\epsilon_r = 11.7$) [6]. Moreover, most porous silicon substrates studied in the literature for RF applications are mesoporous and made from p-type silicon of resistivity below $10 \text{ m}\Omega \cdot \text{cm}$. The materials are generally of moderate thicknesses (10 to $200 \mu\text{m}$) with porosities of 70 to 80 % [7, 8]. Furthermore, porous silicon on n-type substrates in the field of radio frequencies has also been demonstrated in terms of electrical insulation while maintaining low mechanical stresses in the substrate and good thermal conduction [9].

Additionally, the ease and low cost of obtaining porous Si and its particular electrical, optical and thermal properties make this material a field of development for microsystems. It is in this context that it appears possible to combine the use of several of these properties in a single integrated micro device. As of the use of its dielectric properties, porous silicon implementation has been most often made in the form of thick insulating boxes mainly in the field of radio frequencies [10, 11].

In this work, we report an electrochemical study, where new parameters are used in order to anodize a thick porous silicon layer of the starting silicon substrate formed on p-type Si of different resistivity, current density and anodization time. The microporous silicon layer before and after oxidation is characterized by energy dispersive spectroscopy (EDS), X-Ray diffraction (XRD) and the FTIR. The CPW lines are integrated on the porous Si layer and their RF characteristics are measured. RF properties of porous Si substrate will be compared with those of a trap-rich high resistivity (HR) Si substrate.

2. Porous silicon formation

The substrates used in this study were standard p-type silicon (100) wafer with resistivity in the range of $1 - 10 \Omega \cdot \text{cm}$. Electrochemical etching in hydrofluoric acid (HF) solution is a well-known technique to fabricate different structures in silicon for a wide range of applications. The electrolytes used for the anodic etching process were based on 2 : 1 a mixture of (50 %) HF and ethanol. Ohmic contact was made through a Ga–In alloy at the back side of the samples. An adhesive tape was used to mask all the substrate except the area where anodization and electrodeposition were carried out as shown in **Figure 1**. The sample was mounted in an electrochemical cell connected to a potentiostat—galvanostat PAR 362. Distinct morphologies of meso- and macro-pores can be achieved depending on the Si wafer doping as well as by changing the electrochemical parameters. For the fabrication of a microporous layer structure, a current density of $15 \text{ mA} \cdot \text{cm}^{-2}$ and an etching time of 90 min were applied during the etching process. All specimens were fabricated in the dark on an electrochemical etching platform inside a fume-hood at room temperature ($18 \pm 1 \text{ }^\circ\text{C}$). Finally, the samples were rinsed in deionised water and dried by blowing argon gas.

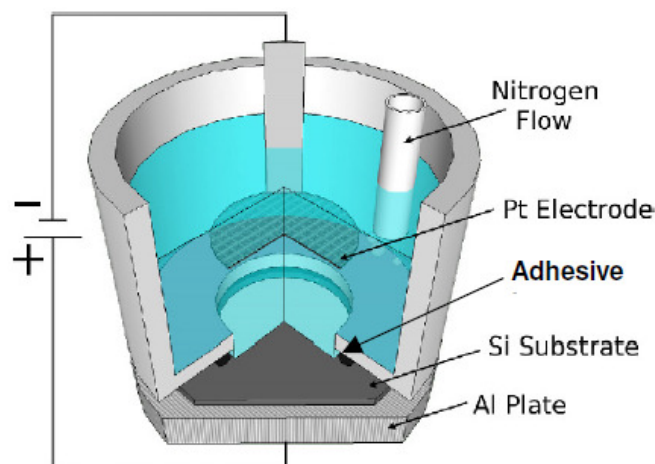


Figure 1. Electrochemical cell used for electrochemical etching [12].

Surface morphology and microstructure of the etching area were investigated using JEOL JSM 6360 LV Scanning Electron Microscope (SEM) equipped with energy dispersive X-ray Spectroscopy (EDS). Analysis tool XRD patterns were measured with $\text{Cu } K\alpha$ radiation (1.54 \AA) using a D8 advance Bruker diffractometer. The FTIR adsorption spectrum, on the other hand, was obtained with a Thermo-Nicolet Nexus 670 Fourier transform infrared spectrometer.

3. Experimental results and discussion

3.1. XRD spectra measurement

In order to reduce the mechanical constraints in porous silicon and have a good electrical isolation between metallic devices and the porous Si layer, it is necessary to oxidize at least partially the porous silicon substrate. The XRD spectra of the porous Si p-type layer are shown in **Figure 2** with each Bragg peak, assigning its identification and Miller indices. **Figures 2a** and **b** present the spectrum before and after oxidation, respectively. We notice a bump on the left of the spectrum in **Figure 2b** indicating the amorphous oxidation of the porous silicon while the [400] plane of the silicon peak does not change.

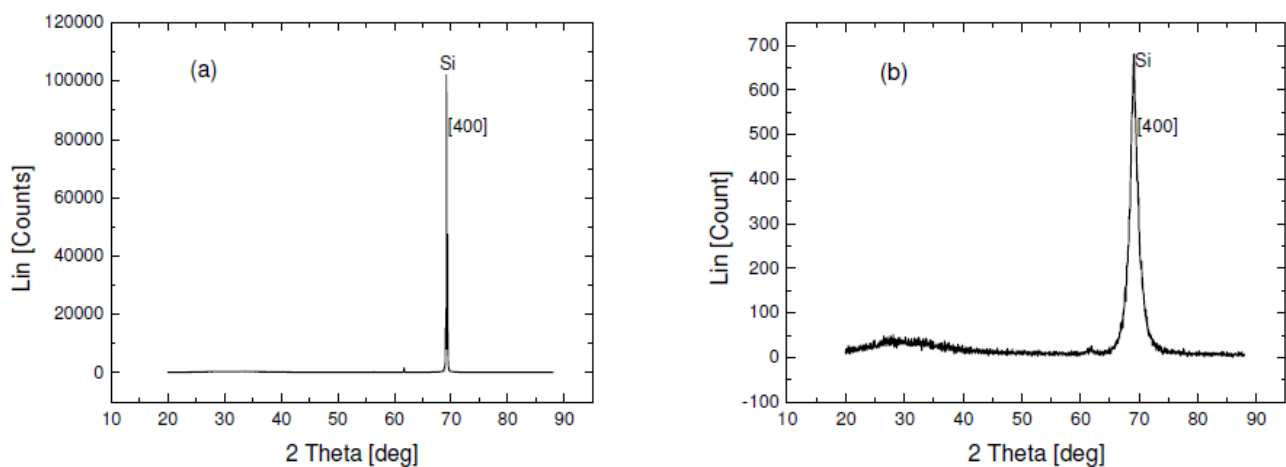


Figure 2. DRX spectrum of porous Si (100) p-type, (a) before and (b) after oxidation.

3.2. Investigation of surface morphology

The morphology of the porous silicon substrate was characterized by SEM. **Figure 3** shows the cross-sectional SEM image of a microporous silicon layer formed with moderately doped p-type Si substrate in HF solution at the condition described in the experimental section. The pores are found to have a diameter ranging from 1 to 5 nm for a substrate resistivity of $1 - 10 \Omega \cdot \text{cm}$ and a current density of $15 \text{ mA} \cdot \text{cm}^{-2}$. On the other hand, for substrate resistivity $10 - 20 \Omega \cdot \text{cm}$ and high current density, we obtained mesopores with diameter varying from 10 to 50 nm. The depth of the pores can be varied depending on the time period of the electrochemical process.

In the present work, the thickness of porous silicon layer is about $50 \mu\text{m}$ for an etching time of 90 min and current density of $15 \text{ mA} \cdot \text{cm}^{-2}$. However, the thickness decreases for an etching time shorter than 90 minutes for the same current density. The recorded energy dispersive spectroscopy analysis spectrum reveals the presence of oxygen after oxidation through the whole layer thickness and into the filled pores indicating that the sample contains silicon and oxygen. The presence of gold is due to the metallization of the samples. The average compositions of the anodization and oxidation have been estimated quantitatively with value of 84 % for Si and 16 % for O in the anodized layer as shown in **Figure 4**.

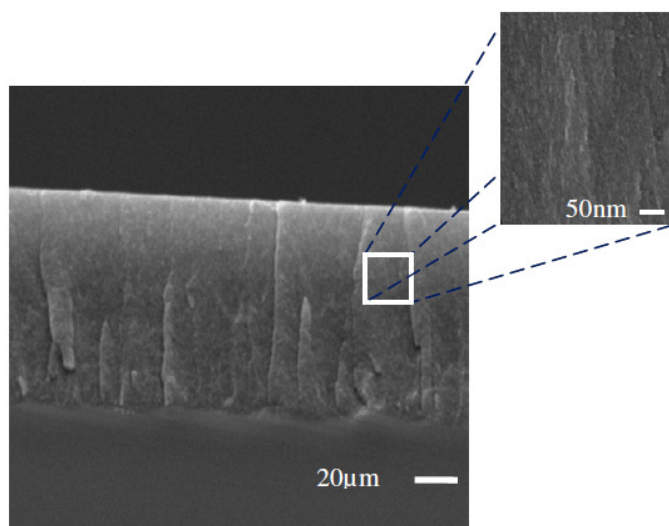


Figure 3. A cross-section SEM image of a porous silicon layer. The inset is a zoom-in image in which the micro-pores can be visualized.

Element	Wt%	At%
O K	09.92	16.21
SiK	90.08	83.79

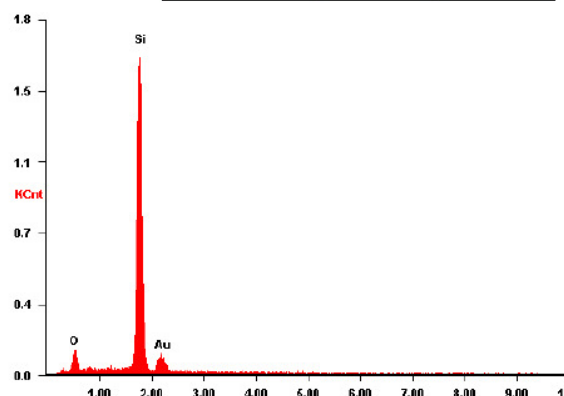


Figure 4. The EDAX spectrum of porous silicon layer after oxidation.

3.3. FTIR spectra measurement

The FTIR analysis is widely used to characterize the bonding properties of porous silicon surfaces. **Figure 5a** shows the IR spectra of porous silicon sample. The infrared spectra of silicon were measured in absorbance mode and were referenced against a single silicon crystal sample. The sample has a small peak at about 1100 cm^{-1} , corresponding to the stretching vibration of Si-O bond (oxygen present in interstitial sites in the silicon crystal lattice). Another more intense peak around 611 cm^{-1} was also observed, corresponding to the stretching vibrations of the Si-Si and Si-C which are combined. We observe a periodicity, which is due to interference phenomena in thin layers. Porous silicon is commonly highlighted by the stretching vibrations of Si-H, Si-H₂ and Si-H₃, respectively, at 2110 , 2087 and 2140 cm^{-1} [13, 14].

Furthermore, other modes have been observed such as deformation vibration at 915 cm^{-1} of the Si-H₂ bond and at 626 cm^{-1} from rocking mode of the Si-H bond. The torsional and the rotation modes have also been observed at 665 and 512 cm^{-1} , respectively.

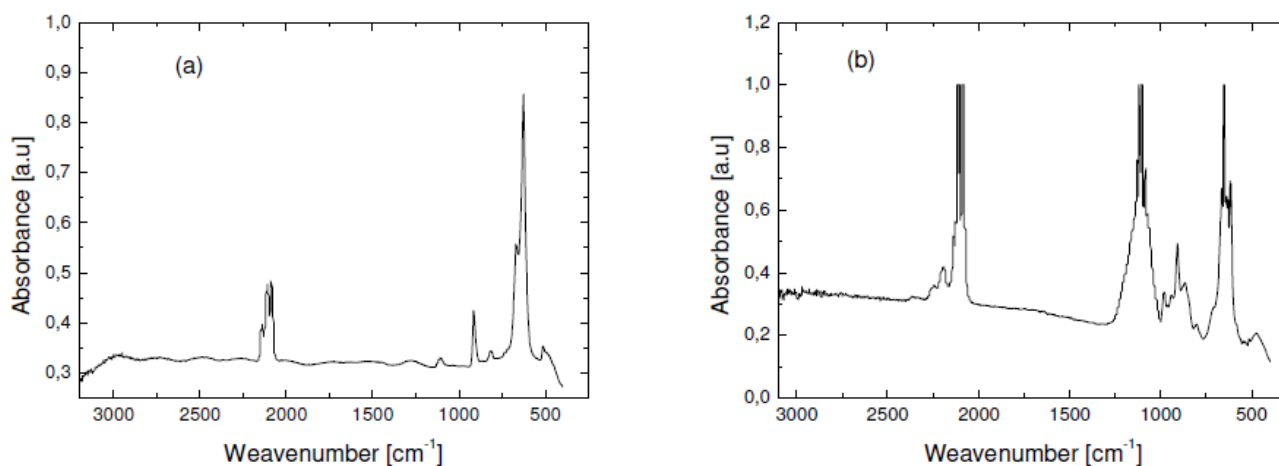


Figure 5. FTIR Spectrum of porous silicon layer, (a) before and (b) after oxidation.

Figure 5b presents the FTIR spectrum of the sample after oxidation. Besides the porous silicon peaks, a strip of significant vibration of Si–O bond containing the vibration of symmetric and asymmetric stretching modes of Si–O–Si at, respectively, 1073 and 1169 cm^{-1} , as well as the stretching vibration of SiO₂ at 1069 and 464 cm^{-1} were observed. A wide band at 1084 cm^{-1} and two simultaneous peaks at 1100 and 1124 cm^{-1} corresponding to the stretching vibration of Si–O bond coincide with the vibration of the Si–OC and the deformation vibration at 879 cm^{-1} . A peak at 800 cm^{-1} corresponds to the stretching vibration of Si–O–Si and Si–OH. Low intensities of peaks that appear at 2186 and 2266 cm^{-1} are assigned, respectively, to the stretching vibration of O₂Si–H or OSi–H₂ and O₃Si–H bonds.

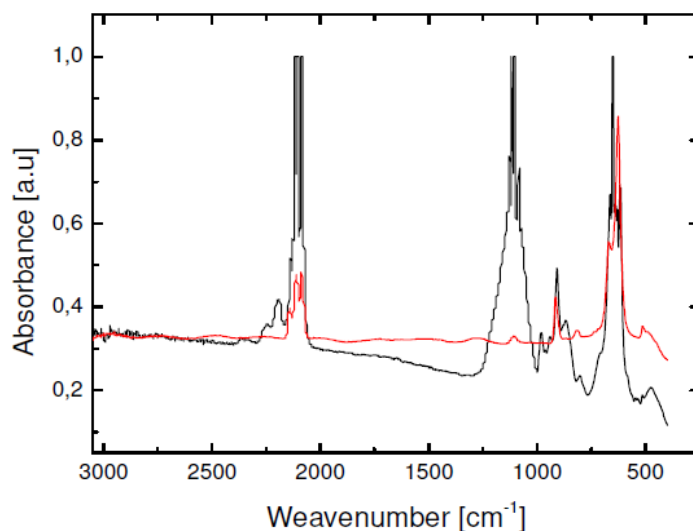


Figure 6. Superposition of FTIR spectra of the 50 μm porous Si film after oxidation.

Finally, the superposition of the two spectra in **Figure 6** highlights the oxidation of porous silicon with intense peaks.

3.4. Electrical measurements

It has been demonstrated that the trap-rich high resistivity (HR) Si substrate can present negligible substrate losses [15, 16]. A comparison is made between this trap-rich HR Si substrate and the porous Si substrate investigated in this work in terms of effective permittivity and effective resistivity by integrating identical CPW lines on both substrates. Also, a same thickness of a 500 nm-thick layer of SiO₂ was deposited on top of which the metal lines were integrated. The CPW lines were fabricated on the porous Si layer using 1 μm -thick Al metallization with a length of 8 000 μm . RF measurements of transmission lines on porous silicon substrate were then conducted in the frequency range from 1 to 25 GHz. The values of the effective permittivity and the effective resistivity were extracted from S -parameters measurements of the CPW line. The experimental results demonstrate that the porous Si shows reduced effective permittivity, ϵ_{eff} , three times lower compared with the trap-rich HR Si substrate. The effective resistivity ρ_{eff} of the porous Si is also significantly higher than the original resistivity of the substrate, i.e. 1 – 10 $\text{k}\Omega \cdot \text{cm}$, and similar to the trap-rich HR Si. As shown in **Figure 7**, the measure of effective permittivity is as low as 2.5, and **Figure 8** shows an effective resistivity larger than 10 $\text{k}\Omega \cdot \text{cm}$.

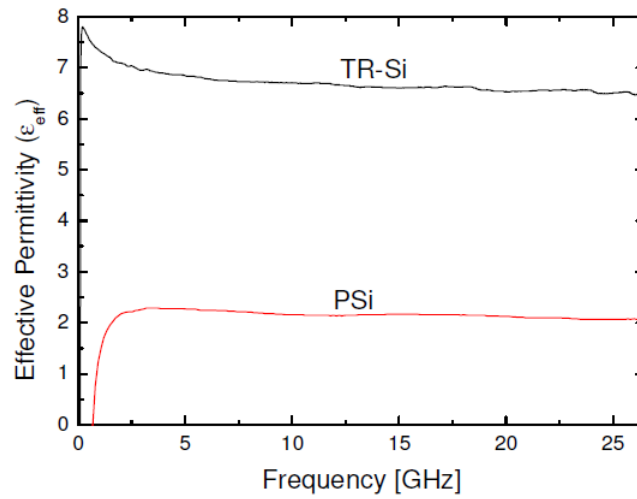


Figure 7. Effective dielectric permittivity (ϵ_{eff}) versus of frequency of CPW line on the porous Si substrate and trap-rich HR-Si

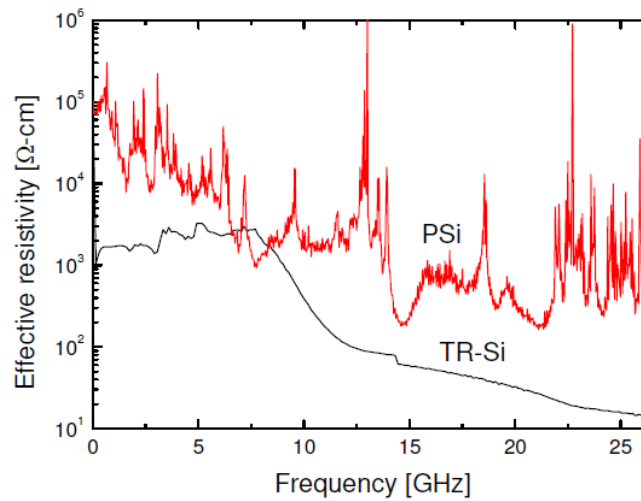


Figure 8. Effective resistivity (ρ_{eff}) versus frequency of CPW line on the porous Si substrate and trap-rich HR-Si.

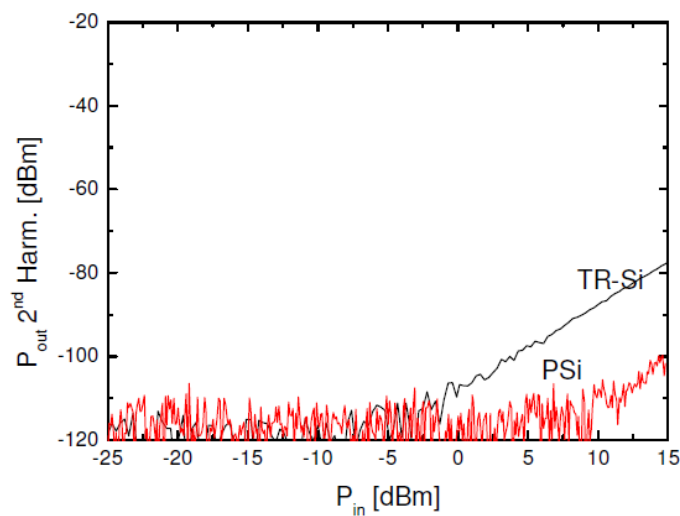


Figure 9. Second harmonic distortion measurement of CPW line on the porous Si substrate and trap-rich HR-Si.

Several 50- Ω CPWs with different lengths were fabricated on top of oxidized porous Si substrate. The formation of trap-rich layer on the Si wafer has been described in detail elsewhere [16]. The nonlinear behavior of the substrate is measured using a characterization setup based on a four-port Agilent PNA-X vector network. It allows measuring the amplitude of the corresponding harmonics and S-parameters from 10 MHz to 26.5 GHz. The measured second harmonic (H2) from a CPW line lying on HR-Si and porous Si substrates are presented in **Figure 9**, the introduction of porous Si substrate drastically reduces the harmonics distortion.

4. Conclusions

After different anodizations of porous silicon with different experimental parameters (applied current density, composition of electrolyte and the time of anodization), we have chosen the best parameters in this work. We have demonstrated the influence of those parameters on physical characteristics of porous silicon layer before and after oxidation according to a range of applied current densities. The results show controllable porous silicon morphologies, including spongy micropores formed on p-type silicon under dark conditions, by current density of 15 mA \cdot cm⁻². Oxidized porous silicon was fabricated successfully, and the functionalization of the oxidized porous silicon into a RF application was implemented. RF measurements of transmission lines demonstrate the successful reduction of the permittivity and an increased resistivity. A porous silicon layer on standard substrate is an efficient technological solution to reduce the harmonic distortion originating from the substrate.

According to the obtained results, the porous Si, with regard to the simplicity of its fabrication and its compatibility with CMOS processing, could be a good candidate for RF applications compared with the trap-rich HR –Si substrate.

Acknowledgements

The authors would like to thank Dr. N. Gabouze, Dr. S. Sam and PhD student S. Belhouse for the valuable discussions and FTIR analysis. This work has been partially funded by the Directorate-General for Scientific Research and Technological Development (DGRSDT), and CDTA (Algiers).

References

1. H. Ohji, P. J. French, K. Tsutsumi. Fabrication of mechanical structures in p-type silicon using electrochemical etching. *Sensors & Actuators A* 82 (2000) 254-258.
2. V. Lehmann. Electrochemistry of silicon: Instrumentation, science, materials and applications. In: *Electrochemistry of Silicon*. 2002, John Wiley & Sons, 127-166.
3. X. Q. Bao, J. W. Jiao, Y. L. Wang, Y. Zhang, D. H. Ge, K. W. Na, H. Choi. One-dimensional mesopore-array formation on low doped n-type silicon. *Electrochem. Commun.* 9 (2007) 1491-1496.

4. M. Masahara, Y. Liu, K. Endo, T. Matsukawa, K. Sakamoto, K. Ishii, Sh. O'uchi, E. Sugimata, H. Yamauchi, E. Suzuki. Fabrication and characterization of vertical-type double-gate metal-oxide-semiconductor field-effect transistor with ultrathin Si channel and self-aligned source and drain. *Appl. Phys. Lett.* 88 (2006) 072103 1-2.
5. H. Contopanagos, A. G. Nassiopoulou. Design and simulation of integrated inductors on porous silicon in CMOS-compatible processes. *Solid State Electronics* 50 (2006) 1283-1290.
6. H.-S. Kim, K. Chong, Y.-H. Xie. The promising role of porous Si in mixed-signal integrated circuit technology. *Phys. Status Solidi A* 197 (2003) 269-274.
7. I. K. Itotia, R. F. Drayton. DC bias effects on bulk silicon and porous silicon substrates. In: *Int. Symp. IEEE Antennas & Propagation Soc.* 2 (2003) 663-666.
8. K. Chong, Y.-H. Xie, K.-W. Yu, D. Huang, M.-C. F. Chang. High-performance inductors integrated on porous silicon. *IEEE Elect. Dev. Lett.* 26 (2005) 93-95.
9. M. Capelle, J. Billoue, P. Poveda, G. Gautier. n-type porous silicon substrates for integrated RF inductors. *IEEE Trans. Elect. Dev.* 58 (2011) 4111-4114.
10. C. M. Nam, Y. S. Kwon. High-performance planar inductor on thick oxidized porous silicon (OPS) substrate. *IEEE Microwave & Guided Wave Lett.* 7 (1997) 236-238.
11. A. S. Royet, R. Cuchet, D. Pellissier, P. Ancey. On the investigation of spiral inductors processed on Si substrates with thick porous Si layers. In: *Eur. Solid State Dev. Res. (ESSDERC'03)*, 2003, 111-114.
12. M. Bassu, G. Scheen, L. A. Francis Thick macroporous silicon membranes: Influence of the masking layer on the under etching characteristics. *Sensors & Actuators A* 185 (2012) 66-72.
13. A. Teyssot, A. Fidélis, S. Fellah, F. Ozanam, J.-N. Chazalviel. Anodic grafting of organic groups on the silicon surface. *Electrochim. Acta* 47 (2002) 2565-2571.
14. S. Gardelis, A. G. Nassiopoulou, M. Mahdouani, R. Bourguiga, S. Jaziri. Enhancement and red shift of photoluminescence (PL) of fresh porous Si under prolonged laser irradiation or ageing: Role of surface vibration modes. *Physica E* 41 (2009) 986-989.
15. C. Roda Neve, D. Lederer, G. Pailloncy, D. C. Kerr, J. M. Gering, T. G. mc Kay, M. S. Carroll, J.-P. Raskin. Impact of Si substrate resistivity on the non-linear behaviour of RF CPW transmission lines. In: *Proc. 3rd Eur. Microwave Integrated Circuits Conf.* 2008, 36-39.
16. C. Roda Neve, J.-P. Raskin. RF harmonic distortion of CPW lines on HR-Si and trap-rich HR-Si substrates. *IEEE Trans. Elect. Dev.* 59 (2012) 924-932.

NANOCRYSTALLINE NICKEL COBALT FERRITE ($\text{Ni}_{1/2}\text{Co}_{1/2}\text{Fe}_2\text{O}_4$) FOR ELECTROMAGNETIC INTERFERENCE (EMI) SHIELDING APPLICATIONS

D. K. Tiwari¹, A. K. Thakur², S. E. Borjas-García¹,
L. M. Villaseñor Cendejas¹, N. Dasgupta-Schubert¹

¹Universidad Michoacana de San Nicolás de Hidalgo
Morelia, México
dkt@ifm.umich.mx

²Indian Institute of Technology Kharagpur
Kharagpur, India

Accepted September 19, 2013

1. Introduction

The role of electromagnetic field is predominantly very much crucial to determine the content and quality of data transfer at very high frequency ranges. The number of electromagnetic signals has increased with the advancement of technology and its ever growing use in telecommunication, biomedical and other electronic systems causes a serious issue due to electromagnetic interference (EMI). EMI is high frequency signal, disturbs the function of a circuit, cable or other electronic component originated from other equipment or from the self-affected components [1, 2]. The EMI caused by these signals necessitate protective materials to avoid diminished product performance or product failure. EMI is coupled between circuits or equipment having some mutual impedance through which one circuit can affects the other circuit [3]. The mutual impedance can be conductive, capacitive, inductive, or combination of these. When electromagnetic energy affects any equipment adversely by causing it to have an emergent response then this electromagnetic energy is called EMI and the affected equipment is said to be susceptible to EMI. EMI may leave a source or enter susceptible equipment by conduction, coupling, or radiation. Interference occurs between one part of the equipment to another or through power supply to nearby circuits [3]. EMI is conducted via signal lines, antenna leads, power cables, and even ground connections, between EMI sources and EMI-susceptible equipment.

EMI shielding makes plastic enclosures to protect equipment with EMI; also, increases emphasis on storage, protection and safe transmission of data, such as, cyber security, crime prevention [1, 2]. EMI shielding reflects, absorbs or transmits the electromagnetic waves to prevent interference from a particular device or zone via an effective placement of shielding materials to reduce the level of electromagnetic energy radiated by the equipment. There are many kind of materials are used for removal or minimization of EMI shielding e.g. sheet metal, conductive paints, electroless plating, ferrites, polymers, composites, etc.

The materials used for EMI shielding are; sheet metal, conductive paint, electroless plating, conductive plastics and ferrites. Depending on the materials property there are certain limitations regarding their design versatility and environmental reliability. Ferrite designs are

made with solid and split beads arranged in versatile geometries and with many types of material compounds, and they offer many installation alternatives. The shielding property of ferrites is strongly influenced by the chemical composition, crystalline structure, grain size, nature of porosity, secondary phase thickness of the grain boundary, magneto crystalline anisotropy and magnetostriction. Electrical characteristics of these components depend on the geometry of conductive material and permeability of the core material.

EMI shielding measures in term of shielding effectiveness (SE) which is defined in decibel (dB), as the ratio of the electric / magnetic field that is incident on the barrier to the magnitude of electric / magnetic field that is transmitted through the barrier (**Figure 1**) [4, 5]:

$$SE = 10 \log \frac{P_i}{P_0} = 20 \log \left| \frac{E_i}{E_0} \right|, \quad (1)$$

where E_i and E_0 are incident and transmitted electric fields respectively.

SE as given by the above equation can also be divided into three terms of reflection loss, absorption loss and multiple reflections, i.e.

$$SE = R + A + B, \quad (2)$$

where R = reflection loss caused by reflection at the left and right interfaces; A = absorption loss of the wave as it proceeds through the barrier; B = multiple reflections and transmissions.

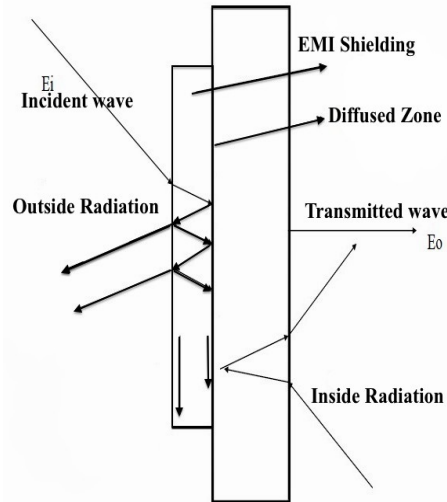


Figure 1. EMI shielding pattern.

The multiple reflections and transmissions can be neglected because of the shield thicknesses that are much greater than skin depth, so that the effective parameter which will affect the SE only initial reflection and transmission at the left and right interfaces [5, 6], i.e.

$$SE = A + R. \quad (3)$$

Absorption loss

Absorption loss of a sample can be defined as

$$A = 20 \log \exp \frac{t}{\delta}, \quad (4)$$

where, t is thickness of the sample and δ is the skin depth, which can be defined as

$$\delta = \sqrt{\frac{2}{\mu \omega \sigma}} = \sqrt{\frac{1}{\pi f \mu \sigma}} \quad (5)$$

when $\sigma \gg \omega\epsilon$, and

$$\delta = \frac{2}{\sigma} \sqrt{\frac{\epsilon}{\mu}} \quad (6)$$

when $\sigma \ll \omega\epsilon$, so that

$$A = 20 \log \exp \frac{t}{\delta} = 8.7x \frac{t}{\delta}, \quad (7)$$

$$A = 8.7t \sqrt{\frac{\mu\sigma\omega}{2}} \quad (8)$$

or

$$A = 8.7t \sqrt{\pi f \mu \sigma} = 131t \sqrt{f \mu_r \sigma_r}. \quad (9)$$

Reflection loss

The reflection loss depends on the mismatch between the incident wave impedance and the impedance of the shield. Ignoring the multiple reflections, the reflection loss for a plane wave of frequency f can be defined as

$$R = 31.5 + 10 \log \frac{\sigma}{\mu f} = 168 - 10 \log \frac{\mu_r f}{\sigma_r}. \quad (10)$$

From equation (3), (9) and (10), SE can be calculated with the formula:

$$SE = 131t \sqrt{f \mu_r \sigma_r} + 168 - 10 \log \frac{\mu_r f}{\sigma_r}, \quad (11)$$

where, σ_r is the conductivity of the material relative to copper, f is the frequency in Hz and μ_r is the relative permeability.

SE can also be defined for the composite materials using Simon formula:

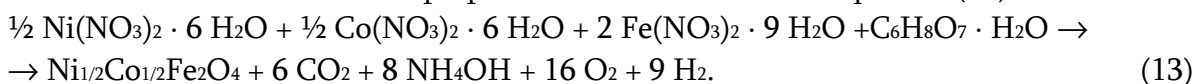
$$SE = 50 + 10 \log \frac{\sigma}{f} + 1.7t \sqrt{f\sigma}, \quad (12)$$

where σ is the conductivity of the material (S / cm), t is the thickness of the sample in cm, and f is the frequency (MHz) of the electromagnetic radiation. The first two terms of equation (12) represent the reflection loss and the third term is the absorption loss.

2. Experimental

2.1. Material preparation

Nanocrystalline $\text{Ni}_{1/2}\text{Co}_{1/2}\text{Fe}_2\text{O}_4$ powers were prepared using citrate route method [7]. The chemical reaction of the material preparation has been noted in equation (13):



The precursors citric acid, nickel, cobalt and iron nitrates were dissolved in distilled water to prepare the Ni – Co ferrite. The resulting solution was heated mechanically on magnetic stirrer at 50 °C for 1 h and final suspension was filtered adding NH_4OH after fixing pH at 10. The precipitate was washed, dried and calcined for 3 h at 300 °C. Homogeneous powders were obtained after milling in mortar about 15 – 20 min.

2.2. Pellet preparation

The pellets were prepared using 1 % wax as a binding agent at 6 ton / cm² pressures. The selected die-punch has area 133 mm². The pellets have diameter 13.06 mm and thickness 2.13 mm.

2.3. Characterization

The crystal structure and particle size of prepared sample is characterized by X-ray diffraction (XRD) pattern by using X-ray diffractometer Rigakuminiflex (Japan) and the particle size were calculated using Scherer's formula:

$$D = \frac{0.9\lambda}{\beta \cos \theta_b}, \quad (14)$$

where D = particle size; λ = X-ray wavelength; β = full width at half max (FWHM) and θ_b = Bragg angle.

The structural and morphological property of the prepared material is analysed using transmission electron microscope (TEM) Philips CM 12 at 25 and 50 kV. TEM had been carried out by ultrasonic dispersion of powder samples in acetone and placing a small drop on thin carbon film supported on the copper grid until it dry.

Electrical property of the material is characterized using impedance analyser (Hioki 3522-50 LCRHiTESTER, Hioki 9700-10 Head Amp Unit). The sample is sandwiched between two electrodes, which measure the impedance as a function of frequency of the applied signal. The apparatus evaluate and separates contribution to the overall electrical properties in the frequency domain due to electrode reaction at the electrode interface and the migration of ions through the bulk and across the grain boundaries of materials.

Variation of relative permeability component with respect to frequency was calculated using Agilent 4294 A precision impedance analyser at current 10 mA. The pellet sample was placed as a coil and an electric current 10mA were applied in transverse direction of the placed sample. The flowing current produces a magnetic field, hence a magnetic flux generated through the circuit and the ratio of the magnetic flux to the current will give the inductance (L) of the circuit. The real and imaginary parts of the permeability components can be calculated using

$$\mu' = \frac{L_s}{L_0}$$

and

$$\mu'' = \frac{R_s - R_0}{2\pi f L_0}, \quad (15)$$

where, L_s is the inductance of the coil in presence of pellet sample, L_0 inductance of the empty coil (without sample), R_s is the coil resistance in presence of sample, R_0 is resistance of coil without sample and f is the frequency.

Magnetic loss tangent can be calculated using formula:

$$\tan \delta = \frac{\mu''}{\mu'}. \quad (16)$$

3. Results and discussion

3.1. Crystal structure and powder size of prepared Ni – Co ferrite

The material preparation and single-phase formation of Ni – Co ferrite ($\text{Ni}_{1/2}\text{Co}_{1/2}\text{Fe}_2\text{O}_4$) samples were confirmed by XRD pattern and POWD technique was used to analyse the lattice parameter (a). **Table 1** shows the Miller indices values of the obtained peaks with respective angle (2θ) and the material shows cubic structure [8] with lattice parameter value 8.3584 Å. The formation of the material is confirmed by JCPDS no. 742081 [7]. Powder of the prepared nickel-cobalt ferrite ($\text{Ni}_{1/2}\text{Co}_{1/2}\text{Fe}_2\text{O}_4$) is calculated by Scherer's formula, obtained 27.7 nm, which confirms the prepared material is nanocrystalline.

Table 1. XRD Pattern of prepared samples using POWD analytical technique.

Angle 2θ , °	Miller indices (h, k, l)	Lattice parameter a , Å
30.26	(2, 2, 0)	8.3584
35.62	(3, 1, 1)	
43.26	(4, 0, 0)	
53.64	(4, 2, 2)	cubic structure
57.25	(5, 1, 1)	
62.86	(4, 4, 0)	
74.31	(5, 3, 3)	

3.2. Transmission electron microscope (TEM) analysis

TEM micrographs of citrate derived prepared nickel-cobalt ferrite ($\text{Ni}_{1/2}\text{Co}_{1/2}\text{Fe}_2\text{O}_4$) were shown in **Figure 2**. The particle size estimated by TEM indicates that the calcined powders composed of mono-dispersive, nanometer size particles. The polycrystalline behaviour of the material on scales; 21, 50 and 100 nm are shown in **Figures 2b – d**. The particle size estimated by TEM and XRD peak broadening indicates that the calcined powder composed of mono-dispersive nanocrystalline particles (**Figure 2a**). Such results confirm that citrate route is fairly effective to produce fine powders without any use of esterification agents.

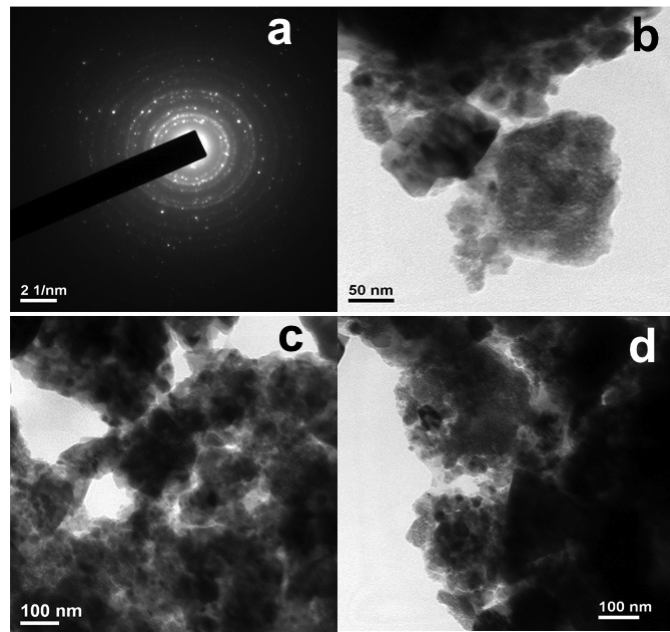


Figure 2. TEM of $\text{Ni}_{1/2}\text{Co}_{1/2}\text{Fe}_2\text{O}_4$.

3.3. Impedance behaviour

Impedance measurement of prepared material has been analysed using impedance analyser at 30 – 200 °C temperature range shown in **Figure 3**. We can see that as temperature increases the impedance value decreases (**Figure 3a**). The magnitude of Z' is dominated with respect to frequency, which decreases with increase of frequency and same with magnitude of Z'' . **Figure 3b** shows the Cole–Cole plot at lower scale, which indicates the clear evidence of the bulk as well as grain boundary behaviour of the material that shows the porous nature of material. Conductivity of the sample calculated at room temperature was $3.234 \cdot 10^{-5} \text{ S/cm}$. Bulk and grain boundary resistivity of the samples at different temperatures are quoted in **Table 2**.

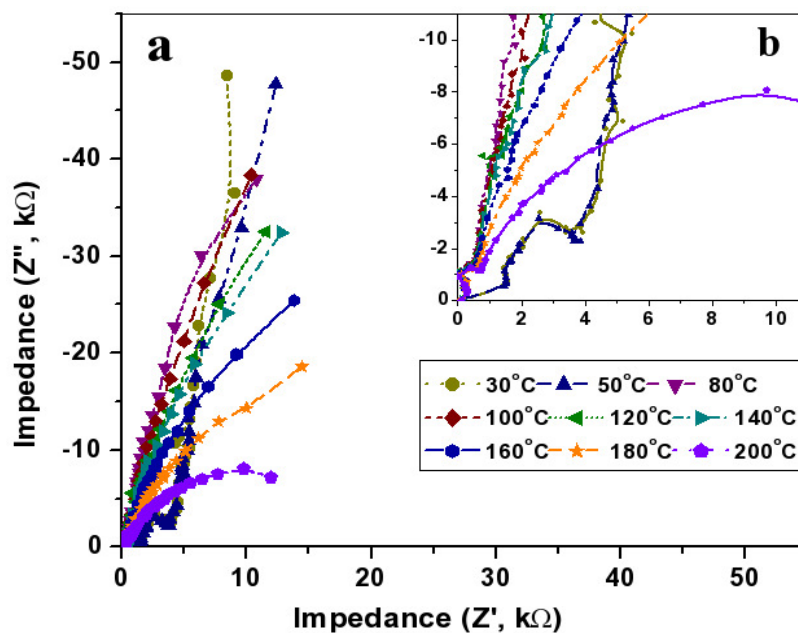


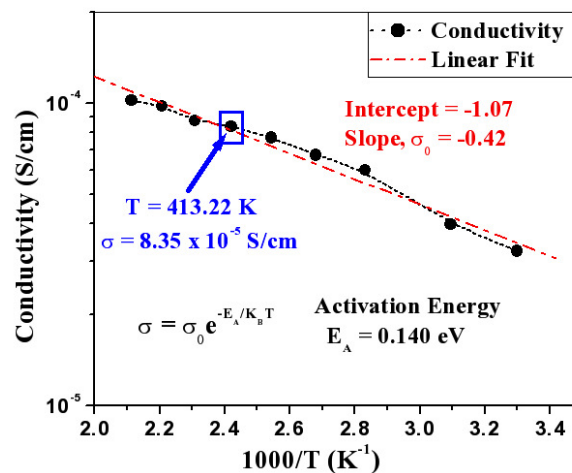
Figure 3. Impedance spectrum of prepared ferrite samples.

Table 2. Resistivity of material with temperature.

Temperature, °C	Bulk resistivity, Ohm · cm	GB resistivity, Ohm · cm
30	$3.09 \cdot 10^4$	$8.93 \cdot 10^5$
50	$2.52 \cdot 10^4$	$6.97 \cdot 10^5$
80	$1.67 \cdot 10^4$	$6.00 \cdot 10^5$
100	$1.49 \cdot 10^4$	$5.89 \cdot 10^5$
120	$1.30 \cdot 10^4$	$5.10 \cdot 10^5$
140	$1.20 \cdot 10^4$	$4.28 \cdot 10^5$
160	$1.15 \cdot 10^4$	$2.90 \cdot 10^5$
180	$1.03 \cdot 10^4$	$1.25 \cdot 10^5$
200	$9.83 \cdot 10^3$	$8.24 \cdot 10^4$

3.4. Conductivity and activation energy

The conductivity of the material at various temperature $\log \sigma$ is plotted with respect to $1000/T$ (Figure 4), the slope of the plot gives the constant value and the activation energy obtained using Arrhenius equation with $E_A = 0.140$ eV.

**Figure 4.** Arrhenius plot of ferrite sample.

3.5. Dielectric constant variation with frequency

Figure 5 shows the variation of dielectric constant of the prepared Ni – Co ferrite with frequency at varying temperatures. We see that as temperature increases, the dielectric constant increases at lower frequencies (100 kHz) but as frequency increase the dielectric constant decreases. From Figure 5 we can see that the polarization effect is taking places at 5, 10 and 12 MHz frequencies, this show the presence of interfacial and dipolar polarization effect at high frequencies. The variations of dielectric constant of ferrite have mainly been attributed to the variation of Fe ions, the greater the Fe concentration, higher the expected dielectric constant [9]. The polarizability of atoms with a larger number of electrons in their outer shells is more than that of atoms having relative fewer electrons. The smaller dielectric constant value at higher frequency in the present work may possibly be explained in terms of smaller grain size. The dielectric constant of the material at high temperature and high frequency is tending towards the dielectric constant of the material at low temperature and lower frequencies.

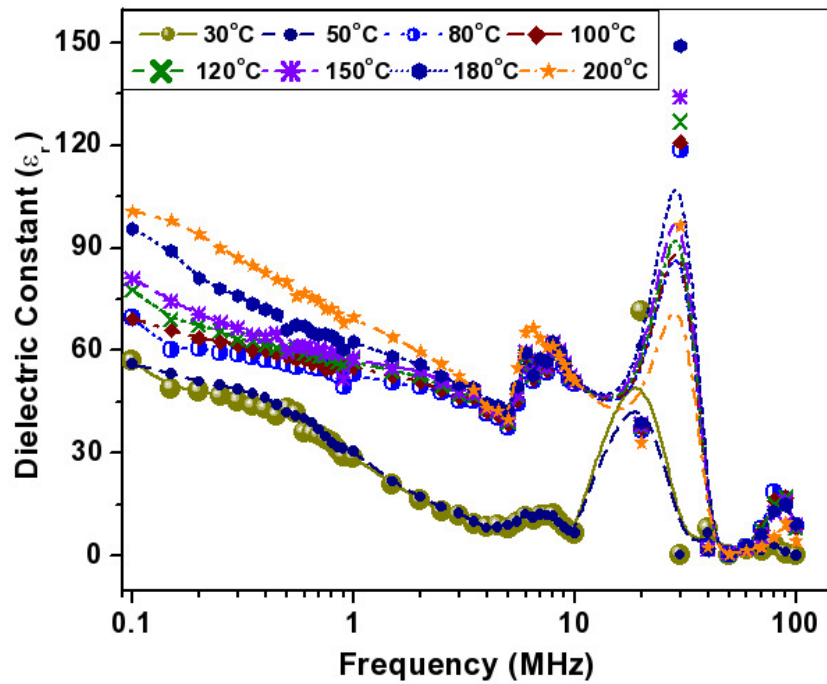


Figure 5. Dielectric constant variation with frequency at different temperatures.

3.6. Magnetic loss tangent ($\tan \delta$)

The $\tan \delta$ value of the sample has been calculated using equation (16) and the variation with frequency is shown in **Figure 6**. Permeability of the ferrite is mainly contributed by spin rotation and the spin in ferrite precess with a certain frequency ω_p known as the larmor frequency. When $\omega = \omega_p$ the maximum value of permeability is obtained and for $\omega > \omega_p$, permeability decreases. From **Figure 6**, there is certain change occurs in $\tan \delta$ value at frequency range of 8 – 10 MHz, this change is caused by the change in spin rotation because of larmor frequency. These values could be correlated with the resonance phenomena in ferrite.

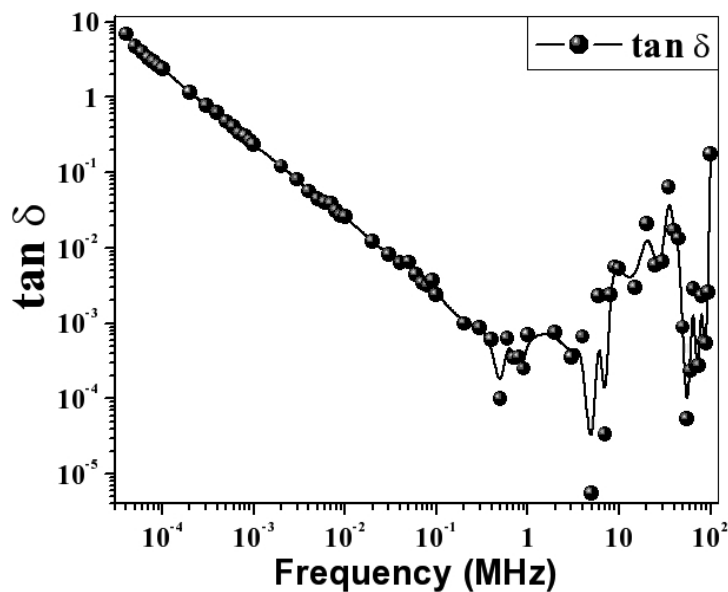


Figure 6. Tangent delta plot with respect to frequency x and y axes are plotted on log scale.

3.7. Shielding effectiveness

The shielding parameters of prepared $\text{Ni}_{1/2}\text{Co}_{1/2}\text{Fe}_2\text{O}_4$ material with frequency are shown in **Figure 7**. The absorption and reflections losses were calculated using equations (9) and (10) and the addition of these two parameters gives the value of shielding effectiveness at 100 kHz – 100 MHz frequency ranges. From the **Figure 7**, we see that, the shielding effectiveness of our laboratory prepared material is completely depends on the reflection loss at 100 kHz – 100 MHz frequency range because the value of absorption loss is in $10^{-3} - 10^{-1}$ range. **Figure 8** shows the shielding effectiveness of our prepared Ni – Co ferrite samples at different temperature ranges. The increase in temperature increases the conductivity of the sample exponentially and the shielding effectiveness is calculated as a function of conductivity and frequency using equation (12).

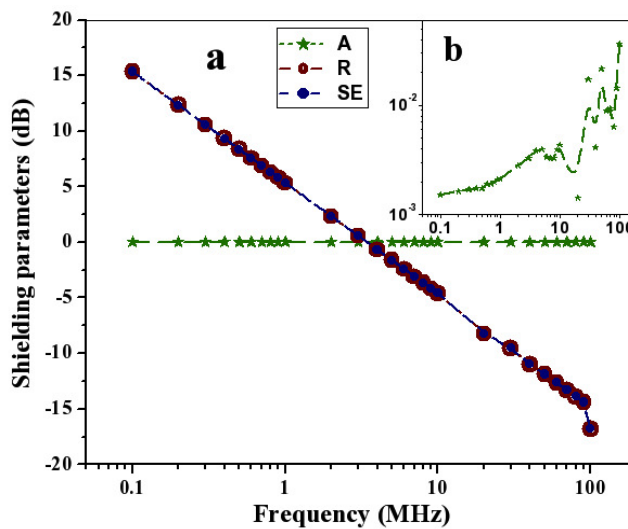


Figure 7. Variation of shielding parameters with frequency. (a) absorption loss (A), reflection loss (R) and shielding effectiveness (SE) with respect to frequency – frequency is plotted on log scale; (b) absorption loss variation with frequency.

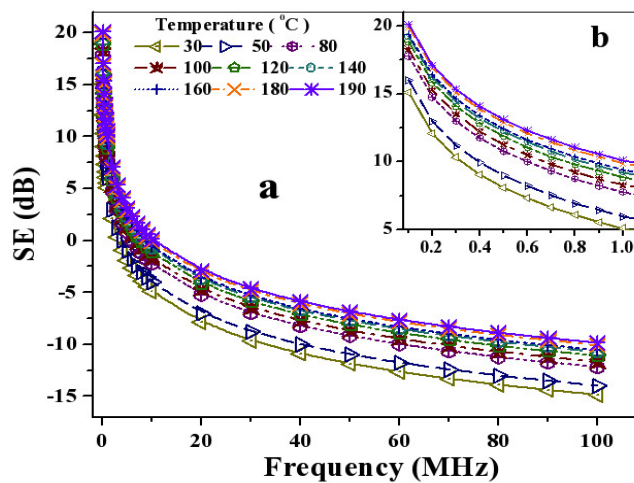


Figure 8. Variation of shielding effectiveness (SE) with frequency. Shielding effectiveness calculation based on equation (12) for composite materials as a function of conductivity and frequency with varying temperature. (a) SE variation at frequency 100 kHz – 100 MHz range; (b) SE variation at 100 kHz – 1 MHz frequency range.

4. Summary and conclusions

The monodispersiveness of the prepared nickel–cobalt ferrite powders were confirmed by TEM measurement and the calculated powder size is 27.7 nm using Scherer's formula. The activation energy of the samples is about 0.140 eV and the sample has semi-conducting behaviour. The magnetic loss measurement calculated with frequency and shows the resonance phenomenon through spin rotation about 8 MHz frequencies. The SE calculated at frequencies 100 kHz – 100 MHz and temperature 30 °C is 15 dB to – 17 dB while the SE calculated, as a function of conductivity with different temperature is 20 to – 15 dB. The calculated SE of the material decrease with frequency and it is strongly influenced with the reflection factor in these frequency ranges. We can see that in 100 kHz – 100 MHz frequency range the absorption loss is not so effective in comparison to the reflection loss while as frequency increasing the absorption loss factor taking place.

References

1. P. B. Jana, K. Mallick, S. K. De. Effects of sample thickness and fiber aspect ratio on EMI shielding effectiveness of carbon fiber filled polychloroprene composites in the X-band frequency range. *IEEE Trans. Electromagn. Compatibility* 34 (1992) 478-481.
2. R. G. Chandran, R. M. Cursetji. Development of an EMI shielding ferrite: A case study. In: *Proc. Int. Conf. Electromagn. Interference & Compatibility*. 1999, 8C.7: 380-383.
3. Metal Textile Corporation: http://www.metexcorp.com/emirfi_theory.cfm.
4. E. Håkansson, A. Amiet, S. Nahavandi, A. Kaynak. Electromagnetic interference shielding and radiation absorption in thin polypyrrole films. *Eur. Polymer J.* 43 (2006) 205-213.
5. A. Kaynak. Electromagnetic shielding effectiveness of galvanostatically synthesized conducting polypyrrole films in the 300 – 2000 MHz frequency range. *Mater. Res. Bull.* 31 (1996) 845-860.
6. Park, Sung-Hoon et al. (2009) Enhanced electromagnetic interference shielding through the use of functionalized carbon nanotube-reactive polymer composites. http://nanomaterials.ucsd.edu/Publications_files/IEEE%20formatted_CNT_Polymer%20composites_Bandaru_Sep14_2009.pdf.
7. D. K. Tiwari, L. M. Villaseñor–Cendejas, A. K. Thakur. Magnetic properties of nanocrystalline nickel–cobalt ferrites ($\text{Ni}_{1/2}\text{Co}_{1/2}\text{Fe}_2\text{O}_4$). *Int. J. Thermophys.* 34 (2013) 1838-1843.
8. S. Singhal, J. Singh, S. K. Barthwal, K. Chandra. Preparation and characterization of nanosize nickel-substituted cobalt ferrites ($\text{Co}_{1-x}\text{Ni}_x\text{Fe}_2\text{O}_4$). *J. Solid State Chem.* 178 (2005) 3183-3189.
9. A. Verma, D. C. Dubey. Processing of nickel–zinc ferrites via the citrate precursor route for high frequency applications. *J. Am. Ceram. Soc.* 88 (2005) 519-523.

CHARACTERIZATION OF AlN THIN FILMS ANNEALED BY CO₂ LASER

J.-Sh. Chen, J.-Y. Wang, Y.-J. Yao, Ch.-T. Chiang

Chung Yuan Christian University
Chung Li, Taiwan – Republic of China
jschen123@gmail.com

Accepted September 19, 2013

1. Introduction

AlN is wurtzite structure material with the largest direct band gap (6.2 eV) in III–V compound [1]. It possesses excellent properties of thermal conductivity, surface acoustic wave velocity, piezoelectric coefficient, chemical stability and high refractive index. These characteristics make it be a proper material for applications of surface acoustic wave (SAW) device [2], UV optoelectronic device [3], high electron mobility transistor [4], high frequency and power device [5], etc.

Compared with conventional tube furnace (CTF) and rapid thermal annealing (RTA) method, the rapid localized heating process of scanning focused CO₂ laser beam can reduce thermal expansion, lattice mismatch and film cracks issues caused in CTF and RTA annealing process [6 – 9].

2. Experiment

We use purity 99.999 % aluminum as the target of sputtering system. The sputtering ion gas and reactive ion gas are purity 99.999 % argon and purity 99.999 % nitrogen. The flow rate ratio of Ar / N₂ is 50 %. The base pressure and deposition pressure of sputtering chamber are $7 \cdot 10^{-8}$ torr and 1 mtorr, respectively. The substrates temperature of deposition are room temperature. The sputtering DC powers are operated at 225 and 210 W for sapphire and Si (111) substrates, respectively. The thickness of AlN films are 200 nm on sapphire substrate and 400 nm on silicon substrate. All substrates are cleaned respectively with acetone, methanol, and isopropanol. Additionally, the Si (111) substrate is cleaned by BOE to remove the native oxide of its surface. The scan power of CO₂ laser annealing is 12 W for AlN / sapphire and 30 W for AlN / Si (111). The CO₂ laser scan rates are 2.5 and 3 mm / s for samples of sapphire substrate and Si (111) substrate. The X-ray diffraction (XRD), atomic force microscopy (AFM) and ellipsometer are used dividedly to characterize the crystallinity, surface roughness and refractive index of AlN thin films.

3. Results and discussion

3.1. X-ray diffraction – θ - 2θ scan

Figures 1 and 2 are XRD θ - 2θ scans of AlN films grown on sapphire and Si (111) substrates at room temperature without annealing and with CO₂ laser annealing. From the

results, the XRD (002) preferred orientation of AlN films are increased after CO₂ laser annealing. It indicates that AlN films and substrates absorb the energy of CO₂ laser, then inducing AlN films recrystallized to improve the crystallinity of AlN films.

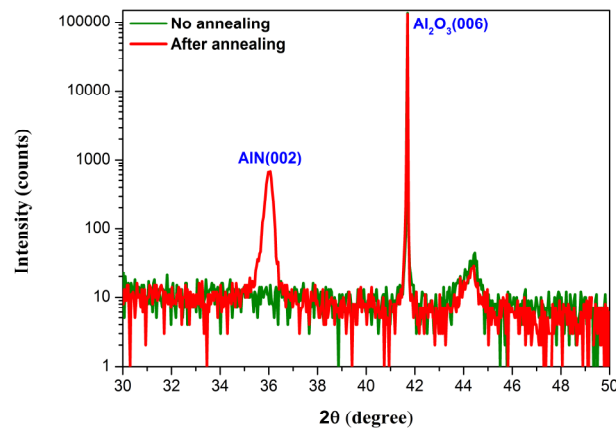


Figure 1. XRD θ - 2θ scan of a 200 nm AlN film grown on Al₂O₃ substrate at room temperature before and after CO₂ laser annealing.

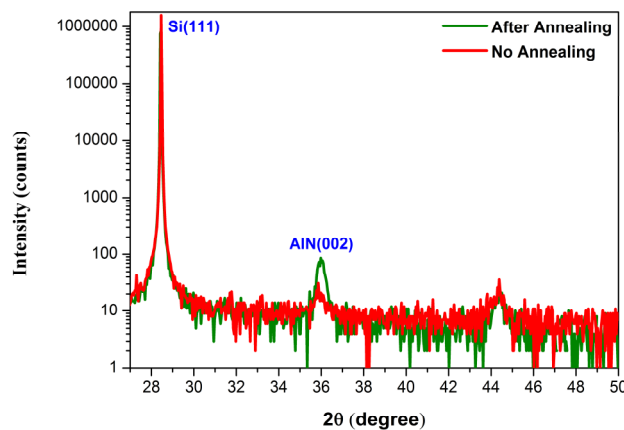


Figure 2. XRD θ - 2θ scan of a 400 nm AlN film grown on Si (111) substrate at room temperature before and after CO₂ laser annealing.

3.2. X-ray diffraction – rocking curve

Figures 3 – 5 are the rocking curves (ω scans) of the AlN films grown on sapphire and Si (111) substrates at room temperature without annealing and with CO₂ laser annealing. **Figure 3** is the AlN film grown on Sapphire after annealing, the FWHM of the rocking curve is about 2.717° following the θ - 2θ scan. The non-annealing AlN film grown on sapphire at room temperature has no (002) crystallization, so it does not have the result of rocking curve. **Figures 4** and **5** are the rocking curves (ω scans) of AlN film grown on Si (111). From these results, the crystallization of non-annealing AlN film is not good, so the FWHM of rocking curve is broad and we can't estimate the FWHM. After CO₂ laser annealing, the FWHM becomes 10.26°, and the counts of peak is higher than non-annealing condition. From **Figures 3 – 5**, the FWHMs of rocking curves become smaller after annealing. It proves the crystallinity of AlN film becomes better after CO₂ laser annealing, so to achieve improving the quality of AlN film.

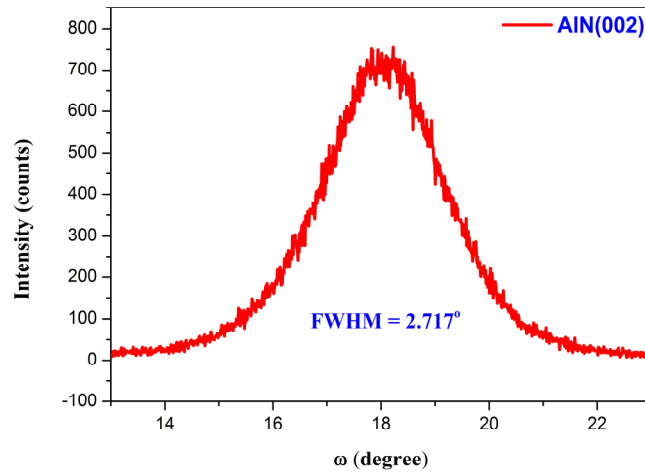


Figure 3. ω scan of a 200 nm AlN film grown on Al_2O_3 substrate at room temperature after CO_2 laser annealing.

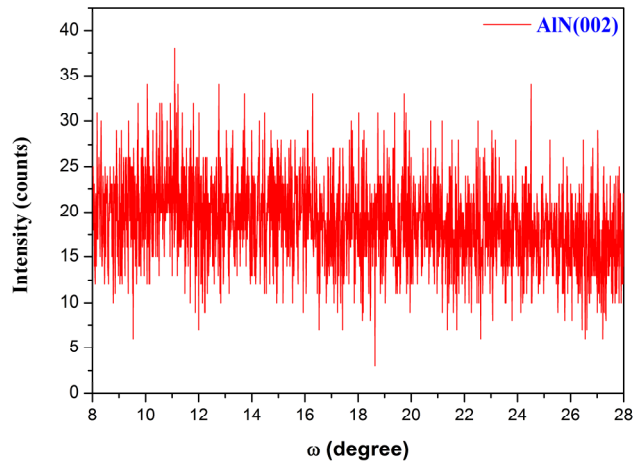


Figure 4. ω scan of a 400 nm AlN film grown on Si (111) substrate at room temperature before CO_2 laser annealing.

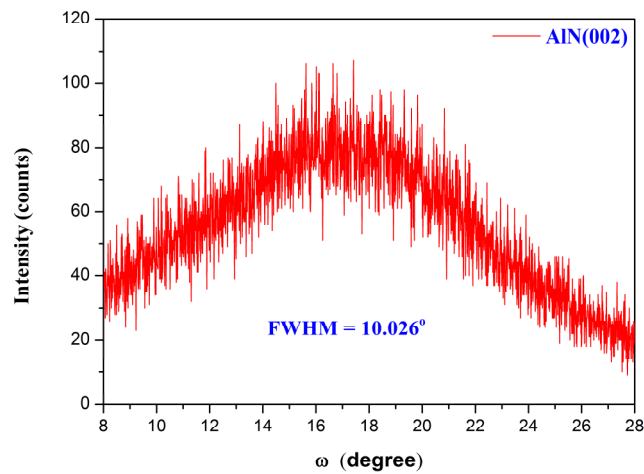
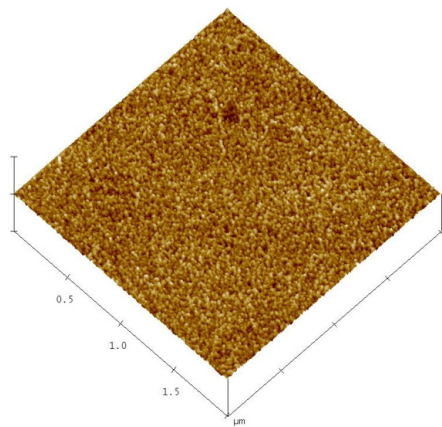


Figure 5. ω scan of a 400 nm AlN film grown on Si (111) substrate at room temperature after CO_2 Laser annealing.

3.3. The surface morphology and roughness of AlN film

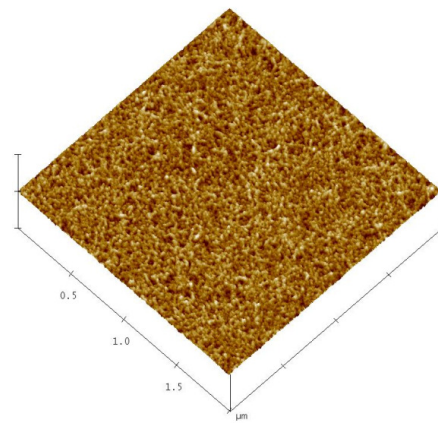
Figures 6 and 7 are AFM measurements of 200 nm thickness AlN film grown on sapphire substrate at room temperature before annealing and after 12 W and 2.5 mm / s scanning velocity CO₂ laser annealing. According to AFM images, the surface roughnesses of AlN films before annealing and after annealing are 0.600 and 0.549 nm.

Figures 8 and 9 are AFM measurements of 400 nm thickness AlN film grown on Si (111) substrate at room temperature before annealing and after 30 W and 3.0 mm / s scanning velocity CO₂ laser annealing. According to AFM images, the surface roughnesses of AlN films before annealing and after annealing are 0.672 and 0.679 nm.



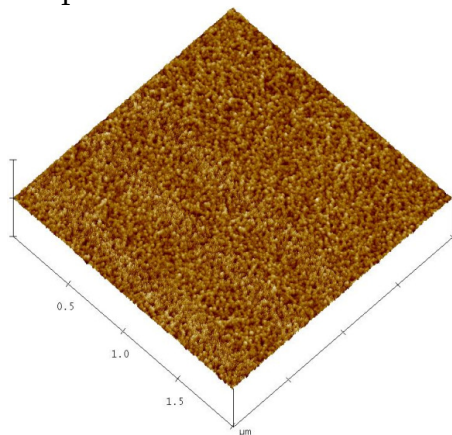
RMS = 0.600 nm

Figure 6. AFM image of non-annealing AlN film grown on sapphire substrate at room temperature for 200 nm thickness.



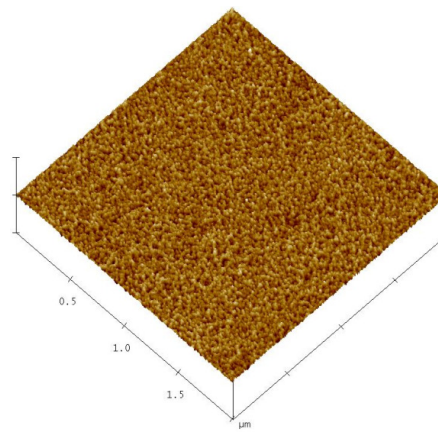
RMS = 0.54 nm

Figure 7. AFM image of annealing AlN film grown on sapphire substrate at room temperature for 200 nm thickness.



RMS = 0.672 nm

Figure 8. AFM image of non-annealing AlN film grown on Si (111) substrate at room temperature for 400 nm thickness.



RMS = 0.67 nm

Figure 9. AFM image of annealing AlN film grown on Si (111) substrate at room temperature for 400 nm thickness.

From **Figures 6 – 9** results, the roughness of samples after CO₂ laser annealing don't have any obviously decay. Compared with CFT and RTA methods. CFT method causes film surface interacting with oxygen, then increases the surface roughness. Besides, the annealing AlN films grown on Si (111) appear cracks, due to the lattice mismatch and thermal expansion coefficient between AlN films and substrates are huge difference [10]. When using RTA over 800 °C, the surface roughness become worse [6, 8].

From the above results, the crystallinity of AlN films are improved and the surface roughness of AlN films do not become worse after CO₂ laser annealing. Compare CO₂ laser annealing with CFT and RTA methods, CO₂ laser is to anneal thin film locally, then to scan the whole sample surface, CFT and RTA are to anneal the whole films in the same time. Therefore, CO₂ laser annealing can avoid causing cracks and poorer surface roughness of AlN / sapphire and AlN / Si (111) films. The surface roughness of AlN films will influence the application of devices. For example, surface roughness may cause loss in the propagation of sound wave [11]. The AlN films surface roughness by sputtering at room temperature is about 0.6 nm for a flatter substrate surface in this paper. It's a good property for application in the future.

3.4. The refractive index of AlN film annealing by CO₂ Laser

Figures 10 and 11 are the refractive index comparisons of AlN film grown on sapphire and Si (111) substrates at room temperature before annealing and after annealing. The annealing conditions are the same with AFM measurement samples. These measurements show that the refractive indices of AlN films are 2.017 and 2.019 at $\lambda = 550$ nm before annealing for sapphire and Si (111) substrates. The refractive indices of AlN films grown on sapphire and Si (111) substrates after annealing are obviously increasing than the results before annealing. These results indicate that the crystallinity of thin film is better, the porous structure in film is less, and the film compactness is better after CO₂ laser annealing.

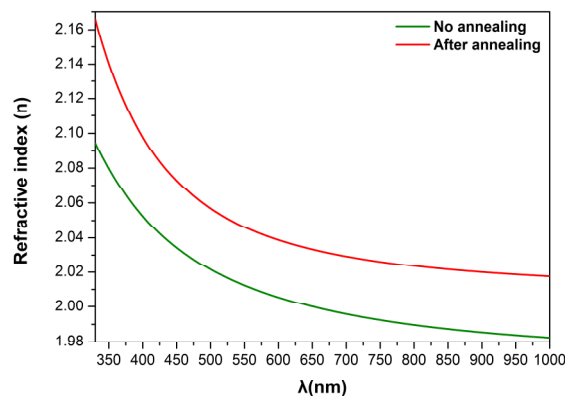


Figure 10. The refractive index comparison of AlN film grown on sapphire substrate at room temperature before annealing and after annealing.

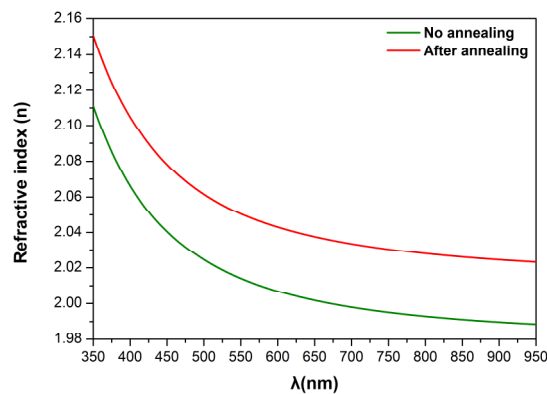


Figure 11. The refractive index comparison of AlN film grown on Si (111) substrate at room temperature before annealing and after annealing.

4. Conclutions

From XRD ω scan results, the FWHMs of rocking curve are decreased and prove the improvement of AlN films *c*-axis crystallinity quality after CO₂ laser annealing. From the AFM results, the roughness of samples after CO₂ laser annealing don't have any obviously decay and prove that CO₂ laser annealing can avoid causing crack and poorer surface roughness of AlN / sapphire and AlN / Si (111) films. The results of ellipsometer show the refractive indices of AlN films after CO₂ laser annealing are increasing. Indicating CO₂ laser annealing improving the compactness of AlN films. All these results show CO₂ laser annealing for AlN films will be a good method to improve its properties and reduce any possible negative effects.

References

1. C. Morosanu, T. A. Stoica, T. F. Stoica, D. Necsoiu, M. Popescu. Optical, Electrical and structural properties of AlN thin films. In: Semicond. Conf. (1995) 183.
2. C. Caliendo, P. Imperatori. High-frequency, high-sensitivity acoustic sensor implemented on AlN / Si substrate. Appl. Phys. Lett. 83 (2003) 1641.
3. J. J. Zhou, R. L. Jiang, X. L. Ji, B. Wen, P. Chen, S. J. Chua, R. Zhang, B. Shen, Y. D. Zheng. Effects of the polarization fields on the responsivity of the AlN / GaN photodetectors. In: 13th Int. Conf. Semicond. & Insul. Mater. (2004) 281.
4. M. Germain, M. Leys, S. Boeykens, S. Degroote, W. Wang, D. Schreurs, W. Ruythooren, K.-H. Choi, B. van Daele, G. van Tendeloo, G. Borghs. High electron mobility in AlGaIn / GaN HEMT grown on sapphire: Strain modification by means of AlN interlayers. Mater. Res. Soc. Symp. Proc. 798 (2004) Y10.22.1.
5. C.-M. Yang, K. Uehara, S.-K. Kim, S. Kameda, H. Nakase, K. Tsubouchi. Highly *c*-axis-oriented AlN Film using MOCVD for 5 GHz-band FBAR filter. In: IEEE Ultrasonics Symp. (2003) 170.
6. J. P. Kar, G. Bose, S. Tuli. Influence of rapid thermal annealing on morphological and electrical properties of RF sputtered AlN films. Mater. Sci. Semicond. Proc. 8 (2005) 646.
7. L. Vergara, J. Olivares, E. Iborra, M. Clement, A. Sanz-Hervás, J. Sangrador. Effect of rapid thermal annealing on the crystal quality and the piezoelectric response of polycrystalline AlN films. Thin Solid Films 515 (2006) 1814.
8. B. Liu, J. Gao, K. M. Wu, C. Liu. Preparation and rapid thermal annealing of AlN thin films grown by molecular beam epitaxy. Solid State Commun. 149 (2009) 715.
9. L. Riuttanen. Thermal Annealing of AlN Thin Films Fabricated by Plasma-Enhanced Atomic Layer Deposition for GaN Epitaxy (Thesis). Aalto Univ. Sch. Sci. (2010).
10. J. N. Stranski, L. Krastanov. Theory of orientation separation of ionic crystals. Ber. Akad. Wiss. Wien. 146 (1938) 797.
11. M. B. Assouara, O. Elmazria, P. Kirsch, P. Alnot. High-frequency surface acoustic wave devices based on AlN / diamond layered structure realized using e-beam lithography. J. Appl. Phys. 101 (2007) 114507 1-5.

ANALYSIS OF DIELECTRIC RESONATOR ANTENNAS (DRA)
BASED ON COMPLEX PEROVSKITE CNBTOX – $\text{Ca}(\text{Nb}_{1/2}\text{Bi}_{1/2})_x\text{Ti}_{1-x}\text{O}_3$

A. D. S. Bruno Costa^{1,2}, R. C. S. Costa²,
F. W. de O. Amarante², A. S. B. Sombra²

¹ Physics Institute
Cidade Universitária São Paulo
São Paulo, Brazil
antonia_daniele@yahoo.com.br

² LOCEM – Teleinformatics Department
Federal University of Ceará
Fortaleza, Brasil

Accepted September 19, 2013

1. Introduction

The rapid development of microwave dielectric materials as important materials operating in microwave frequencies have been extensively applied in the fields as resonators, antennas, cellular phones, wireless local area networks, direct broadcasting satellite and the global position system and many others [1]. These fields require new materials with singular and important characteristics such as small size, low power loss, and temperature stable microwave components [2, 3]. Another challenge in these materials is the high temperature sintering required, usually above 1400 °C [4, 5].

The dielectric resonator (DR) has greatly influenced the microwave-based wireless communication industry by reducing the size, weight, and cost. The DR also presents reasonable bandwidth, low profile, high radiation efficiency, and ease of excitation [6]. DR ceramics also enable the filter units in the mobile telephone base stations to remove unwanted sidebands and secondary signals, ensuring transmission of high quality primary signals with minimum interference [7].

The feed mechanisms vary from probes, slot, microstrip lines, and coplanar waveguide [8, 9]. Then, various physical characteristics such as input impedance and radiation patterns can be controlled through different choices for the parameters and feed mechanisms [10].

DR ceramics offers very high radiation efficiency due to its low dielectric loss and it has no metallic loss [11]. In fact, for conventional metallic resonators, the conductive loss increases as frequency increases, diminishing its radiation efficiency [12]. The DR present high radiation efficiency since there is little or no loss due the presence of metals. The use of DRs beyond the microwave band and up to the millimeter-wave region [13], is under study in the literature for applications in microwave electronics.

The change of position between the DR and the excitation probe, may also significantly affect the resonator performance, not only because of the resulting possible change in resonant

frequency, but also because of the change in the coupling factor between the resonator and the excitation probe [12].

The perovskite ceramic CaTiO_3 has been widely used in the electronic devices [14]. This ceramic exhibit high dielectric ($\epsilon_r = 162$), low dielectric loss and high temperature coefficient ($\tau_f \approx 850 \text{ ppm} / ^\circ\text{C}$) [15, 16]. Some authors reported that complex perovskites with general formula $\text{Ca}(\text{X}_{1/2}\text{Nb}_{1/2})\text{O}_3$ present better dielectric properties than calcium titanate [17, 18].

This paper presents the numeric simulation of a probe-feed cylindrical DRA of a modified perovskite ceramic based on the substitution of Ti^{4+} in CaTiO_3 by $(\text{Nb}^{5+}_{1/2}\text{Bi}^{3+}_{1/2})$. This paper studies the effects at antenna features in the 2 – 6 GHz frequency range (E, F, and G microwave bands) as concentration range of b-site substitution in CNBTOX ($\text{CaTi}_{1-x}(\text{Nb}_{1/2}\text{Bi}_{1/2})_x\text{O}_3$) increases (for $x = 0$ through 0.8). The DR is excited by a coaxial probe placed at different positions to achieve the position with less air gap between the DR and the ground plane.

2. Experimental methods

This section describes details of methods used to produce the sample materials and the experimental.

The oxides and carbonates were weighed according to the compositions of each sample. The mixtures were high-energy ball milling during 4 h using a high energy planetary ball mill (Fritsch Pulverisette 6). The rotation speed of the disks carrying the sealed vials was 400 rpm. The milled powders were dried and then calcinated at 900°C for 5 h. The calcinated powders were mixed with an appropriate amount of glycerine (5 wt. %) as a binder and pressed into cylindrical disks of diameter 15 mm and height about 7.5 mm at a pressure of $1.5 \text{ ton} / \text{cm}^2$. These pellets were preheated at 600°C for 1 h to expel the binder and then sintered at temperature of 1100°C during 3 h.

2.1. Resonator configuration

The resonator consist of the cylindrical disc of the dielectric based on CNBTO placed above a conducting ground plane ($35.5 \text{ cm} \times 30 \text{ cm} \times 2.14 \text{ mm}$), and excited by a coaxial probe, as shown in **Figure 1**.

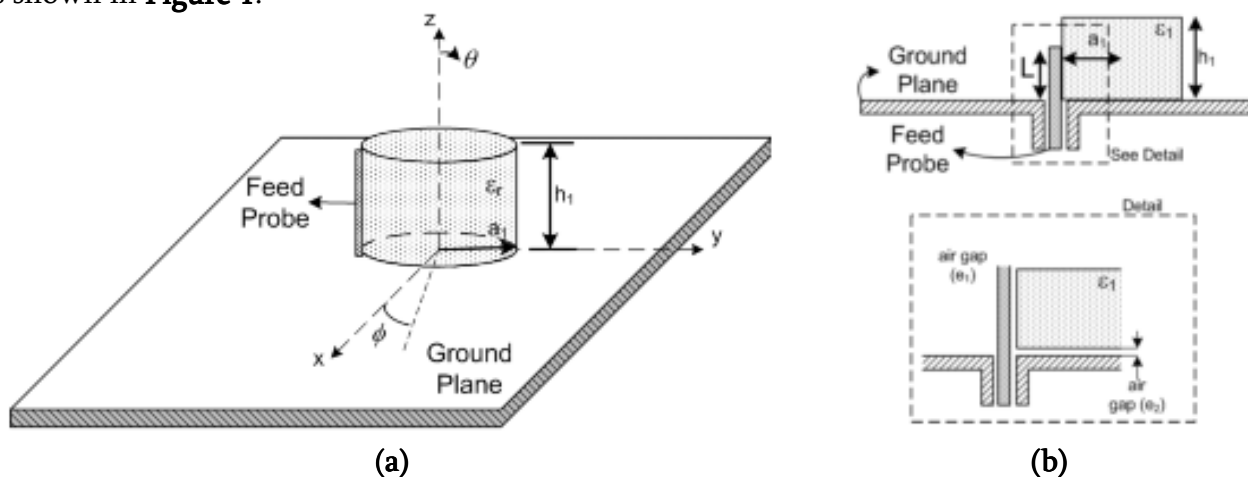


Figure 1. The geometry of the cylindrical DR.

The lateral of the cylindrical DR is placed against a coaxial probe, which excites the $HEM_{11\delta}$ mode. The DR is placed above a conducting ground plane, and excited by a coaxial probe. The coaxial probe goes through the ground plane and is connected to a SMA connector. In **Figure 1a**, the DR has radius a , height h and dielectric permittivity k . The probe is located on x axis at $x = a$ and $\varphi = 0$.

The resonant frequency can vary with presence of an air gap between the DR and the metallic conductors. This effect has been thoroughly studied by Junker et al. [19] and Rocha et al. [12]. To illustrate the effect, the resonator configuration used in this paper assumes a existence of two parameters associated to the air gap ϵ_1 between the dielectric and the probe, and ϵ_2 between the dielectric and the ground plane, as defined in **Figure 1**.

2.2. Resonant frequency measurement

Because of the highly resonant structure of the DR, the input impedance $Z = R + jX$ at the feeder port presents a frequency response due to the resonant response of each mode. Neglecting the overlap between the first and second mode, at the resonant frequency f_0 , the resistance R shows a maximum and the reactance X is null.

According with [12], the resonant frequencies can also be determined from the minimum of the return loss parameter (S_{11}) due its relationship to Z , given by

$$S_{11} = \frac{z-1}{z+1} \quad \text{with} \quad z = \frac{Z}{R_c} .$$

When antenna is resonating, the return loss is high (different than 0 dB). With this assumption, in this paper the produced resonator antennas arrangement were excited by a coaxial probe at the reflection port of a HP8716T network analyser to measure return loss in 1 – 3 GHz frequency band and with it, evaluate the resonant frequency.

2.3. Hakki–Coleman’s experiment

The antenna losses could be represented by quality factor ($Q = 1 / \tan \delta$). Typically, there radiation conduction, dielectric, and surface wave losses. Therefore, the total quality factor is influenced by all of these losses [11]. This property is very required of microwave dielectric, because it is related how easily the dielectrics resonate when the material are irradiated in an electromagnetic wave [20].

The dielectric permittivity is also very important antenna property. It is relationship with size of mobile equipment, time delay and the signal transmission speed [20]. These important dielectrical properties at RF (radio-frequencies) and MW (microwave frequencies) are deduced from the sizes of the sample and the value of the resonant frequency, performing the Hakki and Coleman’s dielectric resonant TE_{011} and $TE_{01\delta}$ methods [21] and later modified by Courtney [22, 23].

A HP 8716ET network analyzer is employed to make the measurements. From the resonant frequency of the TE_{011} mode, the dielectric permittivity (ϵ_r) and loss ($\tan \delta$) are obtained.

3. Numerical simulation

The objective of this study is also a numerical validation of the experimental measurements, shown in **Figure 1**. The frequency response around the first mode ($HEM_{11\delta}$) is determined by the HFSS and the result is compared to the experimental setup. In this procedure, important parameters of the DR were obtained, such as: return loss, input impedance and resonator bandwidth. In the numerical study we calculate the S parameters using a 3D distribution of the fields inside the passive structures. It is based on a FEM method, dividing the model in a great number of small regions, as shown in **Figure 2**.

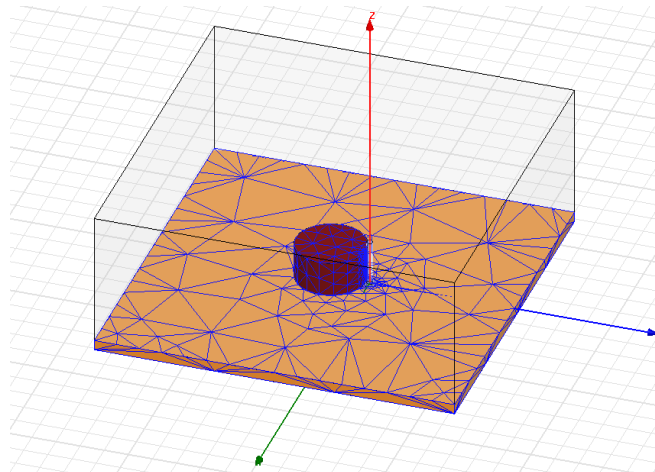


Figure 3. DRA model simulate in HFSS.

As an alternative to the previous eigenmode analysis, the results that will be presented in this paper are issued from a harmonic analysis for which the feeder is excited. This method enables the determination of the port characteristics, such as the input impedance and the return loss. In a single run, the so-called Fast Frequency Sweep provides these quantities in the 1 – 3 GHz.

The results that will be presented in this paper are issued from a harmonic analysis for which the feeder is excited. This method enables the determination of the port characteristics, such as the input impedance and the return loss. In a single run, the so-called fast frequency sweep provides these quantities in the 1 – 5 GHz frequency band.

In order to take into account the effect of an air gap between the probe and the DR the ϵ_1 and ϵ_2 parameters are optimized to complete the simulation with less than 1 % of error.

4. Results and discussions

This section presents the results of operation of the studied samples. The experimental return loss (RL) of the cylindrical DRA constructed from the dielectrics CNBTOX and the numerical fitting using HFSS are presented in **Figure 3**.

For each DRA, several return losses and input resistance measurements were obtained. The result with lower resonance frequency is adopted as the real operation of the produced DRA. The CNBTO1 presents the lowest resonant frequency due its higher permittivity. There is shift in frequency when increase the amount of niobium and bismuth in solid solution.

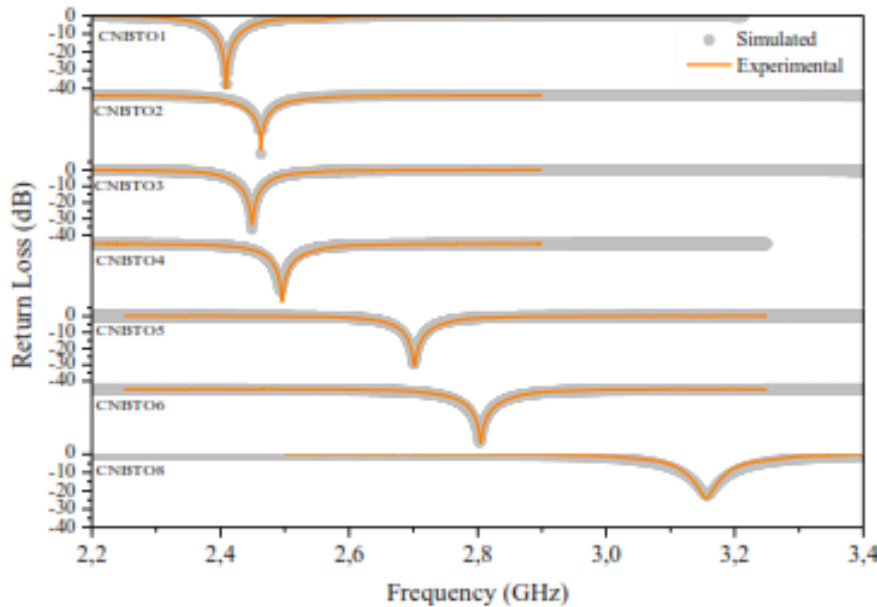


Figure 3. Experimental and calculated return loss (RL) for studied DRAs. For the calculated RL, the geometry and dielectric characteristics were listed in **Table 1**.

The frequency for each the return loss (S_{11}) is minimum, whose values are presented in **Table 1** and compared with calculated values. In Table 1, the dielectric permittivities obtained from the DRA operation are also showed.

Table 1. Simulation parameters.

Amostras	a , mm	h , mm	$a : h$	ϵ_r	HEM _{11δ} , GHZ	e_1	e_2
CNBTO1	8.309	8.300	1.001	58.536	2.408	0.100	0.073
CNBTO2	8.121	8.084	1.010	48.030	2.463	0.075	0.022
CNBTO3	7.729	7.734	0.999	54.409	2.449	0.070	0.021
CNBTO4	7.634	7.346	1.039	57.742	2.496	0.100	0.040
CNBTO5	7.522	6.512	1.155	58.573	2.702	0.080	0.038
CNBTO6	7.409	7.145	1.037	38.728	2.805	0.055	0.014
CNBTO8	7.994	6.951	1.150	28.960	3.156	0.099	0.050

The dielectric permittivities measured by Hakki–Colleman experiment using a HP 8716ET network analyser were used as simulated permittivity (ϵ_r). According to the results, the permittivity reduces as b-site substitution increases, so its resonance frequency increases as x increases.

Figure 4 exhibit simulated and experimental frequencies response of input resistance and impedance of proposed series, using parameters shown in **Table 1**. According to these results, the input impedance becomes more inductive when the permittivity increases. The CNBTO1 sample demonstrates the most inductive behavior (lowest permittivity). For all samples, at the resonant frequency f_0 , the resistance R is maximum and the reactance X is null.

The input impedances for the dielectric resonators obtained in experimental data diverge slightly from simulation curves. In the numerical study, the air gap increase leads to a frequency shift upward. The resistance values oscillate with bismuth content.

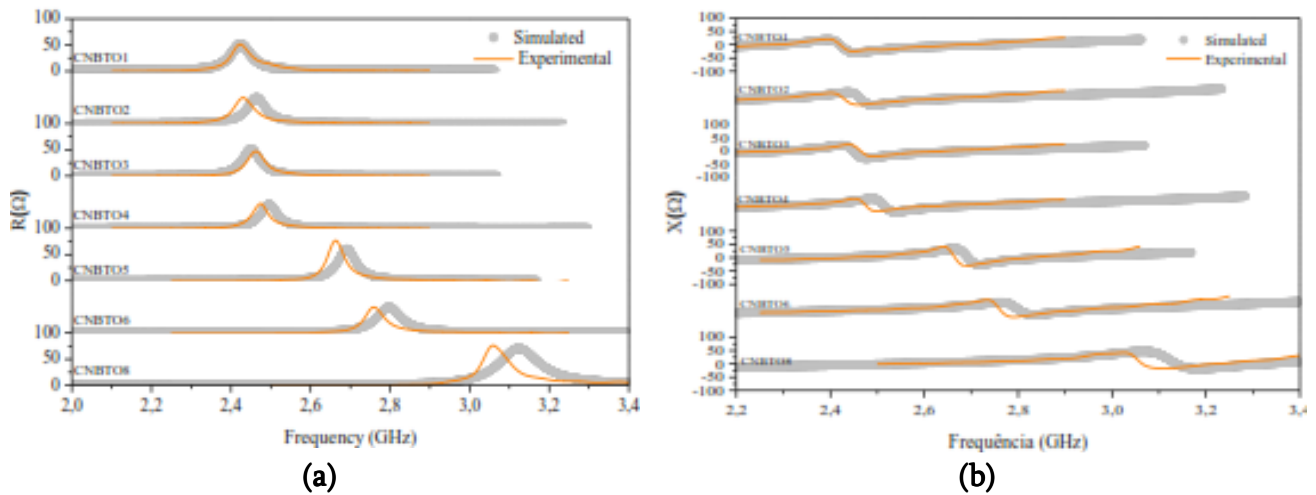


Figure 4. Experimental and calculated input impedance (Z) for CNBTOX series: (a) resistance (R) and (b) reactance (X).

Both simulated and measured values for frequencies resonance, input impedances, and 10 dB bandwidths are presented in **Table 2**. There is a good agreement between the calculated and experimental values of f_0 , whose error percentage are less than 0.2 %. The resistances values is general present also present a satisfactory concordance between experimental and simulated results, with errors amount less than 10 %. Nevertheless, CNBTO5 displays an error of 20.8 %. The return loss of the series were -48 , -41 , -33 , -32 , -30 , -32 , and -24 dB for CNBTO1, CNBTO2, CNBTO3, CNBTO4, CNBTO5, CNBTO6, and CNBTO8, respectively.

Table 2. Experimental and calculated resonant frequencies, input impedances and 10 dB bandwidth of the DRAs for the first mode $HEM_{11\delta}$

Sample	Resonant frequency, GHz		Input resistance at resonance, Ω		Bandwidth (10 dB), MHz		
	Measured	Calculated	Measured	Calculated	Measured	Calculated	Error, %
CNBTO1	2.408	2.409	51.238	51.288	40.094	40.826	3.40
CNBTO2	2.463	2.463	49.510	49.293	45.033	42.856	15.6
CNBTO3	2.449	2.449	51.668	46.981	38.725	35.741	4.81
CNBTO4	2.496	2.493	45.567	47.213	33.173	34.883	1.64
CNBTO5	2.702	2.701	60.735	76.651	38.120	37.309	3.70
CNBTO6	2.805	2.803	48.984	49.115	45.970	50.203	8.51
CNBTO8	3.156	3.157	70.463	76.137	67.677	91.649	17.5

4. Conclusions

In this work, a new electroceramic $\text{Ca}(\text{Nb}_{1/2}\text{Bi}_{1/2})_x\text{Ti}_{1-x}\text{O}_3$ (CNBTOX), with x between 0.1 and 0.8 were investigated in the microwave frequency range. Experimental and theoretical characteristics of the resonator (return loss, bandwidth and input impedance) were in good agreement. The numerical study was done taking into account the air gaps between the dielectric resonator and the metallic conductors. These measurements confirm the possible use of such material for small dielectric resonator antenna.

Acknowledgements

This work was partly sponsored by CELESTICA, Fundação Cearense de Apoio ao Desenvolvimento Científico e Tecnológico (FUNCAP), Coordenação de Aperfeiçoamento de Pessoal de Nível Superior (CAPES), Conselho Nacional de Desenvolvimento Científico e Tecnológico (CNPq) and the U.S. Air Force Office of Scientific Research – AFOSR (FA9550-08-1-0210).

References

1. J. Zhou, R. Li, R. Li, W. Chen. Effect of heterogeneous interface on the microwave dielectric properties of $\text{Ca}(\text{Mg}_{1/3}\text{Nb}_{2/3})\text{O}_3 / \text{CaTiO}_3$ thin films. *Appl. Surf. Sci.* 259 (2012) 29-33.
2. R. Umemura, H. Ogawa, A. Yokoi, H. Ohsato, A. Kan. Low temperature sintering-microwave dielectric property relations in $\text{Ba}_3(\text{VO}_4)_2$ ceramic. *J. Alloys & Comp.* 424 (2006) 388-393.
3. H.-P. Sun, Q.-L. Zhang, H. Yang. Silver cofireble $(\text{Ca}_{0.9}\text{Mg}_{0.1})\text{SiO}_3$ microwave dielectric ceramics with $\text{Li}_2\text{CO}_3 - \text{Bi}_2\text{O}_3$ additive. *Ceram. Int.* 35 (2009) 637-641.
4. G. Dou, D. Zhou, M. Guo, Sh. Gong. Low-temperature sintered $\text{Zn}_2\text{SiO}_4 - \text{CaTiO}_3$ ceramics with near-zero temperature coefficient of resonant frequency. *J. Alloys & Comp.* 513 (2012) 466-473.
5. L. Wang, Q. Sun, W. Ma, Zh. Huan. Microwave dielectric characteristics of $\text{Li}_2(\text{Mg}_{0.94}\text{M}_{0.06})\text{Ti}_3\text{O}_8$ ($\text{M} = \text{Zn}, \text{Co}, \text{and Mn}$) ceramics. *Ceram. Int.* 39 (2013) 5185-5190.
6. Y.-B. Chen. New dielectric material system of $\chi\text{La}(\text{Mg}_{1/2}\text{Ti}_{1/2})\text{O}_3 - (1-\chi)\text{SrTiO}_3$ in the microwave frequency range. *J. Alloys & Comp.* 491 (2010) 330-334.
7. R. Freer, F. Azough. Microstructural engineering of microwave dielectric ceramics. *J. Euro. Ceram. Soc.* 28 (2008) 1433-1441.
8. Zh. Peng, H. Wang, X. Yao. Dielectric resonator antennas using high permittivity ceramics. *Ceram. Int.* 30 (2004) 1211-1214.
9. A. Buerkle, K. Sarabandi, H. Mosallaei. Compact slot and dielectric resonator antenna with dual-resonance, broadband characteristics. *IEEE Trans. Anten. & Propag.* 53 (2005) 1020-1027.
10. A. Petosa. *Dielectric Resonator Antenna Handbook*. Norwood: Artech House (2007).
11. Y.-B. Chen. Microwave dielectric properties of $0.95\text{MgTiO}_3 - 0.05\text{CaTiO}_3$ for application in dielectric resonator antenna. *J. Alloys & Comp.* 471 (2009) 347-351.
12. H. H. B. Rocha, F. N. A. Freire, R. C. S. Costa, R. S. T. M. Sohn, G. M. Y. Orjubin, C. C. M. Junqueira, T. Cordaro, A. S. B. Sombra. Dielectric resonator antenna operation of the magnetodielectric Composites $\text{Cr}_{0.75}\text{Fe}_{1.25}\text{O}_3$ (CRFO) / $\text{Fe}_{0.5}\text{Cu}_{0.75}\text{Ti}_{0.75}\text{O}_3$ (FCTO). *Microwave & Opt. Technol. Lett.* 49 (2007) 409-413.
13. A. A. Kishk, X. Zhang, A. W. Glisson, D. Kajfez. Numerical analysis of stacked dielectric resonator antennas excited by a coaxial probe for wideband application. *IEEE Trans. Anten. & Propag.* 51 (1993) 1996-2006.

14. S. Parida, S. K. Rout, N. Gupta, V. R. Gupta. Solubility limits and microwave dielectric properties of $\text{Ca}(\text{Zr}_x\text{Ti}_{1-x})\text{O}_3$ solid solution. *J. Alloys & Comp.* 546 (2013) 216-223.
15. R. C. S. Costa, A. D. S. Bruno Costa, F. N. A. Freire, M. R. P. Santos, J. S. de Almeida, R. S. T. M. Sohn, J. M. Sasaki, A. S. B. Sombra. Structural Properties of $\text{CaTi}_{1-x}(\text{Nb}_{2/3}\text{Li}_{1/3})_x\text{O}_{3-\delta}$ (CNLTO) and $\text{CaTi}_{1-x}(\text{Nb}_{1/2}\text{Ln}_{1/2})_x\text{O}_3$ (Ln = Fe (CNFTO), Bi (CNBTO)) modified dielectric ceramics for microwave applications. *Physica B* 404 (2009) 1409-1414.
16. A. D. S. Bruno Costa, D. G. Sousa, R. C. S. Costa, F. W de O. Amarante, T. S. M. Fernandes, G. D. Saraiva, M. A. S. da Silva, A. S. B. Sombra. High thermal stability of the microwave dielectric properties of $\text{CaTi}_{1-x}(\text{Nb}_{2/3}\text{Li}_{1/3})_x\text{O}_{3-\delta}$ alloys. *Physica Scripta* 84 (2011) 055701 1-7.
17. A. D. S. Bruno Costa, M. C. Romeu, R. C. S. Costa, T. S. M. Fernandes, F. W. de O. Amarante, M. A. S. da Silva, G. D. Saraiva, A. S. B. Sombra. High thermal stability of microwave dielectric properties of $\text{CaTi}_{1-x}(\text{Nb}_{1/2}\text{Fe}_{1/2})_x\text{O}_3$ ceramics. *J. Adv. Dielec.* 4 (2011) 1-11.
18. S. R. Kiran, G. S. Babu, Ch. Narayana, V. R. K. Murthy, V. Subramanian. Long range B-site cation ordering and Briet–Wigner–Fano line shape of A_{1g} -like Raman mode in $\text{Nd}_{1-x}\text{Sm}_x(\text{Mg}_{0.5}\text{Ti}_{0.5})\text{O}_3$ microwave dielectric ceramics. *Mater. Res. Bull.* 48 (2013) 194-199.
19. G. P. Junker, A. A. Kishk, A. W. Glisson, D. Kajfez. Effect of air gap on cylindrical dielectric resonator antenna operation in TM₀₁ mode. *Electronics Lett.* 30 (1994) 97-98.
20. H. Ohsato. Research and development of microwave dielectric ceramic for wireless communications. *J. Ceram. Soc. Jpn.* 113 (2005) 703-711.
21. B. W. Hakki, P. D. Coleman. A dielectric resonator method of measuring inductive capacities in milimeter range. *IRE Trans. Microwave Theo. & Tech.* 3 (1960) 402-410.
22. W. B. Courtney. Analysis and evaluation of a method of measuring the complex permittivity and permeability of microwave insulators. *IEEE Trans. Microwave Theo. & Technol. MIT* 18 (1970) 476-485.
23. J. Krupka, K. Derzakowski, B. Riddl, J. Baker–Jarvis. A dielectric resonator for measurements of complex permittivity of low loss dielectric materials as a function of temperature. *Measur. Sci. & Technol.* 9 (1998) 1751-1756.

FAST SET-UP OF CLASSICAL MOLECULAR DYNAMICS SIMULATIONS OF NANOMATERIALS USING WOLFFIA

J. O. Sotero–Esteve, F. Matrínez, R. Quiñones, W. Cuadrado, A. de Jesús

Universidad de Puerto Rico en Humacao
Humacao, Puerto Rico
jose.sotero@upr.edu

Accepted September 19, 2013

1. Introduction

Simulations based on the iterative application of Newton's laws have been used to simulate the dynamics of molecule systems for many years. There exist several general purpose molecular dynamics computer programs. They have been optimized for several architectures ranging from common personal computers to massively parallel computers and, more recently, to sophisticated general purpose graphics processing units (GPGPU). However, despite of those technological advances, the process of assembling a simulation of this type is hard. All of these software applications were, and still are, command-line driven and configured by means of editing complex data and configuration files in text format.

In a recent review paper [1] on the state of the art in classical molecular simulations E. Maginn explained that although advances in computer hardware has reduced the time scale to perform simulations in almost all areas of application to a few hours or a few days “setting up a particular calculation can often take longer than the simulation itself” often requiring months of preparations. He concludes that “the human “setup” and “analysis” times for simulation are a major barrier to the more widespread adoption of molecular simulations”. As he also states, “easy-to-use commercial software is available, but in general these closed proprietary codes lack the capabilities and power of modern open source codes”. In fairness, there are a few easy to use computer applications for CMD but they address only a small aspect of the simulation assembly or have a very narrow scope of application.

Moreover, CMDs have reached the nanoscale, even without considering the use of coarse grained representation of matter that may increase feasible simulations by a time and scale by factors from tens to hundreds. Prototypes for nanodevices that have been simulated using CMD include nanopore-based DNA sequencers and supercapacitor membranes among others. Developing CMD simulation systems that enhance productivity and widens its user base will be a major development.

This presentation demonstrates how the use of Wolffia, a recently released [2] open-source graphical user interface for setting up CMDs. After a brief description of the software a test case consisting of developing a simulation that describes several stages of the process of preparing the precursor solution for electrospinning of nanofibers consisting of a mixture of PMMA with carbon nanotubes dispersed in a water-SDS solution. In this way the capability of the software to significantly reduce the preparation time of many CMD simulations is

demonstrated. The implications of the resulting simulation to the electrospinning and to the physical properties of the nanofibers are, however, out of the scope of the presentation and are addressed in a separate paper.

2. Description of the software

Wollfia is a graphical user interface to setup molecular dynamics simulations. The actual execution of the simulation is done with a well established general purpose CMD simulator, currently NAMD [3]. A LAMMPS version is expected to be released in October. However, it is not meant as a graphical front end to any existing software. It runs on Ubuntu 11.04 and later as well as in many Debian-based LINUX distributions and Windows 8. A detailed description of the software, its design and features are being published elsewhere [2]. The software is available at <http://wollfia.uprh.edu/>.

The interface is organized based on four stages of the preparation of CMD simulations: building the system, defining force field parameters, defining a container, minimizing energies and the actual simulation. A visualization area allows the user to monitor the conformation of the molecules as well as plots of the energies, kinetics and messages on the progress of the simulation. **Figure 1** shows the general disposition of the features of the interface. The arrangement of tools serves as a guidance through the preparation CMD simulation without imposing a linear process such as the ones used by wizards.

```

ATOM  3748 CL1  CLF A  1      9.052  2.807  3.761  0.00  0.00      CL
ATOM  3749 CL2  CLF A  1      8.141  5.123  4.524  0.00  0.00      CL
ATOM  3750 CL3  CLF A  1      8.374  4.612  1.867  0.00  0.00      CL
ATOM  3751 O2   LIG A  1     23.202 38.466 19.073  0.00  0.00      O
ATOM  3752 C3   LIG A  1     21.434 36.177 16.401  0.00  0.00      C
ATOM  3753 C3   LIG A  1     22.884 35.921 18.744  0.00  0.00      C

```

Figure 1. Portion of a PDB formatted coordinate file.

The *Build* section is the areas where molecules are incorporated into the system, called *mixture* in Wollfia. Molecules can be incorporated from the *molecule catalog*, or imported from coordinate files in PDB format, imported from the PDB [4] or NCI-CADD [5] data banks, or even drawn atom by atom.

With the *Force Field* editor a user may enter the parameters for a CHARMM-type potential. Parameter values for molecules selected from the molecule catalog appear with predefined. Those parameters have been adapted from published work. Molecules drawn atom by atom will have provisional values for the non-bonded interactions. A mechanism is provided to search in publicly available CHARMM [6] force field parameters for values that may be used to complete the preparation of the simulation that will run. Although occasionally these values very close to rigorously validated ones, as it is the case with glycerol, the user is warned that simulations performed with those parameters are not validated in any rigorous way and that the simulation results that use such parameters may fail to reflect actual physical behavior more often than validated ones.

The *Container* area is used to define periodic boundary conditions and to solvate the system. A minimal box containing all the molecules in the system is presented as a starting boundary which the user modify to suit her needs.

The *Minimization* and *Simulation* areas are used to configure energy minimizations and the simulation of the dynamics of the system respectively. It presents default values that can be modified.

Complete production runs of small systems with tens of thousands of atoms can be done within *Wolffia* assuming it is being installed in a workstation with the minimal recommended configuration of an Intel Core I–5 processor and 4 GB of memory. However, the configuration files for larger simulations may be packed and transferred to a server for the production run. Then the coordinates of the molecules can be transferred back to the workstation where the simulation was prepared to update the coordinates of the atoms in the system within *Wolffia*.

3. Preparation of the simulations

Preparing CMD simulations to be run using general purpose simulators such as NAMD and LAMMPS requires preparing at least four sets of values: the initial positions of the atoms, a specification of the connectivity between them, often called the topology, the values for the parameters used by the force field, and the configuration of the simulator. In this section we compare how this is often done compared to how it is done with *Wolffia*. For the traditional way we will follow loosely the methods explained in the tutorials from the NAMD website. The simulation of a carbon nanotube CNT surrounded by the surfactant sodium dodecyl sulfate (SDS) in water. This is the product of a standard method for dissolving CNC by the addition of the surfactant and sonication. The conformation of the surfactant around the CNT depends non the concentration of the surfactant and the surfactant nanotube ratio. Detailed simulations of the process are scarce, though.

3.1. Building the mixture

Conventionally, the concrete goal of this first phase is to produce a file that contains, at the least, the x , y , z coordinates of the atoms and their type. A PDF formatted file, a format commonly used, the information of each atom is in one line of text as it can be seen in **Figure 1**. Atoms have to be numbered in columns 6 to 12 coordinates from 26 through 54, 8 characters for each one, the segment names and element symbols. There are other fields that hold information, in the case of PDB files, mostly designed to describe proteins. Column 63, the occupancy field, will be mentioned later in this narrative.

The thousands of lines included in the PDB file may come from data banks, such as the Protein Data Bank. Small molecules may be drawn using molecule editing software such as Avogadro, periodically structured molecules such as a CNT may require access to software particularly written or this purpose, more often than not, by the research group that is arming the simulation. Coordinate files for individual molecules may have to be merged into one file depending on the simulator. Special care has to be taken with type names and other information. Placing them in precise initial positions may require another piece of software, custom programming or even manual editing of the file.

So far only the positions of the atoms have been defined. Sometimes the PDB file may include a CONNECT section that defines which atoms are bonded. Anyway, additional topological information has to be described by means of another file. **Figure 2** shows a segment

of such a file in the PSF format. This file format is somewhat more lenient than the PDB format, but still, attempting to manually edit the file requires adhering to a number of format rules. Here nonbonded characteristics of the atoms, bonds, angles, dihedrals and improper may be defined.

```

42 !NATOM
1 MAIN A LIG C3 CG00 +0.000000 12.0107 0
2 MAIN A LIG C3 CG00 +0.000000 12.0107 0
3 MAIN A LIG C3 CG00 +0.000000 12.0107 0
4 MAIN A LIG C3 CG00 +0.000000 12.0107 0
5 MAIN A LIG C3 CG00 +0.000000 12.0107 0
    
```

Figure 2. Portion of a PSF formatted topology file.

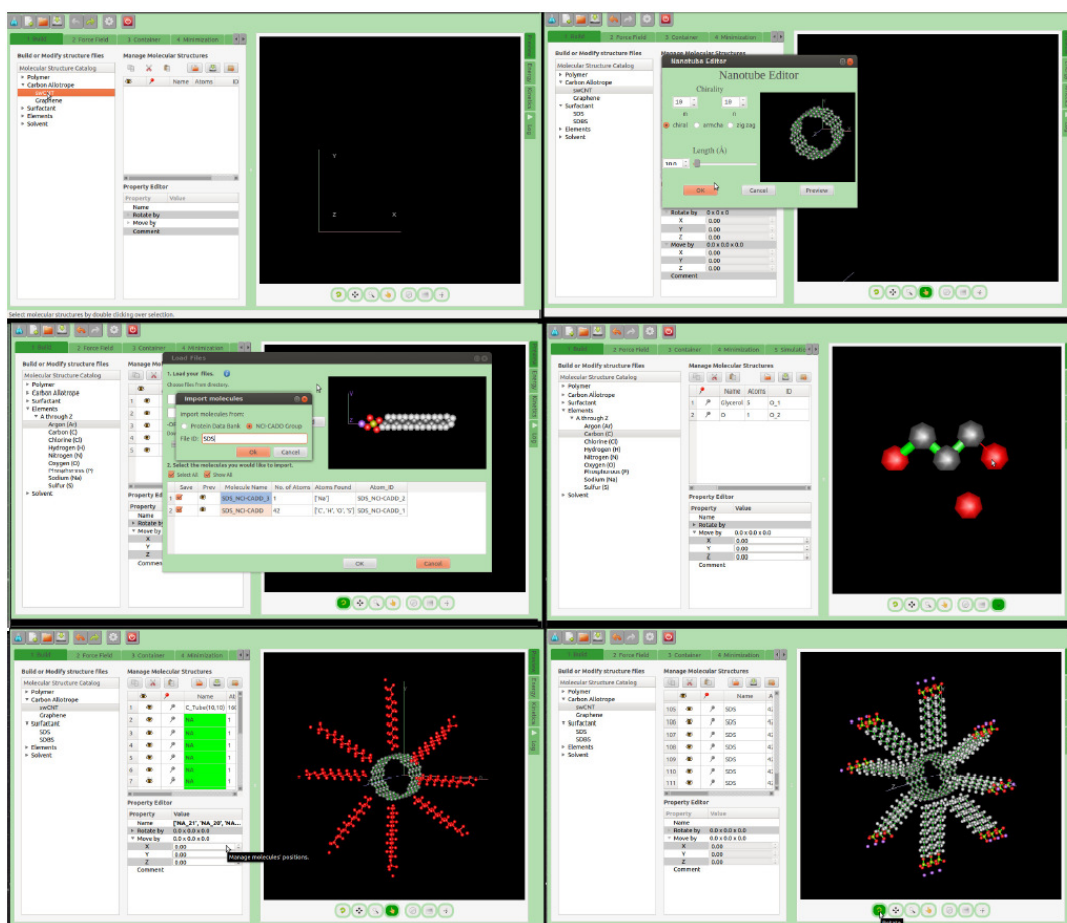


Figure 3. Wolffia being used to build a molecule system. From top to bottom, left to right, (a) the molecule catalog is being used to add molecules, (b) a nanotube editor is used to specify its geometry, (c) a molecule structure is fetched from the NCI-CADD database, (d) another molecule is being constructed atom by atom, (e) surfactants are being replicated and placed in the desired positions, and (f) the final system is completed.

Figure 3 shows various options available in Wolffia. A molecule found in the *molecule catalog* can be created by a simple double click (**Figure 3a**). Some complex molecules such as allotropic or polymer pup up a custom dialog to set, for example, the chirality of a CNT or its length (**Figure 3b**). In case a molecule is not in the catalog, a simple search in online data banks (**Figure 3c**) or from a PDB file or, if everything else fails, drawn atom by atom (**Figure 3d**).

Placing them at the desired positions is done by selecting the molecule and specifying its position. Molecules can be replicated by the common cut-and-paste mechanism, one by one or in groups (**Figure 3e**). **Figure 3f** shows a final conformation for our test case. For the sake of this illustration two versions of the SDS have been kept, one from the molecule catalog, the other imported from a data bank. Final conformations can be saved for later use, in this case, for example, for examining the effect of other solvents.

The PDB coordinates file and the PSF topology file produced for this example have a total of NNN lines of text combined. A person using Wolffia with the intent of simulating a small system may even dismiss the fact that these files will be produced.

3.2. Defining force field parameters

Once the molecules have been defined and put in place a force field has to be defined. A common procedure described in literature is selecting a predefined force field such as the ones provided by CHARMM and AMBER [7]. In concrete terms, this means inspecting the file where the values of the force field are defined (or a other documentation) in search of type names corresponding to each of the atoms of the molecules (**Figure 4**), then assigning those type names to the atoms by editing the PSF file or by other means to update this file. Other more automated methods, but less reported in literature are the use of programs such as the *psfgen* plugin of VMD [8], or other similar programs.

```

CEL2 CEL1 CTL2 CEL1      1.300  3      180.00 !1,4-dipentene
CEL1 CTL2 CEL1 HEL1      0.000  2          0.00 !1,4-dipentene
CEL1 CTL2 CEL1 HEL1      0.000  3          0.00 !1,4-dipentene
! 2,5-diheptene, adm jr., 2/00
! for CIS double bonds in polyunsaturated lipids (default)
CEL1 CEL1 CTL2 CEL1      1.000  1      180.00 !2,5-diheptane
CEL1 CEL1 CTL2 CEL1      0.100  2          0.00 !2,5-diheptane
    
```

Figure 4. Portion of a PRM formatted coordinate file.

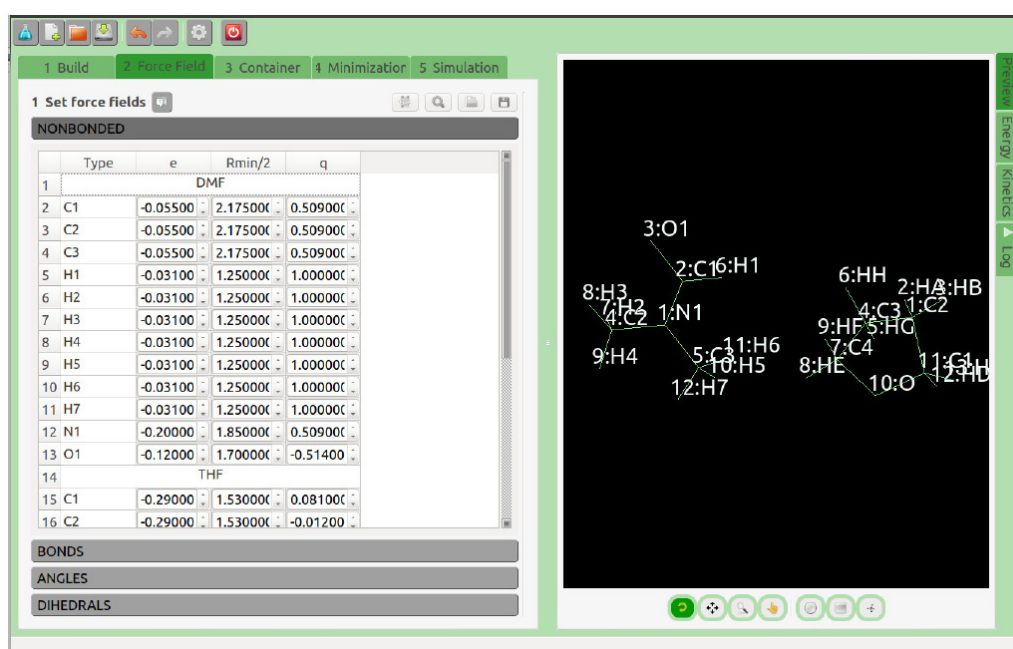


Figure 5. The force field editor.

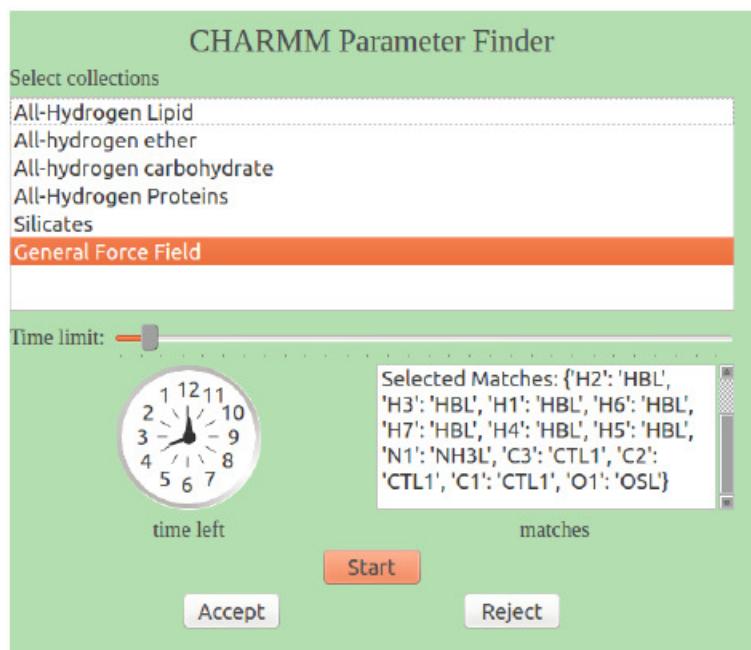


Figure 6. The force field finder.

The force field editor in Wolffia (**Figure 5**) lets the user directly define the values of the parameters of force field of the type in equation (1). For molecules selected from the molecule catalog these values will be predefined but they could be modified. For other molecules Wolffia offers various options besides entering the values manually. They can be loaded from a PRM formatted force field file. Also, a CHARMM parameter finder tool can be used to search in publicly available CHARMM force field file for the combination of atom-type matches that maximize the number of parameters from within those matches that are compatible with the structure of the molecule (**Figure 6**). Atoms types can be edited and an additional tool automatically sets type names to atoms according to the structure of the molecule if needed.

3.3. Energy minimization and dynamics simulation

When all the information about the topology and physics of the system have been defined it is ready for the energy minimization and, after that, the dynamics simulation. Here the configuration of the simulators have to be specified in at least one other file. A relatively simple simulation using basic integration parameters, PME electrostatics, Langevin temperature control, and Nose–Hoover pressure control in NAMD consists of close to a hundred lines. One often have to reuse configuration files and edit the necessary changes.

Wolffia provides menus to configure the simulator (**Figure 7**). It checks for the consistency of several parameters and warn the user about problems before the simulation is submitted. The minimization or simulation is started, paused or stopped by pressing a button. Energies and kinetic measurements and the conformation of the molecules can be monitored while the simulation progresses. This is an important feature, for example, for determining if a energy minimization has reached a local minimum: all the energy plots should be flat or nearly flat.

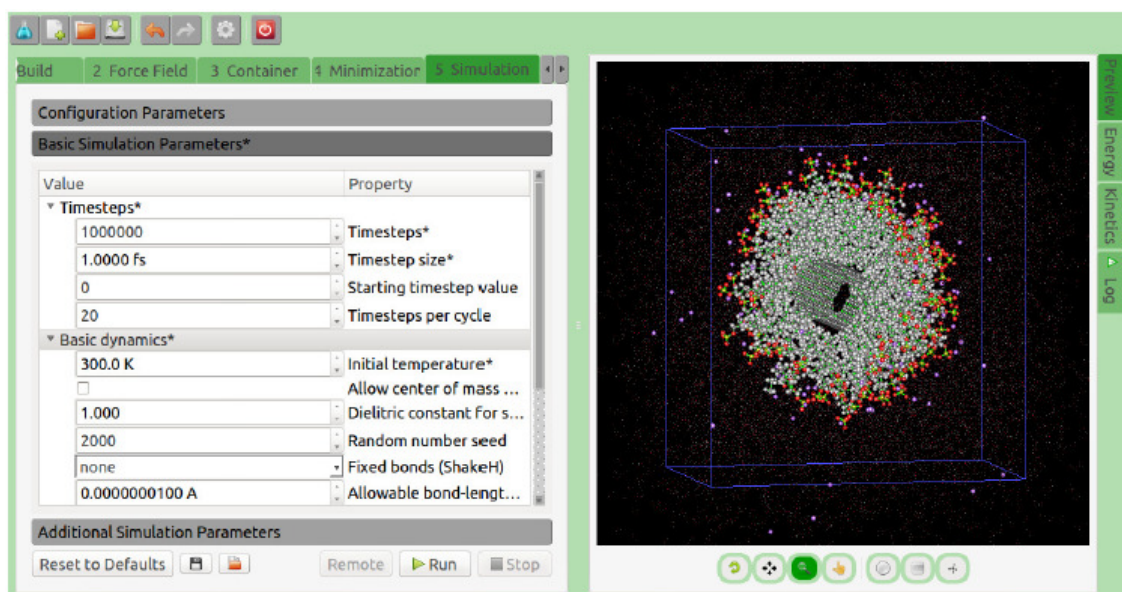


Figure 7. The result of the simulation after a production run was packed in Wolffia, transferred to a server and executed and imported back into the interface.

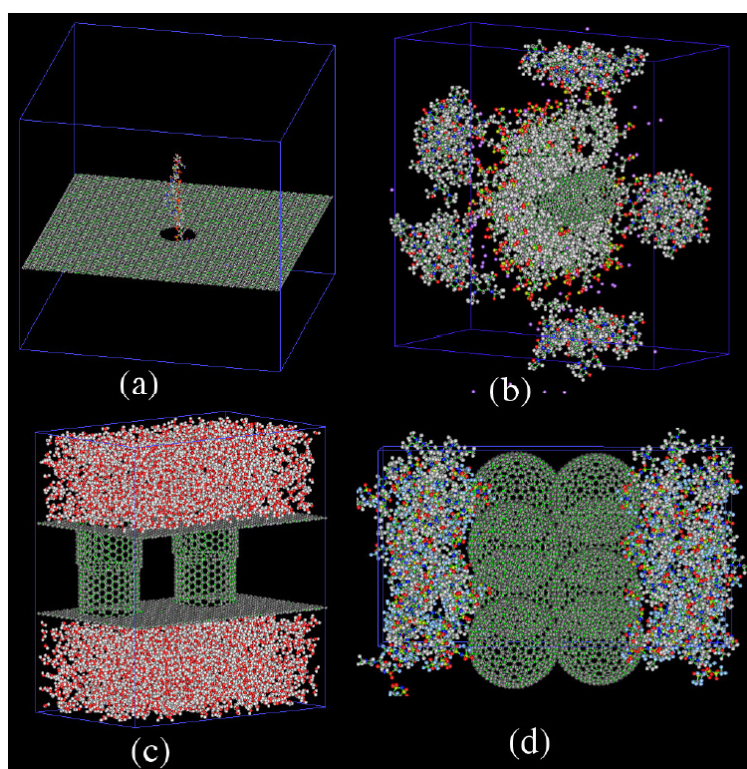


Figure 8. Examples of simulations prepared with Wolffia.

Figure 8 shows other systems that have been recently simulated with the help of Wolffia: (a) a DNA translocation through a nanopore on a graphene sheet by means of an electric field, (b) the effect of adding the polymer PMMA to a CNT-surfactant system similar to the one shown above, (c) tubular carbon pores filled with an electrolyte in water to study activated carbon electrodes of supercapacitors, and (d) fullerenes to simulate the impregnation of ionic liquids supercapacitor electrodes made with packed nanodiamonds.

4. Conclusion

The capabilities of Wolffia, a new tool for the preparation of classical molecular dynamics simulations, have been examined. A test case was followed through the different stages of preparation compared to conventional ways of developing such simulations. The software has shown the potential for significantly reducing the time to prepare classical molecular dynamics simulations. Additional effort is being made to be able to run the simulations prepared by this software with more CMD simulator engines.

Acknowledgements

This work has been supported by the National Science Foundation under Grant NSF–DMR–0934195, PENN–UPRH Partnership for Research and Education in Materials (PREM). Mr. Giovanni Sepúlveda produced most of the figures shown in this paper.

References

1. E. J. Maginn. From discovery to data: What must happen for molecular simulation to become a mainstream chemical engineering tool. *AICHE J.* 55 (2009) 1304-1310.
2. M. Medina–Cuadrado. Wolffia: An environment with a graphical user interface to prepare and monitor classical molecular dynamics simulations, 2013 – in press.
3. J. C. Phillips, R. Braun, W. Wang, J. Gumbart, E. Tajkhorshid, E. Villa, C. Chipot, R. D. Skeel, L. Kalé, K. Schulten. Scalable molecular dynamics with NAMD. *J. Comput. Chem.* 26 (2005) 1781-1802.
4. RCSB (2012). Protein Data Bank: <http://www.rcsb.org/pdb/home/home.do>.
5. NCI / CADD Group. NCI / CADD: <http://cactus.nci.nih.gov/>.
6. A. D. MacKerell Jr., B. Brooks, C. L. Brooks III, L. Nilsson, B. Roux, Y. Won, M. Karplus. CHARMM: The energy function and its parameterization with an overview of the program. In: *The Encyclopedia of Computational Chemistry*, 1. Chichester: John Wiley & Sons (1998) 271-277.
7. AMBER 12 Reference Manual. San Francisco: Univ. California (2012).
8. H. Williams, D. Andrew, K. Schulten. Visual molecular dynamics. *J. Mol. Graphics* 14 (1996) 33-38.

APPARENT HALL MOBILITY OF CHARGE CARRIERS IN SILICON WITH NANO-SIZED “METALLIC” INCLUSIONS

L. Chkhartishvili, T. Pagava

Georgian Technical University
Tbilisi, Georgia
chkharti2003@yahoo.com

Accepted September 19, 2013

1. Introduction

Any foreign inclusion in the ordered crystalline structure creates a field of elastic stresses, by which it attracts a variety of defects existing in the matrix. As a result, defective shells appear around the inclusions. If the matrix is semiconducting, these shells may contain defects creating discrete energy levels in the band gap – the majority carrier’s traps. In this case, charge carriers and shells of inclusions are like-charged. It means electrostatic screening of the inclusions from passing the electric current. Below, for definiteness we speak on a semiconductor material with n-type conductivity and, therefore, electron-traps. Material with p-type conductivity can be considered similarly.

Obviously, mean thickness of the shells and concentration of the traps ionized by electron-capturing in shells determine the character of the defects influence on the effective electron Hall mobility μ_{eff} . When inclusions are “dielectric”, i.e. their conductivity is much lower than that of the matrix, regardless of the degree of screening, current lines bypass them. The degree of the screening determines distortion of the inner-potential relief in the matrix and, consequently, leads to additional scattering of charge carriers. Effect of screening is more palpable in the presence of “metallic” inclusions, whose conductivity is much higher than that of the matrix. If the screening is weak, the shell will be transparent for electrons. However, in the case of strong screening essentially “metallic” inclusions effectively behave as “dielectric” ones.

In general, the shell of a “metallic” inclusion is transparent for some electrons, but not for the rest of them. Therefore, it is too difficult task to find a first principles theoretical description of the electron transport in semiconductors with “metallic” inclusions. For example, negatively charged shells of nanoscale inclusions differ from common electron scattering charged centres and to account for their influence on electron transport one needs to construct a realistic model of the electron traps distribution in the shell, calculate the electron transmission coefficient through the related potential barrier, etc. Instead, in this paper we propose a phenomenological approach, which for physically reasonable parameters of the theory provides a satisfactory description of the temperature-dependence of the effective electron Hall mobility $\mu_{eff}(T)$ in a semiconductor with “metallic” inclusions.

2. Theorizing

Let μ_m and μ_d denote the electron effective Hall mobilities, respectively, for the completely unscreened, i.e. ideally “metallic” (with infinite conductivity), and completely screened, i.e. ideally “dielectric” (with zero conductivity), inclusions in a semiconductor material. If μ is the electron Hall mobility in the semiconducting matrix, we can write:

$$\mu_m = c_m \mu,$$

$$\mu_d = c_d \mu,$$

where c_m and c_d are some dimensionless coefficients satisfying the conditions: $c_m > 1$ and $0 \leq c_d < 1$. Therefore, always

$$\frac{c_m}{c_d} > 1.$$

These values are determined by volume fractions of inclusions, as well as their size, shape, and orientation relative to the electric current direction, interconnections between inclusions, etc. [1]. Pay attention to the dependence of these factors on the prehistory of the sample, e.g. its radiation- and thermal-treatments.

From the point of view of applications in the solid state electronics, one has to analyze the temperature-region where electrons obey the Boltzmann statistics. This means that the probability of the absence of an electron on the trap-level E (assuming that the energy is counted from the bottom of the conduction band) at the temperature T is proportional to the exponent $\exp(-E/kT)$. When the concentration of screening traps in the shell is too high, they are located closely to each other. For this reason, the parameter E can include the correction for the electrostatic interaction between electrons trapped on adjacent centres.

Apparently, the probability w_m that inclusions are unscreened, i.e. behave like “metallic” inclusions, is proportional to the probability of the electron absence on the trap:

$$\frac{w_m}{w} = \exp\left(-\frac{E}{kT}\right).$$

Here w is the temperature-independent coefficient. Its value is determined by the concentration of traps in the screening shells, their mean thicknesses, and also external influences on the sample during the electrical measurements, such as IR illumination with the photon energy sufficient to excite electrons from trap-levels in the conduction band of the semiconducting matrix. For simplicity, we assume that electron traps of only single-type are responsible for the screening of “metallic” inclusions. Of course, shells of inclusions may contain traps of different origins. However, the differences in their concentrations and the energy levels are likely to lead to dominance one of them in the temperature-range under the consideration. The concentrations of electron traps of different types are determined by the sample prehistory, such as parameters of irradiation and annealing processes.

Probability w_d that “metallic” inclusions are screened by their shells from conduction electrons, i.e. these inclusions act as “dielectric”, is:

$$w_d = 1 - w_m.$$

Now the effective Hall mobility can be expressed by weighted effective mobility in samples with ideally “metallic” and ideally “dielectric” inclusions:

$$\mu_{eff} = w_m \mu_m + w_d \mu_d$$

OR

$$\frac{\mu_{eff}}{\mu} = c_d + (c_m - c_d)w \exp\left(-\frac{E}{kT}\right).$$

To find the temperature-dependence of the effective Hall mobility $\mu_{eff}(T)$, one should take into account the temperature-dependence of the mobility in the matrix $\mu(T)$. Within the phonon-scattering temperature-range, which is of interest for applications in electronics, this dependence is the decreasing exponential function

$$\mu(T) = \frac{M}{T^n},$$

where $M > 0$ is the temperature-independent coefficient characterizing semiconducting material and $n > 0$ is the dimensionless exponent. Thus, we have to explore the behaviour of the function

$$\mu_{eff}(T) = \frac{c_d M}{T^n} \left(1 + \left(\frac{c_m}{c_d} - 1 \right) w \exp\left(-\frac{E}{kT}\right) \right).$$

If the main trapping level is sufficiently deep it meets the condition

$$\frac{E}{nkT_{min}} > 1,$$

and then at the point $T = T_{min}$ determined by the transcendental equation

$$w \left(\frac{c_m}{c_d} - 1 \right) \left(\frac{E}{nkT_{min}} - 1 \right) = \exp\left(\frac{E}{kT_{min}}\right),$$

the first derivative of this function equals to zero,

$$\mu'_{eff}(T_{min}) = 0,$$

while the second derivative is expressed by the positively defined form:

$$\mu''_{eff}(T_{min}) = \frac{nc_d E \mu(T_{min})}{kT_{min}^3} > 0.$$

Consequently,

$$\mu_{eff}(T_{min}) = \frac{c_d \mu(T_{min})}{1 - \frac{nkT_{min}}{E}}.$$

is the value of the function at the minimum. The equivalent form of this expression,

$$\frac{\mu_{eff}(T_{min})}{\mu(T_{min})} = \frac{c_d}{1 - \frac{nkT_{min}}{E}},$$

determines the ratio of the effective electron mobility in material with inclusions and electron mobility in the matrix at the temperature-minimum.

3. Experimental procedure and testing

Experimentally we have studied changes in the character of the temperature dependences of the concentration N and the electron Hall mobility μ_{eff} in irradiated silicon

crystals subjected to isochronous annealing at different temperatures. The samples studied were 1 mm × 3 mm × 10 mm n-Si or p-Si single crystals doped, respectively, with P or B to the concentration of $\sim 6 \cdot 10^{13} \text{ cm}^{-3}$. The samples were irradiated with significant doses of high-energy protons and / or electrons at 300 K. The irradiated crystals were subjected to isochronous annealing at temperatures in the range 80 – 600 °C; the annealing temperature T_{ann} was varied with a step of 10 °C. The time of sample exposure to a particular temperature was 10 min. After each isochronous annealing cycle, we recorded the temperature dependences of the Hall mobility and the charge carrier concentration in the range from the nitrogen boiling point up to room temperature (77 – 300 K). Hall measurements were conducted not only in the dark, but also under the IR monochromatic illumination. The ohmic contacts used in the measurements were fabricated by rubbing Al into the sample surface. The ionization energies of defect levels were determined from the slope of the dependences $N(T)$. The concentrations of various radiation defects were calculated using the stepwise dependences $N(T)$ and $N(T_{ann})$ in the temperature ranges 77 – 300 K and 80 – 600 °C, respectively. The sample temperature was monitored with a copper–constantan thermocouple, and the annealing temperature with a chromel–alumel thermocouple. In the measurements of T and T_{ann} , the error was no higher than $\sim 10\%$.

3. Comparison between theory and experiment

In the temperature range from the nitrogen boiling point to room temperature, we sometimes have measured the charge carriers Hall mobilities in silicon crystals irradiated by high-energy particles and isochronously annealed significantly more or significantly less than those in the initial samples. In such cases, the temperature-characteristics often reveal the minima located in the phonon-scattering region. In light of the above constructed theoretical framework, such behaviour is a reliable indicator of the presence of “metallic” inclusions in form of clusters of certain radiation-induced defects, which can be screened by the radiation defects of other types, when those are charged by capturing the majority carriers from the matrix. The degree of screening should be influenced by the irradiation and annealing conditions.

Before the analysis of the experimental data, we should note that the scattering of electrons or holes by the acoustic phonons in silicon leads to the exponent of $n = 3/2$, and the molar thermal energy of the crystal at room temperature is $kT \approx 0.025 \text{ eV}$. On the other hand, the trapping levels in silicon are quite deep. For example, for A- and E-centres, which should be responsible for the screening of “metallic” inclusions in n-Si, the corresponding levels are of 0.17 and 0.44 eV, respectively. Same order of magnitude is characteristic for trap-levels related to the complexes of vacancies with boron dopant atoms $V + B$, which seem to screen such inclusions in p-Si: 0.45 eV. Thus, below room temperature the condition $E/nkT_{min} > 1$ for silicon is satisfied within a larger margin: $nkT_{min}/E \ll 1$. This fact greatly simplifies transcendental relation between the temperature-minimum point and magnitude of the effective Hall mobility at that minimum:

$$\frac{\mu_{eff}(T_{min})}{\mu(T_{min})} \approx c_d.$$

Thus, the minimum should be observed in case of almost complete screening of “metallic” inclusions, i.e. at low effective mobility. This ratio will be used for estimating of the parameter c_d in different silicon crystals of n- and p-type conduction irradiated by high-energy particles.

The $\mu_{eff}(T)$ dependences for n-Si crystals irradiated by protons were measured by us previously [2]. As for the data on n-Si crystal irradiated by protons and electrons and p-Si crystals irradiated by electrons, they are published in this paper for the first time. Obtained curves are shown in **Figures 1 – 3**.

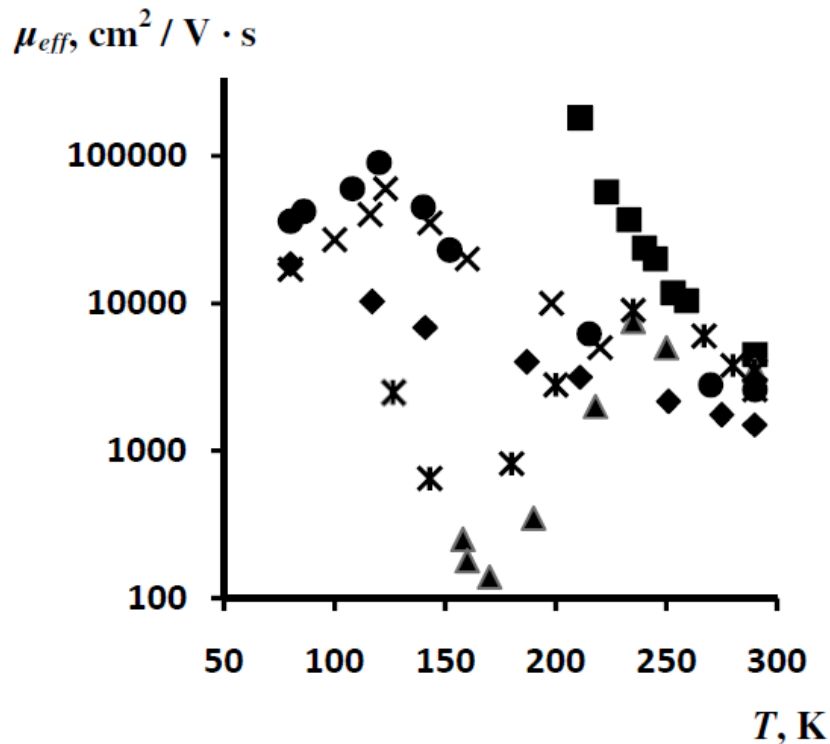


Figure 1. Temperature-dependences of the electron effective Hall mobility in zone-melted n-Si samples irradiated by 25 MeV protons with the dose of $8.1 \cdot 10^{12} \text{ cm}^{-2}$ at 300 K: 1 (♦) – before irradiation, 2 (■) – after irradiation, 3 (▲) and 4 (×) – after irradiation and annealing for 10 min at 110 and 160 °C, respectively, 5 (✱) and 6 (●) – after irradiation and annealing for 10 min at 110 and 160 °C and under IR illumination with photon energies of 0.44 and 0.17 eV, respectively [2].

The temperature-dependence of the electron Hall mobility in the initial zone-melted n-Si crystals (**Figure 1**, Curve 1) after the high-dose irradiation by protons with energy of 25 MeV is significantly shifted upward (Curve 2). The strong increase in the effective Hall mobility clearly indicates that such irradiation leads to the formation of “metallic” inclusions with ohmic junctions at the boundaries with n-Si matrix. Isochronous annealing at 110 °C strongly reduces the effective Hall mobility in the irradiated material compared with that in initial one (Curve 3) indicating formation of the screening shells around the “metallic” inclusions. The observed temperature-dependence, revealing a minimum, allows the evaluation of the reducing in the effective Hall mobility value: $c_d \approx 0.028$. Next isochronous annealing at 160 °C increases the effective mobility (Curve 4) and its values at fixed temperatures become much higher than those for initial sample, however, still much lower compared to those in the

irradiated, but unannealed material. Thus, such annealing weakens the screening. Because screening in n-Si is attributed to A- and E-centers (see below), for the samples annealed at 110 and 160 °C we also carried out photo-Hall effect measurements, i.e. utilize IR illumination with photon energies of 0.44 and 0.17 eV, respectively (Curves 5 and 6). As noted above, these are energy levels of E- and A-centers. Therefore, such illuminations should lead at least to a partial (depending on intensity) depletion of trapping levels and thus weakening in the screening. This effect manifests itself in upward shifts of the temperature-characteristics of effective Hall mobility regarding the dark-characteristic.

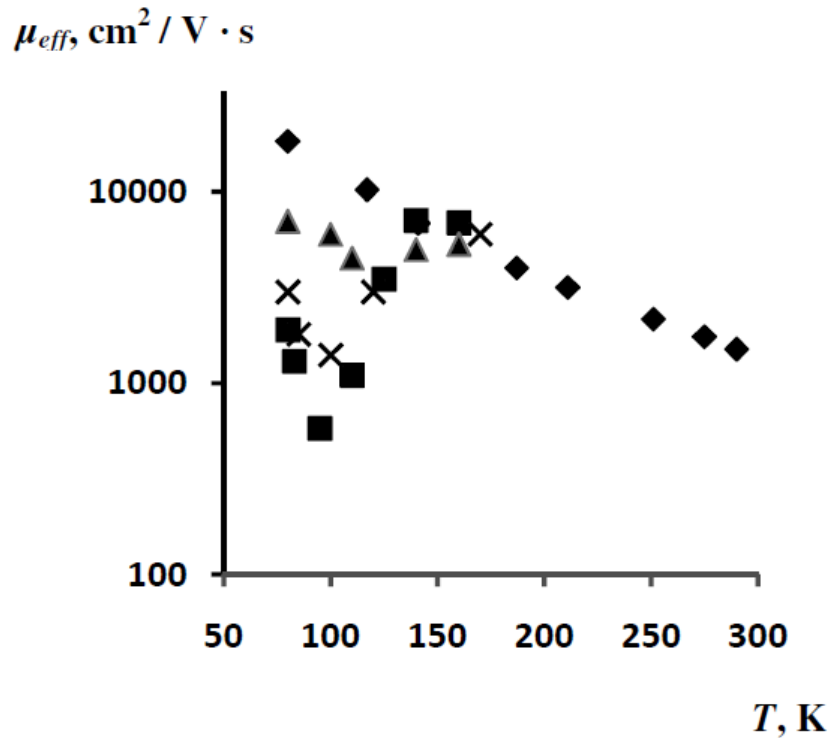


Figure 2. Temperature-dependences of the electron effective Hall mobility in zone-melted n-Si samples irradiated by 25 MeV protons and 2 MeV electrons with doses of $1.0 \cdot 10^{11}$ and $1.0 \cdot 10^{14}$ cm⁻², respectively, at 300 K: 1 (♦) – before irradiation, 2 (■) – after irradiation, 3 (▲) and 4 (×) – after irradiation with IR illumination with photon energies of 0.44 and 0.17 eV, respectively.

The temperature-dependence of the electron effective Hall mobility in the initial n-Si sample (**Figure 2**, Curve 1) after the irradiation with the relatively low dose of 25 MeV protons and the high dose of 2 MeV electrons is mostly shifted down (Curve 2). This result suggests that such kind of combined irradiation leads to the formation of “dielectric” inclusions in the n-Si matrix. From the corresponding temperature-minimum we find: $c_d \approx 0.038$. Apparently, these inclusions are not truly dielectric, but screened “metallic”. The plausibility of this conclusion is confirmed by the photo-Hall measurements performed for irradiated samples under the IR illumination with photon energies of 0.44 and 0.17 eV (Curves 3 and 4, respectively): optical depletion of the traps associated with E- and A-centers increases the electron effective mobility and this is manifested in the weakening of the screening.

The temperature-dependence of the hole effective Hall mobility in the initial p-Si samples (**Figure 3**, Curve 1) after irradiation by 8 MeV electrons with high dose and annealing

at 90 and 170 °C moves down (Curves 2 and 3), but after annealing at 180 °C moves up (Curve 4). With increasing annealing temperature, curves move upwards. The reducing in the effective mobility for samples annealed at 90 and 170 °C equal to $c_d \approx 0.008$ and $c_d \approx 0.265$, respectively. As the annealing at 180 °C greatly increases the holes effective Hall mobility in the irradiated samples if compared with initial sample, we come to the conclusion that in this case the radiation inclusions are “metallic”.

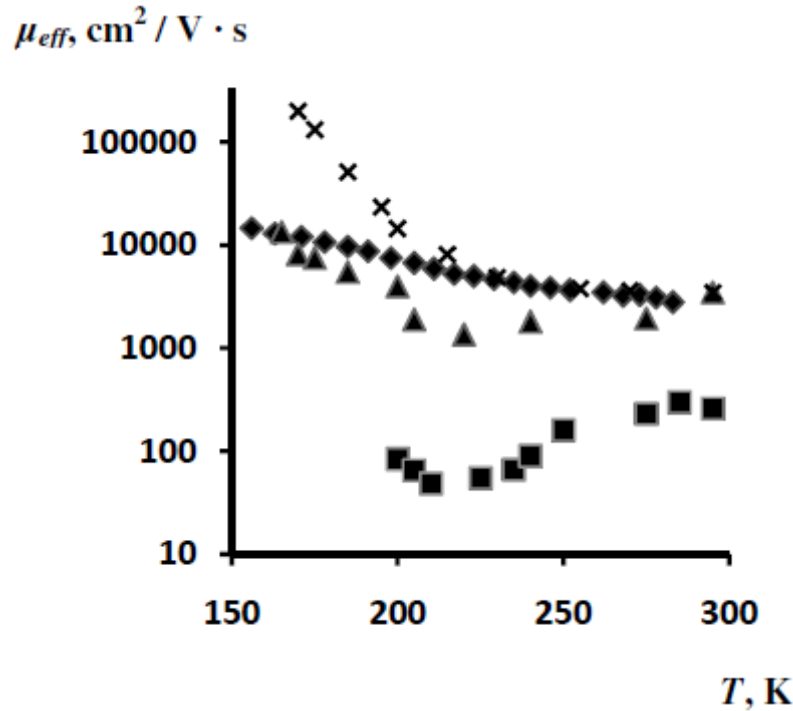


Figure 3. Temperature-dependences of the hole effective Hall mobility in zone-melted p-Si samples irradiated by 8 MeV electrons with the dose of $1.0 \cdot 10^{15} \text{ cm}^{-2}$ at 300 K: 1 (♦) – before irradiation, after irradiation and annealing at 2 (■) – 90, 3 (▲) – 170 and 4 (x) – 180 °C for 10 min.

4. Discussion

In the framework of the above suggested phenomenological theory and based on the available experimental data, we can offer formation and screening mechanisms for “metallic” inclusions in silicon. For this purpose, it will be separately analyzed the temperature-dependences of the effective charge carrier Hall mobility.

All the curves presented in **Figure 1** find a consistent explanation within the following model. As is well known [3], irradiation by high-energy protons (with energies above the threshold of $\sim 8 \text{ MeV}$) induces so strong displacement of silicon atoms from their regular lattice sites that along with separate pairs of non-equilibrium vacancies and interstitials, there are formed nanoscale disordered regions in form of clusters of these structural point defects. Since at room temperature vacancies in silicon are highly mobile and tend to form stable complexes, mostly – divacancies, the inclusions formed mainly consist of interstitial atoms [4]. The sharp increase in the electron effective Hall mobility in n-Si after irradiation with high-energy

protons indicates that n⁺-Si inclusions are formed in the sample: only in this case it is possible to detect highly conductive inclusions with ohmic junctions with the matrix. This conclusion seems quite plausible, if we recall the property of the dopant phosphorus in silicon to diffuse towards the interfaces and segregate at phase inclusions [5]. During isochronal annealing at 110 °C, quasi-chemical reactions between free (remained outside the complexes) vacancies with background oxygen O and dopant P impurity-atoms yield defect complexes $V + O$ and $V + P$. These are deep electron traps, A- and E-centers, the levels of which are located at $E_c - 0.17$ and $E_c - 0.44$ eV, respectively. On the other hand, clusters of interstitial atoms generate elastic stresses in the lattice, which are possible attract vacancy-complexes. Therefore, around the “metallic” inclusions it is formed defective shell consisting of A- and E-centers, divacancies, etc. Due to electrons capturing by A- and E-centers, these shells become negatively charged and, consequently, prevent penetration of conduction electrons inside the “metallic” inclusions. This explains the strong decrease in effective electron Hall mobility in the irradiated and annealed at 110 °C material in comparison with the initial one. It is clear that as the temperature increases the degree of screening by the charged A- and E-centers in the shells reduces. The relative contribution of A- and E-centers in screening depends on the temperature: below ~ 200 K both are involved in the screening, but above this temperature mainly E-centers are responsible for screening as almost all the A-centers are depleted because of the lower-laying electron-level. Thermal treatment at 160 °C leads to the annealing of the E-centers and, consequently, weakening of the screening, which reveals in increasing in the effective electron Hall mobility. IR illumination with photon energies of 0.17 and 0.44 eV leads to the de-ionization of A- and E-centers. Naturally, increasing in mobility is pronounced at low temperature region, where the screening of highly conducting inclusions in the dark is substantial.

In the case shown in **Figure 2**, pre-irradiation of n-Si by protons only negligibly affects the effective electron Hall mobility, because the dose is relatively low and for this reason “metallic” inclusions are formed in low concentration. However, due to high-energies of protons the sizes of individual disordered regions are significant and they are able to create strong elastic stresses in the matrix. Therefore, vacancy complexes formed after the high-dose irradiation by high-energy electrons move toward these inclusions and form the screening shells. Similarly to the above case, the main role in screening will play ionized A- and E-centers because the formation of divacancies from a pair of negatively charged vacancies is unlikely due to the electrostatic repulsion force. The presence of screening shells naturally explains the decrease (especially, in low-temperature region) in electron effective Hall mobility. Same mechanism is confirmed by the photo-Hall effect measurements.

The high value of the hole effective Hall mobility in p-Si irradiated by high-energy electrons and annealed at 180 °C (**Figure 3**) indicates that in this material p⁺-Si inclusions are formed. This fact is not surprising, since dopant B atoms in silicon easily form complexes with intrinsic interstitials [6]. These boron clusters actively migrate to the structurally disordered regions, where again dissociate [7]. All this leads to the accumulation of boron dopants. The formed p⁺-Si inclusions are screened by the shells containing vacancy complexes $V + B$ characteristic of boron-doped silicon [8]. These centers are quite deep acceptors with energy-level located at $E_v + 0.45$ eV and, therefore, the majority of them are positively charged (by the capturing of holes) within the almost the entire temperature range of Hall measurements. A significant decrease in the effective mobility after the irradiation and relatively low-temperature (at 90 °C) annealing compared to that in the initial material must be caused by the

onset of annealing of tetravacancies V_4 [9]. Fragments of their dissociation – nonequilibrium monovacancies – in these conditions actively migrate [10] to inclusions in form of disordered regions. Quasi-chemical reaction between vacancies and dopant boron atoms results in creation of additional $V + B$ complexes in the screening shells around the inclusions. However, by the thermal treatment at 170 °C most of the $V + B$ centers taking part in the screening are annealed, which results in the increased effective mobility. These defects are finally annealed at 180 °C and the screening of highly conducting inclusions completely disappears.

5. Concluding remarks

In summary, we have proposed the phenomenological theory of the mobility of charge carriers in the semiconductor with “metallic”, i.e. highly conductive compared with the matrix, inclusions, which can be screened by the defective shells containing trap-centers for major carriers. In such heterogeneous samples, depending on the degree of screening the effective Hall mobility of charge carriers μ_{eff} can be either higher or lower than the Hall mobility μ in the semiconductor matrix itself. On the decreasing part of the temperature-characteristic of μ_{eff} it is expected to appear the minimum. With the proposed theory, it has been analyzed $\mu_{eff}(T)$ dependences from the nitrogen boiling point up to room temperature in the dark and under monochromatic IR illumination of n-Si and p-Si samples doped with phosphorus P or boron B, respectively, irradiated with different doses of high-energy protons ($\sim 10^{11} - 10^{13} \text{ cm}^{-2}$ and 25 MeV) and / or electrons ($\sim 10^{14} - 10^{15} \text{ cm}^{-2}$ and 2 – 8 MeV) at room temperature. We conclude that screening of “metallic” inclusions is caused by the irradiation-induced defects in silicon: complexes of vacancies with background oxygen O and dopants. In n-Si these are $V + O$ (A-centers): $E_C - 0.17 \text{ eV}$ and $V + P$ complexes (E-centers): $E_C - 0.44 \text{ eV}$, while in the p-Si – $V + B$ complexes: $E_V + 0.45 \text{ eV}$.

References

1. E. V. Kuchis. *Galvanomagnetic Effects and Methods of Their Investigation*. 1990, Moscow: Radio & Communications.
2. T. A. Pagava, M. G. Beridze, N. I. Maisuradze, Isochronous annealing of n-Si samples with 25-MeV protons. *Semiconductors*, 2012, 46, 10, 1251-1255.
3. J. R. Srouf, Ch. J. Marshall, P. W. Marshall. Review of displacement damage effects in silicon devices. *IEEE Trans. Nucl. Sci.*, 2003, 50, 3, 653-670.
4. A. L. Aseev, L. I. Fedina, D. Höehl, H. Barsch. *Clusters of Interstitial Atoms in Silicon and Germanium*. 1994, Berlin: Akademie.
5. O. V. Aleksandrov, N. N. Afonin. Specific features of the segregation-related redistribution of phosphorus during thermal oxidation of heavily doped silicon layers. *Semiconductors*, 2005, 39, 6, 615-622.
6. O. V. Aleksandrov, V. V. Kozlovski. Simulation of near-surface proton-Stimulated diffusion of boron in silicon. *Semiconductors*, 2008, 42, 3, 257-262.

7. K. V. Feklistov, L. I. Fedina, A. G. Cherkov. Precipitation of boron in silicon on high-dose implantation. *Semiconductors*, 2010, 44, 3, 285-288.
8. J. Adey, R. Jones, D. W. Palmer, P. R. Briddon, S. Öber. Theory of boron–vacancy complexes in silicon. *Phys. Rev. B*, 2005, 71, 165211, 1-6.
9. T. A. Pagava. A Study of recombination centers in irradiated p-Si crystals. *Semiconductors*, 2004, 38, 6, 639-643.
10. T. A. Pagava, Z. V. Basheleishvili. Migration energy of vacancies in p-type silicon crystals. *Semiconductors*, 2003, 37, 9, 1033-1036.

PHASE TRANSITION OF NANOPARTICLES OF ORGANIC PIGMENTS

M. Kakuichi, K. Kasatani, Y. Morita

Graduate School of Science and Engineering
Yamaguchi University
Ube, Japan
kasatani@yamaguchi-u.ac.jp

Accepted September 19, 2013

1. Introduction

Nanoparticles are particles having a size range from 1 nm to several hundred nm. Physical properties of nanoparticles are different from those of bulk crystals, atoms, and molecules. For example, if particles are smaller than tens of nanometers, phenomena such as quantum size effect [1] and quantum confinement effect [2] can be observed. The practical applications of nanoparticles are optical materials [3], catalysis [4], and medical materials [5]. While nanoparticles of inorganic semiconductors have a lot of practical application, organic nanoparticles have not yet been used widely. Since organic compounds have huge variety, we can expect wide practical application of organic nanoparticles. For example, the use of organic nanoparticles rather than inorganic nanoparticles can be expected to reduce the invasiveness of the human body in the medical field.

Preparation of organic nanoparticles is classified to the build-up method and top-down method. Examples of the former are a mechanical grinding method and a method of laser ablation in a liquid [6 – 10], and those of the latter are a reprecipitation method [11 – 16] and chemical synthesis. The reprecipitation method is a method to fabricate nanoparticles, in which a material is dissolved in a good solvent and the solution is diluted in a stirred poor solvent drop wise. The reprecipitation method is convenient and easy to modify; properties of nanoparticles, such as, particle size [15 – 17], size distribution, morphology [17] melting point, crystallinity, etc. can be changed.

In a previous paper, we reported phase transition of nanoparticles of violanthrone 78 (V78) [18]. Nanoparticles of V78 were made by a reprecipitation method using aqueous ethanol as a poor solvent, and then the nanoparticles were annealed to obtain J-like aggregate. Temperature of annealing was as low as 60°C.

In the present study, adding ethanol to the poor solvent and heating the nanoparticles made by reprecipitation method, we have obtained DPP nanoparticles with properties of J-like aggregates. We think this is a kind of phase transition. In the present paper, we report details of fabrication and the properties of the J-like aggregate nanoparticles of DPP. Phase transition of nanoparticles of V79 was also observed.

2. Experimental

Figure 1 shows structural formulas of organic pigments used. DPP was purchased from Tokyo Chemical Industry Co. and used without further purification. V79 was purchased from Aldrich Co. and used without further purification.

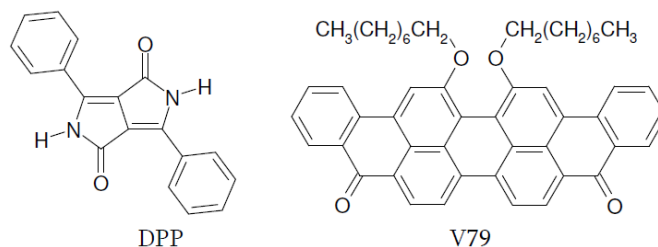


Figure 1. Structural formulas of organic pigments used.

Typical condition for preparing nanoparticles of DPP was as follows: about 0.2 ml of N-methylpyrrolidone (NMP) solution of DPP (ca. $1.0 \cdot 10^{-3}$ M) was injected using a microsyringe into 10 ml of vigorously stirred aqueous ethanol at 5 °C. The obtained nanoparticles were filtrated with membrane filter of 800 nm pore size, and the filtrate was annealed at 60 °C for at least 2 h.

Typical condition for preparing nanoparticles of V79 was as follows: about 0.2 ml of tetrahydrofuran (THF) solution of V79 (ca. $1.0 \cdot 10^{-3}$ M) was injected using a microsyringe into 10 ml of vigorously stirred aqueous acetone at room temperature. The obtained nanoparticles were filtrated with a paper filter, and the filtrate was annealed at 60 °C for at least 15 h.

UV / visible spectra were measured with a JASCO spectrometer V-550.

3. Results and discussion

We optimized fabrication conditions for DPP nanoparticles of J-like aggregates. The optimized conditions were concentration of DPP in good solvent, amount of the DPP solution, drip rate, composition of the poor solvent, temperature of poor solvent, stirring rate, annealing temperature, and annealing time.

Figure 2 shows UV / visible spectra of DPP nanoparticles together with a spectrum of NMP solution of DPP. The light blue line shows the spectrum of nanoparticles made under optimized conditions. The blue line shows that of the same nanoparticles before annealing. Annealing made the main band sharper and shifted from 530 to 545 nm. A sharp and red-shifted band is a characteristic of J-aggregates. However, the sharpness of the main band does not look sufficient to describe the particles as J-aggregates; we describe the nanoparticles as J-like aggregates.

We were unable to obtain J-like aggregates of DPP at any annealing temperature when we used pure water as a poor solvent. We also used pure ethanol as a poor solvent, but only large microparticles were obtained. Finally we found that a mixture of water and ethanol was suitable to obtain nanoparticles of DPP with J-like characteristics. We believe ethanol molecules are included in a nanoparticle, and ethanol molecules work as a lubricant in a nanoparticle upon phase transition.

Figure 3 shows the dependence of UV / visible absorption spectra of DPP nanoparticles on the composition of the poor solvent. The other experimental conditions were optimized ones. The best ethanol concentration of the poor solvent was 25 vol. %.

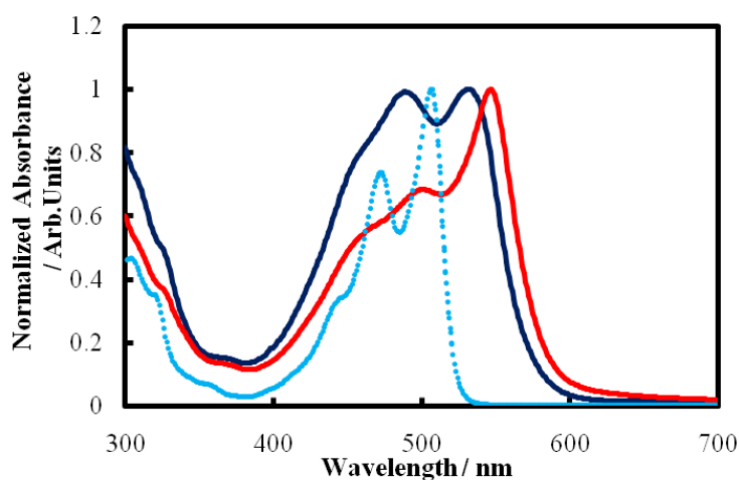


Figure 2. UV / visible absorption spectra of DPP nanoparticles with (red solid line) and without (dark blue solid line) annealing. Spectrum of DPP in an NMP solution (light blue dotted line) is also shown.

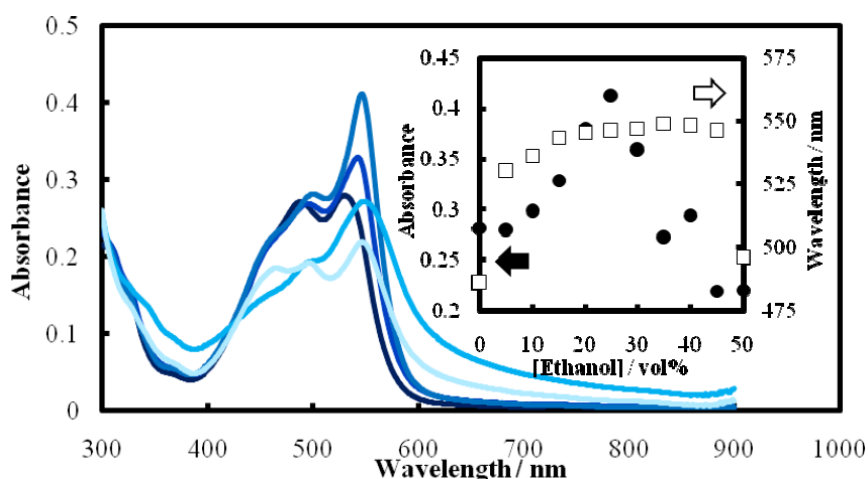


Figure 3. Dependence of UV / visible absorption spectra of DPP nanoparticles on the ethanol concentration of the poor solvent. The ethanol concentration was in a range from 5 vol. % (the darkest blue line) to 45 vol. % (the lightest blue line). The inserted figure is a plot of maximum absorbance and wavelength of maximum absorption vs. ethanol concentration.

Figure 4 shows the dependence of UV / visible absorption spectra of DPP nanoparticles on annealing temperature. The other experimental conditions were optimized ones. The dependence was rather critical; 60 °C was the best annealing temperature. UV / visible absorption spectrum of nanoparticles annealed at 70 °C has a broad band which was often observed for microparticles. We think that aggregation at a high temperature is the cause of the broad band. Thought we observed phase transition of DPP nanoparticles at as low as 60 °C, generally phase transition of organic crystals needed much higher temperature than nanoparticles. For example, the single crystals of 2,3-bis(phenylethenyl)-5,6-dicyanopyrazine underwent a morphological phase transformation from a yellow crystal to an orange one via a

thermal phase transition without the crystal state collapsing. The transformation began at a single starting point in the yellow crystal and then spread out into the whole crystal like a domino at 174.5 °C [19]. We expected that phase transition of organic crystals in small size, i.e. in nanoparticles, can occur much more easily.

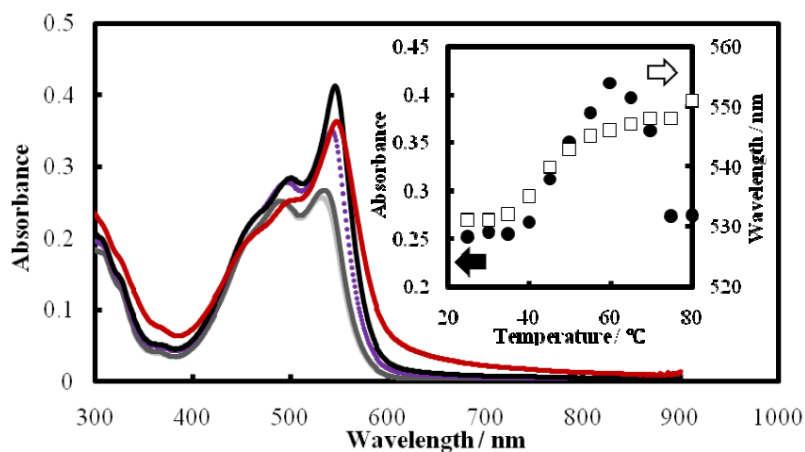


Figure 4. Dependence of UV / visible absorption spectra of DPP nanoparticles on annealing temperature. Annealing temperature is 50 (light gray solid line), 55 (dark gray solid line), 60 (black solid line), 65 (purple dotted line), and 70 °C (dark red broken line).

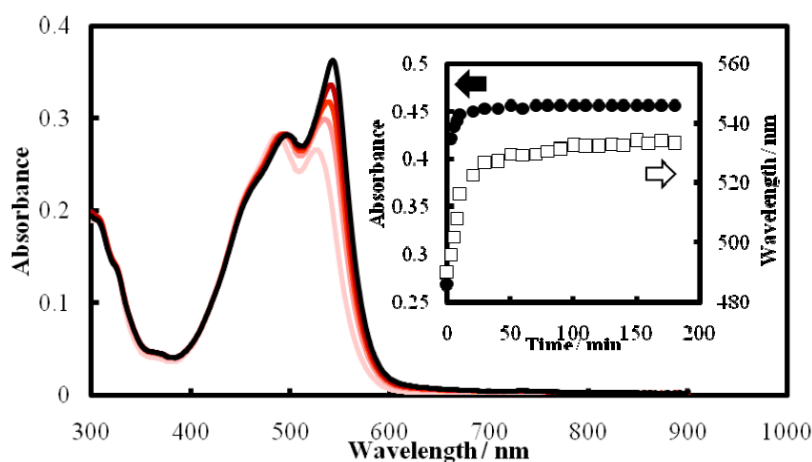


Figure 5. Dependence of UV / visible absorption spectra of DPP nanoparticles on annealing time. Annealing time is in a range from 0 (the lightest red line) to 10 min (the black line). The increment is 2.5 min. The inserted figure is a plot of maximum absorbance and wavelength of maximum absorption vs. annealing time.

Figure 5 shows the dependence of UV / visible absorption spectra of DPP nanoparticles on annealing time. The other experimental conditions were optimized ones. Annealing time must longer than 0.5, and 2 or 3 h are desirable.

Figure 6 shows the dependence of UV / visible absorption spectra of DPP nanoparticles on the temperature of the poor solvent in which a solution of DPP was diluted. The other experimental conditions were optimized ones. First, we thought if we diluted DPP solution in the poor solvent at 60 °C, annealing process might not be necessary. However, the best temperature range for the poor solvent was from 5 to 15 °C. Nanoparticles made at high temperature in the poor solvent may be in great disorder and it is a little difficult to change them to J-like aggregates upon annealing.

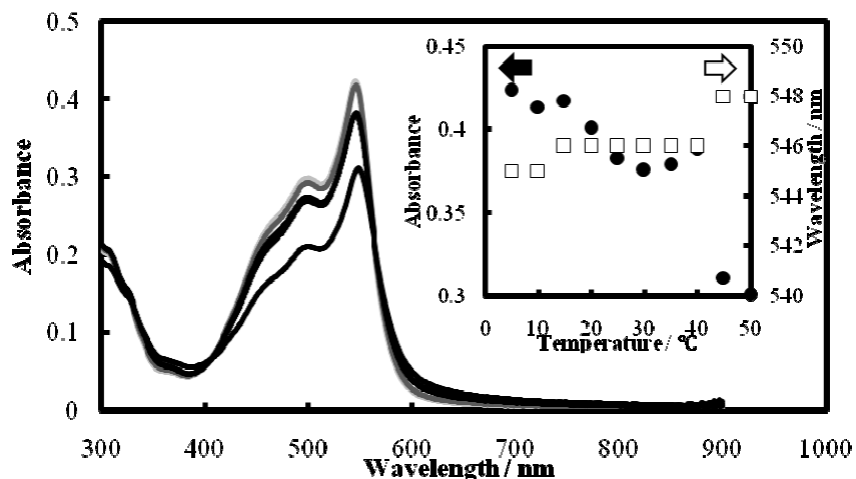


Figure 6. Dependence of UV / visible absorption spectra of DPP nanoparticles on temperature of the poor solvent. Temperature of the poor solvent is 10 (light gray solid line), 20 (dark gray solid line), 30 (black solid line), 40 (black dotted line), and 50 °C (black broken line).

In a previous paper, we reported that addition of poly(vinyl alcohol) (PVA) even at concentration as low as 1 ppm in water as a poor solvent improved production of anthracene nanoparticles drastically [20]. We only obtained anthracene microparticles instead of nanoparticles without PVA. This time we studied the effect of addition of PVA to the poor solvent for DPP nanoparticles.

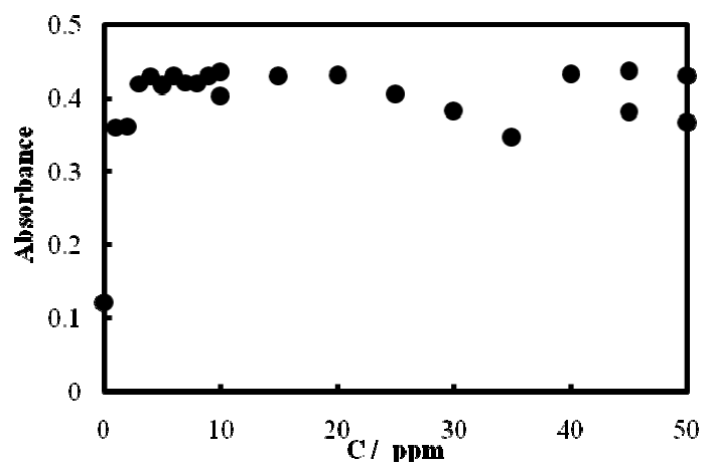


Figure 7. Dependence of absorbance of DPP nanoparticles of J-like aggregates on poly(vinyl alcohol) concentration in the poor solvent.

Figure 7 shows the results; absorption spectrum of DPP nanoparticles made without PVA shows very low absorbance, which means existence of few particles. Addition of PVA into water at a concentration of as low as 1 ppm drastically improved nanoparticle formation. We also changed stirring rate of poor solvent. Final concentration of J-like aggregate nanoparticles increased with stirring rate, but this effect was very limited.

The diameter distribution of the J-like aggregate nanoparticles was estimated by measuring UV / visible absorption spectra after filtration with membrane filters. **Figure 8** shows the results; most particles have diameters in a range from 300 to 450 nm.

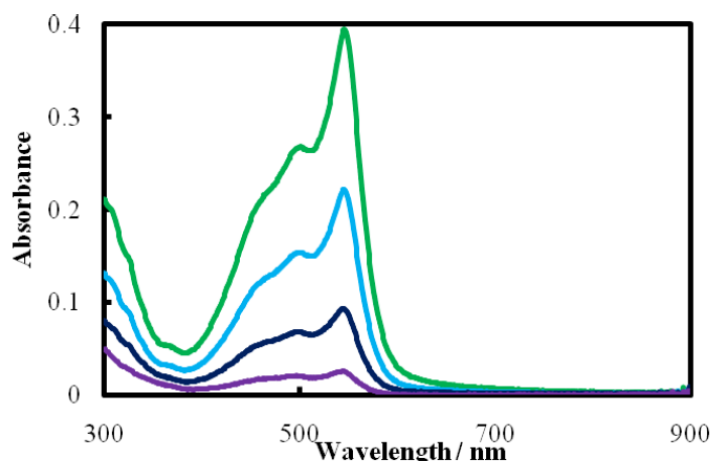


Figure 8. UV / visible absorption spectra of DPP J-like aggregate nanoparticles after filtration with membrane filters of specified pore size. Pore size was 800 (green solid line), 450 (light blue broken line), 300 (blue dot-and-dash line), and 200 nm (purple dotted line)

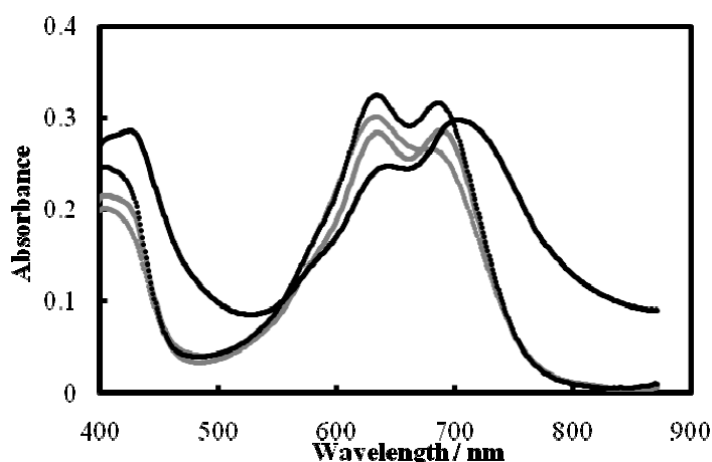


Figure 9. Dependence of UV / visible absorption spectra of V79 nanoparticles on the concentration of the poor solvent. Etanol : Water = 35 : 65 (gray lines), Acetone : Water = 50 : 50 (black lines). V79 nanoparticles with (solid lines) and without (dotted lines) annealing. Annealing time is 17 and 22 h respectively. Temperature of annealing: 60 °C.

Figure 9 shows the dependence of UV / visible absorption spectra of V79 nanoparticles on the composition of the poor solvent. Phase transition of V79 did not occur in water. Also, phase transition of V79 nanoparticles did not occur in aqueous ethanol. Only the phase transition of V79 nanoparticles occurred in aqueous acetone. The best acetone concentration of the poor solvent was acetone : water = 50 : 50. The best annealing temperature was 60 °C, and the annealing time should be longer than 15 h. The best temperature of the poor solvent was 25 °C. However, the UV / visible absorption band of V79 J-like aggregates was a little broad.

4. Conclusions

Phase transition of DPP nanoparticles to J-like aggregates was observed. Nanoparticles of DPP were made by a reprecipitation method using aqueous ethanol as a poor solvent, and then

the nanoparticles were annealed to obtain J-like aggregates. The fabrication conditions for J-like aggregate nanoparticles of DPP were optimized as follows:

Ethanol concentration of poor solvent: 25 vol. %

Annealing temperature: 60 °C

Annealing time: longer than 0.5 h

Temperature of the poor solvent: 5 °C

The fabrication conditions for J-like aggregate nanoparticles of V79 were optimized as follows:

Acetone concentration of poor solvent: 50 vol. %

Annealing temperature: 60 °C

Annealing time: longer than 15 h

Temperature of the poor solvent: 25 °C

References

1. M. Cini, P. Ascarelli. Quantum size effects in metal particles and thin films by an extended RPA. *J. Phys. Met. Phys.* 4 (1974) 1998-2008.
2. T. Takagahara, K. Takeda. Theory of the quantum confinement effect on excitons in quantum dots of indirect-gap materials. *Phys. Rev. B* 46 (1992) 15578-15581.
3. K. L. Kelly, E. Coronado, L. L. Zhao, G. C. Schatz. Photoinduced conversion of silver nanospheres to nanoprisms. *J. Phys. Chem. B* 107 (2003) 668-677.
4. R. M. Crooks, M. Zhao, L. Sun, V. Chechik, L. K. Yeung. Dendrimer-encapsulated metal nanoparticles: Synthesis, characterization, and applications to catalysis. *Acc. Chem. Res.* 34 (2001) 181-190.
5. A. Ito, M. Shinkai, H. Honda, T. Kobayashi. Medical application of functionalized magnetic nanoparticles. *J. Biosci. & Bioeng.* 100 (2005) 1-11.
6. Y. Tamaki, Ts. Asahi, H. Masuhara Tailoring nanoparticles of aromatic and dye molecules by excimer laser irradiation. *Appl. Surf. Sci.* 168 (2000) 85-88.
7. F. Mafune, J.-Y. Kohno, Y. Takeda, T. Kondow. Formation of gold nanoparticles by laser ablation in aqueous solution of surfactant. *J. Phys. Chem. B* 105 (2001) 5114-5120.
8. T. Tsuji, K. Iryo, Y. Nishimura, M. Tsuji. Preparation of metal colloids by laser ablation technique in solution: Effects of irradiation wavelength on the efficiency of colloid formation. *J. Photochem. Photobiol. A* 145 (2001) 201-207.
9. Y. Tamaki, Ts. Asahi, H. Masuhara. Nanoparticle formation of vanadyl phthalocyanine by laser ablation of its crystalline powder in a poor solvent. *J. Phys. Chem. A* 106 (2002) 2135-2139.
10. Y. Tamaki, Ts. Asahi, H. Masuhara. Solvent-dependent size and phase of vanadyl phthalocyanine nanoparticles formed by laser ablation of VOPc crystal-dispersed solution. *Jpn. J. Appl. Phys.* 42 (2003) 2725-2729.
11. H. Kasai, H. S. Nalwa, H. Oikawa, Sh. Okada, H. Matsuda, N. Minami, A. Kakuta, K. Ono, A. Mukoh, H. Nakanishi. A novel preparation method of organic microcrystals. *Jpn. J. Appl. Phys.* 31 (1992) L1132-L1134.
12. X.-M. Duan, T. Kimura, Sh. Okada, H. Oikawa, H. Matsuda, M. Kato, H. Nakanishi. Second-order hyperpolarizabilities of aromatic carboxylates without visible absorption. *Jpn. J. Appl. Phys.* 34 (1995) L1161-L1163.

13. H. Kasai, H. Kamatani, Sh. Okada, H. Oikawa, H. Matsuda, H. Nakanishi. Size-dependent colors and luminescence of organic microcrystals. *Jpn. J. Appl. Phys.* 35 (1996) L221-L223.
14. H. Katagi, H. Kasai, Sh. Okada, H. Oikawa, K. Komatsu, H. Matsuda, Zh. Liu, H. Nakanishi. Size control of polydiacetylene Microcrystals. *Jpn. J. Appl. Phys.* 35 (1996) L1364-L1366.
15. H. B. Fu, J. N. Yao. Size effects on the optical properties of organic nanoparticles. *J. Am. Chem. Soc.* 123 (2001) 1434-1439.
16. Zh. Tan, A. Masuhara, H. Kasai, H. Nakanishi, H. Oikawa. Multibranched C₆₀ micro / nanocrystals fabricated by reprecipitation method. *Jpn. J. Appl. Phys.* 47 (2008) 1426-1428.
17. R. O. Al-Kaysi, A. M. Müller, T.-S. Ahn, S. Lee, Ch. J. Bardeen. Effects of sonication on the size and crystallinity of stable zwitterionic organic nanoparticles formed by reprecipitation in water. *Langmuir* 21 (2005) 7990-7994.
18. M. Kakuichi, K. Kasatani, Y. Morita. Preparation of nanoparticles of a violanthrone derivative with properties of J-like aggregates. *Trans. Mater. Res. Soc. Jpn.* 37 (2012) 471-474.
19. K.-S. Ahn, D. K. Lee, J. H. Kim, S. H. Kim. Domino-like thermal phase transition of 2,3-bis(phenylethenyl)-5,6-dicyanopyrazine crystal. *Dyes & Pigments* 89 (2011) 93-95.
20. K. Kasatani. Fluorescent organic nanoparticles. *Trans. Mater. Res. Soc. Jpn.* 36 (2011) 421-424.

INVESTIGATION OF THE MECHANICAL PROPERTIES OF
POLYAMIDE 6 / CHITOSAN / HYDROXYAPATITE BASED
ELECTROSPUN NANOFIBROUS BIOCOMPOSITES

R. Erdem¹, E. Sancak², S. S. Pazarlioglu², M. Akalin², O. Atak²

¹Serik Vocational School of Higher Education

Akdeniz University

Antalya, Turkey

erdemramazan@gmail.com

²Marmara University

Istanbul, Turkey

Accepted September 19, 2013

1. Introduction

Electrospinning is a unique and facile technique which has recently attracted many researchers for producing ultrafine and continuous sub-micron fibers and / or nanofibers. While electrospinning of purely polymer material systems had gained significant interest by scientific world, recent studies also proved that incorporating inorganic nanoparticles into nanofibers to form nanofibrous composites have made electrospinning very attractive in fulfilling some specific functional applications, in particular, for bone tissue engineering [1].

Natural bone structure is an innate example of inorganic–organic biocomposite form which is consist of the composition of nearly 70 wt. % inorganic crystals (mainly hydroxyapatite with a chemical formula of $\text{Ca}_{10}(\text{PO}_4)_6(\text{OH})_2$) and 30 wt. % of organic matrix (mainly Type I collagen) [2].

It is difficult to electrospin HAp-incorporated collagen nanofibers for bone tissue engineering applications because of high cost, low spinnability, and lack of a proper solvent for collagen. Hence, it is appropriate to use an alternate polymer with high spinnability that mimics collagen chemically and structurally might have potential in this field. Nylon 6 (PA6) has some similarities to collagen protein in terms of its backbone structure and has satisfactory stability in human body fluid. In addition, it can be easily electrospun by applying a wide range of process and solution parameters [3].

Chitosan is a potential candidate for bone tissue engineering applications due to its structural similarity to the glucoseaminoglycan found in bone, biocompatibility, biodegradability, antimicrobial activity and substantial mechanical properties. Since, there are many studies focusing on the electrospinning of chitosan successfully in the literature, it might be possible to use chitosan to form novel nanofibrous biocomposites for potential uses in bone tissue engineering [2].

In the past few years, various types of electrospun nanocomposite fibers, such as; PCL / CaCO_3 [4], Hap / gelatin [1], silk / HAp [5], PLA / HAp [6], and triphasic Hap / collagen / PCL [7] have been investigated and characterized for potential bone regeneration applications. It is a

strong belief that related studies has provided a huge contribution to the field with amazing concepts and ideas as well as impressive experimental results, because, nanofibrous forms could help the osteoblast cells in terms of proliferation, differentiation, and mineralization [8].

The purpose of this study is to realise a successful electrospinning process from the blended solution including polyamide 6 / chitosan / hydroxyapatite, and to explore the morphological and mechanical properties of the final nanofibrous biocomposite structures that may be used in the field of bone tissue engineering.

2. Materials and methods

Polyamide 6 (PA6) was acquired from Eurotec (Turkey). Chitosan (CS) which has a molecular weight of 60.000 – 120.000 g / mol was purchased from Sigma Aldrich (Germany). Hydroxyapatite powder was obtained from Acros Organics (Belgium). All polymers and solvents were used as received without any additional chemical processing.

PA6 (11 wt. %) was dissolved in Formic Acid (FA) at 80 °C for 6 h. CS (2 wt. %) was dissolved in 90 % aqueous acetic acid for 24 h in room temperature. After the polymers were completely dissolved, they were blended with a blend ratio of 90 / 10 % (PA6 / CS) by laboratory type magnetic stirrer (Stuart, SB 162) for three hours at room temperature. Then, HAp was added to the blended solution in different amounts (1 and 3 wt. %) and stirred for about 24 h. pH values of each blended homogenous solutions were measured with pH indicator strips (Merck, Germany). The viscosities of the solutions were identified with a Brookfield Digital Viscometer by using s21 type spindle with a rotational speed of 30 rpm / min. The electrical conductivity of the blended solutions was also measured with a laboratory type conductivity meter (WTW, Cond 3110) under ambient atmosphere.

Electrospinning was performed in the laboratory spinning unit (NS24, NanoFMG), which was designed in terms of a vertical working principle. Each solution was placed in a 3 ml syringe and sent to the drum collector (covered with aluminum foil) through a 20 gauge nozzle. The power supply (AC) was set up for a positive voltage of 34 kV. The flow rate of the solution was also determined by setting up the syringe pump at 0.50 ml / h. The rotational speed of the drum collector was 35 rpm / min and its distance was set to 15 cm (optimum distance based on preliminary tests) away from the nozzle. At the time of the experiments, relative humidity and temperature values ranged from 35 – 42 % RH and 26 – 31 °C.

Electrospun fibers were characterized by Scanning Electron Microscopy (SEM, JSM–5910 LV from JEOL), equipped with an Oxford Instruments INCA Energy Dispersive Spectrometer (EDS) at 5 kV with the SE 2 detector using a 30 mm final aperture. First of all, fibers were coated with a thin gold palladium (20 / 80 %) layer using a sputter coater from Polaron (SC7620) and the morphology of the nanofibrous membranes were observed by SEM analysis at an accelerating voltage of 20 kV. The fiber diameter distribution was calculated over 50 fibers with the Image J software (Image J, 2011) from the SEM images obtained at a magnification of 20 000 ×.

In order to determine the mechanical properties (tensile strength and extension rate) of the PA6 / CS / HAp blended nanofibrous biocomposites, tensile and recovery tests were carried out using an Instron Machine (Instron 4411) in the textile laboratory at Marmara University. The mechanical properties of the blended nanofibrous composites were examined at ambient

environment (22 ± 3 °C temperature and 50 ± 5 % relative humidity). The specimens were cut into approximately 30 mm \times 10 mm (length \times width) in both machine direction and width direction in order to be loaded into the uniaxial testing machine. During the experiment, 50 N load cell under a cross-head speed of 10 mm / min was applied to the specimens. Three repetitions were taken for each specimens in order to calculate the tensile strength and elongation at break values.

3. Results and discussion

3.1. Solution properties

Solution viscosity and conductivity are two major parameters for electrospinning process. Thicker fibers are obtained from more viscous polymer solutions, however, thinner fibers are fabricated from more conductive polymer solutions, because of the increase in the conductivity of polymer solution which is subjected to more stretching under the high electrical field [9]. Solution properties (viscosity, conductivity and pH values) of the electrospun polymers are shown in **Table 1**. According to the table, viscosity of the solution was increased when CS was added to the blend. It could be explained by the chain entanglements among the Chitosan molecules as well as the molecules between CS and PA6 [10]. Solutions, which were prepared from neat PA6, were found highly conductive. The conductive behaviour of PA6 solution was explained by the ionization of polymer amide groups in formic acid [11]. Also, increasing the amount of HAp in the blend resulted more conductive solutions. This was hypothesized that an acidic solvent used for dissolution of PA6 could ionize HAp when mixed with PA6 solution prior to electrospinning [3].

Table 1. Solution Properties of electrospun polymers.

Polymer	Blend ratio, %	Viscosity, cp	Conductivity, mS / cm)	pH
PA 6	100	142	4.43	0–1
PA6 / CS	90 / 10	198	3.34	0–1
PA6 / CS / HAp (1 %)	90 / 10	110	3.75	0–1
PA6 / CS / HAp (3 %)	90 / 10	124	3.99	0–1

3.2. Morphological and structural properties of nanofibrous biocomposites

It is very well known that the morphology of the nanofibers is significantly influenced by the electrospinning parameters such as; applied voltage, polymer solution feeding rate and the distance between feeding unit and the collector [12]. Therefore, in order to explore precisely the effect of HAp amount in the solution to the morphology of resulting electrospun nanofibers, all electrospinning parameters were remained the same. The morphologies of the as-prepared electrospun PA6 / CS nanofibrous biocomposites with different amounts of HAp are presented in **Figure 1**. In general, beadless and uniform nanofibers were obtained through the electrospinning process. In **Figure 1C** and **D**, deposition of HAp particles onto fibers as well

as composite surface could be observed easily. Increasing HAp content in the blends caused fiber break up and fragmentations in some of the regions of the nanofibrous composites. It could be explained by the increase in conductivity of the polymer solution in where polymer jets would be exposed to stronger electrostatic forces during electrospinning. In addition, agglomeration might be happened among the HAp particles which could be a reason for fiber fragmentation.

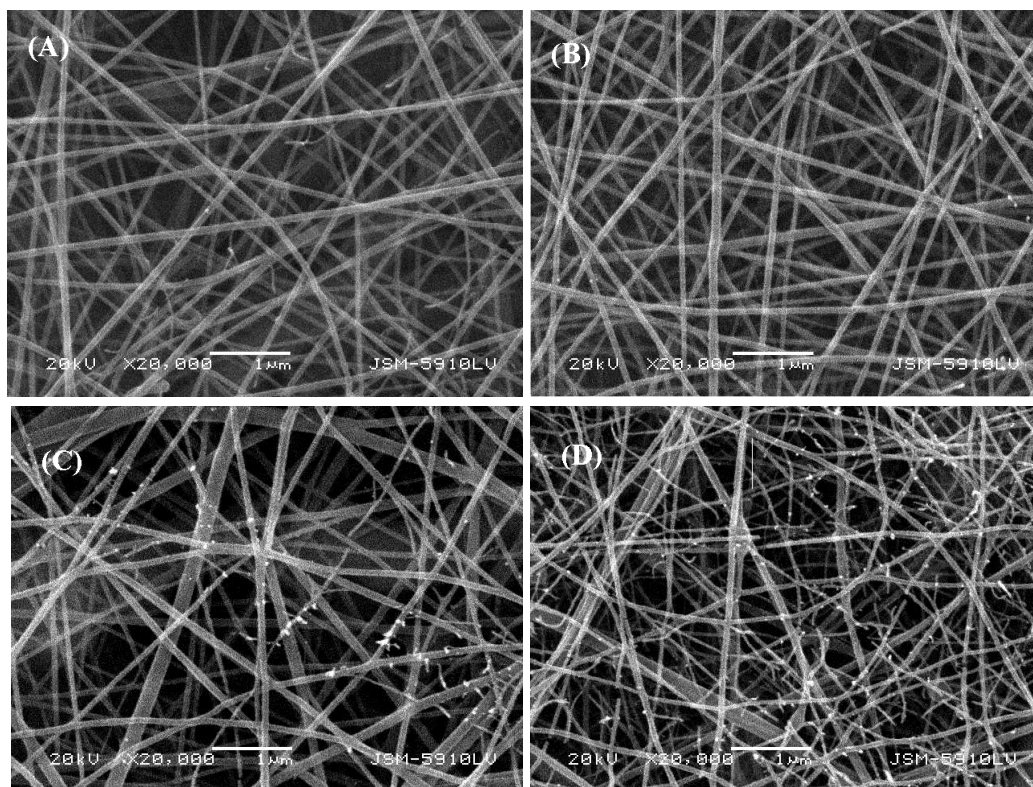


Figure 1. SEM images electrospun nanofibers. A: PA6 (100 %); B: PA6 / CS (90 / 10 %); C: PA6 / CS / HAp (1 %); D: PA6 / CS / HAp (3 %).

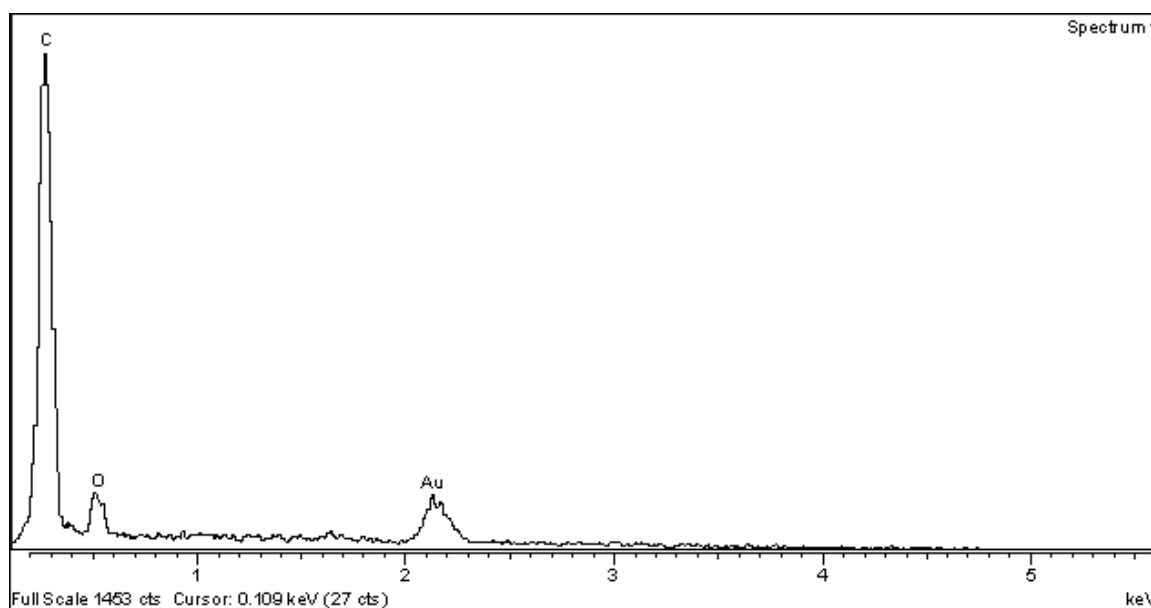


Figure 2. EDS diagram of PA6 based electrospun nanofibers.

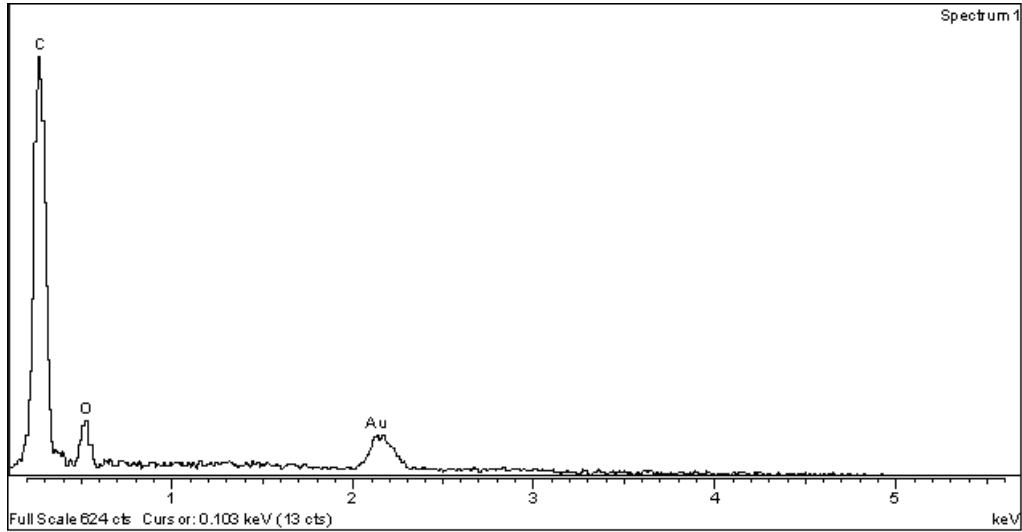


Figure 3. EDS diagram of PA6 / CS based electrospun nanofibers.

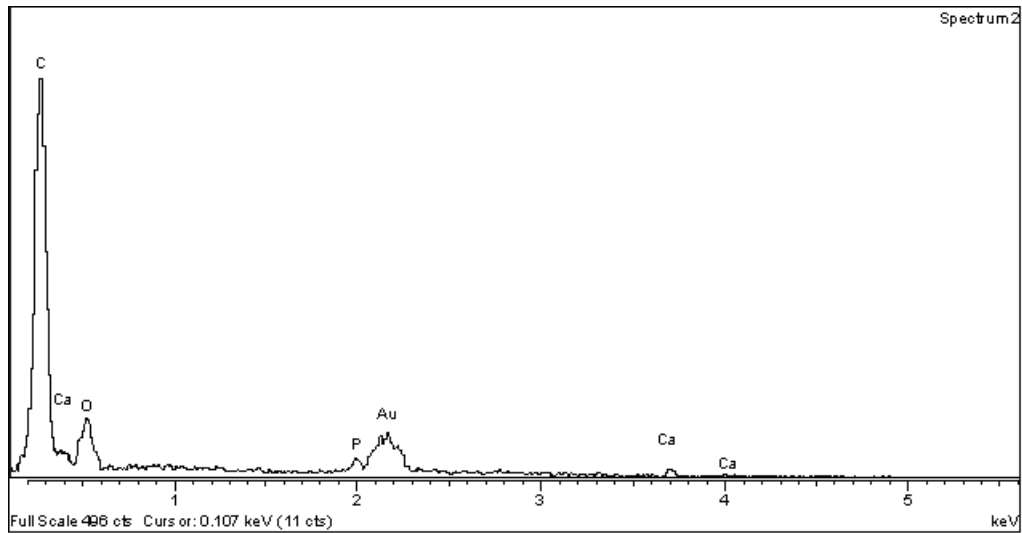


Figure 4. EDS diagram of PA6 / CS / HAp (1 %) based electrospun nanofibers.

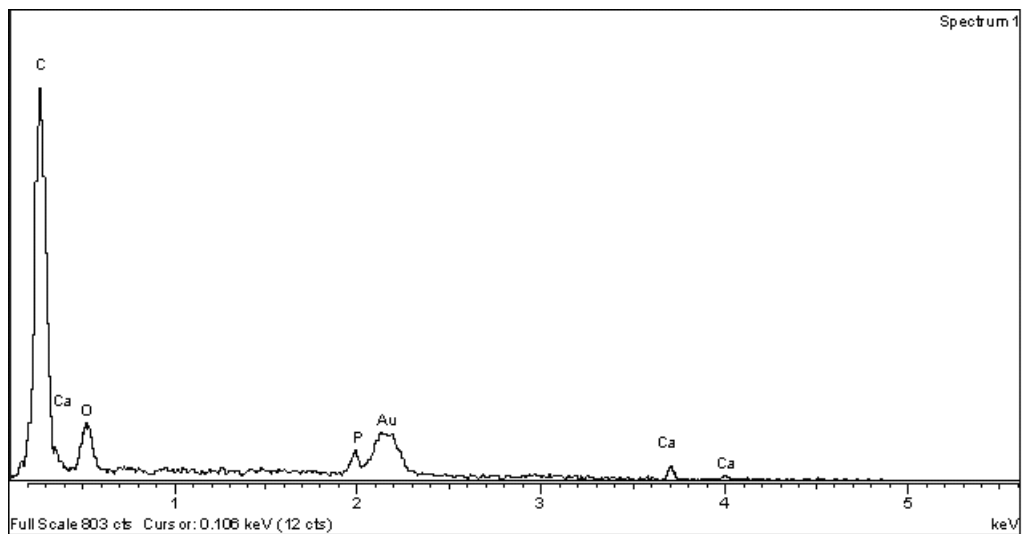


Figure 5. EDS diagram of PA6 / CS / HAp (3 %) based electrospun nanofibers.

Structural details (elemental composition) of the electrospun nanofibers can be seen in **Figures 2 – 5**. Figures belong to electrospun PA6 and PA6 / CS nanofibers showed C, O and Au peaks. C and O are the main elements found in the structure of PA6 and CS. Au was also found because of the sputter coated nanofibrous composites surfaces before SEM analysis. In **Figures 4 and 5**, peaks for Ca and P were also recorded unlike the other EDS graphs. This was attributed to the addition of HAp ($\text{Ca}_{10}(\text{PO}_4)_6(\text{OH})_2$) in the blend.

The diameters of electrospun nanofibers are shown in **Figure 6**. The thicker fibers were obtained from neat PA6 polymer solution. Adding CS into the blend solution slightly decreased the fiber diameters. This was explained by the decrease in the solution surface tension, because of the introduction of acetic acid to the solution system [13].

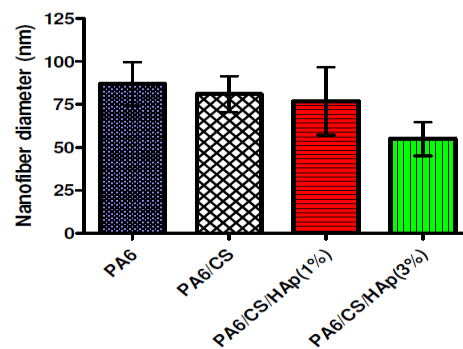


Figure 6. Diameters of electrospun nanofibers: PA6 (100 %), 87 ± 22 ; PA6 / CS (90 / 10 %), 81 ± 18 ; PA6 / CS / HAp (1 %), 77 ± 34 ; PA6 / CS / HAp (3 %), 55 ± 17 .

Increasing the amount of HAp in the blend declined dramatically the final fiber diameter. This was due to the formic acid which caused the dissociation of HAp molecules and the degradation of polymer molecules, rising the amount of short-chain ionic molecules in the solution system. These ionic species can easily increase the conductivity of the solution. Furthermore, PA6 ionic species could form ionic bonds via electrostatic interaction and promote the formation of thinner fibers [3].

3.3. Mechanical properties of nanofibrous biocomposites

The mechanical behaviour of electrospun blend fibrous composites is exhibited in **Figure 7**. Mechanical characteristics of the fibrous structures depend on the properties of the blend components, and the interaction between each polymer fiber [14]. According to the figures, tensile strength of the nanofibrous composites was increased with the addition of CS and HAp into the blend system. As it has previously been mentioned in the literature that Chitosan possesses amino groups and hydroxyl groups in its backbone and it is a rigid and brittle natural polymer [15]. As a result of that when Chitosan added into the blend, the average value of tensile strength of the materials increased, however, elongation at break decreased. Results also clearly showed that the incorporation of HAp enhanced the tensile strength and elongation at break values of the composite materials. The ultimate tensile strength slightly increased at higher HAp reinforcement. The high mechanical strength may be due to the strengths of hydrogen bonding formed during electrospinning process of the nanocomposites and presence of noticeable chemical interaction between PA6 molecules and Ca^{2+} from HAp. Also, it is possible to state that incorporation of HAp into the nanofibrous composites might alter the crystalline structure of the materials [3].

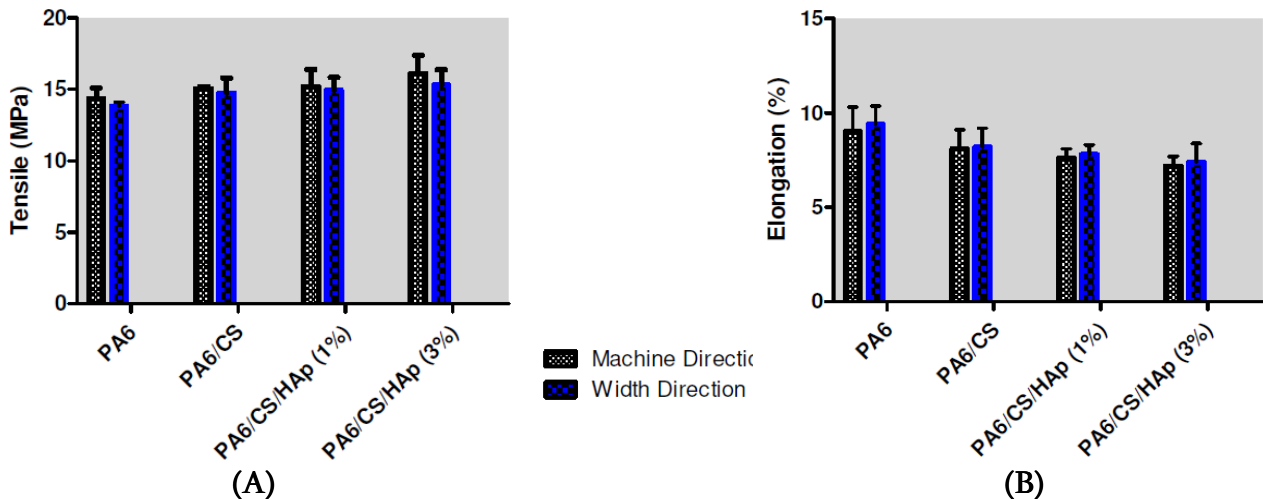


Figure 7. Tensile strength (A) and elongation (B) of the electrospun nanofibrous composites.

It was observed that the tensile strength of the nanofibrous scaffolds was greater in the machine direction comparing with the width direction, however, reverse is true for the elongation at break values. This is due to the fibers laid in parallel along with the same rotation direction of the drum collector.

Although coherent results obtained through the experiments, in literature, there are critical challenges were emphasized for accurate determination of the tensile properties of nanofibers. For example; fiber size distribution in the mats, porosity, individual fiber orientation in the structure, fiber–fiber interaction, entanglement of the fibers, existence of imperfections (beads, etc.) and branching of fibers are important parameters that have great influence on the tensile response of the nanofibrous composites [16].

4. Conclusions

Polyamide 6 (PA6) / Chitosan (CS) based nanofibers containing different amount of Hydroxyapatite (HAp) were electrospun successfully. Properties of the blended solutions were explored before electrospinning. Viscosity of the solutions was increased when chitosan and HAp were introduced to the system, however, conductivity was declined when adding chitosan into the solution. On the other hand, HAp enhanced the conductivity of the blend solutions. Smooth and beadless nanofibers were obtained through the electrospinning process. The diameters of the electrospun nanofibers were ranged from 55 ± 17 to 87 ± 22 . The results revealed that uniform nanofibers were obtained with the addition of a various amount of HAp. It was observed that HAp particles were deposited onto both fibers and the composite surface. Tensile strength and elongational characteristics of the nanofibrous biocomposites were also measured. Results indicated that tensile strength of the blend composites including CS and HAp was greater than the composites made of neat PA6. On the other hand, elongation at break results were smaller for the blend nanofibrous composites compared with the composites including only neat PA6. It can be mentioned that electrospun nanofibrous composites showed well performance for developing novel materials which may be potential candidates to be used in bone tissue engineering applications.

References

1. H. W. Kim J.-H. Song, H.-E. Kim. Nanofiber generation of gelatin–hydroxyapatite biomimetics for guided tissue regeneration. *Adv. Func. Mater.* 15 (2005) 1988-1994.
2. Y. Zhang, J. R. Venugopal, A. el-Turki, S. Ramakrishna, B. Su, Ch. T. Lim. Electrospun biomimetic nanocomposite nanofibers of hydroxyapatite / chitosan for bone tissue engineering. *Biomater.* 29 (2008) 4314-4322.
3. A. Abdal-Hay, H. R. Pant, J. K. Lim. Super-hydrophilic electrospun nylon-6 / hydroxyapatite membrane for bone tissue engineering. *Euro. Polymer J.* 49 (2013) 1314-1321.
4. K. Fujihara, M. Kotaki, S. Ramakrishna. Guided bone regeneration membrane made of polycaprolactone / calcium carbonate composite nano-fibers. *Biomater.* 26 (2005) 4139-4147.
5. Ch. Li, Ch. Vepari, H.-J. Jin, H. J. Kim, D. L. Kaplan. Electrospun silk–BMP–2 scaffolds for bone tissue engineering. *Biomater.* 27 (2006) 3115-3124.
6. G. Sui, X. Yang, F. Mei, X. Hu, G. Chen, X. Deng, S. Ryu. Poly-L-lactic acid / hydroxyapatite hybrid membrane for bone tissue regeneration. *J. Biomed. Mater. Res. A* 82 (2007) 445-454.
7. S. A. Catledge, W. C. Clem, N. Shrikishen, S. Chowdhury, A. V. Stanishevsky, M. Koopman, Y. K. Vohra. An electrospun triphasic nanofibrous scaffold for bone tissue engineering. *Biomed. Mater.* 2 (2007) 142-150.
8. K. M. Woo, J.-H. Jun, V. J. Chen, J. Seo, J.-H. Baek, H.-M. Ryoo, G.-Sh. Kim, M. J. Somerman, P. X. Ma. Nano-fibrous scaffolding promotes osteoblast differentiation and biomineralization. *Biomater.* 28 (2007) 335-343.
9. D. Fallahi, M. Rafizadeh, N. Mohammadi, B. Vahidi. Effect of applied voltage on jet electric current and flow rate in electrospinning of polyacrylonitrile solutions. *Polymer Int.* 57 (2008) 1363-1368.
10. H. Zhang, Sh. Li, Ch. J. B. White, X. Ning, H. Nie, L. Zhu. Studies on electrospun nylon-6 / chitosan complex nanofiber interactions. *Electrochim. Acta.* 54 (2009) 5739-5745.
11. J. R. Schaefgen, C. F. Trivisonno. Polyelectrolyte behavior of polyamides. I. Viscosities of solutions of linear polyamides in formic acid and sulfuric acid. *J. Am. Chem. Soc.* 73 (1951) 4580-4585.
12. V. Beachelya, X. Wen. Effect of electrospinning parameters on the nanofiber diameter and length. *Mater. Sci. Eng. C* 29 (2009) 663-668.
13. P. Supaphol, Ch. Mit-Uppatham, M. Nithitanakul. Ultrafine electrospun polyamide-6 fibers: Effects of solvent system and emitting electrode polarity on morphology and average fiber diameter. *Macromol. Mater. Eng.* 290 (2005) 933-942.
14. J. S. Kim, D. H. Reneker. Mechanical properties of composites using ultrafine electrospun fibers. *Polymeric Composites* 20 (2004) 124-131.
15. W. H. Park, L. Jeong, D. I. Yoo, S. Hudson. Effect of chitosan on morphology and conformation of electrospun silk fibroin nanofibers. *Polymers* 45 (2004) 7151-7157.
16. X. Wei, Zh. Xia, Sh.-Ch. Wong, A. Baji. Modelling of mechanical properties of electrospun nanofibre network. *Int. J. Exp. & Comp. Biomech.* 1 (2009) 45-57.

MECHANICAL PROPERTIES OF NANOSTRUCTURED COPPERCOATINGS MADE BY COLD GAS DYNAMIC SPRAY

R. Maev, V. Leshchynsky, E. Strumban,
D. Dzhurinskiy, J. Kocimski, E. Maeva

Institute for Diagnostic Imaging Research
Windsor, Canada
leshynsk@uwindsor.ca

Accepted September 19, 2013

1. Introduction

Grain refinement by severe plastic deformation is increasingly being developed as a way of processing materials with improved mechanical properties, such as high mechanical strength and plasticity. Cold gas dynamic spray (CS) is widely known as a surface coating technique in which a coating is formed due to bombardment of a metallic substrate by metallic particles accelerated to high velocities and consolidation of these particles due to impact. This process can generate nanocrystalline layers in the impact zone of both the particles impinging upon the substrate and the substrate itself. Understanding the physical mechanisms underlying the severe deformation of the impact zones and grain refinement of material being deposited by CS is crucial for the optimization and improvement of the CS technology.

Localised shear is known to be an important mode of deformation which leads to super high strains and development of interparticle bonding in various powder composites. The CS technology is known to be the process of metallic particles impacting the substrate with a velocity of about 600 – 1000 m / s that results in particle deformation at strain rates in the range of $10^3 - 10^9 \text{ s}^{-1}$. That is why it is well recognized that localization of deformation induced by an adiabatic shear band formation in the impacting particles is one of the dominant mechanisms for successful bonding in CS [1–6]. However, there is a lack of experimental data demonstrating the contribution of SPD to CS coating bonding as well as numerical simulation of the process.

In this article, an experimental investigation of properties and structure formation of the CS deposited Cu coatings has been conducted together with the finite element (FE) simulations of multiparticle impact to characterize the severe deformation in the areas impacted by the impinging particles; the influence of SPD on the nanocrystalline structure of the formed coatings-substrate interface has been shown.

2. Experimental procedure

The CS process was used for depositing Cu coatings on A516 low carbon steel substrates. Commercially available Cu powder, with particles ranging in size from 5 to $100 \mu\text{m}$, has been

used. The particles were accelerated to a high velocity by injecting them into a stream of high pressure carrier gas which was subsequently expanded to supersonic velocity through a converging–diverging de Laval nozzle. After exiting the nozzle, the particles were impacted onto a substrate, where the solid particles deformed and created a bond with the substrate. As the process went on, particles continued to impact and form bonds with the previously consolidated material resulting in a uniform deposit with very little porosity and high bond strength.

The A516 Gr.70 low carbon steel substrates were grit blasted (blasting air pressure 0.75 MPa, stand off distance 150 mm, traverse speed 20 – 40 mm / s) with alumina (mesh 36) to remove the scale layer formed due to the hot rolling process used to produce the substrate material. Commercially available low oxygen Cu powder (Tafa, Inc., Concord, NH, USA) with an average diameter of about 22 μm was used. To form a Cu coating, the following CS parameters were utilized with Plasma Giken CS machine: propellant gas – Nitrogen, gas pressure – 5 MPa, gas temperature – 800 °C; powder feed rate – 100 g / min, and nozzle traverse speed – 500 mm / s.

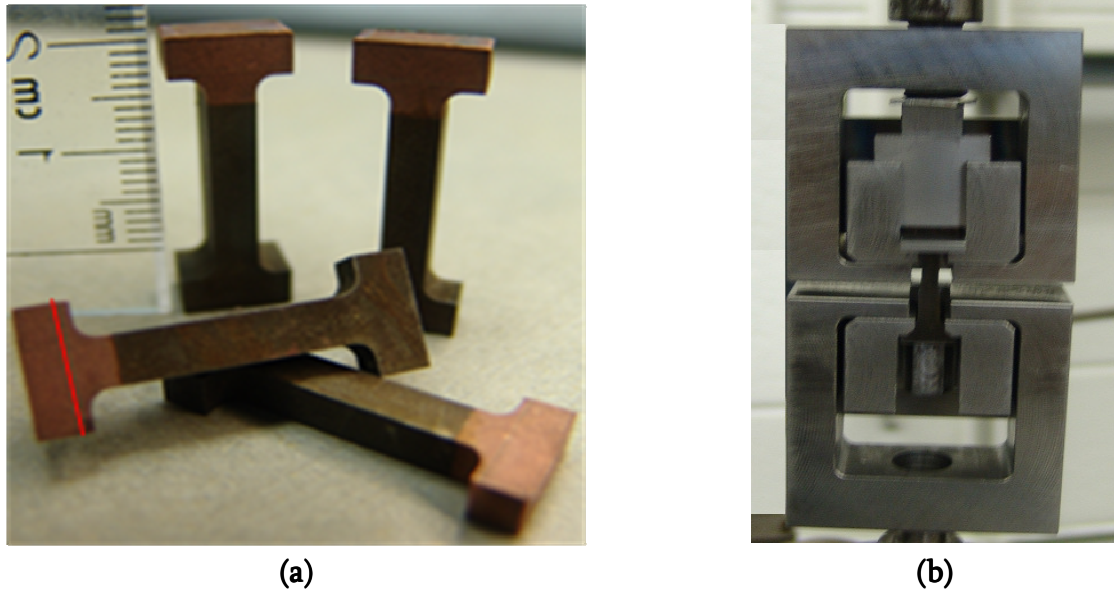


Figure 1. Cut out “dog bone”-shaped samples for adhesion tests (a) and the sample holder (b).

To determine the adhesion strength of the deposited Cu coatings, tensile testing was carried out according to ASTM E8 / E8M–09 and the following steps have been carried out: “dog bone”-shaped samples (**Figure 1a**) were cut out across the coating substrate interface, so that one of the sample shoulders would be cut out of the deposited Cu coating, while the second shoulder and the gauge would be cut out of the A516 low carbon steel substrate; a small copper insert was brazed to the coating surface to make the Cu shoulder of the sample larger for a more convenient gripping; a special sample holder was designed and fabricated (**Figure 1b**) to fit the dimensions of the “dog bone”-shaped sample with a working length of 20 mm; the sample holder was placed in the ZWIK machine, which was used for Cu coating adhesion testing.

Optical light microscope Leica DMI5000 M with a digital camera DFS 320 R2 was used for metallographic characterization of Cu coating / A516 (Gr.70) low carbon steel interfaces. The FEI Quanta 200 FEG scanning electron microscope (SEM) was used for microstructural analysis of Cu coating/A516 (Gr.70) low carbon steel interfaces, including characterization of

both the substrate and the coating, as well as adhesion and cohesion interactions. The TEM examinations were conducted using JEOL 2010 ARP (200KV) analytical scanning TEM. The details are described in [7]. The surface roughness of the grid based A516 Gr.70 low carbon steel substrates was measured by Seimitsu 2800 E roughness measurement machine. The profile diagram is shown in **Figure 2**.

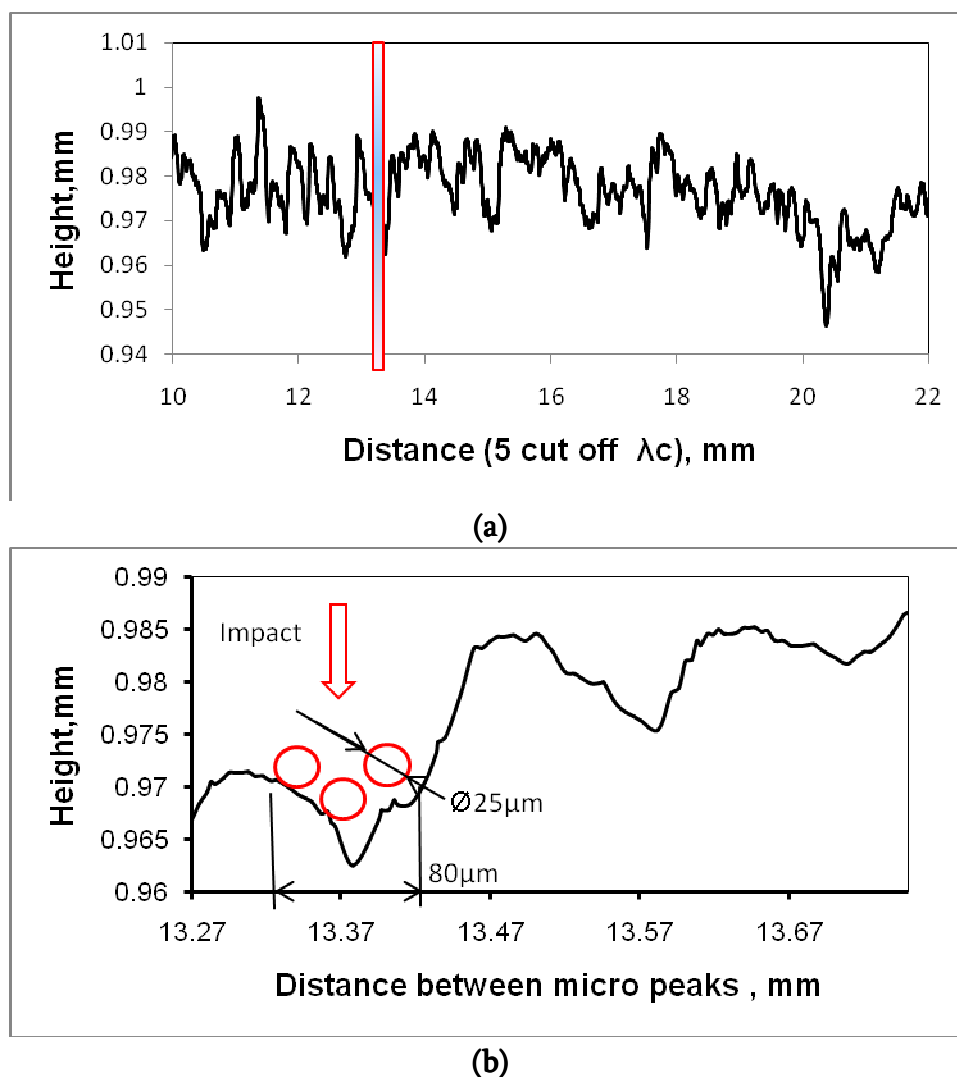


Figure 2. Roughness of the substrate after grit blasting with Al_2O_3 0.7 mm grit: (a) roughness profile of the cut off distance 10 mm; (b) the profile of a shaded area (length – 400 μm). The impinging upon the substrate particles are shown in red.

3. Numerical simulation of multiparticle impact

3.1. Simulation procedure

To study the Cu particle deformation during deposition with the CS process, a dynamic simulation of multiple impact of the Cu particles impinging upon the carbon steel substrate was run, using commercial Lagrangian Finite Element software Abaqus / Explicit Version 6.9 [8]. A 3D FEM analysis was performed for 25 and 50 μm particle size configurations. **Figure 3** shows

the scheme of the simulated model. The bottom surface of the simulated substrate was fixed and additionally the horizontal movement of the substrate in two perpendicular directions was limited by fixing the substrate sides. For both the 25 and 50 μm Cu particles impinging upon the substrate, their temperature was $T_p = 80\text{ }^\circ\text{C}$, the substrate temperature was $T_s = 20\text{ }^\circ\text{C}$ and the impact velocity was $V_p = 800\text{ m/s}$.

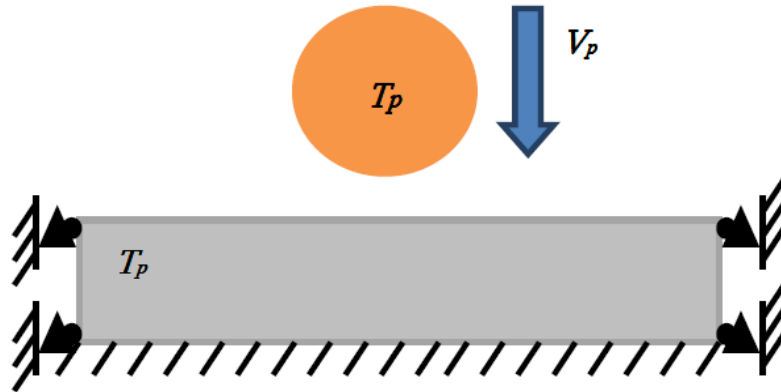


Figure 3. The schematic diagram of impact model with boundary conditions.

Flow stress of both materials was defined using the Johnson–Cook model which is described by the following equation:

$$\sigma = (A + B\varepsilon^n)(1 + C \ln \dot{\varepsilon}^*)(1 - T^{*m})$$

where σ is the (von Mises) flow stress, A is the yield stress at reference temperature and reference strain rate, B is the coefficient of strain hardening, n is the strain hardening exponent, ε is the plastic strain, $\dot{\varepsilon}^* = \dot{\varepsilon} / \dot{\varepsilon}_0$ is the dimensionless strain rate with $\dot{\varepsilon}$ being the strain rate and $\dot{\varepsilon}_0$ the reference strain rate, and T^* is the homologous temperature and expressed as:

$$T^* = \frac{T - T_{ref}}{T_m - T_{ref}}$$

A , B , C , m and n are Johnson–Cook constants which were taken from [1, 5].

3.2. Numerical simulation results

Figures 4a and c demonstrate the von Mises stress distribution in the particles and substrate during impact of two parallel particle columns (shown in Figures 4b and d). It can be seen from the images in Fig. 4a,c that the plastic deformation of the substrate due to impact is considerable in spite of the fact that the yield strength of carbon steel substrate is higher than that of Copper particles.

The calculated particle penetration depth into the substrate is about 32.1 μm for the case shown in Figure 4a, and 14.8 μm for Figure 4b. A comparison of Figures 4a and c shows the influence of the distance between columns and eccentricity of the particle location on the plastic deformation of both the particles and the substrate. In the case of the gap between particle columns in the range of 5 μm (Figure 4a) the substrate material is severely deformed in the area between particles which results in the formation of substrate material jets. Another specific feature of multiparticle impact is nonuniformity of the particle deformation in the case of non-symmetric impact (Figure 4c).

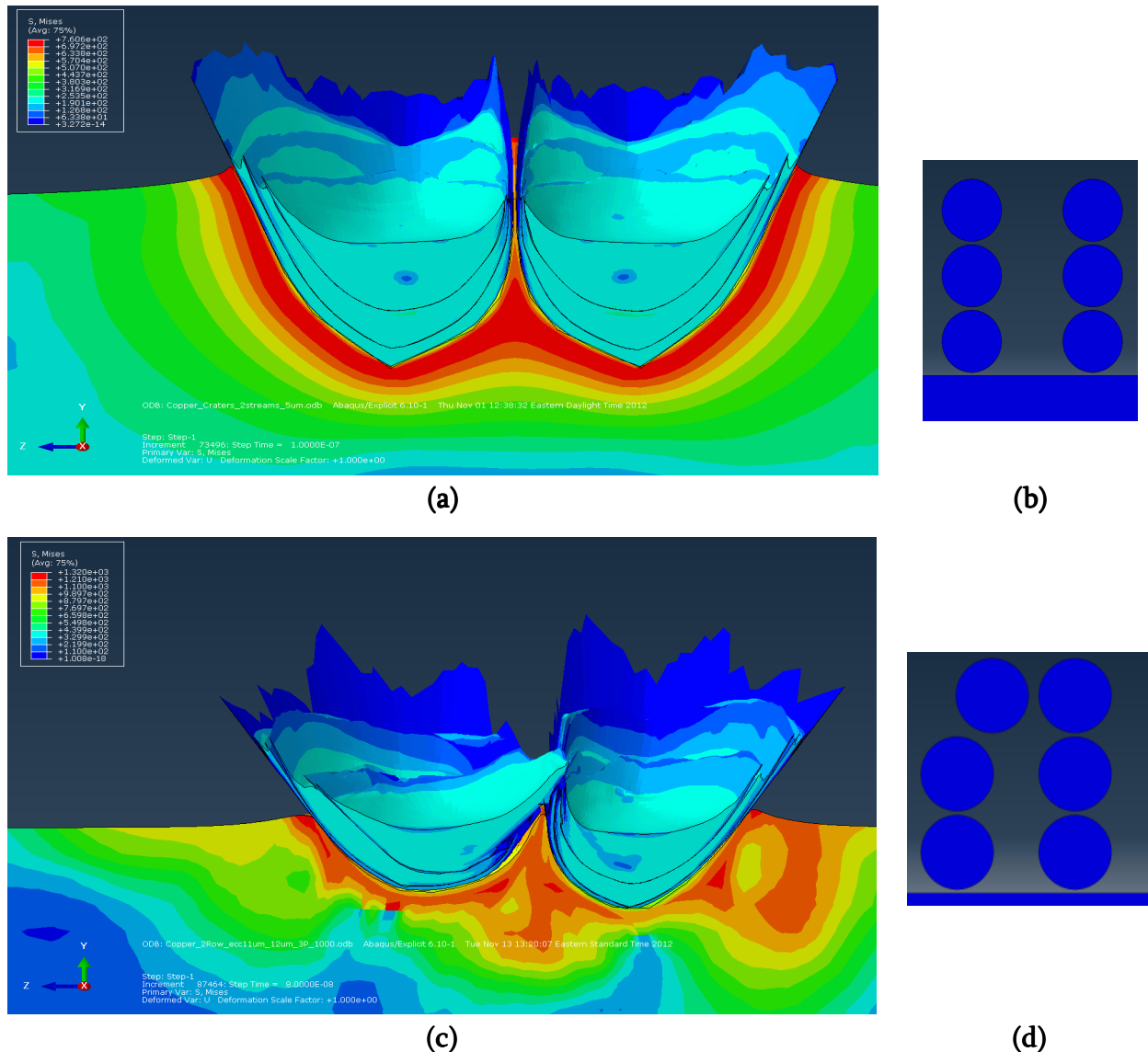


Figure 4. Numerical simulation results of the multiparticle impact with the carbon steel substrate. (a, c) von Mises stress distribution for symmetric (b) and non symmetric (d) particle impact. Particles – copper, diameter of 20 μm ; impact velocity – 1000 m / s; eccentricity – 11 μm (d); gap between particle columns 5 μm (b) and 12 μm (d); impact time – 80 ns; depth of penetration – 32.1 μm (a) and 14.8 μm (b); crater diameter – 34.5 μm (a) and 36.4 μm (c).

To characterize the particle deformation process during multiparticle impact the equivalent strains in various nodes (**Figure 5a**) on the particle surface were calculated. The results are shown in **Figure 5b**. One can note that the total strain of the nodes # 6 – 10 varies in the range of $\varepsilon = 15 - 25$, which is related to the severe strains due to localization of deformation at the interface. The strains of the nodes in the particle core are in the range of $\varepsilon = 2 - 5$ in the case of multiparticle impact. Thus the main conclusion of numerical modeling is that CS technology is characterized by severe deformation of both the particles and the substrate, which depends on the technological parameters of CS. The localization of deformation, severe deformation and formation of material jets seem to be the main processes that lead to obtaining nanostructured coatings with high mechanical properties.

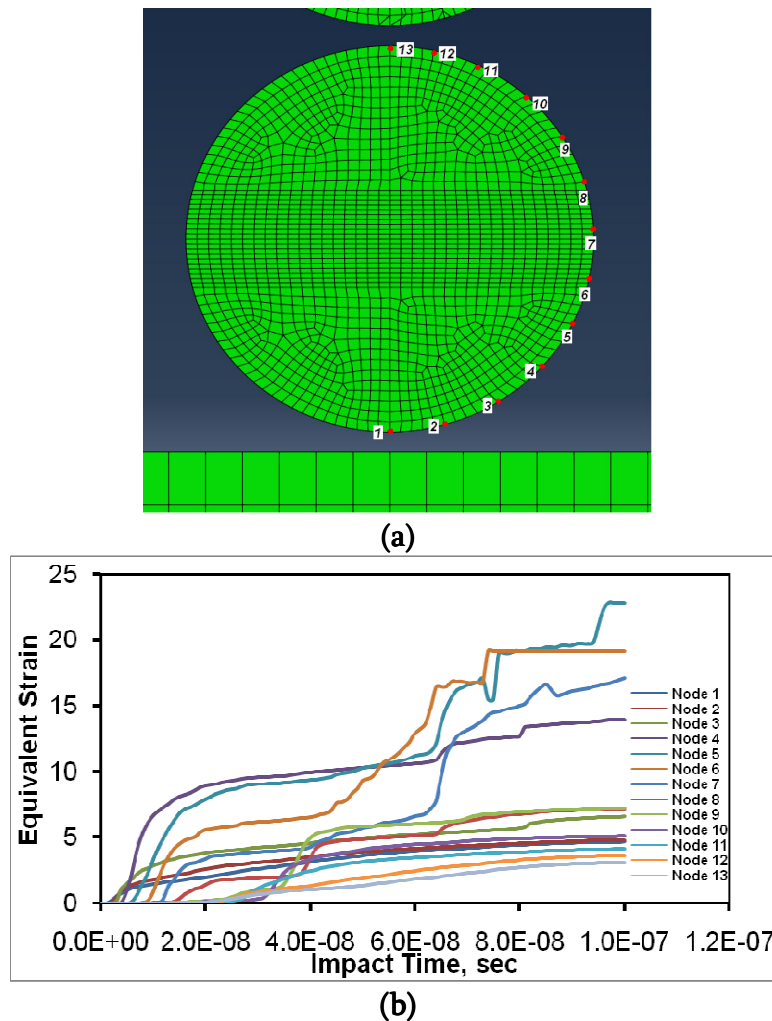


Figure 5. Equivalent strains in the various nodes of the bottom particle: (a) nodes location; (b) equivalent strains at the various times of impact.

4. Experimental results and discussion

4.1. Coating surface morphology and structure at the interface

The morphology and structure of the cold spray deposited coatings in general depend on the substrate roughness is usually reflected in the topography of the formed coating. The morphology also depends on the mechanical properties of the substrate and the impact conditions of the powder material sprayed at high velocity. It also depends on the coating/substrate interface formation mechanism. In the case of Cu coating / A516 Gr.70 low carbon steel substrate, the interface is formed by the deposition of Cu by high pressure Nitrogen carrier gas which accelerated Cu particles at a velocity around 800 m / s [9]. It was found that the initial substrate surface roughness at the interface produced by alumina grit-blasting (**Figure 2**) was considerably altered by the accelerated Cu particles impacting the grit blasted substrate surface. As can be seen in **Figure 6**, the formed interface structure is comprised of micropeaks up to 50 μm high and craters with a mean diameter of 20 – 40 μm and a depth of 10 – 15 μm .

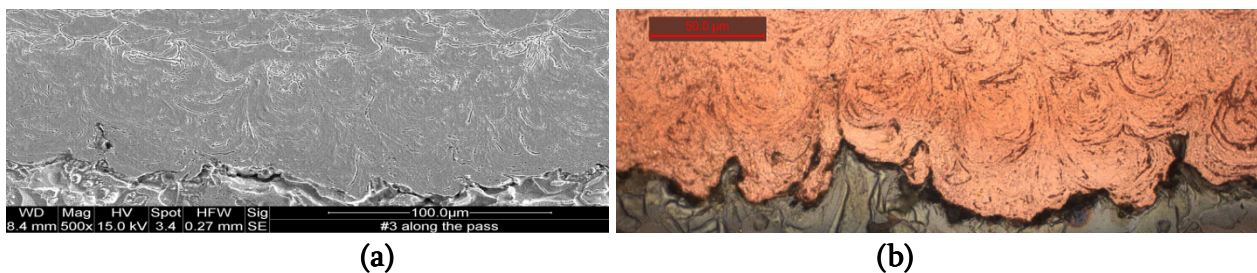


Figure 6. Vortex morphology of the sublayer. Substrate preprocessing grit size: (a) 0.4 mm and (b) 0.7 mm.



Figure 7. Structure of coating / substrate interface.

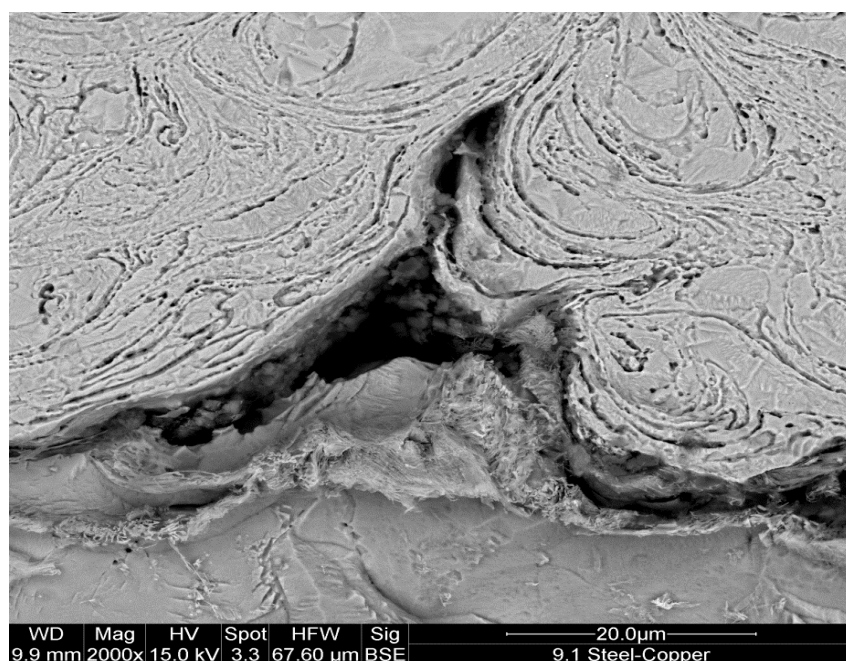


Figure 8. The “turbulent” structure of the sublayer in angled cross-sections. Deep etching with nital.

The alumina grit size increase, which results in higher surface roughness, leads to obtaining the mechanical interlocking of Cu particles at the interface. The presence of the interlocked Cu localized in the substrate craters can be seen (Figure 7). The substrate surface roughness considerably influences the vortex structure of the Cu layer. The role of the substrate surface roughness micropeaks in mechanical interlocking of the impinging copper particles and forming the vortex structure of the Cu layer is well observed (Figure 8) in prepared 45 °-angled cross-sections.

4.2. Nanostructure of cold sprayed coatings

The severe deformation of the deposited material and strain localization result in formation of the vortices that are presented in **Figures 6 – 8**. It is interesting to note that the vortices have a 3D structure, which is shown in the microstructure of coatings cut parallel to the substrate surface (**Figure 9**).

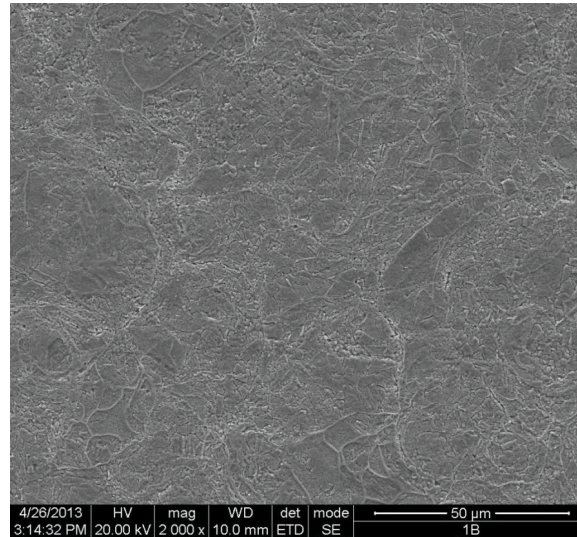


Figure 9. Microstructure of Cu coating in the plane parallel to a substrate surface.

The vortices seen consist of small grains being generated during recrystallization of Cu because of high temperature and strain created at the interface due to multiple particle impact. The influence of the nozzle traverse speed on the grain structure of copper coating is shown in **Figure 10**.

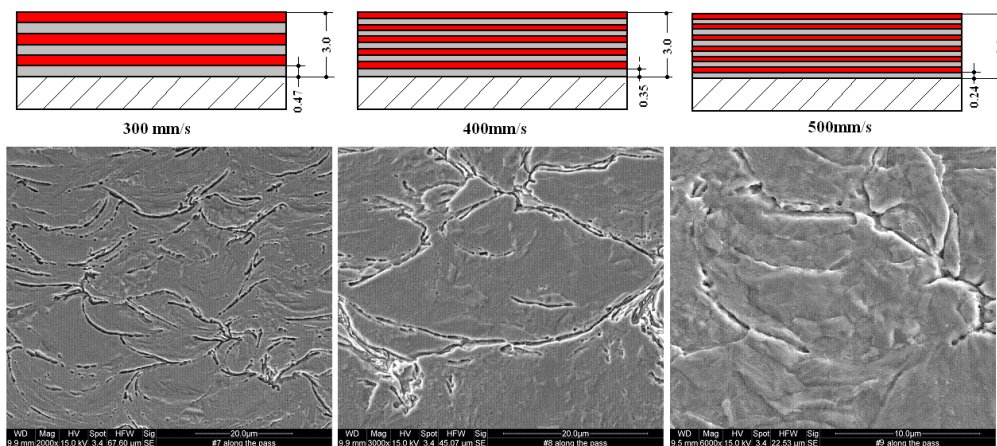


Figure 10. Effect of secondary deformation during the following pass deposition on the coating structure (core of coating).

The increase of the nozzle traverse speed from 300mm/s to 500mm/s results in diminishing of a single pass thickness, which leads to an additional strain accumulation and increase of total strain of the Cu grains. This leads to submicro and nanograins similar to those shown on TEM micrograph (Fig. 11)

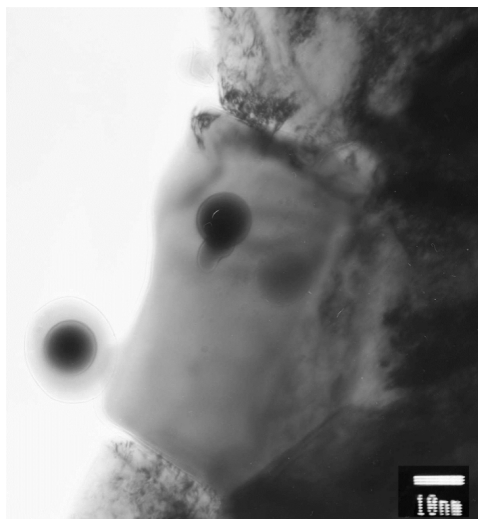


Figure 11. HRTEM image of the copper nanograins at the interface.

The separate recrystallized nanograins free from dislocations and similar to those described by Borchrts et al. [10] can be seen. The presence of low angle boundaries confirms the assumption about the influence of severe plastic deformation taking place during the CS process on the nanocrystalline structure formation at the coating-substrate interface.

4.3. Adhesive strength of copper coatings

To single out the separate mechanisms contributing to the Cu layer / low carbon steel substrate bonding, the adhesion tension tests were performed in accordance with the procedure described above. The results are shown in **Figure 12**.

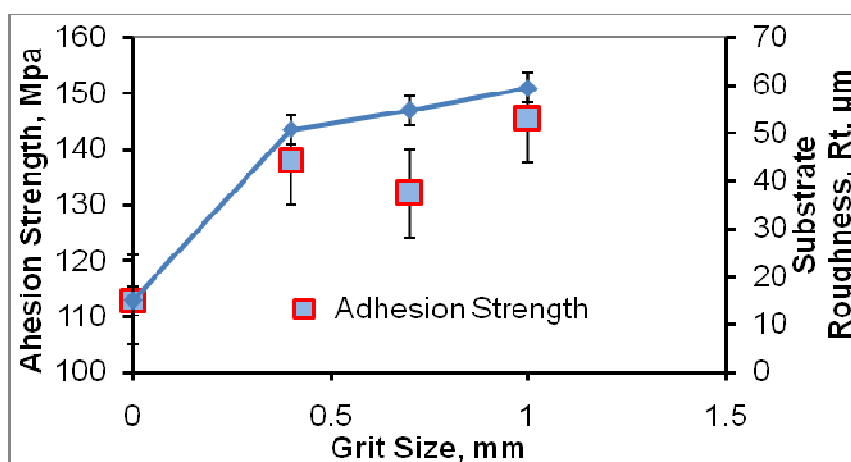


Figure 12. Dependence of roughness on adhesion strength of copper coatings deposited on carbon steel substrates.

The microstructures of the Cu – carbon steel interface shown in **Figures 6 – 8** exhibit the effect of interlocking. Moreover, fracture topography (image is not shown) examination shows that the fractures take place in the localized “necks” within the interlocked particles. In other words, a partly ductile fracturing of Cu grains is taking place in some areas of the formed interface.

The interlocking effect is associated with the effect of nanostructuring, which allows to achieve the proper bonding between Cu and Fe. Both effects caused by severe plastic deformation result in considerable increase of adhesion strength. As can be seen in **Figure 12** the adhesion strength reaches approximately 150 – 160 MPa which is 2.5 – 3 times higher than that of thermal spray coatings.

5. Conclusion

The experimental and simulation study of nanostructured Cu coating formation by cold spray allows us to make the following conclusions:

- Severe deformation of both particles and substrate is defined by numerical modeling of multiparticle impact. The total strains of the nodes at the particle interface are found to be in the range of $\varepsilon = 15 - 25$.
- Considerable vortex formation process is experimentally demonstrated by the proper selection of the CS process parameters.
- Severe deformation of Copper particles results in effective nanostructuring processes. TEM microscopy confirms the presence of nanograin in the copper – carbon steel interface.
- Coupling of nanostructuring and interlocking effects due to strain localization and severe deformation at CS results in obtaining a coating with high adhesion strength.

References

1. H. Assadi, F. Gartner, T. Stoltenhoff, H. Kreye. Bonding mechanism in cold spraying. *Acta Mater.* 51 (2003) 4379-4394
2. T. Schmidt, F. Gartner, H. Assadi, H. Kreye. Development of a generalized parameter window for cold spray. *Acta Mater.* 54 (2006) 729-742.
3. T. Schmidt, F. Gaertner, H. Kreye Jr. New developments in cold spray based on higher gas and particle temperatures. *Thermal Spray Technol.* 15 (2006) 488-494
4. A. Papyrin, V. Kosarev, S. Klinkov, A. Alkhimov. *Cold Spray Technology*. Elsevier (2006) 125-210.
5. Ed. V. K. Champagne. *The Cold Spray Materials Deposition Process: Fundamentals and Applications*. Cambridge: Woodhead Publ. Ltd (2007) 230-312
6. R. G. Maev, V. Leshchynsky. *Introduction to Low Pressure Gas Dynamic Spray*. John Willey & Son – VCH (2007).
7. S. Dumek, M. Blicharski, J. Morgiel, E. Fras. TEM investigation of ductile iron alloyed with vanadium. *J. Microscopy* 237 (2010) 461-464.
8. ABAQUS / Explicit 6.9-1 Manual. Pawtucket: Hibbitt, Karlsson and Sorensen (2002).
9. R. Huang, H. Fukunuma Study of the influence of particle velocity on adhesive strength of cold spray deposits. *J. Thermal Spray Technol.* 21 (2012) 541-549.
10. C. Borchers, F. Gartner, T. Stoltenhoff, H. Kreye. Microstructural bonding features of cold sprayed face centered cubic metals. *J. Appl. Phys.* 8 (2004) 4288-4292

STRUCTURAL AND DIELECTRIC STUDIES
OF Cr³⁺ DOPED ZnFe₂O₄ NANOPARTICLES

R. M. Sebastian¹, K. Maniammal², Sh. Xavier¹, E. M. Mohammed¹

¹Maharaja's College
Ernakulam, India
emmohammed_2005@yahoo.com
²University of Kerala
Trivandrum, India

Accepted September 19, 2013

1. Introduction

Spinel ferrites with general formula MFe₂O₄ shows unique and interesting structural and electrical properties depending on their chemical composition, method of preparation, nature of ions and their site preference among tetrahedral and octahedral sites in the lattice. Nano ferrites is extensively studied due to their various technological applications in sensors, electronic communication devices like digital diary, video camera, recorder, cellular phones, floppy drives etc., bubble devices, high density magnetic storage devices, also for magnetically guided drug delivery [1 – 3]. Preparation method plays a vital role in obtaining ferrites with high quality. Several synthesis techniques like solid state reaction, sol-gel, co-precipitation, citrate precursor technique, ball milling etc., could be used for the fabrication of ferrites [4, 5]. Good stoichiometric control and production of ultra fine particles in the nano range at a relatively low temperature makes sol-gel method as an attractive preparation technique for ferrites [6]. Normal spinel zinc ferrite (ZnFe₂O₄) is commercially important due to its wide application as gas sensors, absorbent material and photo catalyst [7, 8].

The incorporation of metal ions to the spinel structure can considerably change the magnetic and electrical properties. Several reports on the magnetic properties of nano crystalline zinc ferrite are available in literature [4, 9, 10]. However the structural and electrical properties of Cr³⁺ substituted zinc ferrite has not been investigated in detail. In the present paper, the effect of Cr³⁺ substitution on structural and electrical properties of nano crystalline zinc ferrite prepared by Sol-gel technique is reported.

2. Experiment

2.1. Synthesis

Ferrite Sample with chemical formula ZnCr_xFe_{2-x}O₄ ($x = 0.0, 0.2, 0.4, 0.8$) were prepared by simple sol-gel technique. AR grade of zinc nitrate, chromium nitrate, ferric nitrate in the Stoichiometric ratio were used as chemical precursors in ethylene glycol as the solvent. The sol

was heated at 60 °C until a wet gel of metal nitrates was obtained. The gel was dried at 120 °C, which self ignites to form a fluffy product by the redox reaction of the gel where ethylene glycol acts as the reducing agent and the nitrate ions act as the oxidant. The obtained powder was ground well and sintered at 400 °C for 2 h. For dielectric measurements, cylindrical disc shaped pellets of diameter 13 mm and height 1 – 2 mm were made using a hydraulic press by applying a uniform pressure of 5 tons.

2.2. Characterization

The structural characterization of the prepared samples were done using the X-ray diffraction (XRD) patterns recorded using BRUKER make AXS D8 ADVANCE powder X-ray diffractometer with Cu – K_α radiation ($\lambda = 1.5406 \text{ \AA}$) at 40 kV and 35 mA from 20 to 80 ° in steps of 0.02 ° per second. The Fourier Transform Infrared (FTIR) absorption spectra of the prepared sample were recorded using FTIR spectrometer (Thermo Nicolet, Avatar 370) in the wave number range 4000 to 400 cm⁻¹ with potassium bromide (KBr) as binder. Morphological analysis of the zinc ferrite samples were performed by transmission electron microscope (Hitachi Japan H7650). Dielectric measurements were carried out using precision impedance analyzer Wayne Kerr 6500B in the frequency range (20 Hz to 5 MHz) at 300 K. The two faces of the pellet are coated with silver paste to form a parallel plate capacitor with zinc ferrite as the dielectric material.

The capacitance of the parallel plate capacitor is given by

$$C = \frac{\epsilon_0 \epsilon' A}{d}, \quad (1)$$

where A is the area, d the thickness of the pellet, ϵ_0 is the permittivity of free space and ϵ' is the permittivity of the dielectric material. Thus real part of permittivity of the sample can be calculated from the relation

$$\epsilon' = \frac{Cd}{\epsilon_0 A}. \quad (2)$$

From the values of dielectric permittivity and loss tangent the imaginary part of permittivity and AC conductivity of the sample can be calculated using equations (3) and (4),

$$\epsilon'' = \epsilon_r \tan \delta, \quad (3)$$

where $\tan \delta$ is the dielectric loss factor, the energy dissipated in the form of heat when field is applied to the sample

$$\sigma_{ac} = 2\pi f \epsilon_0 \tan \delta. \quad (4)$$

The XRD patterns of all the samples were refined using the GSAS program developed by Larson & van Dreele [11], from X-ray powder diffraction data. The space group and initial structural parameters for all the samples were taken as: F_{d3m} and Wycokoff positions of metal and iron atoms as (0.125, 0.125, 0.125) and (0.5, 0.5, 0.5) respectively and oxygen in (x, x, x) special position, where $x = 0.2555$. All the octahedral, tetrahedral and oxygen sites were assumed to be fully occupied. Multi term Simpson's rule integration of the pseudo-Voigt function was used to model the diffraction profiles. The fitting quality of the experimental data is assessed using the following parameters: the goodness of fit (χ^2) which must tend to 1 and 2 reliability factors R_p and R_{wp} (weighted difference between measured and calculated values), which must be close to or less than 10 % [12].

3. Result and discussion

3.1. Structural analysis

XRD pattern of $ZnCr_xFe_{2-x}O_4$ ($x = 0.0, 0.2, 0.4, 0.8$) nano particles is depicted in **Figure 1**. The patterns were compared with standard data (JCPDS card No: 82 – 1042).

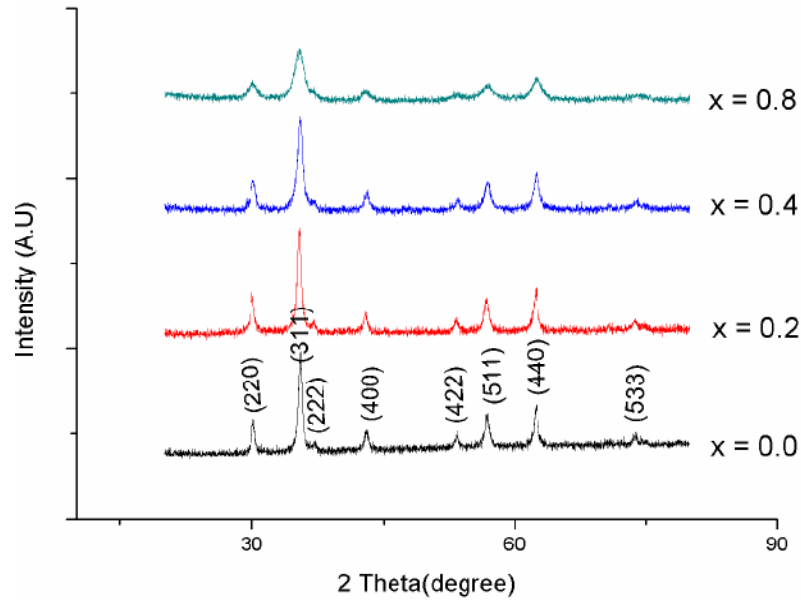


Figure 1. XRD pattern of $ZnCr_xFe_{2-x}O_4$ nanoparticles ($x = 0.0, 0.2, 0.4, 0.8$)

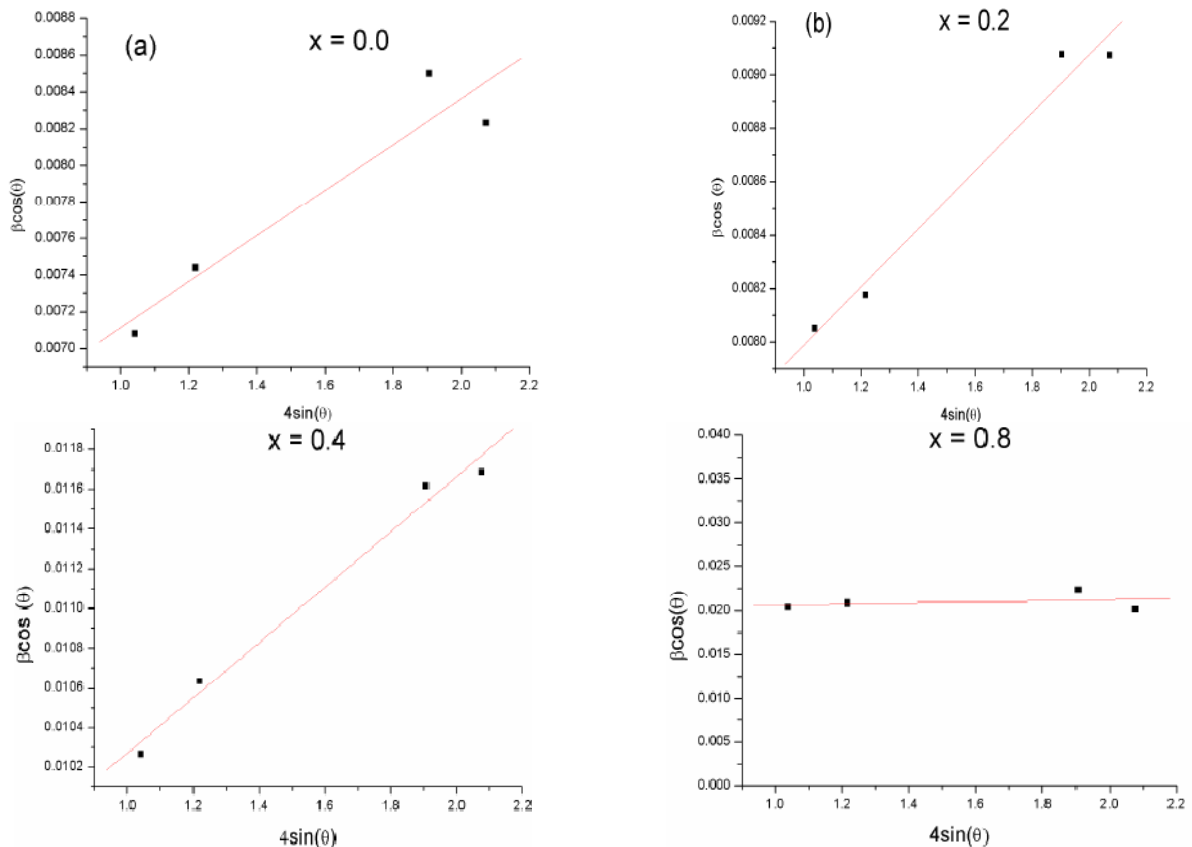


Figure 2. Hall–Williamson plots for $ZnCr_xFe_{2-x}O_4$ series.

The crystallite size of all the samples was calculated using the Scherrer formula. The angle θ for maximum intensity and full width at half maximum (FWHM or β) were determined by fitting the peaks with Lorentzian curve. The β values were calculated using the equation [13]

$$\beta = \beta_{obs} - \beta_{inst}, \quad (5)$$

where β_{obs} is the observed FWHM from the XRD pattern of the sample and β_{inst} is the FWHM of the standard sample. For Lorentzian shape

$$\beta \cos \theta = \frac{\lambda}{D} + 4\varepsilon_{str} \sin \theta, \quad (6)$$

where ε_{str} is the strain due to imperfections in the crystal. Hall–Williamson plots between $\beta \cos \theta$ and $4 \sin \theta$ for all prominent peaks for all the samples is shown in **Figure 2**.

From the graph strain as well as average crystallite size corrected for micro strain has been tabulated in **Table 1**. From the table it is clear that the crystallite size obtained by Hall–Williamson method is greater than that obtained by Scherrer’s formula. It is because the strain correction factor has been taken into account in Hall–Williamson method, where as it was not taken into account in Scherrer’s method.

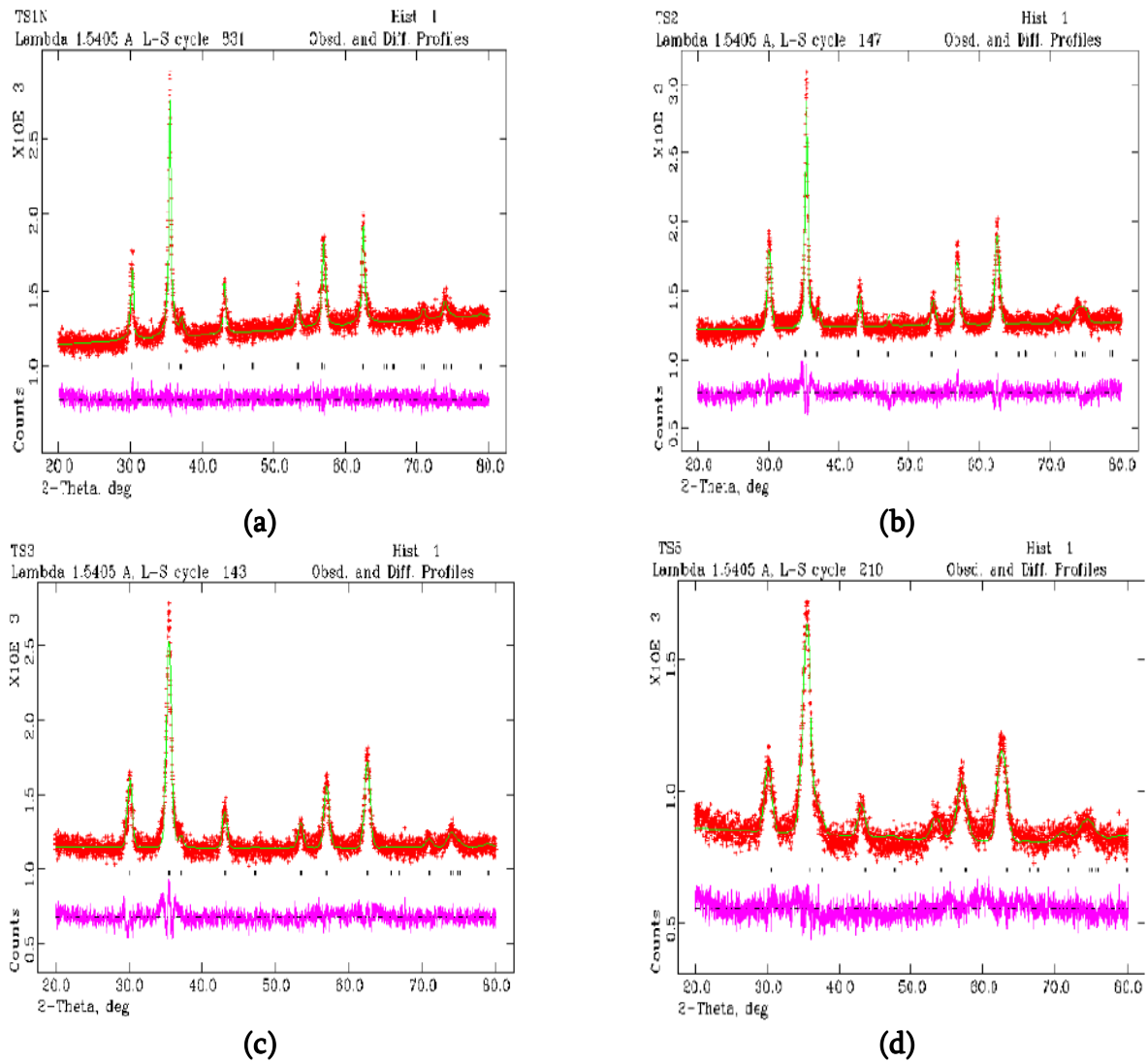


Figure 3. (a) to 3 (d): Rietveld refinement pattern for ZnCr_xFe_{2-x}O₄ nanoparticles ($x = 0.0, 0.2, 0.4, \text{ and } 0.8$).

Table 1. Structural parameters of the Zn–Cr ferrite series.

Doping concentration	Average particle size calculated by Scherrer's method, nm	Average particle size calculated by Hall–Williamson method, nm	Strain calculated by Hall–Williamson method, %
$x = 0.0$	18.64 ± 0.3	23.66 ± 1.7	0.125
$x = 0.2$	16.69 ± 0.2	20.09 ± 0.5	0.109
$x = 0.4$	12.90 ± 0.1	15.61 ± 0.3	0.139
$x = 0.8$	6.67 ± 0.1	6.89 ± 0.6	0.052

Rietveld refinement pattern for the samples is represented in **Figure 3a – d**. X-ray data points are shown by plus marks; the solid line is the best fit to the data and the tic marks show the positions for the allowed reflections. The lower curve represents the difference between the observed and calculated profiles.

The values of goodness of fit (χ^2), reliability factors (R_p and R_{wp}), and the lattice constant calculated from Rietveld method are listed in **Table 2**. The low values of χ^2 , R_p and R_{wp} confirms the goodness of refinement.

Table 2. Lattice constant and Rietveld agreement factors for zinc chromium mixed ferrite series.

Parameter	$x = 0.0$	$x = 0.2$	$x = 0.4$	$x = 0.8$
R_p , %	2.850	2.700	2.700	3.130
R_{wp} , %	2.290	3.400	3.430	3.920
χ^2	1.049	1.505	1.414	1.347
Lattice constant, Å	8.433	8.427	8.410	8.325
Unit cell volume, Å ³	599.717	598.438	594.823	576.969

From **Table 2** it is clear that the lattice constant decreases with increase in chromium content. This decrease in lattice constant with Cr³⁺ content can be explained on the basis of the difference in ionic radii of Fe³⁺ (0.67 Å) and Cr³⁺ (0.64 Å).

**Figure 4.** TEM image of the sample ZnCr_{0.4}Fe_{1.6}O₄.

Figure 4 shows the representative TEM image of the sample ZnCr_{0.4}Fe_{1.6}O₄. From **Figure 4** it is clear that most of the nano particles are spherical in shape and agglomerated.

3.2. FTIR Spectra

FTIR spectra of the investigated samples are shown in **Figure 5**. The two main absorption bands in the ranges 600 – 550 and 450 – 385 cm⁻¹, the typical bands of spinel structure are attributed to the stretching vibrations of the unit cell of the spinel in the tetrahedral (A) site and the metal–oxygen vibration in the octahedral (B) site [14].

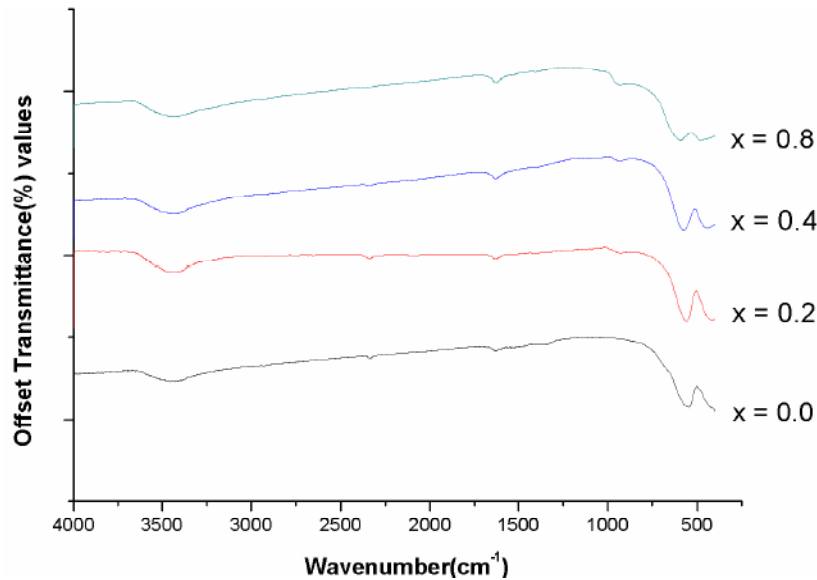


Figure 5. FTIR spectra of ZnCr_xFe_{2-x}O₄ series.

From **Figure 5** it is clear that Cr³⁺ ion doping, the absorption band ν_2 broadens and shift to the higher frequency side which indicates that Cr³⁺ ions occupies the octahedral site. It can also be noted that as the band broadens and intensity decreases which can be explained on the basis that more disorder states give broader and less intense bands in IR spectra [15]. The bands around 3400 and 1600 cm⁻¹ are the contribution of the stretching vibration of free and absorbed water.

3.3. Electrical properties

3.3.1. Dielectric constants

Variation of real and imaginary part of permittivity with frequency at 300 K is depicted in **Figures 6** and **7**.

It can be clearly seen that both real and imaginary part of permittivity exhibits an inverse dependence on frequency. The decrease in both real and imaginary part of permittivity is sharp at the lower frequency region and remains almost a constant at high frequencies. The rapid decrease of permittivity in the low frequency range can be explained by the basic Koop's phenomenological theory [16], which considers the dielectric structure as an inhomogeneous medium of Maxwell–Wagner type [17]. In this model, the dielectric structure of ferrites is assumed to be consisting of highly conducting grains, separated by poorly conducting boundaries. It is known that the grain boundaries are more effective at low frequencies and the grain at high frequencies [18].

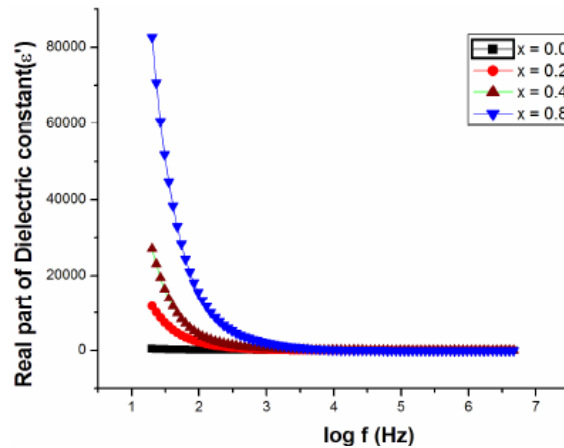


Figure 6. Frequency variation of real part of dielectric constant.

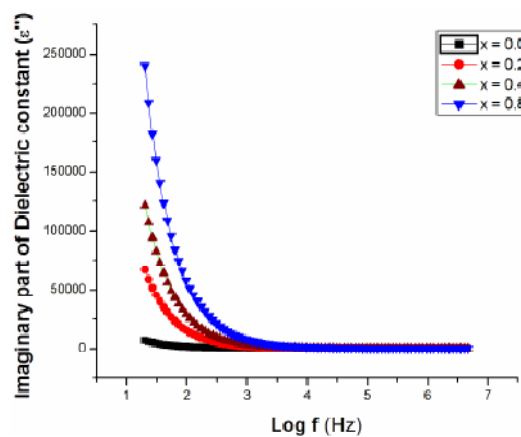


Figure 7. Frequency variation of imaginary part of dielectric constant.

During the electron hopping process between Fe^{2+} to Fe^{3+} , the high resistance of the grain boundaries makes the electrons accumulate on the grain boundaries, producing space charge polarization, resulting in comparatively high value of dielectric constant at low frequencies, But as frequency increases the grains come into action reducing the dielectric constant rapidly due to decrease in space charge polarization. Even if the conductivity increases with frequency the hopping of electrons cannot follow the applied frequency of the alternating field, consequently the dielectric permittivity attains a constant value at higher frequencies.

It is evident from the figure that both real and imaginary part of dielectric constant increases with Cr^{3+} ion doping. It should be noted that the dielectric constant is higher for Cr^{3+} substituted zinc ferrite than zinc ferrite. Similar result has been reported for Nd^{3+} substituted zinc ferrite [19]. The electron exchange between $\text{Fe}^{2+} \leftrightarrow \text{Fe}^{3+}$ ion pairs determines the dielectric polarization and whose magnitude depends on the percentage of Fe^{2+} and Fe^{3+} ion pairs at A and B sites. The increase in dielectric constants (ϵ' and ϵ'') in the present case can be explained by low concentration of Fe^{2+} ion at the B site leading to low value of resistivity, hence high value of dielectric parameter [20].

3.3.2. AC Conductivity

The frequency variation of AC conductivity at room temperature for zinc chromium mixed ferrite is depicted in **Figure 8**.

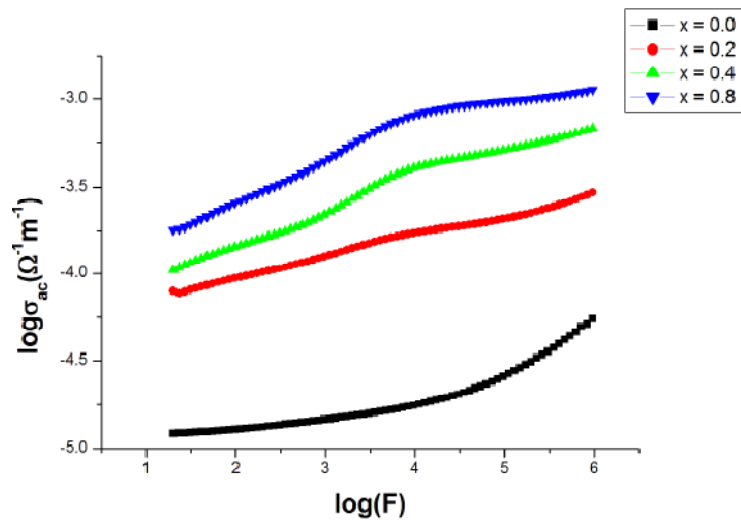


Figure 8. Variation of AC conductivity with frequency.

The increase in AC conductivity with frequency for all the compositions can be explained using Maxwell Wagner two layer model of polycrystalline ferrite [21]. At low frequency the poorly conducting grain boundaries are more prominent hence leading to low value of conductivity. But as frequency increases, conductive grains become active, which results in increase of conduction. The plots of all the Zn–Cr ferrite samples are almost linear, which points to conduction due to small polaron hopping [22]. The AC conductivity is found to increase with chromium ion concentration.

3.3.3. Dielectric loss tangent

The energy loss within the ferrite is termed as dielectric loss tangent ($\tan \delta$). The variation of $\tan \delta$ with frequency at room temperature for all the samples is shown in **Figure 9**.

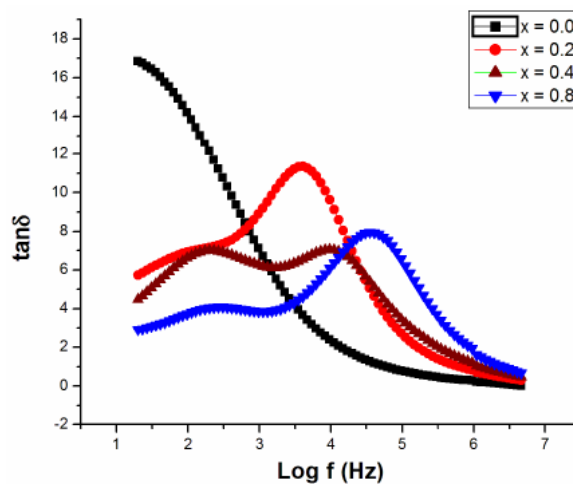


Figure 9. Variation of dielectric losstangent with frequency.

Relaxation peak is observed in all the samples except for un-doped zinc ferrite. This peaking behaviour can be explained by Rezlescu–Rezlescumodel [23]. According to this model, the conduction mechanism in ferrites is considered to be due to hopping of electrons between

divalent and trivalent iron ions situated in octahedral sites. The peaking behaviour is obtained when the hopping frequency exactly matches with the frequency of the external applied field.

It is also observed that all the samples show greater values of dielectric loss at low frequencies and there after decreases rapidly with frequency. This can be explained well using Maxwell-Wagner two layer model of poly-crystal ferrite. As the grain boundaries are active at low frequency region, more energy is required for electron hopping, resulting in high loss, where as in high frequency region, a small energy is required for electron transfer between the two Fe ions as grains are prominent.

4. Conclusions

A series of Cr³⁺ substituted zinc ferrite were synthesized by the sol-gel technique. All the studied samples were pure cubic spinel type ferrite without any impurity phase. The lattice constant of all the samples calculated from Rietveld analysis suggests the contraction of the unit cell with chromium doping. The crystallite size is observed to decrease with chromium doping. The TEM image shows that the particles are spherical in shape and agglomerated. The absorption bands in FTIR spectra are found in the expected range of ferrites and this corroborates the spinel structure of the samples. The absorption bands ν_2 broadens and shifts to the higher frequency side which indicates the substitution of Fe³⁺ ions on octahedral sites by Cr³⁺ ions. Frequency dependence of dielectric constant shows normal behaviour and agrees well with Koops theory. AC conductivity increases with frequency in all the samples. Low value of dielectric loss at high frequencies makes nano sized chromium doped zinc ferrite particularly useful in high frequency applications.

References

1. A. Goldman. *Modern Ferrite Technology*. New York: Springer (2006).
2. W. Ch. Kim, S. J. Kim, S. W. Lee, Ch. S. Kim. Growth of ultrafine NiCuZn ferrite magnetic property synthesized by sol gel method. *J. Magn. & Magn. Mater.* 226 (2001) 1418-1420.
3. M. Hashim, Alimuddin, Sh. Kumar, B. H. Koo, S. E. Shirsath, E. M. Mohammed, J. Shah, R. K. Kotnala, H. K. Choi, H. Chung, R. Kumar. Structural electrical and magnetic properties of Co-Cu ferrite nanoparticles. *J. Alloys & Comp.* 518 (2012) 11-18.
4. L. W. Yeary, J.-W. Moon, C. J. Rawn, L. J. Love, A. J. Rondinone, J. R. Thompson, B. C. Chakoumakos, T. J. Phelps. Magnetic properties of biosynthesized zinc ferrite nanoparticles. *J. Magn. & Magn. Mater.* 323 (2011) 3043-3048.
5. K. R. Krishna, D. Ravinder, K. V. Kumar, U. S. Joshi, V. A. Rana, A. Lincon. Dielectric properties of Ni-Zn ferrites synthesized by citrate gel method. *World J. Cond. Matter* 2 (2012) 57-60.
6. M. Srivastava, S. Chaubey, A. K. Ojha. Investigation on size dependent structural and magnetic behaviour of nickel ferrite nanoparticles prepared by sol-gel and hydrothermal methods. *Mater. Chem. & Phys.* 118 (2009) 174-180.
7. P. Hu, D.-A. Pan, X.-F. Wang, J.-J. Tian, J. Wang, Sh.-G. Zhang, A. A. Volinsky. Fuel additives and heat treatment effect on nano crystalline zinc ferrite phase composition. *J. Magn. & Magn. Mater.* 323 (2011) 569-573.

8. Y. Xu, Y. Liang, L. Jiang, H. Wu, H. Zhao, D. Xue. Preparation and magnetic properties of ZnFe₂O₄ nanotubes. *J. Nanomater.* 10 (2011) 525967 1-5.
9. J. P. Singh, R. S. Payal, R. C. Srivastava, H. M. Agrawal, P. Chand, A. Tripathi, R. P. Tripathi. Effect of thermal treatment on the magnetic properties of nano structured zinc ferrite. *J. Phys. Conf. Ser.* 217 (2010) 012108 1-4.
10. P. M. P. Swamy, S. Basavaraja, A. Lagashetty, N. V. S. Rao, R. Nijagunappa, A. Venkataraman. Synthesis and characterization of zinc ferrite nano particles obtained by self propagating low temperature combustion method. *Bull. Mater. Sci.* 34 (2011) 1325-1330.
11. C. Larson, R. B. van Dreele. General Structure Analysis System. Los Alamos National Laboratory (2001): <ftp://ftp.lanl.gov/public/gsas>.
12. J. A. Gomes, M. H. Sousa, F. A. Tourinho, J. Mestnik-Filho, R. Itri, J. Depeyrot. Rietveld structure refinement of the cation distribution in ferrite fine particles studied by X-ray powder diffraction. *J. Magn. & Magn. Mater.* 289 (2005) 184-187.
13. S. Thankachen, B. P. Jacob, Sh. Xavier, E. M. Mohammed. Effect of neodymium substitution on structural and magnetic properties of magnesium ferrite nano particles. *Phys. Scripta* 87 (2013) 025701 1-7.
14. R. D. Waldron. Infrared spectroscopy of ferrites. *Phys. Rev.* 99 (1955) 1727-1735.
15. A. B. Gadkari, T. J. Shinde, P. N. Vasambekar. Structural analysis of Y³⁺ doped Mg-Cd ferrites prepared by oxalate co-precipitation method. *Mater. Chem. & Phys.* 114 (2009) 505-510.
16. C. G. Koops. On the dispersion of resistivity and dielectric constant of some semiconductors at audio frequencies. *Phys. Rev.* 83 (1951) 121-124.
17. K. W. Wagner. Zur Theorie der unvollkommenen Dielektrika. *Ann. Phys.* 40 (1913) 817-855.
18. B. P. Jacob, S. Thankachan, Sh. Xavier, E.M. Mohammed. Dielectric behavior and AC conductivity of Tb³⁺ doped Ni_{0.4}Zn_{0.6}Fe₂O₄ nano particles. *J. Alloys & Comp.* 541 (2012) 29-35.
19. T. J. Shinde, A. B. Gadkari, P. N. Vasambekar. Effect of Nd³⁺ substitution on structural and electrical properties of nano crystalline zinc ferrite. *J. Magn. & Magn. Mater.* 322 (2010) 2777-2781.
20. E. Pervaiz, I. H. Gul. Structural electrical and magnetic studies of Gd³⁺ doped cobalt ferrite nanoparticles. *Int. J. Curr. Eng. & Technol.* 2 (2012) 377-387.
21. M. George, S. S. Nair, K. A. Malini, P. A. Joy, M. R. Anantharaman. Finite size effects on the electrical properties of sol-gel synthesized CoFe₂O₄ powders: Deviation from Maxwell-Wagner theory and evidence of surface polarization effects. *J. Phys. D* 40 (2007) 1593-1602.
22. R. S. Devan, B. K. Chougule. Effect of composition on coupled electric, magnetic and dielectric properties of two phase particulate magnetoelectric composite. *J. Appl. Phys.* 101 (2007) 014109 1-6.
23. N. Rezlescu, E. Rezlescu. Dielectric properties of copper containing ferrites. *Phys. Status Solidi A* 23 (1974) 575-582.

COMPACT LOW-PASS FILTER USING COMPLEMENTARY ROSE CURVE RESONATORS (CRCRs)

I. Sassi¹, L. Talbi¹, K. Hettak²

¹ Université du Québec en Outaouais
Gatineau, Canada,
sasi01@uqo.ca

² Communication Research Center
Ottawa, Canada

Accepted September 19, 2013

1. Introduction

Artificial magnetic materials provide a wide range of exciting physical phenomena that are not achievable with the omnipresent materials. These magnetic materials are realized with metal and dielectrics elements [1]. These elements can be found in different shapes (SRR, Spiral, Rose curve ...). Periodic arrangement of these particles provides enhanced positive or negative permeability at radio frequencies [2]. Since metamaterials offer new exciting physical phenomena, there is an increasing amount of interest in these materials and they are considered as a good candidate for several applications. Recently, complementary split ring resonators (CSRRs) defined as the negative image of a split ring resonators (SRRs) have been investigated for negative permittivity and left handed metamaterial in microwave application [3].

Low-pass filters are circuit structure very attractive in modern microwave communication systems. These circuits allow removing undesired harmonics or spurious mixing products in radio frequency front-end circuits. For these purposes, various low-pass filter structures have been proposed. Stepped impedance resonators [4], Defected ground structure [5] and compact microstrip resonator cell [6] are the studied structure to implement low-pass filter with good performance.

All the sub-mentioned structures of low loss filters present a gradual cut-off response and don't permit to have a sharp pass-band to stop-band transition which is a very important quality to design low pass filter. In fact, by increasing the number of cascade subdivision, the rejection characteristic of circuit structure can be improved. Nevertheless, adding more parts to the circuit structure will deteriorate the pass-band insertion loss and also increase the physical size of the low-pass filter.

In fact, complementary split ring resonators (CSRRs) are new categories of structures used to design planar microwave circuits [7]. The complementary split ring resonator must be etched either the ground plane or the conductor strip line. In fact, the electric field in this specific region is maximal. Therefore, the electric field must be applied in axial direction to have the maximum coupling between the conductor strip line and the CSRRs.

In 2006, Mandal et al. propose low-pass filter using complementary split ring resonators (CSRRs) for the first time. To eliminate spurious response an open stub was added as a

capacitive load, but this added stub has increased the dimension of the circuit structure. Recently, complementary split ring resonators (CSRRs) are used to improve the rejection characteristics of the low-pass filter without increasing the size of the proposed circuit structure [8]. Using complementary split ring resonator etched to the ground plane, the slow-wave factor of the microstrip line increase and can be improved by using this structure which also indicates a reduction of the geometry size of the proposed filter [8].

The proposed low-pass filter by Zhang et al. was designed using multi-CSRR cells cascaded perpendicularly to the conductor microstrip line. To obtain a set of gradual transmission zero frequencies, the complementary split ring resonator CSRR was modelled by changing the radius and line width. In fact, compared to the complementary split ring resonator CSRR, the complementary rose curve resonator CRCR could enhance the miniaturization factor and decrease the circuit dimension [9].

In this letter, a low-pass filter is realized by cascading complementary rose curve resonator cells to obtain controllable transmission zeroes with reduced dimension circuit structure and large bandwidth. Several CRCRs are used to underscore the geometrical effect on the microstrip line performance and size. First, the complementary rose curve resonator will be presented and its frequency response will be analysed. The second part deals with the new design of the low-pass filter. Finally, the new low-pass filter will be compared to other structures and its performance will be discussed.

2. Complementary rose curve resonator (CRCR)

The complementary rose curve resonator is the only broken looped resonator which can be tuned to provide specific resonant behaviour [10]. In fact, it is based on a circular shape and for highly miniaturized cases, it creates spurious resonances. For that, this structure has more degrees of freedom compared to the split ring resonator SRR, which provide more design flexibility in filter synthesis.

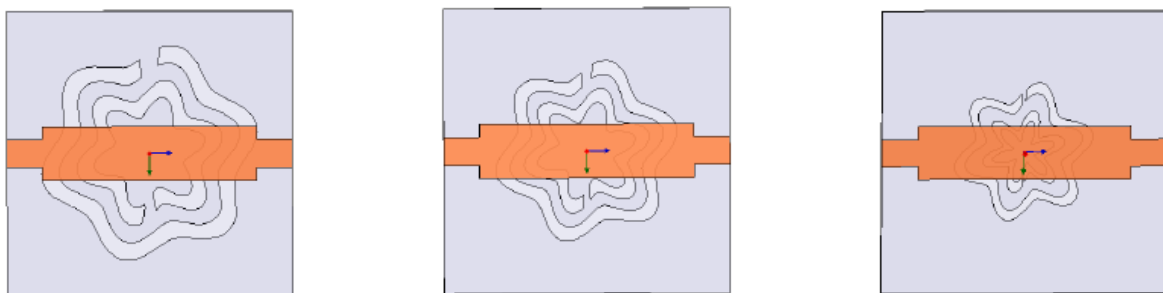


Figure 1. Different CRCRs unit cells (The upper metallization is represented by color orange and the ground plane are is represented by color grey).

Figure 1 shows different complementary rose curve resonator CRCR cells etched in the ground plane and the microstrip on the surface located between two 50Ω lines. There first microstrip line is wider and it is located just above the complementary rose curve resonator cell. This microstrip is applied as compensated shunt capacitance which is usually realized by open stub. Furthermore, there are no discontinuity elements to connect the open subs (the small and the wide microstrip line). In fact, three complementary rose curve resonators are modelled by

modifying the geometrical parameters (the radius, the gap, the slit, the trace width). **Figure 2** is an illustration of the geometrical parameters of the three complementary split ring resonators. The **Table 1** lists with more details the parameter configuration of the CRCR.

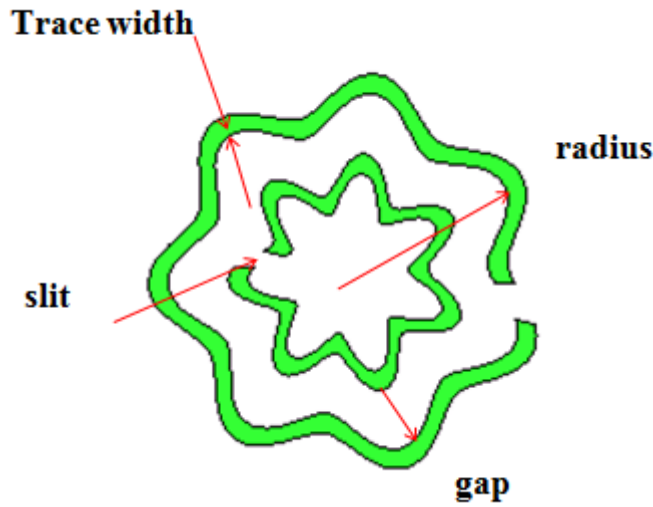


Figure 2. Geometric parameters of the CRCR unit cell.

Table 1. Geometric parameters of different CRCR unit cells,

Unit cell	Radius, mm	Trace width, mm	Gap, mm	Slit, mm
CRCR_1	2.8	0.5	1.0	0.10
CRCR_2	2.3	0.4	0.8	0.07
CRCR_3	1.8	0.3	0.6	0.03
CRCR_4	1.5	0.2	0.5	0.02

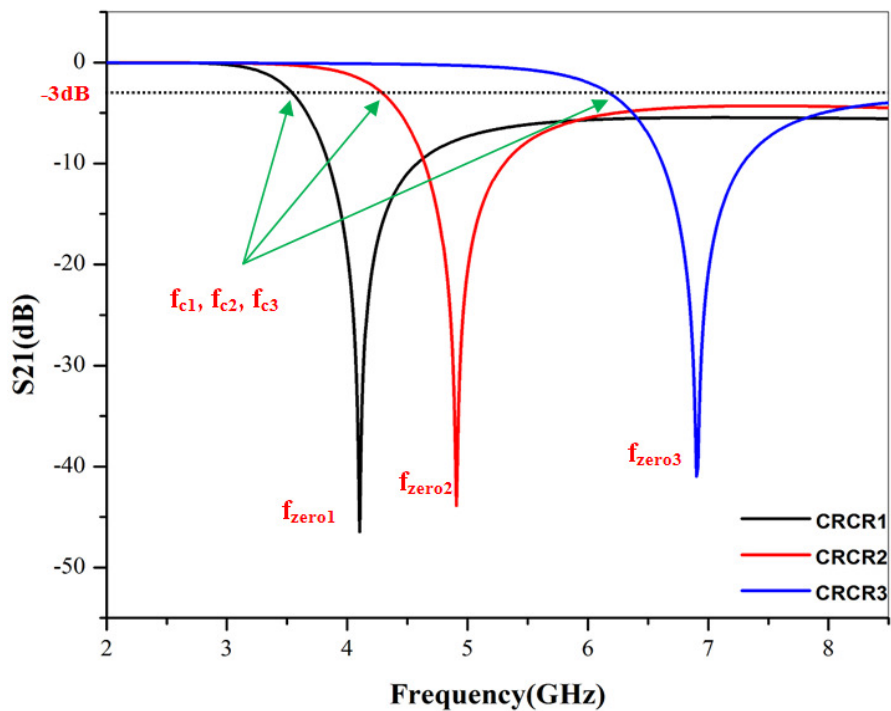


Figure 3. Frequency response of three CRCR units cells with different geometric parameters.

Using Ansoft HFSS, the S-parameters of the complementary rose curve resonators have been simulated. This full-wave three-dimensional electromagnetic commercial software is used to perform the numerical analysis of the frequency response of the CRCRs. **Figure 3** describes the simulated frequency response of the three CRCR cells with different geometrical parameters. f_{zero} is described as the transmission zero frequency which nulls the shunt impedance [8]. From **Figure 3**, it can be noticeable that the frequency at 3 dB is very close to the transmission zero frequency f_{zero} . Consequently, there is a sharp rejection from pass-band to stop-band in this frequency range. By changing the geometry parameters of the CRCR cell, the frequency response of the complementary rose curve resonator change drastically. In fact, by decreasing the radius of the rose, the width of the two rings and the slit, the frequency at 3 dB and transmission zero of the CRCR cell increase considerably. As a result, the frequency response of the complementary rose curve resonator could be tuned by a simple altering in the geometry parameters of CRCR cell.

3. Low-pass filter design

In this section, a low-pass filter will be presented by using two different categories of complementary unit cells resonators. First, the complementary split ring resonators CSRRs are etched in the ground plane, beneath the microstrip line in two different positions. Then, to reduce the circuit dimension and to perform his response, the complementary rose curve resonator will be introduced.

3.1. Wide stop-band LPF using complementary split ring resonators (CSRRs)

Figure 4 illustrates the layout of the low-pass filter using CSRR proposed by Zhang et al. [8]. In fact, this structure consists in three CSRRs cascaded in position 1. Position 1 indicates that the slits of the CSRRs are positioned in the direction perpendicular to the host microstrip line.

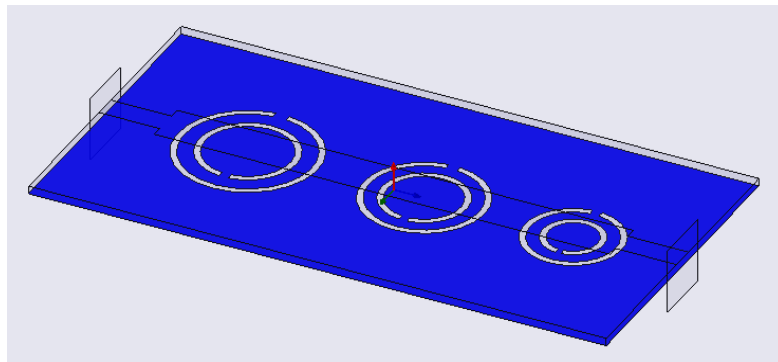


Figure 4. Low-pass filter with CSRR in position 1.

The frequency response of the low-pass filter based on the CSRR in position 1 is illustrated by **Figure 5**. In this structure, the transmission zero of the CSRR unit cells were adjusted at 4.0, 4.9, and 5.9 GHz. The design is done by tuning the geometric parameters of the three CSRRs. From **Figure 5**, the return loss in pass-band is better than -20 dB. The 20 dB stop-band width is from 3.8 to 6.1 GHz.

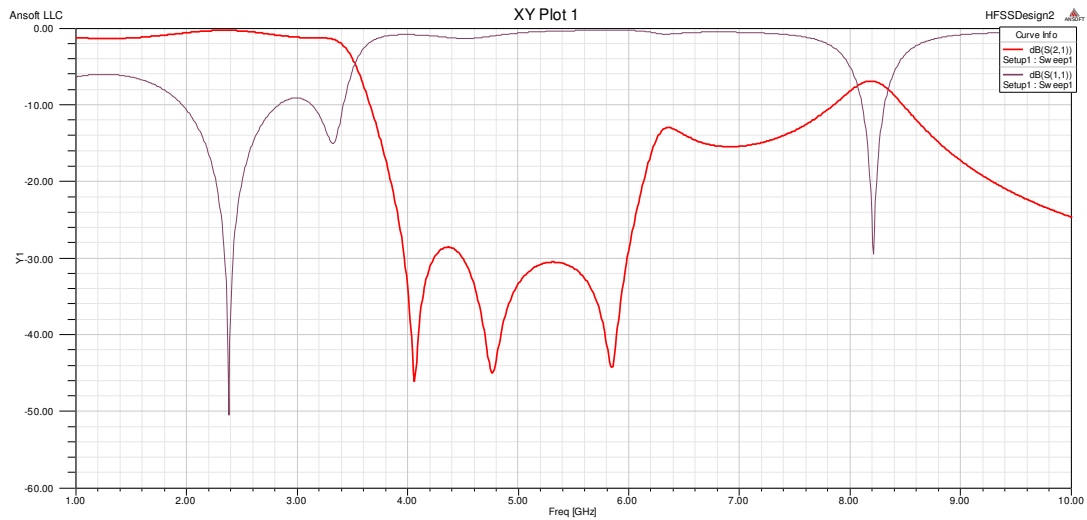


Figure 5. Frequency response of the low-pass filter with CSRR in position 1.

In order to have a wide stop-band, the complementary split ring resonators CSRRs are now etched in the ground plane, beneath the microstrip line in position 2. Position 2 shows that slits are positioned along the microstrip line. **Figure 6** shows the structure of the low-pass filter with CSRRs in position 2.

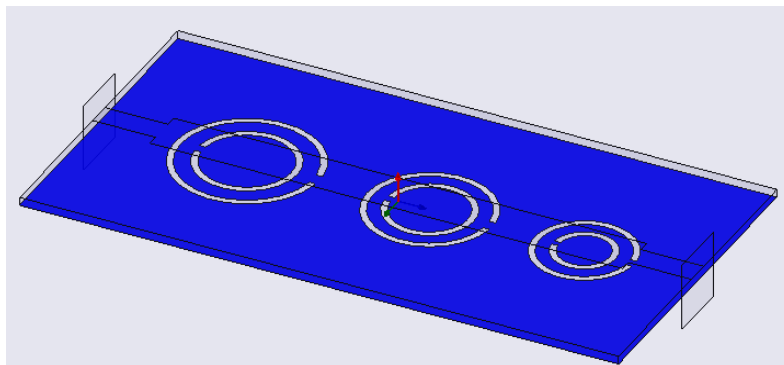


Figure 6. Low-pass filter with CSRR in position 2.

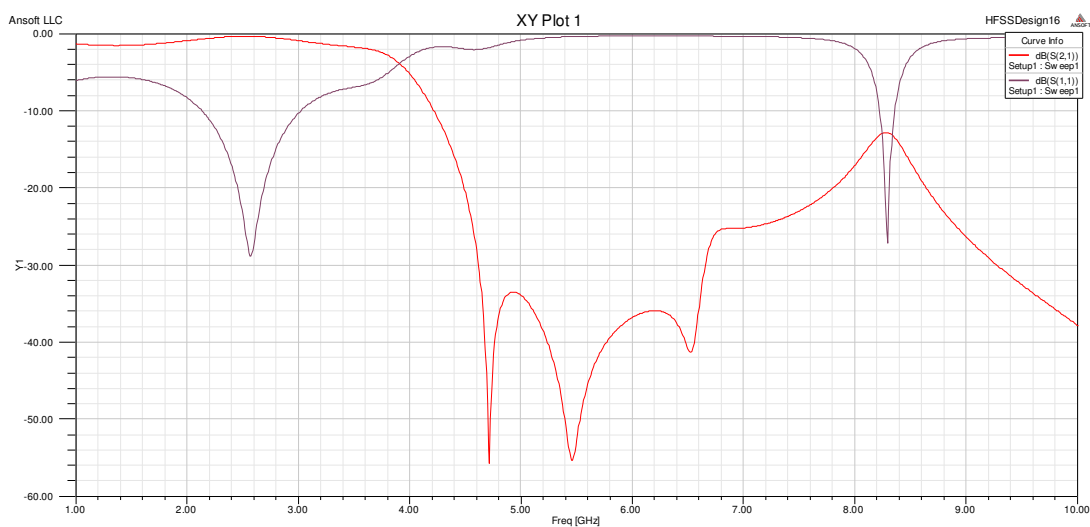


Figure 7. Frequency response of the low-pass filter with CSRR in position 2.

The simulated results of the low-pass filter with CSRR in position 2 are presented by **Figure 7**. It can be seen from this graph, that stop-band width is increased. In fact, this stop-band is from 4.4 to 7.9 GHz. Moreover, the return loss in pass-band is better than -20 dB. Accordingly, by changing the CSRR from position1 to position 2, the response of the low-pass filter has been noticeably performed. In addition, the stop-band width has increased by 35 %.

3.2. Novel LPF using complementary rose curve resonators CRCRs

In order to reduce the size of the low-pass filter based on the CSRRs unit cells, the complementary rose curve resonators will be applied to the microstrip line instead of the CSRRs. The complementary rose curve resonators CRCRs are applied to enhance the miniaturization factor. The miniaturization factor is defined as the ratio of the wavelength at which the CRCR resonate to the length of the microstrip line. In **Figure 8**, three CRCR cells with adjustable zeros transmission frequencies are cascaded and etched to the ground plane. These CRCR cells are modelled by tuning their geometric parameters as shown in **Table 1**.

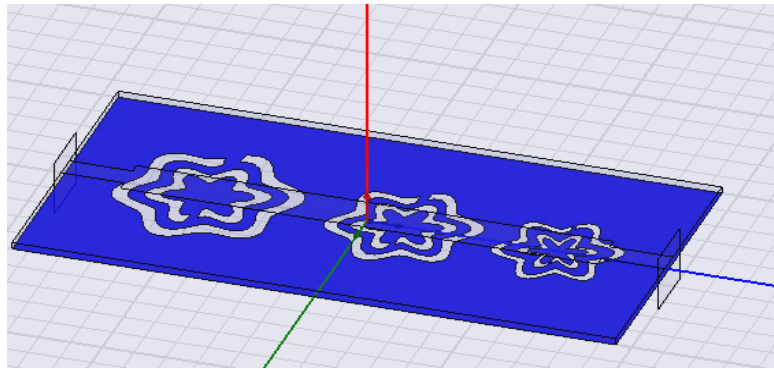


Figure 8. Low-pass filter using three complementary rose curve resonators etched to the ground.

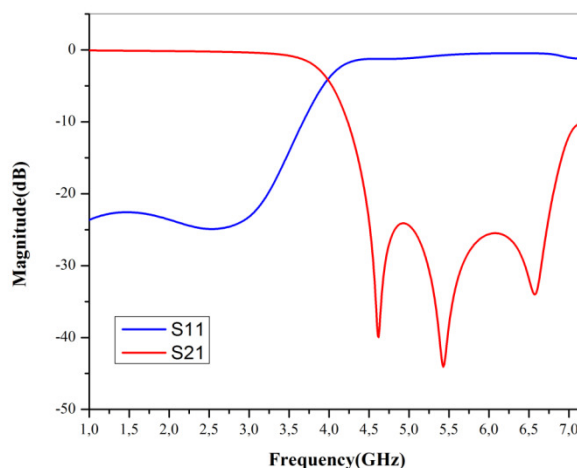


Figure 9. Frequency response of the low-pass filter with three CRCRs.

Simulation results for the low-pass filter using three CRCRs are shown in **Figure 9**. In fact, the stop-band width is from 4.3 to 6.8 GHz. We can notice from this graph, that stop-band width is increased compared to the stop-band width of low-pass filter with CSRRs in position1.

Additionally, the return loss in pass-band is better than -25 dB. Moreover, the size of the low-pass filter is reduced by 30 % compared to low-pass filter loaded by the CSRRs.

For the same size of the low-pass filter based on the CSRRs unit cells, four complementary rose curve resonators have been applied to the microstrip line instead of the CSRRs as shown in **Figure 10**. The geometrical characteristics of the CRCRs unit cells are depicted in the **Table 1**.

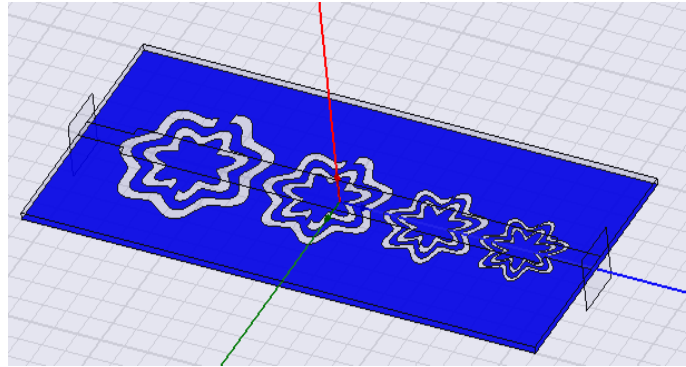


Figure 10. Low-pass filter using four complementary rose curve resonators etched to the ground.

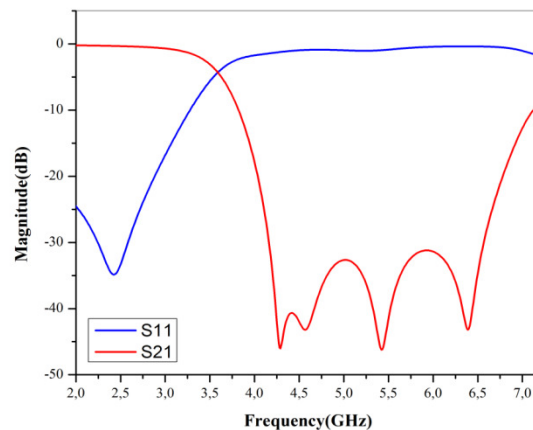


Figure 11. Frequency response of the low-pass filter with four CRCRs.

By cascading four different CRCRs unit cells, the transmission zeros frequencies could be tuned. Four transmission zeros of the CRCR cells were adjusted at 4.2, 4.7, 5.5 and 6.5 GHz. Consequently, the 20 dB stop-band frequency range of the filter increase. In fact, the stop-band width is from 3.8 to 7.0 GHz. Furthermore, the return loss in pass-band is better than -25 dB as shown in **Figure 11**.

4. Conclusions

In this work, we proposed a novel low-pass filter based on complementary rose curve resonators CRCRs. The transmission zeros of the filter are tuned by adjusting the geometric parameters of the CRCRs leading to smaller circuit structure. In fact, a size reduction factor up to 30 % is achieved compared to the filter based on the CSRRs. It was observed that the stop-

band bandwidth of the filter using CRCRs is increased by 35 % compared to the filter based on the CSRRs. Finally, this new filter can be easily implemented in microwave integrated circuit.

References

1. D. R. Smith, S. Schultz, P. Markos, C. M. Soukoulis. Determination of effective permittivity and permeability of metamaterials from reflection and transmission coefficients. *Phys. Rev. B*, 2002, 65, 195104, 1-5.
2. J. B. Pendry, A. J. Holden, D. J. Robbins, W. J. Stewart. Magnetism from conductors and enhanced nonlinear phenomena. *IEEE Trans. Microwave Theo. & Tech.*, 1999, 47, 11, 2075-2084.
3. F. Falcone, T. Lopetegi, J. D. Baena, R. Marques, F. Martin, M. Sorolla. Effective negative- ϵ stopband microstrip lines based on complementary split ring resonators. *IEEE Microwave & Wireless Comp. Lett.*, 2004, 14, 6, 280-282.
4. Sh. Y. Huang, Y. H. Lee. Compact stepped-impedance lowpass filter with a slot-back microstrip line. *Microwave & Opt. Technol. Lett.*, 2005, 50, 4, 1058-1061.
5. J.-S. Lim, Ch.-S. Kim, D. Ahn, Y.-Ch. Jeong, S. Nam. Design of low-pass filters using defected ground structure. *IEEE Trans. Microwave Theo. & Tech.*, 2005, 53, 8, 2539-2545.
6. J. Gu, X. Sun. Compact lowpass filter using spiral compact microstrip resonant cells. *Electronis Lett.*, 2005, 41, 19, 1065-1066.
7. W. Xu, L.-W. Li, H.-Y. Yao, T.-S. Yeo, Q. Wu Left-handed material effects on waves modes and resonant frequencies: Filled waveguide structures and substrate-loaded patch antennas. *J. Electromag, Waves & Appl.*, 2005, 19, 15, 2033-2047.
8. J. Zhang, B. Cui, S. Lin, X.-W. Sun. Sharp-rejection low-pass filter with controllable transmission zero using split ring resonators (CSRRS). *Prog. Electromagn. Res.*, 2007, 69, 0, 219-226.
9. B. Savitri, I. Sassi, L. Talbi, K. Hettak, A. Kabiri. Effect of complementary rose curve resonator (CRCRs) on the effective negative permeability. In: *IEEE Antennas & Propagation Soc. Int. Symp.*, 2012, 1- 2.
10. A. Kabiri, O. M. Ramahi. n th order rose curve as a generic candidate for RF artificial magnetic material. *Appl. Phys. A*, 2011, 103, 3, 831-834.

FORMATION AND EVOLUTION OF NICKEL SILICIDES IN SILICON NANOWIRES

A. Katsman, M. Beregovsky, Y. E. Yaish

Technion
Haifa, Israel
akatsman@technion.ac.il

Accepted September 19, 2013

1. Introduction

Quasi-one-dimensional semiconducting structures have been recently studied as potential candidates for electronic applications. Semiconducting nanowires (NW) have been implemented as the active channel of field effect transistor (FET) with linear and Schottky barrier source and drain contacts [1, 2]. SiNW FETs are of particular interest because they could allow the combination of one-dimensional transport and self-assembly techniques with the well-established Si technology. Of fundamental importance is the method in which contacts to the nanowire channel are being formed. Nickel silicide / silicon contacts used in FET can be formed by thermally activated axial intrusion of nickel silicides into the silicon NW (SiNW) from e-beam lithography pre-patterned Ni reservoirs located at both ends of the NWs. However, the formation of a precisely controlled nanostructure remains one of the most challenging problems in nanotechnology today.

Transformation of the longitudinal NW segments into single-crystalline nickel silicides throughout the entire NWs bulk has been interpreted by some investigators as evidence of a volume diffusion control process. However, the volume diffusion coefficients of nickel in Ni₂Si at 300 – 400 °C are inconsistent with observable nickel silicide intrusion lengths. The experimental results published so far show a distinct dependence of nickel silicide intrusion length on the silicon NW diameter [3], which is indicative of a surface diffusion or a surface reaction controlled process.

The kinetics of nickel silicide growth in Si NWs found by different authors [3 – 13] varies substantially, and the growth rates may differ by some orders of magnitude at the same temperature (for example, from ~ 0.01 nm / s at 500 °C [5] to ~ 4 nm / s at 450 °C [9] and ~ 5 nm / s at 420 °C [10]). Kinetic analysis of nickel silicide formation through point contact reaction between Si and Ni nanowires in the temperature range 500 – 650 °C was performed by Kuo-Chang Lu et al. [5]. A linear time dependence of the silicide length was found for all temperatures investigated, with growth rates of 0.01 – 0.1 nm / s [5]. Activation energies were obtained for the case of nickel diffusion through the silicon part of the NW (1.25 eV) and for diffusion through the nickel silicide phase (1.7 eV). The authors [5] proposed that the observed epitaxial growth of NiSi may be an interface reaction controlled process limited by the rate of dissolution of Ni into Si at the point contact interface and accompanied by very fast volume diffusion of interstitial nickel atoms. The kinetics of Ni silicide phase formation was studied by Dellas et al. [9] in the temperature range 400 – 550 °C for 50 – 75 nm-thick SiNWs grown in

$\langle 112 \rangle$ and $\langle 111 \rangle$ directions. For $\langle 112 \rangle$ oriented SiNWs, growth of the θ -Ni₂Si phase exhibited parabolic kinetics with activation energy of 1.45 ± 0.07 eV / atom. In the case of $\langle 111 \rangle$ oriented SiNW, the NiSi₂ was the only formed phase and the NiSi₂ growth demonstrated linear kinetics with activation energy of 0.76 ± 0.10 eV / atom [9]. Square root time dependence of the total silicide intrusion length was found by Ogata et al. [10] for different crystallographic orientations of SiNWs and core diameters ranging from ~ 10 to 100 nm. They found that the NiSi₂ was the first forming phase whereby Ni-rich silicide phases subsequently nucleate close to the Ni reservoir. Ogata et al. [10] also observed the retardation of silicide growth in oxidized SiNWs. A square root time dependence of the total intrusion length was found for nickel silicides formation in SiNWs at temperatures 350 – 440 °C [11]. Subsequent anneals of the samples at different temperature revealed Arrhenius-type temperature dependence of the square intrusion length increase with an activation energy of 1.45 ± 0.11 eV [11]. Transition from linear to parabolic growth of nickel silicides in SiNWs was analyzed by Yaish et al. [12]. The linear regime can be realized when transition of Ni atoms from the Ni reservoir towards the wire is hindered and limits the silicide growth, while the parabolic regime corresponds to fast transition of Ni atoms from the reservoir and the silicide growth is controlled by diffusion of Ni atoms along the silicide surface toward the silicon part. Intermediate regimes are realized in many cases [12]. Analysis of published experimental results [14] revealed that in many cases formation of nickel silicides in SiNWs can be controlled by diffusion of nickel along the silicide surface or silicide / SiO₂ interface.

The axial intrusion consists usually of different nickel silicides which grow simultaneously during thermal annealing. The kinetics of their growth inside the intrusion can be different with (or without) predominant growth of one of the silicides [15]. The growth is often accompanied by local thickening and tapering of the silicide NW [16 – 20], up to full disintegration of a NW segment adjacent to Si. Up to date, comprehensive understanding of these processes is still missing.

Simultaneous growth of different silicides in SiNWs during rapid thermal annealing (RTA) was recently analyzed in the framework of the model, taking into account the balance between transition of Ni atoms from the Ni reservoir to the NW surface, diffusion transport of these Ni atoms from the contact area to the interfaces between different silicides and nickel silicide / Si interface, and corresponding reactions of Ni atoms with Si and the nickel silicides formed [15]. Thickening and tapering of the silicide intrusion during repeated anneals can be explained by the presence of opposite atomic fluxes caused by curvature gradients. The latter are connected with the presence of two or more different nickel silicide phases along the intrusion segment [19, 20]. In order to understand what processes actually control the nickel silicide formation, corresponding activation energies should be found. For this purpose, time and temperature dependences of the silicide intrusion length should be properly measured.

In the present work we analyzed the experimental results on time and temperature dependencies and possible instability of two-phase nickel silicide intrusions in $\langle 110 \rangle$ and $\langle 112 \rangle$ oriented SiNWs for a temperature range of 300 – 440 °C and nanowire diameters of 30 – 60 nm obtained previously in our laboratory [11, 12, 19, 20]. The results were analyzed in the framework of diffusion model which was developed. This model includes the fluxes of Ni and Si atoms along the nickel silicides formed as well as the reactions at Si / silicide and silicide / silicide interfaces. Quantitative agreement between experiments and theory was obtained and discussed.

2. Experimental details

The SiNWs were synthesized by the vapor-liquid-solid growth technique in an ultrahigh vacuum chemical vapor deposition chamber, with silane as the silicon precursor and gold as the catalyst [21, 22]. Typical diameters of NWs grown in the $\langle 112 \rangle$ and $\langle 110 \rangle$ directions were 35 – 60 nm and 25 – 40 nm, respectively. SiNWs were oxidized at 700 °C by CVD reactor in oxygen flow with rate of 200 sccm and pressure of 1 atm. Samples were fabricated by a method described previously [11], with the lone exception being that the SiNWs were randomly dispensed from an ethanol suspension onto a sacrificial 150 nm-thick PMMA resist layer (deposited on the Si_3N_4 / Si substrate) which allowed to obtain a suspended SiNW structure. In order to form nickel silicide/silicon contacts, a series of anneals of the Ni/SiNW sample were performed: the first, at 420 °C for 15 s, followed by a few subsequent anneals, each at 440 °C for 5 s. Each anneal was carried out in a rapid thermal annealing (RTA) machine in a nitrogen atmosphere and included heating to (and cooling from) the annealing temperature with the rate of 1 °C / s. After every annealing, the silicide intrusions were investigated by high resolution scanning electron microscopy (HRSEM) and atomic force microscopy (AFM).

3. Main experimental results

The axial nickel silicide intrusions were formed as a result of a series of subsequent anneals at 420 and 440 °C. Simultaneous growth of two nickel silicides in SiNWs was observed in a number of works [11, 12, 15]. The typical results obtained in our laboratory are presented in **Figures 1 – 6**. Two-phase nickel silicide intrusions with different thickness of particular intrusion segments are shown in **Figure 1**. Time evolution of intrusion length in different SiNWs at 420 and 440 °C are presented in **Figure 2**. In order to estimate effective activation energy of the process, a number of samples were annealed for 30 s subsequently at 300, 350, 400, 420 and 440 °C. One of such samples is shown in **Figure 3**.

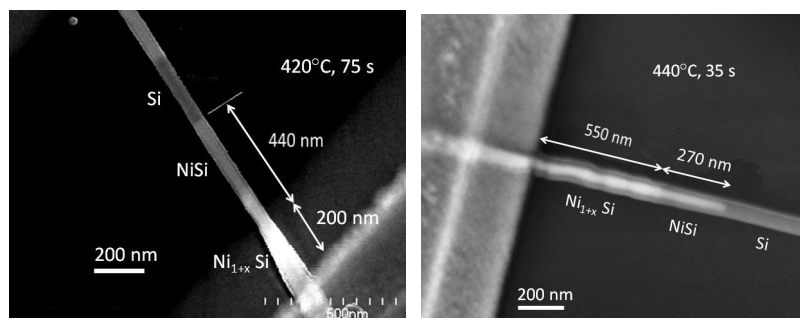


Figure 1. Two-phase nickel silicide intrusions in SiNWs after different rapid TA.

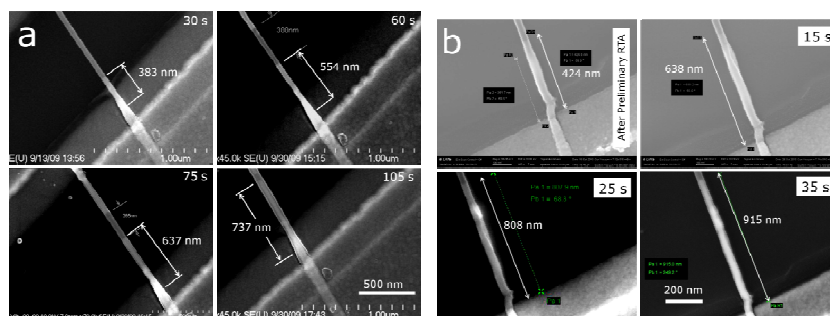


Figure 2. HRSEM micrographs of SiNWs with Ni-silicide intrusions formed during rapid thermal annealing (RTA) for different times at 420 (a) and 440 °C (b).

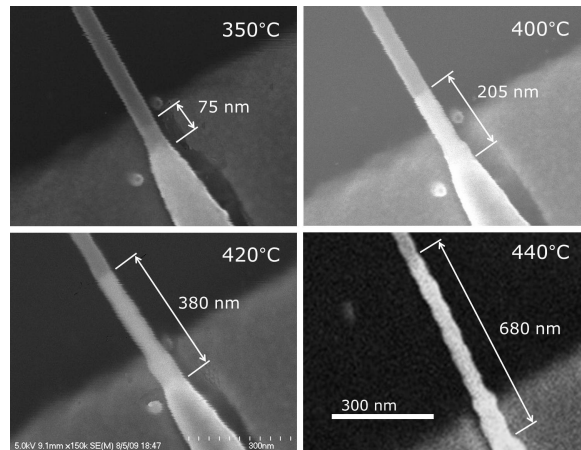


Figure 3. HRSEM images of SiNW covered by 140 nm Ni / 2 nm Au after subsequent RT anneals at 350, 400, 420, and 440 °C for 30 s each; the SiNW has the core diameter of 30 nm and native oxide shell of 3 nm.

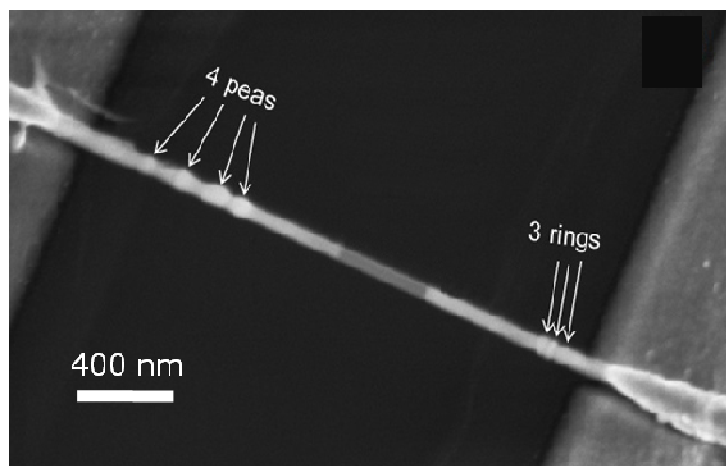


Figure 4. HRSEM images of a 28 nm-thick Ni / SiNW structure after five subsequent thermal cycles with annealing temperatures of 420 °C for 15 s (two first) and 440 °C for 5 s (three last).

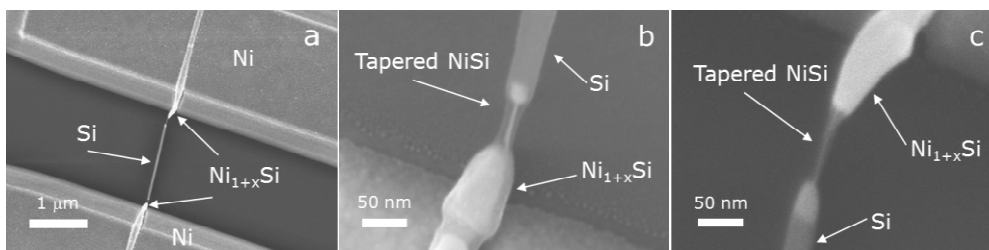


Figure 5. HRSEM image of Ni / SiNW structure after thermal annealing at 420 °C for 1 s: (a) total view of the NW structure with two tapered NiSi regions; (b) and (c) bottom and upper parts of the NW structure.

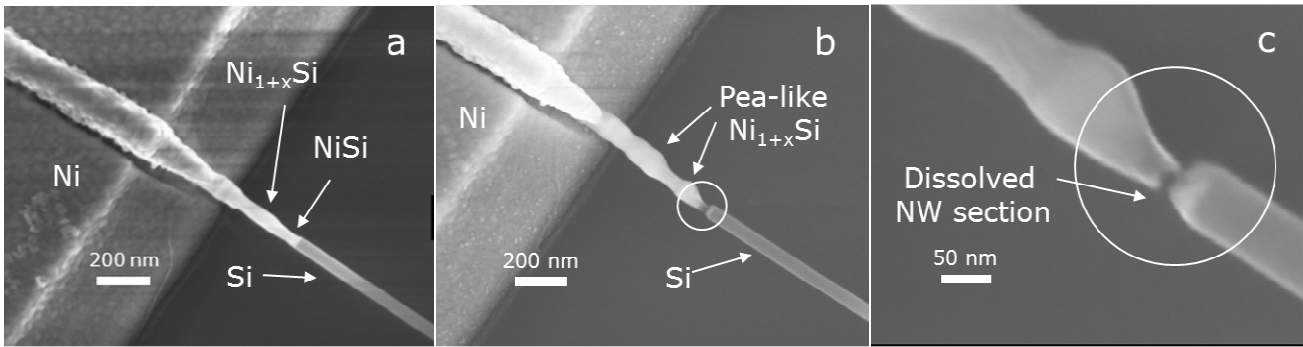


Figure 6. HRSEM images of the a 52 nm-thick Ni / SiNW structure as a result of TA at 420 °C for 15 s (a), followed by two subsequent anneals each at 440 °C for 5 s (b); (c) magnification of the dissolved NW section in (b). (The NW integrity is apparently kept here by a 5 nm-thick thermal oxide shell).

The morphological peculiarities of the silicide intrusions observed sometimes as alternate thickening (pea- and ring-like structures, **Figure 4**), and tapering of the NW segments (**Figure 5**). In some instances the NW tapering continued up to full dissolution / disintegration of the silicide segment adjacent to the Si NW (**Figures 6b** and **c**).

4. Theoretical model

Simultaneous growth of several nickel silicides in Si nanowires (SiNWs) is controlled by some sequential processes: (a) transition of Ni atoms from the e-gun deposited Ni reservoir through an intermediate contact layer (formed by Si oxides or another contamination of the Si surface before Ni deposition) to the silicon or the nickel silicide surface; (b) diffusion transport of these Ni atoms from the contact area to the reaction interfaces; (c) reaction of Ni atoms with Si or nickel silicides at the reaction interfaces resulting in the growth of different nickel silicides (**Figure 7**).

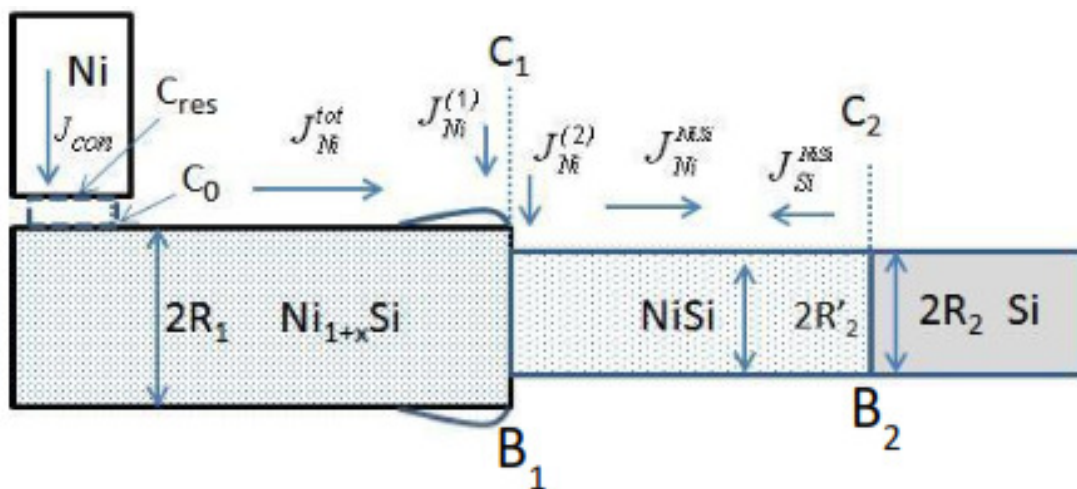


Figure 7. Evolution of nickel silicide intrusion during RTA, schematic diagram.

Experimentally observed thickening and thinning of different parts of the nickel silicide intrusion, up to full dissolution of some part of the intrusion, cannot occur without some diffusion of silicon atoms. In the model considered below, the Si atoms diffuse along the NiSi surface, reach the boundary NiSi / Ni_{1+x}Si ($x > 0$) and react there with the Ni atoms arriving this boundary from the Ni source to form a new portion of Ni_{1+x}Si phase (**Figure 7**). Without loss of generality, we use $x = 1$ in the following discussion.

The flux of Ni atoms from the reservoir through the contact layer of thickness h is proportional to the contact area, s_{con} :

$$J_{con} = -\Lambda_{tr} \frac{\mu_{res} - \mu_0}{h} s_{con}, \quad (1)$$

where Λ_{tr} is the kinetic coefficient for transition of Ni from the reservoir to the silicide surface, μ_{res} and μ_0 are the Ni chemical potentials in the Ni reservoir and on the intrusion surface near the Ni source, respectively. This flux is equal to the total flux of nickel atoms, J_{Ni}^{tot} , diffusing then along the nickel-rich silicide surface:

$$J_{Ni}^{tot} = J_{con}. \quad (2)$$

The total flux of nickel atoms arriving the Ni₂Si / NiSi boundary (B₁) can be divided into three parts:

$$J_{Ni}^{tot} = J_{Ni}^{NiSi} + J_{Ni}^{(1)} + J_{Ni}^{(2)}, \quad (3)$$

where $J_{Ni}^{(1)}$ and $J_{Ni}^{(2)}$ are the fluxes of Ni atoms reacting with Si atoms arriving this boundary and with NiSi phase, respectively. J_{Ni}^{NiSi} is the flux of nickel atoms that diffuse along NiSi surface and reach the NiSi / Si boundary (B₂). The corresponding reactions at boundary B₁ can be written as follows:



The reaction (4) is provided by supply of Si atoms along the NiSi surface by the flux J_{Ni}^{NiSi} . Assuming $J_{Ni}^{NiSi} = \theta J_{Ni}^{Si}$ and $J_{Ni}^{(1)} = 2J_{Si}^{NiSi}$, Eq. (3) can be rewritten:

$$J_{Ni}^{tot} = J_{Ni}^{NiSi} (1 + 2\theta) + J_{Ni}^{(2)}. \quad (7)$$

In a steady state condition, diffusion fluxes of Ni atoms are the following:

$$J_{Ni}^{tot} = \Lambda_1 \frac{\mu_0 - \mu_1}{L_1} s_1, \quad (8)$$

$$J_{Ni}^{NiSi} = \Lambda_2 \frac{\mu_1 - \mu_2}{L_2} s_2, \quad (9)$$

where Λ_1 and Λ_2 are the kinetic coefficients along the Ni₂Si and NiSi segments of intrusion, L_1 and L_2 are the lengths of Ni₂Si and NiSi segments, μ_1 and μ_2 are the Ni chemical potentials at the Ni₂Si / NiSi boundary (B₁), and at the NiSi / Si boundary (B₂), respectively. $s_1 = 2\pi R_1 \delta$, and $s_2 = 2\pi R_2 \delta$, where δ is the diffusion surface layer thickness. The reaction flux $J_{Ni}^{(2)}$ can be written by analogy to the fluxes (8) and (9):

$$J_{Ni}^{(2)} = \Lambda_{reac} \frac{\mu_1 - \mu_{reac}}{R_1} s_{reac}, \quad (10)$$

where Λ_{reac} is the kinetic coefficient of reaction (5) and μ_{reac} is the chemical potential of Ni atoms at the NiSi / Ni₂Si interface (B₁) after reaction.

Using Eqs. (1, 7 – 10) one can find the values of μ_0 and μ_1 as functions of μ_{res} , μ_{reac} , μ_2 and of dimensionless intrusion lengths $l_1 = L_1 / R_1$ and $l_2 = L_2 / R_1$:

$$\mu_0 = \frac{l_1 \mu_{res} + q_0 \mu_1}{l_1 + q_0}, \quad (11)$$

$$\mu_1 = \frac{f_0 l_2 \mu_{res} + (q_0 + l_1)(\mu_2 + p_0 l_2 \mu_{reac})}{f_0 l_2 + (q_0 + l_1)(p_0 l_2 + 1)}, \quad (12)$$

where $f_0 = L_1 s_1 / L_2 s_2 (1 + 2\theta)$, $q_0 = L_1 s_1 h / L_{tr} s_{con} R_1$, and $p_0 = L_{reac} s_{reac} / L_2 s_2$. When the fluxes of nickel, described by Eqs. (8) and (9), are directed from the Ni reservoir to the silicon part of the NW (“positive” direction), the silicide intrusions, l_1 and l_2 , grow with different kinetics, from linear to parabolic, depending on kinetic, geometric and contact parameters.

The nickel-rich silicide grows due to reactions (4) and (5) at a rate proportional to corresponding fluxes:

$$\frac{dL_1}{dt} = \frac{(2+x)\Omega_1}{x\pi R_1^3} (J_{Ni}^{(2)} + xJ_{Si}^{NiSi}) = \frac{3\Omega_1}{\pi R_1^2} (J_{Ni}^{(2)} + \theta J_{Ni}^{NiSi}). \quad (13)$$

The monosilicide grows at the NiSi / Si interface due to reaction (6) and it is contracted due to reaction (5) at the intersilicide interface:

$$\frac{dL_2}{dt} = \frac{2\Omega_2}{\pi R_2^3} J_{Ni}^{NiSi} - \frac{(2+x)\Omega_2}{x\pi R_2^2} J_{Ni}^{(2)}. \quad (14)$$

In the dimensionless form it can be rewritten as follows:

$$\frac{dl_1}{d\tau} = \frac{6\delta}{R_1(1+2\theta)} \frac{((\bar{\mu}_{res} - \bar{\mu}_{reac})l_2 p_0 + (\bar{\mu}_{res} - \bar{\mu}_2)\theta) - p_0(q_0 + l_1)(\bar{\mu}_{reac} - \bar{\mu}_2)(1-\theta) / f_0}{l_2 f_0 + (q_0 + l_1)(p_0 l_2 + 1)}, \quad (15)$$

$$\frac{dl_2}{d\tau} = -\frac{4R_1\delta\nu}{R_2^2(1+\theta)} \frac{(\bar{\mu}_{res} - \bar{\mu}_2) + (\bar{\mu}_{reac} - \bar{\mu}_2)(q_0 + l_1)p_0 / f_0}{l_2 f_0 + (q_0 + l_1)(p_0 l_2 + 1)} - \frac{2R_1^2\nu}{(2+x)R_2^2} \frac{dl_1}{d\tau}, \quad (16)$$

where $\tau = \Lambda_1 \Omega_1 k T t / R_1^2$, $\nu = \Omega_2 / \Omega_1$, and $\bar{\mu}_i \equiv \mu_i / kT$.

It should be noted that for zero initial values $l_1^0 = 0$ and $l_2^0 = 0$, a solution of the equation system (15) and (16) satisfying the following initial conditions has to be found:

$$l_1 = 0, \quad l_2 \leq \bar{l}_2 \equiv \frac{q_0(\mu_{reac} - \mu_2)(1-\theta) - (\mu_{res} - \mu_2)\theta f_0 / p_0}{f_0(\mu_{res} - \mu_{reac})}, \quad (17a)$$

$$l_2 = 0, \quad t = 0, \quad (17b)$$

The first condition corresponds to the requirement $\mu_1 > \mu_{reac} - \theta(\mu_1 - \mu_2) / p_0 l_2$ providing the growth of the nickel-rich silicide. It means, that the monosilicide starts to grow first, and the nickel-rich silicide starts to grow only when the length of the monosilicide reaches a critical value \bar{l}_2 . If $\theta = 0$, the requirement (17a) simply provides reaction (5) as has been found in [14].

Introducing the contact “window”: $\bar{w} \equiv s_{con} \delta / s_1 h$ and dimensionless parameters $r_1 = R_1 / \delta$, $r_2 = R_2 / \delta$, $d_{12} = L_2 / L_1$, $d_{1tr} = L_{tr} / L_1$, and $d_{1reac} = L_{reac} / L_1$, one can write $f_0 \equiv r_1 / (1+\theta) r_2 d_{12}$, $q_0 \equiv 1 / r_1 d_{1tr} \bar{w}$, and $p_0 \equiv r_1 d_{1reac} \bar{w} / r_2 d_{12}$.

The system of Eqs. (13) and (14) was solved numerically for different parameters μ_{res} , μ_{reac} , μ_2 , θ , r_1 , r_2 , ν , d_{12} , d_{1tr} and d_{1reac} . Typical solutions shown in **Figure 8** demonstrate possible dominant growth of one of two phases.

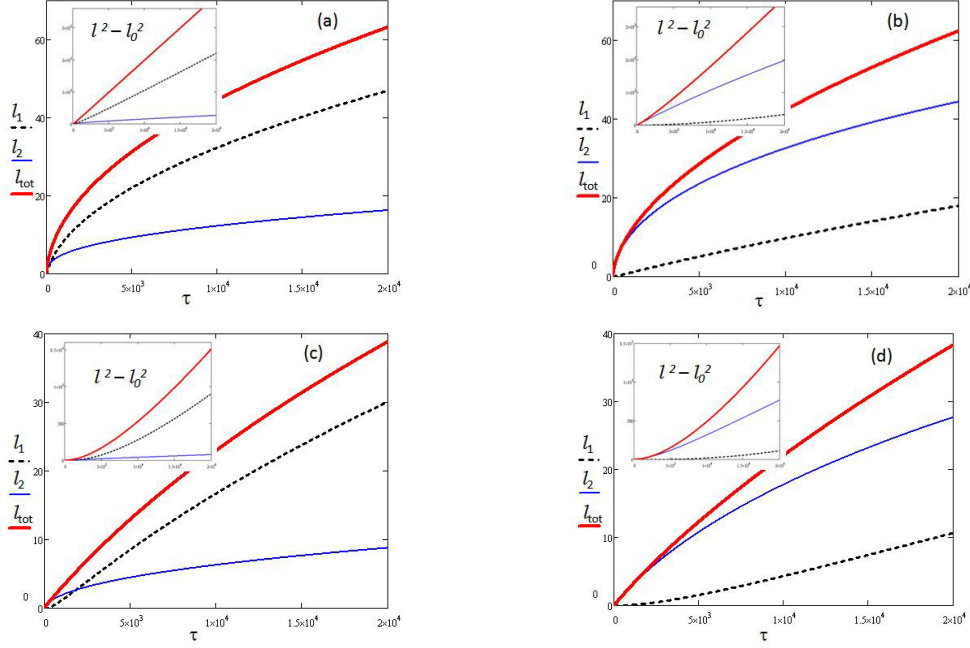


Figure 8. Calculated dimensionless nickel silicide lengths for different kinetic and geometrical parameters: (a, b) – square root like and (c, d) linear-like dependencies with dominant growth of mono- (b, d) or Ni-rich silicide (a, c).

In two limiting cases: (1) $L_2 = 0$ and (2) $L_{reac} = 0$, $\theta = 0$ – only one silicide phase grows (Ni-rich or NiSi, respectively). In these cases the system of Eqs. (13) and (14) is reduced to one equation

$$\frac{dl_i}{d\tau} = \frac{n_i}{r} \frac{\bar{\mu}_{res} - \bar{\mu}_2}{l_i + q_i} \quad (18)$$

with the following solution:

$$l_i = \sqrt{\alpha_i \tau + (l_0 + q_i)^2} - q_i, \quad (19)$$

where $\alpha_i = 2(\bar{\mu}_{res} - \bar{\mu}_2)n_i / r_i$ and $q_i = \Lambda_i / \Lambda_{tr} r_i \bar{w}$, $i = 1$ or 2 for the two limiting cases mentioned above. Eq. (18) is similar to the relationship obtained earlier for the case of one nickel silicide growth [8]. The dependence $l_i(\tau)$, Eq. (18), is linear-like for experimental times:

$$\tau \ll \tau_{crit} \equiv (l_0 + q_i)^2 / \alpha_i. \quad (20)$$

Such a case may be realized for sufficiently small contact “windows”, \bar{w} , and can be referred to as “contact” growth regime. In the opposite case, $\tau \gg \tau_{crit}$, the dependence $l_i(\tau)$ is square root-like, and the silicide growth is diffusion controlled.

5. Analysis of experimental results

The silicide intrusions were obtained by annealing of SiNWs for different temperatures and times as described in [12]. Examples of linear and square root-like time dependences observed for the Ni-rich part and NiSi part of intrusions at 420 and 440 °C are presented in **Figure 9**.

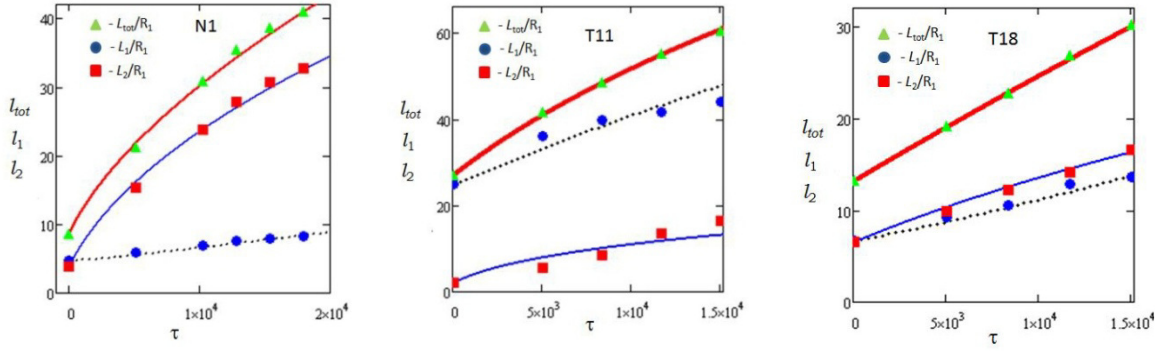


Figure 9. Typical kinetics of total and particular silicide intrusion lengths; dots are experimental values [12], solid lines are calculated with parameters given in **Table 1**.

Table 1. Fitting parameters used in the calculation of particular silicide intrusion lengths.

	$T, ^\circ\text{C}$	l_{01}	l_{02}	$\bar{w}, 10^{-3}$	d_{21}	d_{1reac}	d_{1tr}	r_1	r_2	\bar{C}
N1	420	4.7	3.9	3.03	1	0.01	1	36	30	0.56
T11	440	25.6	2.1	10	2.7	0.7	1	36	30	0.51
T18	440	6.7	6.5	0.43	2.7	0.2	1	36	30	0.50

The experimental results are well described by Eqs. (15, 16) with the corresponding parameters mentioned in **Table 1**. It should be noted that preliminary heating of SiNWs to 400 °C, exposure at this temperature followed by slow heating to 420 or 440 °C resulted in preliminary formation of both Ni-rich and NiSi parts; their lengths are used in the present calculation as initial lengths l_{01} and l_{02} .

Substantial growth of NiSi at 420°C and 440°C as compared to the dominant growth of Ni-rich silicides at lower temperatures (usually $l_{01} > l_{02}$) is indicative of relatively lower rates of reactions (4) and (5) at higher temperatures. Surface diffusion coefficients along Ni-rich silicide can be evaluated as $5 \cdot 10^{-14} \text{ m}^2/\text{s}$ at 420 °C and $1 \cdot 10^{-13} \text{ m}^2/\text{s}$ at 440 °C. The diffusion coefficient along the monosilicide surface is of the same order at 420 °C ($d_{21} = 1$), but of about 3 times higher at 440 °C ($d_{21} = 2.7$). For sample N1, the critical time, $\tau_{crit} = 1.5 \cdot 10^3$, Eq. (20), the growth occurs mainly at $\tau > \tau_{crit}$, and the time dependence of the total intrusion length is square root-like; the same is true for the NiSi part, but the Ni-rich silicide part grows almost linearly, due to a low reaction rate, d_{r1} . For sample T11, the “window” value, $\bar{w} = 0.1$, is sufficiently high, $\tau_{crit} = 140$, and the growth occurs in the diffusion controlled regime for both parts of the intrusion. For sample T18, the contact “window” is small, $\bar{w} = 4.3 \cdot 10^{-4}$, the experimental times $\tau < \tau_{crit} = 7.3 \cdot 10^4$, and both parts of the intrusion increase linearly with time; in this case the total growth rate is determined by the transfer of Ni atoms from the reservoir, and the particular rates depend on the reaction rate, d_{1tr} , at the $\text{Ni}_{1+x}\text{Si} / \text{NiSi}$ interface. In general case, square root time dependence can be realized for the total silicide length (in the diffusion controlled regime), while particular silicides may have different kinetics (square root, linear or intermediate) depending on the reaction rate of the silicide transformations. In this case, assuming close values of diffusion coefficients of Ni along different silicide / SiO_2 interfaces, or, at least, their close activation energies, the total silicide length can be well described by the simplified dependence

$$L^2 - L_0^2 = 8D_s \Delta t (C_{res} - C_f) \frac{\delta}{R} \equiv A_0^2 \exp\left(-\frac{E}{kT}\right) \Delta t \equiv A^2(T) \Delta t. \quad (21)$$

Analysis of temperature dependence of the square length increase, ΔL_n^2 , after RTAs at subsequent temperatures, T_n and T_{n+1} , each for 30 s, allows evaluating the activation energy of the process by using L_{T_n} as the initial length, $L_{0,T_{n+1}}$, for the subsequent anneal at temperature T_{n+1} :

$$\Delta L_n^2 \equiv L_{T_{n+1}}^2 - L_{0,T_{n+1}}^2 \approx L_{T_{n+1}}^2 - L_{T_n}^2 = A^2(T_{n+1}) \Delta t, \quad (22)$$

Such analysis should take into account the silicide growth during heating to and cooling from the annealing temperature. The increase of the silicide intrusion length during heating / cooling with the rate α from T_0 to T_{n+1} , can be evaluated with the following expression:

$$\begin{aligned} L_{0,T_{n+1}}^2 - L_{T_n}^2 &= A_0^2 \int_0^{\Delta t} \exp\left(-\frac{E}{k(T_0 + \alpha t)}\right) dt = A^2(T_0) \int_0^{\Delta t} \exp\left(\frac{E\alpha t}{kT_0(1 + \alpha t)}\right) dt \approx \\ &\approx A^2(T_0) \frac{kT_0^2}{E\alpha} \left(\exp\left(\frac{E\alpha\Delta t}{kT_0^2}\right) - 1 - \frac{1}{2} \sqrt{\frac{\pi E}{kT_0}} \operatorname{erf}\left(\frac{\alpha\Delta t}{T_0} \sqrt{\frac{E}{kT_0}}\right) \right), \end{aligned} \quad (23)$$

where $\Delta t = (T_{n+1} - T_0) / \alpha$ is the heating time. The activation energy of the diffusion process, E , can be found by the iteration procedure described in detail in [9]. The activation energy averaged over the examined NWs is $E = 1.45 \pm 0.11$ eV. This activation energy is typical for nickel silicide growth in thin film silicide reactions controlled by interface and grain boundary diffusion processes [23 – 26].

5.1. Possible instabilities of two-phase nickel silicide intrusions

The sign of the flux J_{Ni}^{NiSi} , Eq. (9), is determined by the difference of the chemical potentials:

$$\mu_1 - \mu_2 = \frac{f_0(\mu_{res} - \mu_2) + p_0(q_0 + l_1)(\mu_{reac} - \mu_2)}{f_0 + (q_0 + l_1)(p_0 + 1/l_2)}. \quad (24)$$

As stated before, the chemical potentials μ_{res} , μ_{reac} , and μ_2 depend on the surface curvature [18]:

$$\mu_{res} = \mu_{res0} + \gamma\Omega/R_1, \quad \mu_{reac} = \mu_{reac0} + \gamma\Omega/R_1, \quad \mu_{2s} = \mu_{20} + \gamma\Omega/R_2, \quad (25)$$

where γ is the surface energy. If $\mu_{reac} < \mu_2$ (can be possible due to the curvature term), the difference $\mu_1 - \mu_2$ decreases with increasing of the nickel-rich silicide length, l_1 , and reaches zero at a critical value:

$$l_1^{crit} = \frac{f_0 \mu_{res0} - \mu_{20} - \gamma\Omega\Delta R / R_1 R_2}{p_0 \mu_{20} - \mu_{reac0} + \gamma\Omega\Delta R / R_1 R_2} - q_0. \quad (26)$$

For values $l_1 > l_1^{crit}$, the flux J_{Ni}^{NiSi} reverses its direction, and the nickel atoms are transferred from the NiSi to the Ni-rich part of intrusion. The critical value l_1^{crit} can be estimated assuming $f_0 = 1$, $\mu_{res0} - \mu_{20} \approx kT \gg \gamma\Omega\Delta R / R_1 R_2$ and $|\mu_{20} - \mu_{reac}| \ll \gamma\Omega\Delta R / R_1 R_2$ and using typical values $\gamma = 2$ J / m², $\Omega = 1.2 \cdot 10^{-29}$ m³, $kT = 9.29 \cdot 10^{-21}$ J, $R_1 = 12$ nm, $R_2 = 10$ nm:

$$l_1^{crit} \approx \frac{kTR_1 R_2}{p_0 \gamma \Omega \Delta R} - q_0 \approx \frac{30}{p_0} - q_0. \quad (26a)$$

This length can vary over a wide range of values depending on parameters of reaction (5) (incorporated in parameter p_0) and on supply of Ni atoms from reservoir (parameter q_0). For example, for $p_0 = q_0 = 1$, $l_1^{crit} = 29$. It should be noted that the flux J_{Ni}^{tot} does not change its direction since the difference of chemical potentials, $\mu_0 - \mu_1$, remains positive for all values of l_1 :

$$\mu_0 - \mu_1 = \frac{\mu_{res} - \mu_2 + p_0 l_2 (\mu_{res} - \mu_{reac})}{f_0 l_2 / l_1 + (1 + q_0 / l_1)(p_0 l_2 + 1)}. \quad (27)$$

5.2. Local thickening: formation of rings and pea-like bulges

As it was found, first anneals resulted in formation of two-phase silicide intrusion consisted of two segments with different radii (**Figures 1a, b, and 3a**). Repeated anneals are often resulted in local thickening of the intrusion with formation of periodic rings and pea-like bulges. Annealing at comparatively low temperatures (during heating and cooling in the temperature range 350 – 400 °C) may cause evolution of the intrusion in the Ni₂Si / NiSi boundary region: the critical length, l_1^{crit} , decreases with temperature (mainly, due to increase of $p_0 \sim L_{reac} / L_2$, Eq. (23)). As a result, the length l_1 , achieved in a previous annealing may exceed the critical value, l_1^{crit} . Then, the flux of Ni atoms along the NiSi part of intrusion reverses its direction, and the net flux of atoms along the NiSi part becomes negative, since the flux of Si atoms is always directed from Si towards the nickel pad. It provides dissolution of the NiSi phase and thinning of its segment adjacent to the Ni₂Si and thickening of the latter. The result of such process can be seen, for example, in **Figure 3a**. The Ni atoms diffusing from the Ni pad reach the Ni₂Si / NiSi boundary region and accumulate here, in the region of the minimal chemical potential, μ_1 . In order to evaluate possible thickening of the Ni₂Si / NiSi boundary region, one can estimate the number of additional Ni atoms reaching this region for the case $f_0 = p_0 = q_0 = 1$ and $l_1, l_2 \gg 1$:

$$\frac{\Delta N}{\Delta t} = \Lambda_1 \frac{\mu_0 - \mu_1}{L_1} s_1 + \Lambda_2 \frac{\mu_2 - \mu_1}{L_2} s_1 \approx \Lambda_1 \frac{\mu_{res} - \mu_{reac}}{L_1} s_1 + \Lambda_2 \frac{\mu_2 - \mu_{reac}}{L_2} \frac{\Delta l}{l_1} s_1, \quad (28)$$

where $\Delta l = l_1 - l_1^{crit}$. Using the following expressions for kinetic coefficients: $\Lambda_i = D_i \bar{c}_i / kT\Omega$, where D_i and \bar{c}_i are the surface diffusion coefficient and average Ni concentration on segment i of intrusion ($i = 1, 2$) and Eqs. (25), one can obtain:

$$\frac{\Delta N}{\Delta t} = 2\pi \frac{\delta}{\Omega} \left(D_1 \frac{c_0 - c_1}{l_1} + D_2 \frac{\gamma\Omega}{kT} \frac{c_2}{l_2} \frac{\Delta R}{R_1^2} \right). \quad (28a)$$

Assuming thickening in the shape of torus with the tube radius Δr , additional volume can be written as $\Delta V = \Delta N\Omega = \pi^2 R_1 (\Delta r)^2$. The thickening Δr can be estimated as

$$\Delta r = \sqrt{\frac{2\delta}{\pi R_1} D_1 \Delta t \frac{\Delta c}{l_1} \left(1 + \frac{D_2 \gamma\Omega}{D_1 kT} \frac{\bar{l}_1 \bar{c}_2}{l_2 \Delta c} \frac{\Delta R}{R_1^2} \right)}, \quad (29)$$

For $D_1 = D_2 = 4 \cdot 10^{-15} \text{ m}^2 / \text{s}$, $\Delta t = 30 \text{ s}$, $\delta = 0.5 \text{ nm}$, $l_1 = 40$, $l_2 = 10$, $R_1 = 15 \text{ nm}$, $\Delta R = 2 \text{ nm}$, and $\gamma\Omega / kT = 2.6 \text{ nm}$, one can obtain $\Delta r \approx 5 \text{ nm}$, that is close to real size of pea-like bulges.

Next annealing at higher temperature (when l_1 , turns out to be less than the critical value, l_1^{crit}), providing supply of nickel atoms from the Ni pad causes further growth of both parts of the silicide intrusion.

5.3. Tapering and dissolution of the NiSi segment

Thickening and formation of rings and bulges in the Ni₂Si / NiSi boundary region during repeated anneals may cause substantial decrease of the critical length l_1^{crit} due to local increase of ΔR (see Eq. (23a)). By this way the condition $l_1 > l_1^{crit}$ can be met at higher temperature, and the flux of Ni atoms along the NiSi part of intrusion reverses its direction. In this case the flux cannot be longer constant along the NiSi intrusion. At the Si / NiSi interface the flux of Ni atoms should be equal zero (there is no a source of Ni atoms here). Maximum atomic flux from the NiSi to the Ni₂Si will be realized at the NiSi / Ni₂Si interface where the gradient curvature is maximal. For $l_1 \geq l_1^{crit}$ the difference of chemical potentials, Eq. (9), can be approximated as follows:

$$\mu_1 - \mu_2 = \frac{\Delta l_1 p_0 (\mu_{reac} - \mu_2)}{f_0 + (q_0 + l_1)(p_0 + 1/l_2)} \approx -\frac{\Delta l_1}{l_1} \frac{\gamma \Omega \Delta R}{R_1 R_2}. \quad (30)$$

The corresponding Ni flux determines the rate of dissolution of the NiSi part of intrusion. It should be emphasized that dissolution of NiSi phase requires both Ni and Si fluxes being equal in their value and direction. Then, the total atomic flux along the NiSi intrusion, $J_{tot}^{NiSi} = 2J_{Ni}^{NiSi}$.

Assuming a linear increase of J_{tot}^{NiSi} from zero to $2J_{Ni}^m$, the rate of dissolution can be written as:

$$\frac{dR_2}{dt} = \Omega \delta \frac{\partial J_{tot}^{NiSi}}{\partial x} = \Omega \delta \frac{2J_{Ni}^m}{L_2} = -D_2 C_1 \frac{\Delta l_1}{l_1 l_2} \frac{\gamma \Omega \delta (R_1 - R_2)}{kTR_1^3 R_2}. \quad (31)$$

Furthermore, let R_1 and l_2 be constant, and $l_1 = l_1^{crit} + \alpha \sqrt{t}$, where $\alpha = (2/R_1) \sqrt{D_1 \delta / R_1}$ [8], then integration of Eq. (28) results in the following equation:

$$R_1 \ln \frac{R_1 - R_2}{R_1 - R_2^0} - R_2^0 + R_2 = B \left(t - \frac{2l_{crit} \sqrt{t}}{\alpha} + \frac{2l_{crit}^2}{\alpha^2} \ln \left(1 + \frac{\alpha \sqrt{t}}{l_{crit}} \right) \right), \quad (32)$$

where $B = D_2 C_1 \gamma \Omega \delta / kTR_1^3 l_2$. The time of full dissolution (when $R_2 = 0$) can be found from Eq. (32). For the case $\alpha \sqrt{t} \ll l_1^{crit}$ it can be estimated by the expression:

$$t_{dis} \approx \left(\frac{3l_{crit}}{2\alpha B} \left(R_1 \ln \frac{R_1}{R_1 - R_2^0} - R_2^0 \right) \right)^{2/3}. \quad (33)$$

For $D_1 = D_2 = 2 \cdot 10^{-14} \text{ m}^2 / \text{s}$, $R_1 = 15 \text{ nm}$, $R_2^0 = 13 \text{ nm}$, $\delta = 0.5 \text{ nm}$, $\alpha = (2/R_1) \sqrt{D_1 \delta / R_1} = 5.4 \text{ s}^{-1/2}$, $l_{crit} = 30$, $C_1 = 0.67$, $\gamma \Omega = 2 \text{ nm}$, $l_2 = 10$ one can obtain $B \approx 1.0 \text{ nm} / \text{s}$ and $t_{dis} \approx 70 \text{ s}$. Such values of dissolution time were often observed in the experiments.

6. Conclusion

Evolution of nickel silicide intrusions in the NiSi / Si NWs after a series of rapid thermal anneals at different temperatures of 350–440 °C was analyzed in the framework of the phenomenological model taking into account the balance between transition of Ni atoms from

the Ni reservoir to the NW surface, diffusion transport of these Ni atoms and corresponding Ni/Si and Ni/nickel silicide reactions. Simultaneous formation of different nickel silicide phases during RTA was considered. Linear or square root-like growth kinetics of particular silicides and of total silicide intrusion length can be realized depending on both the “contact window” value and the relative rate of Ni-rich silicide formation. A square root time dependence of the total intrusion length was indicating of diffusion controlled process. The NW curvature gradients appearing due to different radii of different silicides may play substantial role in tapering and dissolution of monosilicide segment of intrusion. Subsequent anneals of the samples at different temperature revealed Arrhenius-type temperature dependence of the square intrusion length increase with an activation energy of 1.45 ± 0.11 eV typical for diffusion of Ni along the nickel silicide surface or nickel silicide / SiO₂ interface. Thermal cycling resulted in sequential thickening of nickel-rich part with formation of rings or pea-like bulges at different sides of the same NW. It was accompanied by tapering of the monosilicide part up to its full dissolution and breaking of the NW. For a certain set of model parameters formation of the pea-like profile on the nickel-rich silicide surface, tapering and dissolution of the monosilicide part of intrusion were obtained.

References

1. Y. Cui, Z. Zhong, D. Wang, W. U. Wang, C. M. Lieber. *Nano Lett.* 3 (2003) 149.
2. M. Mongillo, P. Spathis, G. Katsaros, P. Gentile, S. de Franceschi. *Nano Lett.* 12 (2012) 3074.
3. J. Appenzeller, J. Knoch, E. Tutuc, M. Reuter, S. Guha. In: *Int. Electron Devices Meeting* (2006).
4. W. M. Weber, L. Geelhaar, A. P. Graham, E. Unger, G. S. Duesberg, M. Liebau, W. Pamler, C. Chze, H. Riechert, P. Lugli, F. Kreupl, *Nano Lett.* 6 (2006) 2660.
5. K.-Ch. Lu, W.-W. Wu, H.-W. Wu, C. M. Tanner, J. P. Chang, L. J. Chen, K. N. Tu. *Nano Lett.* 7 (2007) 2389.
6. Y. Hu, J. Xiang, G. Liang, H. Yan, C. M. Lieber. *Nano Lett.* 8 (2008) 925.
7. W. M. Weber, L. Geelhaar, E. Unger, C. Chèze, F. Kreupl, H. Riechert, P. Lugli, *Phys. Status Solidi B* 244 (2007) 4170.
8. N. S. Dellas, B. Z. Liu, S. M. Eichfeld, C. M. Eichfeld, T. S. Mayer, S. E. Mohny. *J. Appl. Phys.* 105 (2009) 094309.
9. N. S. Dellas, M. Abraham, S. Minassian, C. Kendrick, S. E. Mohny. *J. Mater. Res.* 26 (2011) 2282.
10. K. Ogata, E. Sutter, X. Zhu, S. Hofmann. *Nanotechnol.* 22 (2011) 365305.
11. M. Beregovsky, A. Katsman, E. M. Hajaj, Y. E. Yaish, S. S. Elect. 80 (2013) 110.
12. Y. E. Yaish, A. Katsman, G. M. Cohen, M. Beregovsky. *J. Appl. Phys.* 109 (2011) 094303.
13. S. Habicht, Q. T. Zhao, S. F. Feste, L. Knoll, S. Trellenkamp, B. Ghyselen, S. Mantl. *Nanotechnol.* 21 (2010) 105701.
14. A. Katsman, Y. Yaish, E. Rabkin, M. Beregovsky. *J. Elect. Mater.* 39 (2010) 365.
15. A. Katsman, Y. Yaish, M. Beregovsky. *Def. & Diff. Forum* 323-325 (2012) 427.
16. Y.-Ch. Lin, Y. Chen, D. Xu, Y. Huang. *Nano Lett.* 10 (2010) 4721.
17. W. Tang, S. A. Dayeh, S. T. Picraux, J. Y. Huang, K. Tu. *Nano Lett.* 12 (2012) 3979.

18. Y. Chen, Y. C. Lin, C. W. Huang, C. W. Wang, L. J. Chen, W. W. Wu, Y. Huang, *Nano Lett.* **12** (2012) 3115.
19. A. Katsman, M. Beregovsky, Y. Yaish. In: *MRS Proc.* **1408** (2012) 93.
20. A. Katsman, M. Beregovsky, Y. Yaish. *J. Appl. Phys.* **113** (2013) 084305.
21. J. Westwater, D. P. Gosain, S. Tomiya, S. Usui, H. Ruda. *J. Vac. Sci. & Technol. B* **15** (1997) 554.
22. A. M. Morales, C. M. Lieber. *Science* **279** (1998) 208.
23. J. W. Mayer, J. M. Poate, K. N. Tu. *Science* **190** (1975) 228.
24. J. O. Olowolafe, M. A. Nicolet, J. W. Mayer. *Thin Solid Films* **38** (1976) 143.
25. L. R. Zheng, L. S. Hung, J. W. Mayer, G. Majni, G. Ottaviani. *Appl. Phys. Lett.* **41** (1982) 646.
26. J. C. Ciccariello, S. Poize, P. Gas. *J. Appl. Phys.* **67** (1990) 3315.

SEPARATION OF NANOPARTICLES FROM NANOPARTICLE ENHANCED PHASE CHANGE MATERIAL

M. H. Sheikh, M. A. R. Sharif, P. A. Rupa

The University of Alabama
Tuscaloosa, USA
msharif@eng.ua.edu

Accepted September 19, 2013

1. Introduction

Phase change materials (PCM) are used in thermal energy storage applications where energy is stored (as latent heat of fusion) by melting the PCM and is released during solidification [1 – 3]. Dispersing highly-conductive nanoparticles into the PCM enhances the effective thermal conductivity of the PCM, which in turn significantly improves the energy storage capability [4 – 6]. The resulting colloidal mixture with the nanoparticles in suspension is referred to as nanoparticle enhanced phase change materials (NEPCM). A commonly used PCM for energy storage application is the family of paraffins (C_nH_{2n+2}). Mixing copper oxide (CuO) nanoparticles (treated with surfactants for stability) in paraffin produces a stable and highly conductive NEPCM for energy storage. However, after long term application cycles, the functionality of the NEPCM deteriorates and it is required to replace it with fresh supply. Disposal of the used NEPCM containing the nanoparticles is a matter of great concern as it cannot be discarded directly into the environment because of the short and long term environmental and health hazards [7 – 10]. Due to the widespread application potential of NEPCM, it is very important to develop proper technology to separate the nanoparticles before the disposal of the NEPCM. This is the motivation behind the present study.

Separation of particles / impurities from a solid-liquid mixture has been an age old problem. Various separation methods have been developed for various types of applications over the years. The separation method for a specific class of solid-liquid mixture depends on various factors such as the size of the particles, type / class of the liquid, mass / volume fraction of the particles in the mixture, physical properties of the base liquid and the particles, etc. Following methods are most widely used to separate particulate matter from solution: filtration, distillation, centrifugation, electrophoresis, magnetic separation, chromatography and chemical methods. Every separation method has various operating requirements and one of the most critical one being physical, chemical and electrical properties of entities to be separated and solution to be processed [11 – 16]. By studying and analysing such properties of NEPCM, various methods have been attempted. In this work following methods: distillation, centrifugation, chemical methods, and chromatography which have produced successful results have been reported with brief description followed by analysis and conclusion.

2. NEPCM configuration

In this work Dodecane ($C_{12}H_{26}$) was used as a PCM base fluid and CuO (copper oxide) nanoparticles [17] were employed to enhance thermal conductivity of dodecane. Dodecane of 99 % pure technical grade was used. Dodecane is a colourless liquid with a slight gasoline-like odour, has density of 0.753 g / cm^3 and boiling point of $216 \text{ }^\circ\text{C}$ [18]. The spherical shaped copper oxide nanoparticle size varies from 5 – 15 nm with majority of them being about 9 nm. The density of CuO is 6.31 g / cm^3 and they appear black in colour [17]. A weight basis approach was adopted to prepare NEPCM with required nanoparticles concentration.

3. Experimental setup and procedures

3.1. Atmospheric pressure distillation

Generally, distillation is used to separate a liquid from a liquid mixture containing components of different volatilities or boiling points. In the simplest form of distillation, the liquid mixture is heated in a container until the liquid component with lower boiling point is vaporized and then subsequently condensed to yield the distillate [19 – 22].

The distillation process can also be used to separate suspended solid particles from a colloidal mixture. In the present context, the separation of the nanoparticles from the NEPCM was accomplished by evaporating the dodecane (base fluid) at $218 \text{ }^\circ\text{C}$ using a distillation process.

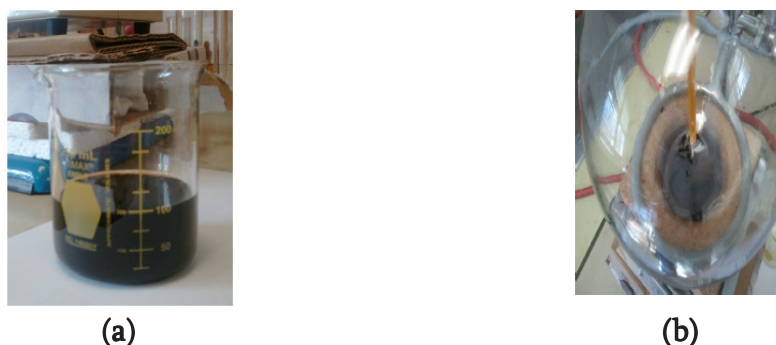


Figure 1. Distillation at atmospheric pressure: (a) before distillation – sample 100 ml 1 mas. % NEPCM and (b) after distillation – flask bottom showing nanoparticle residue.

A standard distillation unit was used to carry out the distillation process at atmospheric pressure. An energy meter measured the amount of energy consumed during each experiment. **Figure 1a** depicts the 100 ml NEPCM with a 1 % by mass concentration of the CuO nanoparticles. The black colour of the colloid is due to the presence of black CuO nanoparticles. **Figure 1b** shows the nanoparticle residue left in heating flask after completion of distillation. Nanoparticles were deposited in the form of a layer at the bottom of the flask.

3.2. Vacuum distillation

The boiling point of the liquid varies depending upon the surrounding environmental pressure. A liquid at high pressure has a higher boiling point than when the liquid is at atmospheric pressure. Conversely at lower pressure or under vacuum boiling point of liquid is lower than that at atmospheric pressure conditions. Distillation has long been criticized as slow

and highly energy intensive process. Hence, in order to make distillation more energy efficient distillation, distillations were performed at reduced temperature. To perform distillation under reduced pressure a complete new setup was required, as the distillation unit for this purpose has to be airtight and of sufficient strength to withstand applied vacuum. Hence a new vacuum distillation unit with vacuum pump of 1/6 HP power rating, 2.4 CFM free air displacement and 10 Pa ultimate vacuum was used. All the standard procedures and safety measures were followed while conducting the trials. **Figure 2** shows the vacuum distillation setup used to conduct trials.

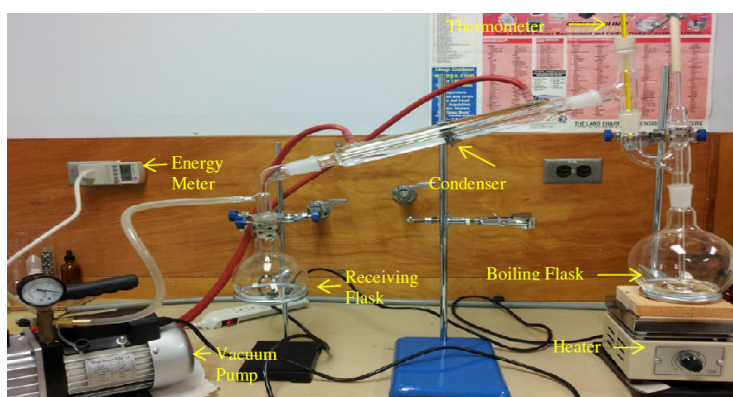


Figure 2. Laboratory vacuum distillation unit.

3.3. Centrifugation of NEPCM

Due to the density gradient between CuO nanoparticles (6.31 g/cm^3) and base fluid dodecane (0.753 g/cm^3), it is anticipated that centrifugation at higher speeds would sediment the nanoparticles. Initial trials were performed on a micro-centrifuge at speed up to 10 000 rpm and no sedimentation was observed for centrifugation duration of 30 min. Hence, in order to bring the nanoparticles out of the suspension it is required to apply larger centrifugal forces to overcome the stabilization effect. This force can be applied using higher centrifugation speeds on a large size centrifugation machine. A SORVALL RC6 super-speed centrifuge floor model with maximum speed rating of 21 000 rpm which is equivalent to over $50\,000 \times$ gravity or relative centrifugal force (RCF) was used to conduct high speed trials in conjunction with SM-24 rotor which is fixed angle rotor. Initial trials were done for up to 6 h duration at 18 000 rpm which showed partial sedimentation of nanoparticles indicating RCF for this duration is not enough to overcome stabilization completely. Further trials were done using 0.5, 2, and 5 % concentration (by mass) of NEPCM for the same operating conditions of 18 000 rpm for 19.5 h.

3.4. Nanoparticle ligands / surfactants destabilization

The nanoparticles in the NEPCM are stabilized by means of steric stabilization by chemically attaching large and bulky oleate ligands on to the particle surface that provide a physical “cushion” between colliding particles and stable suspension of the particles in the base fluid after mixing [23]. In this type of stabilization, the ligands have their polar heads attached to the nanoparticle surface and non-polar tails lying in non-polar base fluid (dodecane). This kind of stabilization is proved to be very efficient and strong due to the fact that being heavier than base fluid (density: 0.753 g/cm^3), nanoparticles (density: 6.31 g/cm^3) stay stable for

months with no or negligible precipitation [17]. Hence, if the ligand end attached to nanoparticle surface is detached, then steric stabilization will break down leading to nanoparticle destabilization and consequential precipitation due to gravity. After conducting several experiments and getting unsatisfactory results, interaction of potassium hydroxide (KOH) with NEPCM in the presence of ethanol produced the desired result. It was observed that KOH interaction with NEPCM results in steric stabilization break down which makes nanoparticles fall down primarily due to gravity.

3.5. Silica column chromatography

Chromatography is a separation process in which sample mixture to be processed is distributed between two phases in the chromatography bed (column or plane). One phase is stationary known as stationary phase while the other phase passes through the chromatography column and is known as mobile phase or eluent. The substances in the mixture to be processed or separated must have different affinities for these two phases. The substance with a relatively higher affinity for the stationary phase moves with a lower velocity through the chromatography column than the substance with lower affinity. This difference in migration velocities of the components of the sample ultimately leads to physical separation of the components [24, 25]. A component of the sample mixture that leaves the stationary phase and moves with mobile phase is said to be eluted in a process known as elution.



Figure 3. NEPCM chromatography.

A manual column chromatography using powder silicate was used to carry out NEPCM chromatography trials. A glass chromatography column of 10.5 mm internal diameter and 200 mm length was purchased from The Lab Dept., Inc., which came with a straight stopcock with a poly-tetrafluoroethylene (PTFE) plug. A cotton plug, sand (coarse) and silicagrain size (230 – 400 mesh), were used to establish the column where cotton plug and coarse sand served as column base. In this formation silica gel was used as stationary phase and hexane was used as mobile phase. **Figure 3** shows NEPCM chromatography set-up. A silica column of 4 inch (approx.) was used for all the trials. After the column is established, NEPCM sample to be processed was added followed by hexane to aid in elution process. Hexane was added till the top end of the glass column, this hexane column (5 ml approx.) on the top of NEPCM sample to help in faster elution. Due to the pressure exerted by the hexane, movement of NEPCM was observed through silica column, which was easier to observe due to its black colour. After reaching a certain length of the column the nanoparticle elution stopped. At this point nanoparticles are considered to be trapped by silica matrix or column allowing only transport of base fluid dodecane under action of hexane as an eluting agent.

4. Results and discussion

Distillation

Figures 4 and 5 show distillate collected after atmospheric pressure and vacuum pressure distillation respectively. Distillate collected resembles to pure colourless dodecane used to prepare the nano-colloid. Absence of any colour clearly indicates that collected distillate is free from any trace of copper oxide.



Figure 4. Distillate: atm. pressure distillation.

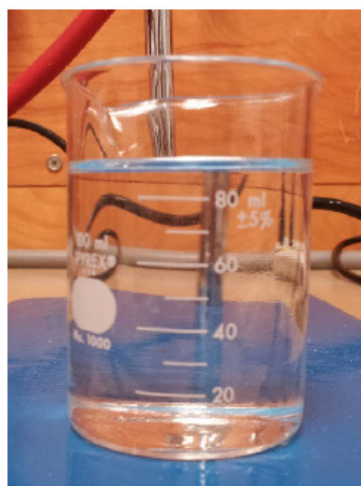


Figure 5. Distillate: vacuum distillation.

Table 1 summarizes the data collected using the atmospheric pressure distillation process. A total of six trials were performed for different combinations of NEPCM volume and nanoparticles concentration. The mass concentration of nanoparticles chosen was 0, 1 and 3 %. A trend was observed for time required and energy consumed in relation to the amount of NEPCM used. Also it was observed that for the same volume, NEPCM with higher concentration of NPs distilled faster than NEPCM with lower NP concentration. This is consistent with an increase in thermal conductivity claim of the dodecane upon the addition of copper oxide nanoparticles.

Table 1. Atmospheric pressure distillation trials summary.

Trial number	NEPCM volume, mL	Nanoparticles mass fraction, %	Total time, min	Total energy consumed, kW · h	Distillate volume, mL	Energy / volume, kW · h / mL
1	100	0	40	0.68	96	0.0068
2	50	1	35	0.6	48	0.0120
3	100	1	40	0.63	95	0.0063
4	150	1	40	0.65	146	0.0043
5	200	1	40	0.66	197	0.0033
6	100	3	32	0.51	97	0.0051

Table 2 shows the data collected for vacuum distillation trials conducted at 33.6 kPa vacuum. For a 100 ml volume of NEPCM, it was found that, as the amount of nanoparticles increased, the time required for vacuum distillation decreased which resulted in less power consumption. This is consistent with the fact that high heat conducting nanoparticles present in NEPCM increases the rate of distillation as was observed in atmospheric distillation case as well (*vide supra*). The final volume of distillate measured was found to be lower than initial volume of 100 ml due to the removal of nanoparticles and loss of dodecane vapours.

Table 2. Vacuum (33.6 kPa) distillation data summary.

Trial number	NEPCM volume, mL	Nanoparticles mass fraction, %	Total time, min	Total energy consumed, kW · h	Distillate volume, mL	Energy / Volume, kW · h / mL
1	100	0	20	0.35	96	0.0035
2	100	1	15	0.24	97	0.0024
3	100	3	12	0.18	96	0.0018

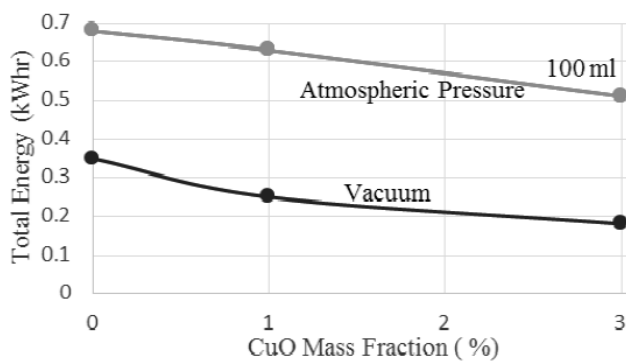


Figure 6. Distillation data comparison on energy basis.

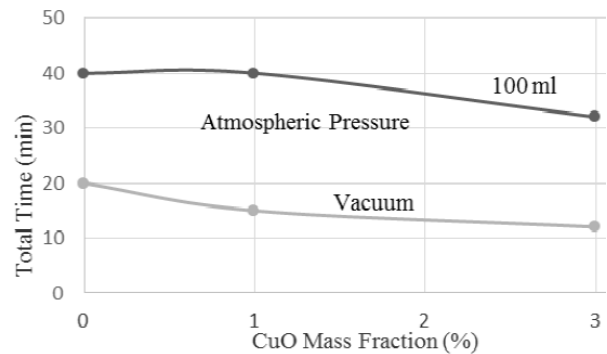


Figure 7. Distillation data comparison on total time basis.

Figures 6 and **7** presents the distillation data for atmospheric pressure and vacuum distillation processes on energy required and time basis, respectively. It is evident that vacuum distillation is much more efficient process to carry out distillation of NEPCM, as it consumes lower energy and takes lesser time than distillation at atmospheric. Based on calculations it is found that for the same volume and nanoparticle concentration of NEPCM distilled, vacuum distillation consumes about 60 % less energy as well as time. Though initial equipment cost for vacuum distillation setup is higher than that for atmospheric distillation the operating cost for vacuum distillation is much lower. Thus it can be concluded that for long term applications and higher volumes of NEPCM to be processed, vacuum distillation is a better alternative.

To verify the nanoparticle removal efficiency of the distillation processes, Scanning Electron Microscope (SEM) was utilized. All samples were prepared on a standard nickel grid having carbon coating and were dried for 48 h before imaging. **Figure 8** shows comparison of SEM images taken for base fluid (pure dodecane), NEPCM before distillation, distillate at atmospheric pressure, and distillate collected by vacuum distillation. **Figure 8a** shows the SEM image of the 99 % pure dodecane, which has been used as a base fluid for the NEPCM preparation. The structure of carbon coating on the grid is clearly discernible from this image

which shows no signs of any nanoparticle present. **Figure 8b** shows the structure of the NEPCM containing 0.5 % (by mass) concentration of the CuO nanoparticles. The lump of nanoparticles sticking to the carbon web structure is clearly visible in the image. As 0.5 % by mass is a higher concentration especially after preparing SEM sample where it is dried which makes nanoparticles to agglomerate. These two images in Figs. 8a and 8 were compared with the SEM images of the distillate samples. **Figure 8c** shows the image of the distillate collected from the atmospheric pressure distillation while **Figure 8d** shows the image of the distillate collected from the vacuum distillation. No trace of the nanoparticle is detected in the distillate in these images asserting that the distillation results in complete separation of nanoparticles from the NEPCM.

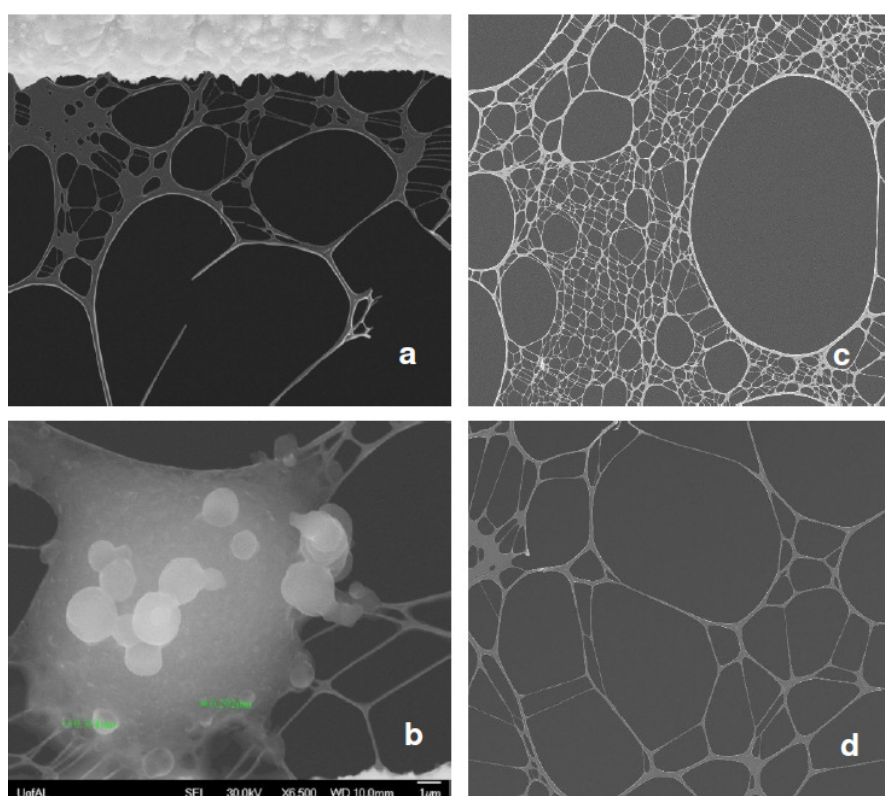


Figure 8. Scanning electron microscope (SEM) images of: (a) dodecane, (b) NEPCM, (c) distillate after atmospheric pressure distillation, and (d) distillate after vacuum distillation.

Centrifugation

Figure 9 shows the results for trial 1 and 2, showing partial precipitation of nanoparticles. It is observed that centrifugation could not remove all of the nanoparticles from the given sample volume, as all the centrifuged samples have reddish colour indicating some of the nanoparticles are still in suspension. As the pure dodecane is colourless, an unclear centrifuged sample indicates presence of nanoparticles. As the centrifugal force is proportional to the particle volume, the larger particles are precipitated and the smaller ones remain in suspension. The nanoparticles still in suspension after the centrifugation giving the reddish colour to the centrifuged samples are of lower size in the nanoparticle size range of 5 – 15 nm, this is due to the fact that being light in weight small particles need greater force to sediment than that required by nanoparticles of large size. **Figure 10** shows SEM image of non-precipitated particles after trial 1, which indicates these are particles of size less than 10 nm.

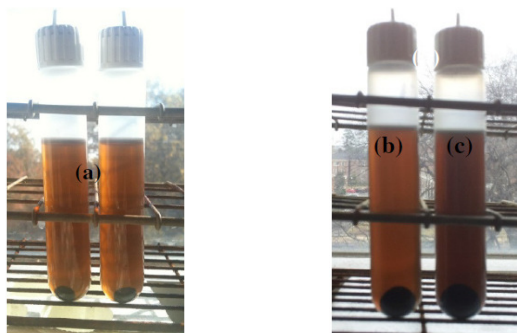


Figure 9. Centrifugation: nanoparticle precipitation. Sample: volume – 13 ml, speed – 18 000 rpm, duration –19.5 h. Trial 1: (a) 0.5, Trial 2: (b) 2 and (c) 5 mas. %.

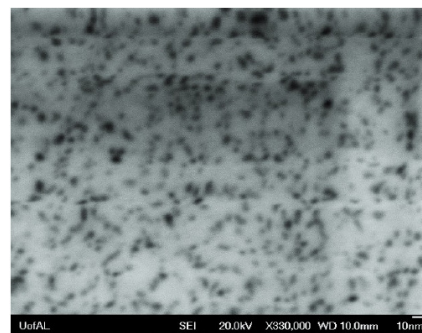


Figure 10. SEM image of centrifuged sample (a).

Table 3. Centrifugation results.

Sample	NEPCM Concentration, NP mas. %	Sample volume, mL	Centrifugation, rpm (\times gravity)	Time, h	Separation, efficiency, %
A	0.5	12	15 000 ($27.820 \times g$)	19.5	58.68
B	2.0	13	18 000 ($40.173 \times g$)	19.5	69.15
C	5.0	13	18 000 ($40.173 \times g$)	19.5	78.42

In order to quantify the particle removal efficiency of the centrifugation trials, a weight based analysis was done by neglecting the volume occupied by individual nanoparticles which introduced maximum 1% error in the calculations. The efficiency is estimated by measuring the weight of the same volume of the NEPCM before and after centrifugation. The difference in the weight when normalized by the weight of the nanoparticles in the measured sample volume before centrifugation gives the normalized fraction of the precipitated nanoparticles. This was done by using 5 ml pipetted out volume of sample before and after centrifugation. **Table 3** shows the separation efficiencies and summary of trial results. It can be seen that for the same duration and speed, the efficiency of the centrifugation increases linearly with the concentration of the nanoparticles in the given sample, which proves the general hypothesis of centrifugation.

Nanoparticle ligands / surfactants destabilization

An initial trial was conducted using 5 ml of 0.5 % CuO mass fraction NEPCM, 3 ml of saturated aqueous solution of KOH, and 0.5 ml of ethanol. The 5 ml of NEPCM was taken in a test-tube and 3 ml of KOH solution was added followed by manual shaking for about 1 min. At this point little mixing was observed with no sedimentation of nanoparticles. A few drops of ethanol were added followed by continuous shaking. Nanoparticles were observed to form a dense black layer at bottom and a colourless top layer. **Figure 11** shows the end result of trial 1. The clear layer on top of precipitated nanoparticles is thought of as a mixture of base fluid dodecane and ethanol. Hexane was added to wash the test-tube walls and to make layers look distinct. The removal of the oleate ligands from the CuO nanoparticles is believed to occur via the reaction mechanism is illustrated in **Figure 12**. On left hand side, a CuO nanoparticle is shown with the oleate group attached to its surface.

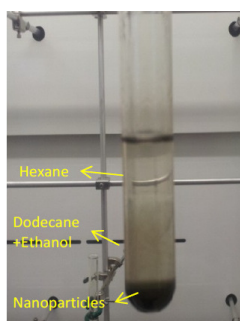


Figure 11. Nanoparticle destabilization using saturated KOH solution.

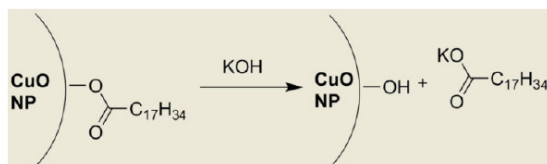


Figure 12. Schematic of the chemical reaction between oleate and KOH.

It is proposed that KOH saponifies the oleate ester linkage, resulting in the formation of potassium oleate. The detachment of oleate from the nanoparticle surface makes the particles unstable and results in precipitation as shown in **Figure 11**. The top clear layer in the test tube in **Figure 11** was analysed by UV–Vis spectrometry to detect the presence of nanoparticles. To record data a freshly prepared sample was irradiated at 20 °C by a dual source of light. The solution was removed at fixed times and its UV spectrum recorded until no further spectral changes occurred. Pure dodecane (99 % technical grade) was used as reference sample (baseline). For the same sample UV–Vis spectrum was recorded and was compared with spectrum of 99 % pure dodecane and 0.0167 % conc. NEPCM as shown in **Figure 13**.

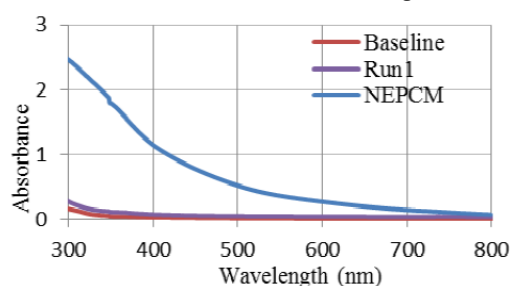


Figure 13. UV–Vis spectrum of trial 1.

Absorbance spectrum of sample i.e. run 1 resembles to spectrum of baseline where as NEPCM spectrum possess very different behaviour with high absorbance values. Hence it can be concluded that treated sample is free from the CuO nanoparticles. This demonstrates that aqueous KOH in the presence of ethanol is capable of removing oleate ligands from the particle surfaces resulting in the precipitation of all of the nanoparticles from the sample NEPCM yielding 100% separation efficiency.

Chromatography

Table 4 shows the chromatography data for different volume and concentrations of NEPCM. It was observed that elution length of the column varies in relation with NEPCM volume and concentration, whereas time required for the complete elution is a function of elutant volume used.

Table 4. Silica column chromatography results.

Trial No.	NEPCM volume, mL	NP concentration, mas. %	Elusion length, inch	Elutant volume, mL	Time, min
1	0.5	0.5	0.25	15	70
2	1	1	0.3	15	70
3	1	2	0.3	15	75
4	2	2	0.3	10	55

UV-Vis spectrometry was employed to confirm complete removal of nanoparticles. **Figure 14** shows UV-Vis spectrum of the elutant obtained after trial 3. To record data a freshly prepared sample of elutant was irradiated at 20 °C by a dual source of light. The solution was removed at fixed times and its UV spectrum recorded until no further spectral changes occurred. To capture the data pure dodecane was used as a base or reference solution. UV-Vis spectral range captured (**Figure 14**) incorporates the UV and visible portions of the electromagnetic spectrum from 300 to 800 nm. This spectrum was compared with pure dodecane (baseline) and 0.0167 % conc. NEPCM spectra as shown in **Figure 14**. Comparing three spectra reveals that for chromatography sample spectrum resembles closely to baseline spectrum where no light absorbance is detected for the entire wavelength spectrum indicating absence of any particulate matter. Difference in NEPCM spectrum and sample spectrum provides additional evidence that processed sample is free from nano-particles. Hence Silica gel chromatography is proved to be an efficient, simple, and cost-effective alternative for nanoparticle separation from the NEPCM.

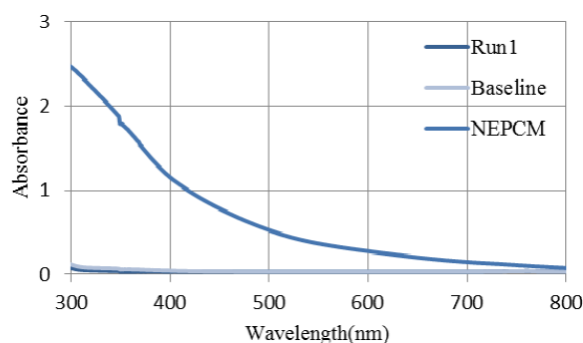


Figure 14. Trial 3 (2 % nanoparticle conc., 1 ml NEPCM) UV spectrum.

5. Conclusions

Out of numerous methods attempted some of the successful methods have been presented to facilitate safe disposal of NEPCM by removing CuO nanoparticles. With the primary objective of establishing simple, safe, and economical methods of separating CuO nanoparticles from an alkane based nano-colloid: Distillation, centrifugation, chemical treatment, KOH reaction, and silica gel chromatography produced successful results. Among presented methods using resources available centrifugation was found to be only 80% successful as compared to other methods which yield 100 % separation efficiency. Every method has some merits and demerits over other methods. Distillation works best by offering complete nanoparticle separation along with operational simplicity. However it has drawback of high

energy requirements and in case of vacuum distillation initial set up costs are high. Though it demands careful separation of phases NEPCM reaction with KOH in presence of ethanol is one of the efficient methods to have nanoparticles separated. Even being comparatively slow, chromatography was found to be one of the safest and simple methods.

Acknowledgements

This material is based upon work supported by the US Department of Energy under Award No. DE-SC0002470 (<http://www.eng.auburn.edu/nepcm>). This report was prepared as an account of work sponsored by an agency of the United States Government. Neither the United States Government nor any agency thereof, nor any of their employees, makes any warranty, express or implied, or assumes any legal liability or responsibility for the accuracy, completeness, or usefulness of any information, apparatus, product, or process disclosed, or represents that its use would not infringe privately owned rights. References herein to any specific commercial product, process, or service by trade name, trademark, manufacturer, or otherwise do not necessarily constitute or imply its endorsement, recommendation, or favouring by the United States Government or any agency thereof. The views and opinions of authors expressed herein do not necessarily state or reflect those of the United States Government or any agency thereof.

References

1. Q. Meng, J. Hu. A poly(ethylene glycol)-based smart phase change material. *Solar Energy Mater. Solar Cells*, 2008, 92, 10, 1260-1268.
2. T. Nomura, N. Okinaka, T. Akiyama. Impregnation of porous material with phase change material for thermal energy storage. *Mater. Chem. & Phys.*, 2009, 115, 2-3, 846-850.
3. F. Kuznik, D. David, K. Johannes, J. Roux. A review on phase change materials integrated in building walls. *Renewable & Sustainable Energy Rev.*, 2011, 15, 1, 379-391.
4. L. Fan, J. M. Khodadadi. Thermal conductivity enhancement of phase change materials for thermal energy storage: A review. *Renewable & Sustainable Energy Rev.*, 2011, 15, 1, 24-46.
5. M. Liu, W. Saman, F. Bruno. Review on storage materials and thermal performance enhancement techniques for high temperature phase change thermal storage systems. *Renewable & Sustainable Energy Rev.*, 2012, 16, 4, 2118-2132.
6. J. M. Khodadadi, L. Fan, H. Babaei. Thermal conductivity enhancement of nanostructure-based colloidal suspensions utilized as phase change materials for thermal energy storage: A review. *Renewable & Sustainable Energy Rev.*, 2013, 24, 0, 418-444.
7. C. Gunawan, W. Y. Teoh, C. P. Marquis, R. Amal. Cytotoxic origin of copper (II) oxide nanoparticles: Comparative studies with micron-sized particles, leachate, and metal salts. *ACS Nano*, 2011, 5, 9, 7214-7225.
8. M. Heinlaan, A. Kahru, K. Kasemets, B. Arbeille, G. Prensier, H. Dubourguier. Changes in the *Daphnia magna* midgut upon ingestion of copper oxide nanoparticles: A transmission electron microscopy study. *Water Res.*, 2011, 45, 1, 179-190.

9. L. Manusadžianas, C. Caillet, L. Fachetti, B. Gylytė, R. Grigutytė, S. Jurkonienė, R. Karitonas, K. Sadauskas, F. Thomas, R. Vitkus, J.-F. Férard. Toxicity of copper oxide nanoparticle suspensions to aquatic biota. *Environ. Toxicol. Chem.*, 2012, 31, 1, 108-114.
10. Z. Wang, N. Li, J. Zhao, J. C. White, P. Qu, B. Xing. CuO nanoparticle interaction with human epithelial cells: Cellular uptake, location, export, and genotoxicity. *Chem. Res Toxicol.*, 2012, 25, 7, 1512-1521.
11. F. Liu, F. Ko, P. Huang, C. Wu, T. Chu. Studying the size / shape separation and optical properties of silver nanoparticles by capillary electrophoresis. *J. Chromatogr. A*, 2005, 1062, 1, 139-145.
12. H. Chen, M. D. Kaminski, A. D. Ebner, J. A. Ritter, A. J. Rosengart. Theoretical analysis of a simple yet efficient portable magnetic separator design for separation of magnetic nano / micro-carriers from human blood flow. *J. Magn. & Magn. Mater.*, 2007, 313, 1, 127-134.
13. B. van der Bruggen, M. Mänttari, M. Nyström. Drawbacks of applying nanofiltration and how to avoid them: A review. *Separation & Purification Technol.*, 2008, 63, 2, 251-263.
14. F. Liu. Using micellar electrokinetic chromatography for the highly efficient preconcentration and separation of gold nanoparticles. *J. Chromatogr. A*, 2009, 1216, 12, 2554-2559.
15. K. F. Lam, E. Sorensen, A. Gavriilidis. Towards an understanding of the effects of operating conditions on separation by microfluidic distillation. *Chem. Eng. Sci.*, 2011, 66, 10, 2098-2106.
16. B. Xiong, J. Cheng, Y. Qiao, R. Zhou, Y. He, E. S. Yeung. Separation of nanorods by density gradient centrifugation. *J. Chromatogr. A*, 2011, 1218, 25, 3823-3829.
17. D. Clary, G. Mills. Preparation and thermal properties of CuO particles. *J. Phys. Chem. C*, 2011, 115, 5, 1767-1775.
18. <http://www.vertellus.com/Documents/MSDS/N-Dodecane%20English.pdf>. (2005).
19. W. Shi-Chang. Ten years' development on distillation in China. *Desalination*, 1987, 64, 0, 211-215.
20. L. M. G. Sánchez, G. W. Meindersma, A. B. Haan. Potential of silver-based room-temperature ionic liquids for ethylene / ethane separation. *Ind. Eng. Chem. Res.*, 2009, 48, 23, 10650-10656.
21. A. K. Coker. Ch. 10: Distillation, Part 1: Distillation Process Performance. In: Ludwig's Applied Process Design for Chemical and Petrochemical Plants. 2010, Boston: Gulf Prof. Publ., 1-268.
22. D. Yang, R. Martinez, B. Fayyaz-Najafi, R. Wright. Light hydrocarbon distillation using hollow fibers as structured packings. *J. Membr. Sci.*, 2010, 362, 1-2, 86-96.
23. D. Clary. The Extension of colloid chemistry from aqueous to non-aqueous media with application to nanofluid research. 2011, Auburn: Auburn Univ.
24. C. H. Bryant, A. Adam, D. R. Taylor, R. C. Rowe. A review of expert systems for chromatography. *Anal. Chim. Acta*, 1994, 297, 3, 317-347.
25. M. Gaborieau, J. Nicolas, M. Save, B. Charleux, J. Vairon, R. G. Gilbert, P. Castignolles. Separation of complex branched polymers by size-exclusion chromatography probed with multiple detection. *J. Chromatogr. A*, 2008, 1190, 1-2, 215-223.

COMPARATIVE STUDIES OF TiO₂ NANOMATERIAL WITH ITS PHOTO-CATALYTIC APPLICATIONS

Y. H. Ng, Y. H. Leung, M. T. Wong,
A. B. Djurišić, F. C. C. Leung, W. K. Chan

The University of Hong Kong
Hong Kong, China
dalek@hku.hk

Accepted September 19, 2013

1. Introduction

Antibacterial and photocatalytic activity of metal oxide nanomaterials has been extensively studied [1]. Materials such as TiO₂ and ZnO are usually considered for these applications [2]. In particular, TiO₂ photocatalysts are the most commonly used in industrial products and applications [3]. However, comparative studies of both photocatalytic pollutant degradation and photocatalytic antibacterial activities for different TiO₂ nanostructures morphology have been scarce. In this study, TiO₂ nanotubes are synthesized by simple anodization method, while single crystalline particles are produced by one-step solution method. The morphology is confirmed by scanning electron microscopy (SEM) and transmission electron microscopy (TEM). The antibacterial and photocatalytic activities have been investigated.

2. Experimental section

2.1. Sample preparation

Synthesis of TiO₂ nanotube array (TNT) – titanium foils (0.25 mm thickness) were cleaned by sonication in acetone, ethanol, and deionized (DI) water sequentially and then dried by N₂ gas. Then the foils were immersed in the electrolyte consisting of 1.36 g NH₄F (99+ %, Aldrich) and 8 mL DI water in 400 mL ethylene glycol (99.8 %, Aldrich) for 2 h at 30 V, similar to previously reported procedures [4]. The as-grown TNT samples were sonicated in DI water and dried in N₂ gas. After that, the samples were annealed in tube furnace in air at 450 °C with ramping rate 1 °C / min. The TNT sample after annealing is labeled as TNT450. The morphology of the prepared samples was examined by SEM using JEOL JSM-7001F field emission SEM.

Synthesis of single crystalline particles (SC) – in typical preparation similar previous reported procedures [5], 22.5 mL of 73 mM TiCl₄ in 2.0 M HCl was added to 45 mL teflon-lined

autoclave with 0.015 M NaF and kept at 100 °C for 72 h in an oven. After the reaction, the white powder was collected by centrifugal separation and washed with DI water several times. All products were dried in a vacuum oven for 1 day at 80 °C. The prepared powder was dispersed in DI water (1 mg / mL) and then drop-cast on Ti foil and then dried in ambient for 1 day. After that, the samples were annealed in tube furnace in air at 450 °C with ramping rate 1 °C / min. The SC sample after annealing is labeled as SC450.

2.2. Test of antibacterial activities

A Gram-positive bacterium *B. atrophaeus* ATCC 9372 was used for antibacterial activity testing. Luria–Bertani (LB) broth was used for culturing *B. atrophaeus* at 30 °C, while 0.9 % (w / v) NaCl solution was used as suspension medium [6]. All samples before the antibacterial experiment were sterilized by UV–C illumination. Blank Ti foil without any treatment was used as a control. Both TNT and SC samples with / without annealing were tested. 10 µL of bacteria suspension (10⁸ CFU / mL) was dropped on the plates and then 500 µL 0.9 % (w / v) NaCl solution was added on the plates in order not to dry up under UV or ambient illumination. For the UV illumination, the plates were then exposed to UV illumination (365 nm, Blak-Ray® B-100 AP Lamp, 50 mW / cm² measured by power meter) with cooling (maintaining the temperature at 25 °C) for 15 min, while for the ambient illumination, the plates were exposed to ambient 1 h. Serial dilution was then performed and 10 µL of dilution was pipetted onto a culture agar in triplicate to ensure reproducibility of the results. The agar plates were then kept at 30 °C for 24 h.

2.3. Test of degradation of dye under UV illumination

The dye solution was prepared by dissolving 10 mg of Acid Red 27 (AR 27) in 1 L of DI water. Samples with/without annealing were placed on the Petri dish and covered with 50 mL AR 27 dye solution for 30 min and stirred with a magnetic stirrer in dark to achieve equilibrium. Then the solution was exposed to UV illumination (365 nm, Blak-Ray® B-100 AP Lamp, 60 mW / cm² measured by power meter) for a specified time. Absorption spectrum of the solution was measured immediately before the start of UV illumination, and at 10 min intervals. 3 mL of the solution was withdrawn for absorption measurements at each time.

3. Results and discussion

Figures 1 and **2** show the SEM and TEM images of TNT and SC with / without annealing. From the SEM images, it can be observed that there is negligible difference of morphologies of both TNT and SC before and after annealing. From SAED patterns in TEM, the crystalline structure of both SC before and after annealing is anatase. While from the TEM images, SC samples seem to become rough after annealing. TNT samples are single wall nanotube according to TEM images shown in **Figure 2**, but annealing would make the nanotube more fragile. So the tube-shape morphology cannot be observed in the TEM image (**Figure 2b**) of TNT450 (unlike SEM images, **Figures 1c** and **d**).

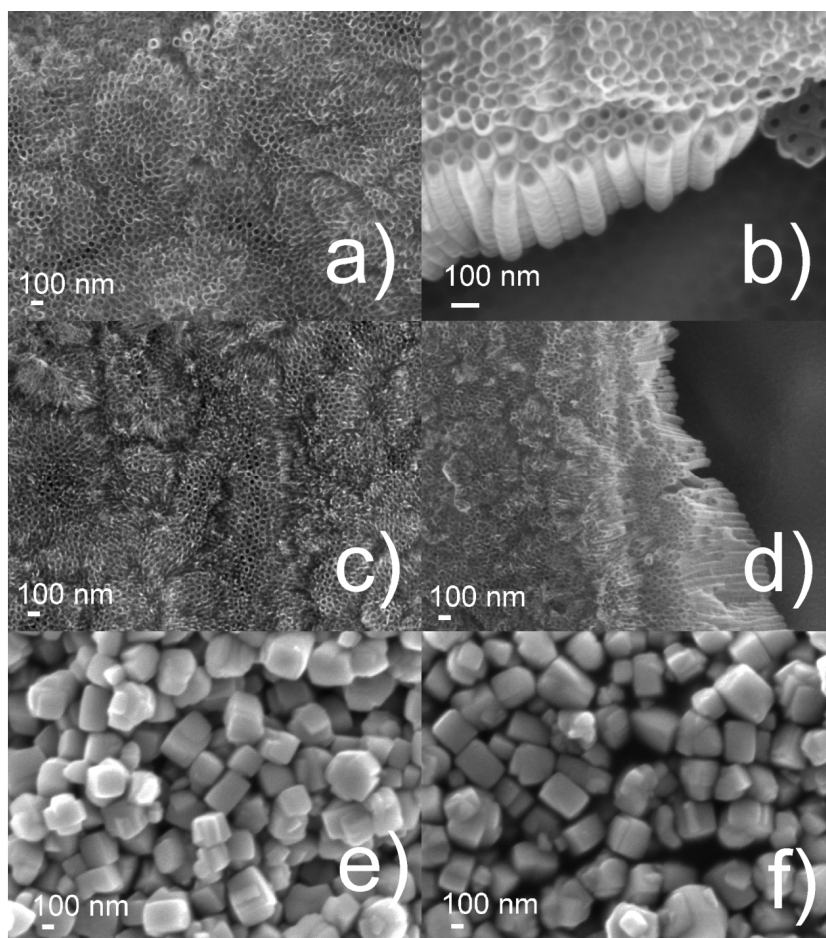


Figure 1. SEM of different TiO₂ nanostructures a) top view and b) side view of TNT; c) top view and d) side view of TNT450; e) SC; f) SC450.

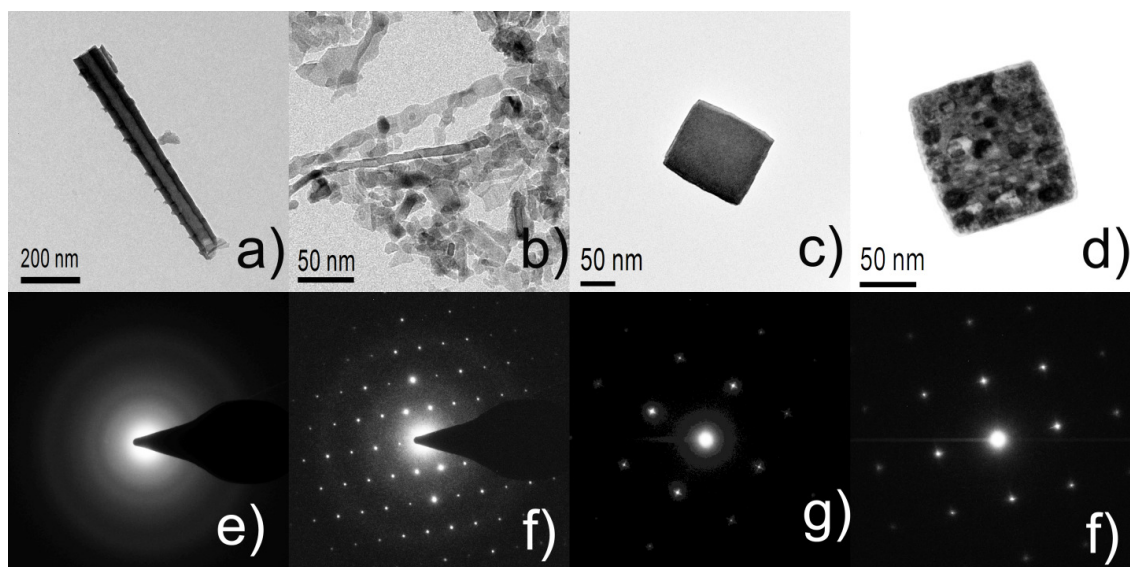


Figure 2. TEM images of a) TNT, b) TNT450, c) SC, and d) SC450. SAED image of e) TNT, f) TNT450, g) SC, and h) SC450.

The results of antibacterial tests for *B. atrophaeus* are summarised in **Table 1** and **Figure 3**. All samples exhibited excellent antibacterial activities under UV illumination. Under ambient illumination, the antibacterial activity of TiO₂ nanostructures is decreased. Annealed samples have better antibacterial activities under ambient illumination. The antibacterial activities under ambient illumination of TiO₂ nanostructures follow the trend TNT450 > SC450 > SC > TNT. Annealed nanotubes exhibited improved performance compared to SC450 samples under ambient illumination. This indicates that the sample morphology plays a significant role in its antibacterial activities.

Table 1. Number of bacteria colonies for different TiO₂ nanostructures with / without annealing under UV and ambient illumination.

	UV 15 min						Mean	S.D.
	Set 1		Set 2					
Blank	850	993	893	995	1045	1100	979	85
TNT	0	0	0	0	0	0	0	0
TNT450	0	0	0	0	0	0	0	0
SC	0	0	0	0	0	0	0	0
SC450	0	0	0	0	0	0	0	0
	Ambient 1 h						Mean	S.D.
	Set 1		Set 2					
Blank	500	595	488	430	420	388	465	59
TNT	389	486	377	320	298	307	361	66
TNT450	0	0	0	0	0	0	0	0
SC	289	209	198	141	130	108	179	61
SC450	32	28	19	86	45	68	46	24

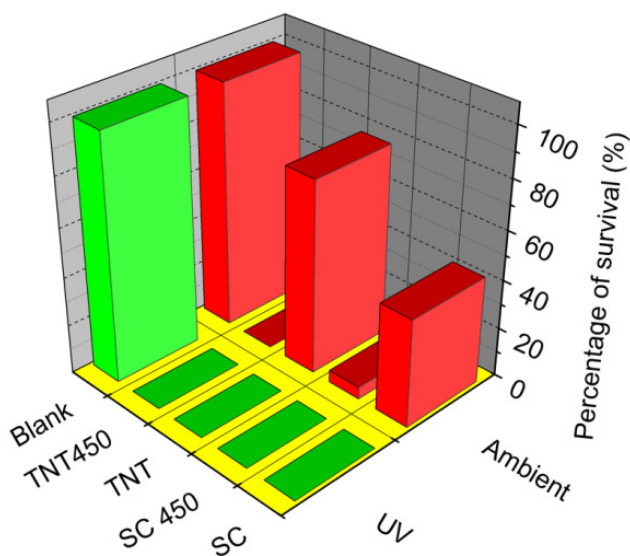


Figure 3. Percentage of survival of *B. atrophaeus* bacteria colonies for exposure to different TiO₂ nanostructures with / without annealing under UV and ambient illumination.

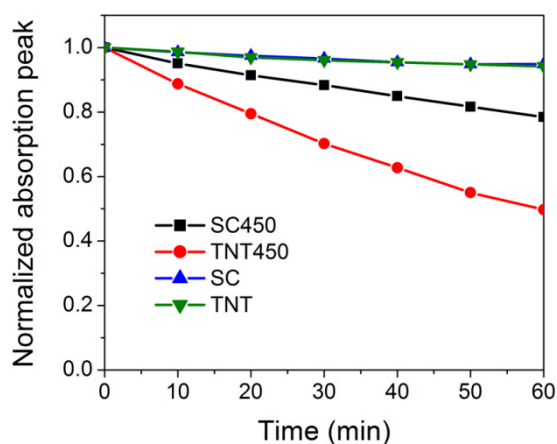


Figure 4. Degradation of Acid red 27 dye for different TiO_2 nanostructures under UV illumination.

On the other hand, the result of photocatalytic degradation of AR 27 under UV illumination shown in **Figure 4** was strongly dependent on morphology and annealing. Both SC and TNT have better ability of dye degradation after annealing. It also shows that TNT sample has better performance compared to SC sample after annealing.

4. Conclusions

We have studied the properties, dye degradation and the antibacterial activity of different TiO_2 nanostructures prepared by anodization and a solution method. The antibacterial activities and dye degradation were highly dependent on the morphology and crystalline structure. Nanotubes exhibited improved performance compared to SC samples. Regardless of morphology, the performance was improved after annealing at 450 °C.

Acknowledgements

Financial support from Innovation Technology Fund project ITS/086/12 and the Strategic Research Theme, University Development Fund, and Small Project Funding of the University of Hong Kong is acknowledged.

References

1. K. R. Raghupathi, R. T. Koodali, A. C. Manna. Size-dependent bacterial growth inhibition and mechanism of antibacterial activity of zinc oxide nanoparticles. *Langmuir* 27 (2011) 4020-4028.
2. Y. H. Leung, C. M. N. Chan, A. M. C. Ng, H. T. Chan, M. W. L. Chiang, A. B. Djurišić, Y. H. Ng, W. Y. Jim, M. Y. Guo, F. C. C. Leung, W. K. Chan, D. T. W. Au. Antibacterial

- activity of ZnO nanoparticles with a modified surface under ambient illumination. *Nanotechnol.* 23 (2012) 475703 1-12.
3. D. Jassby, J. F. Budarz, M. Wiesner. Impact of aggregate size and structure on the photocatalytic properties of TiO₂ and ZnO nanoparticles. *Environ. Sci. & Technol.* 46 (2012) 6934-6941.
 4. A. Man, Ch. Ng, Ch. May, N. Chan, M. Y. Guo, Y. H. Leung, A. B. Djurišić, X. Hu, W. Kin Chan, F. Chi, Ch. Leung, Sh. Y. Tong. Antibacterial and photocatalytic activity of TiO₂ and ZnO nanomaterials in phosphate buffer and saline solution. *Appl. Microbiol. & Biotechnol.* 97 (2013) 5565-5573.
 5. Zh. Lai, F. Peng, Y. Wang, H. Wang, H. Yu, P. Liu, H. Zhao. Low temperature solvothermal synthesis of anatase TiO₂ single crystals with wholly {100} and {001} faceted surfaces. *J. Mater. Chem.* 22 (2012) 23906-23912.
 6. T. P. T. Cushnie, P. K. J. Robertson, S. Officer, P. M. Pollard, C. mc Cullagh, J. M. C. Robertson. Variables to be considered when assessing the photocatalytic destruction of bacterial pathogens. *Chemosphere* 74 (2009) 1374-1378.

NANO-SPHERE OF METAL CARBONATES: SYNTHESIS AND CHARACTERIZATION AS ENERGY STORAGE MATERIALS

Y. Sharma, A. Kumar, P. Chaturvedi

Indian Institute of Technology
Roorkee, India
yksptfpt@iitr.ernet.in

Accepted September 19, 2013

1. Introduction

Presently, lithium ion batteries (LIBs) are the canonical rechargeable power sources suitable for portable appliances and have the enough higher energy densities than the other available secondary batteries and are being used for the low power consumed appliances successfully [1, 2]. For hybrid vehicles, defense and space applications, the parameters to be noted to grade a material as perspective LIBs anode are: high volumetric and gravimetric capacities, high energy and power densities [1]. Much improvement is required to achieve the above mentioned goals and immense research is underway on LIB components (cathode, anode and electrolyte). Since the commercialization of LIBs in 1990, mainly the LiCoO_2 and specialty graphite are being used as the cathode (positive) and anode (negative) materials, respectively [1, 2]. The battery works on intercalation and de-intercalation of Li-ion in to the host structure of cathode as well as anode [3 – 5]. The theoretical capacity of graphite is relatively smaller, 372 mA h g^{-1} to find its application in hybrid vehicles, space crafts and defense applications, various compounds in different shape, size and morphologies have been investigated and proposed as a prospective anode material for Li-ion batteries depending upon their reaction mechanism with Li [1 – 5]. These are: $\text{Li}_4\text{Ti}_5\text{O}_{12}$ (intercalation-deintercalation), Sn, Sb and Zn-based compounds (alloying-de-alloying) and transition and non-transition metal oxides ('conversion' or 'displacement' reaction).

Conversion reactions have been realized for metal-oxides [6 – 9], nitrides [3], sulphides [3], fluorides [10], and hydrides [11], become a general equation for their Li-cyclability. Apart from above mentioned inorganic compounds, the metal carbonates may also be considered as the subject of interest and exploring the feasibility of their conversion reactions involving the carbonate anions. Recently, Tirado's group reported the preliminary studies on Li-cyclability of sub-micron MnCO_3 prepared by reverse micelles method and showed the different Li-reactivity than the MnO prepared by the thermal decomposition of MnCO_3 [12]. Their results, shown for MnCO_3 indicate the feasibility of conversion reaction involving the carbonate anion. However, the observed capacity of 650 decreased to 450 mA h g^{-1} with in 25 cycles. Detailed studies need to be carried out to show the feasibility of conversion reactions involving the carbonates anions and therefore stable long-term Licycling.

Nano- CdCO_3 which could be prepared at ambient temperature and pressure without water of crystallization [13], can be considered as a viable material to investigate its licyclability

involving alloying-de-alloying and conversion reactions. Studies on nano-phase ZnCo_2O_4 [7] and nano- $(\text{Cd}_{1/3}\text{Co}_{1/3}\text{Zn}_{1/3})\text{CO}_3$ [13] have shown that it is viable strategy to achieve high and stable capacity of given compound employing the dual mechanism of reactivity (alloying-dealloying and conversion). Despite the toxicity of metal cation Cd, it is worth to consider this as a subject of interest because it can consume 3.0 moles of Li to form alloy- Li_3Cd [14] and 2.0 moles of Li for conversion [13]; as a result total 5.0 moles of Li do contribute to capacity as high as of 777 mA h g^{-1} . Therefore, in the present work, nano- CdCO_3 is prepared and investigated as an anode material for LIBs. The observed reversible capacity was found to be deteriorated extensively up on cycling and to improve the Li-storage properties of CdCO_3 , strategy of using an active matrix element (Co in present case) along with electrochemical active host (Cd) is used.

The results showed a noticeable improvement in the Li-cycling of CaCO_3 . Further, based on the observed capacity values, CV results, ex-situ XRD and ex-situ TEM of charged electrode to 3 V, a Li-storage mechanism is proposed and results are discussed.

2. Experimental

The Stoichiometric amount of $\text{CdCl}_2 \cdot \text{H}_2\text{O}$ (Merck; > 98 %) and $\text{CoCl}_2 \cdot \text{H}_2\text{O}$ (M & B; > 98 %) was separately dissolved in to distilled water (300 ml each) and then mixed together for about 30 min at magnetic stirrer cum-hot-plate at 50°C . $\text{Na}_2\text{CO}_3 \cdot \text{H}_2\text{O}$ (300 ml, J. T. Baker; > 99 %) solution was added drop by drop to the metal chloride solution using burette. The white, pink and brown colored precipitates were obtained of final product $(\text{Cd}_{1-x}\text{Co}_x)\text{CO}_3$ for $x = 0, 0.25$ and 0.5 , respectively. The precipitate were filtered, washed, and dried at 80°C in hot air oven for 12 h and finally dried powders were grounded using pestle and mortar. XRD (Philips, Expert equipped with $\text{Cu } K_\alpha$ radiation) and SEM (FESEM / EDX – JEOL6700 F) and HR-TEM (JEOL JEM 3010) were used for the structural and morphological characterization, respectively. The doping of Co in CdCO_3 was confirmed by the Electron dispersive spectroscopy (EDX) using SEM / EDX analyzer (JEOL FESEM / EDX). Thermogravimetric analysis (TGA) and differential thermal analysis (DTA) were carried out by TA Instruments (SDT-2960 Simultaneous DTA-TGA) at a heating rate of 5°C min^{-1} , in N_2 - atmosphere.

The composite electrodes were fabricated on Cu-current collector ($\sim 10 \mu\text{m}$) using the 70 : 15 : 15 weight ratio of active material, binder (Kynar 2801) and super P carbon (Ensaco), respectively. The electrode fabrication procedure is described in our earlier reports [7 – 9]. Coin cells (size, 2016: 20 mm diameter and 1.6 mm thickness) were assembled in the glove box (MBraun, USA) which maintained the O_2 and H_2O content < 1 ppm. Li metal (Kyokuto Metal Co., Japan) foil as the counter electrode, glass micro-fiber filter (Whatman) as separator and 1M LiPF_6 dissolved in ethylene carbonate (EC) and diethyl carbonate (DEC) (1 : 1, v / v, Merck Selectipur LP40) as electrolyte were used.

The mass of active material and area of the electrodes were in the range of $\sim 3 - 4 \text{ mg}$ and 2 cm^2 , respectively. Galvanostatic charge-discharge cycling and cyclic voltammetry were performed on several duplicate cells after ageing the cells for 24 h to ensure the homogenous percolation of electrolytes in to the grains of the electrode before test using the computer controlled Bitrode Multiple battery tester (Model SCN, Bitrode, USA) and Mac-pile II (Bio-logic, France), respectively.

For doing ex-situ XRD and TEM analysis, the coin cells were dismantled in the glove box and composite electrode was recovered. The identical cells were discharged or charged to various voltages and aged for 3 h at that specific voltage. These were then dismantled and the recovered composite electrode was washed with DEC to get rid off the electrolyte. Then electrodes were dried inside the Glove box at about 50 °C and stored inside the vacuum tight container and transfer to the XRD sample holder to ensure the minimal contact to air atmosphere.

3. Results and discussion

3. 1. Structural and morphological characterization

As prepared dry powders of CdCO₃ and Co-doped CdCO₃ were characterized by XRD and corresponding patterns are shown in **Figure 1**. These were found in pure-phase form with the rhombohedral–hexagonal crystal structure (space group $R\bar{3}C(167)$). The lattice parameters were evaluated using the Rietveld refinement of XRD pattern using software TOPAS R2 (version 2.1). The evaluated hexagonal lattice parameters $a = 4.920$ and $c = 16.28$ Å for bare CdCO₃ match well with literature [12] and values, $a = 4.930$ and $c = 16.27$ Å reported in JCPDS # 08–0456.

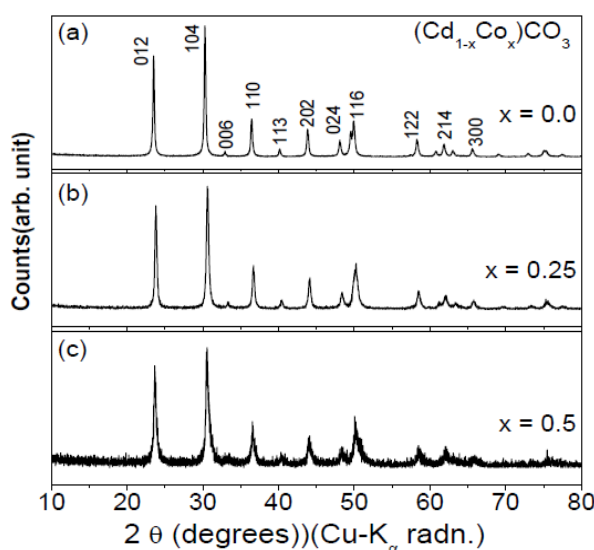


Figure 1. XRD pattern.

Although it is well known that CoCO₃ can only be prepared under hydrothermal conditions, but, presently, the smaller ionic radius of Co²⁺ (~ 0.74 Å: high spin) than the ionic radius of Cd²⁺ (~ 0.95 Å) [15] made it possible to prepare solid solution containing Cd- and Co-carbonates. A small variation in the c axis is noted when Co was doped into the CdCO₃ and the corresponding lattice parameters are $a = 4.90$ and $c = 16.13$ Å for $x = 0.25$ and $a = 4.90$ and $c = 16.10$ Å for $x = 0.5$.

The morphological characterization was carried out by scanning electron microscopy (SEM) and HRTEM. The agglomeration of fine particles of the order of 10 – 20 nm for CdCO₃ and sphere-like morphology of agglomerated fine particles is seen for $x = 0.25$ and 0.5. HR-TEM

also shows the nanophase nature and the agglomeration of fine particles. (Figures are not shown). The crystallite sizes of prepared compounds are evaluated and tabulated in **Table 1** using the maximum intensity peaks of corresponding XRD patterns in the Scherrer's formula, $P = K\lambda / \beta_{1/2} \cos \theta$ [8, 9, 13]. Here, K is a constant (0.9), λ is the wavelength of Cu $K\alpha$ radiation in Å (1.54059), $\beta_{1/2}$ is the full width at half maximum (FWHM) of maximum intensity peak (104) in radians after subtracting the instrumental broadening of 0.15° and θ is the scattering angle. As can be seen in **Table 1**, the crystallites size decreases as Co-content increases in the solid solution from 75 to 25 nm. The calculated particles sizes < 100 nm establish them as a nano-phase materials.

Table 1. Values of lattice constant, crystallite size, observed capacities at different cycles.

Value of x in $(\text{Cd}_{1-x}\text{Co}_x)\text{CO}_3$	Lattice parameters (Å)	Crystallite size* (± 5) nm	Reversible cap. (Theor.) (± 10) mAhg ⁻¹ (moles of Li)	1 st cycle exp. Cap (± 10) mAhg ⁻¹ (moles of Li)			25 th / 50 th cycle exp. Cap, (± 10) mAhg ⁻¹
				disch	charge	ICL	
x = 0	a = 4.92 c = 16.27	75	777 (5.00)	1270 (8.1)	630 (4.0)	640 (4.1)	300 (1.9)
x = 0.25	a = 4.91 c = 16.13	38	716 (4.25)	1300 (7.7)	750 (4.5)	550 (3.3)	475 (2.98)
x = 0.50	a = 4.91 c = 16.10	28	643 (3.50)	750 (9.5)	920 (5.0)	830 (4.5)	500 (2.71)

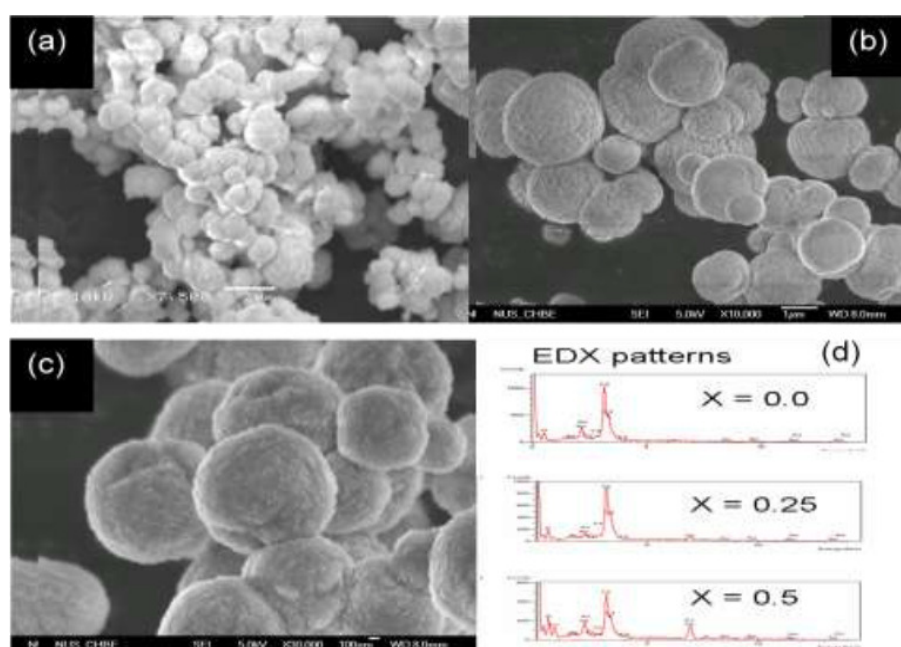


Figure 2. SEM micrographs (a) $x = 0$, (b) $x = 0.25$, (c) $x = 0.5$, and (d) EDX pattern.

As mentioned earlier that CoCO_3 can only be prepared under hydrothermal condition therefore, one may suspect the presence of Co-ion in the solid solution of $(\text{Cd}_{1-x}\text{Co}_x)\text{CO}_3$, because both, bare and Co-doped CdCO_3 exhibit the similar hexagonal-rhombohedral crystal structure therefore it is difficult to distinguish using XRD. To elucidate, the EDX analysis is

carried out and pattern are shown in the **Figure 2d**. EDX pattern shows the several peaks which can be assigned to Co-metal and the corresponding intensity increases as the Co-content in the solid solution increases. The ratio of Co and Cd, 2.8 : 1.0 for $x = 0.25$ and 0.95 : 1.0 for $x = 0.5$ was observed in solid solution $(\text{Cd}_{1-x}\text{Co}_x)\text{CO}_3$, respectively, matches well with the stoichiometric proportion of starting material.

3.2. Electrochemical characterization

3.2.1. Galvanostatic cycling

The capacity vs. voltage profiles are shown in **Figure 3** for $(\text{Cd}_{1-x}\text{Co}_x)\text{CO}_3$ for $x = 0.0, 0.25$ and 0.50 at a constant current, 60 mA g^{-1} in the voltage window, $0.005 - 3.0 \text{ V}$ vs. Li. Only selected cycles are shown for clarity. As can be seen in **Figure 3a**, for $x = 0$ (CdCO_3), first discharge commences from the open circuit voltage (OCV – 2.6 V) and the cell potential drops quickly to $\sim 1.1 \text{ V}$ where a flat plateau is seen till the capacity, 450 mA g^{-1} (2.61 Li) is reached. This is followed by a large slopping region till the cut-off potential, 0.005 V and the total first discharge capacity, $1300 (\pm 10) \text{ mA g}^{-1}$ which corresponds to 7.5 moles of Li per mole of CdCO_3 is obtained.

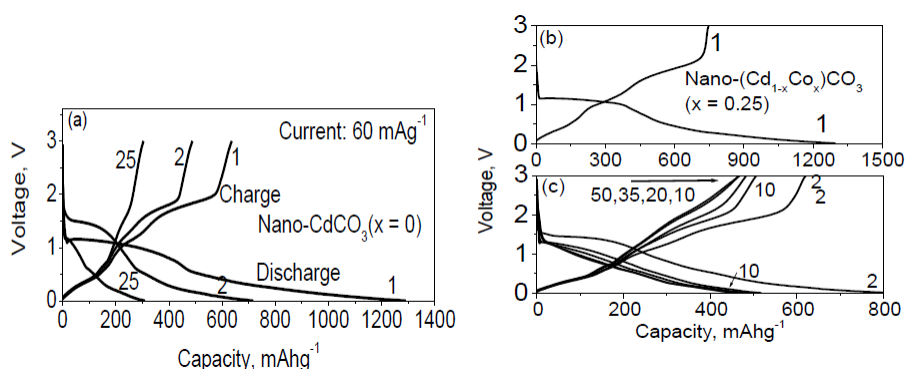


Figure 3. (a) galvanostatic cycling for Nano- CdCO_3 ($x = 0$), (b) $x = 0.25$ (first cycle) and (c) $x = 0.25$ (second cycle to 50 cycles). Only selected cycles are shown. Number refers the cycle number.

During charge process, the small kinks in the charge profiles within the range of $0.25 - 0.75 \text{ V}$ followed by two plateau at ~ 1.35 and $\sim 1.85 \text{ V}$ are seen. Beyond 2.0 V , an almost vertical line shows a small capacity contribution to the total first charge capacity. The observed first charge capacity of $630 (\pm 10) \text{ mA g}^{-1}$ corresponds to the 4.0 moles of Li per mole of CdCO_3 .

During 2nd discharge, the plateau seen at $\sim 1.1 \text{ V}$ during first discharge now shifts to the higher potential $\sim 1.5 \text{ V}$ and the observed total discharge capacity $\sim 730 \text{ mA g}^{-1}$ is quite smaller than the first discharge $\sim 1250 (\pm 10) \text{ mA g}^{-1}$ but nearer to the first charge $\sim 630 (\pm 10) \text{ mA g}^{-1}$. This indicates that electrochemical behavior of CdCO_3 during 2nd discharge is different than first discharge but almost identical to first charge. The capacity vs. voltage profiles for selected cycles shown in **Figure 3a** displays the continuous capacity-fading upon cycling. Nano- $(\text{Cd}_{0.75}\text{Co}_{0.25})\text{CO}_3$ is also subjected to galvanostatic cycling in the potential range, 0.005 to 3.0 V cathodically vs. Li metal at the current rate of 60 mA g^{-1} and the capacity vs. voltage plots are shown in **Figures 3b** and **c**. As it is evident in **Figure 3b**, the first discharge starts from the OCV and similar to bare CdCO_3 potential drops quickly to $\sim 1.1 \text{ V}$ where a flat plateau is seen. The

observed total first discharge capacity of 1300 mA h g^{-1} corresponds to 7.71 moles of Li per mole of $(\text{Cd}_{0.75}\text{Co}_{0.25})\text{CO}_3$. 2nd discharge curve shows a flat plateau region at higher potential $\sim 1.5 \text{ V}$ followed by a slopping tail extending to the capacity $\sim 820 \text{ mA h g}^{-1}$ (**Figure 3b**). A small capacity fading till 8 – 10 cycles and thereafter almost constant capacity of 475 mA h g^{-1} is achieved (**Figure 3c**).

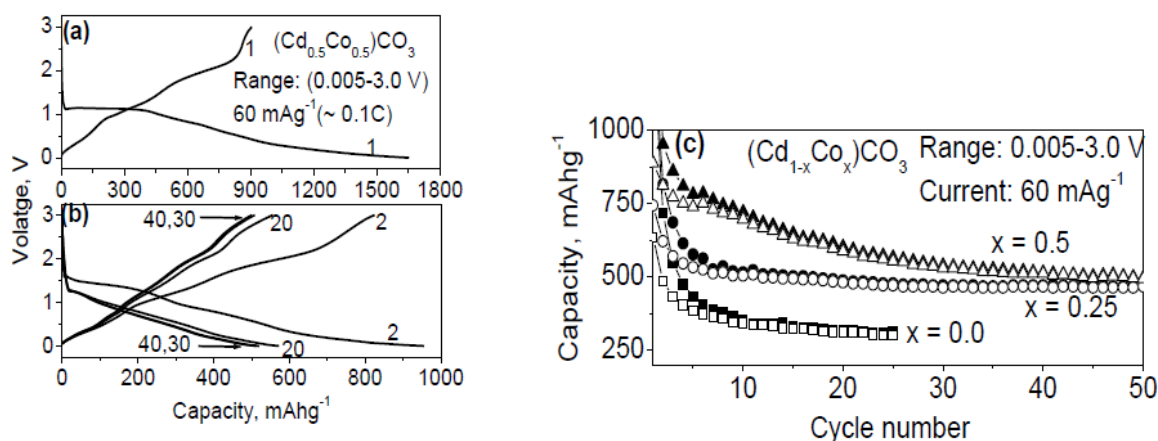


Figure 4. (a) galvanostatic cycling for nano- $(\text{Cd}_{1-x}\text{Co}_x)\text{CO}_3$ ($x = 0.5$, first cycle), (b) $x = 0.5$, second cycle to 40 cycles. Only selected cycles are shown. Number refers the cycle number, and (c) capacity vs. Cycle number plot.

As Co increases till $x = 0.5$ in $(\text{Cd}_{1-x}\text{Co}_x)\text{CO}_3$, similar charge–discharge profiles to $x = 0.25$ are observed except a higher capacity contribution during first discharge and charge. The observed first discharge- and charge capacities of $1750 (\pm 10)$ and $920 (\pm 10) \text{ mA h g}^{-1}$ correspond to the 9.50 and 5.0 moles of Li per mole of compound, respectively. Diminishing plateau regions, seen in **Figure 4b** indicates capacity fading upon cycling. To illustrate better the Li-cyclability of bare nano- CdCO_3 and Co-doped CdCO_3 , the discharge and charge capacities vs. cycle number plot up to 50 cycles (25 cycles for CdCO_3) are shown in **Figure 4c**. As can be seen, the first discharge capacity is larger than the first charge capacity for all the synthesized carbonates. The irreversible capacity loss (ICL) varies as the value of x in $(\text{Cd}_{1-x}\text{Co}_x)\text{CO}_3$ changes. The co-responding values of ICL are tabulated in **Table 1**. For $x = 0$, the reversible capacity fads extensively till the end of 6 – 8 cycles, thereafter slow capacity fading is noted. At the end of 25 cycles, the reversible capacity, $320 (\pm 10) \text{ mA h g}^{-1}$ is achieved. For $x = 0.25$, unlike to the bare CdCO_3 , slow capacity fading is noted for first few cycles and then almost constant capacity of $475 (\pm 10) \text{ mA h g}^{-1}$ which corresponds to the ~ 3.0 moles of Li per mole of compound is obtained with the coulombic efficiency, $> 98\%$ in the range of 15 – 50 cycles. In the case of $x = 0.5$, a drastic fading in capacity from $920 (\pm 10)$ to $500 (\pm 10) \text{ mA h g}^{-1}$ till 30 cycles and thereafter slow fading is noted. At the end of 50th cycle the observed reversible capacity of $500 (\pm 10) \text{ mA h g}^{-1}$ is achieved. The Li-cyclability of nano- $(\text{Cd}_{0.5}\text{Co}_{0.5})\text{CO}_3$ was inferior to the nano- $(\text{Cd}_{0.75}\text{Co}_{0.25})\text{CO}_3$.

3.2.2. Ex-situ XRD and TEM

The identical cells were discharged / charged to a specific voltage and aged for 2 h. Composite electrode was recovered after dismantling the cell in the Ar-filled glove box and

washed with DEC to remove the electrolyte and processed as described in our earlier reports. **Figure 5** shows the XRD patterns recorded on bare nano- $\text{Cd}_{0.5}\text{Co}_{0.5}\text{CO}_3$ and on those discharged to 1.5 and 0.005 V during first discharge, and at 3.0 V (charged state) after 15 cycles. The characteristic peaks of hexagonal–rhombohedral system are seen in the XRD patterns of bare electrode and discharged to 1.5 V. The peaks are disappeared in the pattern recorded at 0.005 V and charged to 3.0 V after 15 cycles, and only peaks due to substrate Cu are seen. This indicates the products formed up on fully discharged (0.005 V) and charged (3.0 V) are either amorphous or crystalline regions which are smaller than coherence length of X-rays. This implies that XRD may be unable to detect them.

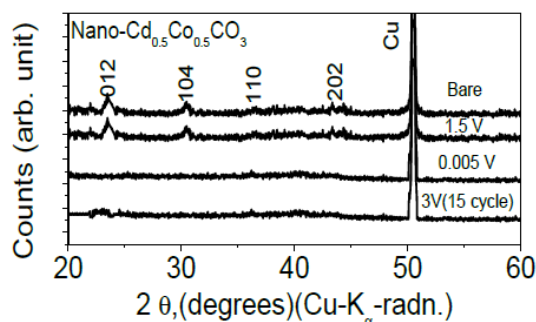


Figure 5. Ex-situ XRD pattern recorded on the composite electrode of nano- $\text{Cd}_{0.5}\text{Co}_{0.5}\text{CO}_3$ at different depth of discharge during first cycle and charged to 3 V after 15 cycles.

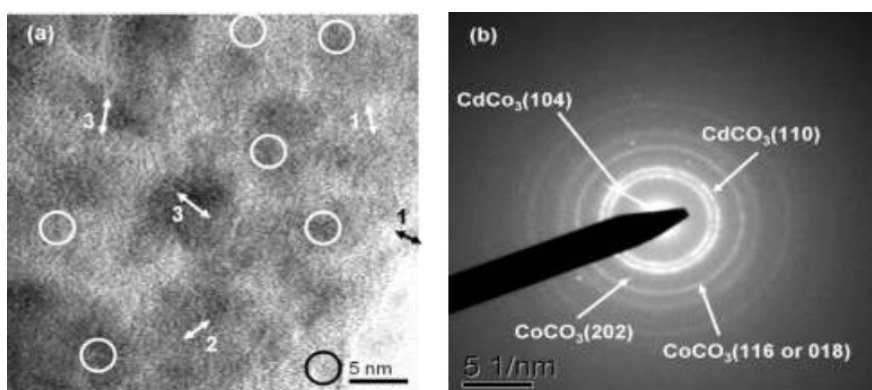


Figure 6. Ex-situ TEM recorded on the composite electrode of nano- $\text{Cd}_{0.5}\text{Co}_{0.5}\text{CO}_3$ charged to 3 V after 50 cycles (a) lattice image. Encircled regions refer to small crystalline regions dispersed in amorphous regions. (b) corresponding electron diffraction pattern. Rings are referred to metal carbonates formation.

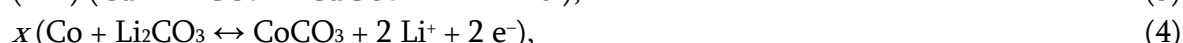
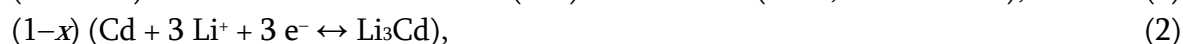
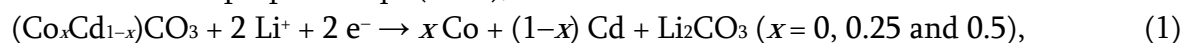
To investigate the charged product formed upon charging the electrode of nano- $\text{Cd}_{0.5}\text{Co}_{0.5}\text{CO}_3$ to 3.0 V after 30 cycles which could not be detected by XRD, HR-TEM analysis along with SAED studies were carried out corresponding lattice image and SAED pattern are shown in **Figures 6a** and **b**. Careful investigation was executed by analyzing the various parts of sample. The lattice image (**Figure 6a**) shows the dispersion of small crystalline region (4 – 6 nm) in to amorphous matrix. The darker and bright regions seen in lattice image can be referred as crystalline and amorphous regions. From the HR-TEM lattice images, the evaluated d-values (interplanar distance) corresponding to some of the regions marked as 1, 2 and 3 are 2.74, 2.52 and 2.43 Å, respectively. These values are assigned to the hexagonal- CoCO_3 (JCPDS file No.

11–0692), and CdCO₃ (JCPDS file No. # 72–1939). Within the range of experimental error in the *d*-values measurement from the lattice image, we also cannot rule out the presence of partially unreacted Li₂CO₃ in the charged samples. However, the presence of Li₂CO₃ is unlike since during first charge we get higher capacity than the theoretical where complete reversible consumption of Li₂CO₃ is assumed (proposed reaction mechanism in next section). The observed *d*-values of 2.74 and 2.43 Å can be ascribed to the hexagonal-CoCO₃ and CdCO₃ separately, respectively.

SAED pattern shown in the **Figure 6b** is comprised of concentric diffuse rings overlapped by occasional diffuse spots which indicate the dispersion of nano-crystalline regions in to the amorphous matrix complements HR-TEM lattice image data. The derived *d*-values using diameter of the rings / spots with in the limit of experimental error (± 0.05 Å) are 2.88, 2.43 and 1.65 Å, respectively. The former two values can be ascribed to the (104) and (110) planes of hexagonal-CdCO₃, respectively. The *d*-value of 1.65 Å is attributed to the (202) plane of hexagonal-CoCO₃. On the basis of ex-situ-XRD, TEM and SAED analysis, we can conclude that the first discharge cycle is the crystal structure or amorphisation of the lattice and the formation of very small particles (3 – 5 nm) embedded in to the amorphous matrix. The CdCO₃ and CoCO₃ formation occurs when electrode is charged to 3.0 V. We do not see any oxide or other decomposition products of carbonates in our ex-situ TEM analysis.

3.2.3. Reaction mechanism

Based on the ex-situ-XRD, TEM, SAED and observed capacity values, a plausible reaction mechanism is proposed Eqs. (1 – 4),



in which the first discharge reaction is the crystal structure destruction or amorphisation of the lattice process in which the metal carbonates first reduce to metal nano-particles (Cd and / or Co, depending upon the value of *x*) embedded in to amorphous matrix of Li₂CO₃, corresponding plateau potential seen at ~ 1.1 V in galvanostatic cycling (**Figure 4**) can be assigned for structure destruction – forward reaction of Eq. (1). Further deep discharge to cut-off potential, 0.005 V, the alloy-Li₃Cd formation occurs as per forward reaction of Eq. (2). During first discharge, a long tail without any clear plateau is seen which indicates that alloying reaction of Li and Cd occurs in the stages ranging from 1 to 3.

Theoretically envisaged number of moles of Li participating in the 1st discharge reaction are 5, 4.25 and 3.5, respectively for *x* = 0, 0.25 and 0.5 in (Cd_{1-*x*}Co_{*x*})CO₃ as per forward reactions of Eqs. (1) and (2). The experimentally observed capacity values of 1270 (± 10), 1300 (± 10) and 1750 (± 10) mA h g⁻¹ correspond to ~ 8.2, 7.7 and 9.5 moles of Li per mole of compounds, respectively for *x* = 0, 0.25 and *x* = 0.5. These values are higher than theoretically predicted ones by 3.2, 3.45 and 6.0 moles of Li, respectively. The excess consumption of Li can be attributed partly to solid electrolyte interphase (SEI) formation at the electrode–electrolyte interface [7 – 9], partly to polymeric gel-type layer formation on Cd and / or Co metal nano-particles due to the catalytic decomposition of solvent of the electrolyte [7 – 9, 13]. The formerly mentioned factor becomes more prominent when the nano-phase of starting materials is used. It is also

evident in our experiment that observed discharge capacity increases as the Co-content increases. Electrochemically in-situ formed Co-metal has some catalytic effect either on SEI formation or on polymeric gel type-layer formation, thereby huge extra capacity is observed specially for $x=0.5$. Studies have shown that the adsorbed water also plays a significant role in enabling extra capacity through the reduction of H_2O to form $LiOH$ upon reaction of H_2O with Li [16].

During first charge, firstly the de-alloy reaction (backward reaction of Eq. (2)) of $Li-Cd$ followed by the metal carbonate formation occur. Similar to alloying reaction, this de-alloy process occurs in stages and corresponding phase changes are depicted by small kinks in the capacity–voltage profiles in the range 0.005 to 1.0 V (**Figures 3** and **4**). The de-alloying of $Li-Cd$ completes at ~ 1.5 V where a plateau is seen.

Upon further charging, the newly formed Cd -metal nano-particles react with amorphous Li_2CO_3 and forms $CdCO_3$ as per forward reaction of Eq. (3) corresponding voltage plateau is seen at ~ 1.85 V. The observed first charge capacity of $630 (\pm 10)$ mA h g^{-1} corresponds to the 4.0 moles of Li per mole of $CdCO_3$. This is almost 150 mA h g^{-1} smaller than the theoretically envisaged value of $777 (\pm 10)$ mA h g^{-1} , this indicates incomplete participation of $CdCO_3$ in the reaction with Li . Co-doping does not show any significant change in the plateau potential ~ 1.85 V of carbonate formation but increases the capacity significantly. The observed first charge capacity increases as the Co-content in $(Cd_{1-x}Co_x)CO_3$ increases from $x=0 \rightarrow 0.25 \rightarrow 0.5$ (**Table 1**, and **Figures 3** and **4**). The observed first charge capacities of $750 (\pm 10)$ and $920 (\pm 10)$ mA h g^{-1} respectively for $x=0.25$ and 0.5 , correspond to 4.45 and 5.0 moles of Li per mole of compounds. These values of capacities are slightly higher for $x=0.25$ and quite high for $x=0.5$ than the theoretically predicted ones. Part of this excess capacity can be attributed to the dissolution of the polymeric layer, formed during the first-discharge reaction, and possibly, the catalytic decomposition of the $LiOH$, aided by the metal nano-particles. However, the observed huge capacity for $x=0.5$ degrades extensively up on cycling till 35th cycles. The observed high capacity during cycling extensively degrades in the range 2 – 8 cycles for $x=0$ and 0.25 after which a stable and reversible capacity of $320 (\pm 10)$ mA h g^{-1} (2 moles of Li) and $475 (\pm 10)$ mA h g^{-1} (3 moles of Li) is observed. Thus, we conclude that the proposed reaction mechanism in which the metal carbonates first reduced to the metal Cd - and / or Co -nanoparticles embedded in the Li_2CO_3 matrix followed by formation of the alloy- $Li-Cd$ upon deep discharge and metal carbonates re-form upon charging (**Figure 5**) is well supported by the experimental data.

3.2.4. Cyclic voltammetry

Cyclic voltammetry is used to complement the galvanostatic data and support the proposed reaction mechanism. Cyclic voltammograms during 1 – 6 cycles for $Cd_{1-x}Co_xCO_3$ ($x=0, 0.25$ and 0.5) at a slow scan rate of $58 \mu V s^{-1}$ in the range of 0.005 – 3.0 V vs. Li are shown in **Figure 7**. The cathodic scans commence from OCV with an intense peak at ~ 0.9 V and a broad peak at ~ 0.3 V followed by a split to fully discharge to 0.005 V (**Figure 7a**). The former intense peak is attributed to the crystal structure destruction or amorphisation of lattice followed by the nano-metal particles formation embedded in to the Li_2CO_3 matrix as per forward reaction of Eq. (1). The broad peak along with a small splitting is ascribed to the alloying reaction of Li and Cd in stages Li_xCd ($x=1-3$), therefore a distinct peak is not seen **Figure 7a**. Upon charging to

3.0 V, the anodic scan exhibits multiple peaks at ~ 0.30 , 1.12 and 1.85 V along with small humps in the range of 0.50 – 0.75 V indicating different electrochemical processes occurring in this range of voltage than the first discharge. The former peak along with the minor shoulders in the range of 0.50 – 0.75 V ascribed to the de-alloy of Cd in stages which finally completes at ~ 1.12 V. The latter peak at ~ 1.85 V is ascribed to CdCO_3 -formation.

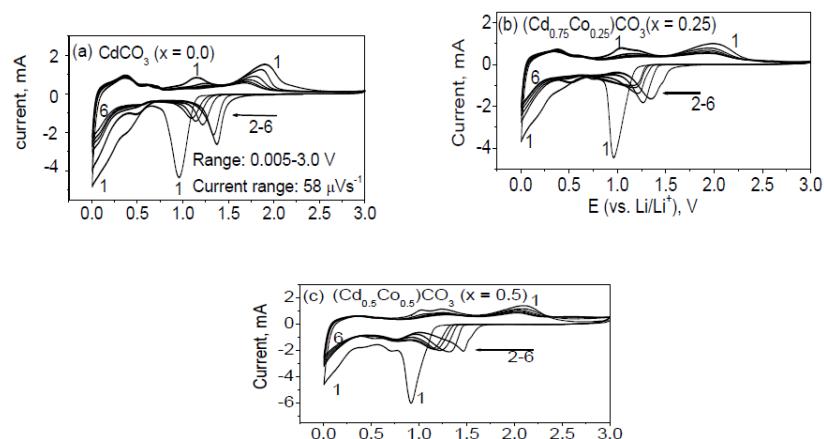


Figure 7. Cyclic voltammetry scans recorded for the electrode of nano- $\text{Cd}_{1-x}\text{Co}_x\text{CO}_3$ (a) $x = 0$, (b) $x = 0.25$ and (c) $x = 0.5$. Numbers refer the cycle number.

Second discharge, in which cathodic peak position shifts towards higher potential at ~ 1.35 V followed by the alloying reaction depicted by a broad peak from 0.50 – 0.005 V, is different than the first discharge. Anodic peak shows a continuous decrease in the peak intensities with slight shift in redox peak positions for metal carbonate formation / decomposition, inferring the capacity fading analogous to the galvanostatic cycling.

During first discharge the CVs for Co-doped CdCO_3 are similar to the bare CdCO_3 in nature as a whole and Co-doping does not show any effect on the peak position for crystal structure destruction (**Figures 7b** and **c**). However, upon charging, a significant difference in the peak positions and their shape is noted. For $x = 0.25$, peak which is assigned to complete de-alloy of Li–Cd moves slightly towards lower potential 1.1 V and becomes broader. For $x = 0.5$, two separate peaks are seen in the range of 0.8 – 1.4 V. One of them can be assigned to the complete de-alloy and other may be ascribed to onset of CoCO_3 formation which finally completes. However, the peak, seen at ~ 1.85 V in **Figure 7a** for CdCO_3 shifts towards higher potential (~ 2.1 V) for $x = 0.5$ (**Figure 7c**). The peak intensities decrease faster in CdCO_3 than the Co-doped CdCO_3 indicating capacity fading upon cycling. The findings are in good agreement for at least first few cycles that capacity fads quickly in two cases: bare CdCO_3 and $\text{Cd}_{0.5}\text{Co}_{0.5}\text{CO}_3$. However, slow fading is noted for $\text{Cd}_{0.75}\text{Co}_{0.25}\text{CO}_3$.

3.2.5. Theoretical consideration

The feasibility of the any electrochemical / chemical reaction can be established using the thermodynamics calculations. Change in Gibbs free energy of a system is one of the tools which can be used to estimate the electromotive force in the reaction using Nernst's equation [3]:

$$\Delta G = -nEF, \quad (5)$$

where ΔG is the change in Gibbs free energy of formation of a product from the initial compound. E is electromotive force (emf), and F is the Faraday's constant ($\sim 96500 \text{ J K}^{-1} \text{ V}^{-1}$). If the calculated emf is positive then the proposed reaction is feasible. We also have carried out some thermodynamic calculations using Gibbs free energy. The change in Gibbs free energy of formation of forward reaction of Eq. (1)

$$\Delta G = \Delta G_f(\text{Li}_2\text{CO}_3) - \Delta G_f(\text{CdCO}_3) = -nEF, \quad (6)$$

The theoretical emf value, $E \sim 2.38 \text{ V}$ is calculated using the Gibbs free energy of $\text{Li}_2\text{CO}_3 = -1132$ and $\text{CdCO}_3 = -671 \text{ kJ mol}^{-1}$ at 25°C from the literature [17], number of Li involved in the reaction were $n=2$. The emf value refers to a cell where Li activity is given by the Li-metal on one side and by three phase contact of Li_2CO_3 , CdCO_3 and Cd on the other side. Li-solubility is negligible and hence, neglected in calculation.

The solid solution of CoCO_3 and CdCO_3 does not show any significant difference in Gibbs free energy of formation. Gibbs free energy of the solid solution is calculated using the general Eq. (7), given for ideal mixing [17]:

$$\Delta G(\text{Cd}_{1-x}\text{Co}_x\text{CO}_3) = x\Delta G(\text{CoCO}_3) + (1-x)\Delta G(\text{CdCO}_3) + RT(x \ln x + (1-x) \ln(1-x)), \quad (7)$$

Calculated ΔG for $x=1/4$ and $1/2$ were -668 kJ and -665 kJ mol^{-1} , respectively at 25°C using the $\Delta G = -650 \text{ kJ mol}^{-1}$ [17.]. The emf values, $\sim 2.40 \text{ V}$ ($x=1/4$) and $\sim 2.42 \text{ V}$ ($x=1/2$) for these solid solutions were slightly higher than the bare CdCO_3 ($\sim 2.38 \text{ V}$). On the basis of calculated values of emf, which is always positive, supports the feasibility of proposed reaction of Eq. (1). The slight increase in emf values is noted up on the Co-doping in to CdCO_3 .

4. Conclusions

Solid solution of nano- $\text{Cd}_{1-x}\text{Co}_x\text{CO}_3$ ($x=0, 0.25$ and 0.50) is prepared by aqueous precipitation method at ambient temperature and pressure. Rhombohedral-hexagonal structure is confirmed by XRD. Sphere-like morphology of agglomerated nano-particles was observed. Solid solution of Cd-Co CO_3 was prepared at ambient temperature and pressure. EDX analysis confirmed the presence of Co in the solid solution. As prepared metal carbonates are tested as anode materials for LIBs at a constant current rate of 60 mA g^{-1} in the voltage range $0.005 - 3.0 \text{ V vs. Li}$. The reaction of Li with metal carbonates leads the crystal structure destruction or amorphisation of the lattice followed by the formation of metal nanoparticles (Cd and / or Co) embedded in the amorphous Li_2CO_3 matrix. Further, electrochemically in-situ formed Cd reacts with Li to form alloy Li_3Cd during deep discharge. The first discharge capacities of $630, 750$ and 920 mA h g^{-1} are noted for $x=0, 0.25$ and 0.5 , respectively. The reversible capacity fads extensively for $x=0$ and 0.5 and the capacities of $320 (\pm 10)$ and $500 (\pm 10) \text{ mA h g}^{-1}$ are observed after 25 and 50 cycles, respectively. However, for $x=0.25$, the slow capacity fading is noted for first few cycles and thereafter a capacity of $475(\pm 10) \text{ mA h g}^{-1}$ is noted within 15 – 50 cycles with good Coulombic efficiency of more than 98 %. Ex-situ XRD, HR-TEM and SAED analysis is carried out to support the reaction mechanism. We have shown that alloying-de-alloying and conversion reaction aids each other to get stable and high capacity involving the carbonate anion similar to oxides. Cyclic voltammetry (CV) supports the galvanostatic cycling. To support the feasibility of proposed reaction mechanism, electromotive force (emf) values were calculated using Nernsts' equation. Theoretical studies were found to be in good agreement with experimental values.

Acknowledgement

Y. Sharma acknowledges the technical / experimental support received from Prof. B. V. R. Chowdari's group, Department of Physics, National University of Singapore.

References

1. B. L. Ellis, K. Town, L. F. Nazar. New composite materials for lithium-ion battery. *Electrochim. Acta* 84 (2012) 145-154.
2. C. M. Hayner, X. Zhao, H. H. Kung. Materials for rechargeable lithium-ion batteries. *Ann. Rev. Chem. & Biomol. Eng.* 3 (2012) 445-471.
3. G. A. Nazri, G. Pistoia. *Lithium Batteries – Science and Technology*. 2003, New York: Kluwer Acad.
4. J. L. Tirado. Inorganic materials for the negative electrode of lithium-ion batteries: State-of-the art and future prospects. *Mater. Sci. & Eng. R* 40 (2003) 103-136.
5. A. S. Aricò, P. Bruce, B. Scrosati, J.-M. Tarascon, W. van Schalkwijk. Nanostructured materials for advanced energy conversion and storage devices. *Nat. Mater.* 4 (2005) 366-377.
6. P. Poizot, S. Laruelle, S. Grugeon, L. Dupont, J.-M. Tarascon. Nano-sized transition-metal oxides as negative-electrode materials for lithium-ion batteries. *Nature* 407 (2000) 496-499.
7. Y. Sharma, N. Sharma, G. V. S. Rao, B. V. R. Chowdari. Nanophase ZnCo_2O_4 as a high performance anode material for Li-ion batteries. *Adv. Func. Mater.* 17 (2007) 2855-2861.
8. Y. Sharma, N. Sharma, G. V. S. Rao, B. V. R. Chowdari. Li-storage and cyclability of urea combustion derived ZnFe_2O_4 as anode for Li- ion batteries. *Electrochim. Acta* 53 (2008) 2380-2385.
9. Y. Sharma, N. Sharma, G. V. S. Rao, B. V. R. Chowdari. Studies on nano- CaOSnO_2 and nano- CaSnO_3 as anodes for Li-ion batteries. *Chem. Mater.* 20 (2008) 6829-6839.
10. M. V. Reddy, S. Madhavi, G. V. S. Rao, B. V. R. Chowdari. Metal Oxyfluorides TiOF_2 and NbO_2F as anodes for Li-ion batteries. *J. Power Sources* 162 (2006) 1312-1321.
11. Y. Oumellal, A. Rougier, G. A. Nazri, J.-M. Tarascon, L. Aymard. Metal Hydrides for lithium-ion batteries. *Nat. Mater.* 7 (2008) 916-921.
12. A. Askarinejad, A. Morsali. Syntheses and characterization of CdCO_3 and CdO nanoparticles by using a sonochemical method. *Mater. Lett.* 62 (2008) 478-482.
13. Y. Sharma, N. Sharma, G. V. S. Rao, B. V. R. Chowdari. Nano- $(\text{Cd}_{1/3}\text{Co}_{1/3}\text{Zn}_{1/3})\text{CO}_3$: A new and high capacity anode material for Li-ion batteries. *J. Mater. Chem.* 19 (2009) 5047-5054.
14. J. Wang, P. King, R. A. Huggins. Investigations of binary lithium-zinc, lithium-cadmium and lithium-lead alloys as negative electrodes in organic solvent-based electrolyte. *Solid State Ionics* 20 (1986) 185-189.
15. R. D. Shannon. Crystal physics, diffraction, theoretical and general crystallography. *Acta Crystalllograp. A* 32 (1976) 751-767.
16. Analytical Methods for Detection of LiOH and Li_2CO_3 : NASA – Ames Research Center under Cooperative Agreement Number NASA-CR-192771.
17. P. A. Rock, W. H. Casey, M. K. mc Beath, E. M. Walling. A new method for determining Gibbs energies of formation of metal-carbonate solid solutions: 1. The $\text{Ca}_x\text{Cd}_{1-x}\text{CO}_3(\text{s})$ system at 298 K and 1 bar. *Geochim. et Cosmochim. Acta* 58 (1994) 4281-4291.

STUDY OF ION BEAM MIXING OF Te / In AND Se / In SYSTEMS BY CASCADE COLLISIONAL MIXING MODEL

B. A. M. Ibrahim

Diyalla University
Baquba, Iraq
buth_oubaidi2@yahoo.com

Accepted October 19, 2013

1. Introduction

Ion implantation is becoming an important technique in physical metallurgy by which surface composition changes are produced by introducing controlled amounts of selected atomic species into the near surface region of material, but unfortunately a maximum concentration of the implanted species is imposed by sputtering phenomena. It is possible to overcome this by using ion beam mixing technique by the deposition of a layer of element on another layer of different element and subsequent irradiation with energetic ions will introduce a cascade of atomic collisions in the solid [1]. If the ion energy is sufficient to penetrate at least to the interface between two layers then the amount of different atoms can be intermixed.

Therefore a controllable amount of the material can be incorporated into solid at a depth which is dependent on the energy of incident ions and on the stopping power of the target material to be implanted [2].

Different processes such as a collisional mixing can bring intermixing of elemental layers. In the collisional mixing process, target atoms are either displaced directly by the incoming ions (recoil mixing) or displaced in the cascade of low energy recoils (cascade mixing) [3].

Electrical resistivity measurements detected interface structural changes since it is sensitive to the presence of defects and changes in the structural state of material. In addition, Rutherford backscattering spectrometry (RBS) is an ideal tool to study the inter-diffusion in bilayer thin film system (diffusion profiles) or kinematics of compound formation.

In this work, the ion beam mixing at normal incidence of 400 keV Ar⁺ ions in Te / In-glass and Se / In-glass bilayer thin film systems are studied by means of AC-electrical resistivity measurements, our main purpose is to show that a simple conduction model allows to estimate the volume fraction of the mixed layers at the interface of these systems, and 2 MeV He⁺ RBS, which indicate that the width of intermixed layers are 50 and 100 nm of (Te–In) and (Se–In) layers, respectively [4].

Also these systems are studied theoretically by means of collisional cascade mixing [5], which shows that the amount and width of mixed layer of (Se–In) is larger than that of (Te–In) layer, which are in good agreement with experimental results.

In this paper, I only want to introduce collisional mixing model as a tool for studying ion beam mixing and to estimate the mixing efficiency between materials of layers.

2. Experimental

Bilayer thin film were prepared by leybold thin film evaporator with vacuum of 10^{-5} mbar, during deposition, was used with a mean evaporation rate of nearly $4 \text{ \AA} / \text{s}$.

The inner layer (In) with lateral dimensions $1.4 \text{ cm} \times 0.2 \text{ cm}$ was first deposited, then Ag contacts of 500 \AA thickness were deposited on both sides of glass such that they touch the inner layer on both ends, at the top of the inner layer – a Te- or Se-layer with the same lateral dimensions as the inner layer. In this investigation, bilayer systems Te / In and Se / In are prepared. It is worth mentioning that the layer thickness of Te / In and Se / In systems was chosen such that the projected range of incident ion exceeded the over laying layer and were calculated from the TRIM computer code [6].

The samples were mounted in vacuum of 10^{-5} mbar and then irradiated, at room temperature with 400 KeV Ar^+ ions. In situ AC resistance measurements were carried out using the component evaluation technique by means of AC voltage and current measurements utilizing a lock-in-amplifier [7]. The RBS measurements were performed using 2 MeV He^+ ions, the surface barrier detector was mounted at scattering angle 135° [8].

3. Results and discussion

3.1. Electrical resistivity measurements

Variation in the electrical resistivity of the irradiated thin film were calculated from continuously measured electrical resistance and film geometry after each ion irradiation with a certain fluence ϕ .

Figures 1 and 2 show the variations in the electrical resistivity of Se / In and Te / In systems with fluence. The initial resistivity for Se / In and Te / In systems are 38 and $212 \mu\Omega \cdot \text{cm}$, respectively. As a decrease of the electrical resistivity (increase of conductivity) of these systems are observed for low fluence up to a critical fluence. The observed increase of electrical conductivity of Te / In and Se / In systems is due to growth of an intermixed layer at Te–In or Se–In interfaces, after the critical fluence there is no dependence of resistivity upon fluence, which means that the mixing process is ended.

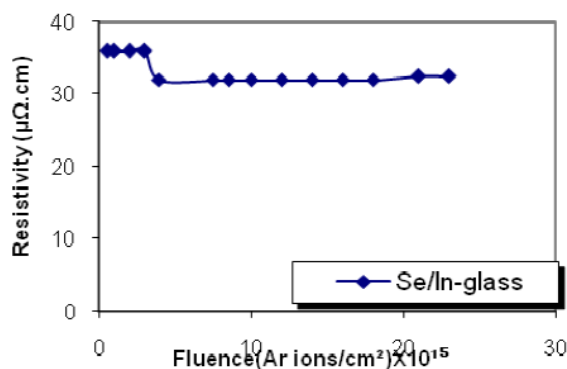


Figure 1. Resistivity of Se / In system versus fluence.

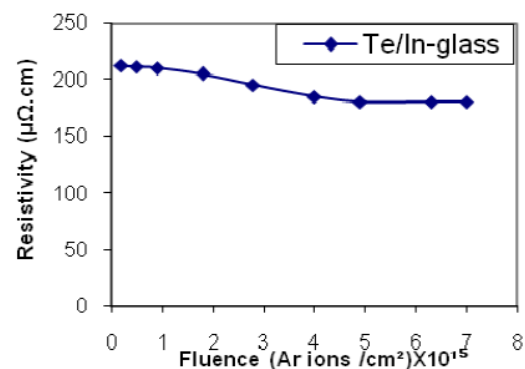


Figure 2. Resistivity of Te / In system versus fluence.

A semi-empirical conduction model [1], which allows the estimation of the volume fraction of the intermixed layer, $C(\varphi)$ was used to study the mixing kinetics of the bilayer thin film, as shown in Eq. (1):

$$C(\varphi) = \frac{\sigma(\varphi) - \sigma_0}{\sigma_f - \sigma_0}, \quad (1)$$

where σ_0 , σ_f , and $\sigma(\varphi)$ are the initial, final and instantaneous conductivities respectively.

The value of volume fraction, at certain fluence, gives an idea of the growth of intermixed layer at the interface. Thus, the mixing kinetics can be understood via the dependence of the volume fraction on the ion fluence. Since the volume fraction of the intermixed layer is proportional to the number of intermixed atoms, it can be used to explain the relative contributions to ion mixing of each of the collisional processes. $C(\varphi)$ will have at least two components. Independent events such as recoil mixing will introduce a linear (φ) dependence while a $\sqrt{\varphi}$ behavior will result from collisional cascade mixing. Therefore, $C(\varphi)$ can be expressed as [2]:

$$C(\varphi) = D\sqrt{\varphi} + R\varphi. \quad (2)$$

It was shown that the systems Se / In and Te / In follow collisional cascade mixing [4].

The critical (saturation) fluencies are estimated from **Figures 3** and **4** for both systems which are $3.955 \cdot 10^{15}$ ion / cm^2 for Se / In system, and $4.954 \cdot 10^{15}$ ion / cm^2 for Te / In system, indicating that the mixing efficiency of Se / In system is larger than that for Te / In system. It is noted that volume fraction of Se / In system is larger than that of Te / In system, which means a large extent of mixing for Se / In.

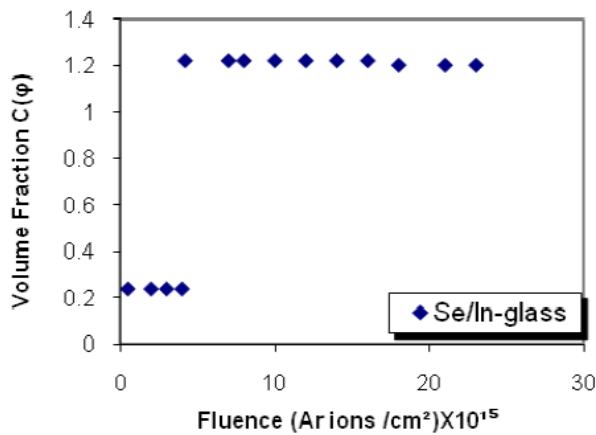


Figure 3. Variation of $C(\varphi)$ versus fluence for Se / In system.

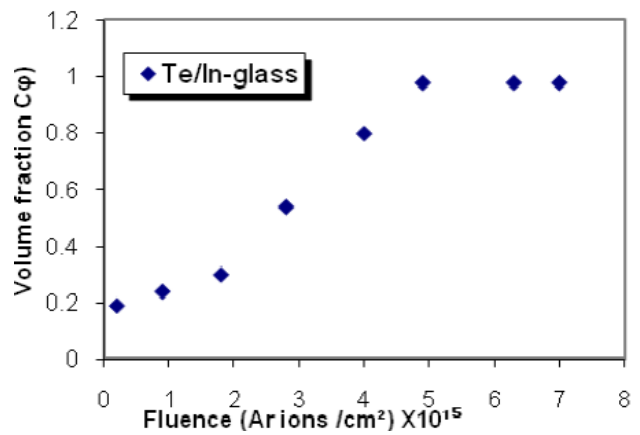


Figure 4. Variation of $C(\varphi)$ versus fluence for Te / In system.

3.2. RBS measurement

Figures 5 and **6**, show the backscattering spectra of Se / In and Te / In systems before and after irradiation by 400 KeV Ar^+ ions, the depth distribution of the Te and Se concentration deduced from the RBS data using the RUMP-computer code for Te / In and Se / In systems, a mixed layer with nearly uniform composition of a thickness 50 and 100 nm for Te / In and Se / In systems respectively.

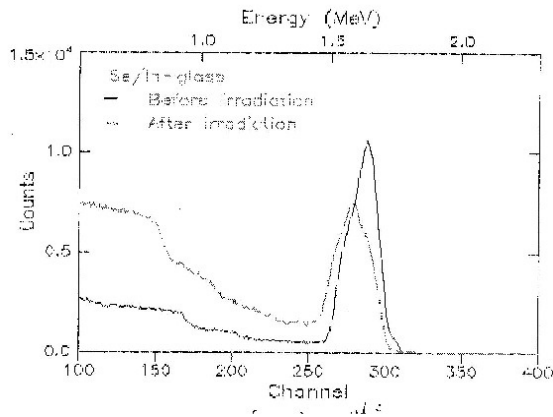


Figure 5. RBS spectrum of Se / In-glass before and after irradiation.

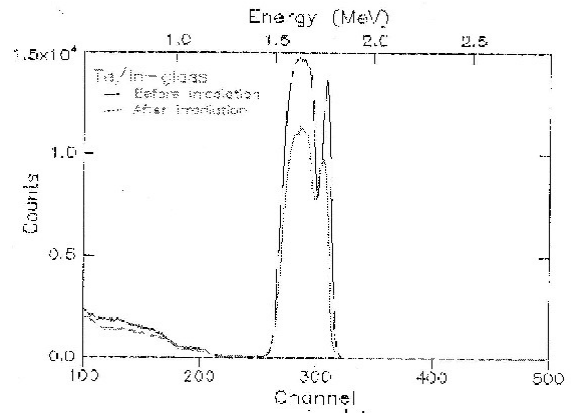


Figure 6. RBS spectrum of Te / In-glass before and after irradiation.

4. Theoretical aspect

Ion beam mixing is a process for adhering two multilayers, especially a substrate and deposited surface layer. The process involves bombarding layered samples with doses of ion radiation in order to promote mixing at the interface.

As an ion penetrates a solid, it slows down by depositing energy to both the atoms and the electrons of the solid. During the nuclear collision portion of the slowing process, target atoms can be permanently displaced from their lattice sites and relocated several lattice sites away. When this process takes place at the boundary separating two different materials, interface mixing results.

Recoil mixing, a highly directed process, in which one atom receives a large amount of kinetic energy in a single displacement. **Collision cascade** – atoms in a collision cascade undergo many multiple uncorrelated low-energy displacement and relocation events. Atomic mixing resulting from a series of uncorrelated low-energy atomic displacements is referred to as **cascade mixing**.

It is found experimentally that amount of mixing (Q) depends on fluence (φ) as shown in the following equation [9]:

$$Q = A\varphi + B\sqrt{\varphi}. \quad (3)$$

The first term on the right hand side of the Eq. (3) represents recoil mixing, but the second term represents collisional cascade mixing.

4.1. Collisional cascade model [5]

There are many models suggested to interpret physical processes occur during ion beam mixing, which are: collisional models, and relaxational and diffusion mixing models.

Haff & Switkowski are the first who beginning with collisional cascade model, and their calculations depend on diffusion model.

The mixing rate (Dt) expressed by the following formula:

$$Dt = \frac{\varphi l d}{NE_d} \left(\frac{dE}{dx} \right)_n, \quad (4)$$

where:

- D – diffusion coefficient,
- t – diffusion time,
- E_d – displacement energy,
- l – interatomic spacing ,
- N – atomic density,
- φ – irradiation fluence (ion / cm²),
- d – mean free path,
- $\left(\frac{dE}{dx}\right)_n$ – nuclear energy loss.

Depending on Thomas–Fermi model [10], the parameter d is expressed by the following formula:

$$d = \frac{(T_m E T_0)^m}{3NC_m(T_m^m - T_0^m)}, \quad (5)$$

where:

- E – projectile ion energy,
- T_m – maximum energy transfer to the target

$$T_m = \frac{4M_1M_2}{M_1 + M_2} E, \quad (6)$$

- T_0 – minimum energy transfer to the target,
- M_1 – projectile atomic mass,
- M_2 – target atomic mass,
- C_m – parameter expressed by the following formula

$$C_m = \frac{\pi}{2} \lambda_m a_{TF}^2 \left(\frac{2Z_1Z_2e^2}{a_{TF}} \right)^{2m}, \quad (7)$$

where:

- Z_1 – projectile atomic number,
- Z_2 – target atomic number,
- a_{TF} – Thomas–Fermi screening distance,
- m – constant $m = 1/3$,
- λ_m – constant $\lambda_m = 1.309$,

Finally, the amount of mixing (Q) is proportional to the fluence and nuclear stopping power, which in turn depends on the diffusion length \sqrt{Dt} , so that:

$$Q \propto \varphi \left(\frac{dE}{dx}\right)_n \Rightarrow Q \propto \sqrt{Dt}. \quad (8)$$

5. Conclusions

The stopping power is calculated by TRIM computer code as shown in **Figures 7 and 8** for Se / In and Te / In systems.

The maximum energy transfer from Ar⁺ ions to the top layers (Te or Se), as shown in **Figure 9**. It is noted that the energy transfer to Se layer larger than that of Te layer because of larger stopping power of Te atoms than that of Se atoms.

The amount of mixing is plotted with square root of fluence as shown in **Figure 10**, which shows the linear dependence, indicating that the mixing occurs upon cascade collisional mixing.

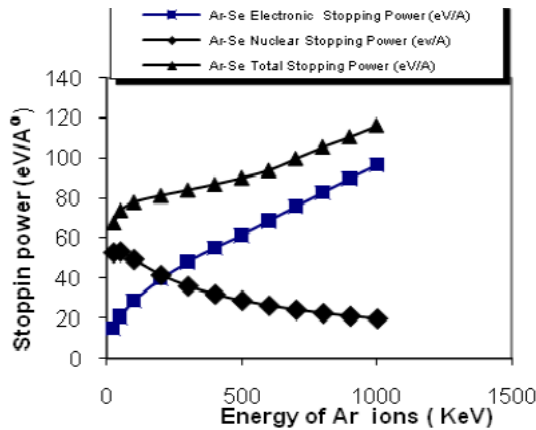


Figure 7. Stopping power versus ions energy for Se / In system.

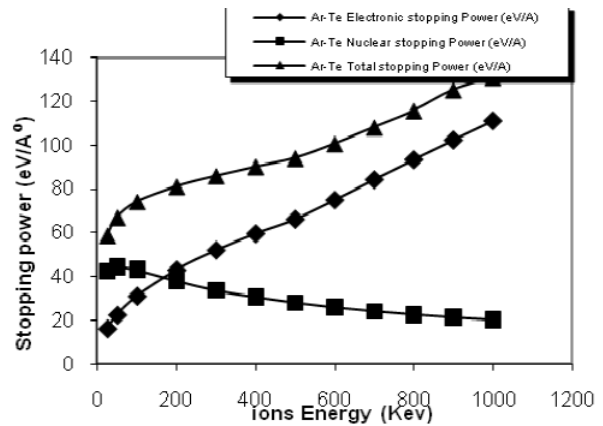


Figure 8. Stopping power versus ions energy for Te / In system.

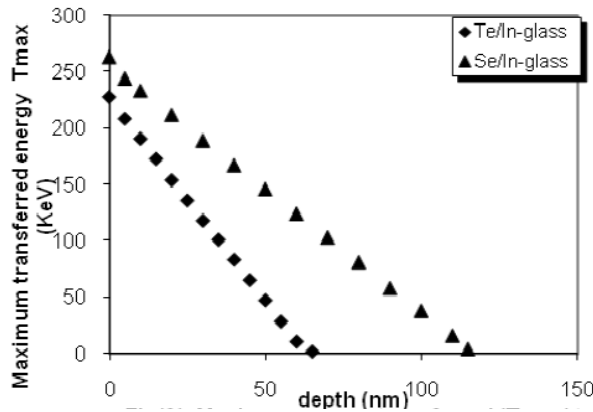


Figure 9. Maximum energy transferred (T_m) to Se or Te versus depth of In layer.

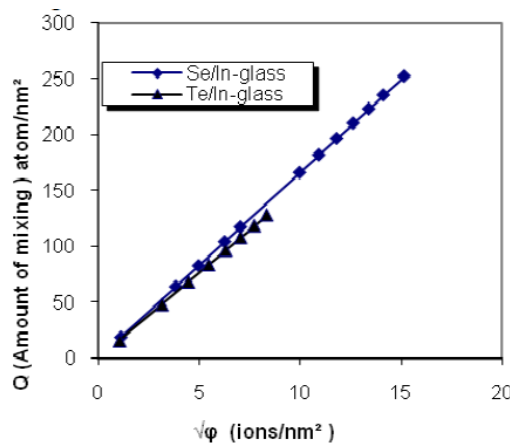


Figure 10. Amount of mixing Q versus $\sqrt{\phi}$.

After that the amount of mixing is plotted with the depth of lower layer as shown in **Figure 11**, which indicate the high mixing efficiency of Se atoms than Te atoms, which agreed the electrical resistivity measurements. Also it is shown that the large extent diffusion of Se atoms than that of Te atoms, which are 117.3 and 62 nm for Se / In and Te / In, respectively, and coincidence with the RBS results.

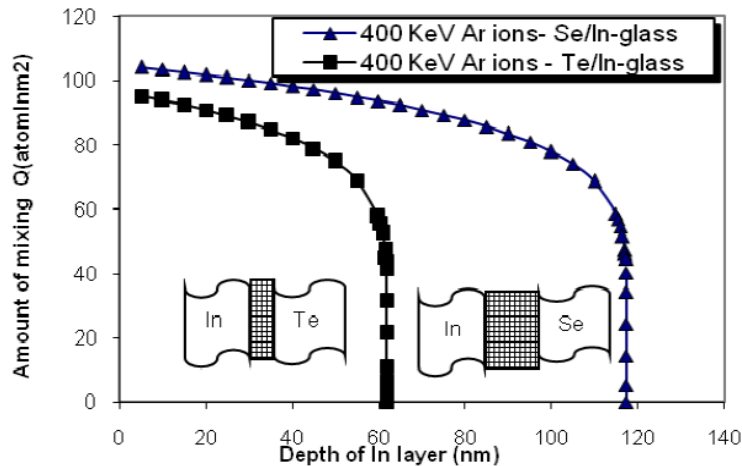


Figure 11. Amount of mixing Q versus depth of In layer.

The conclusion of this study indicate that, there is a large extend of mixing in Se / In system compared with the Te / In system, which give that the mixing efficiency of Se / In system is larger than the mixing efficiency of Te / In system and this result give good coincidence with experimental data.

This study is a tool to determine the possibility of mixing between the upper layer and the lower layer for any bilayer system before the preparation of sample and irradiated by van de Graaff accelerator, which provide the effort and money. It is possible to find out how to penetrate the upper layer atoms in the lower layer for the purpose of determining the incident of ions energy to get the desired width of intermixed layer to achieve the desired purpose.

Acknowledgement

I'd like to thank the Jordan University to help me carry out these experiments in the van de Graaff accelerator laboratory and workshop staff. Also, I'd like to thank my husband for his continued support and encouragement.

References

1. J. P. Riviere, J. Delafond, C. Jaouen, A. Bellara, J. F. Dinhut. Ion-beam mixing kinetics of Fe-Al multilayers studied by in situ electrical resistivity measurements. *Appl. Phys. A* 33 (1984) 77-82 .
2. N. S. Saleh, I. J. Jabr, K. A. Al-Saleh. Ion beam induced atomic mixing kinematics of Te / Cu and Te / Ag. *Nucl. Instrum. & Meth. Phys. Res. B* 7 (1992) 264-270.

3. I. J. Jabr, K. A. Al-Saleh, N. S. Saleh. Ion-beam induced mixing of Cu / Au bilayer thin film (Kinematics and formation of solid solutions). *Appl. Phys. A* 46 (1988) 13-16.
4. B. A.-B. Ibrahim. (Studying ion beam mixing of bilayer systems Te / In, Se / In and S / In (Thesis). Baghdad: Baghdad Univ. (1997).
5. P. K. Haff, Z. E. Switkowski. Ion-beam-induced atomic mixing. *J. Appl. Phys.* 48 (1977) 3383- 3386.
6. J. F. Ziegler, J. P. Biersack, U. Littmark. *The Stopping and Ranges of Ions in Solids*. Pergamon Press: New York (1985).
7. W. Riggs, W. A. Evans. Component evaluation by means of voltage and current measurements. *Trans. Inst.* 3 (1981) 99-105.
8. W. K. Chu, J. W. Mayer, M.-A. Nicolet. *Back Scattering Spectrometry*. New York: Acad. Press (1979).
9. R. Collins. Factors determining radiation – induced mixing at interfaces. *Radiat. Eff.* 98 (1986) 1-20 .
10. M. J. Nastasi, W. Mayer, J. K. Hirvonen. *Ion–Solid Interaction (Fundamentals and Applications)*. Camberdge: Camberdge Univ. Press (2003).

MODEL OF NMR SPECTROSCOPIC ANALYSIS OF AZIDE CONTAINING ORGANIC MOLECULES

T. Chachibaia

University of Santiago de Compostela
Santiago de Compostela, Spain
tamar.chachibaia@usc.es

Accepted April 15, 2013

Introduction

Nanotechnology provides powerful instrumentation tools to solve application-based goals in pharmaco-chemistry, enabling visualization and manipulation at molecular and atomic levels. Structures of more and more protein targets become available through X-ray crystallography, nuclear magnetic resonance (NMR) spectroscopy and bioinformatics methods.

Newly invented pharmacologically active moieties require chemical modification to become drug-like enough to be tested biologically or clinically. One or more of these steps may involve computer-aided drug design.

In this study we use softwares ChemDraw and Mnova, as methods of computational simulation for chemical structure prediction, synthesis and analysis. ChemDraw provides tools for design of molecule and predict its chemical and physical characteristics. ChemDraw is useful for creation of molecules and reactions for generation of associated properties, systematic names and spectra. ChemDraw includes versions for more detailed numerical analysis.

MNova is the software for the processing of NMR spectra of molecular structure. Mnova provides automatic detection and characterization of ^1H – NMR spectral peaks with the applicable molecular structure. Mnova is NMR prediction and analytical software developed by Mestrelab, Mestrelab Research (University of Santiago de Compostela, Spain), which provides an NMR spectrum from molecular structures, providing virtual NMR prediction desktop tools and methods.

In this study is described the NMR spectroscopic analytical model of organic azides and products of cycloaddition reaction with the formation of 1,2,3-triazole molecule.

Why's and how's of "click" chemistry

The first step in drug design is finding of the appropriate chemical structure for the exact target cells, receptors, or particular molecules.

Chemical transformations of small molecules have served as a rich source of "click" reactions for the development of new polymerization processes. The fields of pharmaceutical, materials, and polymer sciences, as well biotechnology industries, enthusiastically embraced the concept of click chemistry, as a versatile tool for introducing structural control [1]. Ideally, these efforts will offer molecular-level control during the preparation of nanostructured materials.

Concept of “click” chemistry was first introduced by the Nobel scientist K. Barry Sharpless, Hawker, Fokin and coworkers in 2001 [2]. Nature served as a source for inspiration of the concept idea. By joining small units together “click” chemistry simplifies compound synthesis and is assessed in chemistry domain as “everything is as easy as a click” [3, 4] for designing small modular components and has the potential to become a powerful polymerization technique [5].

Applications are increasingly found in all aspects of drug discovery making each reaction faster, efficient and reliable. In his breakthrough review published in 2001 Sharpless and coworkers defined click chemistry as reactions that are high yielding, wide in scope, create only byproducts that can be removed without chromatography, are stereospecific, simple to perform, and can be conducted in easily removable or benign solvents.

Among the multiple reactions that could be named “click” the prime example is the copper-catalyzed Huisgen’s 1,3-dipolar cycloaddition of azides and terminal alkynes (CuAAC) [3, 6, 7], which became classic in contemporary chemistry, and has been widely employed to synthesize or modify various polymers and dendrimers [8].

Fundamental and mechanistic aspects are fully described in the several recent reviews of the use of Cu-catalyzed azide–alkyne cycloaddition (CuAAC) for the synthesis of dendritic, branched, linear and cyclic co-polymers [9 – 13]. Materials, polymer and dendrimer sciences were also approached in publications [14], as well the area of drug discovery, bioconjugations, peptidomimetics, chemical ligations, etc [15].

Important aspect of the success of this reaction pertaining to materials science and biotechnology is that the starting materials, azides and terminal alkynes, are exceptionally stable and can be introduced in a wide range of macromolecules.

Variety of the starting monosubstituted alkynes and organic azides are commercially available, or even can be easily be synthesized with a wide range of functional groups.

Cycloaddition reaction selectively gives 1,2,3-triazoles. Several reviews have previously developed applications of the triazole chemistry in many areas [16 – 19]. The copper-(I)-catalyzed 1,2,3-triazole formation from azides and terminal acetylenes is a particularly powerful linking reaction, due to its high degree of dependability, complete specificity, and the bio-compatibility of the reactants. The triazole products are more than just passive linkers; they readily associate with biological targets, through hydrogen bonding and dipole interactions [6].

In spite of the undisputable success of the concept of click chemistry within just a few years, there are still some limitations associated with the concept. Exogenous metals can have mild to severe cytotoxic effects and can thus disturb the delicate metabolic balance of the systems being studied [2]. However, copper is believed to be cytotoxic and demonstrated side effects associated with excessive copper intake include hepatitis, Alzheimer’s disease and neurological disorders [20, 21].

For click reactions to be used in contact with living systems, the copper catalyst must be completely removed or alternatives must be employed.

Remarkable progresses have been made in recent years in the exploration of metal-mediated, as well metal-free click polymerization systems and in the syntheses of linear and hyperbranched polytriazoles with regioregular molecular structures and advanced functional properties [22].

A non-catalytic variation of the 1,3-dipolar azide-alkyne cycloaddition was also utilized with interesting applications in the biochemical area, because of the removal of copper toxicity [23, 24].

A subclass of click reactions which components are inert to the surrounding biological milieu is termed bioorthogonal [25]. This goes one step beyond the typical definition of a click reaction because of the added complications of biocompatibility.

A group of these bioorthogonal reactions that are cycloadditions lacking exogenous metal catalysts, the so-called Cu-free click reactions are another aspect of practical application of click chemistry.

Azides are also often associated with potential toxic side effects, as may bear a very real explosive potential [19]. But the appearance of NaN_3 and organic azides in azide-alkyne cycloaddition reactions was the first step to overcome pre-existing azidophobia. In organic chemistry azides are precursors to amines while participating in the “click reaction”, which is generally quite reliable.

Sodium azide is very toxic, similar to sodium cyanide. The use of additional metals as well as halogenated solvents such as dichloromethane in the presence of the sodium azide must be avoided. Dealing with organic azides “Smith’s rules” must be followed to keep compound non-explosive: (i) the number of nitrogen atoms (N_N) must not exceed that of carbon (N_C), and (ii) $(N_C + N_O) / N_N \geq 3$ [26]. Similarly, the “rule of six” indicates that six carbons (or other atoms of about the same size) per azide provides sufficient dilution to render an organic azide relatively safe.

Some azides are valuable as bioorthogonal chemical reporters [27], and can be carried out in an aqueous environment at physiological temperatures, and also have high efficiency.

In addition, azides for surface decoration of polymer are favorable as they are pluripotent reactants, which eagerly establish hydrogen bonds, also bind to polysaccharides, amino groups and other molecules. Thus, polymeric nanoparticles decorated with the azides-functionalized surface corona opens up the possibility to address challenges in targeted drug delivery [28].

Regardless existing limitations and challenges, click polymerization has promising opportunities and directions to serve as a versatile tool for the construction of new macromolecules with well-defined structures and multifaceted functionalities.

The benefits of the click reaction, namely high yields and biocompatibility, enable the very efficient application of this cycloaddition reaction to the synthesis of molecular architectures for their general application in living systems.

Triazoles in medical applications

Triazole compounds containing three nitrogen atoms in the five-membered aromatic azole ring are readily able to bind with a variety of enzymes and receptors in biological system via diverse non-covalent interactions, and thus display versatile biological activities (**Figure 1**).

The development of 1,2,3-triazoles for drug discovery and industrial use has been shown to be very promising [29]. The uses for triazoles have been found in various areas and are continuously growing. The applications of these triazoles are increasingly found in all aspects of drug discovery. These triazole products are more than just passive linkers; they readily associate with biological targets, through hydrogen bonding and dipole interaction [6]. Derivatives of 1,2,3-triazole have been found to have anti-HIV [30], anti-allergenic [31], antimicrobial,

cytostatic, virostatic, anti-inflammatory [32] and anti-bacterial [33], but also fungicidal and herbicidal activities [34, 35]. Triazoles are also being studied for the treatment of obesity [36] and osteoarthritis [37]. They have xenobiotic metabolizing enzyme Cytochrome P450 aromatasa inhibitory effect, thus widely used as anti-estrogen in cancer treatment and for relevant applications [38].

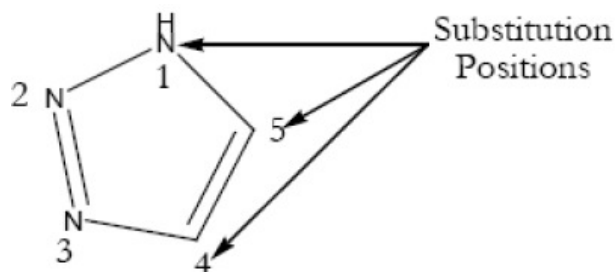


Figure 1.

The increased interest in the 1,2,3-triazole is due to it being non-toxic, benign and stable. Triazoles are particularly interesting for medicinal use because they are more likely to be water soluble than normal aromatic compounds, and are stable in biological systems [39].

This allows for the applications of 1,2,3-triazoles to grow exponentially due to their reliability, tolerance to a wide variety of functional groups, regiospecificity and the readily available starting materials. Through this, 1,2,3-triazoles are very attractive to use and apply in many fields.

Historically there have been many creative methods devised to synthesize 1,2,3-triazoles ranging from complex, step-by-step processes of structural transformation, to the simple cycloaddition of an azide and an alkyne.

The synthesis for the 5-membered triazole ring is accomplished through a synthetic approach known as “click chemistry”. The syntheses of a variety of 1,2,3-triazoles have been carried out via a new “green” synthetic method which involves the absence of solvent and catalyst, and is carried out using a microwave irradiation [40]. This synthetic method provides a fast and efficient technique to obtain various types of triazoles in good to excellent yields.

General concepts of azide–alkyne cycloaddition reaction with triazole ring formation

The products of the click reaction is 1,2,3-triazole, which is a desired target as provides additional functionality, such as hydrogen bonding and coordination prospects. 1,2,3-triazole finds use in research as a building block for more complex chemical compounds, including pharmaceutical drugs.

The perspectives of the foreseeable future in the research and development of triazole-based compounds are also sought rational designs of more active and less toxic triazole medicinal drugs [41, 42].

Specifically, click chemistry has been applied to address dendrimer synthetic concerns. Dendrimer synthesis will dramatically improve as additional clean, efficient reactions are developed to create non-immunogenetic, biofunctional scaffolds [18, 38, 43 – 46].

Another issue concerns the generation of surface-modification of dendrimers with a high density of outer azide–alkyne moieties, which subsequently are reacted with the

appropriate functional groups, capable of attaching a large number of these moieties into the outer shell of the respective dendrimer [6, 32, 47 – 51].

Triazole containing dendrimers can be generated by convergent or divergent methods, using the azide-alkyne click reaction as internal bond for the synthesis. This can lead to hyperbranched polymers either in one step or via sequential reaction [52 – 56]. CuAAC reaction has been widely employed to synthesize or modify various dendrimers [38, 57 – 59].

The whole dendrimer structure may be assembled via the azide-alkyne click reaction, using appropriately functionalized dendrons [1, 2, 6, 7, 43, 60].

A large variety of different dendrimers, such as triazole-containing dendrimers in each generation have been prepared, where the buildup of the central structure has been achieved by linking azide-alkynes [20, 61, 62]. Two monomers (Cl and alkyne) are reacted with an azide in the first step, and in the second step Cl is replaced by an azide using sodium azide (NaN_3). The generations are grown by repeating both steps up to higher generations. They are coupled to a certain core to afford the corresponding dendrimers.

Materials and methods

MNova software is used for the processing of NMR spectra of molecular structure. ChemDraw software was used for selection of starting molecules for the synthesis of dendrimer and core to demonstrate synthetic strategy for dendrimers linked by the 1,2,3-triazole units containing in each generation of corresponding generation. Click cycloaddition performed between the azide and alkyne selected from the virtual library to obtain 1,2,3-triazole ring in each generation, then subsequent generations obtained similarly. Each new generation of dendrimers has corona decorated with azide group, which is reacted with alkyne group.

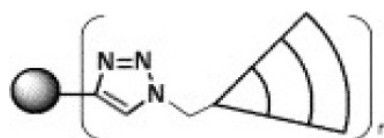


Figure 2.

In the **Figure 2** is presented the schematic demonstration of the model of dendrimer containing the core and 1,2,3-triazole group in each generation, while N is the generation number.

1,2,3-triazole group is a surprisingly stable structure compared to other organic compounds with three adjacent nitrogen atoms. Cleavage is possible at the site of methylene group of ester by means of protease, or influence of pH, or due to photo-sensibility of this locus.

The dendrimer core obtained by cycloaddition reaction contains three azide molecules on the surface corona which is corresponding to six protons of hydrogen molecules (**Figure 3**). Obtained 1st generation of dendrimer contains 6 molecules of azide, which is corresponding to 12 protons. On the spectra are detected 12 protons of the ester from methylene group and 6 protons of triazole ring. In every subsequent generation is doubled amount of protons corresponding to organic azide, thus 2nd generation contains 24 protons corresponding to 12 azide molecules; 36 protons of ester and 18 of triazole ring. In the 3rd generation are 48 protons corresponding to 24 molecules of azide; 96 protons of ester and 42 of triazole ring. This prediction spectrum could be compared with the real time NMR analysis of the reaction.

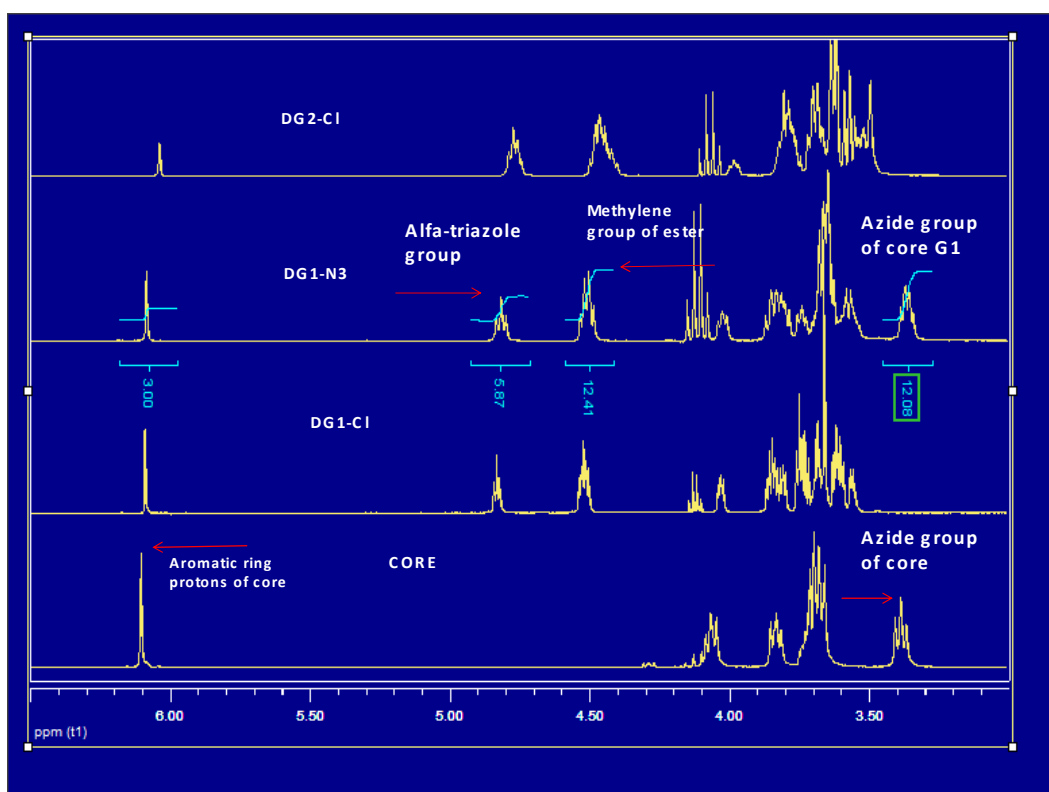


Figure 3.

NMR prediction model is dedicated to compare real time results of the synthesized dendrimers to ensure that reaction is complete and to follow-up reactions with upper generations. This feedback control helps to avoid synthetic pitfalls and to control the efficacy of chemical reaction on every stem of synthesis.

References

1. J. Lahann. Click Chemistry for Biotechnology and Materials Science. 2009, John Wiley & Sons, Ltd.
2. H. C. Kolb, M. G. Finn, K. B. Sharpless. Click chemistry: Diverse chemical function from a few good reactions. *Angew. Chem. Int. Ed.*, 2001, 40, 11, 2004-2021.
3. V. V. Rostovtsev, L. G. Green, V. V. Fokin, K. B. Sharpless. A stepwise Huisgen cycloaddition process: Copper (I)-catalyzed regioselective "ligation" of azides and terminal alkynes. *Angew. Chem. Int. Ed.*, 2002, 41, 14, 2596-2599.
4. R. Lucas, R. Zerrouki, P. Krausz. And if everything was as easy as a "click". Cu(I)-catalyzed 1,3-dipolar cycloaddition between terminal alkynes and azides. *L'actualité Chim.*, 2009, 335, 1, 5-9.
5. R. A. Evans. The rise of azide-alkyne 1,3-Dipolar 'click' cycloaddition and its application to polymer science and surface modification. *Australian J. Chem.*, 2007, 60, 6, 384-395.
6. C. W. Tornøe, C. Christensen, M. Meldal. Peptidotriazoles on solid phase: [1,2,3]-triazoles by regioselective copper (I)-catalyzed 1,3-dipolar cycloadditions of terminal alkynes to azides. *J. Org. Chem.*, 2002, 67, 9, 3057-3064.

7. American Peptide Society (Eds. M. Lebl, R. A. Houghten). 2001, San Diego: Kluwer Acad. Publ., 263-264.
8. P. Wu, M. Malkoch, J. Hunt. Multivalent, bifunctional dendrimers prepared by click chemistry. *Chem. Commun.*, 2005, 41, 46, 5775-5777.
9. D. Fournier, R. Hoogenboom, U. Schubert. Clicking polymers: A straightforward approach to novel macromolecular architectures. *Chem. Soc. Rev.*, 2007, 36, 9, 1369-1380.
10. H. Nandivada, X. W. Jiang, J. Lahann. Click chemistry: Versatility and control in the hands of materials scientists. *Adv. Mater.*, 2007, 19, 17, 2197-2208.
11. J. F. Lutz. 1,3-dipolar cycloadditions of azides and alkynes: A universal ligation tool in polymer and materials science. *Angew. Chem. Int. Ed.*, 2007, 46, 7, 1018-1025.
12. W. H. Binder, C. Kluger. Azide / alkyne-‘click’ reactions: Applications in material science and organic synthesis. *Curr. Org. Chem.*, 2006, 10, 14, 1791-1815.
13. J. E. Hein, V. V. Fokin. Copper-catalyzed azide-alkyne cycloaddition (CuAAC) and beyond: New reactivity of copper (I) acetylides. *Chem. Soc. Rev.*, 2010, 39, 4, 1302-1315.
14. W. H. Binder, R. Sachsenhofer, “Click” chemistry in polymer and materials science. *Macromol. Rapid Commun.*, 2007, 28, 1, 15-54.
15. C. Hartmuth, H. C. Kolb, K. B. Sharpless. The growing impact of click chemistry on drug discovery. *Drug Discov. Today*, 2003, 8, 24, 1128-1137.
16. V. D. Bock, H. Hiemstra, J. H. Maarseveen. CuI-catalyzed alkyne-azide “click” cycloadditions from a mechanistic and synthetic perspective. *Eur. J. Org. Chem.*, 2006, 1, 51-68.
17. A. Dondoni. Triazole: The Keystone in glycosylated molecular architectures constructed by a click reaction. *Chem. Asian J.*, 2007, 2, 6, 700-708.
18. G. C. Tron, T. Pirali, R. A. Billington, P. L. Canonico, G. Sorba, A. A. Genazzani. Click chemistry reactions in medicinal chemistry: Applications of the 1,3-dipolar cycloaddition between azides and alkynes. *Med. Res. Rev.*, 2007, 28, 2, 278-308.
19. M. Meldal, C. W. Tornøe. Cu-catalyzed azide-alkyne cycloaddition. *Chem. Rev.*, 2008, 108, 8, 2952-3015.
20. Gaetke L. M. and Chow C. K. Copper toxicity, oxidative stress, and antioxidant nutrients *Toxicology*, 2003, 189, 147-163.
21. T. Wang, Z. J. Guo. Copper in medicine: Homeostasis, chelation therapy and antitumor drug design. *Curr. Med. Chem.*, 2006, 13, 5, 525-537.
22. A. Qin, J. Lam, B. Tang. Click polymerization: Progresses, challenges, and opportunities. *Macromol.*, 2010, 43, 21, 8693-8702.
23. N. J. Agard, J. A. Prescher, C. R. Bertozzi. A strain-promoted [3 + 2] azide-alkyne cycloaddition for covalent modification of biomolecules in living systems. *J. Am. Chem. Soc.*, 2004, 126, 5, 15046-15047.
24. J. A. Codelli, J. M. Baskin, N. J. Agard, C. R. Bertozzi. Second-generation difluorinated cyclooctynes for copper-free click chemistry. *J. Am. Chem. Soc.*, 2008, 130, 43, 11486-11493.
25. E. M. Sletten, C. R. Bertozzi. Bioorthogonal chemistry: Fishing for selectivity in a sea of functionality. *Angew. Chem. Int. Ed.*, 2009, 48, 38, 6974-6998.
26. S. Braese, C. Gil, K. Knepper, V. Zimmermann. Organic azides: an exploding diversity of a unique class of compounds. *Angew. Chem. Int. Ed.*, 2005, 44, 33, 5188-5240.

27. M. D. Best. Click chemistry and bioorthogonal reactions: Unprecedented selectivity in the labeling of biological molecules. *Biochem.*, 2009, 48, 28, 6571-6584.
28. S. Zhang, K. Chan. R. Prud'homme, A. Link. Synthesis and evaluation of clickable block copolymers for targeted nanoparticle drug delivery. *Mol. Pharmaceutics*, 2012, 9, 2, 2228-2236.
29. C. H. Zhou, Y. Wang. Recent researches in triazole compounds as medicinal drugs. *Curr. Med. Chem.*, 2012, 19, 2, 239-280.
30. R. Alvarez, S. Velazquez, A. San-Felix, S. Aquaro, E. de Clercq, C. F. Perno, A. Karlsson, J. Balzarini, M. J. Camarasa. 4- or 5-monosubstituted and 4,5-disubstituted 1,2,3-triazole analogues of the anti-HIV-1 lead compound. *J. Med. Chem.*, 1994, 37, 24, 4185-4194.
31. D. R. Buckle, C. Rockell, H. Smith, B. A. Spicer. Studies on 1,2,3-triazoles with combined H₁-antihistamine and mast cell stabilizing properties. *J. Med. Chem.*, 1986, 29, 11, 2262-2267.
32. A. R. Katritzky, A. J. Boulton. *Advances in Heterocyclic Chemistry*, 16. 1974, New York: Academic Press Inc., 34.
33. M. J. Genin, D. A. Allwine, D. J. Anderson, M. R. Barbachyn, D. E. Emmert, S. A. Garmon, D. R. Graber, K. C. Grega, J. B. Hester, D. K. Hutchinson, J. Morris, R. J. Reischer, C. W. Ford, G. E. Zurenko, J. C. Hamel, R. D. Schaadt, D. Stapert, B. H. Yagi. Substituent effects on the antibacterial activity of nitrogen-carbon-linked (azolyphenyl) oxazolidinones with expanded activity against the fastidious gram-negative organisms *Haemophilus influenzae* and *Moraxella catarrhalis*. *J. Med. Chem.*, 2000, 43, 5, 953-970.
34. U. Gisi, H. Sierotzki, A. Cook, A. McCaffery. Mechanisms influencing the evolution of resistance to Qo inhibitor fungicides. *Pest Manag. Sci.*, 2002, 58, 9, 859-867.
35. M. B. Klix, J.-A. Verreet, M. Beyer. Comparison of the declining triazole sensitivity of *Gibberella zeae* and increased sensitivity achieved by advances in triazole fungicide development. *Crop Protec.*, 2007, 26, 4, 683-690.
36. L. L. Brockunier, E. R. Parmee, H. O. Ok, M. R. Candelore, M. A. Cascieri, L. F. Colwell, L. Deng, W. P. Feeney, M. J. Forrest, G. J. Hom, D. E. MacIntyre, L. Tota, M. J. Wyvratt, M. H. Fisher, A. E. Weber. Human beta 3-adrenergic receptor agonists containing 1,2,3-triazole-substituted benzenesulfonamides. *Bioorg. & Med. Chem. Lett.*, 2000, 10, 18, 2111-2114.
37. J. S. Tullis, J. C. van Rens, M. G. Natchus, M. P. Clark, B. De, L. C. Hsieh, M. J. Janusz. *Bioorg. & Med. Chem. Lett.*, 2003, 13, 10, 1665-1668.
38. M. J. Balunas, B. Su, S. Riswan, H. H. Fong, R. W. Brueggemeier, J. M. Pezzuto, A. D. Kinghorn. Isolation and characterization of aromatase inhibitors from *brassaiopsis glomerulata* (araliaceae). *Phytochem. Lett.* 2009, 19, 2, 1, 29-33.
39. N. Kaval, D. Ermolat'ev, P. Appukkuttan, W. Dehaen, C. O. Kappe, E. van der Eycken. The application of "click chemistry" for the decoration of 2(1H)-pyrazinone scaffold: Generation of templates. *J. Comb. Chem.*, 2005, 7, 3, 490-502.
40. K. Savin, M. Robertson, D. Gernert, S. Green, E. Hembre, J. Bishop. A study of the synthesis of triazoles using microwave irradiation. *Mol. Diversity*, 2003, 7, 2-4, 171-174.
41. C. H. Zhou, Y. Wang. Recent researches in triazole compounds as medicinal drugs. *Curr. Med. Chem.*, 2012, 19, 2, 239-280.

42. S. Svenson, D. Tomalia. Dendrimers in biomedical applications – Reflections on the field. *Adv. Drug Deliv. Rev.*, 2005, 57, 15, 2106-2129.
43. P. Antoni, D. Nystrom, C. J. Hawker. A chemoselective approach for the accelerated synthesis of well-defined dendritic architectures. *Chem. Commun.*, 2007, 43, 22, 2249-2251.
44. C. N. Urbani, C. A. Bell, D. E. Lonsdale. Reactive alkyne and azide solid supports to increase purity of novel polymeric stars and dendrimers via the click reaction. *Macromol.*, 2007, 40, 19, 7056-7059.
45. R. K. o' Reilly, M. J. Joralemon, C. J. Hawker. Synthesis and applications of click-functionalized dendrimers as crosslinkers for nanoparticle delivery agents. *PMSE Preprint*, 2005, 46, 1, 92-93.
46. R. Vestberg, M. Malkoch, M. Kade. Role of architecture and molecular weight in the formation of tailor-made ultrathin multilayers using dendritic macromolecules and click chemistry. *J. Polymer Sci. A*, 2007, 45, 14, 2835-2846.
47. E. Fernandez-Megia, J. Correa, I. Rodriguez-Meizoso, R. Riguera. A click approach to unprotected glycodendrimers. *Macromol.*, 2006, 39, 6, 2113-2120.
48. E. Fernandez-Megia, J. Correa, R. Riguera. Clickable PEG-dendritic block copolymers. *Biomacromol.*, 2006, 7, 11, 3104-3111.
49. R. K. o' Reilly, M. J. Joralemon, C. J. Hawker. Preparation of orthogonally functionalized core click cross-linked nanoparticles. *New J. Chem.*, 2007, 31, 5, 718-724.49.
50. M. Malkoch, K. Schleicher, E. Drockenmuller. Structurally diverse dendritic libraries: A highly efficient functionalization approach using click chemistry. *Macromol.*, 2005, 38, 9, 3663-3678.
51. D. mc Nerny, D. Mullen, I. Majoros, M. Holl, J. Baker Jr. Dendrimer synthesis and functionalization by click chemistry for biomedical applications. In: *Click Chemistry for Biotechnology and Materials Science* (Ed. J. Lahann). 2009, John Wiley & Sons, Ltd.
52. P. Vogt, S. R. Gondi, B. S. Sumerlin. Hyperbranched polymers via RAFT copolymerization of an acryloyl trithiocarbonate. *Australian J. Chem.*, 2007, 60, 6, 396-399.
53. J. Scheel, H. Komber, B. I. Voit. Novel hyperbranched poly([1,2,3]-triazole)s derived from AB₂ monomers by a 1,3-dipolar cycloaddition. *Macromol. Rapid Commun.*, 2004, 25, 12, 1175-1180.
54. M. Smet, K. Metten, W. Dehaen. Synthesis of new AB₂ monomers for polymerization to hyperbranched polymers by 1,3-dipolar cycloaddition. *Coll. Czech Chem. Commun.*, 2004, 69, 5, 1097-1108.
55. D. E. Bergbreiter, B. S. Chance. Click-based covalent layer-by-layer assembly on polyethylene using water-soluble polymeric reagents. *Macromol.*, 2007, 40, 15, 5337-5343.
56. G. W. Goodall, W. Hayes. Advances in cycloaddition polymerizations. *Chem. Soc. Rev.*, 2006, 35, 3, 280-312.
57. M. J. Joralemon, R. K. o' Reilly, J. B. Matson. Dendrimers clicked together divergently. *Macromol.*, 2005, 38, 13, 5436-5443.
58. M. J. Joralemon, A. K. Nugent, J. B. Matson. Clicking together dendritic macromolecular divergently. *PMS E Preprint*, 2004, 91, 195.

59. Q. Liu, P. Zhao, Y. Chen. Divergent synthesis of dendrimer-like macromolecules through a combination of atom transfer radical polymerization and click reaction. *J. Polymer Sci. A*, 2007, 45, 15, 3330-3341.
60. W. H. Binder, R. Sachsenhofer. Click chemistry in polymer and material science: An update. *Macromol. Rapid Commun.*, 2008, 29, 12-13, 952-981.
61. J. W. Lee, B. K. Kim, H. J. Kim, S. Ch. Han, W. S. Shin, S.-H. Jin. Convergent synthesis of symmetrical and unsymmetrical PAMAM dendrimers. *Macromol.*, 2006, 39, 6, 2418-2422.
62. C. J. Hawker, K. L. Wooley. The convergence of synthetic organic and polymer chemistries. *Science*, 2005, 309, 5738, 1200-1205.

НЕСМАЧИВАНИЕ МЕТАЛЛАМИ СТЕНОК ПОЛОСТЕЙ В ЦЕОЛИТАХ

А. А. Капанадзе, Г. В. Ртвелиашвили, Г. Д. Табатадзе

Грузинский технический университет
Тбилиси, Грузия
a.kapanadze@gtu.ge

Принята 23 апреля 2013 года

При вдавливании различных металлов в цеолиты было обнаружено, что полости в цеолитах заполняются лишь частично. Так, например, при условии полного заполнения ртутью больших полостей в цеолите NaX величина скачка объема должна быть $0.43 \text{ см}^3 / \text{см}^3$ кристалла, а фактически полученный скачок равен $0.24 \text{ см}^3 / \text{см}^3$ кристалла. Аналогичная картина наблюдается при вдавливании металла в цеолиты CaX, NaY, NaA, CaA и NaM.

Как известно, жидкие металлы не смачивают цеолиты. Это означает, что между стенками полости в цеолите и жидким металлом образуется зазор, величину которого обычными методами измерить практически невозможно. Проведенные эксперименты по заполнению пустот цеолитов жидкими металлами позволяют оценить величину зазора на несмачиваемость, сопоставляя полный объем полостей с экспериментально полученной величиной скачка объема.

Для примера вычислим зазор на несмачиваемость висмутом стенок цеолита NaX. Общий объем пустот цеолита NaX складывается из объема больших полостей, имеющих диаметр 12.00 \AA и объема малых полостей, имеющих диаметр 6.60 \AA . Для висмута критическое давление составляет 8.5 кбар. При этом давлении, однако, заполняются, по-видимому, только большие полости. Малые полости остаются пустыми, т.к. для их заполнения требуются гораздо большие давления. Из полученных данных следует, что большие полости заполняются висмутом на 58 % их объема. Объем большой полости в цеолите NaX равен 822 \AA^3 [1]. Предполагая равномерное распределение металла по полостям цеолита, вычислим объем, который занимает металл в одной полости: $0.58 \cdot 822 \text{ \AA}^3 \approx 476 \text{ \AA}^3$.

Поскольку большая полость в цеолите NaX имеет форму, близкую к сферической, можно, по-видимому, предположить, что атомы металла, введенного внутрь полости, образуют каплю сферической формы. Для висмута диаметр этой капли получается равным 9.68 \AA . Как нетрудно видеть, при диаметре большой полости 12.00 \AA зазор на несмачиваемость висмутом цеолита NaX равен 1.16 \AA . Аналогичным образом вычислены зазоры на несмачиваемость металлами Ga, Hg, Sn, In, Pb и Bi цеолита NaX. Эти данные приведены в **таблице 1**.

При вдавливании металла в цеолит NaA, имеющий иные диаметры больших полостей, также наблюдалось только частичное их заполнение. Диаметр большой полости в NaA 11.40 \AA , объем большой полости равен 776 \AA^3 [1]. Используя эти данные, а также данные по заполнению металлами пустот в цеолите NaA способом, изложенным выше,

можно рассчитать зазоры на несмачиваемость этого цеолита различными металлами. Полученные результаты также приведены в **таблице 1**.

Таблица 1.

Вводимый металл	Величина зазора на несмачивание, Å	
	NaX	NaA
Bi	1.16	1.57
Hg	1.22	1.57
Sn	1.90	1.57
Pb	1.72	1.57
In	1.58	1.84
Ga	1.58	1.70

При сравнении приведенных в таблице результатов видно, что зазоры на несмачиваемость металлом разных по типу цеолитов хорошо совпадают. Отличие не превышает 15 %. По-видимому, этого и следовало ожидать, т.к. цеолиты NaX и NaA близки по химическому составу.

Можно ожидать, что и для других цеолитов величина зазора на несмачиваемость останется примерно той же. Эксперименты по введению ртути и висмута в каналы цеолита NaM косвенно подтверждают это предположение. Средний диаметр сечения канала в мордените 6.60 Å. Если учесть зазор на несмачиваемость металлом (Hg или Bi) стенок канала в цеолите, средняя величина которого по данным таблицы составляет ~ 1.5 Å, остается свободный диаметр, примерно равный 4 Å. Эта величина близка к размерам одного атома.

По данным Шульце [2] металлический радиус ртути составляет 1.60 Å, висмута – 1.62 Å. Таким образом получается, что в каждом канале может поместиться только одна одноатомная цепочка металла. При этом объем введенного металла должен составлять 4 – 6 % от объема цеолита (4.3 % для ртути и 5.6 % для висмута). Это существенно меньше, чем для цеолитов типа NaX, где скачок объема в случае Hg и Bi составляет примерно 25 %. В цеолите NaM большая доля объема канала уйдет на «вакуумный» зазор между атомами металла и стенками канала цеолита. Экспериментально найденные объемы, заполненные металлом в каналах цеолита NaM близки к расчетным. Следует отметить, что различие в количествах висмута и ртути, которые можно ввести в один и тот же цеолит, проистекает из различных диаметров атомов висмута и ртути, т.е. эффекты атомного порядка проявляются в макроскопических масштабах.

Ссылки

1. А. В. Киселев, А. А. Лопаткин. Кинетика и катализ 4 (1963) 786.
2. Г. Шульце. Металлофизика. 1971, Москва: Мир.

BOREHOLES WATER LEVEL AND EARTHQUAKE'S DAILY MONITORING

A. Sborshchikovi¹, G. Kobzev¹, S. Ch. Mavrodiev², G. Melikadze¹

¹ M. Nodia Institute of Geophysics
Tbilisi, Georgia
rossoneri08@yandex.ru

² Institute for Nuclear Research and Nuclear Energy
Bulgarian Academy of Sciences
Sofia, Bulgaria
kobzev47@gmail.com

Accepted July 18, 2013

Introduction

The main reason of this research was to find the answer to the question has changing water level in the boreholes the same effect on the earthquake appearance as the variations of magnetic fields or not.

The hypothesis for possible correlations between the earthquakes and the variations of magnetic fields, Earth's horizontal and vertical currents in the atmosphere, was born when in early 1988, the historical data on the Black Sea was systemized. The achievement in the Earth surface tidal potential modeling, with the ocean and atmosphere tidal influences being included, makes an essential part of the research. In this sense, the comparison of the Earth tides analysis codes [1] is very useful. The possible tidal triggering of earthquakes has been investigated for a long period of time [2].

The earthquake-related part of the models has to be infinitely repeated in the "theory-experiment-theory" process, using nonlinear inverse problem methods in looking for correlations between the different fields in dynamically changing space and time scales. Each approximate model supported by some experimental evidence should be included in the analysis. The adequate physical understanding of the correlations among electromagnetic precursors, tidal extremes and the impendent earthquake is related to the progress of an adequate Earth magnetism theory and electrical currents distribution, as well as to the quantum mechanical understanding of the processes in the earthquake source volume before and during the earthquake.

Simultaneous analysis of more accurate space and time measuring sets for the Earth crust condition parameters, including the monitoring data of the electromagnetic field under and over the Earth surface, as well as the temperature distribution and other possible precursors, would be the basis of nonlinear inverse problem methods. It could be promising for studying and solving the "when, where and how" earthquake prediction problem.

The discovery of geomagnetic quake as reliable precursor for increasing of regional seismicity

In December 1989, a continuous measurement of a projection of the Earth's magnetic field (F) with a magnetometer (know-how of JINR, Dubna, Boris Vasiliev) with absolute precision less than one nano-Tesla at a sampling rate of 2.5 samples per second was started. The minute's mean value of F , its error mean value, the minute's standard deviation SDF , and its error were calculated, i.e., every 24 hours, 1440 quartets of data were recorded.

Minute standard deviation of F is defined as:

$$SDF_m = \left(\left(\frac{1}{N} \right) \sum_{i=1}^{N_m} (F_i - F_{mean})^2 \right)^{1/2}, \quad (1)$$

where m is the chosen time interval and n is the number of samples during the period,

$$F_{mean} = \left(\frac{1}{N} \right) \sum_{i=1}^{N_m} F_{mean} \quad (2)$$

with N_m the number of samples per minute.

The connection between variations of local geomagnetic field and the Earth currents was established in INRNE, BAS, Sofia, 2001 Seminar [3]. The statistic of earthquakes that occurred in the region (1989 – 2001), confirmed the Tamrazyan notes [4, 5] that the extremes of tides are the earthquake's trigger. The Venedikov's code [6, 7] for calculating the regional tide force was used [8].

The signal for imminent increasing regional seismic activity (incoming earthquakes) is the "geomagnetic quake" (Gq), which is defined as a jump (positive derivative) of daily averaged SDF. Such approach permits to compare by numbers the daily behaviour of the geomagnetic field with those in other days.

Among the earthquakes occurred on the territory under consideration in certain time period, the "predicted" one is the earthquake with magnitude M and epicentral distance $Dist_p$ which is identified by the maximum value of the function:

$$S_{ChM} = 10^{1.5M+4.8} / (D + Depth_p + Dist_p)^2 \left[energy / km^2 \right], \quad (3)$$

where $D = 40$ km is fit a parameter.

The physical meaning of the function S_{ChM} is a surface density of earthquake's energy in the point of measurement. It is important to stress out that the first consideration of the earthquake magnitude M and epicentral distance dependence was obtained using nonlinear inverse problem methods. Obviously, the close distance strong earthquake (with relatively high value of S_{ChM}) will bear more electropotential variations, which will generate more power geomagnetic quake.

It is very important to note that in the time scale of one minute, the correlation between the time period of increasing regional seismic activity (incoming earthquake), and tide extrema, recognized of predicted earthquake was established using the Alexandrov's code REGN for solving the over determined nonlinear systems [8, 9]. The very big worthiness of Alexandrov's theory and code is possibility to choose between two functions, which describe the experimental data with the same hi-squared, the better one.

Day-difference analysis

The role of the electromagnetic variations as earthquake's precursor can be explained in general by the hypothesis: the strain accumulation in the Earth Crust during the earthquake preparation causes medium's density change, within which a chemical phase ("dehydration") shift and a corresponding electrical charges shift appears. The Earth tides extremum as earthquake's trigger could be based on the hypothesis of "convergence of tidal surface waves" in the region (territory with prominent tectonic activity as consequences of chemical phase shift) of impending seismic activity.

For every occurred earthquake was calculated "day-difference"; the smaller absolute time difference between the hypocentral time and the daily times of pre and post tide's extremum time at that site on the Earth surface (the earthquake epicenter). This procedure was provided on all reported earthquakes in ISC catalogue (<http://www.isc.ac.uk/>) for the time period 1981 – 2011 and MN 3.5 and MN 4.0. The program for calculating of daily averaged module of vector movement *Rmeanis* based on Dennis Milbert TIDE programe (*solid.for*), by which Tide data could be calculated only for the time period after 1981. The DailyTide time of the Tide extremes *Rmeanwere* calculated by analogy of center mass calculation.

The statistic of day-differences for the earthquakes that occurred worldwide (1981 – 2011) and the Gaussian fitted curve (see below), confirmed the Tamrazyan notes [5, 6] from 1960th, that the extremes of tides play a role of earthquake's trigger.

Data and stations

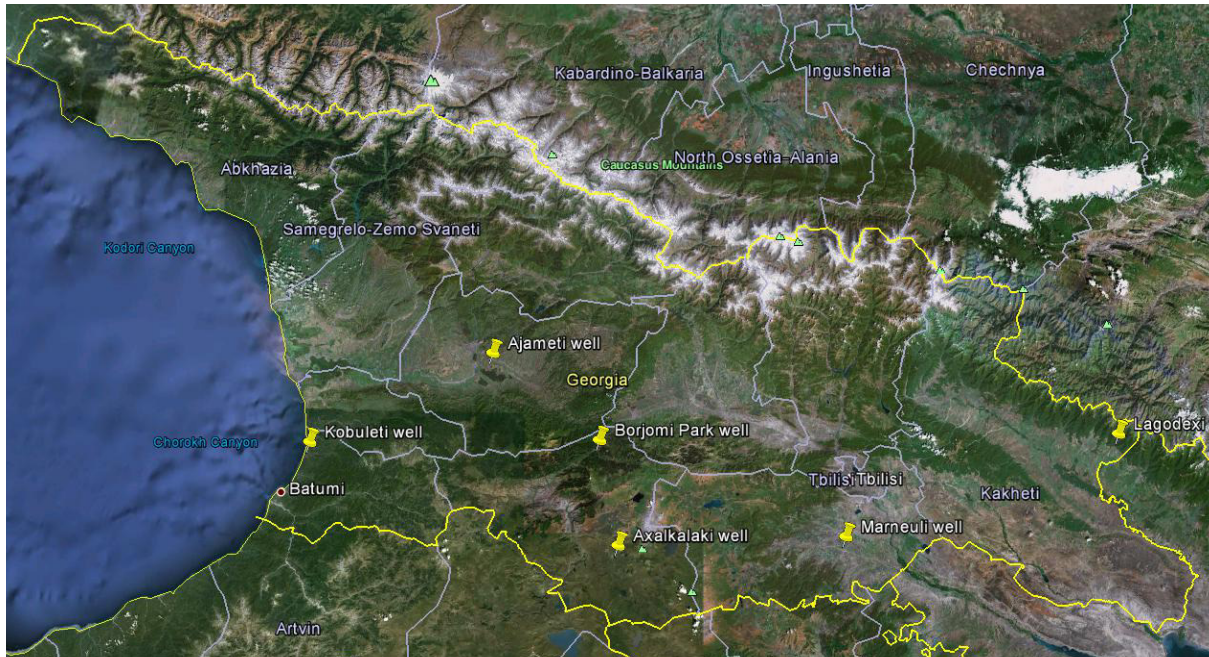
The main reason of this research was to find the answer to the question has changing water level in the boreholes the same effect on the earthquake appearance as the variations of magnetic fields or not.

The hypothesis for possible correlations between the earthquakes, the variations of magnetic fields, Earth's horizontal and vertical currents in the atmosphere, was born when in early 1988, the historical data on the Black Sea was systemized. The achievement in the Earth surface tidal potential modeling, with the ocean and atmosphere tidal influences being included, makes an essential part of the research. In this sense, the comparison of the Earth tides analysis codes [6] is very useful. The possible tidal triggering of earthquakes has been investigated for a long period of time [7].

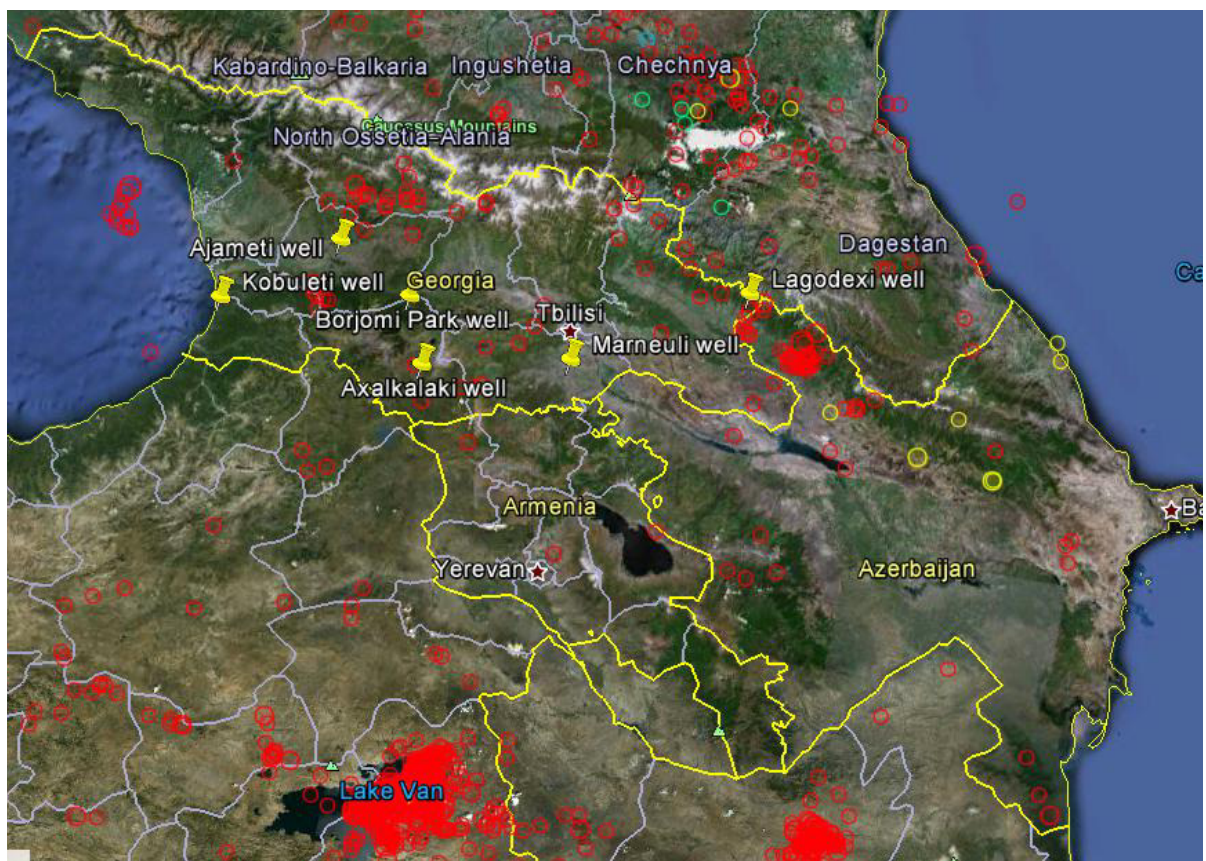
After studying this fact a hypothesis was born may be we can forecast earthquake using the same methodology.

Before discussing our methodology let stop our attention on the boreholes, which are located in different parts of Georgia. We have Ajameti borehole (depth 1300 m); Axalkalaki (1400 m); Borjomi-70 (1300 m); Kobuleti (2000 m); Lagodehi (800 m) and Marneuli (3500 m). The detail description of these boreholes is shown in **Table 1**.

The location of these boreholes is shown in **Figure 1 a**. While the locations of epicenters of earthquakes during 2011 – 2012 are shown in **Figure 1 b**.



(a)



(b)

Figure 1. (a) Map of boreholes in Georgia, (b) Earthquakes during 2011 – 2012.

Table 1. Description of the boreholes located in different parts of Georgia.

Borehole	Depth, m	Filter interval, m	Lithology	Geological intervals, m	Water level, m
Ajemeti	1330	520 – 740	Litostone	520 – 740	– 6.0
Ahalkalaki	1400	1000	Tuff Andezit Basalt Dolomite	580 – 1000	– 0.2
Borjomi-70	1330	1260 – 1300	Clay	0 – 12	– 22.0
Kobuleti	2000	187 – 640	Tuff Andezit Basalt	0 – 150 150 – 2000	– 0.5
Lagodehi	800	255 – 367	Sand + Gravel	0 – 24	– 15.8
Marneuli	3500	1235 – 1600	Gravel	0 – 50	– 5.0

Methodology of analysis

We have selected earthquakes with magnitude ≥ 3.5 at distance ≤ 500 km from boreholes for 2011 and 2012 years. We have modified water-data, calculate water-level-signal, precursors, select earthquakes, which could be connected with precursors and then analyzing the data and their graphic presentations, using Dennis Milbert Fortran code for local tidal behavior, <http://home.comcast.net/~dmilbert/softs/solid.htm>, in accordance of geomagnetic quake's methodology. Like time scale in used methodology is hour normalized standard deviations, mean of them for a day and calculate the precursors. By definition the precursor is the difference (jump) between standard deviation of today and the previous day. Then we have created twelve files with result-data. Each file has result-data for one borehole during 1 year, which is divided on three month intervals.

As we see in **Figure 2** the first graph in the left corner is the picture of tidal behavior [m], the next shows the energy [J / km^2], the next – magnitude, and the last describes precursors (red points) and water level signals (blue points). The blue points has been count using normal standard deviation and the red points so called precursors were obtain by subtraction of the daily standard deviation of today and the previous day [10, 11].

The first graph in the right corner is water mean during 23 October the period of great Turkey earthquake and the next describes standard deviation of water level [12].

The same emplacement is shown for another period in the **Figure 3**.

Boreholes water level and earthquake's daily monitoring.

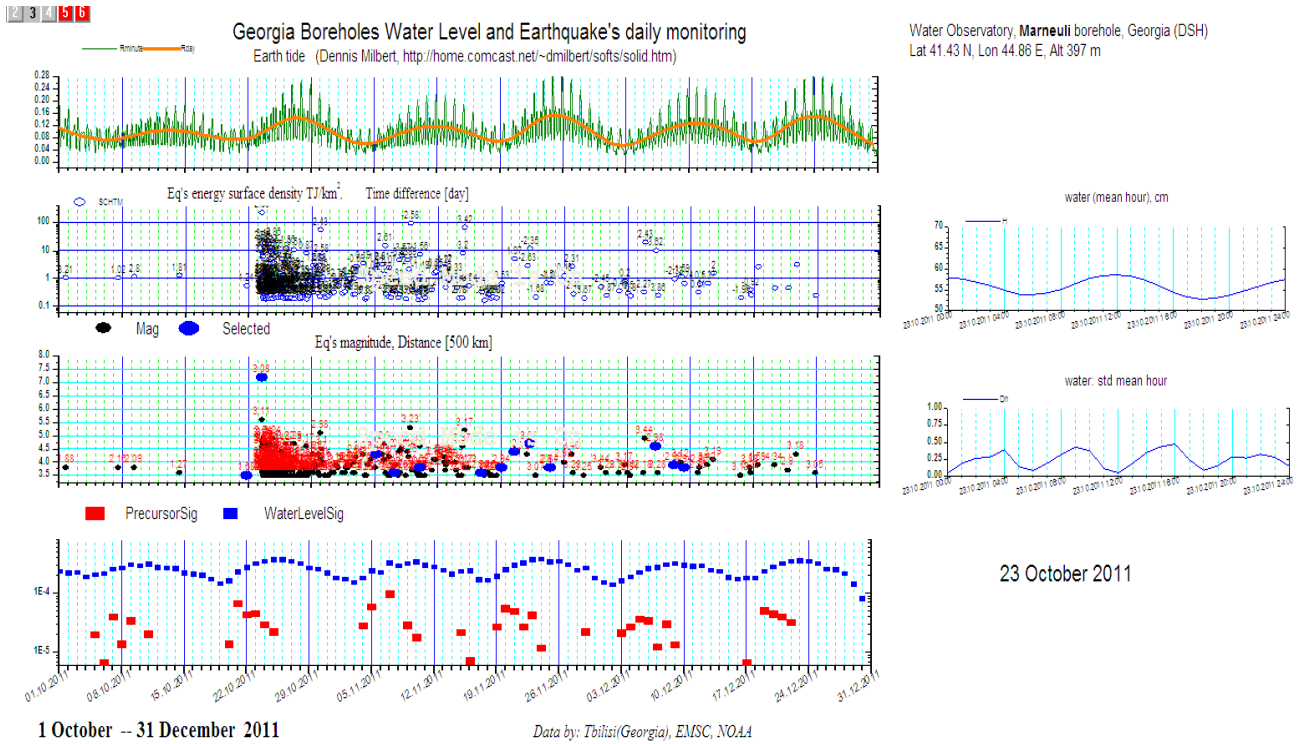


Figure 2. Marneuli borehole daily monitoring including period of great earthquake in Turkey (2011).

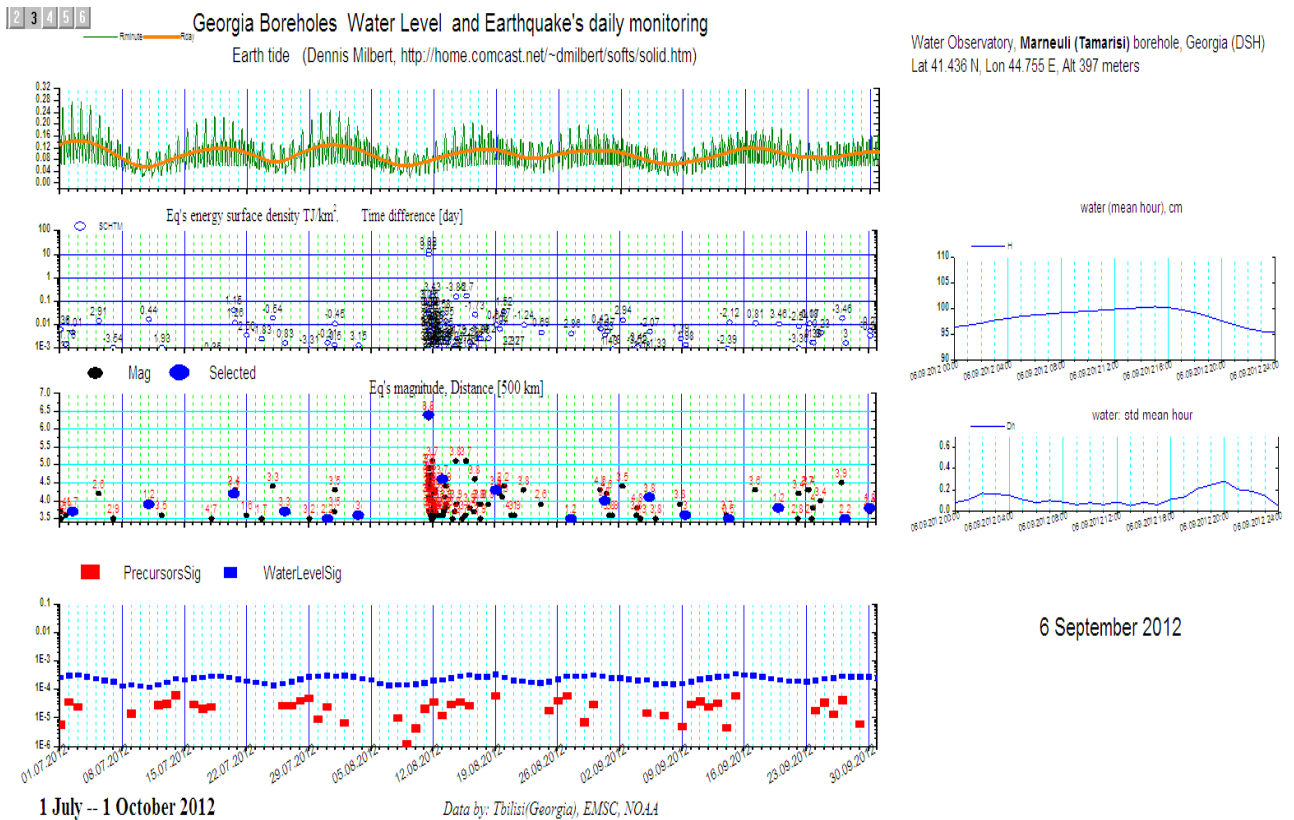


Figure 3. Marneuli borehole daily monitoring (2012).

We have done the Gauss distribution for day difference as for 2012 year period also for the two years from 2011 until 2012 (see **Figures 4 and 5**).

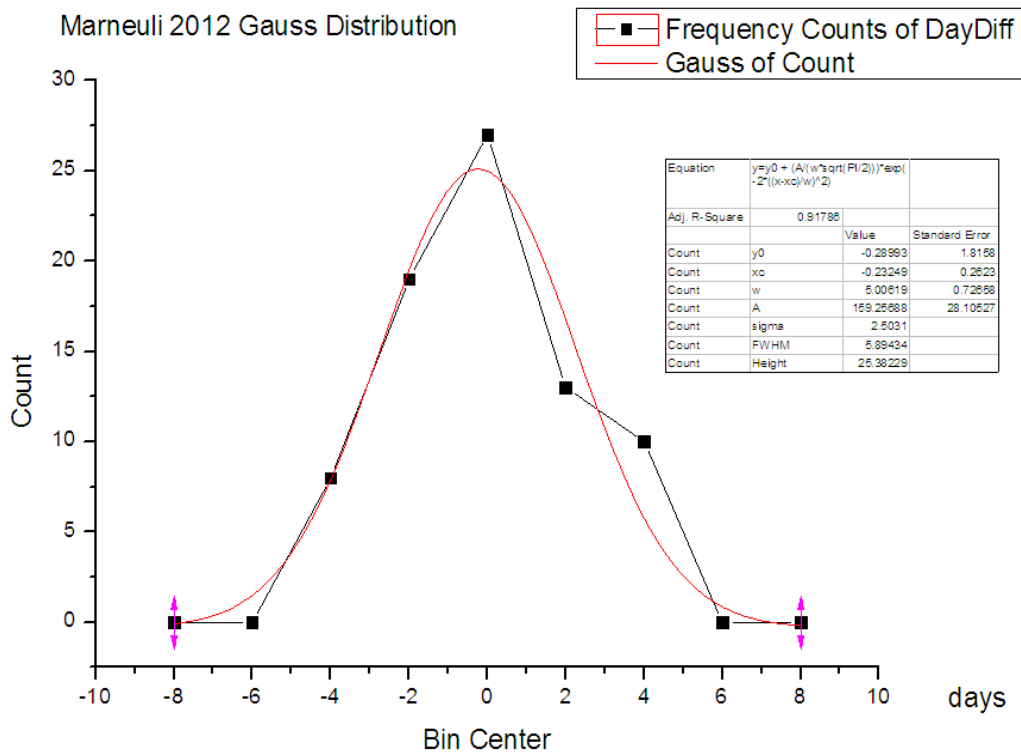


Figure 4. Marneuli borehole Gauss Distribution for day difference (2012).

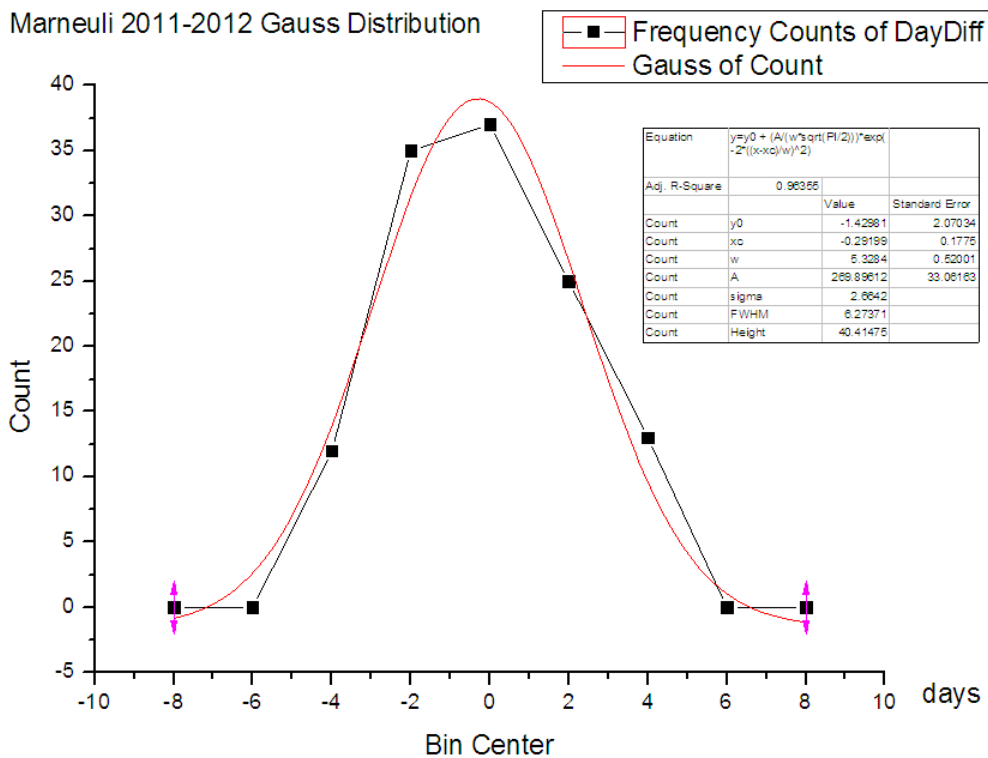


Figure 5. Marneuli borehole Gauss Distribution for day difference (2011 – 2012).

Boreholes water level and earthquake's daily monitoring.

As we can see from the figure according to the results we get very good Gauss distribution with the R-square not less than 0.90.

The next step was finding frequency count for the distance of the selected by precursors quakes, for the whole period 2011 – 2012 (see **Figure 6**).

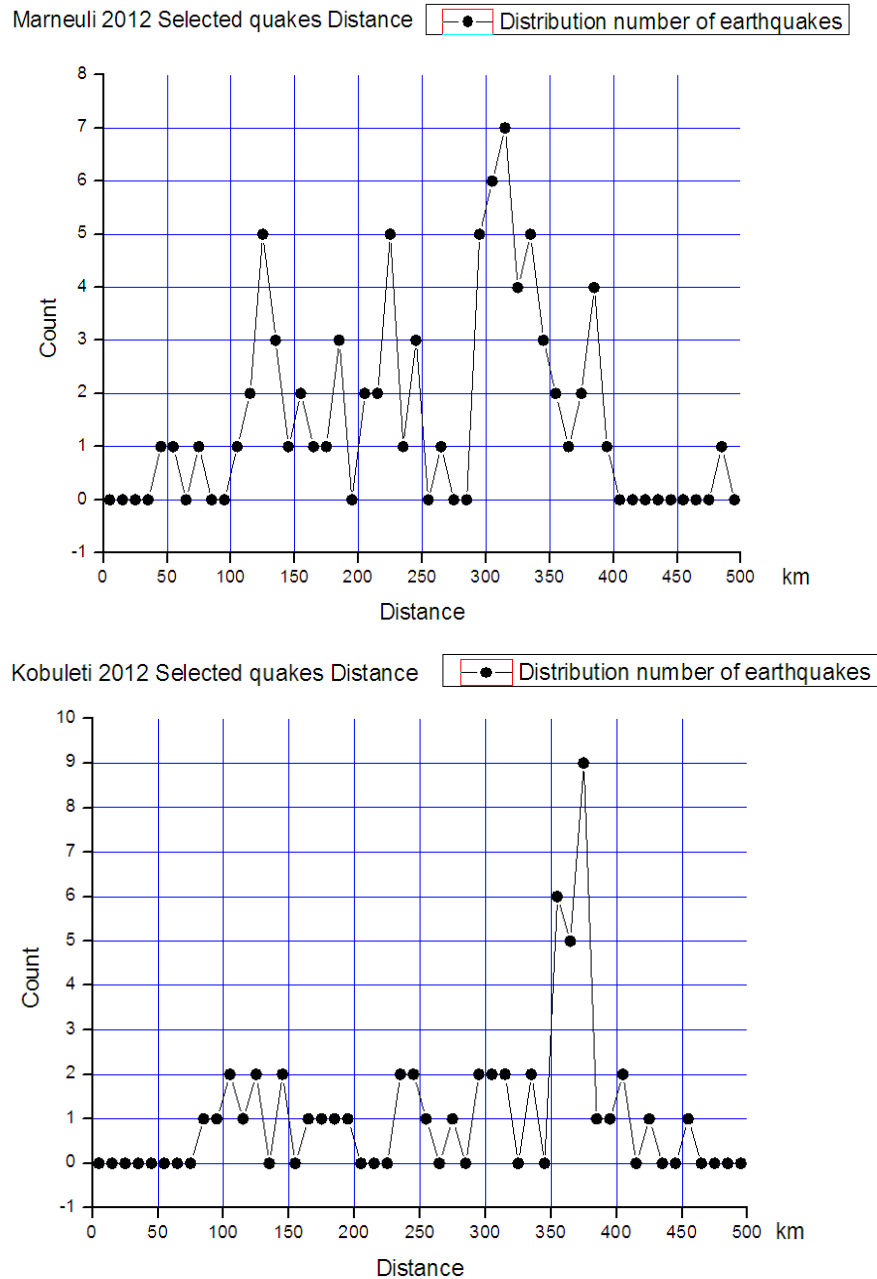


Figure 6. Two boreholes frequency counts for distance of selected by precursors quakes.

The increment was taken 10 km. The highest number of the earthquakes is at the distance 300 – 350 km (Turkey earthquakes), the earthquake at distance 350 – 450 km are Iran earthquakes and the other one that are at distance less than 300 km are regional local earthquakes.

So, as we can see from the material before, our daily monitoring has not the same effect and could not be used as precursors for prediction of regional seismic increase. Another and not

less important idea is to make not daily monitoring of the water level and then count normal standard deviation use another time interval, for example week or two weeks or may be month. And for this period count normal STD and look if it will be possible to use it as precursors [13 – 15].

One more chance to use water-level daily monitoring for predicting regional seismic increase is to use it together with radon monitoring and it will be more useful for getting precursors. So we can discuss some facts about radon as well.

Conclusion

As we could see from the results of experience, using daily water-level changing in the boreholes and after that counting STD and use it as precursors has no physical arguments. It could not be true precursors that could predict the earthquakes at long distance and cause water-level change. The way to overwrite this problem is to use not daily but another time interval for getting precursors. And after this we hope water-level changing in the boreholes will have the same effect on the earthquake appearance as the variations of magnetic fields.

References

1. A. P. Venedikov, R. Arnos, R. Vieira. A program for tidal data processing. *Comput. & Geosci.* 29 (2003) 487-502.
2. G. P. Tamrazyan. Tide-forming forces and earthquakes. *ICARUS* 7 (1967) 59-65.
3. S. Ch. Mavrodiev, C. Thanassoulas. In: Proc. Seminar "Possible Correlation between Electromagnetic Earth Fields and Future Earthquakes". 2001, Sofia: INRNE BAS.
4. L. Knopoff. Earth tides as a triggering mechanism for earthquakes. *Bull. Seismol. Soc. Am.* 54 (1964) 1865-1870.
5. G. P. Tamrazyan. Tide-forming forces and earthquakes. *ICARUS* 7 (1967) 59-65.
6. G. P. Tamrazyan. Principal regularities in the distribution of major earthquakes relative to Solar and Lunar tides and other Cosmic forces. *ICARUS* 9 (196) 574-592.
7. A. Venedikov, R. Arnos. Program VAV / 2000 for tidal analysis of unevenly spaced data with irregular drift and colored noise, *J. Geodetic Soc. Jpn.* 47 (2001) 281-286.
8. A. P. Venedikov, R. Arnos, R. Vieira. A program for tidal data processing. *Comput. & Geosci.* 29 (2003) 487-502.
9. L. Alexandrov. Program code REGN, PSR 165 RSIK ORNL. 1983, Oak Ridge.
10. S. Ch. Mavrodiev. On the reliability of the geomagnetic quake as a short time earthquake's precursor for the Sofia region. *Nat. Hazards & Earth Syst. Sci.* 4 (2004): 433-447.
11. S. Ch. Mavrodiev, L. Pekevski. Complex regional network for earthquake researching and imminent prediction. In: *Electromagnetic Phenomena Related to Earthquakes and Volcanoes* (Ed. B. Singh). 2008, New Delhi: Narosa Publ. House, 135-146.
12. T. Chelidze, T. Matcharashvili, G. Melikadze. Earthquakes' signatures in dynamics of water level variations in boreholes. In: *Synchronization and Triggering – From Fracture to Earthquake Processes* (Eds. V. de Rubeis, Z. Czechowski, R. Teisseyre). 2010, Springer, 287-304.

13. G. Kobzev, G. Melikadze, T. Jimsheladze. New method of hydrodynamical data analysis, In: Mater. Workshop–Seminar Black Sea Haz Net Ser. 2011, Tbilisi, 25-72.
14. T. Jimsheladze, G. Melikadze, G. Kikuashvili, S. Mavrodiev, L. Pekevski, M. Chkhitunidze. Study of geomagnetic variations in Georgia and establishment the anomaly Nature of earthquake precursors. In: Mater. Workshop–Seminar Black Sea Haz Net Ser. 2011, Tbilisi, 205-214.
15. S. Ch. Mavrodiev, L. Pekevski, T. Jimseladze. Geomagnetic-quake as imminent reliable earthquake's precursor: Starring point for future complex regional network. In: Electromagnetic Phenomena Related to Earthquakes and Volcanoes (Ed. B. Singh). 2008, New Delhi: Narosa Publ. House, 116-134.

კაფიუმის აკუმულაცია რეჰანის (*Ocimum basilicum*), ქინძის (*Coriandrum sativum*)
და ზაფრანის (*Crocus sativus* L) მიერ კაფიუმით გამდიდრებული ნიადაგიდან

ა. რჩეულიშვილი¹, ო. რჩეულიშვილი^{1,2}, ნ. რჩეულიშვილი³,
ე. გინტური¹, ლ. ტულუში¹, ე. ლელალუტაშვილი¹

¹ ე. ანდრონიკაშვილის ფიზიკის ინსტიტუტი
ო. ჯავახიშვილის სახ. თბილისის სახელმწიფო უნივერსიტეტი
² ილიას სახელმწიფო უნივერსიტეტი
³ ი. ჯავახიშვილის სახ. თბილისის სახელმწიფო უნივერსიტეტი
თბილისი, საქართველო
archeuli@gmail.com

მიღებულია 2013 წლის 23 ივლისს

როგორც ცნობილია, მეტალური ნანონაწილაკების ტოქსიკურობა ბევრად ნაკლებია მეტალთა იონების ტოქსიკურობაზე, რაც უმნიშვნელოვანეს როლს თამაშობს სოფლის მეურნეობაში. ამ დარგში მიმდინარეობს რიგი პროექტების დამუშავება, რათა მეტალური ნანონაწილაკების გამოყენებით ზუსტად და უსაფრთხოდ მიეწოდოს საკვები ნივთიერებები მცენარეებს. ამ მიზნის განხორციელებისათვის კი აუცილებელია შესწავლილი იქნას მიკროელემენტების აკუმულაციის პროცესი ბუნებრივი ობიექტების, პირველ რიგში საკვები მცენარეების მიერ. ინდუსტრიალიზაციის ზრდასთან ერთად სულ უფრო მეტად დაიკვირვება მძიმე მეტალების კონცენტრაციის ზრდა გარემოში. ბოლო წლებში დიდი ყურადღება ექცევა აგროკულტურების მიერ მძიმე მეტალების აკუმულაციას წყლიდან [1]. მიკროელემენტები მონაწილეობენ ორგანიზმში მიმდინარე ჟანგვა-აღდგენით პროცესებში. როგორც ცნობილია, მცენარეთა ნორმალური ცხოველქმედებისათვის მიკროელემენტების უმნიშვნელო რაოდენობაც საკმარისია. საკვები მცენარეების მიერ მეტალთა აბსორბცია უჯრედთა ისეთ ფუნქციონალურ ჯგუფებთანაა დაკავშირებული, როგორცაა ბუნებრივი პროტეინები, ლიპიდები, კარბოჰიდრატები.

საკვები მცენარეებიდან აღსანიშნავია რეჰანი, ქინძი, ზაფრანა. საქართველოში გავრცელებულია ბოსტნის რეჰანი (*Ocimum basilicum*), რომელიც მრავლდება თესლით. რეჰანის ნათესი საჭიროებს ორგანული და მინერალური (უფრო აზოტისანი) სასუქებით განოყიერებას. სავეგეტაციო პერიოდია (დარგვიდან მოსავლის აღებამდე) 130 – 150 დღე. ქინძი (*Coriandrum sativum*) ერთწლოვანი მცენარეა ქოლგოსანთა ოჯახიდან. ნაყოფი შეიცავს ეთერზეთებს და ცხიმებს. საქართველოში ქინძი გავრცელებულია უძველესი დროიდან. აქ გვხვდება ქინძის რამდენიმე კულტურული სახეობა. საკვები მცენარე ზაფრანა (*Crocus sativus* L) ფართოდ გამოიყენება საკვებად, როგორც მარომატიზირებელი. საქართველოში ზაფრანის ხუთი სახეობაა გავრცელებული. აღნიშნული საკვები მცენარეების როლი ცნობილია ფიტოთერაპიაშიც. სამუშაოში [2] შესწავლილია ბოსტნის რეჰანის ექსტრაქტის პოტენციური დამცველობითი ფუნქცია დელტამეტრინზე, რომელიც გამოწვეულია ალბინურ თაგვებში ნევროტოქსიკურობით. ზაფრანა სასარგებლოა ალცაიმერის [3] და ალერგიული [4] დაავადებებისას. რეჰანის მიერ სპილენძის აბსორბცია დამოკიდებულია pH-ზე [5]. აღნიშნულ საკვებ მცენარეებში

მეტალთა იონების შემცველობა და მათ მიერ მეტალთა აბსორბციისა და აკუმულაციის უნარი თითქმის არაა შესწავლილი, თუ არ ჩავთვლით რამოდენიმე შრომას, სადაც მიკროელემენტებია განსაზღვრული [5 – 9].

მოცემული სამუშაოს მიზანს წარმოადგენს კადმიუმის აკუმულაციის პროცესის შესწავლა რეჰანის, ქინძისა და ზაფრანის მიერ და მათი გადანაწილება ორგანოებში (ფესვები, ღეროები, ფოთლები), როდესაც ეს მცენარეები გაზრდილია ნიადაგში, სადაც წინასწარ იქნა შეტანილი კადმიუმი ქლორიდის სახით.

ობიექტი და კვლევის მეთოდები

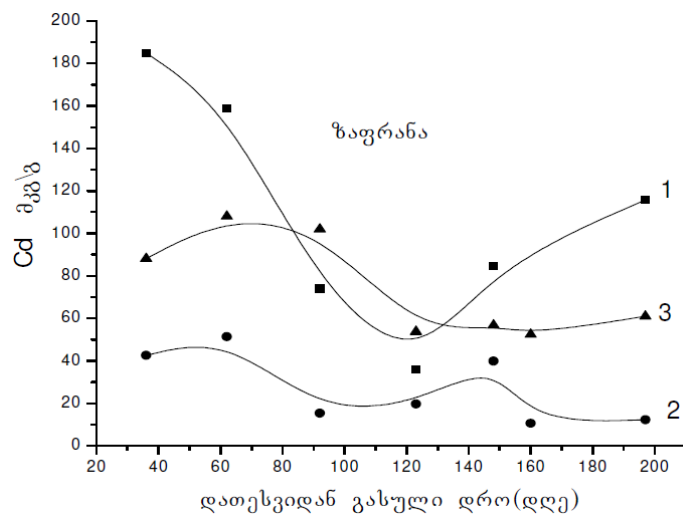
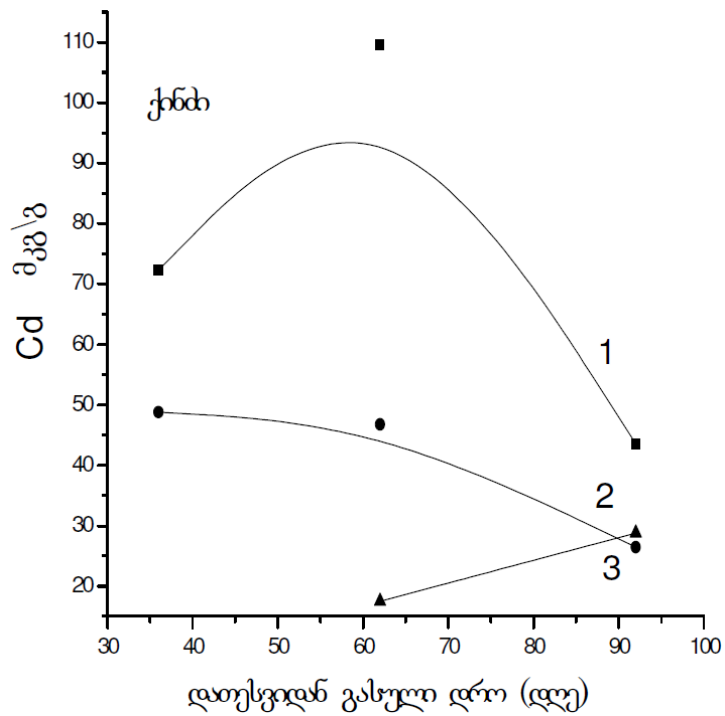
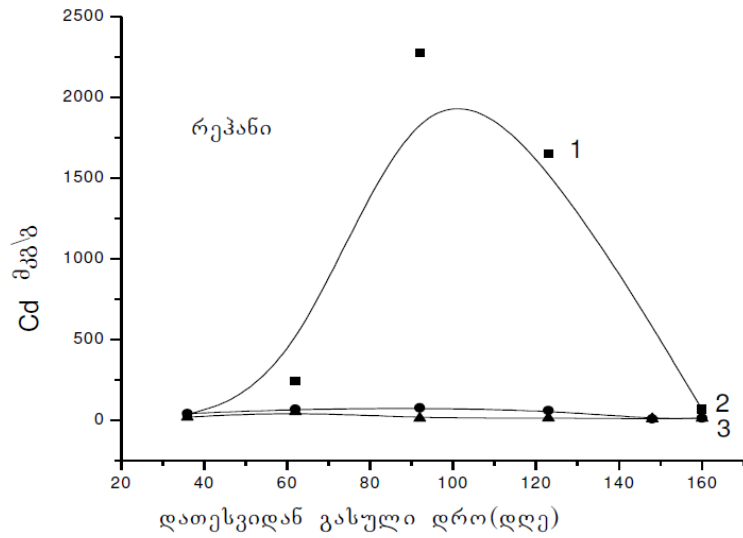
კვლევის ობიექტად აღებული იქნა საკვები მცენარეები რეჰანი (*Ocimum basilicum*), ქინძი (*Coriandrum sativum*) და ზაფრანი (*Crocus sativus* L) და მძიმე მეტალი კადმიუმი. Cd შევიტანეთ ერთჯერადად დიდი ზომის, მინარევებისაგან გასუფთავებულ ნიადაგში CdCl₂ მარილის ხსნარის სახით (1.5 გ Cd 15 ლიტრი მოცულობის მქონე ნიადაგით საკვს სპეციალურ კონტეინერში). მოვახდინეთ ნიადაგის ჰომოგენიზაცია. ნიადაგიანი კონტეინერი მოვათავსეთ ლაბორატორიულ პირობებში და დავთესეთ მცენარეები. ნიადაგი ირწყვებოდა პერიოდულად.

გაზრდილ მცენარეებს ვიღებდით ნიადაგიდან ~ 30 დღიანი ინტერვალით. ამოღებულ მცენარეებს ვრეცხავდით დისტილირებული წყლით და ვახდენდით მათ დანაწევრებას ცალკეულ ორგანოებად (ფოთოლი, ღერო და ფესვები). მიღებულ ნიმუშებს ვაშრობდით, მექანიკური საფქვავის საშუალებით ვახდენდით ნიმუშების დაქუცმაცებას, ვწონიდით და ვათავსებდით სინჯარებში. სინჯარებში ვამატებდით კონცენტრირებულ აზოტმჟავას და ვაცხელებდით ჰომოგენური ხსნარის მიღებამდე. ჰომოგენიზირებულ ნიმუშებს ვაზავებდით ბიდისტილატით 10 მლ მოცულობამდე.

კადმიუმის შემცველობის ანალიზი განხორციელდა ატომურ-აბსორბციული სპექტრომეტრის Analyst – 900-ის გამოყენებით. კადმიუმის ეტალონური ხსნარები დამზადებული იყო Perkin Elmer-ის ფირმის ეტალონური დედა-ხსნარისაგან (1 მგ / ლ).

შედეგები და მათი განსჯა

ნახაზზე 1 ნაჩვენებია კადმიუმის შემცველობა დათესვიდან გასული გარკვეული დროის შემდეგ რეჰანის, ქინძისა და ზაფრანის ცალკეულ კომპონენტებში (ფესვებში, ღეროებში, ფოთლებში). როგორც ნახაზიდან ჩანს, რეჰანის შემთხვევაში კადმიუმის ყველაზე დიდი რაოდენობით აკუმულაცია ფესვებში დაიკვირვება დათესვიდან 92-ე დღეს. რაც შეეხება ფოთლებს და ღეროებს, მცენარის ზრდის მთელი პროცესის განმავლობაში კადმიუმის დაგროვება მათში მცირეა ფესვებთან შედარებით. ზაფრანაში, დაგროვების ყველაზე მეტი ეფექტურობით გამოირჩევა ფესვები, შემდეგ ფოთლები და ყველაზე ნაკლები რაოდენობა Cd-ისა აღმოჩნდა ღეროებში. დათესვიდან გასული დროის ზრდისას მცირდება მცენარის ცალკეული ორგანოების მიერ ზრდის პროცესში აკუმულირებული Cd-ის შემცველობა. 92-ე დღეს ფოთლებში Cd-ის შემცველობამ გადააჭარბა ფესვებში მისი შემცველობის მაჩვენებელს, რაც დაიკვირვება, აგრეთვე, დათესვიდან 123-ე დღესაც. 148-ე დღის მიხედვით, Cd-ის განაწილება შემდეგნაირად ხდება: ფესვები > ფოთლები > ღეროები. აღნიშნულ კომპონენტებში Cd-ის შემცველობებს შორის ნაკლები განსხვავება დაიკვირვება. დათესვიდან 160-ე დღისათვის. Cd-ის დაგროვების და განაწილების ეს ტენდენცია შენარჩუნებულია დათესვიდან 197-ე დღისთვისაც.



ნახაზი 1. რეპანის, ქინბის და ზაფრანის ცალკეულ კომპონენტებში კადმიუმის განაწილება: 1 – ფესვები, 2 – ლეროები და 3 – ფოთლები.

ქინძის მიერ კადმიუმის აკუმულაცია ყველაზე მეტია ფესვებში, შემდეგ ღეროებსა და ფოთლებში. მაქსიმალურ აკუმულაციას ადგილი აქვს დათესვიდან 62-ე დღეს. ქინძში კადმიუმის აკუმულაცია 62-ე დღეს ფოთლებთან შედარებით მეტია, ხოლო დათესვიდან 92-ე დღეს კადმიუმს ფესვები, ფოთლები და ღეროები თითქმის ერთნაირად ითვისებს.

ამრიგად, მიღებული შედეგების ანალიზი ცხადყოფს, რომ ექსპერიმენტებში აღებული სამივე საკვები მცენარისათვის ტოქსიკური ელემენტის – კადმიუმის აკუმულაცია ნიადაგიდან ყველაზე მეტად ხორციელდება ფესვებში. მიღებული შედეგები თანხვდება ლიტერატურულ მონაცემებს, რომლის მიხედვითაც მეტალთა ტრანსპორტი საკმაოდ სწრაფი პროცესია.

Allium sativum-ზე ჩატარებულმა ცდებმა აჩვენა [8], რომ 6 საათის შემდეგ კადმიუმის შემცველობა გაიზარდა ფესვებში და 12 საათის შემდეგ – ფოთლებში. რეჰანი ტოლერანტულია სპილენძის და თუთიის მაღალი კონცენტრაციების მიმართ. სუბუჯრედული განაწილების შესწავლამ ფესვებსა და ფოთლებში აჩვენა, რომ სპილენძის და თუთიის მაღალი კონცენტრაციების აკუმულირება ხდება კედლის ზედაპირზე, ხოლო კობალტის და ნიკელის – ციტოპლაზმის სუპერნატანტულ ფრაქციაში [10]. რეჰანის ექსტრაქტის ფიტოქიმიური სკრინინგი და ელემენტების ანალიზი ცხადყოფს, რომ მცენარე შეიცავს ტანინს, კარდიალურ გლიკოზიდებს, ხოლო მინერალური შემადგენლობის მხრივ, მაღალი კონცენტრაციებით შეიცავს ნატრიუმს, კალციუმს და კალიუმს [5]. შესწავლილი იქნა, აგრეთვე, რეჰანის მიერ Cd³⁺-ის აკუმულაციაც [11]. მცენარის გამშრალი ქსოვილის მიკროანალიზმა აჩვენა, რომ დიდი რაოდენობით ქრომის აკუმულაცია ხდება ფესვების მიერ და ნაკლებად გადაადგილდება დანარჩენი ორგანოებისაკენ.

სამუშაო შესრულებული იქნა გრანტის GNSF / STCU 5635 ფარგლებში.

მითითებები

1. G. H. Pino, L. M. S. de Mesquita, M. L. Toerm. G. A. S. Pinto. Miner. Eng. 58 (2006) 380.
2. S. A. Sakr, W. M. al-Amoudi. J. Appl. Pharmac. Sci. 2 (2012) 22.
3. S. Akhondzadeh, M. S. Sabet, M. H. Harirchian, M. Togha, H. Cheraghmakani, S. Razeghi. J. Clin. Pharm. Ther. 35 (2010) 581.
4. D. Chryssanthi, G. Dedes, P. G. Karamanos, N. K. Cordopatis, F. N. Lamari. Planta Med. 77 (2011) 146.
5. A. Gupte, M. Karjekar, J. Nair. Acta Biol. Ind. 1 (2012) 113.
6. J. X. Xu, J. Q. Liu. Chin. J. Pharm. Anal. 30 (2010) 285.
7. L. H. Jia, Y. Liu, Y.-Zh. Li. J. Chinese Pharmac. Sci. 20 (2011) 297.
8. H. Zhang, Y. Jiang, Z. He, M. Ma. J. Plant Physiol. 162 (2005) 977.
9. V. N. Daniel, I. E. Daniang, N. D. Nimyel. Int. J. Eng. & Technol. 11 (2011) 161.
10. K. Veeranjanyuu, V. S. Ramadas. Proc. Ind. Natl. Sci. Acad. B 1982 (48) 109.
11. R. Bishekolaei, H. Fahimi, S. Saadatmand, T. Nejadstari, M. Lahouti, F. T. Yazdi. Turk. J. Bot. 35 (2011) 261.

СВОЙСТВА НИТРИДА БОРА, СИНТЕЗИРОВАННОГО ПОД ВОЗДЕЙСТВИЕМ КОНЦЕНТРИРОВАННОГО СВЕТОВОГО ИЗЛУЧЕНИЯ

Л. Л. Сартинская¹, Е. В. Войнич¹, А. Ф. Андреева¹, А. М. Касумов¹,
И. И. Тимофеева¹, А. Ю. Коваль¹, Г. А. Фролов¹, Т. Эрен², Э. Алтай²

¹Институт проблем материаловедения им. И. Н. Францевича
Национальная академия наук Украины
Киев, Украина
sart@ipms.kiev.ua

²Илдижский технический университет
Стамбул, Турция

Принята 26 июля 2013 года

1. Введение

Нитрид бора (BN) привлекает значительное внимание благодаря своим уникальным физико-химическим и механическим свойствам, таким как низкая плотность, высокая температурная стабильность, низкая диэлектрическая постоянная, высокая теплопроводность и химическая инертность. Материалы на основе наноструктур из BN, являются перспективными для создания новых полупроводников, сегнетоэлектриков и сверхпроводников. Увеличивается также спрос на компактные лазерные устройства ультрафиолетового спектра, так как они имеют важное применение в таких областях как оптические накопители, фотокатализ, стерилизация, офтальмологическая хирургия и нанохirurgия, и гексагональный нитрид бора (h-BN) является многообещающим материалом для применения в лазерных устройствах [1 – 2].

Известно, что BN наноструктуры являются аналогом углеродных наноструктур, поэтому для их получения используют те же, но, несколько модифицированные, методы синтеза. Процессы синтеза, используемые для получения наноструктур из BN можно разделить на высокотемпературные (≥ 1500 °C,) и низкотемпературные, которые могут использовать даже обычную муфельную печь [3 – 7]. К высокотемпературным (физическим) методам относятся метод дугового разряда, плазменные методы, и метод лазерной абляции, которые обычно используют для изготовления наноструктур. Все высокотемпературные методы включают абляцию и / или поверхностное испарение в соответствующей атмосфере (вакуум или инертные газы) при высоких температурах и конденсацию полученного пара под влиянием высоких градиентов температур. Наличие жидкой фазы является необходимым условием для получения наноструктур. Основными отличиями различных процессов является метод, используемый для абляции и / или поверхностного испарения. Нагрев под воздействием концентрированного светового излучения, используемый авторами, также относится к высокотемпературным (физическим) методам [8 – 10].

Нанотрубки из BN являются структурно-устойчивыми широкополосными полупроводниками. Они вызвали значительный интерес в последние годы в связи с развитием функциональных материалов и наноустройств. Электронные и структурные свойства нанотрубок из BN предсказанные теоретически показали, что имеют большую и стабильную ширину запрещенной зоны, которая не зависит от радиуса трубки, хиральности и количество стенок. Это делает нанотрубки из BN особенно перспективными для наноэлектроники и оптоэлектроники [11].

К сожалению, широкое применение наноструктур и нанотрубок из BN сдерживается, в первую очередь, низкой производительностью методов их получения, а применение в наноэлектронике и оптоэлектронике требует стабильности и воспроизводимости свойств. В связи с этим, исследование влияния условий синтеза на морфологию и свойства BN наноструктур, получаемых под воздействием концентрированного светового излучения, является важной задачей для исследований.

2. Методика проведения эксперимента

Синтез BN был проведен в оптической печи с ксеноновыми источниками света в потоке азота при плотности энергии в фокальной зоне установки $\sim 0.7 \cdot 10^4$ кВт / м² в течение 1 ч. Схема проведения эксперимента представлена на **рисунке 1**.

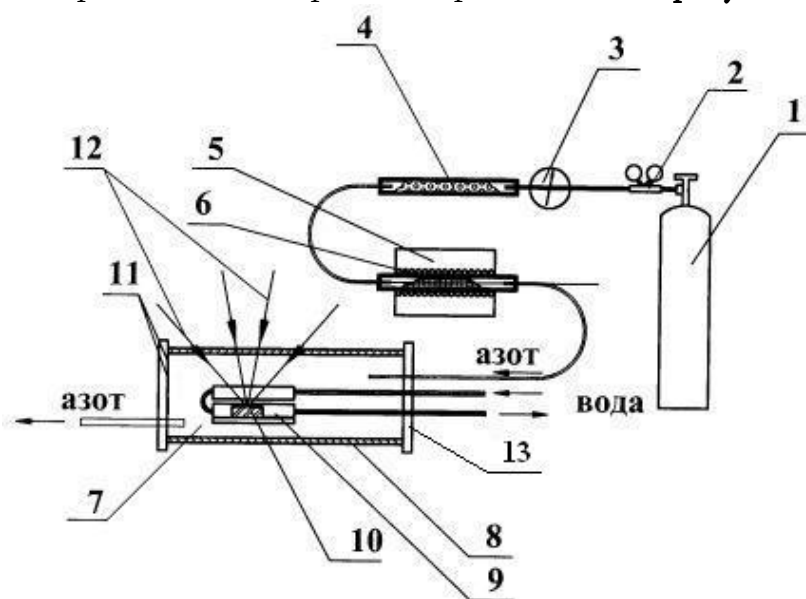


Рисунок 1. Схематическое изображение проведения эксперимента.

- 1 – газообразный азот; 2 – редуктор; 3 – манометр; 4 – стеклянная трубка, заполненная KOH; 5 – печь; 6 – медная стружка; 7 – рабочая камера; 8 – кварцевая труба; 9 – водоохлаждаемые медные экраны; 10 – исходный образец BN; 11 – левый фланец; 12 – концентрированный световой поток; 13 – правый фланец.

Для получения достоверных данных и устранения влияния дополнительных факторов в отдельных экспериментах проводилось дополнительное досушивание при помощи KOH и очищение азота титановой губкой. В качестве исходного был использован аморфный порошок бора (**рисунок 2**).

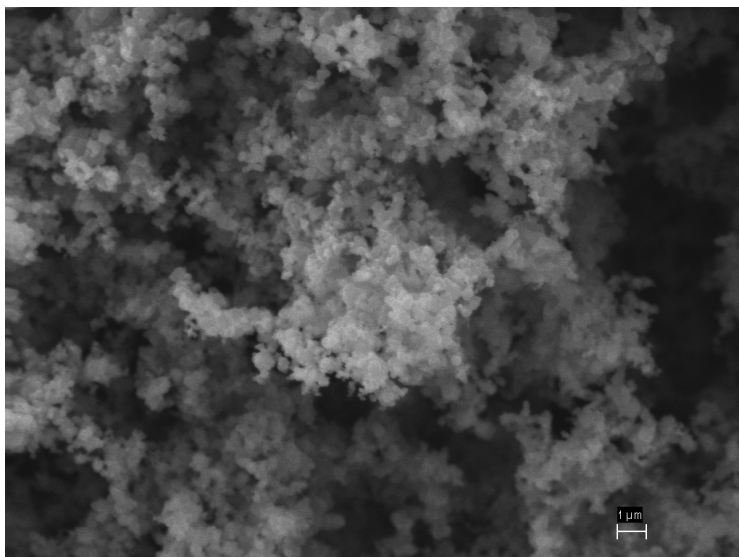
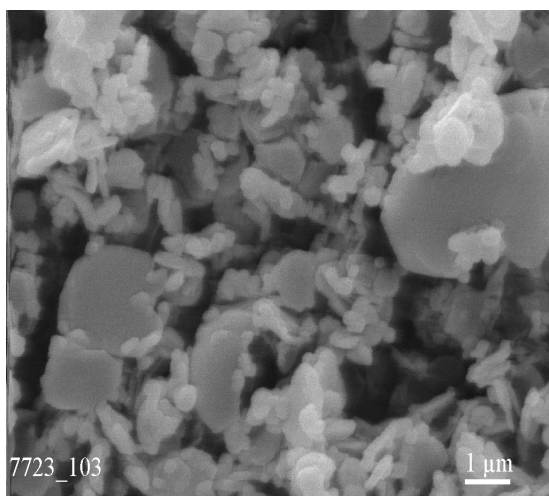


Рисунок 2. SEM изображение исходного бора.

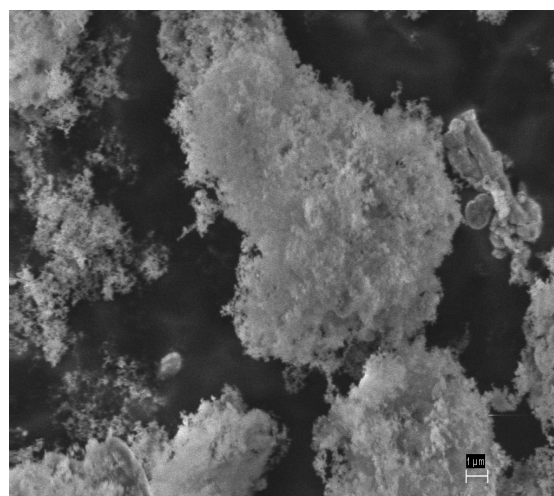
Структуры исходного порошка бора и полученных порошков BN были исследованы с помощью SEM. Изучение спектральной зависимости оптического поглощения было проведено на спектрофотометре Specord UV-VIS. Рентгеновская дифракция (дифрактометр ДРОН-3.0, излучение $K\alpha$ -Cu) дополнила информацию о получаемых BN порошках. В качестве катализатора в исходный порошок бора вводили порошок $NiSO_4$ и Cu.

3. Результаты и обсуждение

SEM исследования показали формирование равноосных и крупных пластинчатых частиц BN различных размеров при прямом синтезе BN (**рисунок 3 а**). Введение катализатора способствует получению нанодисперсных и волокнистых структур из BN, а также, сохранению структуры исходного бора (**рисунок 3 б**).



а



б

Рисунок 3. SEM изображение получаемых при синтезе BN наноструктур: (а) без катализатора и (б) с катализатором.

Поскольку нагрев в оптической печи локализован, было проведено изучение оптических свойств наночастиц, получаемых без катализатора (**рисунок 3 а**) в различных зонах реакционной камеры. Для исследования частицы порошка были взяты на кратчайшем расстоянии от реакционной зоны с поверхности медных экранов, кварцевой трубы, левого (ближайшего) и правого фланцев (**рисунок 1**). Величина ширины запрещенной зоны наноструктур BN, получаемых на различных расстояниях от реакционной зоны, растет с увеличением расстояния и достигает своего максимума 5.1 эВ на максимальном расстоянии – на 20 мм (**рисунок 4**).

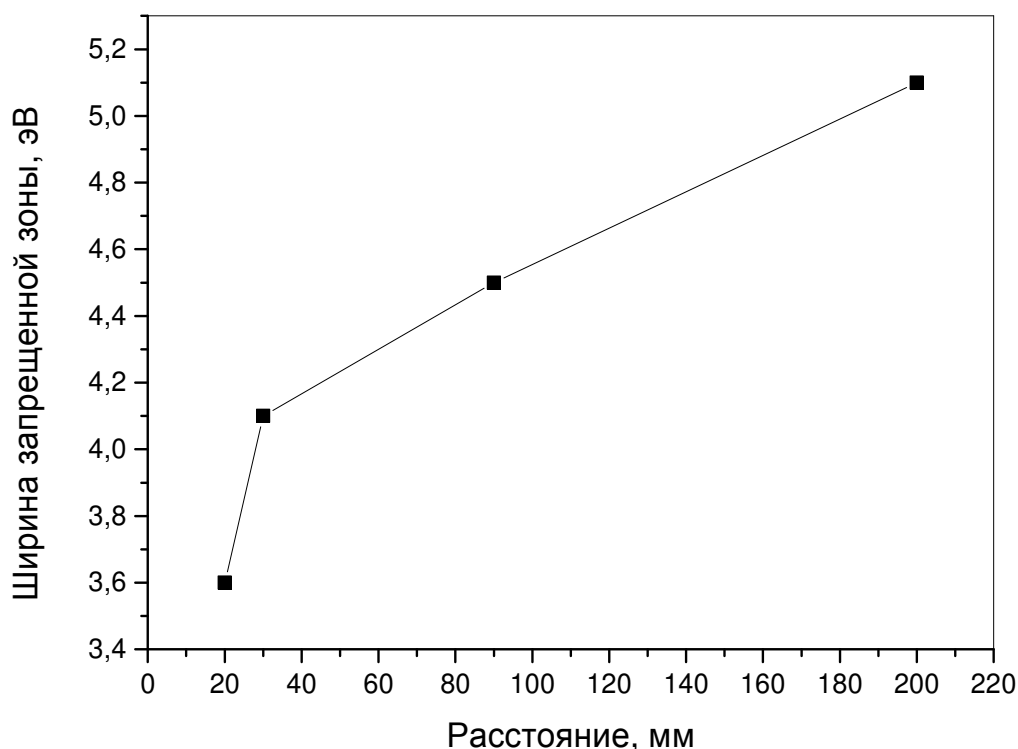


Рисунок 4. Зависимость ширины запрещенной зоны BN наноструктур, получаемых при синтезе под воздействием концентрированного светового излучения от расстояния до реакционной зоны.

Структурных и морфологических особенностей частиц порошка BN с увеличением расстояния от реакционной зоны найти не удалось. Весь порошок из BN, осажденный в камере в процессе синтеза, в основном, является аморфным и состоит из двух, обогащенных бором, тетрагональных фаз BN ($B_{51.2}N$ и $B_{25}N$), а также двух оксидных фаз B_2O и B_2O_3 по данным рентгеновской дифракции. Причем, в больших количествах оксидные фазы B_2O и B_2O_3 присутствуют в порошке, полученном в области, ближайшей к реакционной зоне (**рисунок 5 а**), поскольку в технически чистом азоте присутствует примесь кислорода. Этот результат говорит о том, что понижение величины ширины запрещенной зоны осажденного порошка, полученного при прямом синтезе BN, может иметь место не только за счет нестехиометричности содержания бора в соединении [12], но и за счет примеси кислорода. К изменению величины ширины запрещенной зоны могут приводить также деформации и, как результат, дефекты, которые возникают в порошковом материале при больших градиентах температуры при синтезе под воздействием концентрированного светового излучения

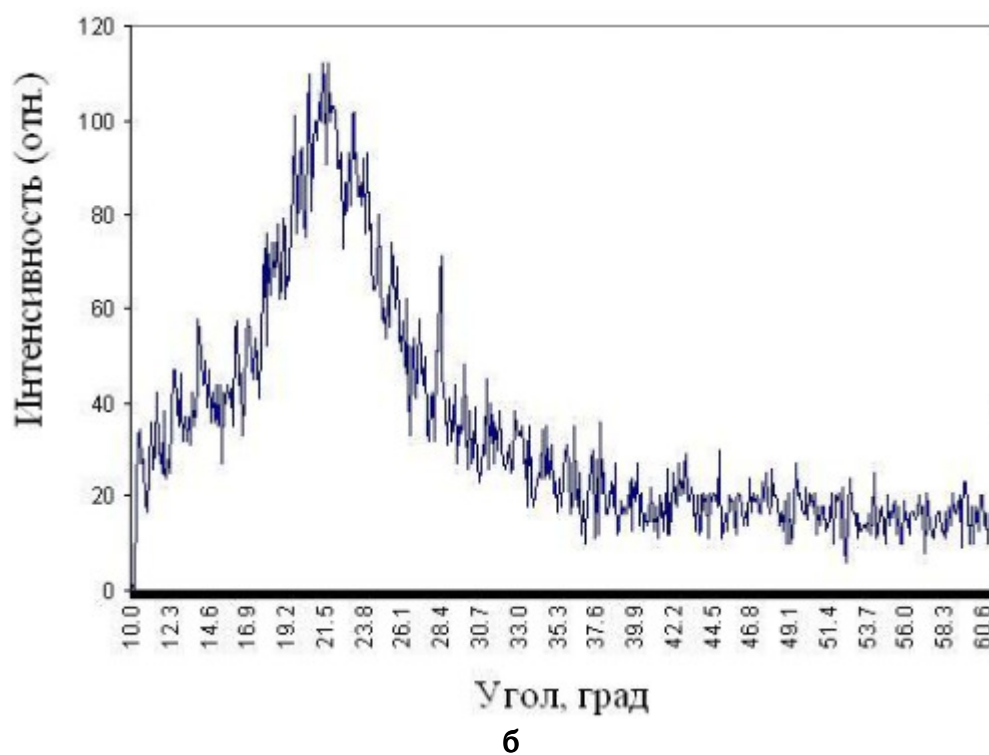
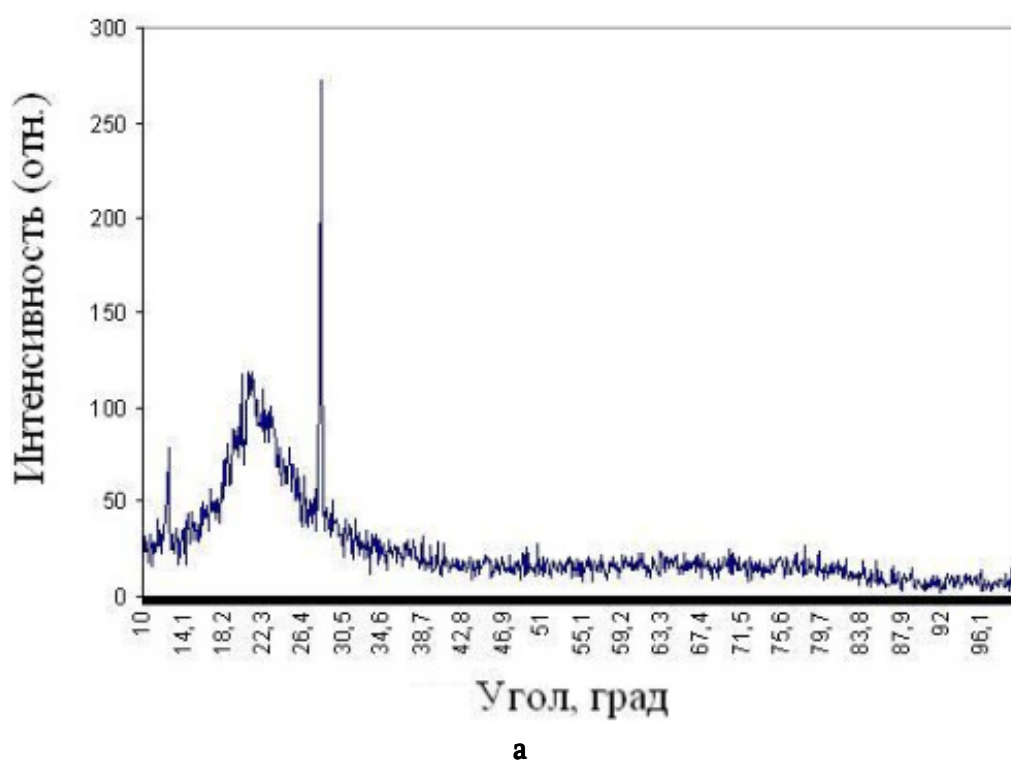


Рисунок 5. Фазовый состав частиц порошка BN с увеличением расстояния от реакционной зоны: (а) вблизи зоны и (б) на максимальном расстоянии.

4. Заключение

Под воздействием концентрированного светового излучения получены нанодисперсные и волокнистые структуры при прямом синтезе BN в присутствии катализатора.

Величина ширины запрещенной зоны структур BN растет с увеличением расстояния от реакционной зоны и достигает своего максимума 5.1 эВ при максимальном расстоянии в камере.

Пониженное значение ширины запрещенной зоны вблизи реакционной зоны может быть вызвано присутствием окислов в порошке.

Ссылки

1. L. Duclaus, B. Nystue, J. P. Issi. Structure and low-temperature thermal-conductivity of pyrolytic boron-nitride. *Phys. Rev. B* 46 (1992) 3362-3367.
2. C. Guimon, D. Gonbeau, G. Pfisterguillouzo, M. Lahaye, O. Dugne, A. Guettea, R. Naslain. XPS study of BN thin-films deposited by CVD on SiC plane substrates. *Surf. Interface Anal.*, 16 (1990) 440-445.
3. T. Laude. Boron Nitride Nanotubes Grown by Non-Ablative Laser Heating: Synthesis, Characterization and Growth Processes (PhD Thesis). 2001, Univ. Tsukuba & Ecole Centrale Paris (t.laude@teijin.co.jp).
4. R. T. Paine, C. K. Narula. Synthetic routes to boron-nitride. *Chem. Rev.* 90 (1990) 73-91.
5. A. Aydogđdu, N. Senviç. Carbothermic formation of boron nitride. *J. Eur. Ceram. Soc.* 23 (2003) 3153-3161.
6. S. I. Hirano, T. Yogo, S. Asada, S. Naka. Synthesis of amorphous boron nitride by pressure pyrolysis of borazine. *J. Am. Ceram. Soc.* 72 (1989) 66-70.
7. J. Duan, R. Xue, Y. Xu, Ch. Sun. Preparation of boron nitride flakes by a simple powder reaction, *J. Am. Ceram. Soc.* 91 (2008) 2419-2421.
8. A. A. Frolov, L. L. Sartinska, A. Yu. Koval', N. A. Danilenko. Application of the optical furnace for nanosized boron nitride production. *Nanomater.* 4 (2008) 115-120.
9. A. A. Frolov, L. L. Sartinska, A. Yu. Koval'. Set-up for obtaining of nanostructure boron nitride by evaporation of concentrated solar radiation and condensation on the cooling surface. In: Proc. Int. Conf. "Science & Develop. Biosphere Proc. Periscii: Exper. & Chall. Period". 2005, Apatity, 128-130.
10. L. L. Sartinska. Catalyst-free synthesis of nanotubes and whiskers in an optical furnace and gaseous model for their formation and growth. *Acta Mater.* 59 (2011) 4395-4403.
11. Ch. Tang, Y. Bando, Y. Huang, Sh. Yue, Cha, Gu, F. F. Xu, D. Golberg. Fluorination and electrical conductivity of BN nanotubes. *JACS Commun.* published on Web 04/15/2005.
12. A. Yu. Golovacheva, P. N. D'yachkov. Effect of intrinsic defects on the electronic structure of BN nanotubes. *JETP Lett.* 82 (2005) 737-742.

INVESTIGATION THE INFLUENCE OF ABSORPTION OF MERCURY
ON THE STRUCTURE AND MORPHOLOGY OF THE GOLD THIN FILMS

N. I. Khachidze, T. I. Khachidze

Georgian Technical University
Tbilisi, Georgia
nixachidze@gmail.com
txachidze@gmail.com

Accepted August 16, 2013

The investigation of interaction of mercury vapor with the sensitive element has been carried out for optimization of the parameters of the mercury vapor sensor developed by us [1 – 3]. In this work, the influence of absorption of mercury on the structure and morphology of gold in a running cycle of the sensor was investigated. The gold film was located in mercury vapor of high concentration (10^{-3} wt. %) for 10 min. Then the structure and morphology of the film was studied by the methods of X-ray diffraction and electronic microscopy. For experimentation it was used the gold film of thickness 300 Å deposited on NaCl crystals by thermal vacuum evaporation.

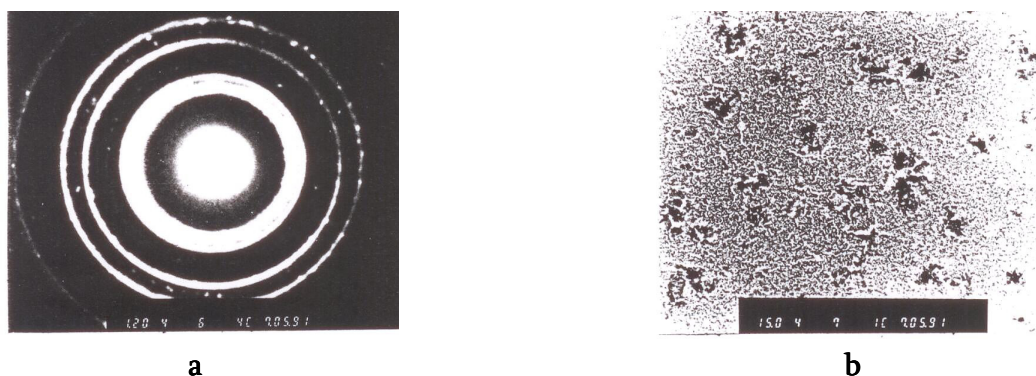


Figure 1. Structure (a) and morphology (b) of the gold film of thickness 300 Å after interaction with mercury vapor.

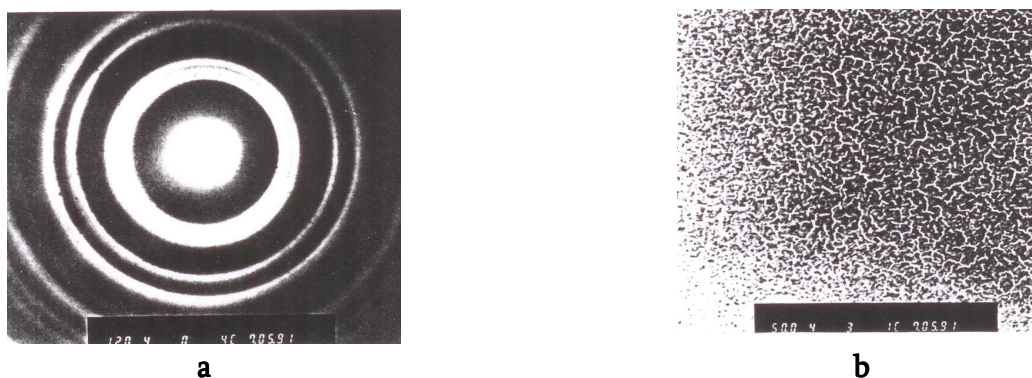


Figure 2. Structure (a) and morphology (b) of the gold film of thickness 300 Å after heat treatment.

In the **Figure 1**, the microphotograph of the gold film after interaction with the mercury vapor is presented. The formed gold–mercury conglomerates are distinctly visible. Presence of mercury is also visible on the electrogram taken from the same film (**Figure 2**).

In addition to the basic diffraction rings belonging to gold, the dot orbits of the rings corresponding to mercury also are visible on the electrogram. The structure of the gold film did not change, i.e. it represents a polycrystal without any distinguished orientation.

For investigation of the structure and morphology of the gold film after its regeneration (removal of mercury), another film prepared similarly was heated in flow up to 400 °C for 5 s. (operating conditions of restoration of the sensitive element). Then the investigation utilizing electronic microscopy and X-ray diffraction was performed. As we can see on the photos, mercury has been completely removed from the gold film.

The investigation of the dependence of resistivity ρ of the gold film on the time of absorption for various thickness of the film was carried out. It was carried at the constant concentration of the mercury vapor of 10^{-3} wt. % and at the film temperature of 20 °C. The thickness of the film varied in the range of 0.06 – 0.15 μm . This dependence is presented in **Figure 3**. As we see from the resulted curves, the increase in ρ for all the samples initially rather intensively and then gradually passes to saturation (approximately in 30 s). After that any changes in ρ do not occur. The fact that saturation takes place practically simultaneously for the gold films with mercury of different thickness of the sensitive element is very intriguing.

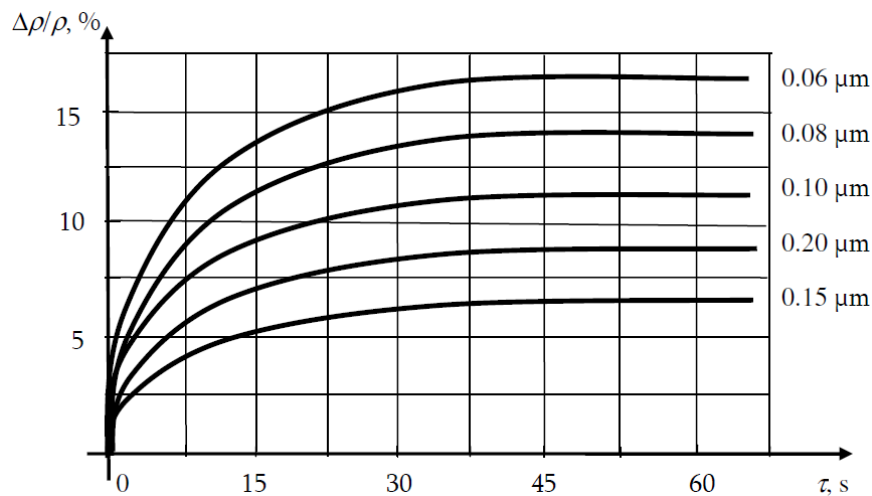


Figure 3. Dependence of the relative change in the resistivity of the gold film on time of absorption of mercury vapor. Concentration of mercury is 10^{-3} wt. % and thickness of the film is within the range of 0.06 – 0.15 μm .

To find the explanation of this phenomenon, it has been studied the mercury distribution in the depth of the gold film.

This study has been carried out for gold film of the thickness 0.25 μm at absorption of mercury vapor of concentration 10^{-4} wt. %. Rather thick film was chosen so that the restriction on thickness would not affect the mechanism of distribution in the depth of the gold film.

In the **Figure 4**, the density of distribution of mercury in the depth of the gold film for various time phases of absorption of mercury (in 5, 10, 20, 30, and 60 s) is shown.

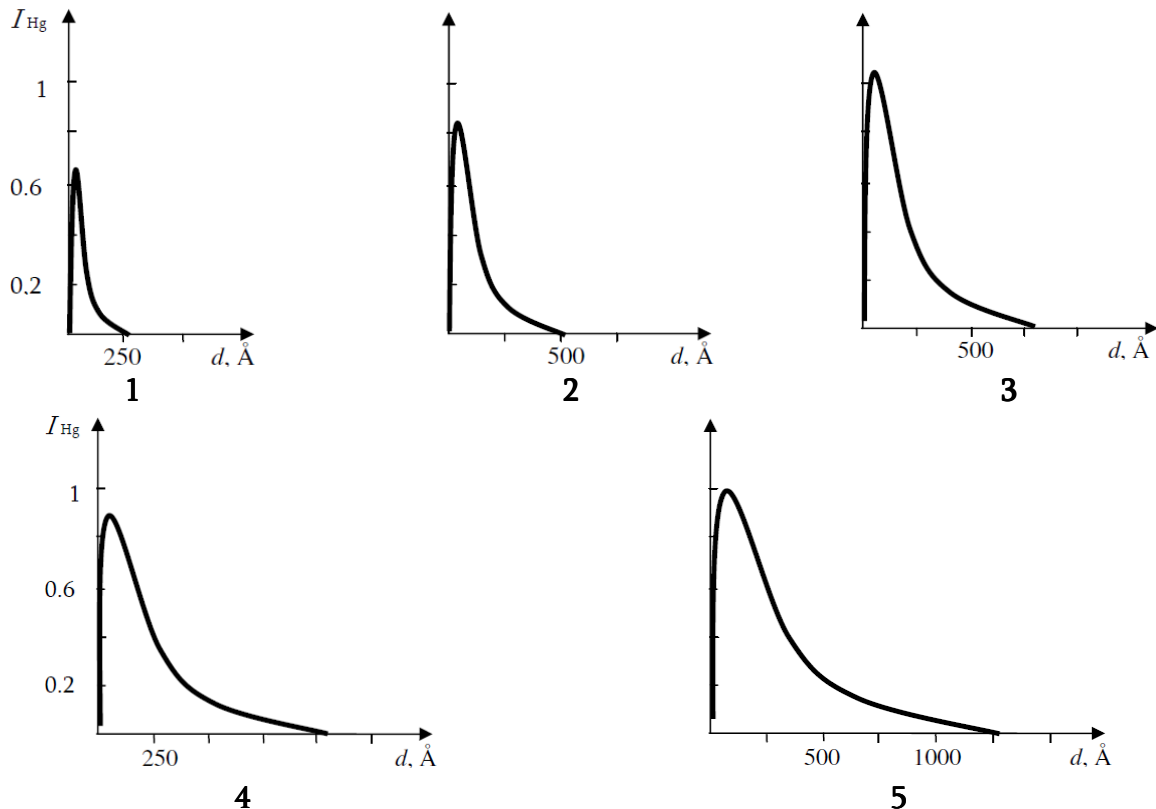


Figure 4. Relative density of distribution of mercury in the depth of the gold film at different stages of absorption: in (1) 5, (2) 10, (3) 20, (4) 30, and (5) 60 s.

It is evident from the **Figure 4** that at the beginning of the process of mercury accumulation, basically, proceeds only in the surface layer of the gold film of thickness $\sim 60 - 80 \text{ \AA}$. To this phase corresponds a fast increase in $\Delta\rho$. Mercury gradually penetrates into the volume of the gold film and in the surface layer accumulation of mercury proceeds not so intensively. The rate of increasing in $\Delta\rho$ decreases as well. After certain time (in this case 30 s.) accumulation of mercury in the surface layer does not proceed any more (there comes saturation), and since this moment $\Delta\rho$ does not change, in spite of the fact that in the volume of the film accumulation of mercury goes on.

The results of the conducted investigation allow draw the conclusion that the changes in the resistivity of the gold film occur due to accumulation of mercury in the near-surface layer of thickness of $\sim 60 - 80 \text{ \AA}$; penetration of mercury into the gold film practically does not affect ρ . That fact indicates that with reduction of the film thickness sensitivity of the sensor accordingly increases.

The study of the distribution of mercury in the depth of the gold film at heating of the substrates at different temperatures was carried out in following way.

Gold film was kept in mercury vapor at 20°C before saturation (till the moment when ρ ceases to change). Then the film was heated at different temperatures for 30 s, and the distribution of mercury in the depth of the film was studied by the method of secondary ionic weight spectroscopy. It appears from the obtained results (**Figure 5**) that at 20°C the accumulation of mercury occurs, basically, in the surface layer of the film. After heating the film up to 100°C , there is some redistribution of mercury in the volume of the film and

reduction in the total amount of the absorbed mercury. At heating the film at higher temperatures (150, 200, 300, and 350 °C), the quantity of absorbed mercury gradually decreases and simultaneously it takes place its redistribution in the volume of the film. This phenomenon explains the fact that at absorption of mercury at lower temperatures, the change in ρ is much more significant. Full evaporation of mercury from the film occurs at temperatures of $\sim 380 - 400$ °C.

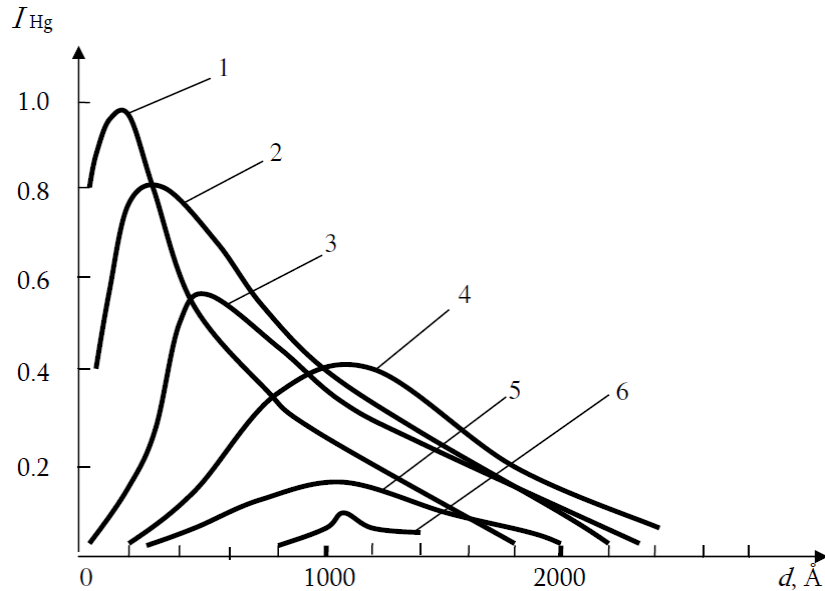


Figure 5. Relative density of distribution of mercury in the depth of the gold film after heating at different temperatures: (1) 20, (2) 100, (3) 150, (4) 200, (5) 300, and (6) 350 °C.

The results of our investigations allow drawing the conclusion that the optimal measurement time of the sensor is 20 – 25 s. Measurements are desirable to be carried out at low temperatures (40 – 50 °C), minimal temperature necessary for restoration of the sensitive element at 400 °C.

References

1. R. Chikovani, N. Khachidze, T. Khachidze. Sensors of environmental parameters based on microelectronic technology. *Microsyst. Res. & Technol. News* 1 (1997) 4-7.
2. A. I. Buturlin, N. I. Khachidze, T. I. Khachidze. A sensor for rapid measurement of the mercury concentration. *Georg. Eng. News* 1 (2000) 40-41.
3. N. Khachidze, T. Khachidze. Sensor for express measurement of mercury concentration. *Abs. Int. Workshop IWRFR1. 2000, St. Petersburg*, 119-119.

**TOMOGRAPHICAL MODEL OF INHOMOGENEOUS STRUCTURE
OF EARTH CRUST FOR GEORGIA AND NEAREST TERRITORIES
DEVELOPED BY DATA OF SURFACE SEISMIC RAYLEIGH WAVES**

T. Gegechkori¹, V. Gotciridze¹, N. Zhukova¹, A. Sborshchikovi¹, I. Shengelia²

¹ M. Nodia Institute of Geophysics
Tbilisi, Georgia
tengeg@gmail.com
rossoneri08@yandex.ru

² Ilia State University
Tbilisi, Georgia

Accepted August 25, 2013

For investigation of horizontal-inhomogeneous structure of Earth crust and upper mantle the most useful is the method of tomographic alradiography by body and surface waves. Tomographical models of inhomogeneous structures of Earth crust based on velocities of surface waves with different resolution levels are created for many regions of World (Eurasia, South America, Arctic and so on). For Georgia and nearest territories such investigations have not been performed. Before the study of surface-wave tomography begin, our team disposed of archive records of surface waves, which had been collected in the past in the Institute of Geophysics of Georgian Academy of Sciences. These were seismograms from Georgian seismic stations and, also the copies of Armenian and Azerbaijan records in period of 1961 – 1985, approximately 1000 seismograms in all recorded on 21 stations of Transcaucasia.

On the first stage these records had been classified by quality and regional basis. Besides the quality, the main criterion of collecting records was the condition of reciprocal crossing of different traces – epicenter–station. This condition is basis of surface wave tomography. After studying of seismic activity in the given period the Eastern Turkey and Southern-Eastern Iran had been chosen as the main regions. In this case the condition of reciprocal crossing of traces was kept. Dispersion curves of group velocities for various traces, which are the initial material for tomography calculations, were built manually using specially developed program of semi-manual method of plotting. The most qualitative records had been digitized and then processed with special developed computer program of frequency-spectral analysis for getting the dispersion curves. Tomography calculations were carried out in two steps as seismic records had been collected. The first tomography models were built for 30 collected earthquakes of Turkey and Iran. For this region 59 traces epicenter-station had been collected. Out calculations were held within beam tomography. It was considered, that wave lengths are much smaller then studied inhomogeneities.

Later, as the works progressed, the new tomography method had been developed, which was able to use remote earthquakes with epicentral distances over 2 000 km. and does not demand the condition of traces crossing [1]. Implementation of this method allowed involving new records for calculations, notably from eastern and western directions – Aegean Sea, Northern Africa, Central Asia, Pakistan and China. After adding of new data the 110 traces from 55 earthquakes were additionally collected. This database served as the basis for aggregate calculations and building of the tomography models.

On the **Figure 1** the traces used for calculations of periods 20 s are shown. After classification and collection of records it became clear, that dispersion data for periods between 10 till 22 s turned out as a representative. The upper interval of periods was determined by the amplitude-frequency characteristics of the applied seismometers.[2].

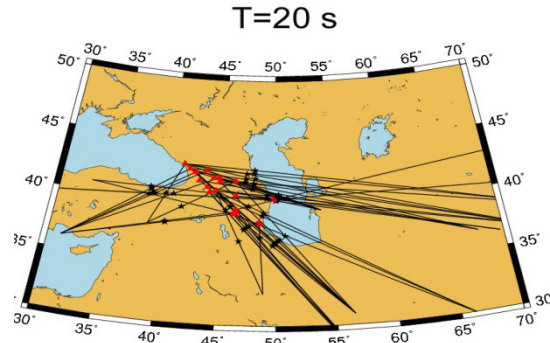


Figure 1. Pattern of traces for periods $T = 20$ s.

It could be approximately considered that the main part of energy of the surface wave propagates in the layer of thickness of half-length of the wave, which accordingly gives information of structure up to these depths. Thus, the depth of “raying” of the Earth’s crust is determined by formula $\lambda = CT/2$ (where λ is the length of the wave, C – phase velocity, T – wave period). Therefore the carried out tomography calculations gives the conception of horizontally-inhomogeneous structure of the Earth’s crust up to 40 km depths.

The tomography calculations were carried out by three ways: (1) semi-manual method, (2) program that demands reciprocal crossing of traces, and (3) program for remote (over 2 000 km) earthquakes. When building solution for lateral distribution of velocities the resolution characterized by the effective radius of smoothing area, simultaneously has been estimated for periods 10 – 20 s. The solution has been considered acceptable if the radius of smoothing area did not exceed 200 km.

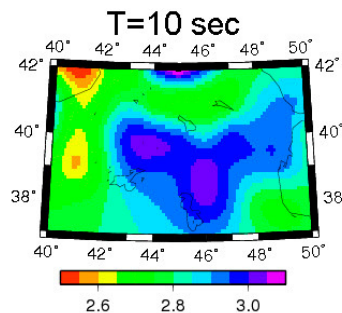


Figure 2. Tomographical model for depth $H = 15$ km ($T = 10$ s).

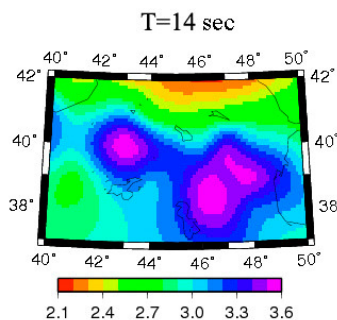


Figure 3. Tomographical model for depth $H = 24$ km ($T = 14$ s).

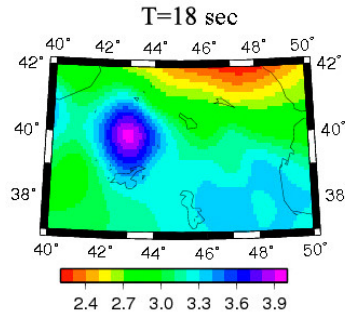


Figure 4. Tomographical model for depth $H = 32$ km ($T = 18$ s).

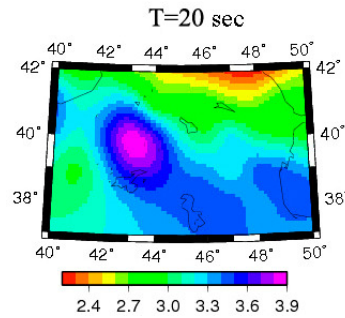


Figure 5. Tomographical model for depth $H = 37$ km ($T = 20$ s).

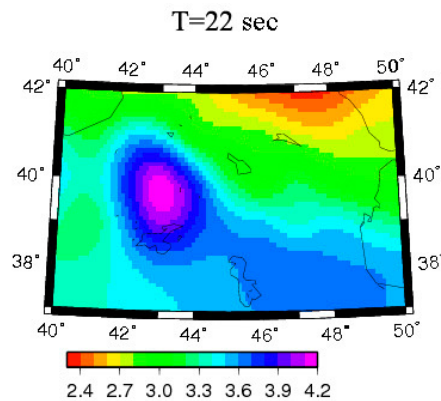


Figure 6. Tomographical model for depth $H = 40$ km ($T = 22$ s).

The main feature of the surface wave is the presence of the free surface of Earth. Thus after tomography calculations for each specific period we receive the averaged model of the horizontally-inhomogeneous structure of the Earth's surface for depths equal to half length of the wave corresponding to this period. On the **Figures 2 – 6** the tomographical models of the Earth's surface for different depths are shown. We can compare tomographical consturctions with available information onstructure of the Earth's crust and area's tectonical peculiarities [3].

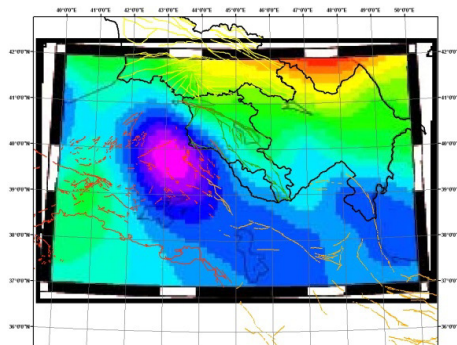


Figure 7. Comparison of depth and regional faults with tomographical model for $T = 20$ s.

On the **Figure 7** the comparison of tomographical constructions for the 20 s with data of depth and regional faults with various penetration in the Earth's crust [4].

The high-velocity inclusion in the southwest part of the region is related to continuation of the mega-anticlinorium of Zagros mountains towards the Small Caucasus direction in Iran. That results into coarse lineament zones: Erevan–Megris and Nakhichevan–Aragats.

The high-velocity inclusion shown on **Figures 2** and – on the Northern latitude 40° in the Eastern part of the map is related to Javakheti upland on the south of Georgia, which is also visible on the northwest part of Armenia. This is area of former volcanic activity and in its structure dominates the formations of volcanic origin.

The presence of extensive high-velocity inclusion in the southwest part of the region for 24 – 37 km depths with phase velocities 3.4 – 3.7 km / s leads to conclusion that thickness of the Earth's crust in this region is the subject of more precise definition. The evidence of reliability of tomographical constructions obtained for big depths is the fact, that models for periods 20 and 22 s (**Figures 5** and **6**) are practically identical. The calculations are more complicated for lesser depths. The Earth's crust in the studied region is far from horizontally-inhomogeneous model and has a block structure, or increasing of the resolving capacity of the method the distance between stations should be 50 – 100 km.

For more precise tomographical study of the upper horizons of Earth's crust the resolving capacity of surface-wave tomography should be increased. This can be achieved only by increasing the quantity of broadband seismic stations in the region. The digital records could make possible to recede the lower level of recorded periods to 4 s. In this case the resolving capacity of the method will reach 10 km. This will allow studying lateral structure of the lower horizons of the sedimentary basin, forecast oilfields, gas fields and mineral products; also carry out works of long-term strong earthquake prediction. The necessity of increasing of initial data and, accordingly the quantity of the reciprocal crossing traces results from the fact that marked high-velocity zone for period 18 s is shifted by 1° of longitude to the East.

The usage of the broadband recordings should also considerably expand the frequency range for big period sideways and allow to make tomographical constructions for periods 30 – 80 s, and obtain information about horizontally-inhomogeneous structure of the Earth's crust foot and upper mantle layers.

References

1. T. B. Yanovskaya. Methodic of surface wave tomography based on data of remote earthquakes. *Earth's Phys.* 3 (2009) 50-55.
2. T. B. Yanovskaya. Assessment of resolution in ray tomography tasks. *Earth's Phys.* 9 (1997) 76-80.
3. T. B. Yanovskaya, P. G. Ditmar. Smoothness criteria in surface wave tomography. *Geophys. J. Int.* 102 (1990) 63-72.
4. G. A. Mikheev, M. G. Makarova. Tectonic interpretation of decrypted satellite-borne photography of Caucasus. *Studying of Earth from Space* 2 (1985) 59-66.

SHORT DICTIONARY (GLOSSARY) ON
NANOCHEMISTRY AND NANOTECHNOLOGY. Part III


Ts. Ramishvili, V. Tsitsishvili

P. Melikishvili Institute of Physical and Organic Chemistry
I. Javakhishvili Tbilisi State University
Tbilisi, Georgia
rtsiuri@yahoo.com

Accepted August 31, 2013

Table 1 lists some of such terms in English, German, and Russian taken from dictionaries and scientific periodic chemical publications [1 – 18] and the corresponding terms in Georgian with appropriate definitions. In comparison with the previous parts in this section are more extended definitions of some terms. Synonyms are designated separate line.

Table 1. English, German, Russian, and Georgian terms used in nanochemistry and nanotechnology.

Terms			
in English	in German	in Russian	in Georgian
Aerogel Aerogels	Aerogel n Aerogele pl / Aerogels pl	Аэрогель Аэрогели	აეროგელი აეროგელები
 <p>სილიციუმის დიოქსიდის აეროგელი http://stardust.jpl.nasa.gov/home/index.html</p>			<p>კოლოიდური ნივთიერებებია, აქვს მცირე სიმკვრივე და მაღალი ფორიანობა, მეზოფორიანი კლასის მასალებია, მათში ფორები იკავებს 50–99%-ს. ისინი ამორფული მასალებია, რომლებსაც აქვს მოცულობითი მაკროსტრუქტურა ნანოსტრუქტურული სფერული ნაწილაკებით ზომებით 4–10 ნმ და რომლებიც წარმოადგენს გელებს, რომლებშიც თხევადი ფაზა მთლიანად ჩანაცვლებულია აირადით (ჰაერით ან სხვა აირით); ამის გამო მათ აქვს რეკორდულად მცირე სიმკვრივე (0.002–0.25 გ/სმ³), გამჭვირვალება, სიმტკიცე (უმცირეს 2000-ჯერ მეტ დატვირთვას საკუთარ მასასთან შედარებით), დაბალი გარდატეხის მაჩვენებელი (1.00–1.05) და სითბოგამტარობა, თერმომდგრადობა, დიდი ხვედრითი ზედაპირი, მაღალი სორბციული თვისებები</p>



ყვავილი მოთავსებულია კვარცის აეროგელის ნაჭერზე, რომელიც ბუნუნენის სანთურის ზემოთაა. აეროგელს აქვს საუკეთესო თერმოსაიზოლაციო თვისება და ყვავილი დაცულია ალისაგან

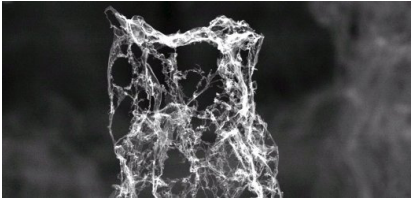

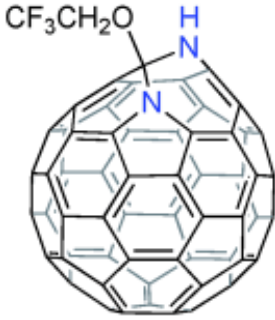
<http://www.sculptors.com/~salsbury/House/panels.html>

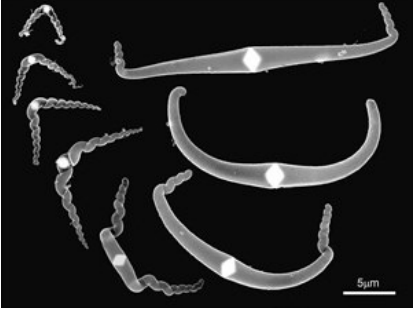
<http://galspace.spb.ru/index143.html>

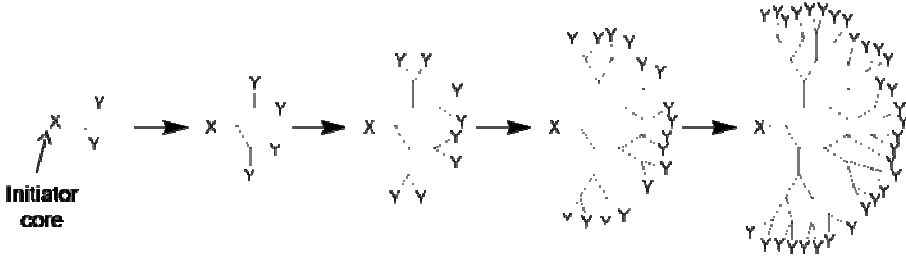
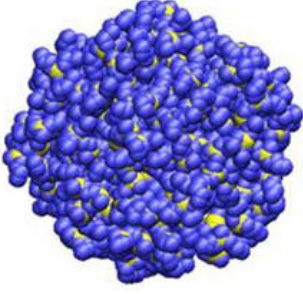
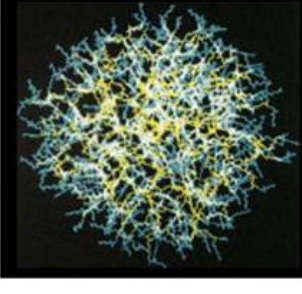
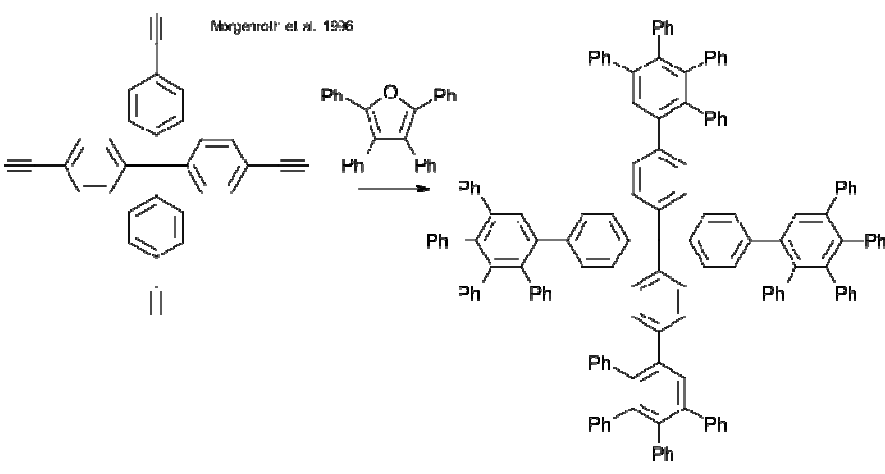
stardust.jpl.nasa.gov

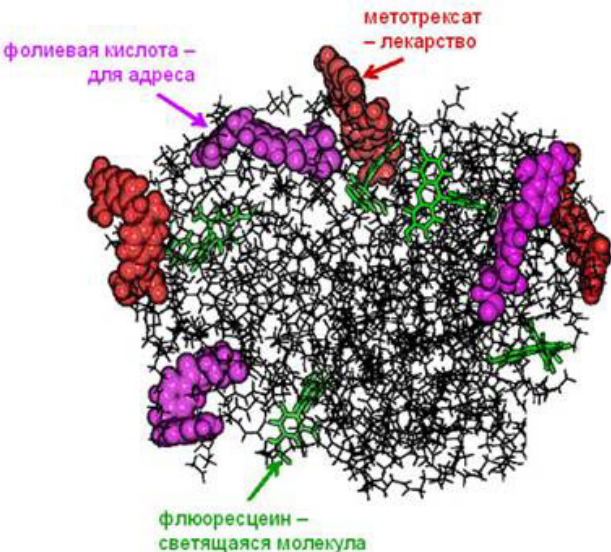
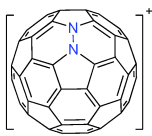

(ეფექტურად შთანთქავს CO-ს, CO₂-ს, NO-ს, NO₂-სა და უჯერ ნახშირწყალბადებს), მწელად განიცდის დაბერებას. აეროგელები თავისი 15 განსაკუთრებული მახასიათებლის გამო შეტანილია გინესის რეკორდების წიგნში. პირველად აეროგელი მიიღო ამერიკელმა მეცნიერმა Samuel Kistler-მა 1920–1930 წლებში კვარცისაგან, რის შესახებაც 1931 წ. გამოაქვეყნა სტატია ჟურნალში Nature. ის მუშაობდა სტოკტონის (კალიფორნია, აშშ) წყნარი ოკეანის კოლეჯში. მასვე მიაწერენ ტერმინის “აეროგელი” დამკვიდრებას. ლათ. “aer” – ჰაერი, “gelatus” – გაყინული. აეროგელებს ადარებენ გამყარებულ საუნის ქაფს. მათ გაყინულ, მყარ კვამლსაც ეძახიან, რადგანაც შეხებისას მყარია. აგრეთვე, გამჭვირვალობის გამო მათ “მყარ ჰაერსაც” უწოდებენ. ისინი 99.99%-თ ჰაერისგან შედგება. იყენებენ ელექტრო- და თერმოსაიზოლაციო მასალად (მაგალითად, ამერიკული კოსმოსური სკაფანდრების და “შატლის” კონსტრუქციისთვის), ნანოდისპერსულ დანამატად ჰიბრიდულ ორგანულ და არაორგანულ კომპოზიციურ მასალებში, კატალიზატორების და სორბენტების სარჩულად, ნანოზომის აირების ფილტრებად (მაგალითად, მძიმე ელემენტებისაგან წყლის გასუფთავების საქმეში), მაღალი ენერჯის დამუხტული ნაწილაკების დეტექტორებში, მინაბოჭკოსა და მაღალი ჰომოგენობის მინის საწარმოებლად. ერთ-ერთი აეროგელის “Airglass” სიმკვრივეა 0.05–0.20 გ/სმ³, ის თბოსაიზოლაციო თვისებებით რამდენჯერმე აღემატება ჩვეულებრივ მინას, აგრეთვე უფრო გამჭვირვალეა ($n = 1.05$) ვიდრე ჩვეულებრივი მინა ($n = 1.5$); შექმნილია ამ მასალის დრეკადი, არამსხვრევადი სახე. ყოველივე ქმნის პერსპექტივას ამ მასალის ფანჯრის მინად გამოსაყენებლად. NASA-ის კოსმოსურმა აპარატმა “Stardust” ერთ-ერთი ასტეროიდის ბირთვთან ახლოს ჩავლისას 2004 წ. გაიარა კომეტის კუდში და შესძლო კოსმოსური მტვრის დაჭერა სილიციუმის დიოქსიდის საფუძველზე მომზადებული აეროგელით – როგორც მტვრის მშთანთქმელით; ზემციერე სიმკვრივის მქონე აეროგელით

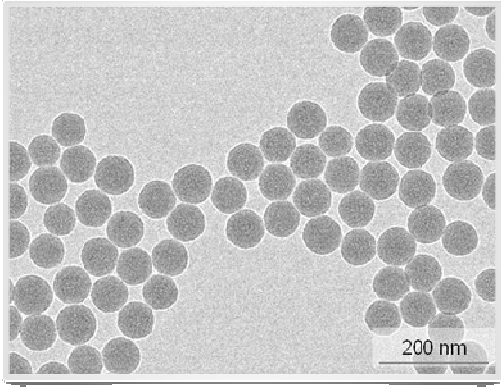
			<p>შესაძლებელი გახდა დიდი სიჩქარით (20–30 კმ/წმ) მოძრავი კოსმოსური ნაწილაკების დამუხრუჭება გადახურების გარეშე და ამგვარად თავიდან იქნა აცილებული მათი დაშლა. მათში აღმოჩნდა მინერალური ნივთიერებების გარდა ორგანული ნივთიერებებიც (მეთილამინი, ეთილამინი), რაც იძლევა წარმოდგენას დედამიწაზე სიცოცხლის წარმოშობის შესახებ http://galspace.spb.ru/index143.html. ცნობილია აეროგელები, მიღებული ამორფული SiO₂-ისა და Al₂O₃-ის საფუძველზე, აგრეთვე შემდეგი ელემენტების ოქსიდების საფუძველზე: Li, Na, Ca, Mg, Ba, Zn, Sn, Cr, Ge, Te, Sb, W, Fe, Ni, Mn, Ti, V, Gr, Sn და სხვ.; მიღებულია ნახშირბადის ნანომილაკების აეროგელები – მაგ., აეროგრაფიტი. SiO₂-ის აეროგელი არის სამგანზომილებიანი განტოტვილი კლასტერი, რომლის ქსელი 4 ნმ-ის ზომის ნანონაწილაკებს შეიცავს; კლასტერებს შორის სივრცე შევსებულია ჰაერით; რადგანაც ამ სიცარიელეთა ზომები (~100 ნმ) ათჯერ და მეტად აღემატება კლასტერების ზომებს, მიიღება მსუბუქი მასალა. SiO₂-ის აეროგელს იღებენ ტეტრაეთილ-ორთოსილიკატის Si(OCH₂CH₃)₄ წყალთან მოქმედებით, მიღებულ გელს შემდგომ წყალს აცილებენ ეთანოლით: გელს ზეკრიტიკულ ტემპერატურასა და წნევაზე გააცხელებენ და ორთქლადქცეულ ეთანოლს მოაცილებენ. სხვა ლითონების ოქსიდების გელებს იღებენ მათი ნადნობების შერჩევითი ჟანგვით. ნახშირბადის აეროგელები შედგება ერთმანეთთან კოვალენტურად შეკავშირებული ნანონაწილაკებისაგან. ისინი დენის გამტარებია და მათ ძალიან დიდი შინაგანი ზედაპირის (800 მ²/გ) გამო იყენებენ სუპერ-კონდენსატორების წარმოებაში.</p>
<p>Aerographite / Carbonnanotube aerogel</p>	<p>Aerographit m</p>	<p>Аэрографит</p>	<p>აეროგრაფიტი შავი ფერისაა, სინთეზური ქაფია, რომელიც შეიცავს ფოროვანი ნახშირბადის მილაკების ბოჭკოების დენდრიტულ ქსელს. 2012 წ. ის მიიღეს გერმანელმა მეცნიერებმა Kiek-ისა და Hamburg-ის უნივერსიტეტებიდან (გფრ).</p>

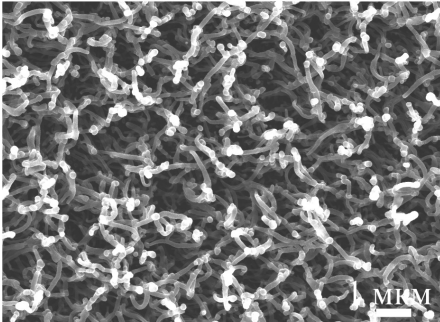
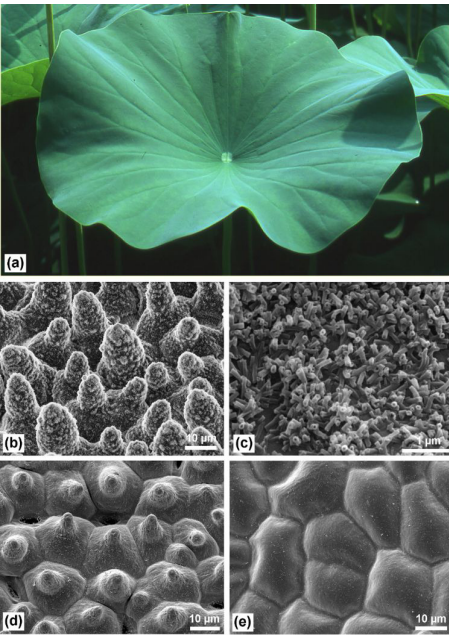
 <p>უმსუბუქესი აეროგრაფიტი ელექტრონულ მიკროსკოპში: ის თითქმის არაფერს იწონის ($d = 0.20$ მგ/სმ³), შედგება 0.004 მმ სიგანის და 0.007 მმ სიმაღლის ფოროვანი ნაწილაკებისაგან http://www.spiegel.de/wissenschaft/technik/aerographit-leichtestes-material-der-welt-entwickelt-a-843819.html</p>  <p>გრაფენის აეროგელი ჰაერზე 7-ჯერ უფრო მსუბუქია და ბალახის ფხაზე შეკავდება; მისი 1 სმ³-ის მასაა 0.16 მგ (Zhejiang University, China). ეს მასალა 12%-ით უფრო მსუბუქია, ვიდრე რეკორდული მაჩვენებლის მქონე ზემტკიცე, ელექტროგამტარი აეროგრაფიტი, ის ჰაერზე 6-ჯერ უფრო მსუბუქია და მისი 1 სმ³-ის მასაა 0.20 მგ (Kiel University, Hamburg University of Technology, German) http://inhabitat.com/newly-developed-graphene-aerogel-is-the-worlds-lightest-material/</p>			<p>აეროგრაფიტს გააჩნია ზეჰიდროფობურობა, მისი შემცველი მასალები მიიზიდება დამუხტული საგნებით, არის ელექტროგამტარი, ჰაერზე 6-ჯერ უფრო მსუბუქია. აეროგრაფიტში 0.01% გრაფიტი და 99.99% ჰაერია. 2013 წლამდე ის ითვლებოდა ყველაზე მსუბუქ მასალად – მისი $d = 0.20$ მგ/სმ³. 2013 წ. ჩინეთში, Zhejiang-ის უნივერსიტეტში მიიღეს გრაფენის აეროგელი (graphene aerogel), რომელიც ჰაერზე 7-ჯერ უფრო მსუბუქია, მისი $d = 0.16$ მგ/სმ³ და ის 12%-ით უფრო მსუბუქი აღმოჩნდა, ვიდრე აეროგრაფიტი. მასკანიტებელ ელექტრონულ მიკროსკოპში 10000-ჯერ გადიდებისას ჩანს, რომ აეროგრაფიტის სტრუქტურა ნახშირბადის ნანომილაკებისგან შედგება, რომელთა შერწყმა ერთმანეთთან სამგანზომილებიანი სტრუქტურის “დრუბელს” წარმოქმნის მრავალრიცხოვანი ფორებით, რომლებშიც ჰაერია.</p>
<p>Azahomoazafullerene C₅₉N(NH)R</p>	<p>Azahomoazafulleren n</p>	<p>Азагомоазафуллерен</p>	<p>აზაჰომოაზაფულერენი C₅₉N(NH)R</p>
 <p>http://onlinelibrary.wiley.com/doi/10.1002/ange.201300973/abstract</p>			<p>პრეფიქსი “ჰომო” აღნიშნავს საწყისი ციკლის გაფართოებას C–C ატომებს შორის მეთილენის ჯგუფის შეყვანით. აზაჰომოაზაფულერენში ფულერენის ნახშირბადატომების ჩონჩხში თითო ატომი ნახშირბადი ჩანაცვლებულია აზოტის ატომით.</p>
<p>Bilateral carbon spirals</p>	<p>Bilaterale (zweiseitige) Kohlenstoff-Spiralen f pl / Kohlenstoff-Nano-Schnurrbart m Kohlenstoff-Nano-Schnurrbärte pl</p>	<p>Двусторонние углеродные спирали</p>	<p>ნახშირბადის ორმხრივი სპირალები</p>

			<p>ნახშირბადის სხვადასხვა ზომის ორმხრივი სპირალების კონსტრუქციები. სპირალები მიიღეს ჰერმეტიკულ მოცულობაში ფეროცენის ორთქლის კატალიზური პირობებით მაღალ წნევაზე.</p>
<p>სხვადასხვა ზომის ნახშირბადის სპირალების ბიკონუსების მასკანირებული ელექტრონულ-მიკროსკოპული გამოსახულებები http://derstandard.at/1363711262171/Wiener-Physiker-lassen-Nano-Schnurrbaerte-wachsen http://www.nature.com/srep/2013/130514/srep01840/full/srep01840.html</p>			
Blue emulsion	Blaue Emulsion f	Голубая эмульсия	<p>ცისფერი ემულსია</p> <p>ემულსია, რომელშიც დისპერგირებული წვეთების ზომა 200 ნმ-ზე მეტი არაა. ამიტომ ისინი განაზღვრენ ციფერ სინათლეს და მას აღვიქვამთ როგორც ცისფერს. ასეთ სისტემებს იყენებენ კოსმეტიკაში.</p>
Carbonaerogel	Kohlenstoffaerogel n / Aerogel-Kohlenstoff m / Nanoschaum m	Углеродный аэрогель / Аэрогель углерода	<p>ნახშირბადის აეროგელი</p>
Carbonaerogels	Kohlenstoffaerogele pl / Nanoschäume pl	Углеродные аэрогели / Аэрогели углерода	<p>ნახშირბადის აეროგელები</p> <p>ნახშირბადის აეროგელები (ნ.ა.) შედგება ერთმანეთთან კოვალენტურად შეკავშირებული ნანონაწილაკებისაგან. მათ აქვს მაღალი ფორიანობა — 50%, ფორის დიამეტრი არანაკლებია 100 ნმ-ისა. ნ.ა. მიიღეს 1990 წ. ისინი დენის გამტარებია, მათ ძალიან დიდ შინაგან ზედაპირს (800 მ²/გ) გამოიყენებენ სუპერკონდენსატორების წარმოებაში, რომელთა ტევადობაა 10⁴ ფ/გ და 77 ფ/სმ³. 0.25–14.3 მკმ გამოსხივების უბანში ნ.ა. არეკლავს გამოსხივების მხოლოდ 0.3 %-ს, რის გამოც ისინი მზის სხივების ეფექტური მშთანთქმელებია. ამ მასალებს არ აქვს მონოლითური შიგა სტრუქტურა და არა აქვს რეგულარული, აეროგელების ფორის დამახასიათებელი, სტრუქტურა.</p>

<p>Dendrimer / Arborol / Cascade molecule</p> <p>Dendrimers / Arborols / Cascade molecules</p>	<p>Dendrimer n</p> <p>Dendrimere pl</p>	<p>Дендример / Арборол</p> <p>Дендримеры</p>	<p>დენდრიმერი</p> <p>დენდრიმერები</p>
<div style="display: flex; justify-content: space-around; align-items: center;"> <div style="text-align: center;">  <p>Initiator core</p> </div> <div style="text-align: center;">  </div> <div style="text-align: center;">  </div> </div> <p>დენდრიმერის მოლეკულის წარმოქმნის სქემა დატოტვილი Z-X-Z მოლეკულისაგან (ზემოთ) და მათი სხვადასხვა სახეები (ქვემოთ)</p> <p>http://en.wikipedia.org/wiki/File:538_Divergent_synthesis.png</p> <div style="text-align: center; margin-top: 20px;">  <p>Moberg et al. 1996</p> </div> <p>პოლიფენილენური დენდრიმერების სინთეზის მაგალითი</p> <p>http://en.wikipedia.org/wiki/File:Dendrimer_DA_Mullen_1996.svg</p>			<p>ბერძნ. “dendron” – ხე; მაკრომოლეკულა სიმეტრიული, ხისებრი, რეგულარულად დატოტვილი სტრუქტურით. პირველად მიიღეს 1978 წ. (F. Fögtle და სხვ., გერმანია). დენდრიმერები (დ.) – ხისებრი პოლიმერები ნანოსამყაროს ერთ-ერთი ელემენტი, მათი ზომებია 1–10 ნმ. დენდრიმერების მრავალსაფეხურიანი სინთეზი ერთ-ერთი ნანოტექნოლოგიაა, რომელიც კიმიასთანაა მჭიდროდ დაკავშირებული. როგორც ყველა პოლიმერი, დ. მონომერებს შეიცავს, მაგრამ დატოტვილი სტრუქტურის; თუ პოლიმერის სინთეზისას არ ხდება ზრდადი ტოტების ურთიერთშეერთება, დენდრიმერი ხეს ემსგავსება სფეროსებრი ვარჯით. მესამე და უფრო მაღალი გენერაციის დ.-ს აქვს მოლეკულური სტრუქტურის მაღალი სიმკვრივე და სფერულთან მიახლოებული ფორმა. ამის გამო დენდრიმერის მოლეკულაში არის ღრუები. თუ მის ღრუებში მოვთავსებთ გარკვეულ ნივთიერებებს, მასკანირებელი ელექტრონული მიკროსკოპის მეშვეობით შესაძლებელი იქნება სხვადასხვა დენდრიმერისაგან ელექტრონული სქემების შექმნა. თანაც ამ დროს სპილენძით შევსებული დენდრიმერი იქნებოდა გამტარის როლში. დენდრიმერის ხსნარებს აქვს უფრო მცირე სიბლანტე, ვიდრე იგივე მოლეკულური მასის სხვა ნივთიერებებს. მათ თვისებას ძირითადად განსაზღვრავს ფუნქციური ჯგუფების ტიპი მათ ზედაპირზე. მაგალითად, თუ დენდრიმერის მოლეკულის ბოლოებში არის ჰიდროფილური კარბოქსილის ჯგუფები, მაშინ ისინი წყალში ხსნადებია, ფტორორგანული ჯგუფების შემცველები კი იხსნება ზეკრიტიკულ CO₂-ში. დენდრიმერის მოლეკულები შეიძლება გამოყენებული იყოს როგორც კონტინერი მეტალების პრაქტიკულად ერთნაირი ზომის ნანონაწილაკების შესაქმნელად, რომლებსაც შემდგომ</p>

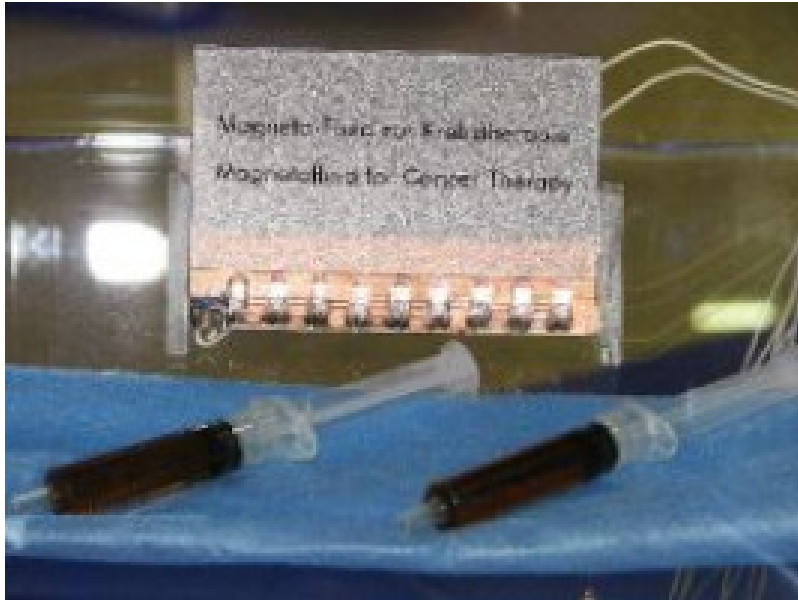
 <p>დენდრიმერი, რომლის გარე გარსთან ფოლის მჟავას მოლეკულებია (იისფერი) მიმაგრებული, ეწეება მხოლოდ სიმსივნურ უჯრედს. ფლუორესცინის მოციმციმე მოლეკულები (მწვანე) გვაძლევს შესაძლებლობას აღმოვაჩინოთ ეს უჯრედები. მეტოტრექსატის მოლეკულები (წითელი) სპობს სიმსივნურ უჯრედებს. ეს იძლევა შესაძლებლობას შერჩევითად იქნეს განადგურებული მხოლოდ კიბოს უჯრედები</p> <p>http://www.med.umich.edu/opm/newspage/2005/nanoparticles.htm</p>			<p>გამოიყენებენ კატალიზატორებად, ელექტრონული მოწყობილობების დამზადებაში, სპეციალური საფარების შესაქმნელად. ფოტოქრომული ჯგუფების შემცველი დ. გარდაქმნის სინათლის ენერჯიას, რაც პერსპექტულია მათი ოპტიკურ ხელსაწყოებში გამოსაყენებლად; დენდრიმერები კომპლექსებს იძლევა, რომელთა სტაბილობა გარემოს მდგომარეობაზეა დამოკიდებული. ეს კი იძლევა პერსპექტივებს მედიცინაში წამლების ორგანიზმში გარკვეული მისამართით გადატანაში. დენდრიმერის მოლეკულების ზომების კონტროლირებადობის და აღწარმოებადობის გამო დენდრიმერებს იყენებენ მას-სპექტრომეტრიაში დაკალიბრებისას; მძიმე ლითონების შემცველი დ. რენტგენოკონტრასტული ნივთიერებებია. დენდრიმერი ნანოსამყაროში “ქვემოდან ზემოთკენ” მიმავალი ბილიკია.</p>
<p>Diazafullerene C₅₈N₂</p>	<p>Diazafulleren n</p>	<p>Диазафуллерен</p>	<p>დიაზაფულერენი</p>
 <p>http://onlinelibrary.wiley.com/doi/10.1002/ange.201300973/abstract</p>			<p>ჰეტეროფულერენების წევრი.</p>
<p>Fluorescent nanobeads</p>	<p>Fluoreszierende nanobeads pl</p>	<p>Флуоресцентный нанобисер / нанобусы</p>	<p>მაფლუორესცირებელი ნანობურთულები / ნანომარცვლები / ნანომძივები</p>
 <p>ვერცხლი ბიოშეთავსებადი ელემენტია, რომლის ნანონაწილაკებს ახასიათებს ფლუორესცენცია, რაც გამოიყენება გამკვალავად (tracer) უჯრედული პროცესების კვლევისას</p> <p>nanobiotechnology.utah.edu hiq-nano.com</p>			<p>ნანოტექნოლოგიის ერთ-ერთი ძირითადი ამოცანაა მაფლუორესცირებელი ნანონაწილაკების მიღება, რომლებსაც ფართოდ იყენებენ ოპტიკურ დამზახსოვრებელ მოწყობილობებში, ბიოქიმიკაში, ბიონალიზში, მედიცინაში. ვიზუალიზაციის არსებული ფლუორესცენციული (ფლ) შეთოდები ეყარება ნიშანდებს საღებარებით (dye markers), მაგრამ მათ გააჩნია შეზღუდული როგორც შუქმედეგობა (photostability), ასევე სხივური ემისია (light emission per</p>

 <p>კვარცის მაფლუორესცირებელი ნანომძივის გვირაბულ-ელექტრონულ-მიკროსკოპული (TEM) სურათი.</p>		<p>molecule), გადათვლილი თითო მოლეკულაზე. ნანონაწილაკებს არ გააჩნია ეს შუზღუდეები – მათ აქვს უფრო სტაბილური და ინტენსიური ფლ სიგნალები. ფლუორესცენციულად ნიშნული ნანონაწილაკები წარმატებით გამოიყენება იმუნოანალიზში, ეკოლოგიაში აირების და სითხეების ნაკადების გაზომვებში გამკვავადავად (tracers), ლაზერულ დოპლერულ ანემომეტრიაში (laser Doppler anemometry, LDA), ნაწილაკების დინამიკურ ანალიზსა (particle dynamic analysis, PDA) და ნაწილაკების გამოსახულების ანალიზში (particle image velocimetry, PIV).</p>	
<p>International Council on Nanotechnology ICON</p>	<p>International Council on Nanotechnology m (Internationaler Rat für Nanotechnologie m) ICON</p>	<p>Международный совет по нанотехнологиям ICON</p>	<p>ნანოტექნოლოგიების საერთაშორისო საბჭო ICON</p> <p>დაარსდა 2004 წ. რაისის (Rice, ჰიუსტონი, ტეხასი, აშშ) უნივერსიტეტში როგორც ამერიკის ბიოლოგიური და ეკოლოგიური ნანოტექნოლოგიების ცენტრის სამეცნიერო ფონდის მემკვიდრე. რისკების შემცირება რომლებიც შეიძლება მიადგეს ახალი ნანოტექნოლოგიების გამოყენებისას ჯანმრთელობას და გარემოს, მათი შეფასება, განიხილვა და ზომების მიღება არის ICON-ის ამოცანები. ამისთვის ის თანამშრომლობს მეცნიერებთან, ინჟინრებთან, მრეწველობის მუშაკებთან, საზოგადოებრივ ორგანიზაციებთან, რომლებიც გარემოს დაცვის პრობლემებზე მუშაობენ. ICON აქტიურად შეისწავლის ნანონაწილაკების უჯრედებთან მოქმედების პროცესებს, ის შეიმუშავებს სტანდარტებს და ტერმინოლოგიას. ICON-ში შექმნა სამეცნიერო-კვლევითი პროექტების ერთიანი საინფორმაციო ცენტრი, აგრეთვე მისი თაოსნობით შეიქმნა სამეცნიერო ლიტერატურის კატალოგი (http://icon.rice.edu/research.cfm), რომელშიც თავმოყრილია უახლესი ლიტერატურა ნანოტექნოლოგიებში ბოლო მიღწევების შესახებ და აგრეთვე ნანომასალების და ნანოტექნოლოგიების პოტენციური საშიშროების</p>

			<p>შესახებ. მონაცემთა ეს ბაზა ნანოტექნოლოგიებში საკონსულტაციო საბჭოს ეგიდით (Consultative Board for Advancing Nanotechnology – CBAN) ხელმისაწვდომია ნებისმიერი მსურველისთვის, თანაც ინტერაქტიურ რეჟიმშიც.</p>
<p>Lotus effect / Superhydrophobicity</p>	<p>Lotos Effekt m / Lotus Effekt m</p>	<p>Эффект лотоса</p>	<p>ლოტოსის ეფექტი /სუპერჰიდროფობურობა</p>
<div style="display: flex; justify-content: space-around;">  </div> <p>პოლიპროპილენის სუპერჰიდროფობური ზედაპირის მიკროფოტოგრაფია http://thesaurus.rusnano.com</p> <div style="display: flex; justify-content: space-around;">  </div> <p>Superhydrophobicity in perfection: the outstanding properties of the lotus leaf. Figure: (a) Lotus leaves, which exhibit extraordinary water repency on their upper side. (b) Scanning electron microscopy (SEM) image of the upper leaf side prepared by 'glycerol substitution' shows the hierarchical surface structure consisting of papillae, wax clusters and wax tubules. (c) Wax tubules on the upper leaf side. (d) Upper leaf side after critical-point (CP) drying. The wax tubules are dissolved, thus the stomata are more visible. Tilt angle 15°. (e) Leaf underside (CP dried) shows convex cells without stomata. Beilstein J. Nanotechnol. 2011, 2, 152-161. Hans J. Ensikat, Petra Ditsche-Kuru, Christoph Neinhuis and Wilhelm Barthlott http://www.google.de/imgres?q=superhydrophobicity</p>			<p>ლოტოსის ეფექტი (ლ.ე.) არის მყარი სხეულის ზედაპირის სითხით თითქმის სრული დაუსველებადობა, რასაც განაპირობებს მიკრო- და ნანოდონეზე მოცემული ზედაპირის რელიეფის თავისებურება და რომელიც იწვევს სითხის საკონტაქტო ზედაპირის შემცირებას მოცემული სხეულის ზედაპირთან. ლ.ე. აღმოაჩინა გერმანელმა ბოტანიკოსმა ვილჰელმ ბარტლოტმა (Wilhelm Barthlott) 1990-იან წლებში მცენარეთა ფოთლებისა და ყვავილების ფურცლების მასკანირებელი ელექტრონული მიკროსკოპით (SEM) კვლევისას. წყლით ცუდი დასველებადობის ბუნებრივი მოვლენა და ზედაპირის თვითაწმენდა, როგორც მისი შედეგი, დიდი ხანია შემჩნეულია სხვადასხვა მცენარეების ფოთლებსა და ყვავილების ფურცლებზე (ლოტოსი, ლერწამი, დედოფლის ყვავილი, წყალიკრეფია, ხანჭკოლა და სხვ.) და აგრეთვე მწერების და პეპლების ფრთებზე). SEM-ით კვლევისას აღმოჩნდა, რომ ამ ზედაპირების განსაკუთრებულობა მდგომარეობს მათ ხორკლიანობაში – მიკრო- და ნანოსკოპიული ზომის ეკლები, ბუსუსები ზედაპირზე წარმოქმნილია ჰიდროფობური ნივთიერებებით (კუტინი, კუტანი); ასეთ ზედაპირზე წყლის წვეთს აქვს შეხების მცირე ზედაპირი, ამიტომ არ შეკავდება მასზე, სცილდება მას და თან მიაქვს მტვერი, სოკოების სპორები, ბაქტერიები, ქუჩყი და სხვ., რასაც მივყევართ თვითაწმენდის ეფექტთან. ლოტოსის ფოთლის ზედაპირს ეხება მაგალითად, წყლის წვეთის ზედაპირის მხოლოდ 1% და დასველების კუთხე ფოთლის ზედაპირსა და წვეთს შორის აღწევს 170°-ს (როგორც</p>

Short dictionary (glossary) on nanochemistry and nanotechnology. Part III.

<p>კუტინი პოლიესტერის მსგავსი ნაერთია, რომელიც ცელულოზასთან, პექტინთან და ცვილთან ერთად შედის მცენარის უჯრედის კუტიკულაში (ლათ. Cuticula – გარსი, თხელი კანი; მცენარეთა კუტიკულა არის ფოთლების, ნაყოფის და ახალგაზრდა ტოტების ეპიდერმისის გარე ფენა) და განაპირობებს მის თითქმის დაუსველებადობას. კუტინი შეიძლება გაიხლიჩოს კუტინაზით და სოკოებით. ქიმიური თვალსაზრისით ის ჰეტეროპოლიმერია რთულეთერული ჯგუფით მონომერებს შორის. მონომერები შედგება C₁₆- ან C₁₈-ჰიდროქსიციხიმოვანი მჟავების ჩონჩხისაგან</p> <p>კუტანი არის კუტიკულის შემადგენელი მეორე პოლიმერი, ის ნახშირწყალბადოვანი პოლიმერია, მისი სტრუქტურა და სინთეზი ბოლომდე შესწავლილი არაა. ის არ შედის ყველა მცენარის კუტიკულაში. მცენარის დაცვითი თვისება კუტანს უფრო მეტი აქვს, ვიდრე კუტინს</p>		<p>ცნობილია, დასველების კუთხე სრული დასველებადობის შემთხვევაში ნულია, ხოლო სრული დაუსველებადობისას – 180°); როგორც აქედან ჩანს, ლოტოსის ფოთლი სუპერჰიდროფობურია. “ლოტოსის ეფექტის” საფუძველზე დღეისათვის შექმნილია მასალები და საფარები, რომელთა სუპერჰიდროფობობა განპირობებულია ზედაპირის დასტრუქტურებით, მათ შორის ნანოდონეზე.</p>	
<p>Magnetic fluid</p>	<p>Magnetofluid n</p>	<p>Магнитная жидкость</p>	<p>მაგნიტური ფლუიდი</p>
	<p>/Magnetisches Fluid n / Magnetierbare Flüssigkeit f / Magnetische Flüssigkeit f / Ferromagnetische Flüssigkeit f</p>	<p>/ Ферромагнитная жидкость</p>	
<p>/ Magnetic liquid</p>	<p>Magnetische Flüssigkeit f / Magnet-flüssigkeit f</p>	<p>Магнитная жидкость</p>	<p>/ მაგნიტური სითხე</p>
			<p>/ მაგნიტური ნანოსითხე</p>
<p>/ Ferrofluid</p>	<p>Ferrofluid n /Ferromagnetische Flüssigkeit f</p>	<p>Феррофлюид / Феррожидкость / Ферромагнитная жидкость</p>	<p>ფეროფლუიდი / ფეროსითხე / ფერომაგნიტური სითხე</p>
<p>/ Magnetic fluids</p>	<p>Magnetofluidе pl / Magnetische Fluidе pl / Magnetierbare Flüssigkeiten pl / Magnetische Flüssigkeiten pl / Ferromagnetische Flüssigkeiten</p>	<p>/ Магнитные жидкости / Ферромагнитные жидкости</p>	<p>მაგნიტური ფლუიდები</p>



მაგნიტომართვადი მაგნეტიტის ნაწილაკები გამოიყენება კიბოს სამკურნალოდ. მკურნალობის ეს მეთოდი – ჰიპერთერმია ეფუძნება იმას, რომ ცვლადი მაგნიტური ველით მოქმედებისას მაგნეტიტის ნაწილაკები ცხელდება და აფერხებს სიმსივნური უჯრედის ზრდას

სურათზე ნაჩვენებია РОСНАНО გამოფენაზე წარმოდგენილი შპრიცი მაგნიტური სითხით

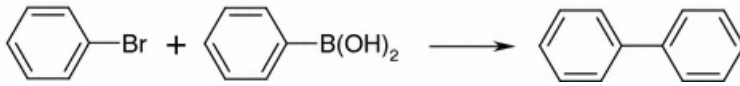
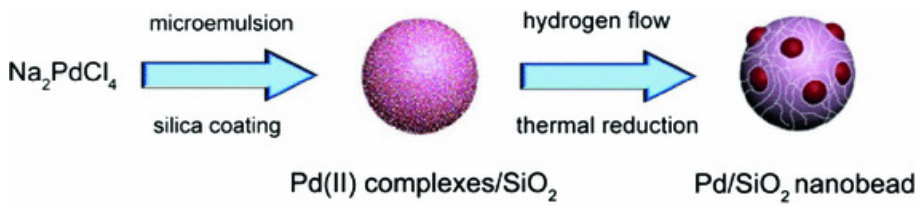
ქირურგიაშიც შეიძლება მ.ნ.ს.-ის გამოყენება ჰიპერთერმიისთვის (Germany); თუ საოპერაციო ადგილის გარშემო მუდმივ მაგნიტს მოვათავსებთ, მაშინ შპრიცით ვენაში ან არტერიაში წინასწარ შეყვანილი მაგნიტური სითხე წარმოქმნის საცობს, რაც გადახურავს სისხლის ნაკადს გაჭრის შემდეგ

<http://magneticliquid.narod.ru/authority/166.pdf>

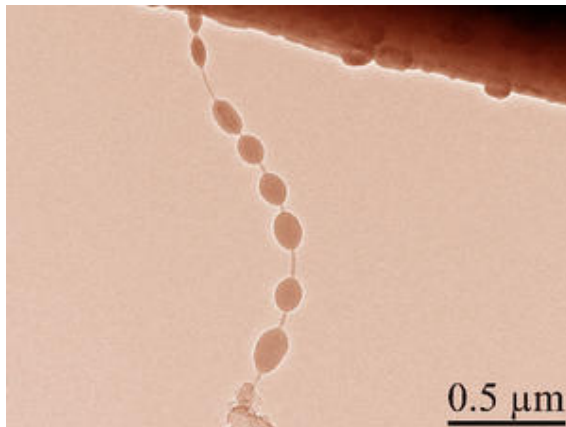
Journal of Magnetism and Magnetic Materials 225 (2001) 118
Успехи современного естествознания. 10 (2006) 6715

მდგრადობისთვის და კოაგულაციის საწინააღმდეგოდ იყენებენ ზან-ს. Fe_3O_4 -დან მიღებული მ.ნ.ს. შავი ფერისაა, ხოლო $\gamma-Fe_2O_3$ -ის და Mn-, Co-, Zn- და Ni-ფერიტების მ.ნ.ს.-ის შეფერილობა იცვლება მუქი ყავისფერიდან ნარინჯისფერ-წითლამდე; სინთეზის პირობებისაგან დამოკიდებულებით მ.ნ.ს.-ის ფერთა გამა შეიძლება ვცვალოთ. სპეციალური საღებარების ჩამატებისას მ.ნ.ს.-ში მიიღება მაღალდისპერსული, ფერთა ფართო სპექტრის სისტემები. მათ იყენებენ ბეჭდვით მრეწველობაში მაგნიტური საღებავების და მელნის მისაღებად. მ.ნ.ს.-ის მიღებისას სადისპერსიო არედ იყენებენ წყალს, ეთანოლს, აგრეთვე არაპოლარულ გამხსნელებს – ნახშირწყალბადებს, სილიკონებს. მ.ნ.ს. მრავალ წელს ინარჩუნებს მდგრადობას. მ.ნ.ს.-ის მომზადებისთვის მაგნიტური ნივთიერების მიკრო- და ნანონაწილაკებს იღებენ ფიზიკური მეთოდებით (დისპერგირებით ან კონდენსაციით, კერძოდ ლითონის ლაზერული აორთქლებით) და ქიმიური გზით. მათ ფართო გამოყენებას განაპირობებს მათი დენადობა და გარე მაგნიტური ველით მართვის შესაძლებლობა. მაგ., მათ იყენებენ: მაგნიტურ საცხებად ბურთულსაკისარებში, ზღვის, ოკეანის, ტბის წყლის ზედაპირებზე დაღვრილი ნავთობპროდუქტების შეგროვებისთვის – დაღვრილ ნავთობპროდუქტზე ვერტმფრენიდან გააშხეფებენ მაგნიტურ ნანოსითხეს, ის სწრაფად იხსნება ნავთობპროდუქტის ლაქაში, შემდეგ წყალში უშვებენ ძლიერ მაგნიტებს, ხდება ლაქის მიზიდვა, "შეკუმშვა", მას ტუმბოებით ამოქაჩავენ და წყლის ზედაპირი გასფთავდება; NASA-მა მ.ნ.ს. გამოსცადა კოსმოსური ხომალდის სივრცეში სტაბილიზაციისთვის; ამ მასალებს აქვს "მეხსიერება", რაც გამოიყენება ინფორმაციის შენახვისთვის; მათ იყენებენ მაგნიტოსითხურ შუასაღებებად როგორც სამჭიდროებელი საშუალებას, მასალების მაგნიტურ გამდიდრებაში, გაცივების სისტემაში, ბიოლოგიაში, მედიცინაში.

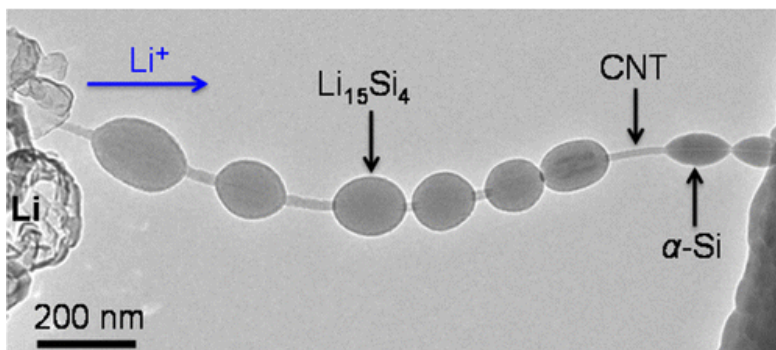
Metamaterial	Metamaterial n	Метаматериал	მეტამასალა
Metamaterials	Metamaterialien pl	Метаматериалы	მეტამასალები
 <p>სითხე უარყოფითი გარდატეხის მაჩვენებლით (მარჯვნივ) ჩვეულებრივ წყალთან – სითხესთან დადებითი გარდატეხის მაჩვენებლით (მარცხნივ) შედარებით</p> <p>http://www.weltderphysik.de/gebiete/stoffe/metamaterialien/ http://www.physik.highlights.de</p>			<p>ბერძნ. “მეტა” – ზღვარს მიღმა, ზემოთ. ბუნებაში არ არსებული, ხელოვნურად მიღებული კომპოზიციური, დასტრუქტურებული მასალები, რომელთა ელექტრომაგნიტური თვისებები არსებითად განსხვავდება მისი შემადგენელი კომპონენტების თვისებებისაგან და ისინი განისაზღვრება არა იმდენად შემადგენელ კომპონენტთა ფიზიკური და ქიმიური თვისებებით, არამედ მათი ხელოვნურად შექმნილი სტრუქტურით (რგოლის, მავთულის, რულონის და ა.შ. მსგავსი) და განსაკუთრებული მოწყობის რეზონანსული თვისებებით. ისინი შედგება მიკრონზე ნაკლები ზომის მიკროსტრუქტურებისაგან – მცირე ზომის ხელოვნური რეზონატორებისაგან. მეტამასალების (მ.მ.) ერთ-ერთი კლასს მიეკუთვნება მ.მ. გარდატეხის უარყოფითი მაჩვენებლით, რომლებსაც აგრეთვე ერთდროულად უარყოფითი აქვს დიელექტრული და მაგნიტური შეღწევადობებიც. მათი ოპტიკური თვისებები განსხვავებულია ტრადიციული მასალების თვისებებისაგან. ისინი ლითონებისა და დიელექტრული კომპონენტების კომპოზიტებია. მ.მ. გარდატეხის უარყოფითი მაჩვენებლით ელექტრომაგნიტური ტალღების რადიოდიამეტრულში მიღებული იყო 1999 წ. (Pendry J.B. et al. Science. 2006. v.312. p.1780.); ხილულული (380–780 ნმ) ოპტიკური უბნისთვის ასეთი მ.მ. მიიღეს აშშ (Iowa State Univ.) 2007 წ. Ag-ის საფუძველზე. 780 ნმ მისი გარდატეხის მაჩვენებელია 0.6; მ.მ.-ის პერსპექტულ კლასს მიეკუთვნება ფოტონური კრისტალები.</p>
Nanobead	Nanobead m	Нанобисер / Нанобусинка	ნანობურთულა / ნანომძივის მარცვალი
Nanobeads	Nanobeads pl / Nanometer-große Perlen f pl	Нанобусы / Нанобусинки	ნანობურთულები / ნანომძივების მარცვლები



ზოლ-გელ პროცესით მიღებულ SiO_2 -ზე Pd-ის კომპლექსური ნაერთის წყალბადით აღდგენით გარკვეულ გარემოში მიიღება Pd / SiO_2 -ის ნანომარცვლები, რომლებიც Pd-ის 2 ნმ დიამეტრის პაწაწვინტელა კლასტერებს შეიცავს. მიღებული ნანოსტრუქტურა ჩინებული კატალიზატორია Suzuki-ის შეუღლების რეაქციაში <http://link.springer.com/article/10.1007/s10562-012-0798-0>



სილიციუმის ნანომილაკზე გაზრდილი სილიციუმის ნანომივივი <http://spectrum.ieee.org/nanoclast/semiconductors/nanotechnology/nano-beads-of-silicon-could-string-together-liion-batteries-of-t>

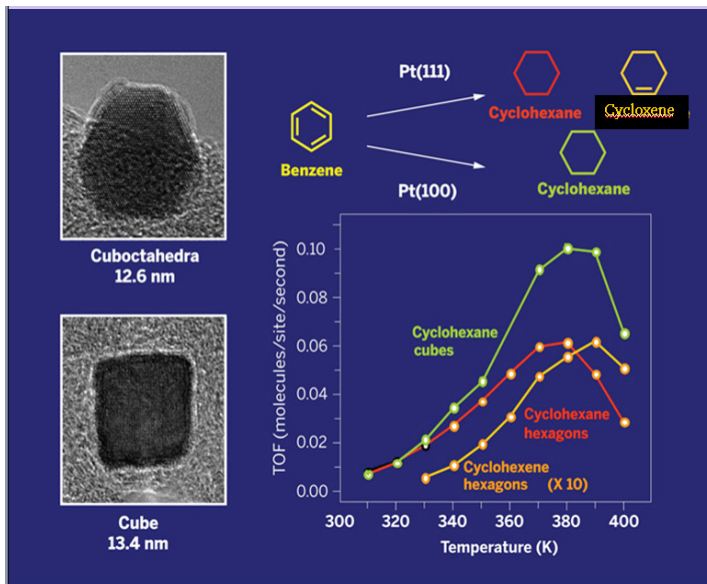


ნახშირბადის ნანომილაკზე გაზრდილი ლითიუმის შემცველი სილიციუმის ნანობურთულები <http://pubs.acs.org/doi/abs/10.1021/nn4001512> ACS Nano, 2013, 7 (3), pp. 2717-2724

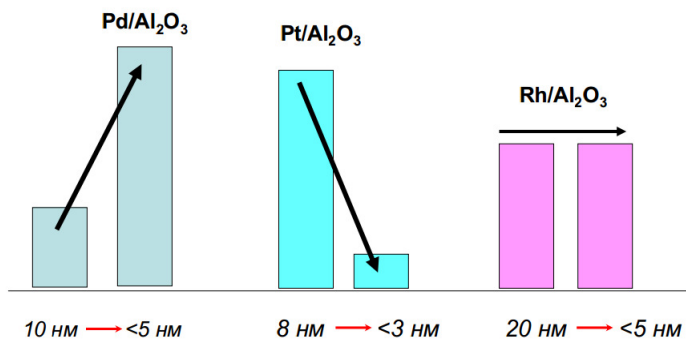
ნივთიერების ნანოზომის მარცვლების ბურთულები. ცნობილია: პოლიმერული ნანობურთულები – polymer beads დიამეტრით 0.1–10 მკმ, ნანოწერტილები – nanodots, ნანოკრისტალები – nanocrystals, ქვანტური ბურთულები – quantum beads; ამ ნანობურთულების ფლორესცენტული კრისტალის ჩიპებით გაჟღერებით შესაძლებელია მრავალგვარი ბიოლოგიური ურთიერთქმედების გაზომვა. აგრეთვე ის გარკვეული საფეხურია დიაგნოსტიკასა და მკურნალობაში. არსებობს ჰეტეროსტრუქტურებში ფაზათაშორისი არასტაბილობის პრობლემა. მისი დაძლევის ერთ-ერთი წარმატებული მაგალითია ნანობურთულების გამოყენება ანოდად ლითიუმ-იონურ ბატარეებში. პრობლემა მდგომარეობს იმაში, რომ ტრადიციულ ლითიუმ-იონურ ბატარეებში გრაფიტის ანოდის სივრცის ხანგრძლივობა დიდი არაა, უკეთესი ალტერნატივაა სილიციუმის ანოდები, მაგრამ ისინი სკდება დამუხტვა-განმუხტვის მცირე რაოდენობა ციკლების შემდეგ. სტენფორდის უნივერსიტეტში (აშშ) დაამზადეს ორკედლიანი სილიციუმის ნანომილაკი, რომელიც დაფარეს სილიციუმის ოქსიდის თხელი ფენით. ამ მასალის ანოდად გამოყენებისას მუხტი 10-ჯერ დიდხანს ინახება, ვიდრე გრაფიტის ანოდის შემთხვევაში და ის მუშაობს დამუხტვა-განმუხტვის 6000 ციკლის განმავლობაში. იგივე მიზნებისთვის მერილენდის უნივერსიტეტში (აშშ) სილიციუმის პაწაწვინტელა ბურთულები გაზარდეს ერთ-ერთი ორგანული ნაერთისა და სილიციუმის წყალბადნაერთის ურთიერთქმედებით ნახშირბადის ნანომილაკებზე, რომელთა დამეტრი ნაკლები იყო 50 ნმ-ზე. მიღებულ სტრუქტურა – “ნანომარცვლების მივივივი” თვითორგანიზებული ნანოსტრუქტურული სილიციუმია, რომელიც ასევე გამოიყენეს ანოდად ლითიუმ-იონიან ბატარეებში. აღმოჩნდა, რომ სილიციუმის ნანობურთულების ზრდა ინტენსიურია მათში ლითიუმის იონების შეყვანისას და მათი მოცილების შემდეგ მიღებული

ბურთულები არ სკდება და არ იშლება. სილიციუმის ნანომარცვლების მძივები ნახშირბადის ნანომილაკზე ერთმანეთის გასწვრივაა ჩალაგებული. Si-ის ნანომძივის მარცვლები (ბურთულები) 10000-ჯერ უფრო თხელია, ვიდრე ჩვეულებრივი ქაღალდის ფურცელი და 10-ჯერ უფრო მტკიცეა. ვიდრე კომერციულ ბატარეებში ანოდად გამოყენებული გრაფიტი.

Nanocatalyst	Nanokatalysator m	Нанокатализатор	ნანოკატალიზატორი
Nanocatalysts	Nanokatalysatoren pl	Нанокатализаторы	ნანოკატალიზატორები



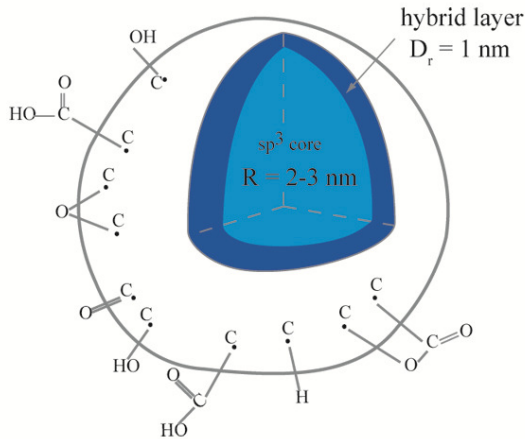
ნანოკატალიზატორის – პლატინის ნანონაწილაკების ფორმისაგან (კუბური და კუბოქტაედრის ფორმის კრისტალების წახნაგები) შერჩევითობის დამოკიდებულება ბენზოლის კატალიზური ჰიდრირების რეაქციაში
Platinum nanoparticle shape effects on benzene hydrogenation selectivity.
Nano Lett., 2007, 7 (10), pp. 3097-3101. Gabor A. Somorjai et al



Al₂O₃-ზე დაფენილი VIII ჯგუფის ლითონთა (Pd, Pt, Rh) ნანონაწილაკების კატალიზური აქტიურობის დამოკიდებულება ნანონაწილაკის ზომისაგან
<http://www.portalnano.ru/db/library/?action=download&num=1&id=182&field=files>

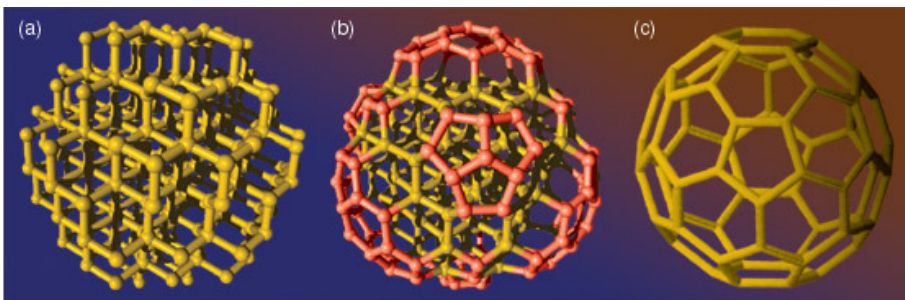
ნანოკატალიზატორი (ნ.კ.) ნანომეცნიერების, ნანომასშტაბური მეცნიერების (Nanoscience, Nanoscale science) დარგის – ნანოქიმიის შესწავლის ობიექტია. ნ.კ. კატალიზური თვისებების მქონე ობიექტია – ნივთიერებების და მასალების შემადგენელი ნანონაწილაკებია, რომელთა კატალიზურ თვისებებს (კატალიზური ცენტრის აქტიურობასა და შერჩევითობას) ჩვეულებრივი, კლასიკური კატალიზატორისაგან განსხვავებით მნიშვნელოვნად განაპირობებს მათი შემადგენელი სტრუქტურული ელემენტების ფორმა და ზომა, რომელიც 1-100 ნმ-ის რიგისაა.

Nanodiamond	Nanodiamant m	Наноалмаз / Ультрадисперсный алмаз, УДА, НА	ნანოალმასი
Nanodiamonds	Nanodiamanten pl	Наноалмазы / Ультрадисперсные алмазы	ნანოალმასები



ნანოალმასის კრისტალიტის სქემატური გამოსახულება

<http://www.google.de/imgres?q=nanodiamond&hl=de&biw=1280&bih=896&tbm=isch&tbnid=ajvh23UNSA-1QM:&imgrefurl=http://eng.thesaurus.rusnano.com/>

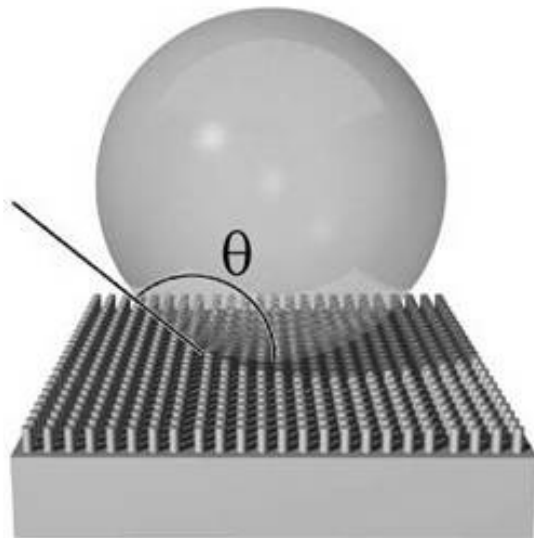


“In first-principles simulations of nanodiamond, (a) the surface of a 1.4-nanometer nanodiamond with 275 atoms spontaneously rearranges itself into (b) a fullerene at about 300 kelvins. These carbon clusters have a diamond core (yellow) and a fullerene-like reconstructed surface (red). (c) A classic 60-atom carbon buckyball”. Science and Technology. When Semiconductors go Nano. Nov. 2003

<http://www.google.de/imgres?q=nanodiamond&hl=de&biw=1280&bih=896&tbm=isch&tbnid=7dGe-VKunLi8PM:&imgrefurl=https://www.llnl.gov/str/November03/va>

ნანოალმასი (ნ.ა.) – ნახშირბადის ნანოკრისტალური მასალა ალმასის კრისტალური სტრუქტურით (იხ. Nano Studies, 6, 2012). ნ.ა.-ს ფხვნილისა თუ აფსკის სახით ალმასის ყველა თვისება აქვს – დიდი სიმაგრე და ინერტულობა. მაგრამ მასში ნაწილაკების ძალიან მცირე ზომების გამო ნახშირბადის ატომების უდიდესი ნაწილი ზედაპირზეა, ამიტომ ჩვეულებრივი ალმასისაგან განსხვავებით, ნანოალმასი ძალიან აქტიურია: ის იჟანგება 450°C-ზე, ჩვეულებრივი ალმასი – 900°C-ზე; ნანოალმასი 1000°C-ზე გადადის გრაფიტში, ჩვეულებრივი ალმასი – 1800°C-ზე; დეტონაციური სინთეზით მიღებული ალმასის ზედაპირი ყოველთვის დაფარულია წყალბადის ან სხვა ფუნქციური ჯგუფებით – სინთეზისას ასაფეთქებელი ნივთიერების შემადგენელი ატომებით. განსაკუთრებულ თვისებებს ამჟღავნებს სრულიად სუფთა, მხოლოდ ნახშირბადის ატომებისაგან შემდგარი, ნანოალმასის ზედაპირი. ამ შემთხვევაში თავისუფალი სავალენტო ერთეულების ხარჯზე ხდება ზედაპირული 5- და 6-წევრიანი ციკლების წარმოქმნა. ქვანტურ-ქიმიური გამოთვლებით 275 ატომის შემცველი ნანოალმასისთვის ნაჩვენებია იყო, რომ ეს ციკლები ერთმანეთთან ისევეა შეერთებული, როგორც ფულერენის (C₆₀) სტრუქტურაში, იხ. სურ. მარცხნივ. ამგვარად, ოთახის ტემპურატურაზე ნანოალმასს აქვს ალმასის ბირთვი და ფულერენის ზედაპირი. ნ.ა.-ს აქვს დიდი ზედაპირი, არის ბიომეთავსებადი, იყენებენ ბიოლოგიასა და მედიცინაში.

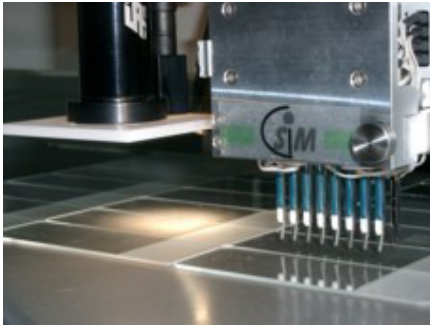
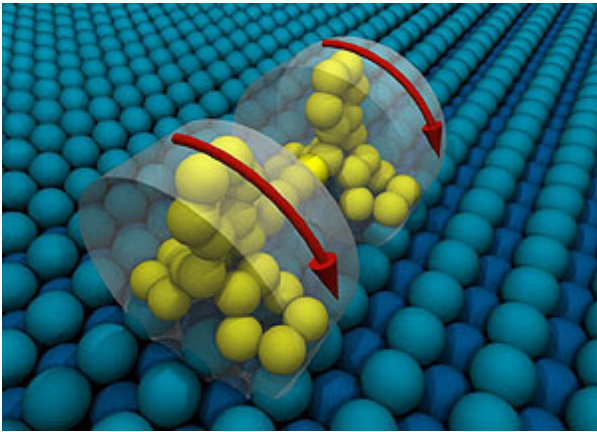
Nanograss	Nanogras n	Нанотрава	ნანობალახი
 <p data-bbox="236 1160 1002 1285">“ნანობალახის” ელექტრონული მიკროფოტოგრაფია. 350 ნმ დიამეტრის და 0.007 ნმ სიმაღლის Si-ის უწვრილეს ღეროებს შორის მანძილია 1 მკმ</p> <p data-bbox="475 1330 767 1368">kbogdanov5.narod.ru</p>			<p data-bbox="1107 344 1444 2078">აშშ ფირმის “Lucent Technologies” კვლევითი განყოფილების Bell Labs თანამშრომლებმა გაზარდეს სილიციუმის ფირფიტაზე ბუსუსებანი (ხაოიანი) ნანოსტრუქტურა “ნანობალახი”; ეს “ნანოგაზონი” ანციფერებს ადამიანს თავისი მკაცრად რეგულარული სტრუქტურით. “ნანობალახის” ნიმუში წარმოადგენს 350 ნმ დიამეტრის და 7 მკმ სიმაღლის Si-ის უწვრილეს ღეროებს, რომელთა შორის ჰაერია და მანძილი ღეროთა შორის ფიქსირებულია, სხვადასხვა ნიმუშებში ის 1–4 მკმ-ია. სილიციუმის ასეთი მოწესრიგებული სისტემა მიიღეს სილიციუმის ფირფიტის ამოჭმით პლაზმაში ფოტორეზისტორით, მერე მასზე ჟანგვით გაზარდეს დიელექტრიკის (სილიციუმის ოქსიდი) თხელი ფენა, ხოლო ზემოდან მთელი ნანოსტრუქტურა დაფარეს ჰიდროფობური პოლიმერის თხელი აფსკით. მიღებული მასალა სუპერჰიდროფობურია: “ნანობალახში” მოხვედრილი წყლის წვეთები თითქოს ჰაერშია გამოკიდებული, ისინი “ნანობალახის” ღეროების წვერობზეა შეკავებული. “ნანობალახის” ნანოღეროებს შორის წყლის წვეთი ვერ ხვდება, რადგან ამას ხელს უშლის სითხის მაღალი ზედაპირული დაჭიმულობა. Si-ის “ნანობალახთან” წყლის წვეთების სფეროების შეხების ზედაპირის ფართობი ძალიან მცირეა (საკონტაქტო კუთხეა 180°), ამიტომ ისინი ძალიან მოძრავია – ზედაპირის უმნიშვნელოდ დახრისას ისინი ჩამოვარდება წვეთის სახით ე.ი. არ განითხვება. “ნანოგაზონი”, რომელიც “ლოტოსის ეფექტის” საფუძველზეა შექმნილი გამოიყენება სუპერჰიდროფობური, თვითგასუფთავებადი საფარების შესაქმნელად. დასველებალობა შეიძლება ვარგულიროთ წვეთსა და ზედაპირს შორის მოდებული ძაბვით – მისი გაზრდისას წყლის სფერული წვეთი თითქოს მიეწებება ზედაპირს, მცირდება კიდური კუთხის სიდიდე; ძაბვის გაზრდა–შემცირებით წვეთი შეიძლება “ვაცეკვოთ”</p>

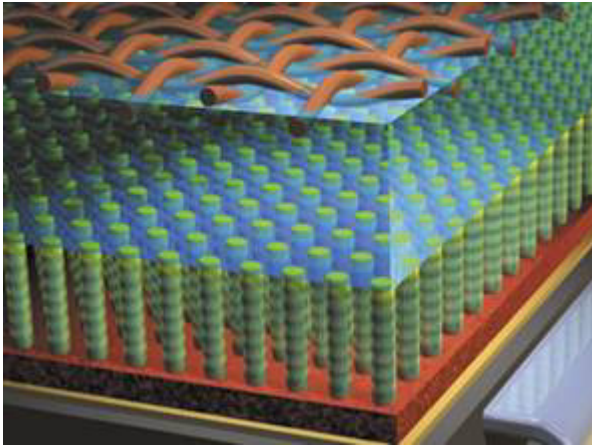


სქემა – წყლის წვეთი “ნანობალახზე”

kbogdanov5.narod.ru

ნანობალახის ნანოდეროვზე. წყლის და ჰაერის გარდატეხის მაჩვენებელი სხვადასხვაა, გაჩერებული წყლის წვეთი ერთგვარი თხევადი ლინზაა. “ცეკვის” დროს იცვლება წვეთის ზედაპირის სიმრუდე და შესაბამისად – გარდატეხის თვისება, მისი ფოკუსური მანძილი. თხევადი ლინზის მოქმედება ჰგავს ადამიანის თვალისას, რომელიც ფოკუსირდება ბროლის სიმრუდით. “თხევადი” დისკლეი და ვიდეო წვეთის “ქალაქზე”, რომელიც ელექტროდასველების ეფექტით იმართება – ეს არა მარტო თხევადი ლინზაა, ის ეფექტური და მაღალსიჩქარიანი მინიატურული გადამრთველიცაა, რომელიც პოულობს გამოყენებას ახალი თაობის დისკლეებში. საკმარისი ძაბვის მოდებისას არათუ შემცირდება წვეთის კიდური კუთხე, არამედ წვეთი ნაწილობრივ ჩაიწოვება ნანობალახში და შეასველებს ნანობალახის ზედაპირს; თანაც ამ დროს ის კარგავს ფორმას, ძვრადობას და გაჩხერილია ნანობალახში. ძაბვის შემცირებით წვეთი კვლავ უკან წავა, ნანობალახის წვეროსკენ და აღიდგენს სფერულ ფორმას და ძვრადობის თავისუფლებას. ნანობალახს იყენებენ აგრეთვე მიკროსტრუქტურების ელემენტთა გასაცივებლად, მიკროფლუიდიკაში, გადამრთველად ოპტიკურბოჭკოვან ქსელებში. ნანოტექნოლოგიები იძლევა შესაძლებლობას შეიქმნას “ნანობალახის” საფუძველზე თვითგასუფთავებადი საფარები და მასალები, რომლებსაც აქვს აგრეთვე წყალუკუდების (წყალგანზიდვის) თვისება. მასალები, მიღებული ასეთი ქსოვილიდან, მუდმივად სუფთაა. უკვე ამზადებენ თვითგასუფთავებად საქარე მინებს, რომელთა გარეთა ზედაპირი ნანობალახიანია. არსებობს ავტომობილების ბორბლების თვითგასუფთავებადი დისკები, იწარმოება საღებავები, რომლითაც გარედან ღებავენ სახლებს და რომლებსაც არასოდეს ეწებება მტვერი. დღეისათვის მიღებულია აგრეთვე GaAs-ის, Ge-ისა და ZnO-ის “ნანობალახები”.

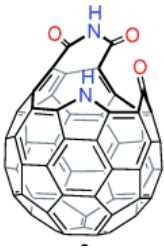
<p>Nanoplotter</p>	<p>Kurvenzeichner m / Plotter m</p>	<p>Наноplotтер</p>	<p>ნანოჩამბაზავი</p>
<div style="text-align: center;">  <p>Nano-plotter NP2.1 http://www.google.de</p> </div>			<p>ნანოკალმისტარი ბევრი წვეროთი. მოწყობილობა, რომელსაც შეუძლია გამოსახოს 30 მოლეკულის სისქის და 1 მოლეკულის სიმაღლის ხაზები. ამავე დროს ერთდროულად ასახავს ათამდე იდენტურ სურათს. გამოიყენება ელექტროსქემების მინიატურიზაციაში, ორგანული და ბიოლოგიური მოლეკულების, როგორცაა დნმ, ზუსტი ასახვისთვის და მრავალგვარი სამედიცინო სენსორის განთავსებისთვის უფრო მცირე ფართობზე, ვიდრე ნემსის წვეროა.</p>
<p>Nanorader</p> <p>Nanoraders</p>	<p>Nanorad n</p> <p>Nanoräder pl</p>	<p>Наноколесо</p> <p>Наноколеса</p>	<p>ნანობორბალი</p> <p>ნანობორბლები</p>
<div style="text-align: center;">  <p>ნანობორბლის გორვითი მოძრაობის სქემატური წარმოდგენა</p> <p>http://derstandard.at/2741026</p> </div>			<p>“ნანობორბალი” შექმნეს სულ რამდენიმე ატომისაგან (Leonhard Grill, Freien Universität Berlin). TEM-გამოკვლევებით ნაჩვენებია, რომ მისი დიამეტრია 0.8 ნმ და ის დაგორავს დამუშავებული სპილენძის ზედაპირზე. ფიზიკოსებმა ტრიპტიცინის 2 მოლეკულა შეაკავშირეს ნახშირბადის 4 ატომის უწვრილესი ღერძით და ის მოათავსეს ნატიფად დასტრუქტურებული სპილენძის ზედაპირზე. მიკროსკოპში აკვირდებოდნენ ამ ღერძის გადაადგილებას, როდესაც მას TEM-ის ნემსით უბიძგებდნენ. ნანობორბალი მრგვალი არაა. მგორავი მოლეკულა ნამცეცა სამეხილა ვარსკვლავს ჰგავს, მისი მოძრაობა რამდენადმე ოღონოლოდო გზაზე გადაადგილებას ჰგავს, ბიჯია 120°. ეს ექსპერიმენტები მიმართულია სამომავლოდ მოლეკულური მოძრაობის კონტროლის შესაძლებლობისკენ და ახალი ნანომანქანების პროექტირებისკენ.</p>
<p>Nanoswitch</p> <p>Nanoswitches</p>	<p>Nanoschalter m</p> <p>Nanoschalter pl</p>	<p>Нановыключатель</p> <p>Нановыключатели</p>	<p>ნანოგადამრთველი</p> <p>ნანოგადამრთველები</p>



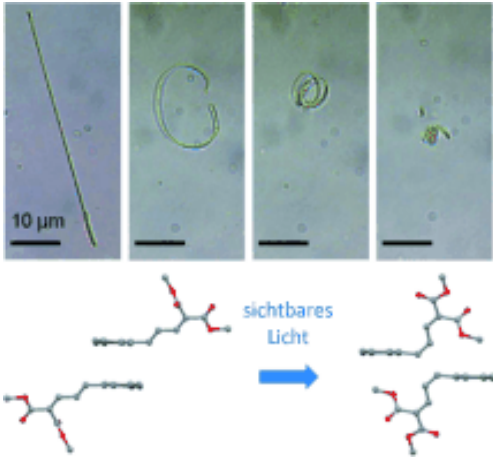
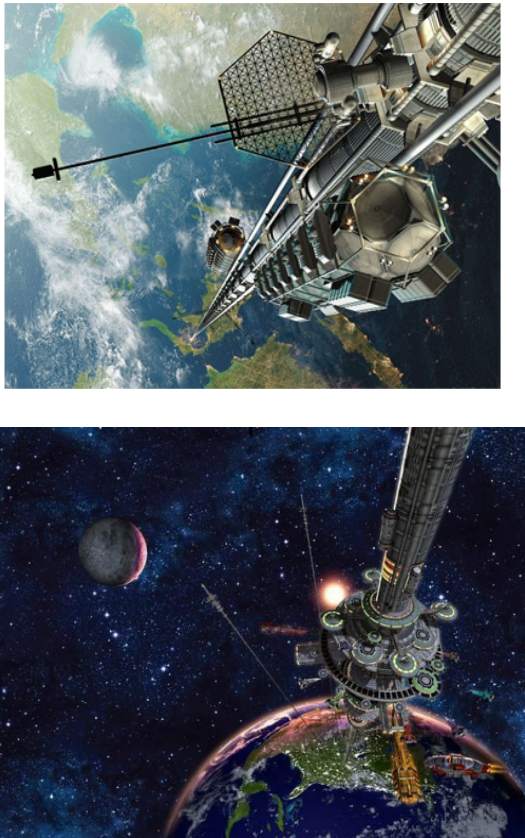
ნანოგადამრთველი ბატარეებისთვის. 3 ნმ დიამეტრის ნანოღეროებიანი “ნანობალახის” სქემატური გამოსახულება, რომელიც იზრდება ბატარეის ერთ-ერთ ელექტროდზე. ნანობუსუსების მასალის ჰიდროფობური თვისებების გამო (ლურჯი ფერის) ელექტროლიტის ხსნარი ვერ უახლოვდება (წითელი ფერის) ელექტროდს და ბატარეა არ კარგავს თავის სიმძლავრეს მრავალი წლის განმავლობაში

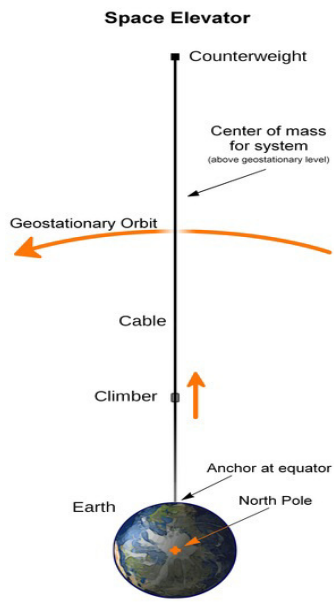
Scientific American, 2006, Feb, p. 73 (kbogdanov5.narod.ru).

საინფორმაციო ტექნოლოგიებში ნანოგადამრთველი (ნ.გ.) არის მოწყობილობა, რომელიც იცვლის თვისებას მდგომარეობებში ჩართვა / გამორთვა (on / off) და არის ძალიან პატარა. მაგალითად, მანჩესტერის უნივერსიტეტში გრაფენისაგან დაამზადეს 10 ატომის სიგანის და 1 ატომის სისქის ნ.გ. ნ.გ.-ის მაგალითია გადამრთველი ბატარეებისთვის: შენახვისას არამომუშავე ბატარეების 85% თითქმის მთლიანად განიმუხტება; ამის მიზეზი ისაა, რომ მათში მუდმივად ერთმანეთთან შეხებაშია ელექტროდები და ელექტროლიტი; თანდათან იცვლება ელექტროლიტის იონური შედგენილობა და ელექტროდების ზედაპირი, რაც ამცირებს ბატარეის ენერგოტევადობას. ამის თავიდან ასაცილებლად ელექტროლიტისაგან ელექტროდების ზედაპირს იცავს წყლით არადასველებადი ნანობუსუსებით, რაც “ლოტოსის ეფექტის” და ელექტრო-დასველების იმიტაციაა (იხ. სურ.). ეს სისტემა ნანოგადამრთველია ბატარეასთვის. სურათზე (მწვანე ფერით აღნიშნული) ნანობუსუსები არ ახებენ (ლურჯ) ხსნარს (წითელი ფერით აღნიშნულ) ელექტროდებს. ბატარეის ამუშავებისთვის ნანობუსუსებს მოსდებენ მცირე ძაბვას, ისინი ხდება დასველებადი, რის გამოც ელექტროლიტი ავსებს ელექტროდებს შორის მთელ სივრცეს და ბატარეა მოდის სამუშაო მდგომარეობაში.

Open-cage azafullerene	Offenes Azafulleren n	Азафуллерен с открытыми клетками	აზაფულერენი გახსნილი ღრუებით
			<p>/ გახსნილ ღრუიანი აზაფულერენი</p> <p>ფულერენების ნაწარმი კეტიმიდური ჯგუფით გახსნის ადგილზე.</p>

<http://onlinelibrary.wiley.com/doi/10.1002/ange.201300973/abstract>

Photoinduced nanowires	Photoresponsive Nanodrähte m pl	Фотоиндуцированные нанопроволочки	ფოტოინდუცირებული ნანომავთულები
 <p data-bbox="156 826 1075 864">http://onlinelibrary.wiley.com/doi/10.1002/ange.201302323/abstract</p>			<p data-bbox="1109 414 1444 719">სინათლის იმპულსის მოქმედებით, მაგალითად, ანტრაცენ-9(1,3-ბუთადიენის) ნაწარმები ფორმას იცვლის ("იგრძობა, იღუნება"), რაც დაკავშირებულია E და Z იზომერების ფოტოიზომერიზაციასთან $E \rightleftharpoons Z$, რის შედეგადაც იზომერების წარმოქმნება მოლეკულური ნანომავთულები.</p>
Space elevator	Weltraumlift m /Weltraumaufzug m	Космический лифт	კოსმოსური ლიფტი
 <p data-bbox="167 1937 1066 2011">იაპონელები აპირებენ 2050 წლისთვის კოსმოსური ლიფტის აგებას http://www.google.de</p>			<p data-bbox="1109 996 1444 2027">კ. ციოლკოვსკიმ (1857–1935) ეიფელის კოშკის დათვალიერების შემდეგ 1895 წ. გამოთქვა იდეა "კოსმოსური კოშკის" შესახებ, რომელიც შედგებოდა კოჭის, კაბელის და გეოსტაციონარული ორბიტისაგან. ეს იდეა შემდეგ ასახული იყო ფანტასტი მწერლის არტურ კლარკის (Arthur Clarke) რომანში "A Space Odyssey", 2001 წ. და წიგნში "The Fountains of Paradise". ზოგიერთი ამერიკული (Southwest nanotechnologies, Lift Port Group, Carbonnanotechnologies) და იაპონური (Obayashi) ფირმა მუშაობს ასეთი ფანტასტიკური პროექტის რეალიზაციაზე. ამ იდეის რეალიზაციაზე მუშაობის დაწყება შესაძლებელი გახდა იაპონელი მეცნიერის Sumio Iijima-ის მიერ 1991–1993 წლებში ნახშირბადის ნანომილაკების (ნ.ნ.მ.) მიღების შემდეგ. მეცნიერებმა ისწავლეს ნ.ნ.მ.-ის დაგრეხვა და მისგან ბოჭკოს მიღება. ის 20-ჯერ უფრო მტკიცეა და 6-ჯერ უფრო მსუბუქია ფოლადისაზე. ასეთი მასალა მისაღებია ზაგირის დამზადებისთვის. იაპონური (Obayashi) ფირმის პროექტით მსუბუქი და ამავედროულად მტკიცე მასალისაგან – ნახშირბადის ნანომილაკებისაგან ან შესაძლოა გრაფენისაგან</p>

 <p>ლიფტი ზემოთ იმომრავებს დედამიწის ზედაპირის კოსმოსურ სადგურთან შემაერთებელი ბაგირით; მისი საჭირო სიგრძეა 96000 კმ; კოსმოსური სადგური იქნება გეოსტაციონარულ ორბიტაზე ე.ი. ის "უძრავად" ჩამოკიდებულია დედამიწის ზემოთ. ბაგირი მხოლოდ აერთებს დედამიწის ზედაპირს კოსმოსურ სადგურთან და არაა მასზე ჩამოკიდებული. ფაქტობრივად ბაგირი თვითონ დგას დედამიწის ზედაპირის პერპენდიკულარულად ცენტრიდანული ძალის მოქმედებით. ის მხოლოდ გრძელი უნდა იყოს, რომ მიწვდეს სადგურს ცაში. კოსმოსური ლიფტის შექმნისას პრობლემა მხოლოდ ბაგირშია; თუ ის ფოლადის იქნება, უკვე 70 კმ სიგრძის, საკუთარი წონის მოქმედებით გაწყდება. გამოთვლები აჩვენებენ, რომ ბაგირს უნდა ჰქონდეს რთული ფორმა. მისი სისქე ექსპონენციალურად უნდა გაიზარდოს დედამიწის რამდენიმე რადიუსის სიმაღლეზე, სადაც იქნება ორბიტალური სადგური, მერე კი თანდათან უნდა შემცირდეს, რათა შეიქმნას ბაგირის სამუშაო ნაწილის ცენტრიდანული საპირწონე. ფოლადის ბაგირის შემთხვევაში დედამიწის ზედაპირთან მისი დიამეტრი 1 სმ უნდა იყოს, ორბიტაზე კი რამდენიმე ასეული კმ! ამიტომ ამ ამოცანების შესრულებისთვის საჭიროა უფრო მსუბუქი ($d < 2000$ კგ/სმ³) და უფრო მტკიცე მასალები (გარღვევა სიმტკიცეზე: 100 გპა). ამ მოთხოვნებთან ახლოს არის მხოლოდ ნახშირბადის ერთკედლიანი ნანომილაკები, თანაც ერთეულოვანი მილაკისთვის, რომლის სიგრძე ასეული. ე.ი. საჭიროა ბაგირის დაწვანა მრავალი მილაკისაგან, მაგრამ ცხადია, ამ დროს სიმტკიცე შემცირდება.</p>	<p>დამზადებული სპეციალური ბაგირი დაჭიმულ მდგომარეობაში იქნება ცენტრიდანული ძალებით. ჯერჯერობით მიღებული ნახშირბადის ნანომილაკების სიგრძე 20 სმ-ია, ხოლო დიამეტრი რამდენიმე ნმ. გრძელდება მუშაობა ამ ნანომასალების სრულყოფაზე. NASA-ის ხელშეწყობით ამერიკული ფირმა High Lift System აწარმოებს ამწის კონსტრუირებას, რომელიც ბაგირზე იმომრავებს. კერძო კომპანია LiftPort გააკეთა ინფორმაცია 400 მ-იანი კოსმოსური ლიფტის პროტოტიპის წარმატებით გამოცდაზე და გააკეთა განაცხადი 2031 წლისთვის ორბიტაზე ტვირთების კომერციულ გადაზიდვაზე და ტურისტების გადაყვანაზე.</p>
------------------------------------------------------------------------------------------------------------------------------------------------------------------------------------------------------------------------------------------------------------------------------------------------------------------------------------------------------------------------------------------------------------------------------------------------------------------------------------------------------------------------------------------------------------------------------------------------------------------------------------------------------------------------------------------------------------------------------------------------------------------------------------------------------------------------------------------------------------------------------------------------------------------------------------------------------------------------------------------------------------------------------------------------------------------------------------------------------------------------------------------------------------------------------------------------------------------------------------------------------------------------------------------------------------------------------------------------------------------------------------------------------------------------------------------------------------------------------------------	-----------------------------------------------------------------------------------------------------------------------------------------------------------------------------------------------------------------------------------------------------------------------------------------------------------------------------------------------------------------------------------------------------------------------------------------------------------------------------------------------------------------------------------------------------------------

References

1. Г. Эрлих. Малые объекты – большие идеи. 2011, Москва: БИНОМ – Лабор. знаний.
2. Л. Уильямс, У. Адамс. Нанотехнологии. Путеводитель. 2010, Москва: Эксмо.
3. Н. Кобаяси. Введение в нанотехнологию. 2008, Москва: БИНОМ – Лабор. знаний.
4. У. Хартман. Очарование нанотехнологии. 2008. Москва: БИНОМ – Лабор. знаний.
5. И. П. Суздалев. Нанотехнологияю физико-химия нанокластеров, наноструктур и наноматериалов. 2009, Москва: Книжный дом “ЛИБРОКОМ”.
6. Англо-русский нанотехнологический словарь. <http://pornano.ru/glossary/index.php?letter=P&ctg=7>
7. Словарь нанотехнологических и связанных с нанотехнологией терминов. Электронный словарь. РОСНАНО. 2009. <http://thesaurus.rusnano.com>
8. Linguee.de – Das Web als Wörterbuch. <http://www.linguee.de/>
9. Dictionary of nanotechnology (Nanodictionary). <http://www.nanodic.com/>
10. ENZYKLO. Online Enzyklopädie. <http://www.enzyklo.de/Begriffe/>
11. <http://www.dict.cc>
12. www.nano.org.uk/nano/glossary
13. <http://www.nano.bam.de/en/glossar/index.htm>
14. <http://www.nano.bam.de/de/glossar/index.htm>
15. <http://dict.leo.org/Englisch-Deutsch/.html>
16. А. А. Елисеев, А. В. Лукашин. Функциональные наноматериалы. 2010, Москва: Физматлит.
17. რუსულ-ქართულ-ინგლისურ-გერმანული ქიმიური ლექსიკონი (რედ. და გამომ. ვ. დოლიძე, ვ. ციციშვილი). 2004, თბილისი: უნივერსალი.
18. ტექნიკური ტერმინოლოგია. ქართულ-რუსული ნაწილი (რედ. რ. დვალი, რ. ღამბაშიძე). 1982, თბილისი: მეცნიერება.

MODELING OF THE QUASI-DIELECTRIC STATE IN
PbSnTe AND PbSnSe NANOLAYERS WITH HIGH
CONCENTRATION OF NONSTOICHIOMETRIC DEFECTS

A. M. Pashaev¹, O. I. Davarashvili², M. I. Erukashvili²,
Z. G. Akhvlediani^{2,3}, L. P. Bychkova², V. P. Zlomanov⁴

¹National Aviation Academy of Azerbaijan
Baku, Azerbaijan

²I. Javakhishvili Tbilisi State University
Tbilisi, Georgia
omardavar@yahoo.com

³E. Andronikashvili Institute of Physics
I. Javakhishvili Tbilisi State University
Tbilisi, Georgia
zairaak@yahoo.com

⁴M. Lomonosov Moscow State University
Moscow, Russia

Accepted September 10, 2013

I. Introduction

In a number of works, it was suggested using the effective “negative” pressure realized when the layers grow on the substrates with a high lattice constant for creation of the dielectric state [1 – 3]. The strain formed due to the mismatch, for instance, in the layers of PbSe and also of PbSnTe and PbSnSe solid solutions, grown on the BaTe and BaF₂ substrates, cause the increase in the forbidden gap width. If such semiconductor layers are doped with the impurities having variable valency, such as In or Cr, the impurity level shifts to the midgap.

Also, if the concentration of impurities exceeds the concentration of nonstoichiometric defects, it compensates the electric activity of the defects and of one another. At the same time, being stabilized, the Fermi level matches with the impurity level. In works [4, 5] the layers of that kind were considered.

In this work, we model the shift of the In and Cr levels in the PbSnTe and PbSnSe solid solutions during their growth on the BaTe and BaF₂ substrates, and analyze the decrease in the concentration of current carriers in the layers.

II. The model of creation of the stabilized Fermi level in the forbidden gap of IV–VI semiconductors under effective “negative” pressure

Showing donor and acceptor properties at their high concentration, In and Cr impurities with variable valency in IV–VI semiconductors compensate the electrically active nonstoichiometric defects (their concentration is $> 5 \cdot 10^{18} \text{ cm}^{-3}$) and one another. For both compositions of solid solutions PbSnTe and PbSnSe, the Fermi level stabilizes, changing its energy level. For binary compounds, the above-mentioned impurity levels are detected in the conduction band, while in the solid solutions they shift first to the bottom of the conduction band and then to the midgap, as the concentration of tin increases [6, 7]. The stabilized Fermi level shifts to the midgap not only with increasing tin concentration in the solid solutions, but also with increasing effective “negative” pressure.

By using both these factors, it is possible to shift the stabilized Fermi level significantly into the forbidden gap depth and to decrease the concentration of current carriers. The **Figure 1** shows the pressure dependence of the changes in the locations of In and Cr impurity levels for the semiconductors of the compositions PbSnTe:In and PbSnSe:Cr.

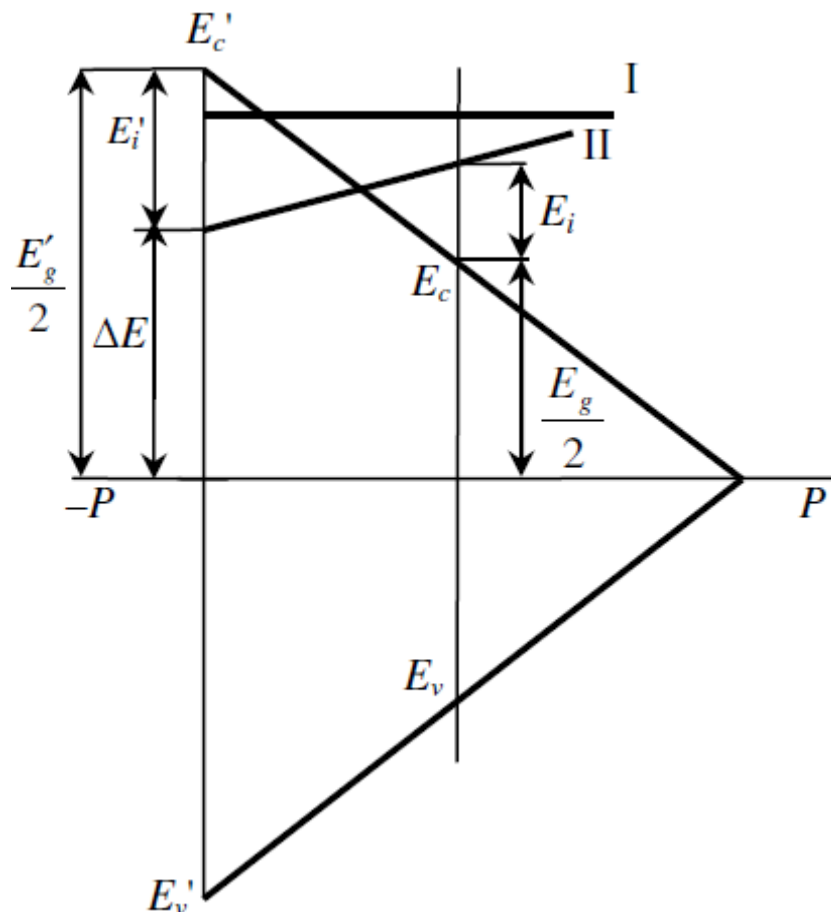


Figure 1. Impurity level shift to the midgap of IV–VI semiconductors under effective “negative” pressure: I – PbSnSe:Cr and II – PbSnTe:In (this case is considered in detail).

It should be noted that the location of the Cr impurity level does not change in respect to the midgap with increasing pressure. In the general case, the modulus of energy distance of the impurity level from the changed edge of the conduction band (as a result of an increase in the forbidden gap width), as is obvious from the **Figure 1**, can be represented by subtracting energy ΔE by which the impurity level is away from the midgap of the new half-width of the forbidden gap. This energy makes up

$$\Delta E = E_i + \frac{\Delta E_g}{2} - \sigma \frac{dE_i}{dp},$$

where E_i is the initial location of the impurity level in the unstrained semiconductor; $\Delta E_g / 2$ is the initial half-width of the forbidden gap; $\sigma dE/dp$ is the impurity level shift under effective “negative” pressure. Then the new location of the impurity level modulo from the new edge of the conduction band will be determined as follows:

$$E'_g = \frac{E'_g}{2} - E_i - \frac{E_g}{2} + \sigma \frac{dE_i}{dp} = \frac{\Delta E_g}{2} - E_i + \sigma \frac{dE_i}{dp}. \quad (1)$$

Here the values of dE_i/dp are taken from the experimental data. The values of σ are calculated by the formula $\sigma = E\varepsilon/(1-\nu)$, where E is the elastic modulus; ν is the Poisson ratio; $\varepsilon = 1 - a_s/a_l$ is the deformation, a_s and a_l being the lattice constants of the substrate and the layer, respectively. The values of ΔE_g for different orientations of substrates are determined by the formulae:

$$\Delta E_g(100) = \frac{2}{3}(3D_d + D_u) \left(1 - \frac{c_{12}}{c_{11}}\right) \varepsilon, \quad (2)$$

$$\Delta E_g(111) = 2 \left(D_d \frac{6c_{44}}{c_{11} + 2c_{12} + 4c_{44}} - D_u \frac{c_{11} + c_{12} - 2c_{44}}{c_{11} + c_{12} + 4c_{44}} \right) \varepsilon, \quad (3)$$

where D_d and D_u are the deformation potential constants; c_{11} , c_{12} and c_{44} are the elastic constants. The locations of impurity levels at partial deformation are calculated via the relation $\varepsilon = \varepsilon_{\max} / r_i$ ($r_i = 2, 4, \dots$). The concentration of current carriers is determined by the formula $n = N_c F_{1/2}(\eta)$, where N_c is the effective density of states, $N_c = 4.82 \cdot 10^{15} (T m_n / m_0)^{3/2} \text{ cm}^{-3}$, $F_{1/2}(\eta)$ is the Fermi–Dirac integral, $\eta = (E_F - E_c)/kT$.

III. The decrease in the concentration of current carriers in PbSnTe:In and PbSnSe:Cr nanolayers

The deformation in the layers ε under effective “negative” pressure is determined by the layer thickness [1, 2]. At $\varepsilon = 0.01$ and higher, the layer thickness is < 200 nm. The **Table 1** gives the data on the components considered in the model and entering formulae (1 – 3) for solid solution compositions PbSnTe and PbSnSe with the value of x (SnTe, SnSe) = 0.1, 0.2. For computation of the strain, the elastic modulus was varied within the range of $E = (5 - 8) \cdot 10^{11} \text{ dyne / cm}^2$, the Poisson ratio $\nu = 0.38 - 0.40$. At computation of ΔE_g , the elastic constants made up $c_{11} = 13.4$, $c_{12} = 1.97$ and $c_{44} = 1.56 \text{ dyne / cm}^2$ for PbSe, and $c_{11} = 10.9$, $c_{12} = 0.77$ and $c_{44} = 1.21 \text{ dyne / cm}^2$ for PbTe. For the In- and Cr-doped solid solutions, the increase in the elastic constants was within 35 – 40 %.

Table 1. The properties of the doped layers of IV–VI semiconductors at 77 K in the conditions of mismatch.

Structure	Content x , impurity	Mismatch $\varepsilon = \Delta a / a$	Initial width of the forbidden gap E_g , meV	Strain under mismatch $\Delta\sigma$, kbar	Changed width of the forbidden gap ΔE_g , meV	New half-width of the forbidden gap $E_g' / 2$, meV	Initial location of the impurity level E_i counted from the midgap, meV	Impurity level shift $\Delta E = \sigma \Delta p$ because of the mismatch, meV	New location of the impurity level from the edge of the conduction band E_i' , meV	Concentration of current carriers n , cm ⁻³
Pb _{1-x} Sn _x Te / BaTe	0.1, In	0.019 $\varepsilon = \varepsilon_{\max} / 2$	162	21	166	164	93	21	- 92	$1.8 \cdot 10^{11}$
	0.2, In	0.020 $\varepsilon = \varepsilon_{\max} / 2$	109	23	167	138	55	23	- 106	$2.2 \cdot 10^{10}$
Pb _{1-x} Sn _x Se / BaF ₂	0.1, Cr	0.014	67	16.5	140	103.5	72	0	- 31	$9.6 \cdot 10^{14}$
	0.15, Cr	0.015	35	19.5	152	93.5	56	0	- 37	$3.9 \cdot 10^{14}$

The deformation potential constants were taken equal to $D_d = 4.57$ eV and $D_u = -2.17$ eV for tellurides, and equal to $D_d = 6.48$ and $D_u = -2.11$ eV for selenides [8]. The derivative dE_i/dp was taken from works [7, 9], and it varied in the range of 1 – 5 meV / kbar.

As is obvious from the **Table 1**, after serial calculations of the new locations of impurity levels in the forbidden gaps of solid solutions of IV – VI semiconductors, the concentration of current carriers decreased by 5 – 8 orders of magnitude. With consideration of some increase in the mobility in uniform layers at stabilization of the Fermi level, the resistivity of layers can reach $10^4 - 10^5$ Ohm · cm.

IV. Conclusions

We developed the model of determination of the locations of the In and Cr impurity levels in the system of semiconductors PbSnTe:In and PbSnSe:Cr at mismatch corresponding to effective “negative” pressure and when Fermi level is stabilized.

At doping of IV–VI semiconductors with those impurities at the level of $> 10^{19}$ cm⁻³, the concentration of current carriers decreases by 5 – 8 orders of magnitude, while the resistivity increases and the narrow width of the forbidden gap is retained.

References

1. A. M. Pashaev, O. I. Davarashvili, M. I. Erukashvili, Z. G. Akhvlediani, R. G. Gulyaev, V. P. Zlomanov. Unrelaxed state in epitaxial heterostructures based on lead selenide. *J. Mod. Phys.*, 2012, 3, 6, 502- 510.
2. A. M. Pashaev, O. I. Davarashvili, Z. G. Akhvlediani, M. I. Erukashvili, L. P. Bychkova, V. P. Zlomanov. Study on the forbidden gap width of strained epitaxial lead selenide layers by optical transmission. *J. Mater. Sci. & Eng.*, 2012, 2, 2, 142-150.
3. A. M. Pashaev, O. I. Davarashvili, M. I. Erukashvili, Z. G. Akhvlediani, R. G. Gulyaev, M. A. Dzaganina. Growth and properties of strained epitaxial nanolayers of lead selenide. In: *Abs. Int. Conf. Func. Mater. & Nanotechnol.* 2012, Riga, 198-198.
4. A. M. Pashaev, O. I. Davarashvili, M. I. Erukashvili, Z. G. Akhvlediani, R. G. Gulyaev, L. P. Bychkova. Epitaxial lead selenide layers over a wide range of their thickness on dielectric substrates. *J. Mater. Sci. & Eng.*, 2013, 3, 2, 97-103.
5. A. M. Pashaev, O. I. Davarashvili, M. I. Erukashvili, Z. G. Akhvlediani, R. G. Gulyaev, V. P. Zlomanov. Nanolayers of lead selenide on potassium chloride substrates: Specific features of formation. *J. Mater. Sci. & Eng.*, 2013, 3, 4, 235-238.
6. B. A. Volkov, L. I. Ryabova, D. R. Khokhlov. Impurities with varying valence in solid solutions based on lead telluride. *Phys. – Uspekhi*, 2002, 152, 1, 1-68.
7. B. A. Kaydanov, Y. I. Ravich. Deep and resonant states in semiconductors type A^{IV}B^{VI}. *Phys. – Uspekhi*, 1985, 145, 1, 51-86.

8. I. I. Zasavitskii. Infrared luminescence and characteristics of the energy spectrum of IV–VI semiconductors (Doctor's Thesis). 1990, Moscow.
9. B. A. Akimov, L. I. Ryabova, O. B. Yatsenko, S. M. Chudinov. Energy spectrum rearrangement in PbSnTe alloys with In impurity at variation of their composition and under pressure. *Semicond.*, 1979, 13, 4, 752-756.

ATTENUATION OF GAMMA-RADIATION CONCOMITANT NEUTRON- ABSORPTION IN BORON-TUNGSTEN COMPOSITE SHIELDS

G. Nabakhtiani¹, L. Chkhartishvili^{1,2}, A. Gigineishvili¹,
O. Tsagareishvili², D. Gabunia², Z. Rostomashvili³, Sh. Dekanosidze

¹Georgian Technical University
Tbilisi, Georgia
giorgi.nabakhtiani@gmail.com
chkharti2003@yahoo.com

²F. Tavadze Institute of Metallurgy & Materials Science
Tbilisi, Georgia
t_otari@hotmail.com
d_gabunia@hotmail.com

³E. Andronikashvili Institute of Physics
I. Javakhishvili Tbilisi State University
Tbilisi, Georgia

Accepted September 16, 2013

To formulate the problem of attenuation of concomitant γ -radiation in the boron-based neutron-shields, let describe construction and operation of a nuclear reactor as it already made in text-books – see, e.g., [1].

Almost all the nuclear reactors can be defined as a device designed to produce and sustain a long term controlled fission chain-reaction, and made from properly selected and placed materials. Their majority is the thermal reactors wherein thermal-neutrons cause the fission reactions (generally, thermal neutrons are associated with a kinetic energy of 0.025 eV that translates into a neutron velocity of 2200 m/s or “room temperature” 300 K neutron-beam). **Figure 1** shows a schematic for a simple thermal reactor of cylindrical form. The tubes containing radioactive fuels such as uranium are called as fuel cladding. The fuel elements are arranged in a regular pattern mainly dictated by the neutronics with the moderator, which slows down the neutrons to sustain the fission reaction with thermal neutrons. The fuel-moderator assembly is surrounded by a reflector, the purpose of which is to direct the neutrons generated toward the reactor core so that neutron leakage can be controlled, thus improving the neutron economy. On the outside, the reactor is lined by shielding materials that absorb neutrons and γ -rays that escape the core and reduce the radiation intensity to a tolerable level so that personnel working near the reactor are not exposed. A rod of regulating or safety types helps to control the chain reaction by absorbing neutrons, maintaining the steady state of operation, or permit shutdown in the case of emergency. Coolant (not shown in this figure) is an important component of a reactor as a huge amount of heat is generated in the fuel elements and needs to be removed continuously in order to maintain a safe, steady-state reactor operation.

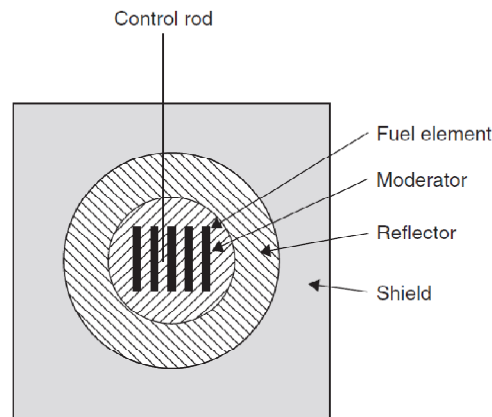


Figure 1. A schematic of a simple reactor design [1].

In the process of reactor operation, the thermal neutrons induced fission of ^{235}U nuclei is the most significant reaction. Note that ^{235}U is the only naturally occurring radioisotope – fissile atom – in which fission can be induced by slow neutrons. When a thermal neutron gets absorbed by a ^{235}U nucleus, it leads to the formation of an unstable radionuclide ^{236}U immediately followed by the creation of smaller fission fragments. The fission reaction of ^{235}U can occur in ~ 30 different ways leading to the possibility of ~ 60 different kinds of fission fragments. About 2.5 neutrons on average are also released per fission. A generally accepted equation for a fission reaction is $^{235}\text{U} + {}^1_0\text{n} \rightarrow {}^{92}\text{Kr} + {}^{142}\text{Ba} + 2 {}^1_0\text{n} + \text{energy}$. To sustain a continuous chain-reaction, released neutrons should be able to initiate the fission of at least another fissile atom.

The neutron energy spectrum is affected by various factors, including the specific type of reactor, positions of components in the reactor, and their immediate surroundings. Neutronic properties are of significant consideration in the design of nuclear reactors because the chain reaction requires continued supply of neutrons. The materials in the reactor can absorb neutrons and undergo nuclear reactions that lead to the production of different radioactive isotopes, which would decay by emitting α -, β - and γ -rays of different energy levels. The energetic radiation plays a significant role in modifying the microstructure of the materials involved. The effects of radiation can be diverse, including radiation hardening and embrittlement, void swelling, irradiation creep, and so forth, with all having significant effects on the performance of the reactor components. Another effect of radiation is the radiolytic decomposition of coolant. Fission fragments also cause damage, but they are limited to the fuel.

So, for selecting materials for a nuclear reactor, designer must know the effects of neutron and concomitant radiations on these materials.

The current understanding (based on the light-water-reactor case study) of radiation-induced degradation in nuclear reactors structural materials induced mainly by thermal neutrons and γ -rays is presented, e.g., in [2]. Results of the spectral emissivity measurements of candidate materials for reactors have been given in [3]. Heat dissipation by radiation is especially important consideration in very-high-temperature-reactor components because of the fourth power temperature dependence of radiated heat. The emissivity was found to be strongly dependant on the alloy chemical composition.

To control the chain reaction, the reactor materials should have high neutron absorption cross section. It is reason why the control rods are made from neutron-absorbing materials, usually B, as well as Hf. For the shielding materials one of the major requirements also is the

absorption of neutrons and γ -radiation as well. Such a material can be broal – a B and Al alloy. However, aluminum is not too good material for gamma absorption and therefore broal is not used for absorption of gamma.

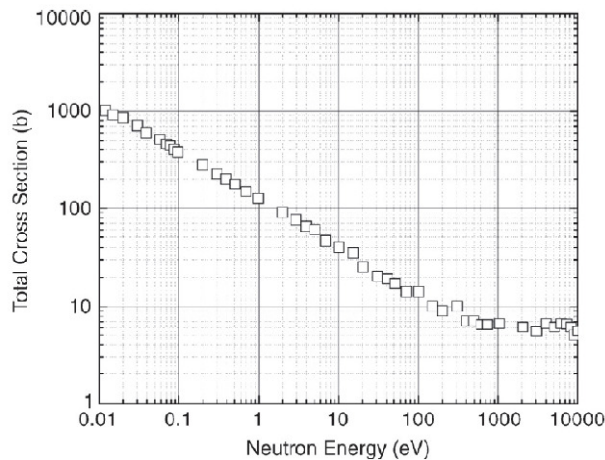


Figure 2. Variation of total cross section of elemental boron of natural isotopic composition as a function of neutron energy [1].

As is known, neutron shield can be made from materials of different chemical composition, not only boron-containing. Water, plastics and other materials containing high concentrations of hydrogen provide protection against relatively weak neutron radiation. But, in case of high neutron flux densities effective shields are those materials that contain boron or cadmium. We focused our attention on the use of boron-rich materials [4 – 8] because boron compounds and composites combine attractive physical-technical characteristics with a very large neutron capture cross section of ^{10}B nucleus: it is equal to 3835 barns for thermal-neutrons and keeps fairly high values also for fast neutrons. One more advantage of boron is the $\sim 1/\sqrt{E}$, where E is the neutron energy, dependence of neutron cross section over the entire possible neutron energy spectrum (**Figure 2**). Most nuclides exhibit both the $\sim 1/\sqrt{E}$ dependence of total neutron cross section as a function of neutron energy and the resonance effects. Other nuclides show abrupt increases in neutron cross section at certain narrow energy ranges due to resonance effects, which happens when the energy of the incident neutron corresponds to the quantum state of the excited compound-nucleus.

Boron carbide, the hardest material after diamond and cubic boron nitride, has been characterized for its neutron shielding behavior in [9]. Experiments were performed using a Howitzer device. The lowest neutron permeability rate (62.1%) and the lowest total macroscopic cross section were found for pellet, which is the sample composed of 12.5 g of boron carbide powder and 3 g of wax. It can be concluded that for equivalent thicknesses, boron carbide is a better shield material than kurnakovite or inderite. Boron carbon oxynitride (BCNO) is a low effective-nuclear-charge (≈ 6.8), near tissue equivalent, material useful in a γ -dosimeter. The thermoluminescence characteristics of doped and undoped BCNO material were studied and compared with each other [10]. The main interesting feature is concerning these properties in a very wide range $5 \cdot 10^2 - 4 \cdot 10^4$ Gy of gamma doses for nanocrystalline BCNO-phosphors. The doping with Cu or Dy leads to the quenching of its thermoluminescence. The synthesized BCNO nanophosphor shows a linear response from

$1.0 \cdot 10^1$ up to $4.5 \cdot 10^2$ Gy, what is the range in which it may be used as thermoluminescence dosimeter material.

Most (~ 93.9 %) of $^{10}\text{B} - \text{n}$ elementary acts is accompanied by radiation of a high-energy γ -quantum: $^{10}\text{B} + ^1_0\text{n} \rightarrow ^{11}\text{B} \rightarrow ^7\text{Li} (0.84 \text{ MeV}) + ^4\text{He} (1.47 \text{ MeV}) + \gamma (0.48 \text{ MeV})$ (energies of the nuclear reaction products shown in parenthesis correspond to the limit of zero-velocity neutron incident on a stationary boron nucleus). For this reason, one of the main problems associated with the use of boron-containing neutron-shields is the need to provide additional protection against the concomitant γ -radiation.

A series of Japanese Evaluated Nuclear Data Libraries (JENDLs) of special and general purpose-types seem to be the most complete database to be used in various fields for nuclear science and technology [11]. The special purpose libraries have been issued in order to meet the needs for particular application fields. As for the general purpose libraries, they have been updated periodically by considering the latest knowledge on experimental and theoretical nuclear physics. The newest library (the fourth version) for nuclear science and engineering released is JENDL – 4.0 [12]. We have analyzed the problem taking into account the compatibility of the various elements with boron in the composition and their γ -absorption capacity, according to JENDLs, and came to conclusion that the layered composites of boron or its compounds with heavy metals, in particular, tungsten, are promising neutron shields, which would allow the protection from the concomitant γ -radiation as well.

The general structural classification of layered composites, which are promising as functional materials, was given in [13]; some of thermophysical and mechanical properties of multilayer metal–ceramic composites that operate under extreme heat and mechanical conditions also were considered [14, 15]. Cases, when the effective properties deviate from the rule of additivity, are of special interest. In particular, ceramic–metal layered composites with a specific set of properties, and also layer thickness, may exhibit marked (by an order of magnitude) higher impact strength and heat resistance compared with monolithic ceramics.

The possible geometries of three types – hexagonal (h), triangular (t) and mixed hexagonal-triangular (ht) – of monolayer boron sheets adsorbed on deferent metal (Mg, Al, Ti, Au, and Ag) surfaces were studied theoretically [16] using density-functional-theory. It has been found that, when adsorbed on metal surfaces, h-B sheet is more energy-favorable than t-B or ht-B sheets, and the atop-site adsorption geometry is the most favored. For all h-B sheet / metal geometries, electrons are observed to transfer from metal to boron sheets, due to intrinsic electron deficiency of all boron structures.

The spectral properties of La / B, La / B₄C, and LaN / B, LaN / B₄C multilayer mirrors consisting of ~ 50 bilayers with a bilayer thickness of approximately 4 nm were investigated in [17]. The measured maximum reflectance at various wavelength values around the boron *K*-absorption edge was compared to theoretical values from model systems. From these calculations, it was shown that the boron chemical state has to be taken into account because a significant amount of boron is probably bound to La. This results in a shift of the B absorption edge to a longer wavelength, which significantly changes the optical properties. The reflectivity of LaN / B and LaN / B₄C multilayers can be well described by using the measured atomic B optical constants, which suggests that in both multilayers boron atoms are in a similar state as in a boron film. Consequently, nitridation of the La layer in the multilayer prevents the formation of La – B compounds.

Present paper provides an assessment of radiation properties of boron–tungsten layered composites as neutron shields of different sizes. All calculations were performed using the computing code Micro Shield.

The calculations were carried out for three geometries of the neutron source, which corresponded to the parameters (standard: diameter of the base \times height) of cylindrical nuclear reactors: (1) 3.84 m \times 4.50 m, (2) 2.88 m \times 3.20 m, and (3) 12.00 m \times 8.80 m [18]. For each of these geometries, there are considered two cases: lead Pb as standard material often used for protection against γ -radiation and tungsten W as a heavy metal forming a number of compounds with boron. It was assumed that these metallic layers are placed on the outer surface of the boron-containing layer, so that the γ -rays concomitant neutron-capture in boron must pass through the γ -absorbing metal layer.

In each of the 6 analyzed cases, the thickness of the protective layer was varied in the range of 0.2 – 2.0 cm, and the calculations were performed in 19 points of the interval. It was obtained the two curves of exposure dose (mR / h) with and without the factor of accumulation. The use of the factor of accumulation meant the account in the main beam of already scattered rays. Flux densities were calculated at the same form (**Figures 1 – 3**). Conventionally, the γ -ray flux incident on the protective layer was assumed to be 10^9 photons / s, i.e., the equivalent of 1 GBq (1 Becquerel is the source of radioactivity, which is 1 decay / s). Since the curves define the degree of attenuation of gamma radiation, the absolute value of output flow from the protective layer is easily counted for each part of the incident flux.

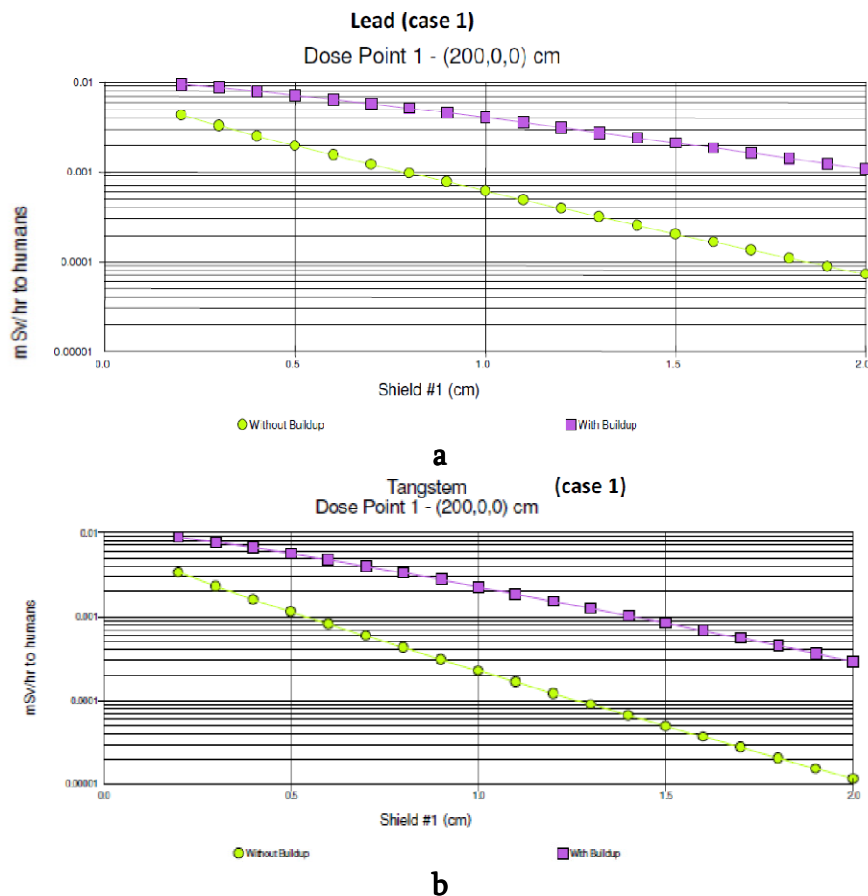


Figure 3. Attenuation of γ -radiation concomitant the neutrons-capture in boron-containing shield of cylindrical shape with base diameter of 3.84 m and height of 4.50 m versus thickness of (a) lead and (b) tungsten.

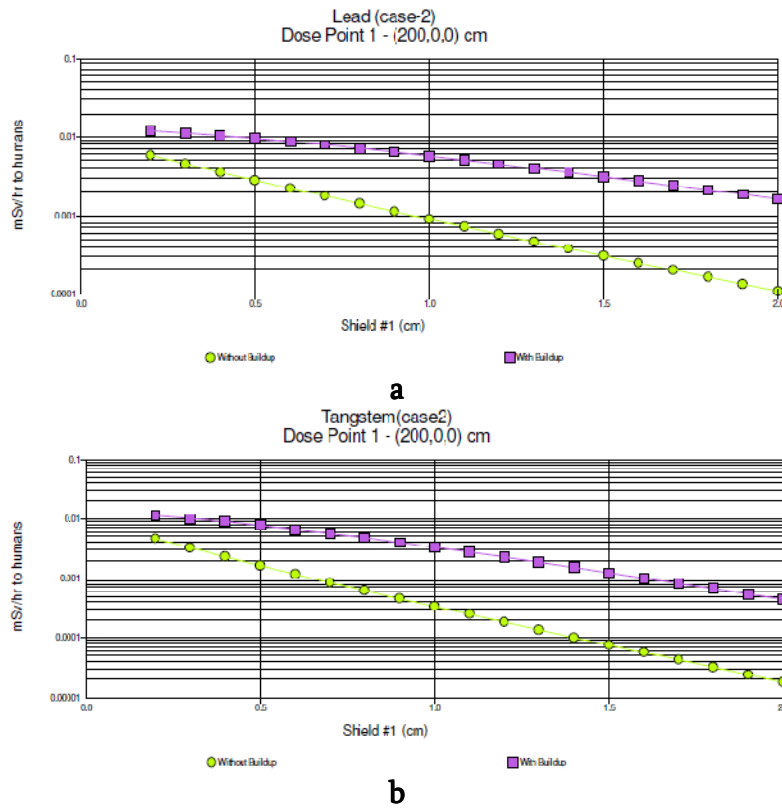


Figure 4. Attenuation of γ -radiation concomitant the neutrons-capture in boron-containing shield of cylindrical shape with base diameter of 2.88 m and height of 3.20 m versus thickness of (a) lead and (b) tungsten.

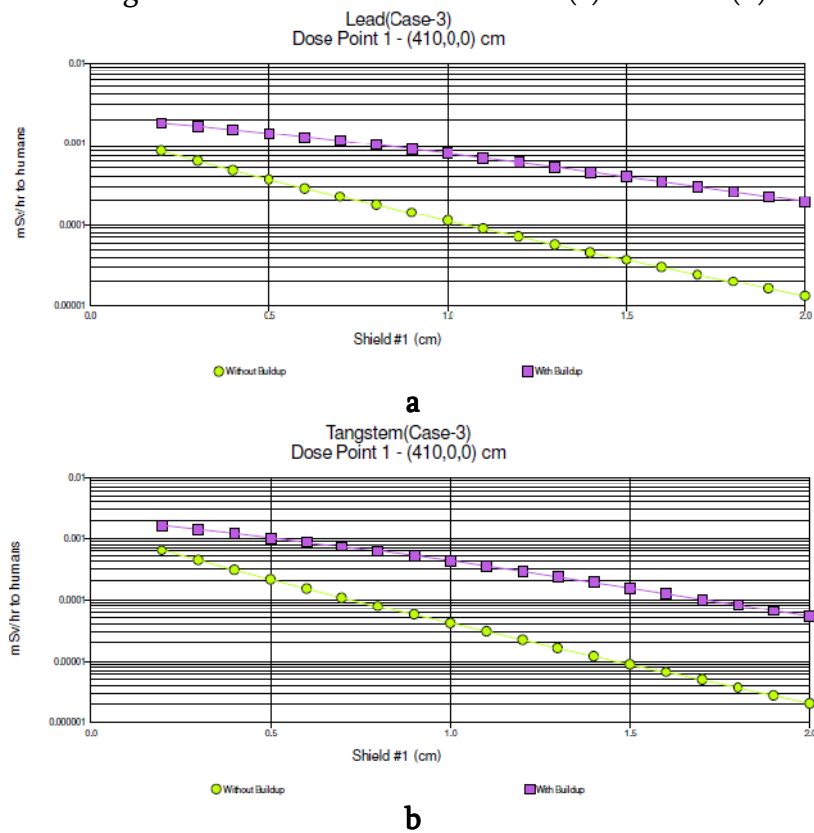


Figure 5. Attenuation of γ -radiation concomitant the neutrons-capture in boron-containing shield of cylindrical shape with base diameter of 12.00 m and height of 8.80 m versus thickness of (a) lead and (b) tungsten.

For geometries (1) and (2) dose rate is calculated for a distance of 200 cm from the center, and for the geometry (3) – 410 cm. These distances correspond approximately to a range of regions near the surfaces of cylinders and, therefore, allow comparison of the results. Since the exposure dose is the old value, graphics are presented for effectively equivalent (or effective) dose in mSv / h ($Sv = J / kg$). As we see, initial dose rates are too low and tungsten layer further reduces them (remember that natural background is in the range of 10 – 20 mSv).

According to international standards, it is acceptable to people (not professionals) receiving a maximum of ~ 1 mSv without an accounting background. If we assume that the person is irradiated from several sources, then the annual dose from each of them should not exceed ~ 0.3 mSv (the so-called dose-limiting). In the general case, if the radiation received from a source does not exceed 10 mSv / h, such a source is not considered as a radioactive (is at the level of acceptability). Getting a dose by man depends on the scenario of his relation to the source. According to most of the considered scenarios, the considered case should be taken out of the regulation. We should emphasize that we talk about protecting only from the concomitant γ -radiation, when the neutron flux is completely absorbed by boron-containing protective layer.

We have also calculated the power of equivalent doses for different organs. In this case, we referred to the ICRP (International Commission on Radiation Protection), which presents the model estimates of such doses.

These results lead to the conclusion that monoisotopic ^{10}B -layered compositions of boron and tungsten can be used successfully to protect against the different neutron flux intensities. Simultaneous protection from neutrons and concomitant γ -radiation associated with formation on the inner surface of the enclosure first tungsten layer and then boron coating of certain thicknesses.

We can say that the state diagram of the W – B system is among the most studied phase diagrams of transition metal–boron systems. This indicates the existence of a series of binary W / B phases which differ in crystal structure and value of the W : B ratio. This allows thinking the adhesion in such layered structures will be good due to the formation of a transition layer, the mixture of tungsten borides, as is the case of well-known technique of growing boron fibers coating a tungsten wire with boron.

When creating the coating that protects against neutron radiation and the concomitant γ -radiation from the boron-containing and tungsten layers, the authors intend to draw on their experience in technologies of boron doping with tungsten and growth of boron-rich tungsten boride phases.

References

1. K. L. Murty, I. Charit. *An Introduction to Nuclear Materials. Fundamentals and Applications*. 2012, Berlin: Wiley–VCH.
2. K. Fukuya. Current understanding of radiation-induced degradation in light water reactor structural materials. *J. Nucl. Sci. & Technol.*, 2013, 50, 3, 213-254.
3. G. Cao, S. J. Weber, S. O. Martin, M. H. Anderson, K. Sridharan, T. R. Allen. Spectral emissivity measurements of candidate materials for very high temperature reactors. *Nucl. Eng. & Design*, 2012, 251, 1, 78-83.

4. O. Tsagareishvili, L. Chkhartishvili, D. Gabunia, A. Gachechiladze, S. Shalamberidze, L. Gabunia, M. Tushishvili. Some aspects of use of boron-containing materials for neutron shield. In: Proc. 4th Int. Boron Symp., 2009, Eskişehir: OGU, 257-266.
5. L. S. Chkhartishvili, O. A. Tsagareishvili, A. A. Gachechiladze, D. L. Gabunia, Z. Sh. Mirijanashvili, G. F. Tavadze, T. A. Peradze, A. G. Eristavi. On possibility of application of boron-containing coatings as neutron shield. In: Proc. 6th Int. Conf. MEE, 2010, Kiev: IPMS, 73.
6. L. Chkhartishvili, D. Gabunia, O. Tsagareishvili. ^{10}B powder-based neutron shield coating materials. In: Abs. 17th Int. Symp. Boron, Borides & Rel. Mater., 2011, Istanbul: ITU, 294-294.
7. L. S. Chkhartishvili, O. A. Tsagareishvili, D. L. Gabunia, T. T. Jmukhadze. Nanostructural ^{10}B as an effective shielding material against neutron irradiation. In: Proc. 3rd Int. Conf. High Mat Tech, 2011, Kiev: IPMS, 270-270.
8. L. Chkhartishvili, O. Tsagareishvili, D. Gabunia. ^{10}B -based materials for neutron-shielding. In: Proc. Int. Conf. Mod. Technol. & Meth. Inorg. Mater. Sci., 2012, Tbilisi: Meridian, 188-202.
9. A. S. Kipcak, P. Gurses, E. M. Derun, N. Tugrul, S. Piskin. Characterization of boron carbide particles and its shielding behavior against neutron radiation. Energy Conver. & Manag., 2013, <http://dx.doi.org/10.1016/j.enconman.2012.08.026>
10. V. Chopra, P. Singh, L. Singh. Thermoluminescence study of gamma irradiated BCNO nanophosphor. Radiat. Phys. & Chem., 2012, 81, 7, 771-775.
11. K. Shibata. JENDL: Nuclear databases for science and technology. J. Nucl. Sci. & Technol., 2013, 50, 5, 449-469.
12. K. Shibata, O. Iwamoto, T. Nakagawa, N. Iwamoto, A. Ichihara, S. Kunieda, S. Chiba, K. Furutaka, N. Otuka, T. Ohasawa, T. Murata, H. Matsunobu, A. Zukeran, S. Kamada, J.-I. Katakura. JENDL – 4.0: A new library for nuclear science and engineering. J. Nucl. Sci. & Technol., 2011, 48, 1, 1-30.
13. V. V. Skorokhod. Layered composites: structural classification, thermophysical and mechanical properties. Powd. Metall. & Met. Ceram., 2003, 42, 9/10, 437-446.
14. V. V. Skorokhod, V. V. Panichkina, P. Ya. Radchenko, S. M. Solonin, V. P. Katashinskii. Sintered metals and alloys effect of metal-layer structure on the mechanical properties of multilayer metal–ceramic composites. I. Fracture energy. Powd. Metall. & Met. Ceram., 2009, 48, 1/2, 21-26.
15. P. Ya. Radchenko, V. V. Panichkina, O. I. Get'man, M. G. Andreeva, V. V. Pasichnyi, S. A. Ostapenko. Sintered metals and alloys effect of metal-layer structure on the mechanical properties of multilayer metal–ceramic composites. II. Heat resistance. Powd. Metall. & Met. Ceram., 2009, 48, 3/4, 196-200.
16. L. Z. Zhang, Q. B. Yan, S. X. Du, G. Su, H.-J. Gao. Boron Sheet adsorbed on metal surfaces: Structures and electronic properties. J. Phys. Chem., 2013, 116, 8, 18202-18206.
17. I. A. Makhotkin, E. Zoethout, E. Louis, A. M. Yakunin, S. Müllender, F. Bijkerk. Spectral properties of La / B-based multilayer mirrors near the boron K -absorption edge. Optics Express, 2012, 20, 11, 11778-11786.
18. V. G. Rodnenkov. Fundamentals of Radiation Safety. 2011, Minsk: Tetra Systems.

ONCE MORE ON EFFECTIVE ELECTRICAL CHARGE OF ATOMIC NUCLEI

L. Chkhartishvili, T. Berberashvili

Georgian Technical University
Tbilisi, Georgia
chkharti2003@yahoo.com
tamo.berberashvili@yahoo.com

Accepted September 17, 2013

Hartree had introduced the concept of the effective charge number for atomic nuclei simultaneously with the self-consistent field (SCF) in multi-electron atoms [1]. Its physical meaning can be understood as follows. The inner electric field is purely Coulomb only for hydrogen-like atoms. As for the atoms with two or more electrons, each of electrons is affected by the Coulomb field of positively charged atomic nucleus, which however is partially screened by the rest of electrons as electrons are negatively charged. Consequently, the SCF acting on the electron with the principal and orbital quantum numbers $n = 1, 2, 3, \dots$ and $l = 0, \pm 1, \pm 2, \dots, \pm (n - 1)$ one can still imagine as the Coulomb field of a “nucleus” with some effective charge number Z_{nl} , which however is less than the charge number of the nucleus Z : $Z_{nl} < Z$, where $Z > 1$.

Parameters Z_{nl} serve for the important characteristics of the intra-atomic SCF. Unfortunately, they are not defined unambiguously – their numerical values are essentially dependent of the chosen scheme of evaluation. The results of calculations performed on the basis of SCF approach by Clementi et al. can be found in web [2]. However, when it comes to the use of Z_{nl} parameters of electrons of the constituent atoms in the calculation of the electron energy spectrum of molecules or condensed matters, it seems more rational to introduce them by direct equating the energies of atomic electron orbitals followed from the analytical expression for the corresponding “hydrogen-like atom”, on the one hand, and ab initio calculations, on the other hand.

Such a parameterization we used in the quasi-classical theory of substance ground state [3] The values of the quasi-classical parameters of electric field potential and the electric charge density distributions in the most of atoms were tabulated by us in [4, 5] based on the energies of the electron orbitals calculated by Froese–Fischer [6] within the Hartree–Fock approximation. Works [7, 8] are the most recent examples of the successful use of such a quasi-classical approach to estimate of relative stabilities of ultra-small radius boron nitride nanotubes, and binding energies and electron energy levels of metallic dopants in boron.

In this paper, we publish our results in the parameters Z_{nl} . They are presented in the **Table 1**. In parentheses, there are shown the values previously obtained in [2].

Table 1. Effective electric charge numbers of atomic nuclei.



Atom	1s	2s	2p	3s	3p	3d	4s
1 H	1.00 (1.00)						
2 He	1.35 (1.69)						
3 Li	2.23 (2.69)	1.25 (1.28)					
4 Be	3.08 (3.68)	1.57 (1.91)					
5 B	3.92 (4.68)	1.90 (2.58)	1.57 (2.42)				
6 C	4.76 (5.67)	2.38 (3.22)	1.86 (3.14)				
7 N	5.59 (6.67)	2.75 (3.85)	2.13 (3.83)				
8 O	6.43 (7.66)	3.16 (4.49)	2.25 (4.45)				
9 Fe	7.26 (8.65)	3.55 (5.13)	2.42 (5.10)				
10 Ne	8.10 (9.64)	3.93 (5.76)	2.61 (5.76)				
11 Na	9.00 (10.63)	4.73 (6.57)	3.48 (6.80)	1.81 (2.51)			
12 Mg	9.90 (11.61)	5.49 (7.39)	4.27 (7.83)	2.13 (3.31)			
13 Al	10.82 (12.59)	6.27 (8.21)	5.07 (8.96)	2.66 (4.12)	1.94 (4.07)		
14 Si	11.73 (13.57)	7.02 (9.02)	5.84 (9.95)	3.12 (4.90)	2.31 (4.29)		
15 P	12.65 (14.56)	7.75 (9.83)	6.57 (10.96)	3.54 (5.64)	2.66 (4.89)		
16 S	13.56 (15.54)	8.49 (10.63)	7.31 (11.98)	3.98 (6.37)	2.81 (5.48)		
17 Cl	14.48 (16.52)	9.21 (11.43)	8.04 (12.99)	4.39 (7.07)	3.02 (6.12)		
18 Ar	15.40 (17.51)	9.93 (12.23)	8.75 (14.01)	4.80 (7.75)	3.26 (6.76)		
19 K	16.34 (18.49)	10.77 (13.01)	9.60 (15.03)	5.61 (8.68)	4.14 (7.73)		2.17 (3.50)
20 Ca	17.28 (19.47)	11.60 (13.78)	10.44 (16.04)	6.36 (9.60)	4.91 (8.66)		2.50 (4.40)
21 Sc	18.22 (20.46)	12.35 (14.57)	11.20 (17.05)	6.80 (10.34)	5.32 (9.41)	2.49 (7.12)	2.59 (4.63)
22 Ti	19.15 (21.44)	13.09 (15.38)	11.93 (18.06)	7.19 (11.03)	5.68 (10.10)	1.99 (8.14)	3.76 (4.82)
23 V	20.08 (22.43)	13.82 (16.18)	12.66 (19.07)	7.57 (11.71)	6.03 (10.79)	2.04 (8.98)	4.04 (4.98)
24 Cr	21.00 (23.41)	14.54 (16.98)	13.38 (20.08)	7.94 (12.37)	6.36 (11.47)	2.07 (9.76)	4.27 (5.13)
25 Mn	21.93 (24.40)	15.26 (17.79)	14.09 (21.08)	8.29 (13.02)	6.68 (12.11)	2.11 (10.53)	4.52 (5.28)
26 Fe	22.86 (25.38)	15.98 (18.60)	14.81 (22.09)	8.66 (13.68)	7.03 (12.78)	2.16 (11.18)	4.55 (5.43)
27 Co	23.79 (26.37)	16.70 (19.41)	15.52 (23.09)	9.02 (14.32)	7.36 (13.43)	2.19 (11.86)	4.65 (5.58)
28 Ni	24.72 (27.35)	14.42 (20.21)	16.23 (24.10)	9.38 (14.96)	7.68 (14.09)	2.23 (12.53)	4.76 (5.71)
29 Cu	25.65 (28.34)	18.13 (21.02)	16.94 (25.10)	9.73 (15.59)	8.00 (14.73)	3.65 (13.20)	3.02 (5.84)
30 Zn	26.58 (29.32)	18.84 (21.83)	17.65 (26.10)	10.07 (16.22)	8.31 (15.37)	3.75 (13.88)	3.06 (5.97)
31 Ga	27.52 (30.31)	19.63 (22.60)	18.44 (27.09)	10.73 (17.00)	8.98 (16.20)	4.63 (15.09)	3.69 (7.07)
32 Ge	28.47 (31.29)	20.43 (23.36)	19.23 (28.08)	11.38 (17.79)	9.64 (17.01)	5.42 (16.25)	4.21 (8.04)
33 As	29.41 (32.28)	21.22 (24.13)	20.03 (29.07)	12.02 (18.60)	10.29 (17.85)	6.17 (17.38)	4.68 (8.94)
34 Se	30.36 (33.26)	22.03 (24.89)	20.84 (30.07)	12.68 (19.40)	10.95 (18.71)	6.91 (18.48)	5.18 (9.76)
35 Br	31.31 (34.25)	22.84 (25.64)	21.64 (31.06)	13.33 (20.22)	11.60 (19.57)	7.61 (19.56)	5.64 (10.55)
36 Kr	32.25 (35.23)	23.64 (26.40)	22.45 (32.05)	13.97 (21.03)	12.25 (20.43)	8.30 (20.63)	6.07 (11.32)
37 Rb	33.21 (36.21)	24.50 (27.16)	23.31 (33.04)	14.78 (21.84)	13.07 (21.30)	9.23 (21.68)	6.98 (12.39)
38 Sr	34.17 (37.19)	25.36 (27.90)	24.17 (34.03)	15.57 (22.66)	13.88 (22.17)	10.12 (22.73)	7.79 (13.44)
39 Y	35.12 (38.18)	26.20 (28.62)	25.01 (35.00)	16.30 (23.55)	14.61 (23.09)	10.90 (25.40)	8.33 (14.26)
40 Zr	36.80 (39.16)	27.04 (29.37)	25.84 (35.99)	17.00 (24.36)	15.31 (23.85)	11.63 (25.57)	8.80 (14.90)
41 Nb	37.03 (40.14)	27.87 (30.13)	26.68 (36.98)	17.69 (25.17)	16.00 (24.62)	12.34 (26.25)	9.24 (15.28)
42 Mo	37.82 (41.13)	28.71 (30.88)	27.51 (37.97)	18.37 (25.98)	16.67 (25.51)	13.03 (27.33)	9.65 (16.41)
43 Tc	38.94 (42.11)	29.54 (31.63)	28.34 (38.94)	19.04 (26.79)	17.34 (26.38)	13.71 (28.35)	10.04 (17.20)



Once more on effective electrical charge of atomic nuclei.



Atom	1s	2s	2p	3s	3p	3d	4s
44 Ru	39.89 (43.09)	30.37 (32.38)	29.18 (39.95)	19.71 (27.60)	18.01 (27.22)	14.39 (29.36)	10.45 (17.66)
45 Rh	40.85 (44.08)	31.21 (33.15)	30.01 (40.94)	20.37 (28.44)	18.67 (28.15)	15.06 (30.41)	10.83 (18.58)
46 Pd	41.80 (45.06)	32.04 (33.88)	30.84 (41.93)	21.03 (29.22)	19.32 (29.02)	15.72 (31.45)	11.21 (18.99)
47 Ag	42.76 (46.04)	32.87 (34.63)	31.67 (42.92)	21.68 (30.03)	19.97 (29.81)	16.37 (32.54)	11.58 (19.86)
48 Cd	43.71 (47.03)	33.71 (35.39)	32.50 (43.91)	22.33 (30.84)	20.61 (30.69)	17.01 (33.61)	11.93 (20.87)
49 In	44.67 (48.01)	34.57 (36.12)	33.37 (44.90)	23.09 (31.68)	21.37 (31.52)	17.79 (34.68)	12.62 (21.76)
50 Sn	45.63 (48.99)	35.44 (36.86)	34.23 (45.89)	23.85 (32.42)	22.13 (32.35)	18.57 (35.74)	13.28 (22.60)
51 Sb	46.60 (49.97)	36.31 (37.60)	35.10 (46.87)	24.60 (33.21)	22.89 (33.18)	19.35 (36.80)	13.93 (23.54)
52 Te	47.56 (50.96)	37.18 (38.33)	35.97 (47.86)	25.37 (34.00)	23.65 (34.01)	20.13 (37.84)	14.58 (24.41)
53 I	48.52 (51.94)	38.05 (39.07)	36.84 (48.85)	26.13 (34.79)	24.42 (34.84)	20.91 (38.90)	15.23 (25.30)
54 Xe	49.49 (52.92)	38.92 (39.80)	37.71 (49.83)	26.89 (35.58)	25.18 (35.67)	21.68 (39.95)	15.86 (26.17)
55 Cs	50.45 (53.90)	39.81 (40.55)	38.61 (50.82)	27.72 (36.38)	26.01 (36.58)	22.54 (40.98)	16.68 (27.04)
56 Ba	51.42 (54.89)	40.71 (41.25)	39.50 (51.81)	28.55 (37.16)	26.85 (37.32)	23.39 (42.02)	17.49 (27.92)
57 La	52.38 (55.87)	41.57 (41.95)	40.36 (52.80)	29.24 (37.94)	27.53 (38.14)	24.08 (43.06)	17.92 (28.80)
58 Ce	53.34 (56.85)	42.42 (42.94)	41.21 (53.78)	29.92 (38.66)	28.21 (38.96)	24.76 (44.09)	18.33 (29.68)
59 Pr	54.31 (57.83)	43.27 (43.46)	42.07 (54.77)	30.59 (39.50)	28.87 (39.82)	25.42 (45.15)	18.71 (30.33)
60 Nd	55.27 (58.81)	44.13 (44.22)	42.92 (55.76)	31.25 (40.34)	29.53 (40.69)	26.08 (46.16)	19.10 (30.99)
61 Pm	56.23 (59.80)	44.98 (44.97)	43.77 (56.74)	31.91 (41.18)	30.19 (41.55)	26.73 (47.10)	19.47 (31.64)
62 Sm	57.19 (60.78)	45.83 (45.73)	44.62 (57.73)	32.57 (42.03)	30.84 (42.42)	27.37 (48.23)	19.84 (32.29)
63 Eu	58.15 (61.76)	46.67 (46.47)	45.46 (58.72)	33.22 (42.87)	31.49 (43.28)	28.02 (49.25)	20.19 (32.87)
64 Gd	59.11 (62.74)	47.53 (47.22)	46.31 (59.71)	33.88 (43.71)	32.14 (44.15)	28.66 (50.28)	20.57 (33.44)
65 Tb	60.07 (63.73)	48.3747.97)	47.1660.69)	34.5344.55)	32.7945.01)	29.3151.30)	20.9334.02)
66 Dy	61.0864.71)	49.22 (48.71)	48.01 (61.68)	35.18 (45.39)	33.43 (45.88)	29.94 (52.33)	21.29 (34.59)
67 Ho	61.99 (65.69)	50.07 (49.46)	48.86 (62.67)	35.83 (46.24)	34.07 (46.75)	30.58 (53.35)	21.65 (35.31)
68 Er	62.96 (66.67)	50.92 (50.20)	49.70 (63.65)	36.47 (47.08)	34.71 (47.61)	31.21 (54.36)	22.00 (36.23)
69 Tm	63.92 (67.66)	51.77 (50.95)	50.55 (64.64)	37.11 (47.92)	35.35 (48.48)	31.85 (55.37)	22.35 (37.14)
70 Yb	64.88 (68.64)	52.61 (51.69)	51.40 (65.63)	37.75 (48.76)	35.98 (49.34)	32.47 (56.40)	22.69 (37.52)
71 Lu	65.84 (69.62)	53.48 (52.45)	52.27 (66.61)	38.48 (49.53)	36.71 (50.10)	33.20 (57.42)	23.28 (38.27)
72 Hf	66.84 (70.60)	54.36 (53.19)	53.14 (67.60)	39.21 (50.31)	37.43 (50.98)	33.93 (58.43)	23.86 (38.98)
73 Ta	67.78 (71.58)	55.23 (53.93)	54.01 (68.59)	39.94 (51.09)	38.16 (51.80)	34.65 (59.44)	24.45 (39.76)
74 W	68.74 (72.57)	56.10 (54.67)	54.89 (69.57)	40.68 (51.87)	38.90 (52.62)	35.39 (60.45)	25.04 (40.56)
75 Re	69.71 (73.55)	56.98 (55.41)	55.76 (70.76)	41.41 (52.65)	39.63 (53.43)	36.13 (61.45)	25.63 (41.36)
76 Os	70.68 (74.53)	57.86 (56.15)	56.64 (71.55)	42.15 (53.43)	40.37 (54.25)	36.87 (62.47)	26.23 (42.10)
77 Ir	71.64 (75.51)	58.73 (56.89)	57.51 (72.54)	42.90 (54.20)	41.11 (55.07)	37.61 (63.43)	26.83 (42.85)
78 Pt	72.61 (76.49)	59.61 (57.63)	58.39 (73.53)	43.64 (54.98)	41.85 (55.89)	38.35 (64.50)	27.42 (43.64)
79 Au	73.58 (77.48)	60.49 (58.37)	59.27 (74.51)	44.38 (55.76)	42.59 (56.70)	39.09 (65.51)	28.02 (44.41)
80 Hg	74.55 (78.46)	61.37 (59.11)	60.15 (75.50)	45.13 (56.54)	43.34 (57.52)	39.83 (66.52)	28.61 (45.24)
81 Tl	75.52 (79.44)	62.26 (59.68)	61.04 (76.49)	45.92 (57.42)	44.13 (58.37)	40.63 (67.53)	29.33 (46.08)
82 Pb	76.49 (80.42)	63.16 (60.43)	61.93 (77.48)	46.71 (58.15)	44.93 (59.15)	41.43 (68.55)	30.05 (46.89)
83 Bi	77.46 (81.40)	64.05 (61.18)	62.83 (78.47)	47.51 (58.89)	45.72 (59.93)	42.23 (69.54)	30.77 (47.71)
84 Po	78.43 (82.38)	64.95 (61.92)	63.73 (79.46)	48.31 (59.62)	46.52 (60.71)	43.03 (70.57)	31.50 (48.52)
85 At	79.41 (83.36)	65.85 (62.67)	64.63 (80.45)	49.11 (60.35)	47.32 (61.50)	43.83 (71.58)	32.22 (49.34)
86 Rn	80.38 (84.33)	66.75 (63.41)	65.52 (81.44)	49.92 (61.09)	48.13 (62.28)	44.64 (72.60)	32.95 (50.15)





<i>4p</i>	<i>4d</i>	<i>4f</i>	<i>5s</i>	<i>5p</i>	<i>5d</i>	<i>6s</i>	<i>6p</i>
8.47 (16.43)	2.77		5.33 (6.48)				
8.84 (17.14)	2.81		5.53 (6.64)				
9.20 (17.72)	2.85		5.73 (0.00)				
9.55 (18.56)	4.75		3.60 (6.76)				
9.88 (19.41)	4.94		3.64 (8.19)				
10.59 (20.37)	5.83		4.32 (9.51)	3.14 (8.47)			
11.27 (21.27)	6.62		4.88 (10.63)	3.64 (9.10)			
11.93 (22.18)	7.35		5.39 (11.61)	4.09 (9.99)			
12.59 (23.12)	8.08		5.92 (12.54)	4.24 (10.81)			
13.23 (24.03)	8.77		6.41 (13.40)	4.49 (11.61)			
13.87 (24.96)	9.43		6.87 (14.22)	4.78 (12.42)			
14.72 (25.86)	10.40		7.85 (15.44)	5.85 (13.65)		2.98 (6.36)	
15.54 (26.80)	11.32		8.70 (16.62)	6.72 (14.80)		3.37 (7.58)	
15.96 (27.71)	11.70	3.48 (1.36)	8.85 (17.81)	6.84 (15.90)		3.39 (9.31)	
16.34 (28.61)	12.05	3.89 (1.68)	8.98 (18.91)	6.93 (16.97)		3.42 (10.80)	
16.71 (29.06)	12.38	4.19 (21.10)	9.10 (17.61)	7.01 (15.28)		3.44 (7.75)	
17.07 (30.01)	12.69	2.30 (22.27)	9.21 (18.74)	7.09 (16.96)		6.55 (9.31)	
17.43 (30.62)	13.01	4.48 (23.13)	9.33 (18.84)	7.17 (16.41)		3.47 (9.40)	
17.77 (31.09)	13.31	4.62 (23.53)	9.43 (18.25)	7.24 (16.28)		3.49 (8.01)	
18.11 (31.87)	13.60	4.77 (24.32)	9.53 (18.59)	7.30 (16.56)		3.51 (8.12)	
18.46 (32.65)	13.91	4.72 (25.01)	9.64 (18.88)	7.37 (16.76)		3.52 (8.22)	
18.81 (33.40)	14.22	4.72 (25.86)	9.75 (19.17)	7.45 (16.96)		3.54 (8.30)	
19.14 (33.83)	14.51	4.74 (26.54)	9.85 (19.30)	7.51 (17.13)		3.56 (8.34)	
19.48 (34.56)	14.80	4.76 (27.47)	9.95 (19.58)	7.58 (17.34)		3.58 (8.44)	
19.81 (35.11)	15.09	4.77 (27.98)	10.05 (19.72)	7.64 (17.47)		3.59 (8.48)	
20.14 (35.99)	15.38	4.80 (28.63)	10.15 (20.04)	7.71 (17.73)		3.61 (8.58)	
20.46 (36.40)	15.66	2.42 (29.43)	10.24 (20.15)	7.76 (17.83)		7.26 (8.59)	
21.05 (37.19)	16.26	5.87 (30.93)	10.76 (20.96)	8.29 (18.68)	3.49 (20.11)	3.78 (8.80)	
21.63 (37.93)	16.86	6.77 (32.31)	11.22 (21.83)	8.75 (19.59)	4.03 (16.62)	3.88 (9.16)	
22.22 (38.73)	17.45	7.60 (33.47)	11.66 (22.69)	9.19 (20.47)	4.40 (16.37)	3.96 (9.53)	
22.80 (39.55)	18.05	8.39 (34.71)	12.09 (23.54)	9.60 (21.33)	4.72 (16.74)	4.02 (9.85)	
23.39 (40.37)	18.64	9.14 (35.92)	12.49 (24.36)	10.00 (22.14)	5.07 (17.38)	4.08 (10.12)	
23.99 (41.14)	19.25	9.89 (37.15)	12.91 (25.10)	10.42 (22.91)	5.18 (18.00)	4.15 (10.32)	
24.58 (41.91)	19.85	10.62 (38.34)	13.31 (25.85)	10.81 (23.66)	5.36 (18.70)	4.20 (10.57)	
25.17 (42.73)	20.44	11.32 (39.51)	13.71 (26.59)	11.20 (24.42)	5.54 (19.41)	4.25 (10.75)	
25.76 (43.55)	21.03	12.00 (40.65)	14.09 (27.33)	11.57 (25.27)	5.75 (20.13)	4.30 (10.94)	
26.35 (44.41)	21.62	12.66 (41.76)	14.46 (28.11)	11.94 (25.97)	5.98 (20.86)	4.34 (11.15)	
27.08 (45.22)	22.38	13.61 (42.87)	15.20 (29.12)	12.71 (27.09)	6.96 (22.03)	5.10 (12.82)	3.72 (12.25)
27.81 (46.03)	23.13	14.51 (43.97)	15.90 (30.13)	13.44 (28.03)	7.81 (23.15)	5.73 (14.10)	4.29 (12.39)
28.53 (46.85)	23.88	15.40 (45.07)	16.58 (31.03)	14.13 (29.02)	8.59 (24.24)	6.30 (15.24)	4.80 (13.34)
29.26 (47.67)	24.63	16.28 (46.16)	17.27 (32.02)	14.83 (30.02)	9.37 (25.30)	6.88 (16.33)	4.96 (14.22)
29.99 (48.48)	25.38	17.14 (47.24)	17.93 (32.93)	15.51 (31.04)	10.09 (26.34)	7.42 (17.30)	5.23 (15.16)
30.72 (49.30)	26.13	17.98 (48.33)	18.58 (33.89)	16.16 (31.97)	10.78 (27.35)	7.93 (18.22)	5.55 (16.08)



We note that our results are largely correlated with previous data both on trends in rows and in columns. Some of the differences in these trends are observed only in atoms with filled $4d$ -states, which were neglected in the electron-configurations considered by Clementi et al. As for our numerical values, they are relatively underestimated in some cases – quite substantially. It points to a more realistic account of the screening effect.

The presence of credible values of the effective charge of atomic nuclei can serve as the basis for the development of a principally new approach to the calculation of the electronic structure of molecular and crystalline, including nano, forms of matter.

References

1. D. R. Hartree. The calculation of Atomic Structures. 1957, New York: Wiley & Sons.
2. http://www.webelements.com/periodicity/eff_nuc_charge_clementi/
3. L. Chkhartishvili. Quasi-Classical Theory of Substance Ground State. 2004, Tbilisi: Technical Univ. Press.
4. L. Chkhartishvili, T. Berberashvili. Atoms constituting nanosystems: Quasi-classical parameterization for binding energy and electronic structure calculations. Nano Studies, 2010, 1, 103-144.
5. L. Chkhartishvili, T. Berberashvili. Intra-atomic electric field radial potentials in step-like presentation. J. Electro Mag. Anal. & Appl., 2010, 2, 4, 205-243.
6. Ch. Froese-Fischer. The Hartree-Fock Method for Atoms: A Numerical Approach. 1977, New York: Wiley.
7. L. Chkhartishvili, I. Murusidze. Relative stability of BN nanotubes. Solid State Sci., 2012, 14, 11/12, 1664-1668.
8. L. Chkhartishvili, I. Murusidze, M. Darchiashvili, O. Tsagareishvili, D. Gabunia. Metal impurities in crystallographic voids of beta-rhombohedral boron lattice: Binding energies and electron levels. Solid State Sci., 2012, 14, 11/12, 1673-1682.

გარემოს მონიტორინგი ბიონდიკაციისა
და ბიოტესტირების საშუალებით

თ. პავლიაშვილი¹, თ. ყალაბეგიშვილი²

¹სსიპ მიკრო- და ნანოელექტრონიკის ინსტიტუტი
თბილისი, საქართველო
pavliashvilitamaz@yahoo.com

²ე. ანდრონიკაშვილის ფიზიკის ინსტიტუტი
ი. ჯავახიშვილის სახ. თბილისის სახელმწიფო უნივერსიტეტი
თბილისი, საქართველო

მიღებულია 2013 წლის 29 სექტემბერს

გარემოს მონიტორინგი განიხილება როგორც სისტემურად ორგანიზებული რეგულარული დაკვირვებები გარემოს მცენარულ და ცხოველურ სამყაროზე, ანთროპოგენური ზემოქმედების ხასიათზე, ატმოსფერული ჰაერის შემადგენლობაზე, წყლისა და ნიადაგის მდგომარეობაზე. ამჟამად ფართოდ გავრცელებულია გარემოს კვლევის ფიზიკო-ქიმიური მეთოდები, რომელიც ყოველთვის არ იძლევა სასურველ შედეგს. ხშირად, გარემოში მოხვედრილი სხვადასხვა ნივთიერებები წარმოადგენს მრავალკომპონენტთან ნაერთებს და ძნელია მათი ფიზიკო-ქიმიური სტანდარტიზაცია. ეს ნივთიერებები შეიძლება იყოს როგორც ბუნებრივი, ასევე სინთეტური წარმოშობის. გარემოს კონტროლისათვის ფიზიკო-ქიმიური მეთოდების გამოყენება განპირობებულია მათი მყარი ნორმატიული ბაზის არსებობით. ამ მეთოდების ნაკლია მაღალი შრომატევადობა, მცირე ოპერატიულობა და სიძვირე. უკანასკნელ ხანს გარემოს ეკოლოგიური მონიტორინგისათვის შეინიშნება ბიოლოგიური მეთოდების სულ უფრო მზარდი გამოყენება. ეს გამოწვეულია როგორც ეკოლოგიური პრობლემების ზრდით, ასევე ბიოლოგიური ობიექტების რაოდენობის მკვეთრი მატებით.

გარემოს მონიტორინგის ბიოლოგიური მეთოდები საშუალებას იძლევა ხშირ შემთხვევებში უფრო სწრაფად განისაზღვროს გარემოს დაბინძურება, ვიდრე ეს შესაძლებელია ქიმიური მეთოდებით. გარემოს კონტროლის ბიოლოგიური მეთოდებია ბიონდიკაცია და ბიოტესტირება. ბიონდიკაციისა და ბიოტესტირების უპირატესობა ფიზიკო-ქიმიურ მეთოდებთან შედარებით გამოიხატება შემდეგში:

- მათ შეუძლიათ დააფიქსირონ ადამიანისათვის და გარემოსათვის ამა თუ იმ ტოქსიკური ნივთიერების არსებობა.
- საშუალებას იძლევა გაკონტროლდეს სინთეზირებული ახალი მასალების ზემოქმედება ადამიანზე და გარემოზე.
- შეუძლიათ რეაგირება მოახდინონ გარემოში ტოქსიკანტების მცირე ზემოქმედებაზე, რადგანაც გააჩნიათ მაღალი მგრძობიარობა და დოზის აკუმულირების შესაძლებლობა.

მოკლე ისტორიული ცნობები ბიოინდიკაციისა და ბიოტესტირების შესახებ

ბიოინდიკაციის, როგორც მეცნიერული მიმართულების ფორმირება მიმდინარეობდა ბიოლოგიური მეცნიერების განვითარების პარალელურად. ანტიკური ხანის მეცნიერთა, ფილოსოფოსთა და აგრონომთა შრომებმა შემოგვინახა ცნობები მცენარეული საფარის პრაქტიკული გამოყენების თაობაზე. კატონის (უფროსის) შრომებში (234 – 149 ჩ.წ.ა.) არსებობს ჩანაწერი იმის თაობაზე, რომ მიწის მოხვნამდე ბალახის დიდი სიხშირე მიუთითებს იმ ადგილებზე, სადაც შეიძლება მუხუდოსნაირი კულტურების მოყვანა.

რომაელი მწერალი და აგრონომი ი. კალუმელა I საუკუნეში ჩ.წ.ა. აღწერს, რომ მცენარეთა ფოთლებისა და მომწიფებული ნაყოფის მიხედვით შეიძლება წარმოდგენა ვიქონიოთ ნიადაგის თვისებებზე და ვიცოდეთ რომელი მცენარეული კულტურები გაიზრდებიან მასზე კარგად. რომელი ინჟინერი ვიტრუვიუსი I საუკუნეში ჩ.წ.ა. აღნიშნავდა, რომ წყლის არსებობას დედამიწის სიღრმისეულ შრეებში მიაჩნებდა ამ ადგილებში ტენის მოყვარული მცენარეების სიჭარბე.

ვერგილიუსს თავის ნაშრომში “გეორგიკები” (36 – 29 ჩ.წ.ა.) გამოთქმული აქვს მოსაზრება იმის შესახებ, რომ კლდოვანი რელიეფი საუკეთესოა ზეთისხილის მოსაყვანად, ხოლო გვიმრებით მდიდარ ადგილებში კი უფრო მიზანშეწონილი იქნებოდა ყურძნის მოყვანა.

აღსანიშნავია რომელი მწერლისა და მეცნიერის პლინიუსის (უფროსის) (79 – 24 ჩ.წ.ა.) აზრი იმის შესახებ, რომ კავშირი მცენარეული საფარის ხარისხსა და ნიადაგის ნაყოფიერებას შორის არც ისე მარტივია. ხშირად, მაღალი ხეები და ბალახით მდიდარი ველების არსებობა არ არის ნიადაგის ნაყოფიერების ნიშანი.

უძველესი დროიდანვე იყო ცნობილი, რომ სეისმურად აქტიურ რაიონებში ცხოველთა ქცევითი ნორმების ცვლილება მიაჩნებდა ადამიანებს მოახლოებული საფრთხის შესახებ. შუა საუკუნეებში მიწისქვეშა მაღაროში მომუშავენი იადონს იყენებდნენ მაღაროს გაზის აღმოსაჩენად. იადონის ქცევითი ნორმების ცვლილება ან მისი სიკვდილი იყო მანიშნებელი, რომ მაღაროში არსებობდა ფეთქებადი აირი.

დიდი მნიშვნელობა ჰქონდა ა. ჰუმბოლტის (17 – 18 საუკუნეები) შრომებს, რომლებშიც აღწერილი იყო მცენარეულობის ზონალურ-კლიმატური განაწილება. აღსანიშნავია ა. ვერნადსკის შრომები, რომლებიც საფუძვლად დაედო გეოლოგიაში ახალი მიმართულების წარმოშობას. ამ მეთოდის არსი მდგომარეობს მადნის წარმომქმნელი ელემენტების დაფიქსირებაში მცენარეებსა და ნიადაგის ზედა ფენებში. ასეთი ადგილების აღმოჩენა ნიადაგის ზედა ფენებში და მცენარეებში მიაჩნებდა დედამიწის სიღრმეში არსებული შესაძლო მადანის არსებობაზე [1].

ატმოსფერული ჰაერის დაბინძურების ხარისხის განსაზღვრა მღიერების საშუალებით წარმოადგენს ერთ-ერთ ძველ მეთოდს. XIX საუკუნის მეორე ნახევარში გამოჩნდა პირველი შრომები, სადაც აღნიშნული იყო, რომ ინდუსტრიული ცენტრების გაჩენამ გამოიწვია მღიერების შემცირება და მათი სახეობების გაღარიბება. 1885 წელს დადგენილ იქნა, რომ ლონდონის მახლობლად მნიშვნელოვნად შემცირდა მღიერების სახეობები. შენიშნული იყო აგრეთვე, რომ სხვადასხვა სახეობების მღიერებს გააჩნიათ განსხვავებული მგრძობიარობა ჰაერის დაბინძურების მიმართ. 1892 წელს ჩატარებულ იქნა პირველი ექსპერიმენტი: რამდენიმე სახეობის მღიერი ადამიანის მიერ

ხელუხლებელ ლანდშაფტური ზონიდან გადარგეს ქალაქში, სადაც ყველა ისინი სწრაფად დაიღუპა. 1926 წელს შვედმა ბოტანიკოსმა რ. სერნარდერმა გამოაცალკევა სხვადასხვა სახეობის მღიერების ზონები ატმოსფერული ჰაერის დაბინძურების ხარისხის მიხედვით. ამით შესაძლებელი გახდა ქალაქებისა და მათი მიმდებარე ტერიტორიების დაყოფა მღიერთა ფლორის სრულად შესწავლის საფუძველზე [2].

გარემოს ბიონდიკაცია

ბიონდიკატორებად შეიძლება გამოყენებული იყოს ყველა ის ცოცხალი ორგანიზმი, რომელსაც გააჩნია რეაქცია გარემოზე ზემოქმედებებზე. ასეთები არიან: სხვადასხვა სახის ბაქტერიები, წყალმცენარეები, სოკოები, მცენარეები, ცხოველები და ა.შ. ბიონდიკატორების არსებით თვისებას წარმოადგენს მათი მგრძობიარობა. როდესაც ბიონდიკატორს გააჩნია მყისიერი რეაქცია გარემოზე მცირე ზემოქმედებაზე, ეს ითვლება ადრეულ ინდიკაციად, ხოლო თუ ბიონდიკატორი გარემოზე ზემოქმედებაზე რეაგირებს გარკვეული დროის შემდეგ, ის ითვლება აკუმულატორულ ბიონდიკატორად. იმ მოთხოვნებიდან, რომელიც წაყენება ინდიკატორებს, შეიძლება გამოიყოს მგრძობიარობა, ექსპრესიულობა, აღრიცხვის სიმარტივე და სიიარაღე. მგრძობიარე ინდიკატორებად ითვლებიან მღიერები, ხავსები, მიკროორგანიზმები და წყალმცენარეები. ბიონდიკაციის ერთ-ერთ ფართოდ გავრცელებულ მეთოდს წარმოადგენს ე.წ. ეტალონების მეთოდი. მეთოდის არსი მდგომარეობს შესასწავლი ეკოსისტემის შედარებაში ე.წ. ფონურ სისტემასთან, რომელიც მიღებულია ეტალონად შესასწავლი პარამეტრების მიხედვით. ამ მეთოდის გამოყენება განსაკუთრებით მიზანშეწონილია იმ შემთხვევაში, როდესაც დაბინძურებული გარემოს შედარება ხდება იმ ბუნებრივ მახასიათებლებთან, რომლებიც არ განიცდიან გარემოზე ანტროპოგენურ ზემოქმედებას. ბიონდიკაციაში მეტად მნიშვნელოვანია ბიონდიკატორების სწორად შერჩევა. დაბინძურებული გარემოს ბიონდიკაციის შემთხვევაში საუკეთესო ბიონდიკატორად ითვლება ორგანიზმი, რომლითაც მიიღწევა წრფივი კორელაცია გარემოს დაბინძურების დონესა და აკუმულირებულ ტოქსიკანტს შორის.

მიკროორგანიზმები გამოირჩევიან სწრაფი რეაგირებით. მათი გამოყენება მიზანშეწონილია ცალკეული ტოქსიკანტის ზემოქმედებისას ცოცხალ ორგანიზმზე და მასში მიმდინარე ბიოქიმიური პროცესების შესწავლის დროს.

ატმოსფერული ჰაერის ბიონდიკაცია

ატმოსფერული ჰაერის ერთ-ერთ გავრცელებულ დამაბინძურებელს წარმოადგენს გამოფრქვეული ტოქსიკური გაზები. ამათგან ყველაზე გავრცელებულია გოგირდის ორჟანგი, ნახშირბადის ორჟანგი, ფტორწყალბადი, გოგირდწყალბადი, აზოტის ჟანგეულები, წყალბადის ქლორიდი და ა.შ. ტოქსიკური გაზებით ატმოსფეროს დაბინძურება ძირითადად ხორციელდება სხვადასხვა საწარმოში მიმდინარე პროცესების შედეგად, ნავის დაწვისას და ავტოტრანსპორტის გამონაბოლქვის შედეგად.

ატმოსფერული ჰაერის დაბინძურების კარგ ინდიკატორებად ითვლება მცენარეები, რადგან ისინი მეტად მგძნობიარენი არიან ჰაერის დაბინძურების მიმართ და უფრო ინტენსიურად რეაგირებენ გარეშე ტოქსიკური ნივთიერებების იმ კონცენტრაციებზე, რომლებიც ადამიანებსა და ცხოველებში არ იწვევს მოწამვლის შესამჩნევ მოვლენებს. მავნე გაზების ზემოქმედება ორგანიზმზე დამოკიდებულია ნივთიერების კონცენტრაციაზე, ზემოქმედების დროზე, ფიზიოლოგიური განვითარების იმ სტადიაზე, რომელშიც იმყოფება მცენარე მასზე გაზების ზემოქმედების მომენტში.

ტოქსიკური გაზების ზემოქმედებისას ირღვევა მცენარის სასიცოცხლო პროცესები, რის შედეგადაც შეინიშნება მცენარეთა ცალკეული ქსოვილებისა და მთლიანად ფორმის შეცვლა. გარეშე ზემოქმედების გამოვლენის უკიდურეს ფორმას წარმოადგენს ტერატების წარმოშობა. მწერებზე მავნე გაზების ზემოქმედებისას შეიძლება მოხდეს მათი სხეულის ზედაპირის სტრუქტურის ცვლილება. ჰაერის დაბინძურების ინდიკატორად შეიძლება ჩაითვალოს ფუტკრების სიკვდილიანობის მაღალი პროცენტულობა. ჰაერის სისუფთავის კარგი ინდიკატორებია მღიერები. მღიერები წარმოადგენენ სიმბიოტიკურ ორგანიზმებს, რომლებიც შედგება ორი კომპონენტისაგან: სოკოსა და წყალმცენარისაგან. მღიერები თავისი საარსებო ადგილის მიხედვით განიყოფიან შემდეგ ძირითად ჯგუფებად: ეპიგენური (ნიადაგზე), ეპილიტური (კლდოვან ადგილზე), ეპიფიტური (ხის ქერქზე) და ეპიფილური (მარადმწვანე მცენარეების ფოთლებზე). ჰაერის დაბინძურების შემთხვევაში ადგილი აქვს ეპიფიტური მღიერების ზედაპირის შემცირებას ან მთლიან გაქრობას. დაფუძნდა ახალი მიმართულება გარემოს ბიოინდიკაციაში ლიქენონდიკაცია, რომელსაც უკვე გააჩნია ასწლიანი ისტორია. დადგენილია, რომ მღიერებზე განსაკუთრებით ძლიერი ტოქსიკური ზემოქმედებით გამოირჩევიან გოგირდისა და აზოტის ჟანგეულები, ოზონი, ფტორიდები, კომპლექსური დამაბინძურებლები და მძიმე მეტალები. ასევე აქტიურად აკუმულირებენ მღიერები რადიონუკლიდებს. მღიერების ასეთი უნიკალური თვისებები განაპირობებს მათ ფართო გამოყენებას ეკოტოქსიკოლოგიურ კვლევებში.

ჰიდრორესურსების ბიოტესტირება

დღეისათვის წყლის ანალიზისათვის ყველაზე გავრცელებულია ქიმიური მეთოდები. ქიმიური ანალიზის სირთულის, ტოქსიკური ნივთიერებების დიდი რაოდენობისა და მეთოდის სიძვირის გამო შეუძლებელია ქიმიური ანალიზის რეგულარულად ჩატარება. ამასთანავე, ქიმიურ-ანალიტიკური კონტროლის შემთხვევაში შეუძლებელია დაფიქსირდეს ნივთიერებათა კომბინირებული მოქმედების შედეგი, როდესაც ერთ-ერთის მოქმედებას შეუძლია გააძლიეროს ან დაასუსტოს მეორის მოქმედება. ამიტომ, ანალიზური ქიმიის მეთოდებთან ერთად გამოიყენება ბიოლოგიური მეთოდები. აღსანიშნავია აგრეთვე, რომ ცოცხალ ორგანიზმებს შესწევთ უნარი აღიქვან ნივთიერებათა უფრო მცირე კონცენტრაციები, ვიდრე ეს შესაძლებელია ანალიზური ქიმიის მეთოდებით. ამჟამად დამუშავებულია მრავალი ბიოტესტი, რომლებშიც ტესტ-ორგანიზმებად იყენებენ სხვადასხვა ჰიდრობიონტებს, როგორც არის ინფუზორიები, ნაწლავურ-ჩხიროვანი ჰიდრები, ჭიაყელები, მოლუსკები, კიბოსებურთა ოჯახიდან (დაფნია, გამმარუსები) და თევზები.

წყლის ხარისხის ეფექტური კონტროლისათვის მეტად მნიშვნელოვანია ექსპრეს-მეთოდების შემუშავება. ამის შესაძლებლობას იძლევა ჰიდრობიონტების გამოყენება. ყველაზე ხშირად გამოიყენება მეთოდიკა, რომელიც დაფუძნებულია დაფნიების (*Daphnia*) სიკვდილიანობაზე და ნაყოფიერების ცვლილებაზე იმ ტოქსიკური ნივთიერებების ზემოქმედებისას, რომელსაც შეიცავს წყალი. შედარება ხდება იმ საკონტროლო წყლის სინჯებთან, რომლებიც არ შეიცავენ ტოქსიკურ ნივთიერებებს.

უკანასკნელ ხანს მრავალი მეცნიერი იყენებს სტანდარტულ მეთოდიკას ცეროდაფნიებზე. ტესტ-ორგანიზმების კულტურა მოთავსებულია კლიმატოსტატში მუდმივი ტემპერატურისა და განათების პირობებში. შესასწავლი წყლის მწვავე ტოქსიკური ზემოქმედება განისაზღვრება ცეროდაფნიების სიკვდილიანობით ექსპოზიციის გარკვეულ პერიოდში. მწვავე ტოქსიკურობის კრიტერიუმად მიღებულია ის მდგომარეობა, როდესაც შესასწავლ წყლის სინჯში 48 საათის განმავლობაში იღუპება 50 % და უფრო მეტი ცეროდაფნია. ამასთანავე, საკონტროლო წყლის სინჯში სიკვდილიანობა არ უნდა აღემატებოდეს 10 %-ს. ბიოტესტები დაფნიების გამოყენებით რეკომენდებულია ჩამდინარე წყლების კონტროლისათვის და პოტენციურად საშიში ტოქსიკანტების გამოსავლენად. აღსანიშნავია, რომ ამჟამად ბიოტესტები დაფნიების გამოყენებით ყველაზე გავრცელებულია, რაც განპირობებულია მათი კულტივირების სიმარტივით და მცირე ზომებით. ამის გამო შესაძლებელია გამოკვლევა ჩატარდეს სინჯებში წყლის მცირე რაოდენობისას.

ევროგაერთიანების ქვეყნებში ჩამდინარე წყლების ბიოტესტირებისათვის მიღებულია სტანდარტი "Daphnia Magna". ბიოტესტირების მეთოდები, რომლებშიც გამოყენებულია დაფნიები, საშუალებას იძლევა შევადაროთ სხვადასხვა სინჯების წყლების ტოქსიკურობა, რომლებიც შეიცავენ სხვადასხვა ნივთიერებებს. ამასთანავე, სხვადასხვა ლაბორატორიებში მიღებული დაფნიები განსხვავდებიან ერთმანეთისაგან და ეს იწვევს შედეგების მნიშვნელოვან განსხვავებას, რომელიც აღწევს 35 %-ს. ამრიგად, მიუხედავად თავისი სიმარტივისა და მთელი რიგი ღირსებებისა, ბიოტესტები დაფნიების გამოყენებით არ შეიძლება ჩაითვალოს უნივერსალურად. მისი გამოყენება მიზანშეწონილია სხვა ბიოლოგიურ და ფიზიკო-ქიმიურ მეთოდებთან ერთად. საყოფაცხოვრებო სასმელი წყლის კონტროლი ძირითადად ხორციელდება წყლის გამანაწილებელ სისტემამდე. ძირითადი მოთხოვნები, რომლებიც წაეყენება ამ შემთხვევაში ბიოტესტებს, არის რეაქციის გამომჟღავნება წყალში საშიში ტოქსიკანტების გაჩენის შემთხვევაში მინიმალური დროის განმავლობაში. ეს მოითხოვს სპეციალური ავტომატური ხელსაწყოების შექმნას, რომელიც გარდაქმნის რეგისტრირებულ ტესტ-რეაქციებს წყლის ტოქსიკურობის მაჩვენებლების ნორმირებულ სიდიდეებად. ამჟამად საყოფაცხოვრებო დანიშნულების სასმელი წყლის კონტროლისათვის გამოიყენება ბიოტესტები, სადაც ტესტ-ობიექტებად გამოყენებულია ინფუზორიები, ტეტრაჰიმენა პერიფორმის (*Tetrahymena pyriformis*), ბაქტერიების შტამები *Escherichia coli*, დაფნიები და ცეროდაფნიები (*Ceriodaphnia*), წყალმცენარეები – ქლორელა (*Chlorella*) და სცენედესმუსი (*Scenedesmus*). აღსანიშნავია, რომ ბიოტესტირების მეთოდის გამოყენებისას არ ფიქსირდება ტესტ-რეაქცია ზღვრული დასაშვები კონცენტრაციის (ზდკ) ფარგლებში. რეალურად დაფიქსირებული ტესტ-რეაქციები დაიმზირება, როდესაც წყალში არსებული ტოქსიკანტების კონცენტრაცია მეტია ზდკ-ზე. მაგრამ, ეს ეხება სიტუაციას, როდესაც წყალი დაბინძურებულია ერთი, ცალკეული სახის ტოქსიკანტით. ბიოტესტირების უპირატესობა გამოიხატება იმაში, რომ ის აფიქსირებს წყალში მოხვედრილი ყველა ტოქსიკანტის ჯამურ ზემოქმედებას ცოცხალ ორგანიზმზე.

საყოფაცხოვრებო დანიშნულების სასმელი წყლის ბიოლოგიური კონტროლი შესაძლებლობას იძლევა სწრაფად გამოვლინდეს წყლის დაბინძურების მაღალი დონე და მიღებულ იქნას საჭირო ადეკვატური ზომები.

ნიადაგის ბიოინდიკაცია

ნიადაგის ბიოინდიკაციის მეთოდი ემყარება იმ აზრს, რომ ნიადაგი, როგორც ყოფითი გარემო წარმოადგენს სხვადასხვა ორგანიზმების ერთიან სისტემას. ნიადაგების ბიოინდიკაციისათვის კარგად დამუშავებულია ფიტოინდიკატორული მეთოდები. მაგალითად, მცენარეული საფარის ქიმიური შემადგენლობისა და სტრუქტურის შესწავლის შედეგად შეიძლება დადგინდეს ნიადაგის ტიპი, მარილების დაგროვების პროცესი, დაჭაობების მიმდინარეობა და სხვ. საინტერესოა ნიადაგების ბიოინდიკაციის ე.წ. ზოოლოგიური მეთოდი. ამ შემთხვევაში ერთი რომელიმე სახეობის გამოყენება არ არის საკმარისი დამაჯერებელი დასკვნებისათვის. უკეთესია გამოყენებული იყოს ორგანიზმების მთელი კომპლექსი, რომელთა შორისაც ზოგიერთი იქნება ინდიკატორი ტენიანობაზე, ხოლო ზოგიერთები ტემპერატურის, ქიმიურ და მექანიკურ შემადგენლობაზე. ამ მხრივ განსაკუთრებით გამორჩეული არიან მსხვილი უხერხემლონი (წვიმის ჭიაყელები, მრავალფეხები და სხვ.).

ნიადაგების მიკრობიოლოგიური და ბიოქიმიური მახასიათებლების განსაზღვრა წარმოადგენს ერთ-ერთ რთულ ამოცანას. ზოგიერთი მეცნიერის აზრით, ნიადაგის მდგომარეობის სრული და ყოვლისმომცველი შეფასების მიღება შესაძლებელია ტესტ-ორგანიზმების კომპლექსების გამოყენებით. ასე მაგალითად, ტესტ-ორგანიზმებად გამოყენებულია ჰიდრობიონტების წარმომადგენელი *Daphnia magna* Straus, მიკროორგანიზმები და უმაღლესი მცენარეების წარმომადგენელი *Avena sativa*. ასევე ნიადაგის ბიოლოგიური აქტიურობის ერთ-ერთ გავრცელებულ ინტეგრალურ მეთოდს წარმოადგენს ნიადაგის “სუნთქვის” შესწავლა, ე.ი. ნიადაგის ბიოტის მიერ ნახშირორჟანგის გამოყოფის პროცესის შესწავლა [3].

ნანონაწილაკებისა და ნანომასალების ბიოტესტირება

უკანასკნელი წლები ხასიათდებოდა ნანოტექნოლოგიების ინტენსიური დანერგვით სხვადასხვა სფეროში. ამჟამად, ნანოტექნოლოგიები ფართოდ გამოიყენება ელექტრონიკაში, ენერგეტიკაში, ქიმიურ მრეწველობაში, მედიცინაში, სამშენებლო ინდუსტრიაში, ბიოლოგიაში, ბიოფიზიკაში, პარფიუმერიაში, კვების მრეწველობაში და სხვა მრავალ დარგში. მთელ რიგ ქვეყნებში ნანონაწილაკებისა და ნანომასალების წარმოებამ მიიღო სამრეწველო ხასიათი. უახლოეს მომდევნო წლებში მოსალოდნელია ნანოტექნოლოგიური მასალების წარმოების მკვეთრი ზრდა [4]. ასეთი ტენდენცია აუცილებლად გამოიწვევს ნანომასალების ემისიას გარემოში. ნანოტექნოლოგიებს შეუძლიათ ბევრი სიკეთე მოუტანონ ადამიანებს, მაგრამ, როგორც ყოველ დიდ აღმოჩენას კაცობრიობის ისტორიაში გააჩნდა უარყოფითი მხარე, ასევეა ნანოტექნოლოგიების შემთხვევაშიც. დადგენილია, რომ მთელ რიგ ნანონაწილაკებს და

ნანომასალებს გააჩნიათ ტოქსიკური თვისებები. მეცნიერებაში დაფუძნდა ახალი მიმართულება – ნანოტოქსიკოლოგია. ტრადიციულად, ნანონაწილაკებს მიაკუთვნებენ 1 – 100 ნმ-ის ზომების ნაწილაკებს. ნანონაწილაკების მცირე ზომები და მრავალნაირი ფორმები ხელს უწყობს მათი შეღწევის უნარის გაზრდას ადამიანის ორგანიზმში. ნანონაწილაკების დიდი ხვედრითი ზედაპირი ზრდის მათ ადსორბციულ ტევადობას, რომელმაც შეიძლება გამოიწვიოს თავისუფალი რადიკალების მკვეთრი ზრდა და ასევე ჟანგბადის აქტიური ფორმების წარმოშობა. ძირითადი გზები, რომლითაც შეიძლება მოხვდეს ნანონაწილაკები ადამიანის ორგანიზმში შეიძლება იყოს ატმოსფერული ჰაერი, წყალი და ნიადაგი [5]. მრავალი მეცნიერი გამოთქვამს შეშფოთებას ნანომასალების მედიცინაში ფართოდ გამოყენებასთან დაკავშირებითაც [6 – 8]. მაგალითად, აღმოჩენილია კადმიუმისა და ვერცხლის ნანონაწილაკების ტოქსიკური თვისებები, კერძოდ, მათი მოქმედება ადამიანისა და ცხოველების სპერმატოგონიალურ უჯრედებზე. ეს განსაკუთრებით შემამფოთებელია ვერცხლის ნანონაწილაკებთან მიმართებაში, რადგან ის მრავალი წელია ფართოდ გამოიყენება მედიცინაში. ეჭვს არ იწვევს, რომ საჭიროა დამატებითი კვლევების ჩატარება. აღსანიშნავია ე.წ. ფორს-მაჟორული სიტუაციები, რის მაგალითადაც შეიძლება დავასახელოთ საომარი მოქმედებები სპარსეთის ყურეში, როდესაც ჯარისკაცებს გაუჩნდათ პათოლოგია, რომელიც არ თავსდებოდა ცნობილი დაავადებების სინდრომოლოგიაში [6, 9, 10]. ჯარისკაცების ბიოლოგიურ ქსოვილებში აღმოჩნდა ტყვიის, ნახშირბადის, კობალტის და ვოლფრამის ნანონაწილაკები. ავტორების აზრით, ეს იყო ნანოპათოლოგია, განპირობებული ნანონაწილაკების ზემოქმედებით ორგანიზმზე. ხოლო თვითონ ამ ნანონაწილაკების წარმოშობა შესაძლებელია ყოფილიყო ვოლფრამული იარაღის, ნავთობის ჭაბურღილის აფეთქების ან გაუმდიდრებელი ურანის შემცველი ბომბის აფეთქების შედეგი.

ნანონაწილაკების დაგროვება და მიგრირება გარემოში შეიძლება მოხდეს ზედაპირული, გრუნტის და ჩამდინარე წყლების საშუალებით. მათი გავრცელება შეიძლება მოხდეს ჰაერის, ნიადაგის ან სამრეწველო ნარჩენების საშუალებით. ამრიგად, კონტაქტის ალბათობა ნანონაწილაკებსა და ცოცხალ ორგანიზმებს შორის საკმაოდ მაღალია. ნანონაწილაკების მოხვედრა ორგანიზმში შესაძლებელია ინჰალაციური, პერორალური ან ტრანსდერმალური გზით. ადამიანის ორგანიზმში შეღწევის მექანიზმის მიხედვით ისინი გადანაწილდებიან მასში სხვადასხვაგვარად. ამჟამად, ნანონაწილაკების მიგრაციის პროცესი ადამიანის ორგანიზმში სათანადოდ არ არის შესწავლილი. ასევე აქტიურად მიმდინარეობს ნანონაწილაკების ბიოლოგიურ უჯრედში შეღწევის მექანიზმების კვლევა.

უკანასკნელი წლების განმავლობაში დადგენილ იქნა, რომ ნანონაწილაკთა ბიოტესტირებისათვის შესაძლებელია გამოყენებული იყოს ჰიდრობიონტები. ამჟამად ცნობილია, რომ ნანონაწილაკების შემცველი დისპერსიული სისტემების ტოქსიკურობის ხარისხი დამოკიდებულია, როგორც ნაწილაკების ზომაზე, ასევე მათ ქიმიურ ბუნებაზე. ნანონაწილაკთა ტოქსიკური თვისებების დამოკიდებულება ნანონაწილაკთა კონცენტრაციაზე უფრო მკვეთრად მაშინაა გამოხატული, როდესაც მათი ზომა არის 5 – 10 ნმ.

ნანოტოქსიკოლოგიაში, მოლეკულური ხსნარების ტოქსიკოლოგიის მეთოდების პირდაპირ გადმოტანას შეუძლია გამოიწვიოს კვლევის შედეგების დამახინჯება. ნანოტოქსიკოლოგიურ კვლევებში გამოყენებული უნდა იყოს ტესტ-ორგანიზმების ფართო წრე სხვადასხვა სისტემატიკური ჯგუფებიდან. ამჟამად გამოვლენილია

ნანონაწილაკების გავრცელების მექანიზმები ატმოსფერულ ჰაერში, წყალში და ნიადაგში, მაგრამ არასათანადოდ არის შესწავლილი ნანონაწილაკების გადატანის მექანიზმები სხვა სახით – ტრაფიკული ქსელების საშუალებით. ამ პროცესის შესწავლისას აუცილებელია ნანონაწილაკების აკუმულაციისა და შემდგომი მიგრაციის პროცესის კვლევა მიკროორგანიზმებში, მცენარეებში, ცხოველებში და, აქედან გამომდინარე, ადამიანის ორგანიზმში.

ზოგიერთი მეცნიერის აზრით, ნანონაწილაკების ასეთი ტრანსლოკაცია შესაძლებელია და მას შეუძლია გამოიწვიოს გარემოს დაბინძურება და შექმნას გარკვეული საფრთხე ადამიანებისათვის [11, 12]. ამ პრობლემის შესასწავლად გამოყენებული იყო ტიტანის დიოქსიდის ნანონაწილაკები, რომლებიც ფართოდ გამოიყენება საღებავებში, სამკურნალო პრეპარატებში, კოსმეტიკურ საშუალებებში და ა.შ. 5 ნმ ზომის ტიტანის დიოქსიდის ნანონაწილაკები მიღებული იყო ელექტროაფეთქებით. ამ ნანონაწილაკების აკუმულირების პროცესის შესწავლა ბიოლოგიურ ქსოვილში ხდებოდა მას-სპექტრომეტრის მეშვეობით. გამოკვლეული იყო სისტემები: “ქლორელა – ნანონაწილაკთა დისპერსიული სისტემა” და “დაფნიები – ნანონაწილაკთა დისპერსიული სისტემა”. ტესტ-ორგანიზმებად *Chlorella vulgaris* Beijer-ისა და *Daphnia magna* Straus-ის არჩევა განპირობებული იყო იმით, რომ ისინი ფართოდ გამოიყენება ეკოტოქსიკოლოგიურ კვლევებში და ჩართული არიან ბიოტესტირების სტანდარტულ პროგრამებში.

აღმოჩნდა, რომ ორივე სისტემაში ინტენსიურად ხდებოდა ტიტანის დიოქსიდის ნანონაწილაკების აკუმულირება. ამასთანავე, ბიოაკუმულაციის ხარისხი დაფნიების გამოყენების შემთხვევაში რამდენადმე მცირეა, ვიდრე ქლორელის გამოყენებისას. დადგინდა, რომ ტიტანის დიოქსიდის ნანონაწილაკები საკმაოდ სწრაფად აკუმულირდებიან, როგორც წყალმცენარეებში, ასევე დაფნიებში. რადგან პლანქტონური ორგანიზმები წარმოადგენენ შუალედურ შემაკავშირებელ რგოლს კვებით და ენერგეტიკულ ჯაჭვში, რომლის პირველადი მომხმარებლები არიან წყალმცენარეები, ხოლო მეორადნი შეიძლება იყვნენ თევზები. მკვლევართა მიერ მიღებული შედეგები მიუთითებს იმაზე, რომ შესაძლებელია მოხდეს ნანონაწილაკთა ტრანსლოკაცია კვებითი ქსელების საშუალებით სამრეწველო მეთევზეობის ზონაში, ხოლო აქედან ადამიანის ორგანიზმში [11].

ამჟამად გარემოს მონიტორინგში ფართოდაა გავრცელებული ფიზიკო-ქიმიური მეთოდები, რომელიც საშუალებას იძლევა განისაზღვროს ტოქსიკანტების ზდკ, მაგრამ მათი გამოყენება უსაფრთხოების კრიტერიუმად არ უზრუნველყოფს გარემოში არსებული ბიოორგანიზმების უსაფრთხოებას. ატმოსფეროს დამაბინძურებლები რეალურად წარმოადგენენ სხვადასხვა ნივთიერებათა ნაზავს და ამკარაა, რომ ცალკეული კომპონენტების კონცენტრაცია, რომელიც ნაკლებია ზდკ-ზე, არ იძლევა უსაფრთხოების გარანტიას. ამასთანავე ნივთიერებათა ზდკ-ის დადგენა ითხოვს დიდ დანახარჯებს. ამერიკელი ექსპერტების მონაცემებით ის შეადგენს დაახლოებით 1 მლნ. დოლარს. რუსი მეცნიერების აზრით, საჭირო თანხა რამდენადმე ნაკლებია, მაგრამ მეთოდის გამოყენება მაინც მნიშვნელოვან ხარჯებთან არის დაკავშირებული.

ეკოსისტემაში მოხვედრილმა ქიმიურმა ნივთიერებებმა შეიძლება იმოქმედონ იქ არსებულ ყველა ცოცხალ ორგანიზმზე, რამაც შეიძლება გამოიწვიოს მეტად მძიმე შედეგები. ასევე შესაძლებელია ბიოტრანსფორმაციის პროცესში ახალი ტოქსიკური ქსენობიოტიკების წარმოქმნა. ცხადია, აუცილებელია შეიქმნას მეცნიერულად დაფუძნებული კრიტერიუმები, რომლებიც განსაზღვრავენ ადამიანისა და სხვა

ცოცხალი ორგანიზმების უსაფრთხოებას ეკოსისტემაში. ამ მხრივ მეტად პერსპექტიულია ეკოსისტემების მდგომარეობის შესწავლა ცოცხალი ორგანიზმების საშუალებით.

ზღვ-ის მნიშვნელობები დადგენილია მხოლოდ ადამიანისათვის და, ცხადია, ის არ შეიძლება გავრცელდეს სხვა ცოცხალ ორგანიზმებზე. ეკოსისტემებში შეიძლება არსებობდეს უფრო მგძნობიარე ორგანიზმები, რომლებიც დიდ როლს ასრულებენ ეკოსისტემების წონასწორობისათვის. ბიომონიტორინგი საშუალებას იძლევა მოვიპოვოთ ინფორმაცია გარემოს ცვლილებების შედეგად წარმოშობილი ბიოლოგიური შედეგების შესახებ. გარემოს მდგომარეობის შეფასებისას სასურველია ფიზიკო-ქიმიური და ბიოლოგიური მეთოდების ერთობლივად გამოყენება.

ბიომონიტორინგის პერსპექტიულობა განპირობებულია აგრეთვე მისი სიმარტივითა და სიიაფით. მთელ რიგ შემთხვევებში ის წარმოადგენს ექსპრეს-მეთოდს. ტრადიციულად ჯერ ტარდება გარემოს ბიონდიკაცია, რომელიც საშუალებას იძლევა სწრაფად იქნას აღმოჩენილი ყველაზე დაზიანებული “ცხელი” უბნები, ხოლო შემდგომი კვლევისას ფიზიკო-ქიმიური მეთოდებით ხდება ტოქსიკანტების იდენტიფიცირება და მათი ბუნების დადგენა.

მითითებები

1. О. А. Ляшенко. Биоиндикация и биотестирование в охране окружающей среды. 2012, Санкт-Петербург.
2. Ю. С. Григорьев, Н. В. Пахарькова, С. В. Прудникова, О. Е. Крючкова. Биологический контроль состояния окружающей среды. 2008, Красноярск.
3. Н. В. Маячкина, М. В. Чугунова. Особенности биотестирования почв с целью их экотоксикологической оценки. Вест. Нижегород. унив. им. Лобачевского 1 (2009) 84-93.
4. А. С. Бугаев, В. В. Васекин, В. А. Гольцов, А. А. Евдокимов, Ю. А. Котляр, В. М. Лазарев, С. Д. Левченко, А. П. Лосюков, Л. Б. Меламед, А. И. Морозов, Л. Э. Морозова, М. Ю. Пискунов, М. П. Романов, А. С. Сигов, Л. А. Спортсмен, В. Н. Фатеев, Х. Д. Чеченов, П. В. Шелищ, В. В. Шинкаренко, В. А. Ястребов. Рынок нанотехнологии. Состояние и перспективы. 2008, Москва: Мир – Икар.
5. თ. პავლიაშვილი, თ. კალაბეგიშვილი. ნანონაწილაკების და ნანომასალების გამოყენების ეკოლოგიური ასპექტები. საქ. ქიმ. ჟურნ. 2 (2012) 225-229.
6. Н. Г. Проданчук, Г. М. Балан. Нанотоксикология: Состояние и перспективы исследований. Совр. проб. токсикол. 3-4 (2009) 4-9.
7. V. E. Kagan, H. Bayir, A. A. Shvedova. Nanomedicine and nanotoxicology: Two sides of the same coin. Nanomed. Nanotechnol. Biology & Medic. 1 (2005) 313-316.
8. G. Oberdorster, E. Oberdorster, J. Oberdorster. Nanotoxicology: An emerging discipline evolving from studies of ultrafine particles. Environ. Health Persp. 7 (2005) 823-839.
9. A. M. Gatti, M. Montana. Detection of micro- and nanosized biocompatible particles in blood. J. Mater. Sci. Mater. Med. 15 (2004) 469-472.

10. Ed. A. M. Gatti. Ch. 12: Risk assessment of micro- and nanoparticles and human health. In: Handbook of Nanostructured Biomaterials and Their Applications. 2005, Am. Sci. Publ., 347- 369.
11. Ю. Н. Моргалев, Н. С. Хоч, Т. Г. Моргалева, Е. С. Гулик, Г. А. Борило, У. А. Булатова, С. Ю. Моргалев, Е. В. Понявина. Биотестирование наноматериалов: О возможности транслокации в пищевые сети. Росс. нанотехнол. 5 (2010)131-135.
12. R. D. Handy, R. Owen. The ecotoxicology of nanoparticles and nanomaterials: Current status, knowledge gaps, challenges, and future needs. Ecotoxicol. 17 (2008) 315- 325.

АКУСТИЧЕСКИЙ СПЕКТРОМЕТР

Д. Г. Дриаев, К. О. Кахиани, Ф. Х. Акопов, С. Дж. Цакадзе

Институт физики им. Э. Андроникашвили
Тбилисский государственный университет им. И. Джавахишвили
Тбилиси, Грузия
drijaev@mail.ru

Принята 4 октября 2013 года

Метод внутреннего трения является одним из наиболее тонких и чувствительных инструментов исследования дефектов кристаллической структуры.

Коэффициент внутреннего трения Q^{-1} – величина обратная механической добротности – является мерой рассеяния механической энергии колеблющегося тела:

$$Q^{-1} = \frac{1}{2\pi} \frac{\Delta W}{W} = \frac{\delta}{\pi} = \frac{1}{\sqrt{3}} \frac{\Delta \nu}{\nu_0}, \quad (1)$$

где ΔW – энергия, рассеянная за период, W – энергия упругих колебаний, δ – логарифмический декремент затухания, $\Delta \nu$ – полуширина резонансного пика, ν_0 – резонансная частота образца. Как видно из (1), внутреннее трение можно определять или по затуханию свободных колебаний образца, или по полуширине его резонансного пика. Однако такие измерения «по точкам» связаны с большими затратами времени и не позволяют фиксировать быстропротекающие процессы.

Мы использовали описанный в литературе [1, 2] способ измерения внутреннего трения, который лишен этих недостатков и позволяет проводить измерения в непрерывном режиме при постоянной амплитуде колебаний образца. Он основан на уравнении колебаний механического вибратора в резонансе:

$$Q^{-1} = F / A m \omega_0^2, \quad (2)$$

где A – амплитуда колебаний, F – амплитуда возбуждающей силы, m – масса, а ω_0 – резонансная частота вибратора.

Разработанный нами акустический спектрометр предназначен для измерения внутреннего трения Q^{-1} и модуля упругости E различных материалов в широком интервале температур в килогерцовом диапазоне частот. Отличительной особенностью прибора является возможность автоматической непрерывной записи Q^{-1} и E в условиях стабилизации амплитуды колебаний образца на заданном уровне.

Образец. Возбуждение и детектирование колебаний

В приборе используется метод вибрирующего язычка.

Одной из важнейших задач техники акустических измерений является повышение механической добротности колебательной системы. Основным каналом потерь энергии механических колебаний являются потери на внешнее трение между образцом и его

зажимом, которые могут достигать $Q^{-1} \approx 10^{-3}$, что ограничивает чувствительность метода и неприемлемо для задач, требующих более низкого уровня диссипации.

Чтобы уменьшить аппаратный фон диссипации и зависимость параметров колебаний резонатора от свойств держателя, мы используем в качестве образца-вибратора изобретенный нами [3] трехязычковый камертон (**рисунок 1**), который представляет собой плоскопараллельную пластинку с тремя язычками одинаковой длины; при этом средний язычок вдвое шире крайних.

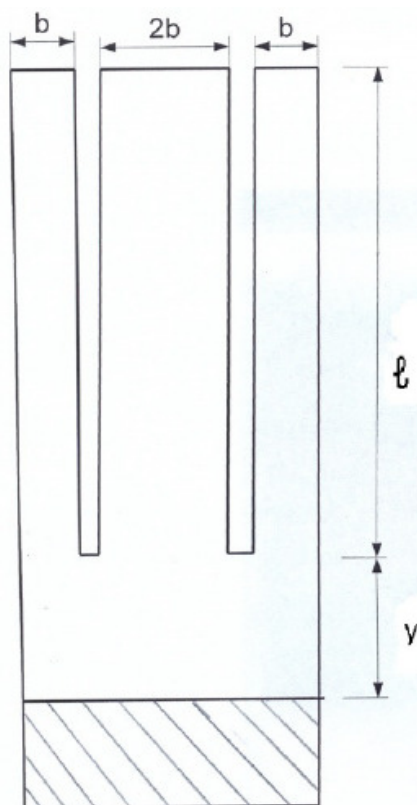


Рисунок 1. Трехязычковый камертон.

При возбуждении изгибных колебаний любого из язычков, остальные тоже приходят в колебательное движение, причем крайние язычки колеблются синфазно друг с другом и в противофазе со средним язычком в направлении перпендикулярном плоскости пластинки. Каждый язычок представляет собой вибратор на изгибных колебаниях с собственной частотой первой гармоники:

$$\nu_0 = 0.162 \frac{h}{l^2} \sqrt{\frac{E}{\rho}}, \quad (3)$$

где h – толщина, l – длина, ρ – плотность, а E – модуль Юнга язычка.

Мы использовали камертоны со средними язычками шириной $b = 4$ мм, толщиной $h = 0.5 - 2$ мм и длиной $l = 10 - 30$ мм. При этих размерах частота первой гармоники измеренных нами материалов лежит в интервале $0.5 - 5$ кГц.

Камертон закрепляется консольно за основание между двумя зажимными блоками, причем эмпирически установлено, что линия зажима должна быть удалена от основания язычков на расстояние y , не меньшее, чем удвоенная ширина b среднего язычка (на **рисунке 1** $y \geq 2b$). Поскольку амплитуда колебаний основания камертона практически

равна нулю, то и потери на трение в зажимах минимальны и добротность колебательной системы определяется свойствами самого образца.

При креплении камертона деформация, обусловленная зажимными блоками, локализована в основании камертона, вследствие этого, один и тот же образец можно зажимать сколько угодно раз без риска повредить его; при этом воспроизводимо обеспечивается минимальный уровень фонового затухания.

На расстоянии $d \approx 0.1$ мм от поверхности среднего язычка камертона располагается плоский электрод, служащий для возбуждения и регистрации колебаний.

Возбуждение колебаний происходит путем подачи на электрод постоянного поляризующего напряжения V и синусоидального возбуждающего напряжения $V_0 \sin \omega t$. Амплитуда электростатической силы, действующей с частотой ω со стороны электрода на образец

$$F = \epsilon'_0 S V_0 V / d^2, \quad (4)$$

где S – площадь электрода, d – зазор между электродом и образцом. Из (2) и (4) следует связь между напряжением на электроде и внутренним трением образца:

$$Q^{-1} = (\epsilon'_0 S V / m \omega^2 d^2 A) V_0. \quad (5)$$

Таким образом, если амплитуду колебаний образца поддерживать постоянной, внутреннее трение будет определяться только амплитудой возбуждающего напряжения:

$$Q^{-1} = k V_0. \quad (6)$$

Константа k вычисляется экспериментально путем определения абсолютного значения внутреннего трения по логарифмическому декременту затухания (согласно (1)).

Регистрация колебаний образца осуществляется емкостным датчиком с частотной модуляцией (этот способ детектирования обладает многими преимуществами и, в первую очередь, высокой чувствительностью). Заземленная грань образца и электрод образуют плоский конденсатор емкостью $C = \epsilon'_0 S / d$, который вместе с индуктивностью L включен в колебательный контур высокочастотного генератора-датчика, работающего на частоте $f \approx 50$ МГц. При колебаниях образца с амплитудой $A \ll d$, зазор между электродом и образцом изменяется на $\Delta d = A$, емкость C системы образец–электрод изменяется на ΔC и, соответственно, несущая частота генератора-датчика $f = 1/2\pi\sqrt{LC}$ изменяется на Δf . Таким образом происходит частотная модуляция высокочастотного сигнала с девиацией частоты Δf , определяемой амплитудой колебаний язычка (связь между Δf и A устанавливается из калибровочных измерений).

Система образец–электрод находится внутри камеры, дающей возможность производить измерения в вакууме (10^{-4} торр) или в инертной среде. Конструкция вакуумной камеры позволяет проводить измерения в диапазоне температур от 4.2 до 400 К (в принципе, конструкцию камеры и держателя образца можно видоизменить так, чтобы можно было проводить измерения и при более высоких температурах).

Блок-схема прибора

Функциональная схема электронной части акустического спектрометра приведена на **рисунке 2**. Вся электронная часть прибора контролируется компьютером через модуль управления и сбора данных (Data Acquisition PCI-6221 фирмы National Instruments).

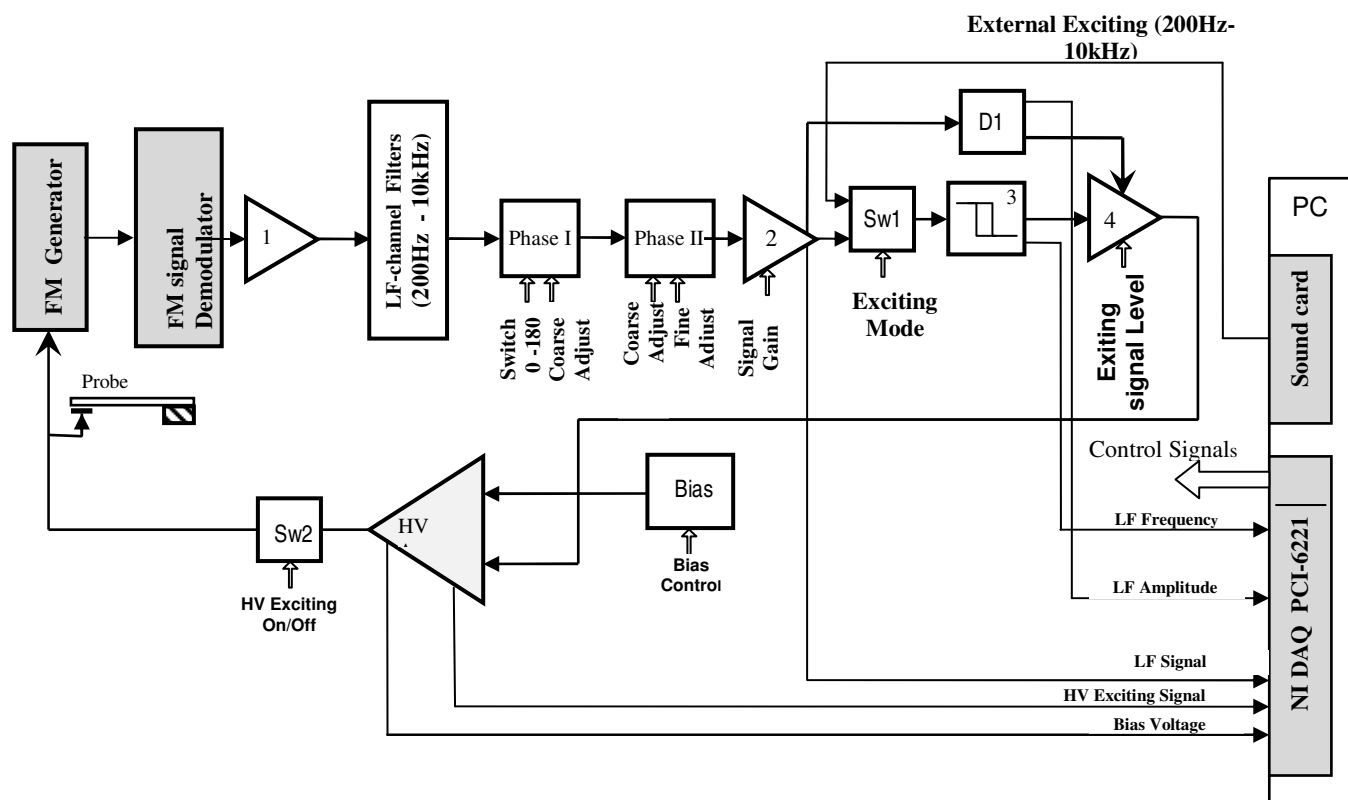


Рисунок 2. Схема электронной части прибора.

Частотно-модулированный сигнал от генератора-датчика (FM Generator) по коаксиальному кабелю подается на вход приёмника с частотным демодулятором (FM Signal Demodulator). На его выходе имеем сигнал с частотой, равной частоте ν_0 собственных колебаний образца, и напряжением U , пропорциональным амплитуде его колебаний. После усилителя 1 этот сигнал подается на вход полосового фильтра с полосой пропускания 0.2 – 10 кГц на уровне -3 дБ. Полосовой фильтр собран на операционных усилителях по схемам фильтров Баттерворта 5-го порядка. После прохождения фильтров сигнал поступает в канал возбуждения колебаний который включает: фазовращатель (Phase I и Phase II), усилитель по напряжению 2, коммутатор Sw1, формирователь прямоугольных импульсов 3, пиковый детектор D1 и регулируемый усилитель 4. Сигнал с усилителя 4 поступает на вход высоковольтного усилителя HV Amp, с выхода которого возбуждающее напряжение, через коммутатор Sw2 (управляющий сигнал HV Exciting On / Off) и развязывающий LC фильтр, подается на электрод. На электрод так же подается поляризующее напряжение V с Bias, величина которого (100 – 600 В) регулируется управляющим сигналом Bias Control. Величину возбуждающего сигнала на выходе усилителя HV Amp можно изменять от 0 до 300 В. В режиме автоколебаний через эти узлы замыкается цепь положительной обратной связи, в которой поддерживаются при $A = const$ незатухающие резонансные колебания образца.

Стабилизация амплитуды колебаний образца на заданном уровне осуществляется следующим образом. Когда внутреннее трение образца по той или иной причине изменяется, механическая добротность колебательной системы убывает / возрастает, что вызывает уменьшение / увеличение амплитуды колебаний образца и напряжение, поступающее с усилителя 2 на пиковый детектор D1, изменяется; пиковый детектор выдает соответствующий сигнал разбаланса, который поступает на управляемый

усилитель 4 и возбуждающее напряжение корректируется таким образом, чтобы амплитуда колебаний образца вернулась к заданному уровню.

Как было указано выше, мерой внутреннего трения в этом случае вынужденных резонансных колебаний служит амплитуда возбуждающего напряжения V_0 , которая и фиксируется в модуле сбора данных компьютера. Кроме того, непрерывно измеряется и поступает в модуль сбора данных резонансная частота образца, из которой вычисляется модуль упругости.

Таким образом, данный акустический спектрометр обеспечивает измерение внутреннего трения и модуля упругости в непрерывном режиме, что значительно увеличивает разрешающую способность любого эксперимента. В режиме автоколебаний возбуждение колебаний образца и их максимальная амплитуда достигается только при определенном значении фазы прикладываемого возбуждающего сигнала. Регулировка фазы осуществляется в Phase I и Phase II. Для полного перекрытия диапазона регулировки фаз ($0 - 180^\circ$) кроме грубого и тонкого изменения фазы используется также и фазоинвертор в Phase I. В качестве регулирующего элемента изменения фазы применены управляемые компьютером электронные сопротивления в составе RC цепей, задающих величину сдвига фазы.

Поскольку при высоких уровнях внутреннего трения ($Q^{-1} \approx 0.1$) декремент затухания определяется со значительной погрешностью, измерения в этом случае необходимо проводить по ширине резонансной кривой. Поэтому, кроме режима автоколебаний, в приборе предусмотрен режим внешнего возбуждения, при котором образец подвергается вынужденным колебаниям с частотой, программно задаваемой звуковой картой используемого компьютера; при сканировании частоты определяется полуширина резонансной кривой, из которой по (1) вычисляется Q^{-1} . Выбор режима возбуждения осуществляется коммутатором Sw1 (управляющий сигнал Exciting Mode).

Программное обеспечение акустического спектрометра включает в себя пакет NI DAQmx v.8.7.1, поставляемый National Instruments вместе с модулем PCI-6221 и созданную для данного прибора программу "Int_Fric3.10".

Программа "Int_Fric" написана в Visual C++ 6.0 с использованием библиотек MFC, Daqmx, fmod и работает в операционных системах Windows XP, 7. Программа позволяет управлять параметрами электронной части спектрометра, принимать и сохранять данные на диске в виде файлов, графически отображать процесс измерений и проводить широкий спектр экспериментов на акустическом спектрометре в ручном и автоматическом режимах.

Заключение

Отметим отличительные достоинства представленного акустического спектрометра.

1. Использование в качестве образца-вибратора трехязычкового камертона обеспечивает минимальный уровень фоновой диссипации ($Q^{-1} \approx 10^{-6}$). Кроме того, использование камертона позволяет исключить самое уязвимое место техники

акустических методов – воздействие крепления образца на уровень фоновой диссипации и воспроизводимость результатов измерений.

2. Измерение внутреннего трения и модуля упругости в непрерывном режиме увеличивает разрешающую способность эксперимента.
3. Поскольку внутреннее трение кристаллов в большинстве случаев зависит от амплитуды деформации, стабилизация амплитуды колебаний образца на заданном уровне (т.е. измерение Q^{-1} при фиксированной колебательной деформации) позволяет избежать неоднозначности при интерпретации результатов эксперимента.
4. Использованный для возбуждения и регистрации колебаний электростатический способ, характеризуется слабой связью между механической и электрической системами, так что утечка энергии через эти связи и влияние параметров электрической цепи на результаты измерений внутреннего трения и модуля упругости весьма незначительны и ими можно пренебречь. Кроме того, мы применяем вариант, который значительно упрощает конструкцию блока-держателя образца – возбуждение и регистрация колебаний осуществляется одним электродом.

Ссылки

1. D. O. Thompson, F. M. Glass. Rev. Sci. Instr. 29 (1958) 1034.
2. W. W. Scott, R. K. mac Crone. Rev. Sci. Instr. 9 (1968) 821.
3. М. В. Галусташвили, Д. Г. Дриаев, И. А. Политов, З. К. Саралидзе. Патент GE P (2005) 3499B.

THE THEORY OF POLARON LOW TEMPERATURE MOBILITY

B. Kotia, D. Khutsishvili

Georgian Technical University
Tbilisi, Georgia
bejankotia@gmail.com
davitiu@gmail.com

Accepted October 5, 2013

1. Introduction

Investigation of kinetics of small subsystem (particle) interacting with a quantum field (thermostat) is an important problem of quantum field theory and condensed matter physics. Electron in polar crystal (polaron) is widely known example of such system [1]. The relaxation processes and behavior of particle interacting with heat bath under the influence of applied field can be conveniently studied by means of the correlation functions and Green functions [2].

The equilibrium two-time correlation functions are the basic quantities in the Kubo linear transport theory [3]. This theory (for example, in case of electrons, which interact with impurities or phonon field in crystal) is free from restrictions on the scattering processes, in contrast to the Boltzmann equation approach in which the scattering processes must be well separated in space and in time. But at the calculation of electrical conductivity $\sigma(\omega)$ (ω is the applied electric frequency) according to Kubo formula, i.e. the current–current correlation function, the difficulties arise connected with the divergency of terms of $\sigma(\omega)$ expansion into a series on the interaction of electrons with scatterers at $\omega \rightarrow 0$. Even in case of weak interaction one must sum up an infinite series of divergent terms to obtain a correct result for conductivity at $\omega \rightarrow 0$ [4] (because the correct order of two limits in such calculation is $\lim_{\alpha \rightarrow 0} \lim_{\omega \rightarrow 0}$ [5], where α is coupling constant for the interaction of electrons with scatterers). There is a number of works dealing with the polaron mobility by means of different approximations in calculation of current–current correlation function [6]. However, these results for low temperature mobility of polaron are different from results obtained with the help of the Boltzmann equation [6].

The above difficulties can be avoided by using an evolution equation for correlation function instead of correlation function itself. Generalized equations for density matrix and correlation functions of subsystem interacting with quantum boson field (thermostat) have been obtained in [7 – 11]. The Boltzmann equation for statistical operator of subsystem follows from the exact obtained at weak electron–phonon interaction and small external field as well as the corresponding approximate equations for correlation functions of subsystem. In case of strong (arbitrary) electron–photon interaction the approximate evolutionary equations can be obtained [10, 11] within the scope of the Feynman model of polaron [12].

The only approximation used in the derivation of the generalized evolutionary equations is the random phase approximation (RPA) (at the initial time moment $t = 0$ a subsystem and

thermostat do not interact with each other or Gibbs factor in an equilibrium two-time correlation function is approximated by product of Gibbs distributions for the subsystem and thermostat). But it is not evident that the results will be the same under various initial conditions.

In the given work we derive the new exact equations for the correlation functions of the subsystem which interacts with boson field (heat bath). The random phase approximation (the product type distribution) is not used at derivation of these equations. With the help of equations obtained the correlation functions for electron–phonon system is considered and a theory of the electrical conductivity within the scope of the Kubo linear transport theory is developed. In particular, the consistent theory of polaron mobility at low temperatures is obtained. We discuss also the influence of the initial correlations on relaxation process and conductivity.

The paper is organized as follows.

In Section 2, we introduce the subsystem correlation functions, Green functions, Liouville superoperator formalism, projection operator techniques and exact equations (not using RPA) for correlation functions of the subsystem interacting with the large system in the equilibrium state (quantum boson field). The procedure of the excluding of boson field operators (amplitudes) is described and transition to the Markovian equations in the second order of a perturbation theory is realized.

In Section 3, we consider electron-phonon system. The current–current (velocity–velocity) correlation functions, which define the conductivity tensor in the Kubo linear transport theory [3] is introduced here. On the basis of the formalism developed in Section 2 we derive in this section the equations for velocity–velocity correlation functions of electron weakly interacting with phonons and with weak uniform external electric field. In the case of single-band model these equations are solvable by quadratures with the aid of approximation which is of relaxation time approximation (RTA) type and is exact at low temperatures. The corresponding expression for conductivity tensor applicable for arbitrary dispersion laws of electrons and phonons and for arbitrary temperature is obtained. The relaxation process and contribution from the initial correlations (in RPA they are absent) are discussed in this section.

In Section 4, conductivity connected with the slow traveling Frohlich polaron is considered (the case of low temperature). The generalized Osaka result for conductivity (Drude formula) including the correction from initial correlations is obtained. Correct low temperature mobility of polaron follows from the result obtained. Further discussion is given in Section 5.

2. Correlation function equation approach

Consider dynamic subsystem S interacting with the boson field Σ . The Hamiltonian of the whole system ($S + \Sigma$) is taken as

$$H = H_S + H_\Sigma + H_i \quad (1)$$

where H_S, H_Σ and H_i are the Hamiltonians of subsystem, boson field and interaction between them respectively

$$H_\Sigma = \sum_k \hbar\omega(k) b_k^+ b_k, \quad H_i = \sum_k [C_k(S) b_k + C_k^+(S) b_k^+] \quad (2)$$

Here $\hbar\omega(k)$ is the energy quantum of boson field characterized by quantum numbers k, b_k, b_k^+ are Bose-operators of annihilation and creation of boson in state $k, C_k(S)$, and $C_k^+(S)$ are operators attributed to the subsystem S . Boson system Σ will be considered as thermostat.

The two-time equilibrium correlation function $F(t)$ and Green functions $G^r(t), G^a(t), G^c(t)$ (retarded, advanced, casual) for subsystem operators A_S, B_S are determined as [2]:

$$\begin{aligned} F(t) &= \langle A_S(t), B_S(0) \rangle \\ G^r(t) &= \theta(t) \langle [A_S(t), B_S(0)]_\eta \rangle \\ G^a(t) &= -\theta(-t) \langle [A_S(t), B_S(0)]_\eta \rangle \\ G^c(t) &= \frac{1}{i\hbar} \langle T_\eta \{ A_S(t), B_S(0) \} \rangle \end{aligned} \quad (3)$$

Here $A_S(t) = e^{\frac{i}{\hbar}Ht} A_S(0) e^{-\frac{i}{\hbar}Ht}$, $\langle \dots \rangle$ defines the averaging over the equilibrium ensemble:

$$\begin{aligned} \langle \dots \rangle &= Z^{-1} Tr \{ e^{-\beta H} \dots \} \\ Z &= Tr e^{-\beta H}, \quad \beta = \frac{1}{k_B T} \end{aligned}$$

$\theta(t) = 1$ at $t > 0$ and $\theta(t) = 0$ at $t < 0$;

$$\begin{aligned} [A_S(t), B_S(0)]_\eta &= A_S(t) B_S(0) - \eta B_S(0) A_S(t); \\ T_\eta \{ A_S(t), B_S(0) \} &= \theta(t) A_S(t) B_S(0) + \eta \theta(-t) B_S(0) A_S(t) \end{aligned}$$

$\eta = 1$ if A_S and B_S are Bose-operators and $\eta = -1$ for Fermi-operators.

The correlation function $F(t)$ may be rewritten in the form

$$\langle A_S(t) B_S(0) \rangle = Z^{-1} Tr_{(S,\Sigma)} [B_S(0) e^{-\beta H} e^{iLt} A_S(0)] \quad (4)$$

Here the Liouville superoperator L acting on the arbitrary operator D according to

$$\begin{aligned} LD &= \frac{1}{\hbar} [HD]_- \\ e^{\pm iLt} D(0) &= e^{\pm \frac{i}{\hbar}Ht} D e^{\mp \frac{i}{\hbar}Ht} \equiv D(\pm t) \end{aligned}$$

is introduced ($L = L_S + L_Z + L_i$) in corresponding with terms of the Hamiltonian (1). $Tr_{(s,\Sigma)}$ is the trace over the whole system ($S + \Sigma$) states.

It is evident form (4) that the dynamics of correlation function can be considered with the help of following superoperators which act on D operator as

$$R(t)D = Z^{-1} Tr_{(\Sigma)} [e^{-\beta H} e^{iLt} PD] \quad (5)$$

$$I(t)D = Z^{-1} Tr_{(\Sigma)} [e^{-\beta H} e^{iLt} QD],$$

where P is the projection operator ($P^2 = P$) realizing average over the heat bath (boson field) states

$$PD = Tr_{(\Sigma)} (\rho_\Sigma D) \equiv \langle D \rangle_\Sigma, \quad \rho_\Sigma = Z_\Sigma^{-1} e^{-\beta H_\Sigma} \quad (6)$$

$$Z_\Sigma = Tr_{(\Sigma)} e^{-\beta H_\Sigma}, \quad Q = 1 - P$$

Then the expression for correlation function $F(t)$ (3) takes the form

$$\langle A_S(t) B_S(0) \rangle = \langle A_S(0) B_S(-t) \rangle = Tr_{(s)} [B_S(0) R(t) A_S(0)] \quad (7)$$

It is easy to obtain the exact system of equations for superoperators $R(T)$ and $I(t)$. The result is

$$\frac{\partial}{\partial t} R(t) = iR(t)PLP + iI(t)QLP \quad (8)$$

$$\frac{\partial}{\partial t} I(t) = iI(t)QLQ + iR(t)PLQ$$

equation (8) for $I(t)$ integrates to the following expression

$$I(t) = I(0)M_Q(t) + i \int_0^t d\tau R(\tau)PLQM_Q(t-\tau), \quad (9)$$

where

$$I(0) = Z^{-1} Tr_{(\Sigma)} e^{-\beta H} Q, \quad (10)$$

is the initial value of $I(t)$ and

$$M_Q(t) = e^{iQLQ t}$$

is the “mass” superoperator.

Substituting (9) in the first equation (8) we obtain the exact inhomogeneous evolutionary equation for $R(t)$

$$\frac{\partial}{\partial t} R(t) = iR(t)PLP + iI(0)M_Q(t)QLP - \int_0^t d\tau R(\tau)PLQM_Q(t-\tau)QLP \quad (11)$$

This equation defines the equation for correlation function (7). Using the definitions (5) and the possibility of operator cyclic rearrangement under the trace sign, one can obtain from (7) and (11) such an equation for the correlation function

$$\begin{aligned} \frac{\partial}{\partial t} \langle A_S(0) B_S(-t) \rangle &= i \langle [PLPA_S(0)] B_S(-t) \rangle + i \langle [QM_Q(t)QLPA_S(0)] B_S(0) \rangle - \int_0^t d\tau \langle [PLQ \times \\ &\times M_Q(t-\tau)QLPA_S(0)] B_S(-\tau) \rangle \end{aligned} \quad (12)$$

Equations (11) and (12) are the exact non-Markovian equations for superoperator $R(t)$ and correlation function (3). The inhomogeneous terms in these equations (the second terms on the right hand sides of (11) and (12) describe the influence of initial (precollision) correlations in time which are caused by interaction between a subsystem S and heat bath Σ (a boson field) in the initial time moment $t = 0$. hence, to solve the Cauchy problem for equation (11) (and thus to find correlation function) one needs not only $R(0)$ but also $I(0)$. If the memory about initial correlations disappears in time, then the effect of collisions predominates in evolution. But, in principle, the presence of precollision term connected with $I(0)$ can influence the relaxation process described by the correlation function $F(t)$ even at weak subsystem thermostat interaction. We will see that initial correlations contribute to the kinetic coefficient (conductivity) of subsystem S (electron).

It is much better to deal with the exact homogeneous equation of evolution in which initial correlations are contained in an implicit form. To obtain such an equation we use the known integral operator identity

$$e^{-\beta H} = e^{-\beta H_0} - \int_0^\beta d\lambda e^{-\beta H} e^{\lambda H} H_i e^{-\lambda H_0}, \quad (13)$$

where $H_0 = H_S + H_\Sigma$. Then, it is easy to obtain the system of equations for superoperators $I(t)$ and $I(0)$ consisting of equation (9) and equation

$$I(0) = -R(t)J_{\rho}(t, \beta) - I(t)J_{\rho}(t, \beta), \quad (14)$$

which follows from (13) and initial condition for $I(t)$ (10). Here the integral superoperator is introduced as follows:

$$J_{\rho}(t, \beta) = \int_0^{\beta} d\lambda e^{-i\lambda t} e^{\lambda H} H_i e^{-\lambda H_0} Q \quad (15)$$

Finding $I(0)$ from equations (9) and (14) and substituting it into (11) we obtain the desired exact homogeneous closed equation for superoperator $R(t)$

$$\begin{aligned} \frac{\partial}{\partial t} R(t) = & iR(t)PLP - iR(t)PJ_{\rho}(t, \beta)[1 + M_{\rho}(t) \times \\ & \times J_{\rho}(t, \beta)]^{-1} M_{\rho}(t)QLP + \int_0^t d\tau R(\tau)PLQM_{\rho}(t - \tau) \times \\ & \times J_{\rho}(t, \beta)[1 + M_{\rho}(t)J_{\rho}(t, \beta)]^{-1} M_{\rho}(t)QLP - \int_0^t d\tau R(\tau) \times \\ & PLQM_{\rho}(t - \tau)QLP \end{aligned} \quad (16)$$

Note: that equations obtained can be simplified slightly due to the following relations which takes place in general:

$$L_2 P = 0; \quad PL_s Q = QL_s P = 0; \quad PL_i P = 0 \quad (17)$$

Finally, using (16) and (17) we have instead of (12) the following exact equations for correlation function

$$\begin{aligned} \frac{\partial}{\partial t} \langle A_s(0)B_s(-t) \rangle = & i \langle [PL_s PA_s(0)]B_s(-t) \rangle - \\ & i \langle \{ [PJ_{\rho}(t, \beta)[1 + M_{\rho}(t)J_{\rho}(t, \beta)]^{-1} M_{\rho}(t)QL_i P \times \\ & \times A_s(0) \} B_s(-t) \rangle + \int_0^t d\tau \langle \{ PL_i QM_{\rho}(t - \tau)J_{\rho}(t, \beta) \times \\ & \times [1 + M_{\rho}(t)J_{\rho}(t, \beta)]^{-1} M_{\rho}(t)QL_i PA_s(0) \} B_s(-\tau) \rangle - \\ & - \int_0^t d\tau \langle [PL_i QM_{\rho}(t - \tau)QL_i PA_s(0)]B_s(-\tau) \rangle \end{aligned} \quad (18)$$

Equations (16) and (18) are rather complicated. The evolution of initial correlations is described by the integral superoperator $J_{\rho}(t, \beta)$ (15) and proceeds both in Markovian and non-Markovian forms (the second and the third terms on right hand sides of (16) and (18)). In RPA when use in the correlation function (4) $e^{-\beta H_0}$ instead of $e^{-\beta H}$, $I(0) = 0$ as it is seen from (5) and (6) ($PQ = 0$). It leads to $J_{\rho}(t, \beta)$, being equal to zero and vanishing of terms in (16) and (18) connected with the initial correlations. As a result we have a correlations function obtained in [9, 11].

Equations for Green functions (3) follow from equation (18). Thus, for the retarded Green functions we have

$$\begin{aligned} \frac{\partial}{\partial t} G^r(t) = & \partial(t) \langle [A_s(0), B_s(0)]_{\eta} \rangle + \theta(t) \frac{\partial}{\partial t} \langle A_s(0)B_s(t) \rangle - \\ & - \eta \theta(t) \frac{\partial}{\partial t} \langle B_s(0)A_s(t) \rangle \end{aligned}$$

and the equation for the correlation function $M_Q(t) = e^{iQLQ^t}$ can be obtained from (18) by the substitution $t \rightarrow -t$.

The superoperators in equation (18) can be expanded in series on Li (Hi) with help of following expressions

$$[1 + M_Q(t)J_Q(t, \beta)]^{-1} = \sum_{k=0}^{\infty} (-1)^k [M_Q(t)J_Q(t, \beta)]^k$$

$$M_Q(t) = \sum_{n=0}^{\infty} M_Q^{(n)}(t); \quad M_Q^{(0)}(t) = e^{iL_0 t}$$

$$M_Q^{(n)}(t) = \int_0^{t_1} dt_1 \int_0^{t_2} dt_2 \dots \int_0^{t_{n-1}} dt_n e^{iL_0(t-t_1)} iQL_i \times$$

$$\times e^{iL_0(t_1-t_2)} iQL_i \dots e^{iL_0(t_{n-1}-t_n)} iQL_i e^{iL_0 t_n} \quad (19)$$

$(n = 1, 2, \dots)$

$$e^{-iLt} = e^{-iL_0 t} T \exp[-i \int_0^t L_i(\xi)]$$

$$e^{\lambda H} = e^{\lambda H_0} T' \exp \left[\int_0^{\lambda} H_i(\gamma) d\gamma \right]$$

$$L_i(\xi) = e^{iL_0 \xi} L_i e^{-iL_0 \xi}, \quad H_i(\gamma) = e^{-\gamma H_0} H_i e^{\gamma H_0}$$

$$L_0 = L_S + L_{\Sigma}$$

where T and T' denote the ordering of operators with respect to variables ξ and γ .

At weak $S - \Sigma$ interaction the expansions (19) can be regarded formally as the perturbation theory series which allow us to calculate the terms of right-hand sides of equations (16) and (18) with the desired accuracy. It is easy to see that at such an expansion on interaction when H_{Σ} and H_i have form (2), in equation (18) only averages $\langle \dots \rangle_{\Sigma}$ containing the equal numbers of boson creation and annihilation operators are different from zero and proportional to products of boson average occupation numbers. Thus boson (phonon) products of operators are entirely eliminated from equation (18).

Let us assume, that owing to weak coupling between subsystem S and thermostat Σ the time hierarchy

$$\tau_{rel} \gg t_0 = \max(t_S, t_{\Sigma}) \quad (20)$$

takes place, where τ_{rel} is the characteristic subsystem relaxation time, t_S is the collision time for subsystem t_{Σ} is the correlation time for heat bath fluctuations. Inequality (20) allows us to pass to Markovian approximation in equations (16) and (18). Restricting ourselves to the second order of perturbation theory on Hi (Li) and using the expansions (19), we can make following approximations

$$[1 + M_Q(t)J_Q(t, \beta)]^{-1} \Rightarrow 1$$

$$M_Q(t) \Rightarrow M_Q^{(0)}(t) = e^{iL_0 t}$$

$$J_Q(t, \beta) \Rightarrow J_Q^{(0)}(t, \beta) = \int_0^{\beta} d\lambda e^{-iL_0 t} e^{\lambda H_0} H_i e^{-\lambda H_0} Q$$

$$B_S(-\tau) \Rightarrow e^{iL_0(t-\tau)} B_S(-t)$$

Then (18) takes the following simpler form of the Markovian equation

$$\begin{aligned} \frac{\partial}{\partial t} \langle A_S(0) B_S(-t) \rangle &= i \langle [L_S A_S(0)] B_S(-t) \rangle - \\ &- i \int_0^\beta d\lambda \langle [P e^{-iL_0 t} e^{\lambda H_0} H_i e^{-\lambda H_0} e^{iL_0 t} L_i A_S(0)] B_S(-t) \rangle - \\ &- \int_0^t d\tau \langle [P L_i e^{iL_0(t-\tau)} L_i A_S(0)] e^{iL(t-\tau)} B_S(-t) \rangle \end{aligned} \quad (21)$$

Using the explicit form (2) for Hamiltonians H_Z and H_i and eliminating from (21) the boson operators as described above, we obtain the final form of equation for correlation function

$$\begin{aligned} \frac{\partial}{\partial t} \langle A_S(0) B_S(-t) \rangle &= -\frac{i}{\hbar} \langle [A_S, H_S]_- B_S(-t) \rangle - \\ &- \frac{1}{\hbar^2} \int_0^t d\xi \sum_k \left\{ e^{i\omega(k)\xi} N_k \langle [[A_S, C_K^+(S)]_- C_K^+(S, -\xi)]_{-\omega(k)} \times \right. \\ &\times B_S(-t) \rangle + e^{-i\omega(k)\xi} (1 + N_K) \langle [[A_S, C_K(S)]_- C_K^+(S, -\xi)]_{+\omega(k)} \times \\ &\times B_S(-t) \rangle \left. \right\} + \frac{i}{\hbar_0} \int_0^\beta d\lambda \sum_K \left\{ e^{-i\omega(k)(t+i\hbar\lambda)} (1 + N_K) \times \right. \\ &\times \left. \langle C_K(S, -t - i\hbar\lambda) [A_S C_K^+(S)]_- B_S(-t) \rangle \right\} \end{aligned} \quad (22)$$

where $N_K = [e^{\beta\hbar\omega(k)} - 1]^{-1}$ is the boson (phonon) average (thermal) occupation number.

$$C_K(S, \pm Z) = e^{\pm iL_S Z} C_K(S); \quad C_k^+(S, \pm Z) = e^{\pm iL_S Z} C_k^+(S)$$

$$[E, D]_{\pm\omega(k)} = ED - e^{\pm\beta\hbar\omega(k)} DE$$

for arbitrary operators E and D , $A_S = A_S(0)$.

At the derivation of equation (22) the following relations have been used

$$e^{\pm iL_S t} b_k = e^{\mp i\omega(k)t} b_k, \quad e^{\mp iL_S t} b_k^+ = e^{\pm i\omega(k)t} b_k^+$$

$$P(b_k^+, b_{k'}) = N_{kk} \delta_{kk'}, \quad P(b_k b_{k'}^+) = (1 + N_k) \delta_{kk'}$$

$$P(b_k b_{k'}) = P(b_k^+ b_{k'}^+) = 0$$

It is easy to obtain also the equation for correlation function $\langle A_S(0) B_S(t) \rangle$ by the substitution $t \rightarrow -t$ in equation (22).

Equation (22) differs from the similar equation obtained earlier in RPA [9, 11] by the third term on the right hand side which describes the influence of the initial correlations.

3. Electron-phonon system

We will consider further a more specific case of a particle interacting with quantum field which is described by the Hamiltonian (1, 2) with

$$H_S = T(\vec{p}), \quad C_{\vec{k}}(S) = V_{\vec{k}} e^{i\vec{k}\vec{r}} \quad (23)$$

where $T(\vec{p})$ is the kinetic energy of particle having momentum \vec{p} , \vec{r} is the particle radius-vector. $V_{\vec{k}}$ is the particle-field interaction energy corresponding to quantum $\hbar\omega(\vec{k})$ characterized by the wave vector \vec{k} (in 2 we must consider K as a vector).

For the Frohlich polaron (an electron moving in the polar crystal and interacting with phonons) we have

$$T(\vec{p}) = \frac{\vec{p}^2}{2m^*}, \quad V_{\vec{k}} = -i \frac{\hbar \omega(\vec{k})}{KU^{1/2}} \left(\frac{4\pi\alpha}{V} \right)^{1/2}$$

$$u = \left(\frac{2m^* \omega(\vec{k})}{\hbar} \right)^{1/2}, \quad \alpha = \frac{1}{2} \left(\frac{1}{\epsilon_\infty} - \frac{1}{\epsilon_0} \right) \frac{e^2 u}{\hbar \omega(\vec{k})} \quad (24)$$

where α is the conventional dimensionless constant of electron-phonon interaction. m^* and e are the effective electron mass in crystal and electron charge, V is the system volume. $\omega(\vec{k}) = \omega_0$ if the interaction of electron only with the optical mode is considered.

The quantity of physical interest is the conductivity tensor. Under small applied electric field of frequency ω it can be expressed through the current-current correlation function. According to the Kubo formula [3] the dissipative part of conductivity tensor can be represented in form

$$\text{Re } \sigma_{\mu\nu}^S(\omega) = \frac{1}{E_\beta(\omega)} \int_0^\infty dt \cos(\omega t) \psi_{\mu\nu}^S(t)$$

$$E_\beta(\omega) = \frac{\hbar\omega}{2} \text{cth} \left(\frac{\beta\hbar\omega}{2} \right) \quad (25)$$

where $\sigma_{\mu\nu}^S(\omega)$ and $\psi_{\mu\nu}^S(t)$ are the symmetric parts of the conductivity tensor $\sigma_{\mu\nu}(\omega)$ and correlation function $\psi_{\mu\nu}(t)$, respectively

$$\sigma_{\mu\nu}^S(\omega) = \frac{1}{2} [\psi_{\mu\nu}^S(t) + \psi_{\nu\mu}^S(t)]$$

$$\psi_{\mu\nu}^S(t) = \frac{1}{2} [\psi_{\mu\nu}(t) + \psi_{\nu\mu}(t)] = \frac{1}{2} [\psi_{\mu\nu}(t) + \psi_{\mu\nu}(-t)] \quad (26)$$

$$\psi_{\mu\nu}(t) = \frac{1}{2} [\langle j_\nu(0) j_\mu(t) \rangle + \langle j_\nu(t) j_\mu(0) \rangle] =$$

$$\frac{1}{2} [\langle j_\nu(0) j_\mu(t) \rangle + \langle j_\nu(0) j_\mu(-t) \rangle]$$

$j_\mu(t) = e^{iL_t} j_\mu(0)$ is the Heisenberg representation of the μ component of the electric current operator \vec{j} .

Consider an electron having in general the kinetic energy $T(\vec{p})$ and interacting with phonons. Then, to obtain the conductivity (25) one needs to calculate the correlation function

$$\psi_{\mu\nu}(t) = \frac{e^2}{2} \left[\langle v_\nu(0) v_\mu(t) + v_\nu(0) v_\mu(-t) \rangle \right] \quad (27)$$

where \vec{v} is the electron velocity operator.

For the calculation of (27) we can use the approach developed in Section 2. Using equation (22) for the electron-phonon system under consideration with H_S , H_Σ , and H_I given by expressions (2) and (23), we obtain the following equation for velocity-velocity correlation function ($A_S(0) = v_\nu$, $B_S(0) = v_\mu$)

$$\begin{aligned}
 \frac{\partial}{\partial t} \langle v_\nu(0) v_\mu(t) \rangle &= \frac{i}{\hbar} \langle [v_\nu, T(\vec{p})]_- v_\mu(t) \rangle - \frac{1}{\hbar^2} \times \\
 &\times \int_0^t d\xi \sum_{\vec{k}} |V_{\vec{k}}|^2 \left\{ \left[e^{-i\omega(\vec{k})\xi} N_{\vec{k}} + e^{i\omega(\vec{k})\xi} (1 + N_{\vec{k}}) \right] \times \right. \\
 &\times \left\langle [v_\nu, e^{i\vec{k}\vec{r}}]_- e^{-i\vec{k}\vec{r}(\xi)} v_\mu(t) \right\rangle - \left[e^{i\omega(\vec{k})\xi} N_{\vec{k}} + \right. \\
 &+ \left. e^{-i\omega(\vec{k})\xi} (1 + N_{\vec{k}}) \right\} \left\langle e^{-i\vec{k}\vec{r}(\xi)} [v_\nu, e^{i\vec{k}\vec{r}}]_- v_\mu(t) \right\rangle \left. \right\} - \\
 &- \frac{i}{\hbar_0} \int_0^\beta d\lambda \sum_{\vec{k}} |V_{\vec{k}}|^2 \left[e^{i\omega(\vec{k})(t-i\hbar\lambda)} N_{\vec{k}} + e^{-i\omega(\vec{k})(t-i\hbar\lambda)} \times \right. \\
 &\times \left. (1 + N_{\vec{k}}) \right] \left\langle e^{-i\vec{k}\vec{r}(t-i\hbar\lambda)} [v_\nu, e^{i\vec{k}\vec{r}}]_- v_\mu(t) \right\rangle
 \end{aligned} \tag{28}$$

Here

$$\begin{aligned}
 v_\mu(t) &= e^{\frac{i}{\hbar}Ht} v_\mu e^{-\frac{i}{\hbar}Ht} = e^{iLt} v_\mu \\
 \vec{r}(\xi) &= e^{\frac{i}{\hbar}T(\vec{p})\xi} \vec{r} e^{-\frac{i}{\hbar}T(\vec{p})\xi} = e^{iL_\nu\xi} \vec{r}
 \end{aligned}$$

is the trajectory of electron free motion and the relations $\omega(-\vec{k}) = \omega(\vec{k})$, $V_{-\vec{k}} = V_{\vec{k}}$ have been supposed.

The equation for correlation function $\langle v_\mu(0)v_\nu(-t) \rangle$ follows from (28) through the substitutions $t \rightarrow -t$, $\mu \leftrightarrow \nu$.

To proceed further we restrict ourselves to the case of single electron band when the electron velocity operator is diagonal in the momentum representation and

$$\begin{aligned}
 v_\mu(\vec{p}) &= \frac{\partial}{\partial p_\mu} T(\vec{p}) \\
 [v_\mu(\vec{p}), T(\vec{p})]_- &= 0 \quad (\mu = x, y, z)
 \end{aligned}$$

We use the notation $v_\mu(p)$ for the matrix element $\langle \vec{p} | v_\mu | \vec{p} \rangle$ of the velocity operator on the electron momentum operator on the electron momentum operator eigenstates $|\vec{p}\rangle$.

It is convenient to introduce the following relevant operator (compare with (5))

$$G_\mu(t, \beta) = Z^{-1} Tr_{(S)} [v_\mu(t) e^{-\beta H}] \tag{29}$$

with the initial condition at $t = 0$.

$$G_\mu(\beta) = v_\mu \frac{Z^S(\beta)}{Tr_{(S)}[Z^S(\beta)]} \tag{30}$$

where $Z^S(\beta) = Tr_{(S)}(e^{-\beta H})$ is the reduced partition function for given electron-phonon system.

The introduced quantity (29) allows us to express the correlation functions (27) and equations for them in such way

$$\begin{aligned}
 \langle v_\nu(0) v_\mu(\pm t) \rangle &= Tr_{(S)} [v_\nu(0) G_\mu(\pm t, \beta)] \\
 \frac{\partial}{\partial t} \langle v_\nu(0) v_\mu(\pm t) \rangle &= Tr_{(S)} [v_\nu(0) \frac{\partial}{\partial t} G_\mu(\pm t, \beta)] = \\
 &= \pm Tr_{(S)} [v_\nu(0) \Gamma_\nu(\pm t, \beta)] G_\mu(\pm t, \beta)
 \end{aligned} \tag{31}$$

Here the operator $\Gamma_\nu(t, \beta)$ is defined immediately from equation (28) and has a form

$$\begin{aligned}
 \Gamma_v(t, \beta) = & \frac{1}{\hbar^2} \int_0^t d\xi \sum_k |V_{\vec{k}}|^2 \left\{ [e^{-i\omega(\vec{k})\bar{r}\xi} N_{\vec{k}} + \right. \\
 & + e^{i\omega(\vec{k})\xi} (1 + N_{\vec{k}})] v_v^{-1} [v_v e^{i\vec{k}\bar{r}}]_- e^{-i\vec{k}\bar{r}(\xi)} - [e^{i\omega\vec{k}\xi} \times \\
 & N_{\vec{k}} + e^{-i\omega\vec{k}\xi} (1 + N_{\vec{k}})] v_v^{-1} e^{-i\vec{k}\bar{r}(\xi)} [v_v, e^{i\vec{k}\bar{r}}]_- \left. \right\} - \\
 & - \frac{i}{\hbar} \int_0^\beta d\lambda \sum_k |V_{\vec{k}}|^2 \left[e^{i\omega\vec{k}(t-i\hbar\lambda)} N_{\vec{k}} + e^{-i\omega\vec{k}(t-i\hbar\lambda)} \times \right. \\
 & \left. \times (1 + N_{\vec{k}}) \right] v_v^{-1} e^{-i\vec{k}\bar{r}(t-i\hbar\lambda)} [v_v, e^{i\vec{k}\bar{r}}]_- \quad (32)
 \end{aligned}$$

where $v_v^{-1}v_v = v_v v_v^{-1} = I$, i.e. these operators are mutually inverse.

The trace over electron (subsystem S) states in equations (31) will be calculated on eigenstates $|\bar{p}\rangle$ of electron momentum operator. Then, these equations can be rewritten as

$$\begin{aligned}
 \langle v_v(0) v_\mu(\pm t) \rangle &= \int d\bar{p} v_v(\bar{p}) G_\mu(\pm t, \beta, \bar{p}) \\
 \int d\bar{p} v_v(\bar{p}) \frac{\partial}{\partial t} G_\mu(\pm t, \beta, \bar{p}) &= \pm \int d\bar{p} v_v \bar{p} \Gamma_v(\pm t, \beta, \bar{p}) G_\mu(\pm t, \beta, \bar{p}) \quad (33)
 \end{aligned}$$

Here we take into account that the electron velocity operator is diagonal in the momentum representation and that in the case of space homogeneity under consideration only the diagonal matrix elements of operator $\Gamma_v(t, \beta)$

$$\Gamma_v(t, \beta, \bar{p}) = \langle \bar{p} | \Gamma_v(t, \beta) | \bar{p} \rangle$$

are not equal to zero (see below). Using the relations

$$\begin{aligned}
 \langle \bar{p}_1 | e^{\pm i\vec{k}\bar{r}} | \bar{p}_2 \rangle &= \delta(\bar{p}_2 \pm \hbar\vec{k} - \bar{p}_1) \\
 e^{\pm i\vec{k}\bar{r}} f(p) &= f(p \mp \hbar k) e^{\pm i\vec{k}\bar{r}} \\
 f(\bar{p}) e^{\pm i\vec{k}\bar{r}} &= e^{\pm i\vec{k}\bar{r}} (p \pm \hbar\vec{k})
 \end{aligned}$$

where $f(\bar{p})$ is an arbitrary function of momentum \bar{p} , we obtain for the matrix element of operator $\Gamma_v(t, \beta)$ defined by (32)

$$\begin{aligned}
 \Gamma_v(t, \beta, \bar{p}) = & \frac{2}{\hbar} \sum_k |V_{\vec{k}}|^2 \frac{v_v(\bar{p} + \hbar\vec{k}) - v_v(\bar{p})}{v_v(\bar{p})} \left\{ N_{\vec{k}} \frac{\sin \left[\frac{t}{\hbar} \Delta^-(\vec{k}, \bar{p}) \right]}{\Delta^-(\vec{k}, \bar{p})} + \right. \\
 & \left. (1 + N_{\vec{k}}) \frac{\sin \left[\frac{t}{\hbar} \Delta^+(\vec{k}, \bar{p}) \right]}{\Delta^+(\vec{k}, \bar{p})} + \frac{i}{2} \left[N_{\vec{k}} e^{-\frac{i}{\hbar} t \Delta^-(\vec{k}, \bar{p})} \times \frac{e^{-\beta \Delta^-(\vec{k}, \bar{p})} - 1}{\Delta^-(\vec{k}, \bar{p})} + (1 + N_{\vec{k}}) e^{-\frac{i}{\hbar} t \Delta^+(\vec{k}, \bar{p})} \frac{e^{-\beta \Delta^+(\vec{k}, \bar{p})} - 1}{\Delta^+(\vec{k}, \bar{p})} \right] \right\} \quad (34)
 \end{aligned}$$

Here $\Delta^\pm(\vec{k}, \bar{p}) = T(\bar{p} + \hbar k) - T(\bar{p}) \pm \hbar\omega(\vec{k})$.

To solve an equation for the correlation function (33) we shall consider the isotopic case, when

$$\sigma_{\mu\nu}^S(\omega) = \sigma^S(\omega) \delta_{\mu\nu}; \quad \psi_{\mu\nu}^S(t) = \psi^S(t) \delta_{\mu\nu}$$

and use approximate equation, which can be obtained from (33)

$$\frac{\partial}{\partial t} G_\mu(\pm t, \beta, \bar{p}) = \pm \Gamma_\mu(\pm t, \beta, \bar{p}) G_\mu(\pm t, \beta, \bar{p}) \quad (35)$$

Equation (35) provides the approximation of RTA type. It can be seen that the approximation equation (35) becomes exact when $\Gamma_\mu(\pm t, \beta, \vec{p})$ doesn't depend on \vec{p} . Such case is realized, e.g. for the Frohlich polaron at low temperatures (see Section 4). Equation (35) integrates the following expression

$$G_\mu(\pm t, \beta, \vec{p}) = e^{\tilde{\Gamma}_\mu(\pm t, \beta, \vec{p})} G_\mu(\beta, \vec{p}), \quad (36)$$

where

$$\tilde{\Gamma}_\mu(\pm t, \beta, \vec{p}) = \int_0^t d\tau \cdot \Gamma_\mu(\tau, \beta, \vec{p}) \quad (37)$$

and the initial condition

$$G_\mu(\beta, \vec{p}) = \langle p | G_\mu(\beta) | \vec{p} \rangle = \frac{V_\mu(\vec{p}) Z^S(\beta, \vec{p})}{\int d\vec{p} Z^S(\beta, \vec{p})} \quad (38)$$

$$Z^S(\beta, \vec{p}) = \langle \vec{p} | Z^S(\beta) | \vec{p} \rangle$$

follows from (30). Substituting expression (34) for $\Gamma_\mu(t, \beta, \vec{p})$ in (37) we obtain as a result of integration

$$\begin{aligned} \tilde{\Gamma}_\mu(t, \beta, \vec{p}) &= \text{Re} \tilde{\Gamma}_\mu(t, \beta, \vec{p}) + i I_m \tilde{\Gamma}_\mu(t, \beta, \vec{p}) \\ \text{Re} \tilde{\Gamma}_\nu(t, \beta, \vec{p}) &= \sum_{\vec{k}} |V_{\vec{k}}|^2 \frac{v_\nu(\vec{p} + \hbar\vec{k}) - v_\nu(\vec{p})}{v_\nu(\vec{p})} \left\{ N_{\vec{k}} \times \right. \\ &\times \left[1 + e^{-\beta\Delta^-(\vec{k}, \vec{p})} \right] \frac{1 - \cos \left[\frac{t}{\hbar} \Delta^-(\vec{k}, \vec{p}) \right]}{[\Delta^-(\vec{k}, \vec{p})]^2} + (1 + N_{\vec{k}}) \left[1 + \right. \\ &\left. \left. + e^{-\beta\Delta^+(\vec{k}, \vec{p})} \right] \frac{1 - \cos \left[\frac{t}{\hbar} \Delta^+(\vec{k}, \vec{p}) \right]}{[\Delta^+(\vec{k}, \vec{p})]^2} \right\}; \end{aligned} \quad (39)$$

$$\begin{aligned} I_m \tilde{\Gamma}_\nu(t, \beta, \vec{p}) &= - \sum_{\vec{k}} |V_{\vec{k}}|^2 \frac{v_\nu(\vec{p} + \hbar\vec{k}) - v_\nu(\vec{p})}{v_\nu(\vec{p})} \times \\ &\times \left\{ N_{\vec{k}} \frac{1 - e^{-\beta\Delta^-(\vec{k}, \vec{p})}}{[\Delta^-(\vec{k}, \vec{p})]^2} \sin \left[\frac{t}{\hbar} \Delta^-(\vec{k}, \vec{p}) \right] + (1 + N_{\vec{k}}) \times \right. \\ &\left. \frac{1 - e^{-\beta\Delta^+(\vec{k}, \vec{p})}}{[\Delta^+(\vec{k}, \vec{p})]^2} \sin \left[\frac{t}{\hbar} \Delta^+(\vec{k}, \vec{p}) \right] \right\} \end{aligned}$$

Note, that $\text{Re} \tilde{\Gamma}_\nu(t, \beta, \vec{p})$ is an even function of t while $I_m \tilde{\Gamma}_\nu(t, \beta, \vec{p})$ is an odd function of t.

The expressions of (36), (38) and (39) give the time dependence of correlation functions (33) and allow us in principle to calculate the conductivity tensor according to (22-27). To be consistent we must make an approximation $e^{-\beta H} \Rightarrow e^{-\beta H_0} = e^{-\beta H_s} \cdot e^{-\beta H_\Sigma}$ in expressions (30) and (38) for the initial values of correlation functions we restrict ourselves to the second order of perturbation theory on $H_i(V_{\vec{k}})$ using equations (22) and (28). Thus, we must put

$$G_\mu(\beta) = \frac{e^{-\beta H_s}}{Tr_{(S)} e^{-\beta H_s}} v_\mu; \quad G_\mu(\beta, \vec{\rho}) = \frac{e^{-\beta T(\vec{\rho})}}{\int d\vec{\rho} e^{\beta T(\vec{\rho})}} v_\mu(\vec{\rho}) \quad (40)$$

Then, equations (33), (36) and (40) result in the following expression for the correlation function

$$\Psi_{\mu\nu}(t) = \frac{e^2 \int d\vec{\rho} e^{-\beta T(\vec{\rho})} v_\nu(\vec{\rho}) v_\mu(\vec{\rho}) \left\{ \exp[\tilde{\Gamma}_\nu(t, \beta, \vec{\rho})] + \exp[\tilde{\Gamma}_\mu(-t, \beta, \vec{\rho})] \right\}}{2 \int d\vec{\rho} e^{-\beta T(\vec{\rho})}} \quad (41)$$

where $\Gamma_\nu(t, \beta, \vec{\rho})$ and $\Gamma_\mu(t, \beta, \vec{\rho})$ are defined by (39).

According to (41) and (39) the subsystem (electron) correlation functions can decay oscillating owing to complexity of the relaxation factor $\Gamma_\nu(t, \beta, \vec{\rho})$ and as well see further these oscillations survive asymptotically at $t \gg t_0$ and give the contribution to the kinetic coefficient (conductivity). This fact follows from exact according to Gibbs distribution in the definition of correlation functions (4). In RPA the imaginary part of $\tilde{\Gamma}_\nu(t, \beta, \vec{\rho})$ as well as the possibility for the mentioned oscillations are absent [9, 11].

We should remind that the consideration performed is valid when the time hierarchy (20) is realized. As is seen from (39) in the considered case of electron interacting with phonons $t_s \sim \hbar\beta$ and $t \sim 1/\omega$, where $\bar{\omega}$ is the characteristic phonon frequency. Moreover, the expression (39) shows that the energy conservation in the process of electron scattering by phonons hold true on the large time scale $t \gg t_0$, $t_0 = \max(t_s, t_\Sigma)$ considering times $t \gg t_0$ we can perform in (39) a limiting procedure $t \rightarrow \infty$ and obtain as a result

$$\begin{aligned} \lim_{t \rightarrow \infty} \text{Re} \tilde{\Gamma}_\nu(t, \beta, \vec{\rho}) &= -\Gamma_v^{rel}(\beta, \vec{\rho}) |t| = -\frac{1}{\tau_v^{rel}(\beta, \vec{\rho})} |t| \\ \Gamma_v^{rel}(\beta, \vec{\rho}) &= -\frac{2\pi}{\hbar} \sum_{\vec{k}} |V_{\vec{k}}|^2 \frac{v_\nu(\vec{\rho} + \hbar\vec{k}) - v_\nu(\vec{\rho})}{v_\nu(\vec{\rho})} \left\{ N_{\vec{k}} \times \right. \\ &\times \delta[\Delta^-(\vec{k}, \vec{\rho})] + (1 + N_{\vec{k}}) \delta[\Delta^+(\vec{k}, \vec{\rho})] \left. \right\} \\ \lim_{t \rightarrow \infty} I_m \tilde{\Gamma}_\nu(t, \beta, \vec{\rho}) &= -\beta\pi \sum_{\vec{k}} |V_{\vec{k}}|^2 \frac{v_\nu(\vec{\rho} + \hbar\vec{k}) - v_\nu(\vec{\rho})}{v_\nu(\vec{\rho})} \left\{ N_{\vec{k}} \times \right. \\ &\times \delta[\Delta^-(\vec{k}, \vec{\rho})] + (1 + N_{\vec{k}}) \delta[\Delta^+(\vec{k}, \vec{\rho})] \left. \right\} \text{Sigt} \end{aligned} \quad (42)$$

where the relations

$$\lim_{t \rightarrow \infty} \frac{1 - \cos(\omega t)}{\omega^2} = \pi |t| \delta(\omega), \quad \lim_{t \rightarrow \infty} \frac{\sin(\omega t)}{\omega} = \pi \delta(\omega) \text{Sigt}$$

have been used. Note, that we must make the thermodynamic limiting procedure

$\sum_{\vec{k}} (...) = \frac{V}{(2\pi)^3} \int d\vec{k} (...)$ in (39) before calculation of $\lim_{t \rightarrow \infty}$. We can see from (42) (that on the large time scale ($t \gg t_0$, $t \rightarrow \infty$)) the relation takes place

$$\lim_{t \rightarrow \infty} I_m \tilde{\Gamma}_\nu(t, \beta, \vec{\rho}) = \frac{\beta\hbar}{2} \Gamma_v^{rel}(\beta, \vec{\rho}) \text{signt} \quad (43)$$

According for the above consideration we can interpret $\Gamma_v^{rel}(\beta, \vec{\rho})$ as the relaxation frequency of electron velocity v -component ($\tau_v^{rel}(\beta, \vec{\rho})$ is the corresponding relaxation time).

Using (25 – 27) and (42 – 43) we obtain finally for the dissipative part of conductivity at $\omega \ll t_0^{-1}$.

$$\begin{aligned} \sigma_{\mu\nu}^S(\omega) = & \frac{ne^2}{2E_\beta(\omega)} \int d\vec{p} \rho_s(\beta, \vec{p}) v_\nu(\vec{p}) v_\mu(\vec{p}) \times \\ & \times \left\{ \cos \left[\frac{\beta\hbar}{2} \Gamma_\nu^{rel}(\beta, \vec{p}) \right] \frac{\Gamma_\nu^{rel}(\beta, \vec{p})}{\omega^2 + [\Gamma_\nu^{rel}(\beta, \vec{p})]^2} + \right. \\ & \left. + \cos \left[\frac{\beta\hbar}{2} \Gamma_\mu^{rel}(\beta, \vec{p}) \right] \frac{\Gamma_\mu^{rel}(\beta, \vec{p})}{\omega^2 + [\Gamma_\mu^{rel}(\beta, \vec{p})]^2} \right\} \quad (\omega \ll t_0^{-1}) \end{aligned} \quad (44)$$

where

$$\rho_s(\beta, \vec{p}) = \frac{e^{-\beta T(\vec{p})}}{\int d\vec{p} e^{-\beta T(\vec{p})}}$$

and the electron density n is introduced as a multiplier to account for a number of electrons existing in a system. We see that the initial correlations of electrons with phonons survive is the expression for the conductivity (44) in form of multipliers $\cos \left[\frac{\beta\hbar}{2} \Gamma_\mu^{rel}(\beta, \vec{p}) \right]$. However, due to condition (20)

$$\beta\hbar \Gamma_\mu^{rel}(\beta, \vec{p}) \ll 1 \quad (\tau^{rel} \sim \frac{1}{\Gamma_\mu^{rel}(\beta, \vec{p})}, t_s \sim \beta\hbar).$$

Note, that these correlations do not influence asymptotically the relaxation time $\tau_\mu^{rel}(\beta, \vec{p})$.

In the RPA for the correlation functions (4) we omit the interaction H_i in Gibbs factor $e^{-\beta H}$ (preserving it in factors $e^{\pm \frac{i}{\hbar} H_i t}$) [9, 11]. This approximation leads to the expression (44) for $\text{Re} \sigma_{\mu\nu}^S(\omega)$ in which the substitutions

$$\cos \left[\frac{\beta\hbar}{2} \Gamma_\mu^{rel}(\beta, \vec{p}) \right] \Rightarrow 1, \quad \cos \left[\frac{\beta\hbar}{2} \Gamma_\nu^{rel}(\beta, \vec{p}) \right] \Rightarrow 1$$

must be made (see also [11]).

Thus the expressions obtained for velocity-velocity correlation functions and conductivity are the most general in the scope of considered model and approximations adopted.

4. The Frohlich polaron mobility (the “3/2βħω₀ problem” in low temperature polaron mobility)

Consider now an electron moving in a polar crystal within the framework of the Frohlich model described by Hamiltonians (1), (2), (23) and (24). Besides, we regard the interaction of electrons only with optical dispersionless phonons for which $\omega(\vec{k}) = \omega_0$. We consider in fact the isotropic case when

$$T(\vec{p}) = \frac{\vec{p}^2}{2m^*}, \quad v_\mu(\vec{p}) = \frac{p_\mu}{m^*} \quad (45)$$

As can be seen from expressions (41), (42) and (44), the problem is to calculate the relaxation frequency $\Gamma_\mu^{rel}(\beta, \vec{p})$ depending in general, on the electron momentum \vec{p} . For

definiteness consider $\Gamma_z^{rel}(\beta, \vec{p})$ as if an electric field is applied along Oz axis. From (24) and (42) we obtain after performing the thermodynamic limiting procedure and integration over modules of $|\vec{k}|$

$$\Gamma_z^{rel}(\beta, \vec{P}) = \frac{\alpha\omega_0}{2\pi} \frac{1}{\tilde{P}_z} \left\{ N_0(\gamma) \int_0^{2\pi} d\varphi \int_0^\pi d\theta \sin\theta \cos\theta \frac{\tilde{P} \cos\Phi}{\sqrt{\tilde{P}^2 \cos^2\Phi + 1}} + \right. \\ \left. + [1 + N_0(\gamma)] \int_0^{2\pi} d\varphi \int_0^\pi d\theta \sin\theta \cos\theta \frac{\tilde{P} \cos\Phi}{\sqrt{\tilde{P}^2 \cos^2\Phi - 1}} \right\} \quad (46)$$

$(\tilde{P}^2 \cos^2\Phi \geq 1)$

Here the dimensionless electron momentum \tilde{P} is introduced

$$\tilde{P}_i = \frac{P_i}{\sqrt{2\hbar\omega_0 m^*}} \quad (i = x, y, z), \quad N_0(\gamma) = (e^\gamma - 1)^{-1}$$

$$\gamma = \beta\hbar\omega_0$$

and Φ is the angle between \vec{k} and $\tilde{\vec{P}}$ connected with the angles Θ and φ defining the direction of \vec{k} by relation $\tilde{P} \cos\Phi = \sin\Theta \cos\varphi \tilde{P}_x + \sin\Theta \sin\varphi \tilde{P}_y + \cos\Theta \tilde{P}_z$. To integrate the expression (46) we restrict ourselves to the case of low temperature

$$\gamma \gg 1 \quad (47)$$

when correlation functions is defined by range of small momentum

$$\tilde{P}^2 \ll 1 \quad (48)$$

In this case a slow moving electron cannot emit phonons due to impossibility of satisfying the conservation of electron momentum and energy in such processes (see (42) and (46)). Thus, the second term on the right hand side of (46) is equal to zero when conditions (47) and (48) hold true. Taking into account that $\tilde{P}^2 \cos^2\Phi \ll 1$ expression (46) integrates to

$$\Gamma_z^{rel}(\gamma, \tilde{P}) = \Gamma_0^{rel}(\gamma) = \frac{2}{3} \alpha\omega_0 N_0(\gamma) \quad (49)$$

$(\tilde{P}^2 \ll 1)$

Hence, the velocity relaxation frequency (or time) of slow moving electron does not depend on electron momentum and is defined only by processes of phonons absorption.

Using (49) we obtain (41) in form

$$\langle v_z(0) v_z(\pm t) \rangle = \frac{\hbar\omega_0}{m^x \gamma} \exp[-\Gamma_0^{rel}(\gamma)|t|] \exp\left[\pm \frac{i\gamma}{2\omega_0} \Gamma_0^{rel}(\gamma)\right] \quad (50)$$

$\left(\gamma \gg 1, \quad t \gg \frac{\gamma}{\omega_0} \right)$

where the known formulae

$$\int d\tilde{P} e^{-\gamma\tilde{P}^2} \tilde{P}_z^2 = \frac{1}{2\gamma} \left(\frac{\pi}{\gamma} \right)^{3/2} \quad \int d\tilde{P} e^{-\gamma\tilde{P}^2} = \left(\frac{\pi}{\gamma} \right)^{3/2} \quad (51)$$

has been used.

Thus, we see from (50) that the electron correlation functions decrease exponentially with the time in the considered case of low temperatures. The relaxation time according to (50) is $\tau^{rel}(\gamma) = [\Gamma_0^{rel}(\gamma)]^{-1}$. It should be stressed that this result is obtained without use of any kind

of RPA. Expression (50) differs from the result obtained in RPA by the factor $\exp\left[\pm\frac{i\gamma}{2\omega_0}\Gamma_0^{rel}(\gamma)\right]$ (see [11]).

Now we can calculate the low-temperature conductivity and mobility of the Frohlich polaron in the case under consideration of small electron-phonon interaction. Taking into account (45) and (49 – 51) we have from (44) for the conductivity

$$\text{Re } \sigma(\omega) = \frac{ne^2}{m^* \omega_0} \frac{2}{\gamma \tilde{\omega}} \text{th}\left(\frac{\gamma \tilde{\omega}}{2}\right) \left[1 - 2 \sin^2\left(\frac{\gamma}{2} \Gamma_0(\gamma)\right)\right] \frac{\Gamma_0(\gamma)}{\tilde{\omega}^2 + \Gamma_0^2(\gamma)}$$

$$(\alpha < 1, \gamma \gg 1, \tilde{\omega} \gamma \ll 1) \tag{52}$$

where

$$\sigma(\omega) = \sigma_{xx}(\omega) = \sigma_{yy}(\omega) = \sigma_{zz}(\omega) \quad \tilde{\omega} = \frac{\omega}{\omega_0}$$

$$\Gamma_0(\gamma) = \omega_0^{-1} \Gamma_0^{rel}(\gamma) = \frac{2}{3} \alpha N_0(\gamma)$$

Expression (52) can be considered as the generalized Osaka result [13] in the case of small electron-phonon interaction and is, in fact, the Drude formula for the low-temperature conductivity which comprises the correction due to initial electron-phonon correlations (the second term in (52)). The first term in (52) corresponds to RPA (see [11]). Since $\tilde{\omega} \gamma \ll 1$ (which follows from the condition $t \gg t_0$) and $\gamma \Gamma_0(\gamma) \ll 1$ (see the condition (20)), we can expand $\frac{2}{\gamma \tilde{\omega}} \text{th}\left(\frac{\gamma \tilde{\omega}}{2}\right)$ and $\sin^2\left(\frac{\gamma}{2} \Gamma_0(\gamma)\right)$ in (52). Thus, the correction connected with the initial correlations, is the small in the considered case ($N_0(\gamma) = e^{-\gamma}$, $\gamma \gg 1$).

For the low-temperature polaron mobility $\mu = \frac{\text{Re } \sigma(0)}{ne}$ we have from (52) and (49)

$$\mu = \frac{3e}{2m^* \omega_0 \alpha} e^\gamma, \quad (\gamma \gg 1) \tag{53}$$

where the correction from initial correlations is omitted.

The result (53) represents the correct and consistently obtained low temperature polaron mobility in the case of weak interaction ($\alpha < 1$). We hope that it gives the solution of “ $3/2\beta\hbar\omega_0$ problem” (see e.g. [5]).

5. Conclusion

We have derived in the given work the exact closed equation for the relevant superoperator (see eq. (16)), which defines the exact equation for correlation function of sub system interacting with a boson field taken as heat bath (eq. (18)).

RPA has not been used anywhere. The developed approach was applied to the electron phonon system, and the theory of conductivity was realized in the case of single band electron weakly interacting with phonons and weak applied electric field. In particular, the consistent theory of low-temperature Frohlich polaron mobility was developed. Note, that formula (50) demonstrates the ergodic properties of considered model of particle interacting with boson heat bath.

The presented formalism can be used for the calculation of higher order on the subsystem-thermostat interaction contributions to correlation functions and related quantities. The case of strong (arbitrary) electron-phonon coupling can be also considered by this method in the framework of the Feynman polaron model [12] or the generalized Feynman model of polaron [14].

Obviously, that the proposed approach may be applied to the derivation of equations for the density matrix of subsystem interacting with boson heat bath under the mixed (not the product-type) initial condition.

The considered possibilities will be realized in subsequent publications.

References

1. С. И. Пекар. Исследования по электронной теорий кристаллов. 1951, Москва – Ленинград: Гостехиздат.
2. Н. Н. Боголюбов, Н. Н. Боголюбов (мл.). Введение в квантовую статическую механику. 1984, Москва: Наука.
3. R. Kubo. J. Phys. Soc. Jpn. 12 (1957) 570.
4. G. V. Chester, A. Thellung. Proc. Phys. Soc. 73 (1959) 745.
5. F. M. Peeters, J. T. Devresse. Phys. Status Solidi B 115 (1983) 539.
6. F. M. Peeters, J. T. Devresse. Solid State Phys. 38 (1984) 81.
7. N. N. Bogolubov. Kinetic Equations for Electron–Phonon Systems. Preprint E 17-11822. 1978, Dubna: JINR.
8. Н. Н. Боголюбов, Н. Н. Боголюбов (мл.). ЭЧАЯЭ 11 (1980) 245.
9. В. Ф. Лось. Теор. Мат. Физ. 39 (1979) 393.
10. V. F. Los', A. G. Martynenko. Physica A 138 (1986) 518.
11. В. Ф. Лось. Теор. Мат. Физ. 60 (1984) 107.
12. R. P. Feynman. Phys. Rev. 97 (1955) 660.
13. Y. Osaka. Prog. Theoret. Phys. 25 (1961) 517.
14. J. Luttinger, Ch.-Y. Lu. Phys. Rev. B 21 (1980) 4251.

КОМПОЗИЦИОННАЯ КЕРАМИКА НА ОСНОВЕ КАРБИДА БОРА,
ОБОГАЩЕННОГО ИЗОТОПОМ ^{11}B – ПЕРСПЕКТИВНЫЙ
РАДИАЦИОННО СТОЙКИЙ КОНСТРУКЦИОННЫЙ МАТЕРИАЛ

И. А. Баирамашвили, М. В. Галусташвили,
Д. Ш. Джобава, В. Г. Квачадзе, З. З. Мествиришвили

Институт физики им. Э. Андроникашвили
Тбилисский государственный университет им. И. Джавахишвили
Тбилиси, Грузия
vkvachadze@yahoo.com

Принята 6 октября 2013 года

1. Введение

Благодаря своим уникальным ядерным свойствам бор занимает особое место среди реакторных материалов.

У естественного бора всего два стабильных изотопа – ^{10}B и ^{11}B , содержание которых в природной изотопной смеси составляет, соответственно, 19.8 и 80.2 ат. %. Указанные изотопы, обладая совершенно сходными химическими свойствами, совершенно различны по своим ядерно-физическим свойствам. Основное различие – во взаимодействии с нейтронами: легкий изотоп бора ^{10}B является эффективным поглотителем (сечение поглощения тепловых нейтронов $\sigma^{10\text{B}} = 3837$ барн), а тяжелый изотоп ^{11}B – очень хорошим отражателем и замедлителем нейтронов ($\sigma^{11\text{B}} = 0.005$ барн).

Большой, чем у изотопа бора ^{10}B , способностью к поглощению нейтронов обладают шесть элементов (самарий, европий, гадолиний, диспрозий, изотопы плутония ^{239}Pu и ^{241}Pu , и кадмий). Однако перед каждым из них у бора есть преимущества. Это – его отличные физико-механические свойства, а также термостойкость, нетоксичность, негорючесть и достаточное распространение. Поэтому у ^{10}B практически нет конкурентов при изготовлении регулирующих систем атомных реакторов.

По своей способности замедлять нейтроны изотоп ^{11}B находится между бериллием и графитом. Однако комплекс своих свойств бора и в этом случае превосходит своих конкурентов.

Бор широко используется в производстве конструкционных сталей. Малые (гомеопатические) добавки бора (0.006 – 0.008 мас. %) в процессе разлива стали способствуют измельчению зерна (модифицирование); увеличивают глубину ее закалки, а следовательно, и прочность. Легирование же специальных сталей бором (до ~ 2 мас. %) повышает их жаропрочность. В случае использования конструкционных сталей в реакторной технике их модифицирование и легирование следует проводить стабильным изотопом ^{11}B .

Таким образом в атомной технике находят применение оба изотопа: ^{10}B используется в системах управления и защиты во всех видах ядерных реакторов; ^{11}B – в реакторостроении для создания жаростойких и «прозрачных» по отношению к нейтронам конструкционных сталей путем их модифицирования и легирования.

Необходимо отметить, что бор в ядерной технике обычно используется в различных соединениях (высокобористые керамики), чаще всего в форме карбида бора B_4C . Этому способствуют такие характеристики карбида бора как – высокая механическая прочность; высокая коррозионная стойкость в большинстве применяемых сред; высокая термическая стойкость; высокая теплопроводность; малая плотность; высокая износостойкость; слабая активация в нейтронном поле.

Ниже будет рассмотрена возможность разработки и создания карбида бора на основе ^{11}B с целью его применения в активной зоне реакторов нового поколения в качестве радиационно стойкого конструкционного материала.

2. Суть проблемы

Карбид бора на основе изотопа ^{11}B может сыграть важную роль в разрешении проблемы хранения отработанного ядерного топлива, которая связана с утилизацией высокоактивных долгоживущих актинидов в ней. Кроме выжигания в быстрых реакторах младших актинидов (нептуния, америция, кюрия) и продуктов деления ядерного топлива (цезия, стронция, йода), желательна трансмутация тяжелых актинидов в короткоживущие нуклиды, для чего необходимо снизить энергию быстрых нейтронов до тепловой с помощью замедлителя (гидриды металлов, бериллий, графит, карбид бора на основе ^{11}B). Карбид бора $^{11}\text{B}_4\text{C}$, обладая высокими эксплуатационными свойствами [1], должен стать основным замедляющим элементом в устройствах ловушечного типа, расположенных в боковом экране активной зоны. Кроме выполнения основной функции, модератор, выполненный на основе указанного материала, способен уменьшить эффект реактивности натриевых пустот (– 23 %) и сильно увеличить константу Доплера (+ 62 %), т.е. улучшить параметры безопасности активной зоны – существенное преимущество перед другими материалами-модераторами!

Свойства, которыми должен обладать модератор для работы в очень мощных радиационных полях, это – в первую очередь, размерная стабильность при больших флюенсах тепловых и быстрых нейтронов в широком температурном интервале и отсутствие фрагментации при больших ресурсах. Испытания, проведенные нами, показали, что карбид бора на основе ^{11}B является именно таким материалом (см. также [2]). Образцы из $^{11}\text{B}_4\text{C}$ облучались в боковом экране быстрого реактора БОР–60 (г. Димитровград) в гелиевой среде при температуре 360 °С в течение 656 эффективных суток, достаточно высоким флюенсом $3.6 \cdot 10^{26} \text{ н / м}^2$ ($E > 0$) и $1.8 \cdot 10^{26} \text{ н / м}^2$ ($E > 0.1 \text{ МэВ}$). Все образцы карбида бора на основе ^{11}B (99.4 ат. %) обнаружили превосходную размерную стабильность (практически – нулевой свелинг!), тогда, как аналогичные по размерам образцы из диборида титана TiB_2 на основе ^{11}B (99.4 ат. %) не сохранили начальных размеров – радиальные и аксиальные размеры увеличились на 0.8 %.

Высокую радиационную стойкость карбида бора на основе ^{11}B подтвердили исследования японских ученых в испытаниях, проводимых при более высокой температуре (530 °С) в экспериментальном реакторе на быстрых нейтронах JOYO (общий флюенс $1.94 \cdot 10^{26} \text{ н / м}^2$) [3]. Это очень важные факты, если учесть, что основным требованием, которое предъявляется к конструкционным или / и другим материалам, предназначенным для работы в жестких радиационных полях (имеются в виду также факторы космического пространства) является, в общем случае, требование их радиационной стойкости – способность не изменять своих физико-механических и размерных характеристик в течение всего срока активного существования соответствующих конструкций (10 – 15 лет).

Исходя из этих результатов, а также из термо-механических свойств указанного соединения [3, 4], авторы пришли к идее разработки высокотемпературного радиационно стойкого конструкционного керамического материала на основе $^{11}\text{B}_4\text{C}$ (с содержанием стабильного изотопа $^{11}\text{B} > 99.4$ ат. %). В настоящее время происходит осуществление этой идеи.

Для полномасштабной характеристики конструкционной керамики кроме свелинга необходимо знать ее конструкционную прочность. Она представляет собой комплекс прочностных свойств, которые находятся в наибольшей корреляции с функциональными свойствами данного изделия, обеспечивают длительную и надежную работу материала в условиях эксплуатации. Таким образом конструкционная прочность вмещает в себя такие критерии, как прочность, надежность и долговечность. Согласно этим критериям, конструкционная прочность радиационно стойкого карбида бора ($^{11}\text{B}_4\text{C}$) должна позволить применение этого материала в тяжело нагруженных конструкциях реактора. Имеется в виду создание антифрикционных узлов трения, работающих в активной зоне реакторов (например, в циркуляционных насосах теплоносителя, в загрузочных и обслуживающих механизмах реактора, механизмах управления регулирующих стержней и в оборудовании для обнаружения неисправных ТВЭЛ-ов).

Особое место занимают малые ядерные энергетические установки для космических аппаратов. Те жесткие требования, которые предъявляются соответствующим потенциальным материалам (высокая температура в активной зоне – $T > 700$ °С, малый удельный вес, необходимость большого ресурса), усиливает интерес к разрабатываемой нами конструкционной керамике ($^{11}\text{B}_4\text{C}$), как перспективному материалу для высокотемпературных газовых реакторов космических аппаратов (ВТГР), в том числе в качестве подшипников скольжения циркуляционных насосов. Кроме того, в космических аппаратах в качестве автономного источника питания может быть использован разработанный в [5] эффективный высокотемпературный термоэлектрический генератор на основе $^{11}\text{B}_4\text{C}$, тем более что механическая, химическая и радиационная стойкость этого материала намного превышает аналогичные характеристики других термоэлектрических материалов.

Однако широкое применение карбида бора пока все еще ограничивается его повышенной хрупкостью, являющейся следствием жесткости и направленности ковалентных связей в его кристаллической решетке.

Одним из путей понижения хрупкости является легирование карбида бора компонентами, вносящими некоторую долю нелокализованных электронов [6]. Предлагается легирование переходными металлами IV – VI групп периодической системы элементов (Ti, Zr, Hf, Cr, V). Из указанных элементов для создания радиационно стойкого конструкционного материала с повышенной трещиностойкостью авторы полагают выбрать цирконий, реакторный материал с наиболее низким сечением поглощения тепловых нейтронов ($\sigma_{\text{Zr}} = 0.185$ барн). На наш взгляд, композиционный материал на основе карбида бора с диборидом циркония ($^{11}\text{B}_4\text{C} - \text{Zr}^{11}\text{B}_2$) будет гармонично сочетать высокую прочность с достаточной пластичностью. Оптимальное содержание циркония в этом материале – в пределах 3 – 5 мас. %.

Заметим, что в настоящее время одним из востребованных керамических материалов, используемых в подшипниках скольжения, является карбид кремния – SiC (см. рекламные данные Ceratec Technical Ceramics BV Company – English, Netherlands, Deutsch, Francais). Эти неоксидные керамики широко используются в различных трибологических приложениях благодаря своим прекрасным механическим свойствам, таким как высокая прочность, высокая твердость и химическая стабильность при высоких температурах [7]. Поэтому не удивительно, что еще ранее, из-за дефицита совершенных радиационно стойких материалов, особое

внимание исследователей было обращено на выяснение радиационной стойкости, как самого карбида кремния, так керамических композитов, созданных на его основе (SiC / SiC). Наиболее полно информация по этой проблеме представлена в [8]. Согласно ей, наблюдается существенное различие между радиационными эффектами (большей частью это распухание и изменение теплопроводности, обусловленное нейтронным облучением флюенсом $\sim 10^{25}$ н / м² при низких и средних температурах 20 – 1000 °С), происходящими в материалах, высокочистых (монокристаллические и CVD SiC) и менее чистых, созданных путем горячего прессования, спекания, конвертирования жидкой фазы или полимер-обработки SiC. В последних случаях характер радиационного изменения свойств материала был нестабильным и непредсказуемым. Что же касается стехиометрических образцов SiC, то они показали «поразительную радиационную толерантность» [8], что еще более убедительным стало при высоких температурах облучения (1000 – 1600 °С): при максимальном флюенсе ($\sim 6 \cdot 10^{25}$ н / м²) и температуре облучения распухание достигало ~ 1.5 %.

Особое внимание к SiC обусловлено тем, что керамические материалы, изготовленные на основе карбида кремния, уже заслужили статус «передовых радиационно-стойких композитов» [9]. Поэтому при анализе или / и прогнозировании радиационных эффектов в керамике $^{11}\text{B}_4\text{C}$, происходящих в реакторе на быстрых нейтронах при средних температурах, авторы главным образом будут апеллировать к результатам, полученным на этих материалах. Особенно к данным [3], где в отличие от других экспериментальных работ, радиационные испытания $^{11}\text{B}_4\text{C}$ и CVD SiC проводились одновременно в одинаковых условиях одного и того же реактора на быстрых нейтронах. Тем более, что эти условия (полный флюенс выше 10^{26} н / м² и средняя температура испытания) близки к тем, которые были использованы в реакторе БОР-60. Исходя из такого сопоставления можно с уверенностью сказать, что радиационная стойкость карбида бора на основе ^{11}B значительно превосходит достаточно высокую радиационную стойкость карбида кремния. Здесь следует также учесть нежелательную аморфизацию кристаллического SiC, которое наблюдается при относительно низких температурах нейтронного облучения (70 °С) и сопровождается сильным распуханием материала (10.8 %) [10, 11].

3. Некоторые технологические вопросы

Основные виды разрушения материалов, работающих в экстремальных условиях, можно разделить на две части: поверхностные или локально катастрофические разрушения (в первую очередь имеются в виду проблемы трибологии) и разрушения путем накопления дефектов в объеме материала. Преждевременные разрушения, в основном, связаны с деградацией свойств материала в результате структурных превращений с течением времени, под воздействием условий эксплуатации (т.н. объемные эффекты). Поэтому при разработке нового радиационно стойкого конструкционного материала для активной зоны реактора, основное внимание необходимо уделить повышению его стойкости к воздействию разрушительных радиационных эффектов объемного характера. Предотвращение накопления повреждений в объеме материала является одной из самых сложных и актуальных проблем в современном радиационном материаловедении.

Такие материалы, как карбид бора на основе ^{11}B должны быть очевидно более стойки также к изнашивающим поверхностным эффектам, сопровождающим их возможную эксплуатацию в узлах трения и других подобных конструкциях реактора.

Получение материалов с указанными выше свойствами возможно лишь при использовании специальных термобарических технологий. Одновременное или

попеременное воздействие температуры и давления позволяет получать материал с заданной структурой, изотропностью и плотностью. Основные этапы технологии – получение порошков карбида бора ($^{11}\text{BF}_3 \rightarrow ^{11}\text{B}_2\text{O}_3 \rightarrow ^{11}\text{B}_2\text{O}_3 + \text{C} \rightarrow ^{11}\text{B}_4\text{C}$) и диборида циркония ($2 \text{ZrO}_2 + ^{11}\text{B}_4\text{C} + 3 \text{C} \rightarrow 2 \text{Zr}^{11}\text{B}_2 + 4 \text{CO}$) с обогащением по изотопу $^{11}\text{B} > 99.4$ ат. % и их смешивание (например, 96.276 мас. % $^{11}\text{B}_4\text{C}$ + 3.724 мас. % Zr^{11}B_2) и горячее вакуумное прессование. Однако для разработки и создания качественного материала в первую очередь необходимо разработать и создать высококачественный дисперсный порошок.

Порошок карбида бора, разрабатываемые авторами (см., например, [12, 13], а также [2]), отличаются высокой чистотой и почти точным стехиометрическим составом. Массовая доля свободного углерода составляет 0.5 – 1.5 %. Средний размер частиц – 0.8 мкм с равноосным средним размером зерен сферической формы, которая способствует изготовлению качественных изделий из такого материала. В связи с этим авторы считают нужным сделать следующее замечание.

Известно, что интенсивные разработки в области наноструктурного материаловедения привели к существенному повышению физико-механических и других свойств материалов. Так, появилась возможность сформировать устойчивую ультрадисперсную структуру с повышенной плотностью, которая характеризуется высоким значением твердости и прочности. Это явление основывается на обратной зависимости прочности материалов от размера зерна (эффект Холла–Петча), а также на том, что образование и рост трещин критического размера в материалах с мелкозернистой структурой тормозится из-за малого размера структурных фрагментов и соответственно наличия большого числа границ зерен. Есть данные о том, что наноматериалы значительно меньше, по сравнению с обычными крупнокристаллическими материалами, подвержены аморфизации (и следовательно охрупчиванию), в меньшей степени склонны к набуханию и образованию поверхностных повреждений (отшелушиванию) [14]. В первом приближении особенности поведения наноструктурных материалов в радиационном поле связаны с наличием в последних указанных выше многочисленных границ зерен (поверхностей раздела), действующих в качестве стоков радиационных дефектов.

В настоящее время получены нанопорошки многих керамических материалов, но сохранение наноструктуры в компактных изделиях пока не удается. Вполне очевидно, что при термических воздействиях, а также в силовых, коррозионных и радиационных полях могут иметь место рекристаллизационные, сегрегационные, гомогенизационные и релаксационные процессы; фазовые переходы; явления распада и образования фаз, аморфизация, спекание и заплывание нанопор [15]. Вот те причины, которые вынуждают авторов при разработке и создании радиационно стойкого конструкционного карбида бора $^{11}\text{B}_4\text{C}$ использовать порошки с субмикронным размером частиц. Эти трудности, вероятно, имеют временный характер, так как за последнее время появились работы, например, [16], которые свидетельствуют не только о сохранении наноструктур $\text{W} - (0.3 - 0.7) \text{TiC}$ в жестком радиационном поле реактора ($2 \cdot 10^{24} \text{ н / м}^2$, $E > 1 \text{ МэВ}$), но и о значительно высокой их радиационной стойкости по сравнению с обычным вольфрамом. Так, в наноструктурах в 3 – 4 раза меньше нанопор и в 10 раз выше сопротивление повреждению поверхности.

Авторы разделяют оптимизм, высказанный в [14] о том, что совершенствование технологии, а также знания о природе радиационных дефектов и их эволюции под влиянием дозы облучения и других внешних факторов, должно обеспечить создание стабильных наноструктур с высокими физическо-техническими свойствами. Соответственно, переход к наноструктурным изделиям на основе $^{11}\text{B}_4\text{C}$ в будущем может еще более значительно увеличить эффективность работы этого материала в активной зоне реактора.

4. Заключение

Повышенное внимания к так называемым реакторам 4-го поколения, в том числе реакторам на быстрых нейтронах, как нельзя кстати способствует разработке и созданию композиционной керамики на основе карбида бора и диборида циркония ($^{11}\text{B}_4\text{C} - \text{Zr}^{11}\text{B}_2$) с целью ее использования в качестве радиационно стойкого конструкционного материала. Не без основания можно предположить, что переход к компактным наноструктурным изделиям на основе $^{11}\text{B}_4\text{C} - \text{Zr}^{11}\text{B}_2$ не только повысит эксплуатационные характеристики и радиационную стойкость таких материалов, но и безопасность и эффективность реактора в целом.

На сегодняшний день основной «недостаток» карбида бора $^{11}\text{B}_4\text{C}$ состоит в том, что он, на наш взгляд, незаслуженно мало исследован. Многие факты (часть из которых приведены выше), свидетельствуют, что эта керамика станет одним из самых востребованных реакторных материалов будущего. Однако окончательное решение о перспективности использования указанного композиционного материала в атомной технике будет возможно после проведения полномасштабных реакторных и постреакторных испытаний.

Ссылки

1. G. Gastaldo, G. Vambenepe, J. C. Garnier. In: Adsorber Materials Control Rods and Designs of Shutdown Systems for Advanced Liquid Metal Fast Reactors. 1996, Vienna: IAEA, TECDOC-884: 225.
2. В. Д. Рисованный, А. В. Захаров, Е. П. Ключков, Т. М. Гусева. Бор в ядерной технике. 2003, Димитровград: ФГУП ГНЦ РФ – НИИ АР.
3. Y. Morohashi, T. Maruyama, T. Donomae, Y. Tachi, Sh. Onose. J. Nucl. Sci. & Technol. 45 (2008) 867.
4. G. A. Gogotsi, Ya. L. Groushevsky, O. B. Dashevskaya, Ya. G. Gogotsi, V. A. Lavrenko. J. Less-Comm. Met. 117 (1986) 225.
5. Г. В. Бокучава, Г. С. Карумидзе, Б. М. Широков. Авиационно-косм. тех. и технол., 3 (2008) 75.
6. Г. Н. Макаренко, Т. Я. Косолапова, Э. В. Марек. Тугоплавкие бориды и силициды. 1977, Киев: Наукова думка.
7. R. Sivakumar, M. I. Jones, K. Hirao, W. Kanematsu. J. Eur. Ceram. Soc. 26 (2006) 351.
8. L. L. Snead, Y. Katoh, S. Connery. J. Nucl. Mater. 367-370 (2007) 677.
9. Y. Katoh, L. L. Snead, T. Nozawa, N. B. Morley, W. E. Windes. Adv. Sci. & Technol. 45 (2006) 1915.
10. L. L. Snead, S. J. Zinkle, J. C. Hay, M. C. Osborne. Nucl. Instr. & Meth. Phys. Res. B 141 (1998) 123.
11. L. L. Snead, S. J. Zinkle. Nucl. Instr. & Meth. Phys. Res. B 191 (2002) 497.
12. И. А. Баирамашвили, Г. Н. Бахия, Ш. А. Лоладзе, З. М. Микадзе. In: Summary Report Meeting of Specialists of Development and Application of Absorber Materials. 1973, Dimitrovgrad: RIAR, 371.
13. I. A. Bairamashvili. In: Adsorber Materials Control Rods and Design of Shutdown Systems for Advanced Liquid Metal Fast Reactor. 1996, Vienna: IAEA, TECDOC-884: 225.
14. Р. А. Андриевский. In: 2nd Nanotechnology International Forum RusNanoTech, 2009.
15. Р. А. Андриевский. Росс. нанотехнол. 6 (2011) 34.
16. H. Kurishita, S. Kobayashi, K. Nakai, T. Ogawa, A. Hasegawa, K. Abe, H. Arakawa, S. Matsuo, T. Takida, K. Takebe, M. Kawai, N. Yoshida. J. Nucl. Mater. 377 (2008) 34.

ИССЛЕДОВАНИЕ СПЕКТРОВ ОПТИЧЕСКОГО ПРОПУСКАНИЯ ТОНКИХ ПЛЕНОК TiN, ПОЛУЧЕННЫХ МЕТОДОМ ВЧ-РЕАКТИВНОГО РАСПЫЛЕНИЯ

А. П. Бибилашвили, З. В. Джибути, Н. Д. Долидзе

Институт микро- и наноэлектроники
Тбилисский государственный университет им. И. Джавахишвили
Тбилиси, Грузия
amiran.bibilashvili@tsu.ge

Принята 8 октября 2013 года

Одним из наиболее перспективных направлений внедрения нанотехнологии в промышленность является создание (получение) и производство новых материалов с уникальными свойствами. Такие материалы должны обладать высококачественными физическими, химическими, механическими и оптическими параметрами. С этой целью, в последнее время большое внимание уделяется новым износостойким, перспективным покрытиям нитрида титана (TiN). Нитрид титана является широкозонным материалом и обладает удачной совокупностью вышеперечисленных параметров: низкое удельное сопротивление, высокий коэффициент оптического пропускания в видимой области и высокий коэффициент отражения в инфракрасной области спектра, высокая твердость, хорошая устойчивость к химическим растворам и коррозии [1 – 5]. Тонкие пленки нитрида титана является перспективным материалом для применения в микро- и наноэлектронных устройствах [2] и солнечных батареях [3]. Нитрид титана имеет следующие основные параметры: постоянная решетки 0.433 нм, температура плавления 2947 °С, плотность 5.44 г / см³, теплопроводность 0.34 Вт / см · К, модуль упругости 620 ГПа, микротвердость 20 ГПа.

Тонкие пленки TiN получают разными методами [6]. Среди них, для получения высококачественных пленок, метод ВЧ-реактивного вакуумного распыления мишени является наиболее подходящим, так как он позволяет в широких пределах контролировать такие технологические параметры, как давление под вакуумным колпаком при распылении, мощность мишени, смещение и температура подложки.

Нужно отметить, что по своим физическим свойствам TiN является перспективным материалом для применения в различных фотоэлектрических приборах.

Исходя из вышеизложенного целью данной работы является исследование оптических свойства тонких пленок нитрида титана, полученного методом ВЧ-реактивного распыления титана в атмосфере азота.

Для исследования в качестве подложек применялось стекло, марки К-8, размером 10 × 5 × 1 мм. Перед напылением пленок подложки обрабатывались химическим способом по общеизвестной технологии. Метод позволяет непосредственно перед началом процесса напыления проводить кратковременное протравление с помощью аргоновой бомбардировки для удаления неконтролируемого загрязнения поверхности мишени и подложек.

Напыление тонких пленок TiN проводилось на универсальной вакуумной установке CIT-ALCATEL ANNECY с помощью ВЧ-реактивного распыления чистого титана в атмосфере смеси аргона и азота при постоянном напряжении. Перед началом процесса напыления вакуумная камера откачивалась до остаточного давления $2 \cdot 10^{-3}$ Па. Осаждение пленок проводилось при давлении газов $5.3 \cdot 10^{-2}$ Па, подаче на мишень – 3 кВ напряжении и температуре подложек 350°C . Подложки размещались над мишени на расстоянии 250 мм. С целью улучшения адгезии пленок к поверхности подложки, после напыления, без нарушения вакуума, производился отжиг пленок при температурах 400°C , в течении 10 мин. После остывания в вакууме до комнатной температуры, образцы изымались из вакуумной камеры и для упорядочения структуры и уменьшения внутренних механических напряжений пленок проводился импульсно-фотонный отжиг. В качестве источника полихроматического излучения служил набор ламп накаливания ЛГ-1000Х-220. Плотность мощности падающего на образец света составлял $92 \text{ Вт} / \text{см}^2$. Длительность импульса менялась от мкс до нескольких с.

Измерение толщины пленок TiN проводилось:

- 1) на стекле с использованием оптического интерферометра МИИ-4 по стандартной методике, и
- 2) на кремний (сопствующий в процессе напыления) на установке ЛЭМ-2 с длиной волны лазера 6328 \AA .

Толщины пленок TiN находились в интервале 50 – 200 нм.

Измерения величины оптического пропускания проводились на спектрофотометре ФС-26 в диапазоне длин волн 0.25 – 1.10 мкм.

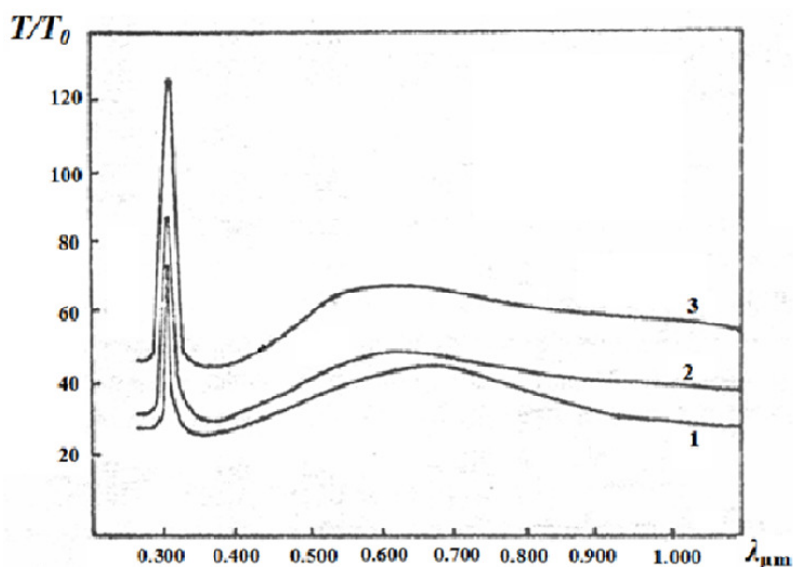


Рисунок 1. Спектры оптического пропускания пленок нитрида титана толщин: 1 – 200, 2 – 160 и 3 – 80 нм.

На **рисунках 1 и 2** показана зависимость величины оптического пропускания пленок нитрида титана от длины волны. Толщина пленок 50 – 200 нм. Как видно из **рисунка 1**, с увеличением толщины пленок наблюдается изменение пропускания света во всем измеряемом диапазоне волн. Характерной особенностью спектра пропускания является наличие резкого пика пропускания в области длин волн 293 – 330 нм (**рисунки 1**

и 2). Второй, более широкий максимум наблюдается в видимой области спектра. Как видно из **рисунка 1**, пленки нитрида кремния обладают большой однородностью пропускания практически по всей видимой области спектра. Неоднородность в диапазоне длин волн 550 – 650 нм не превышает 3%. Отметим, что для образца толщиной 80 нм наблюдается эффект просветления в области коротковолнового пика.

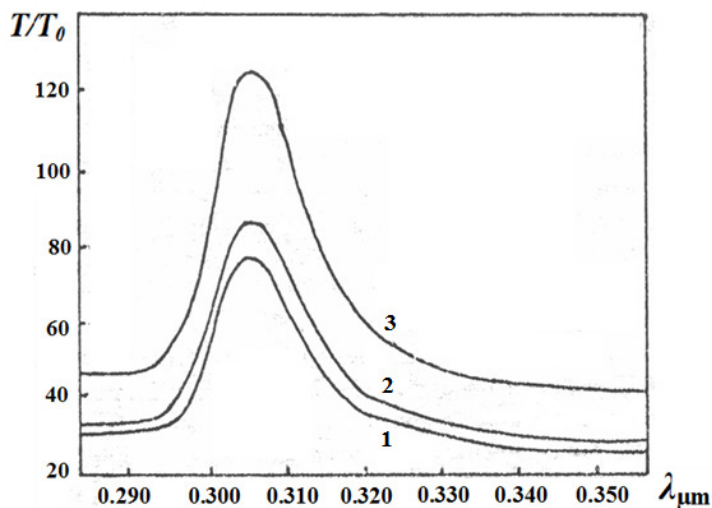


Рисунок 2. Спектры оптического пропускания пленок нитрида титана после: 1 – длительного термического воздействия в печи (200 °С, 14 часов); 2 – импульсного фотонного воздействия (2 с); 3 – импульсного фотонного воздействия (3 с).

Для оценки стабильности оптических свойств пленок TiN проводилось исследование влияния импульсного фотонного, длительного термического и ультрафиолетового воздействий на спектры пропускания образца. Стекло с пленкой TiN освещалось со стороны пленки. Импульсы света длительностью менее 2 с не вызывают изменения спектра оптического пропускания. При увеличении длительности импульса до 2 – 3 с, спектр оптического пропускания изменился в сторону увеличения только в области максимумов пропускания. Увеличение пропускания не превышало 3%. Дальнейшая обработка образцов световыми импульсами не приводит к заметному изменению в спектрах оптического пропускания. Такой же эффект наблюдается при выдержке образцов при температуре 200 °С на воздухе в течении 14 часов.

Как известно [1], TiN обладает высокой отражательной способностью в инфракрасной области спектра, и с учетом кратковременности импульсного фотонного воздействия (2 – 3 с) по сравнению термическим (14 часов), можно заключить, что механизм отжига, вызывающего увеличение оптического пропускания носит атермический характер и связан со снятием внутренних механических напряжений, возникающих в пленках TiN при их выращивании на чужеродных подложках [2].

Исследуемые образцы подвергались также мощному ультрафиолетовому воздействию от лампы ДРШ 1000 в течении 16 часов. В результате, какие либо заметные изменения в спектрах оптического пропускания образца обнаружить не удалось.

Для проверки стабильности изменений, измерения были повторены через четыре месяца. Как показали исследования, изменения в спектрах оптического пропускания не наблюдаются.

Результаты данных экспериментов позволяет оценить оптические свойства полученных пленок TiN и рассчитывать на высокую стабильность параметров в случае их применения в качестве оптических покрытий.

Ссылки

1. М. Н. Солован, В. В. Брус, П. Д. Марьянчук, Т. Т. Ковалюк, J. Rappich, M. Gluba. ФТТ 55 (2013) 2123.
2. А. Е. Вол. Строение и свойства двойных металлических систем, Том 1. 1959, Москва: Физматгиз.
3. E. Valkonen, T. Karlson, B. Karlsson, B. O. Johansson. Thin Films Technol. 401 (1983) 41.
4. U. Ropacz, H. A. John. Vacuum 36 (1986) 81.
B. Nauinzek, A. Zabkar. Vacuum 36 (1986) 111.
5. M. Tao, D. Udeshi, S. Agarwal, E. Maldonado, W. P. Kirk. Solid State Electron. 48 (2004) 335.
6. G. B. Smith, A. Ben-David, P. D. Swift. Renew. Energy 22 (2001) 79.

ულტრაღისაქრონიული α -ალუმინის ოქსიდის ფუნქციონირების
დაბალტემპერატურული სინთეზის ზოგიერთი საკითხი

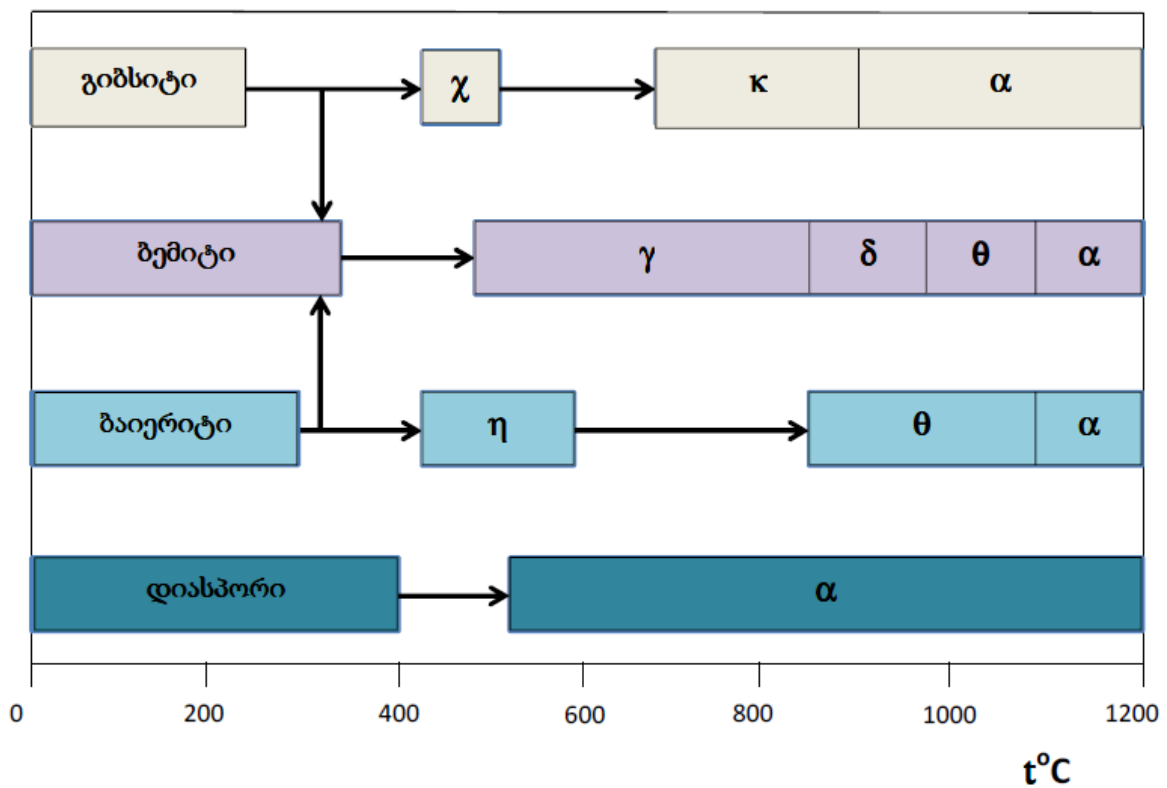
თ. ვ. კუჭუხიძე, თ. ნ. არჩუაძე, ვ. გ. გაბუნია,
მ. ა. ქადარია, ო. ი. ლეკაშვილი, რ. ვ. ჭეღია

სოხუმის ილია ვეკუას ფიზიკა-ტექნიკის ინსტიტუტი
თბილისი, საქართველო
E-mail: sipt@sipt.org

მიღებულია 2013 წლის 18 ოქტომბერს

ნანოფუნქციონირების გააჩნიათ გამოყენების დიდი პოტენციალი მაღალი ხარისხის საინჟინრო, ელექტრონული, ელექტროტექნიკური ბიომეთავსებადი კერამიკული მასალების, კატალიზატორების, ადსორბენტების, მემბრანების, ფილტრების, სინთეზური საიუველირო ქვების, მონოკრისტალებისა და სხვ. მისაღებად. კერამიკული მასალების ფიზიკურ-მექანიკური თვისებები ძირითადად დამოკიდებულია ნანოფუნქციონირების მიღებისა და მათი კონსოლიდაციის მეთოდებზე. კერამიკული მასალების თვისებების მნიშვნელოვანი გაუმჯობესება შესაძლებელია მიღწეულ იქნას ნანოკრისტალური სტრუქტურის ჩამოყალიბებით [1 – 3]. მსხვილკრისტალოვანი სტრუქტურის მქონე კერამიკა ხასიათდება სიმყიფით, ბზარების წარმოქმნის უნარით, ეროზიული და აბრაზიული ზემოქმედების მიმართ მცირე მედეგობით. კერამიკული მასალების თვისებების გაუმჯობესების ტრადიციულმა მეთოდებმა პრაქტიკულად ამოწურეს ყოველნაირი რესურსი. ამ დარგის განვითარების ერთ-ერთი რეალური მიმართულებაა ნანოტექნოლოგიების გამოყენება, ნანოფუნქციონირების მოდიფიცირება მსხვილკრისტალოვანი სტრუქტურის ჩამოყალიბების საწინააღმდეგო ნივთიერებებით, მათი კონსოლიდაცია მზა ნაკეთობაში ნაწილაკების ნანოზომების შენარჩუნებით. ნანოსტრუქტურული კერამიკული ნაკეთობების ფიზიკო-მექანიკური თვისებები რამდენჯერმე აღემატება წარმოების ტრადიციული მეთოდებით მიღებული იმავე მასალების მახასიათებლებს, რაც გამოწვეულია ნანოსისტემების სტრუქტურულ-მორფოლოგიური თავისებურებებით, კერძოდ, ჭარბი ზედაპირული ენერჯის არსებობით, რომელსაც წარმატებით იყენებენ უნიკალური კერამიკული კომპოზიტების მისაღებად. ფუნქციონირების ცალკეული ნაწილაკის განსაკუთრებული თვისებები ვლინდება მაშინ, როდესაც მათი ზომა ნაკლებია 100 ნმ-ზე. ამ შემთხვევაში ნანონაწილაკის ზედაპირზე და მის მოცულობაში არსებული ატომების რაოდენობა თანაზომადია. მაგალითად, 5 ნმ-იანი წახნაგის კუბი შეიცავს 1000 ატომს, რომელთა 40 % განლაგებულია ნანონაწილაკის ზედაპირზე. შედარებისათვის, 0.1 მკმ-ის ზომის ნაწილაკი შეიცავს 10^7 ატომს ან ერთეულ უჯრედს, რომელთაგან მხოლოდ 1 %-ია განლაგებული ზედაპირზე [4]. ნანონაწილაკთა ზომების შემცირებით იზრდება ფარდობა ზედაპირი / მოცულობა. ამ ნაერთების ნანოფუნქციონირების ერთი მოლის ზედაპირის ფართობი რამდენიმე კვ. კმ-ს აღწევს, ხოლო მათი ნაყარის სიმკვრივეა ~ 0.1 გ / სმ³. ამიტომ ნაწილაკების მთელ ენერჯიაში ზედაპირული ენერჯის წილი მკვეთრად იზრდება. სხეულის ზედაპირისა და მოცულობების დამოკიდებულება

ნაწილაკის ზომაზე შესანიშნავად არის დემონსტრირებული ნაშრომში [5]: კუბის ფორმის 50 კგ კვარცის ნიმუშის წახნაგის სიგრძე 27 სმ-ს აღწევს, ზედაპირის ფართობი კი – 0.44 მ²-ს. ამ ნიმუშის დანაწევრება 1მ³ მოცულობის კუბებად ზედაპირს გაზრდის 120 მ²-მდე, ხოლო 5 ნმ³-იანად დანაწევრების შემთხვევაში – 2 კვ.კმ-მდე. ზემოთ აღნიშნულის გამო ნანონაწილაკების სტრუქტურულ-მორფოლოგიური აღნაგობა და თვისებები მკვეთრად განსხვავდება იგივე ნივთიერების მსხვილკრისტალოვანი ნაწილაკისაგან. შესაბამისად, ასეთი ფხვნილებისაგან დამზადებული ნანოსტრუქტურული კერამიკული ნაკეთობების საექსპლუატაციო მახასიათებლები მკვეთრად გაუმჯობესებულია ტრადიციული მეთოდებით მიღებულთან შედარებით. ამავე დროს, ნანონაწილაკების შეცხოების ტემპერატურა რამდენიმე ასეული გრადუსით უფრო დაბალია მსხვილმარცვლოვან ფხვნილებთან შედარებით, რაც ხელს უწყობს ნაკეთობის ნანოსტრუქტურის ჩამოყალიბებას [6, 7].



ნახაზი 1. ალუმინის ჰიდრატების სტრუქტურული გარდაქმნა.

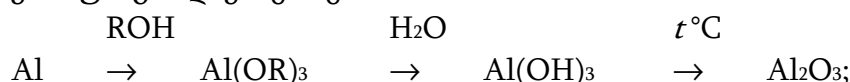
ალუმინის ოქსიდის ფუძეზე მიღებულ კერამიკას გააჩნია გამოყენების ფართო სპექტრი, რადგან მათ გააჩნიათ მთელი რიგი უნიკალური თვისებები, როგორცაა მაღალისი მტკიცე, ცვეთადმედეგობა, დიელექტრიკული მახასიათებლები, მაღალ ტემპერატურაზე და კოროზიულ გარემოში ექსპლუატაციის უნარი. ისინი ფართოდ გამოიყენებიან ელექტროტექნიკაში (იზოლატორები), ელექტრონულ სისტემებში (საფირონის მონოკრისტალებზე გაზრდილი მულტიეპიტაქსიალური შრეები), საავიაციო და აეროკოსმოსურ ტექნოლოგიებში, მედიცინაში (ბიომეთავსებადი კერამიკები), ლაზერულ ტექნიკაში, ოპტიკაში (გამჭვირვალე მინები) და სხვ. ულტრადისპერსული Al_2O_3 -ის მისაღებად გამოყენებულია მრავალი მეთოდი, მათ შორის ზოლ-გელ პროცესი, დალექვის, ქიმიური დაშლის, პლაზმოქიმიური, ელექტროქიმიური, მიკროემულსიური, ჰიდროთერმული, აეროზოლური, კოროზიული, პოლიმერ-პრეკურსორული,

მაღალტემპერატურული დაჟანგვის და სხვ. [8 – 16]. ფხვნილებში მიკრომინარეების არსებობა, ნაწილაკების სტრუქტურულ-მორფოლოგიური აღნაგობა და შეცხოების ტექნოლოგიები განაპირობებენ კორუნდის კერამიკული ნამზადების საექსპლოატაციო მახასიათებლებს. ალუმინის ჰიდრატების ფაზების ტრანსფორმაციისას (ნახაზი 1) მიიღება Al_2O_3 -ის სხვადასხვა ფორმები (α , χ , η , δ , κ , θ , γ , ρ). ტემპერატურის მომატებით ხვედრითი ზედაპირი მცირდება, რადგან იცვლება კრისტალური სტრუქტურა და მცირდება მასალის ფორიანობა. გარდა ამისა, $\gamma \rightarrow \alpha$ გადასვლისას მცირდება Al-OH ბმების რაოდენობა, მცირდება ოქსიდის მჟავიანობა, რაც ხშირად გამოყენებულია სელექტიური კატალიზატორების სარჩულების მისაღებად [17].

დედამიწის ქერქში ალუმინის შემცველობა 8 %-ს აღწევს. როგორც აღვნიშნეთ, ის ფართოდ გამოიყენება მეცნიერებისა და ტექნიკის პრაქტიკულად ყველა სფეროში. ამჟამად ალუმინის ოქსიდის წარმოება მსოფლიოში რამოდენიმე ათეულ მილიონ ტონას აღწევს და ის ძირითადად იწარმოება ბაიერის მეთოდით. ქიმიურად სუფთა Al_2O_3 -გან მიიღება მრავალი ქიმიური ნაერთი თუ კერამიკული მასალა. მაგალითად, იაპონიაში ამ მიზნით ყოველწლიურად გამოიყენება 350 000 ტონა ალუმინის ოქსიდი. ბაიერის მეთოდით მიღებული Al_2O_3 -ის მაქსიმალური სისუფთავე 99.6 – 99.9%-ს აღწევს, რომელიც შეიძლება გამოყენებულ იქნას სხვადასხვა ფუნქციური დანიშნულების კერამიკების მისაღებად, მათ შორის ინტეგრალური სქემების ფუძე-შრეებად (Si / Al_2O_3 , Si-Ge / Al_2O_3 , As-Ge / Al_2O_3 და სხვ.) უფრო მაღალი სისუფთავის (99.99 %) Al_2O_3 გამოყენებულია სცინტილატორების ($Y_3Al_5O_{12}$) მონოკრისტალების (ლალი, საფირონი), გაზის სენსორების, ელექტრონული სისტემების კომპონენტების და სხვ. მასალების მისაღებად.

კორუნდის კერამიკისთვის მაღალი სისუფთავის ალუმინის ოქსიდი ძირითადად იწარმოება შემდეგი მეთოდებით:

1. ალუმინის ალკოქსიდების ჰიდროლიზით, რომელიც დაფუძნებულია შემდეგ ქიმიურ გარდაქმნებზე:



2. ალუმინის ნაერთების ორთქლის დაშლით (chemical vapor deposition – CVD). აქროლადი ალუმინის ნაერთების ($AlCl_3$, AlR_2Cl , $AlRCl_2$, $Al(OR)_3$ და სხვ.) აორთქლებით და მათი დაჟანგვით (H_2O , O_2) მიიღება Al_2O_3 -ის ულტრადისპერსული ფხვნილი (50 ნმ), რომელიც γ - და α -ფაზებისაგან შედგება.

3. ამონიუმ-ალუმინის შაბის დაშლით. ამ მეთოდით მიღებული ალუმინის ოქსიდი გამოყენებულია ლალისა და საფირონის მონოკრისტალების მისაღებად. ამ მიზნით $(NH_4)Al(SO_4)_2 \cdot 12H_2O$ -ის გასუფთავება ხდება გადაკრისტალებითა და შემდგომი დაშლით:



ამ მეთოდის ერთ-ერთი ნაკლია დიდი ოდენობით მავნე გაზების გამოყოფა (NH_3 , SO_3).

4. ალუმინის არაორგანული მარილების დაშლა. ამჟამად ფართოდაა გამოყენებული ამონიუმ-ალუმინის ჰიდროქსიკარბონატის დაშლა მაღალი სისუფთავის ალუმინის ოქსიდის მისაღებად. 99.99 % სისუფთავის Al_2O_3 მიიღება ზემოთ აღნიშნული ნაერთის დაშლით 250 °C-ზე. მიღებული Al_2O_3 -ის ნაწილაკების ზომა 300 – 400 ნმ-ს აღწევს. ასევე გამოყენებულია ალუმინის ფუძე აცეტატების დაშლა 1200 °-ზე [17 – 19].

სპეციალისტების აზრით, ალუმინის ოქსიდის ნანოფხვნილების წარმოება მომავალშიც გაიზრდება, რადგან იზრდება მასზე მოთხოვნა ისეთი დარგებიდან როგორცაა ელექტრონული მრეწველობა (ნახევარგამტარული მასალები, ენერჯის გარდამქმნელები, სენსორები, აეროკოსმოსური ტექნოლოგიები, ლაზერული ტექნიკა, სცინტილატორები, აბრაზივები, მემბრანული ფილტრები ($\text{CO} + \text{H}_2$), პლაზმური დისპლეები, მანქანათმშენებლობა და სხვ.). როგორც აღვნიშნეთ, Al_2O_3 -ის მისაღებად ერთ-ერთი ფართოდ გავრცელებული მეთოდი არის მეტალური ალუმინიდან ალკოქსიდების მიღება და მათი ჰიდროლიზი კონტროლირებად პირობებში. მაღალ ტემპერატურაზე სტაბილურია მხოლოდ α - Al_2O_3 , რომელიც მიიღება ალუმინის ჰიდროქსიდების ან ალუმინის ოქსიდის არამდგრადი შუალედური ფაზების თანდათანობითი გახურებით $\sim 1200^\circ\text{C}$ -ზე ზევით. ამ შემთხვევაში ადგილი აქვს კუბური მესრის ტრანსფორმაციას ჰექსაგონალურში. მცირე ზომის α -სტრუქტურის მქონე კრისტალების ჩამოყალიბება დაბალი სიჩქარით მიმდინარეობს, ხოლო მათი გაზრდა და რამოდენიმე მიკრონის ზომის დენდრიტული სტრუქტურის ჩამოყალიბება სპონტანურად მიმდინარეობს. ამიტომ ერთ-ერთი მნიშვნელოვანი მომენტია ტრანსფორმირების განხორციელება დაბალ ტემპერატურაზე, α - Al_2O_3 -ის კრისტალების წინასწარი შეტანა დაბალტემპერატურული სინთეზისას (პრეკურსორების დაშლის, ჰიდროლიზის, გაშრობა-გახურებისა და გამოწვის პირობებში), რომ მიღებულ იქნას ულტრადისპერსული α - Al_2O_3 -ის ნანოფხვნილები და არ დავუშვათ დიდი ზომის აგლომერატების გაზრდა. დადგენილია, რომ ალუმინის ოქსიდების ფაზათა გადასვლის ტემპერატურა დამოკიდებულია α - Al_2O_3 -ის, წყლის ორთქლის წნევაზე და სხვადასხვა მინარევების არსებობაზე. α - Al_2O_3 -ის კრისტალების დამატებისას მცირდება ფაზათა შორის გადასვლის ენერჯია, ხოლო წყლის ორთქლის არსებობა ხელს უწყობს იონების ზედაპირულ დიფუზიას და α - Al_2O_3 -ის ფაზის ჩამოყალიბებას უფრო დაბალ ტემპერატურაზე. ამ პრობლემაზე მუშაობს მრავალი სამეცნიერო-კვლევითი ცენტრი და გამოყენებულია მთელი რიგი ქიმიური მეთოდები დაბალტემპერატურული γ - α ან θ - α ფაზური გადასვლებისათვის. დაბალტემპერატურული ფაზური გარდაქმნისას აგლომერატების წარმოქმნა ნაკლებად ხდება, ასევე მცირდება პირველადი კრისტალების გამსხვილების პროცესი.

განვიხილოთ ამ პრობლემების გადაჭრის რამოდენიმე მეთოდი. α - Al_2O_3 მიღებულია დაბალ ტემპერატურაზე ალუმინის ჰიდროქსიდის ნაერთებიდან 5 % α -ფაზის დამატებით სარეაქციო არეში, რომელიც ასრულებს კრისტალიზაციის ცენტრების როლს [20]. ავტორის მიერ ულტრადისპერსული ალუმინის ოქსიდის მისაღებად გამოყენებულ იქნა დალექვის მეთოდი. შესწავლილ იქნა შემდეგი სისტემები:

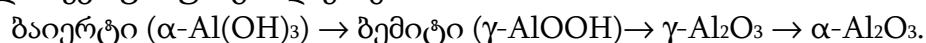
- I. $\text{Al}(\text{OH})_3$ (ნიტრატების იონებისაგან თავისუფალი);
- II. $\text{Al}(\text{OH})_3 + 5\% \alpha$ - Al_2O_3 (ნიტრატების იონებისაგან თავისუფალი);
- III. $\text{Al}(\text{OH})_3 + 45\% \text{NH}_4\text{NO}_3$;
- IV. $\text{Al}(\text{OH})_3 + 5\% \alpha$ - $\text{Al}_2\text{O}_3 + 45\% \text{NH}_4\text{NO}_3$.

დიფერენციალური თერმული ანალიზით (DTA) დადგენილია, რომ I და III კომპოზიტების ფხვნილების გახურებით ($100 - 1300^\circ\text{C}$ -ზე) α - Al_2O_3 -ის ფაზა შესაბამისად წარმოიქმნება 1220 -სა და 1155°C -ზე. რენტგენოფაზური ანალიზის მეთოდით (XRD) α -ფაზა წარმოიქმნება $1150 - 1200$ და $1050 - 1150^\circ\text{C}$ -ზე ტემპერატურულ ინტერვალებში. α -ფაზის 5 %-ის წინასწარი შეტანა საწყის კომპონენტებში მნიშვნელოვნად ამცირებს α - Al_2O_3 -ის წარმოქმნის ტემპერატურებს: II კომპოზიტისათვის გადასვლის

ტემპერატურა აღწევს 1118-სა (DTA) და 600 – 1100 °C-ს (XRD), ხოლო IV კომპოზიტისათვის – 1009-სა (DTA) და 775 – 950 °C-ს (XRD). სინთეზირებული ფხვნილებისაგან დამზადებული კორუნდის კერამიკის ფიზიკურ-მექანიკური თვისებებიც აშკარად განსხვავდება ერთმანეთისაგან: I კომპოზიტისაგან მიღებული ფხვნილის ნაწილაკების ზომა ~ 200 ნმ-ია და მისგან მიღებული კერამიკის შეცხოება აუცილებელია 1600 °C-ზე, IV კომპოზიტისაგან მიღებული ფხვნილის შეცხოებისათვის (ნაწილაკების ზომა < 60 ნმ) საკმარისია 1450 °C, კერამიკის სიმკვრივე თეორიული მნიშვნელობის 99 %-ს აღწევს. ამრიგად, α - Al_2O_3 -ის წარმოქმნის ტემპერატურის დაწვევა მკვეთრად აუმჯობესებს კორუნდის კერამიკის შეცხოების პირობებსა და მიღებული კერამიკის ფიზიკურ-მექანიკურ თვისებებს.

დადგენილია, რომ პოლიმერულ-პრეკურსორული მეთოდით მიღებული γ - Al_2O_3 -ის გარდაქმნის პროცესს α - Al_2O_3 -ში თან სდევს ნაწილაკების ზომის გაზრდა. საწყის ეტაპზე $\text{NH}_4\text{Al}(\text{SO}_4)_2$ -დან ლებულობენ $\text{Al}(\text{OH})_3$ -ს, რომელსაც გარდაქმნიან ჯერ ალუმინის ნიტრატად, შემდეგ კი ეთილენგლიკოლის დამატებით პოლიმერულ გელად. მისი გამოწვით 500 °C-ზე მიიღება ამორფული ფხვნილი, რომელიც 700 °C-ზე წარმოქმნის γ - Al_2O_3 -ს. დადგენილია, რომ α -ფაზის წარმოქმნა იწყება ამორფული ფხვნილის გამოწვით 1000 – 1025 °C-ზე (γ და α -ფაზები), ხოლო 1050 °C-ზე მიიღება მხოლოდ α -ფაზა. რენტგენოფაზური ანალიზის მეთოდით დადგენილია, რომ γ - Al_2O_3 -ის ნაწილაკების ზომა 800 – 950 °C-ზე არის 5 – 10 ნმ, ხოლო მისგან წარმოქმნილი α - Al_2O_3 -ის ნაწილაკების ზომა 10 – 100 ნმ-ს აღწევს (1050 – 1200 °C). ტემპერატურის მომატებით ფაზურ გადასვლას თან სდევს ნაწილაკების ზომის გაზრდა [21].

α - Al_2O_3 -ის მონიკრისტალები მიღებულია კალიუმის სულფატის, ბაიერიტისა (α - $\text{Al}(\text{OH})_3$) და 3 – 8 % α - Al_2O_3 -ის ნანოფხვნილის შემცველი კომპოზიციის 900 °C-ზე გახურებით. მიღებულ α - Al_2O_3 -ს გააჩნია მომრგვალო ფირფიტების ფორმა, დიამეტრით 0.5 – 1.5 მკმ, სისქე 50 – 150 ნმ-ია. α -ალუმინისოქსიდის ნანოფხვნილი შეტანილ იქნა ალუმინის ნიტრატის ხსნარში, რომელსაც ემატება ამონიუმის ხსნარი (pH = 9) და დისპერსანტი პოლიეთილენგლიკოლი (პეგ). წარმოქმნილ ბაიერიტს ერევა K_2SO_4 მოლური თანაფარდობით $\text{K} / \text{Al} = 3 - 12$. დადგენილია, რომ ფხვნილის გამოწვისას ადგილი აქვს ფაზურ გარდაქმნებს:



ავტორთა აზრით, α -ფაზის დაბალტემპერატურული სინთეზი ხორციელდება მცირე რაოდენობით თხევადი ფაზების წარმოქმნით, ამ შემთხვევაში ადგილი აქვს $\text{K}_3\text{Al}(\text{SO}_4)_3$ -ის წარმოქმნას, რომელიც ამ სისტემაში ფორმირდება 612 °C-ზე და ლღვება > 654 °C-ზე. ფირფიტების დიამეტრი მცირდება ფხვნილოვან კომპოზიციაში α - Al_2O_3 -ის ნანოკრისტალების დანამატების მასური წილის გაზრდით 3-დან 8 %-მდე, შესაბამისად, 1000-დან 200 ნმ-მდე [22].

AlF_3 -ის დამატება იწვევს მეტასტაბილური ალუმინის ოქსიდებისაგან α - Al_2O_3 -ის წარმოქმნის ტემპერატურის დაწევას, რაც აიხსნება AlOF -ის შუალედური ნაერთის წარმოქმნით, რომელიც ხელს უწყობს რეგულარული სტრუქტურის დაშლას და Al^{3+} იონების ვაკანსიების წარმოქმნას დიფუზიის დაჩქარებით. საწყისი პრეკურსორი მიღებულ იქნა ალუმინის იზოპროპილატის, ალუმინის ფტორიდისა (2 %) და იზოპროპანოლის წყალხსნარების ჰიდროთერმული დამუშავებით ავტოკლავში 120 °C-ზე 24 სთ-ის განმავლობაში. დადგენილია, რომ AlF_3 -ის კონცენტრაციის გაზრდით α - Al_2O_3 -ის ფხვნილების მორფოლოგია იცვლება არარეგულარულიდან ჰექსაგონალური ფირფიტების წარმოქმნამდე [23].

ალუმინის ოქსიდების ფაზათა ტრანსფორმაციის ტემპერატურული ინტერვალები იცვლება მცირე რაოდენობით სხვადასხვა იშვიათ მიწათა მეტალთა კათიონების სისტემაში დამატებით. დადგენილია, რომ 0.1 % Lu^{3+} იონების შემცველი $\alpha\text{-Al}_2\text{O}_3$ -ის ფხვნილების შეცხოვრით $1400\text{ }^\circ\text{C}$ -ზე მიიღება ნანოსტრუქტურული კორუნდის კერამიკა, რომლის სიმკვრივე თეორიულის 99 %-ს შეადგენს [24].

იაფი კომერციული მეტასტაბილური ალუმინის ფხვნილების ტრანსფორმაცია სტაბილურ α -ფაზაში შესაძლებელია მცირე რაოდენობით $\alpha\text{-Al}_2\text{O}_3$ -ის ნანოფხვნილების შეტანითა და შემდგომი მათი დაფქვით. ასეთი ფხვნილებისაგან მიღებული ნანოსტრუქტურული კერამიკები ხასიათდებიან მაღალი სიმტკიცით ღუნვაზე და დარტყმითი სიბლანტით [25].

დიასპორისაგან ($\alpha\text{-AlOOH}$) $\alpha\text{-Al}_2\text{O}_3$ -ის მიღების ტექნოლოგია დამუშავებულია ნაშრომში [26]. დიასპორი მიღებულია $\text{Al}(\text{OtBu})_3$ -ის კონტროლირებადი ჰიდროლიზით HCl -ით, რეაგენტთა თანაფარდობით ალკოქსიდი / $\text{HCl} = 1$. ამ შემთხვევაში $500 - 800\text{ }^\circ\text{C}$ -ზე მიიღება 64 % α -ფაზა და ამორფული ფაზები. კორუნდის გამოსავალი იზრდება თუ ჰიდროლიზისას სარეაქციო არეში შევიტანთ α -დიასპორის კრისტალებს კონცენტრაციით $7.6 \cdot 10^{16}$ ნაწილი / მოლი Al_2O_3 . ამ შემთხვევაში $700\text{ }^\circ\text{C}$ -ზე ალკოქსიდის პროდუქტი გარდაიქმნება $\alpha\text{-Al}_2\text{O}_3$ -ის ფაზად. კორუნდის ნაწილაკების წარმოქმნა იწყება ჰიდროგელის გაცხელებისას $450\text{ }^\circ\text{C}$ -დან. თუ შევადარებთ ბაიერის პროცესით მიღებული მეტასტაბილური ფორმების გადასვლას თერმოდინამიკურად სტაბილურ $\alpha\text{-Al}_2\text{O}_3$ -ში, შევამჩნევთ, რომ ამ უკანასკნელის მისაღებად აუცილებელია $> 1100\text{ }^\circ\text{C}$ -ზე გახურება. ბაიერის პროცესის ალტერნატიულ მეთოდად ითვლება ალუმინის ნაერთების ან მეტალური ალუმინისაგან ჰიდროქსიდების მიღება და შემდგომ მათი დაბალტემპერატურული გარდაქმნა α -ფაზაში. ზემოთ აღწერილი მეთოდის ნაკლია დიასპორის მიღებისას კონტროლირებადი ჰიდროლიზის განხორციელების ტექნიკური სირთულე და პროცესის ხანგრძლივობა [26].

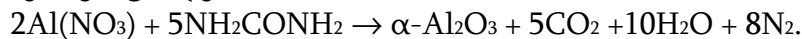
შესწავლილია ფაზათა ტრანსფორმაცია $\gamma\text{-Al}_2\text{O}_3$ -ის 50 ნმ ზომის ფხვნილის დაფქვისას პლანეტარულ წისქვილში. დადგენილია, რომ $\alpha\text{-Al}_2\text{O}_3$ -ის კრისტალების შეტანის გარეშე γ -ფაზა არ განიცდის გარდაქმნას α -ფაზაში (20 სთ). თუ ფხვნილის დაფქვა განხორციელდება ფოლადის ბურთულებით მასური თანაფარდობით m (ბურთულა) / m (Al_2O_3) = 10 : 1, ოთახის ტემპერატურაზე 20 – 27 სთ-ის შემდეგ $\gamma\text{-Al}_2\text{O}_3$ ძირითადად გადადის $\alpha\text{-Al}_2\text{O}_3$ -ში [27].

დადგენილია, რომ $\alpha\text{-Al}_2\text{O}_3$ -ის შეტანა სარეაქციო არეში აუმჯობესებს ასევე YAG ($\text{Y}_3\text{Al}_5\text{O}_{12}$) Al_2O_3 და YAG ნანომაფების ჩამოყალიბებას [28]. ნანომაფები მიღებულია ალუმინისა და იტრიუმის იზოპროპილატების ჰიდროლიზით და ზოლ-გელ პროცესში 200 ნმ ზომის $\alpha\text{-Al}_2\text{O}_3$ -ის ნაწილაკების დამატებით. ალუმინის ნანომაფები ზრდის კერამიკის თერმოსტაბილურობას, განსაკუთრებით ცოცვადობის შემცირების გამო.

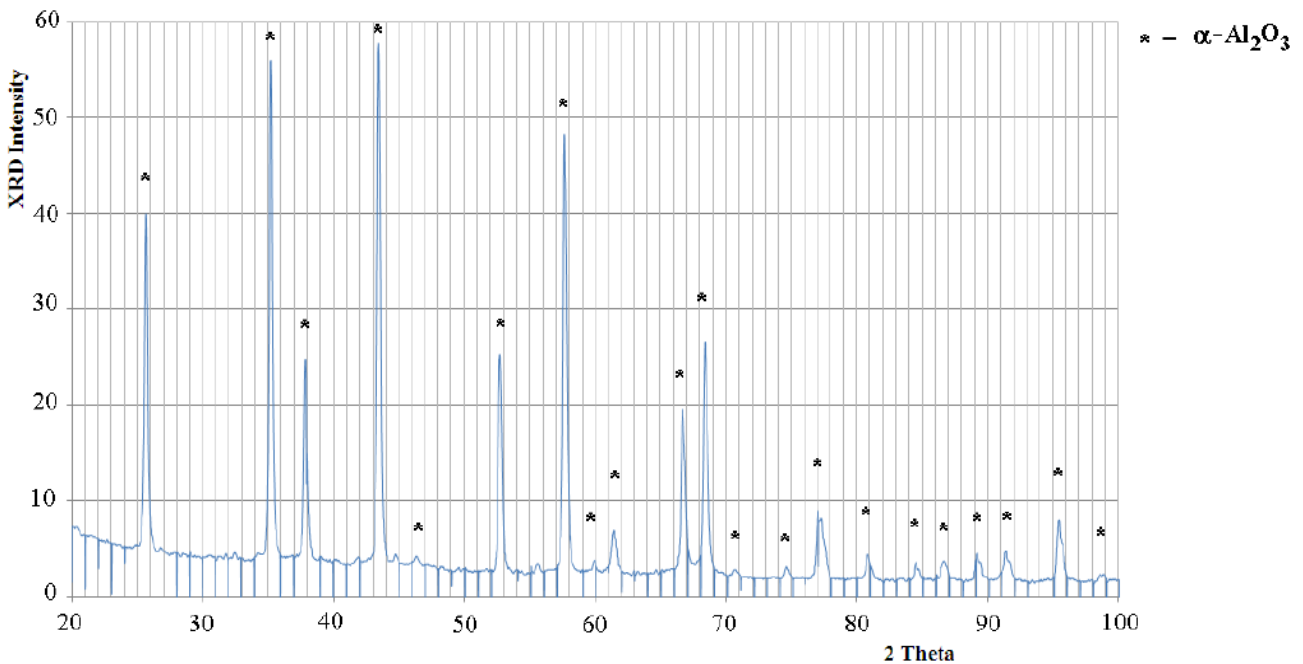
ბემიტისაგან მიღებულ იქნა $\alpha\text{-Al}_2\text{O}_3$ -ის ნანომაფები, როდესაც ალუმინის ნიტრატის ხსნარში შეტანილ იქნა 5 % $\alpha\text{-Fe}_2\text{O}_3$, რომელიც წარმოადგენს $\alpha\text{-Al}_2\text{O}_3$ -ის იზოსტრუქტურულ ანალოგს. დადგენილია, რომ ფაზათა შორის გადასვლის ტემპერატურა მცირდება $1025\text{ }^\circ\text{C}$ -მდე და ძირითადად მიიღება ნაწილაკები ორიენტაციით $[0001]\text{ Al}_2\text{O}_3 // [0001]\text{ Fe}_2\text{O}_3$ და $[1120]\text{ Al}_2\text{O}_3 // [1120]\text{ Fe}_2\text{O}_3$ [29].

ბიოსამედიცინო დანიშნულების შენადნობის (CoCr) თანაობისას ზოლ-გელ მეთოდით მიღებული გამა-ალუმინის ოქსიდი $1200\text{ }^\circ\text{C}$ -ზე გარდაიქმნება ალფა-ფაზად. იგივე მეთოდით მიღებული γ -ფაზა, რომელსაც წინასწარ დაამატეს 40 ნმ ზომის $\alpha\text{-Al}_2\text{O}_3$ ნაწილაკები, $800\text{ }^\circ\text{C}$ -ზე გადადის სტაბილურ $\alpha\text{-Al}_2\text{O}_3$ -ში [30].

ჩვენს მიერ $\alpha\text{-Al}_2\text{O}_3$ მისაღებად გამოყენებულ იქნა მოდიფიცირებული პოლიმერ-პრეკურსორული და თვითგანვითარებადი ჟანგვა-აღდგენითი რეაქცია. საწყის პრეკურსორებად გამოყენებულ იქნა ალუმინის ნიტრატი, ალუმინის ალკოქსიდები, დამჟანგველები და ორგანულ-არაორგანული გელების წარმომქნელი ფუნქციონალური ნაერთები (გლიკოლები, ამინოსპირტები, კარბოქსიმჟავები, ამინომჟავები, ბიოპოლიმერები და სხვ). ორგანულ-არაორგანული გელები მიღებულია ალუმინისა და ორგანული ნაერთების ჰომოგენიზაციით $80 - 200\text{ }^\circ\text{C}$ -ზე და მიღებული მასის კარბონიზაციით სხვადასხვა ტემპერატურულ რეჟიმით $300 - 800\text{ }^\circ\text{C}$ -ზე. კარბონიზაციის შედეგად მიიღება შავი ფხვნილი, რომელიც ძირითადად $\gamma\text{-Al}_2\text{O}_3$ -საგან შედგება. მისი გადაყვანა $\alpha\text{-Al}_2\text{O}_3$ -ში განხორციელდა ჰაერზე $1180 - 1200\text{ }^\circ\text{C}$ -ზე 2 სა-ის განმავლობაში. საწყის სარეაქციო ნარევი 3 - 5 მას. % ალფა-მოდიფიკაციის ალუმინის ოქსიდის დამატებით $\gamma \rightarrow \alpha$ ფაზური გადასვლის ტემპერატურა მცირდება $1020 - 1080\text{ }^\circ\text{C}$ -მდე. $\alpha\text{-Al}_2\text{O}_3$ მიღების ერთ-ერთი მარტივი მეთოდია რეაქცია ალუმინის ნიტრატს (დამჟანგველი) და ორგანულ ნაერთებს (აღმდგენელი) შორის, რომელიც ხორციელდება დაბალ ტემპერატურაზე ($400 - 500\text{ }^\circ\text{C}$). აღმდგენლებად გამოყენებულია მჟავები, ამინომჟავები, სპირტები, პოლიმერები და სხვ. $\alpha\text{-Al}_2\text{O}_3$ მისაღებად ხშირად გამოყენებული ალუმინის ნიტრატსა და შარდოვანას ურთიერთქმედება, რომელიც აღიწერება განტოლებით:

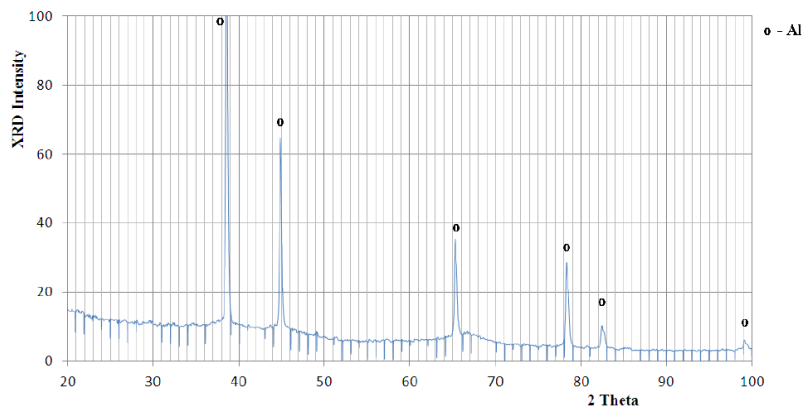


რეაქცია იწყება $500\text{ }^\circ\text{C}$, არის ეგზოთერმული, რის შედეგადაც სარეაქციო არე ცხელდება $\sim 1500\text{ }^\circ\text{C}$ -მდე. მიიღება $\alpha\text{-Al}_2\text{O}_3$, რომლის დიფრაქტოგრამა მოცემულია **ნახაზზე 2**. სარეაქციო არის ტემპერატურა იცვლება დამჟანგველ / აღმდგენელის თანაფარდობის მიხედვით. ზემოთ აღნიშნული განტოლება სრულად არ ასახავს მიმდინარე პროცესებს, რადგან რეაქციისას ადგილი აქვს აზოტის ოქსიდების გამოყოფასაც, ვინაიდან ალუმინის ნიტრატი იშლება ადრე ($< 200\text{ }^\circ\text{C}$ -ზე) ვიდრე ტემპერატურა $\sim 500\text{ }^\circ\text{C}$ -ს მიაღწევს. ამიტომ გამოყოფილი გაზები შეიცავენ NO_2 და O_2 .

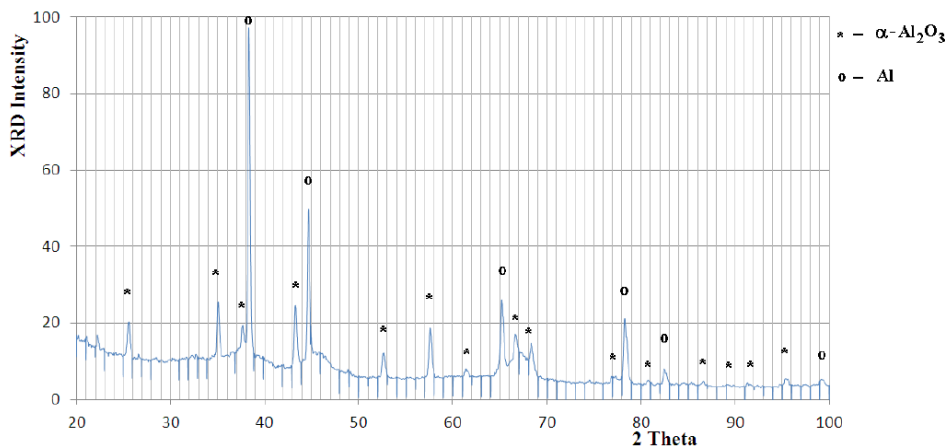


ნახაზი 2. ალუმინის ნიტრატისა და შარდოვანას ურთიერთქმედებით მიღებული $\alpha\text{-Al}_2\text{O}_3$ -ის დიფრაქტოგრამა. რეაქციის ინიცირების ტემპერატურაა $500\text{ }^\circ\text{C}$.

ჩვენს მიერ შესწავლილ იქნა $\text{Al}(\text{NO}_3)_3\text{-NH}_2\text{CONH}_2\text{-Al}$ სისტემისაგან $\alpha\text{-Al}_2\text{O}_3$ -ის მიღების შესაძლებლობა. ალუმინის შეტანა მიზნად ისახავდა ალუმინის ოქსიდის რაოდენობის გაზრდას, რადგანაც $2\text{Al}(\text{NO}_3)_3 \cdot 9\text{H}_2\text{O} + 5\text{NH}_2\text{CONH}_2$ ნარევის დაწვით მიიღებული Al_2O_3 რაოდენობა სარეაქციო მასის მხოლოდ ~ 10 მას. %-ს შეადგენს. რენტგენოგრაფიული ანალიზით დადგენილია, რომ რეაქციის დროს ტემპერატურა ~ 1500 °C-ს აღწევს და მიუხედავად ამისა, ალუმინის ფხვნილი (5 – 75 მკმ) არ იჟანგება, $\alpha\text{-Al}_2\text{O}_3$ -ის მაგივრად წარმოიქმნება ამორფული Al_2O_3 (ნახაზი 3). დარჩენილი რეაქციის პროდუქტის $\text{Al} + \text{Al}_2\text{O}_3$ გახურებით (2 სთ) $\sim 750 - 800$ °C-ზე წარმოქმნება $\alpha\text{-Al}_2\text{O}_3$. ეს ეფექტი აიხსნება იმით, რომ სარეაქციო ნარევი $100 - 200$ °C-ზე წარმოქმნის ბლანტ მასას, რომელიც გარსს ეკვრება ალუმინის ფხვნილის ნაწილაკებს და ხელს უშლის ჟანგბადის დიფუზიას ალუმინის ზედაპირისკენ, მეორეს მხრივ, რეაქციის პროცესში გამოიყოფა დიდი რაოდენობით გაზობრივი ნივთიერებები, რომლებიც ამცირებენ ატმოსფერული ჟანგბადის კონცენტრაციას სარეაქციო არეში. ამავე დროს, რეაქციის სიჩქარე საკმაოდ მაღალია: რეაქციის ფრონტის გავრცელების სიჩქარე 2 – 4 სმ / წმ-ია. ამრიგად სარეაქციო ნარევი 10 %-მდე მეტალური ალუმინის შეტანით ადგილი აქვს $\alpha\text{-Al}_2\text{O}_3$ -ის წარმოქმნის ინჰიბირებას: ის წარმოიქმნება რეაქციის პროდუქტის შედარებით ხანგრძლივი გახურებით ~ 800 °C-ზე (ნახაზი 4). რენტგენოგრაფიული და ქიმიური ანალიზით დადგენილია, რომ მეტალური ალუმინი ამ პირობებში არ იჟანგება, რადგან ნაწილაკების ზედაპირი დაფარულია რეაქციის შედეგად წარმოქმნილი ალუმინის ოქსიდის სქელი ფენით.



ნახაზი 3. ალუმინის ნიტრატი–შარდოვანა–მეტალური ალუმინის ურთიერთქმედებით მიღებული მყარი ნაშთის დიფრაქტოგრამა. რეაქციის ინციტირების ტემპერატურა 500 °C.



ნახაზი 4. ალუმინის ნიტრატი–შარდოვანა–მეტალური ალუმინის ურთიერთქმედებით მიღებული მყარი ნაშთის 800 °C-ზე გამოწვის

შედეგად (2 სთ) მიღებული Al / α -Al₂O₃ კომპოზიტის დიფრაქტოგრამა.

γ - და α -Al₂O₃ ოქსიდების დაბალტემპერატურული სინთეზი განხორციელდა ნაწილობრივ ჰიდროლიზირებული ალუმინის იზოპროქსიდისა და ალუმინის ნიტრატის ნარევის სწრაფი გახურებით ~ 500 °C-ზე. ამ შემთხვევაში დამჟანგველს წარმოადგენს NO₃⁻ იონები, ხოლო აღმდგენელს – იზოპროპილის ჯგუფი (CH(CH₃)), რეაქცია ეგზოთერმულია და სარეაქციო ნარევის ტემპერატურა 800 – 1100 °C-ს აღწევს. რენტგენოფაზური ანალიზით დადგენილია, რომ მიღებული ფხვნილის პირველადი კრისტალიტების ზომა ~ 50 ნმ-ია. ნაწილაკების ზომა გაანგარიშებულ იქნა შერერის ფორმულის გამოყენებით:

$$\Delta(2\theta) = m \lambda / (D \cos \theta),$$

სადაც $\Delta(2\theta)$ არის ინტერფერენციული მაქსიმუმის ნახევარსიგანე (მაქსიმუმის სიგანე სიმალის ნახევარზე) რადიანებში, m – კრისტალის ფორმის ფაქტორი, λ – ტალღის სიგრძე (ნმ), D – მარცვლისზომა (ნმ), ხოლო θ – ბრევისკუთხე (შერერის ფორმულის გამოყენება შესაძლებელია, როცა კრისტალიტების ზომა არ აღემატება ~ 150 ნმ-ს).

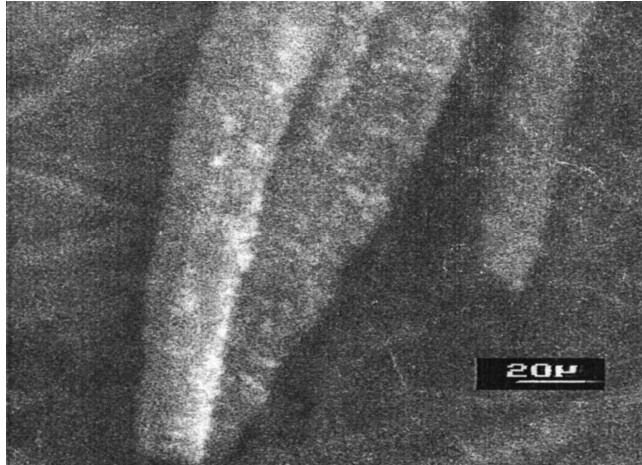
რეაქციის პროდუქტი ფირფიტებია, რომელთა სიგრძე 8 – 15 მკმ-ია. ისინი ადვილად ქუცმაცდებიან ნანოზომის ნაწილაკების წარმოქმნით. მათი ნაყარის სიმკვრივე 30 – 70 მგ / მლ-ს აღწევს. ზემოთ აღწერილი და ალუმინის მარილებიდან დალექვის მეთოდით მიღებული Al₂O₃ ფხვნილის ერთი და იგივე მასის მოცულობები შედარებულია **ნახაზზე 5**.



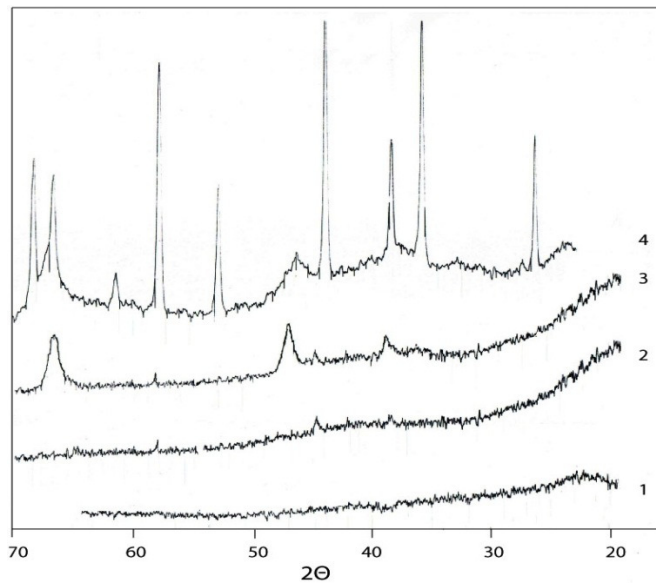
ნახაზი 5. I – თვითგავრცელებადი ჟანგვა-აღდგენის რეაქციით მიღებული ულტრადისპერსული ალუმინის ოქსიდი (მოცულობა – 700 მლ, მასა – 20 გ); II – დალექვის მეთოდით მიღებული ალუმინის ოქსიდი (მოცულობა – 13 მლ, მასა – 20 გ).

α -ალუმინის ოქსიდის ფხვნილის მისაღებად გამოყენებულ იქნა ვერცხლისწყლით გააქტივებული ალუმინის ფირფიტების კოროზიის მეთოდი. ცნობილია, რომ ამალგამირებული მეტალთა ზედაპირები ჰაერზე ადვილად იჟანგებიან შესაბამისი ოქსიდების ან ოქსოჰიდროქსიდების წარმოქმნით [31]. შესწავლილია ალუმინისაგან ნანოფაზური ოქსოჰიდროქსიდების ფხვნილების მიღების შესაძლებლობა დაბალტემპერატურაზე ~ 20 – 90 °C. დადგენილია, რომ ვერცხლისწყლის (I, II) ნაერთების (ქლორიდები, ნიტრატები, სულფატები) განზავებული ხსნარებით ალუმინის ფირფიტების დამუშავების შემდეგ მის ზედაპირზე იზრდება Al₂O₃ · n H₂O ბოჭკოები. მათი წარმოქმნის სიჩქარე დამოკიდებულია

ვერცხლისწყლის ნაერთის ბუნებაზე: ყველაზე მაღალი აქტივობა გამოამჟღავნეს HgCl_2 -ის ფუძეზე მიღებულმა სისტემებმა. 7 – 22 მკმ დიამეტრის ბოჭკოს ზრდის სიჩქარე 0.1 – 0.5 მმ / წთ-ს აღწევს. 5 – 20 მმ სიმაღლის ბოჭკოები იზრდება ფირფიტის პერპენდიკულარულად და იმეორებს გააქტივებული ალუმინის ზედაპირის ფორმას (ნახაზი 5). ბოჭკოს კონის ზრდის პროცესი დაიმზირებოდა ოპტიკური მიკროსკოპით.



ნახაზი 5. მეტალური ალუმინის ფირფიტაზე წარმოქმნილი $\text{Al}_2\text{O}_3 \cdot n\text{H}_2\text{O}$ -ის ბოჭკოების მიკროფოტოგრაფია.



ნახაზი 6. ამორფული $\text{Al}_2\text{O}_3 \cdot n\text{H}_2\text{O}$ -გან α -ალუმინის ოქსიდის მიღება. 1 – 25, 2 – 500, 3 – 800 და 4 – 1100 °C.

როგორც რენტგენოგრამებიდან ჩანს (ნახაზი 6), ოთახის ტემპერატურაზე გააქტივებული ალუმინისაგან მიიღება $\text{Al}_2\text{O}_3 \cdot n\text{H}_2\text{O}$ -ის ამორფული ფხვნილი, რომელიც მცირე რაოდენობით შეიცავს მეტალური ალუმინს (< მას. 2 %) (1). ამ ფხვნილებისაგან კრისტალური ფაზების წარმოქმნა იწყება 500 °C-დან (2, 3). მათი შემდგომი გახურებით (1000 – 1100 °C) მიიღება α - Al_2O_3 -ის ბოჭკოები (4). რენტგენოდიფრაქციული მეთოდით დადგენილია, რომ Al_2O_3 ბოჭკოები შედგება 10 – 30 ნმ-ის ზომის ნაწილაკებისაგან.

ფხვნილები და მისგან მიღებული კორუნდის ნაკეთობების მიკროსტრუქტურა შესწავლილია ოპტიკური და ელექტრონული მასკანირებელი მიკროსკოპებით (Nikon ECLIPSE LV 150, NMM-800TRF, Nanolab-7). მიკროსისალე განსაზღვრულია (DUH – 211S) ხელსაწყოზე. სინთეზირებული ფხვნილის მარცვლის ზომა დადგენილ იქნა (Analysette 12 Dyna Sizer) მეშვეობით. ნიმუშების ფაზური ანალიზი ჩატარდა რენტგენულ დიფრაქტომეტრზე DPOH-3M. თერმული ანალიზი (TG-DTG-DSC) ჩატარებულია ხელსაწყოზე Setsys Evolution (Setaram Tag 24).

მითითებები

1. A. I. Gusev, A. A. Rempel. *Nanocrystalline Materials*. 2004, Cambridge: Cambridge Int. Sci. Publ.
2. M. Niederberger, N. Pinna. *Metal Oxide Nanoparticles in Organic Oxide Solvents. Synthesis, Formation, Assembly, and Application*. 2009, Springer.
3. P. Thrower, T. W. Mason. *Materials in Today's World*. 2008, New York: Mc Graw-Hill.
4. T. Hanemann, D. V. Szabo. Polymer-nanoparticle composites: From synthesis to modern applications. *Mater.* 3 (2010) 3468-3517.
5. Ed. J. F. Gerard. *Fillers and Filled Polymers*, 169. 2001, Weinheim: Wiley-VCH.
6. V. V. Ivanov, A. S. Kaygorodov, V. R. Khrustov, S. N. Paranin. Fine grained alumina-based ceramics produced using magnetic pulsed compaction. In: *Ceramic Materials – Progress in Modern Ceramics*, 2012.
7. Kh. A. Khalil. *Advanced Sintering of Nano-Ceramic Materials*, 2012. <http://www.intechopen.com>.
8. A. Hasmaliza, M. A. Fakhru'l-Razi, A. B. Dayang Radiah, R. Aghababazadeh. Process for producing nano-alpha-alumina powder. *Nanotechnol.* 22 (2011) 692594 1-5.
9. V. Saraswati, G. V. N. Rao, G. V. Rama Rao. Structural evolution in alumina gel. *J. Mater. Sci.* 22 (1987) 2529-2535.
10. H. Hou, Y. Xie, Q. Yang, Q. Guo, C. Tan. Perapration and characterization of γ -ALOOH nanotubes and nanorods. *Nanotechnol.* 16 (2005) 714-721.
11. Y. Xia, Y. Yang, P. Sun, Y. Wu, B. Mayers, A. Gates, Y. Yin, F. Kim, H. Yan. One dimensional nanostructures: Synthesis, characterization, and applications. *Adv. Mater.* 15 (2003) 353-357.
12. G. L. Teoh, K. Y. Liew, W. A. K. Mahmood. Synthesis and characterization of sol-gel alumina nanofibers. *J. Sol-Gel Sci. & Technol.* 44 (2007) 177-180.
13. M. G. Ma, J. F. Zhu. A facile solvothermal route to synthesis of γ -alumina with bundlelike and flower-like morphologies. *Mater. Lett.* 63 (2009) 881-885.
14. K.-L. Huang, L.-G. Yin, S.-Q. Liu, Ch.-J. Li. Preparation and formation mechanism of Al_2O_3 nanoparticles by reverse microemulsion. *Trans. Nonferrous Met. Soc. China* 17 (2007) 633-637.
15. Q. Yang, Y. Deng, W. Hu. Synthesis of alumina nanofibers by a mercury-mediated method. *Ceram. Int.* 35 (2009) 531-537.
16. B. N. Sherikar, A. M. Umarji. Compaction behaviour of solution combustion synthesized alumina ceramic powders. *Int. J. Emerging Technol. & Adv. Eng.* 3 (2013) 1-5.

17. T. Shirai, H. Watanabe, M. Fuji, M. Takahashi. Structural properties and surface characteristics on aluminum oxide powders. *Mater. Chem. & Phys.* 103 (2007) 394-399.
18. S. Fujiwara, Y. Tamura, H. Maki, N. Azuma, Y. Takeuchi. Development of new high-purity alumina. *Sumitomo Kagaku*, 1 (2007).
19. Zibo Litu Aluminum Co., Ltd. Calcined alumina, alumina chemicals, 2011. [www.chinalet.com/page_en/article_disp.asp?id=83&sid=\(2011\)](http://www.chinalet.com/page_en/article_disp.asp?id=83&sid=(2011)).
20. S. Rajendran. Production of ultrafine alpha alumina powders and fabrication of fine grained strong ceramics. *J. Mater. Sci.* 29 (1994) 5664-5672.
21. S. Cava, S. M. Tebcherani, I. A. Souza, S. A. Pianaro, C. A. Paskocimas, E. Longo, J. A. Varela. Structural characterization of phase transition of Al_2O_3 nanopowders obtained by polymeric precursor method. *Mater. Chem. & Phys.* 103 (2007) 394-399.
22. X. Su, J. Li. Low. Temperature synthesis of single-crystal alpha alumina platelets by calcining bayerite and potassium sulfate. *J. Mater. Sci. & Technol.* 27 (2011) 1011-1015.
23. G.-F. Fu, J. Wang, J. Kang. Influence of AlF_3 and hydrothermal conditions on morphologies of α - Al_2O_3 . *Trans. Nonferrous Met. Soc. China* 18 (2008) 743-748.
24. A. Odaka, T. Yamaguchi, T. Fujita, S. Taruta, K. Kitajima. Densification of rare-earth (Lu, Gd, Nd)-doped alumina nanopowders obtained by a sol-gel route under seeding. *Powd. Technol.* 193 (2009) 26-31.
25. Y. Yoshizawa, K. Hirao, S. Kanzaki. Fabrication of low cost fine-grained alumina powders by seeding for high performance sintered bodies. *J. Eur. Ceram. Soc.* 33 (2013) 2365-2830.
26. R. L. Smith, G. S. Rohrer, A. J. Perrotta. The influence of diasporic seeding and chloride concentration on the transformation of "diasporic" precursors to corundum. *J. Am. Ceram. Soc.* 84 (2001) 1896-1902.
27. Y. Wang, C. Suryanarayana, L. An. Phase transformation in nanometer-sized α -alumina by mechanical milling. *J. Am. Ceram. Soc.* 88 (2005) 780-783.
28. A. Towata, H. J. Hwang, M. Yasuoka, M. Sando, K. Niihara. Fabrication of polycrystalline YAG / alumina composite fibers and YAG fibers, 2012. www.iccm-central.org/Proceedings/ICCM12proceedings/site/papers/pap1277.pdf.
29. S. M. Sabol. Development of a textured and tabular grain microstructure in alumina fibers via seeded sol-gel processing. Thesis in *Ceram. Sci.*, 1994.
30. I. J. Bae, O. C. Standard, G. J. Roger, D. Brazil. Phase and microstructural development in alumina sol-gel coatings on CoCr alloy. *J. Mater. Sci. Mater. Med.* 15 (2004) 959-966.
31. Q. Yang, Y. Deng, W. Hu. Synthesis of alumina nanofibers by a mercury-mediated method. *Ceram. Int.* 35 (2009) 531-537.

НОВЫЙ МЕХАНИЗМ ИНДЕНТИРОВАНИЯ МАТЕРИАЛОВ ПРИ НАНОМЕТРОВОМ И СУБМИКРОННОМ УРОВНЕ

А. Б. Герасимов¹, Г. Д. Чирадзе², Т. К. Ратиани¹, М. Т. Вепхвадзе¹

¹Грузинский технический университет
Тбилиси, Грузия

²Государственный университет А. Церетели
Кутаиси, Грузия
gogichiradze@yahoo.com

Принята 28 октября 2013 года

Определение механических свойств материалов на субмикронном и нанометровом уровнях прочно вошло в практику современных исследований. В частности, тонкие пленки (< 1 мкм) представляют собой подобный сложный объект при механических испытаниях. Для их механических испытаний необходимы такие методы, которые обладают высокой степенью локальности (особенно по глубине) [1]. При этом из-за малого размера отпечатков и значительного упругого восстановления в процессе снятия нагрузки, обычное испытание на твердость (с использованием нагрузок, вызывающих проникновение индентора в материал > 1 мкм и определение размеров отпечатков после снятия нагрузки) становится неприемлемым. Поэтому был реализован метод определения твердости, основанный на измерении и анализе зависимости нагрузки от глубины внедрения индентора при вдавливании в поверхность материала [1]. Во время такого испытания регистрируется перемещение индентора как при росте нагрузки (кривая нагружения), так и при его снижении (кривая разгрузки) [1].

На кривой нагружения наблюдались скачкообразные переходы (**рисунок 1**), что указывает на скачкообразное погружение индентора в материал под действием неизменной нагрузки. Несмотря на большой массив экспериментальных данных, накопленных к настоящему времени, полной ясности в природе этой зависимости до сих пор не было [2].

В данной работе предлагаются новые механизмы вышеуказанных явлений. Эти механизмы основаны на новых представлениях о роли химических связей в передвижении атомов (молекул) в конденсированных средах [3, 4], описанных в молекулярно-потенциальной теории [5]. Согласно этой теории, около данного атома может появиться флуктуация не только кинетической но и потенциальной энергии, что соответствует уменьшению высоты потенциального барьера, который должен преодолеть атом (молекула) [3 – 6], в результате уменьшается энергия химической связи данного атома с соседними.

Учитывая, что в конденсированных средах электроны, участвующие в образовании химической связи, могут находиться в двух разных квантовых состояниях – находясь в одном они увеличивают энергию химической связи (связывающие состояния), в другом уменьшают (антисвязывающие состояния) [7] – уменьшение энергии химической связи

происходит за счет появления около данного атома антисвязывающих квазичастиц (АКЧ), т.е. свободных электронов или дырок. В соответствии с теорией молекулярных орбиталей химической связи, распространенной на твердые тела и жидкости [7], энергетический спектр электронов состоит из связывающих и антисвязывающих зон (рисунок 2). В полупроводниках эти зоны разделены запрещенной зоной, в металлах они перекрыты. Нахождение электрона в связывающей зоне усиливает, а его отсутствие (дырка) ослабляет химическую связь. Сила химической связи данного атома (молекулы) с соседними определяется разностью чисел связывающих и антисвязывающих электронов, находящихся около него. Чем меньше эта разность, тем слабее химическая связь, а при равенстве разности нулю химическая связь исчезает (сублимация, испарение, кипение) [4 – 6].

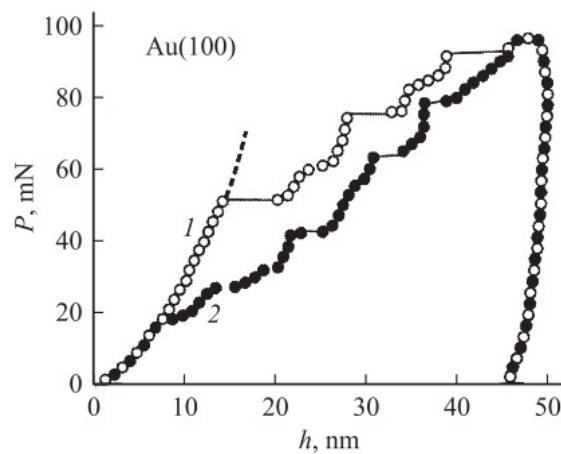


Рисунок 1. Диаграмма $P-h$ (P – нагрузка на индентор, h – глубина проникновения индентора). Монокристаллическое золото: 1 – атомно-гладкая поверхность и 2 – поверхность с ступеньками 2 нм [2].

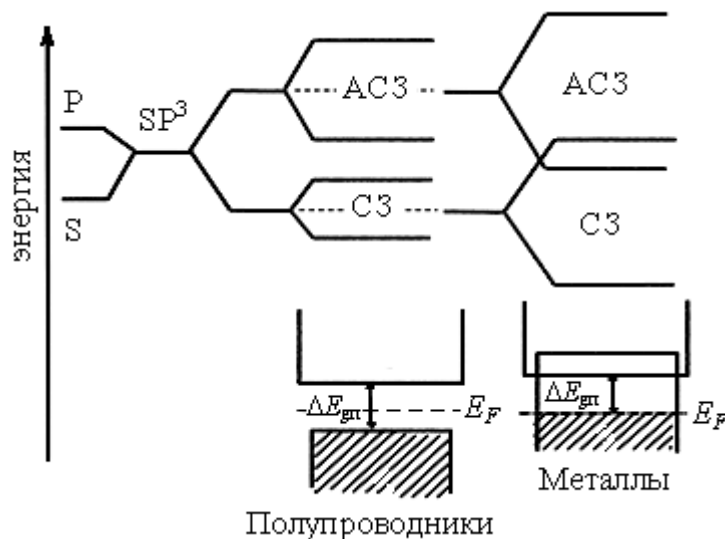


Рисунок 2. Возникновение гибридных sp^3 -орбиталей, их расщепление на связывающие и антисвязывающие орбитали и, при сближении атомов, возникновение из них соответственно связывающих (СЗ) и антисвязывающих (АСЗ) зон. ΔE_g – ширина запрещенной зоны в полупроводниках, ΔE_{gp} – псевдозапрещенная зона в металлах, E_F – уровень Ферми.

Таким образом, перевод электрона из связывающей зоны в антисвязывающую зону (в металлах переходы осуществляются между уровнем Ферми и дном антисвязывающей зоны – это энергетическое расстояние называется псевдозапрещенной зоной – см. **рисунок 2**), означает ослабление химической связи в данном веществе (т.е. если это твердое тело, то оно должно стать более мягким).

Перевод электронов можно осуществить разным способом. В любом случае передвижение атома будет облегчено. При своем хаотическом движении электрон и дырка могут оказаться около определенного атома с вероятностью n/N_a (n – концентрация АКЧ, N_a – концентрация атомов вещества) в разном β количестве (флуктуация потенциальной энергии) с вероятностью $(n/N_a)^\beta$ и по-разному ослабить химическую связь. Чем больше будет концентрация АКЧ при данной температуре, тем больше вероятность передвижения атомов и тем интенсивнее будет протекать наблюдаемый процесс, а при достижении критической концентрации АКЧ $n_k = (m^*/M_a)^{1/2}$ (m^* – эффективная масса свободного электрона, M_a – масса атома (молекулы) вещества) начинается процесс плавления независимо от того, каким способом созданы АКЧ [4 – 6].

При контакте индентора с поверхностью исследуемого образца возникают давления достаточно высоких значений, которые меняют энергетический спектр электронов, участвовавших в создании химических связей, что выражается в изменении энергетического взаиморасположения энергетических зон [8 – 10]. В разных кристаллографических направлениях зоны сдвигаются по-разному, но в каком-то направлении связывающая и антисвязывающая зоны всегда приближаются друг к другу и концентрация АКЧ при неизменной температуре возрастает. В области контакта индентора с образцом происходит локальное уменьшение расстояния между зонами [8] и увеличение концентрации АКЧ, что вначале облегчает передвижение атомов (молекул), т.е. образование точечных дефектов, а при достижении критической концентрации АКЧ происходит локальное плавление, что ведет к скачкообразному увеличению глубины внедрения индентора, под действием неизменной нагрузки. Это, естественно, увеличивает контактную площадь. В результате уменьшается давление, концентрация АКЧ и процесс плавления прекращается. Поэтому далее для увеличения глубины внедрения индентора необходим рост нагрузки (**рисунок 1**). При дальнейшем росте нагрузки может осуществиться вышеописанная ситуация и произойдет новое скачкообразное увеличение глубины внедрения индентора (**рисунок 1**) и так далее. Ясно, что величины нагрузки, при которых осуществляются скачкообразные увеличения глубины внедрения индентора, будут зависеть от природы и обработки материала, геометрии наконечника индентора, скорости нагружения и температуры проведения опыта, которые будут влиять на процесс образования АКЧ. С повышением температуры в достижении критической концентрации АКЧ внесут свой вклад и термические переходы электронов. Поэтому скачкообразное увеличение глубины внедрения индентора будет происходить при меньших нагрузках, что и наблюдается на эксперименте (**рисунок 3**) [2]. При увеличении скорости нагружения не успевает установиться равновесная критическая концентрация АКЧ, для достижения которой уже требуется увеличение нагрузки, что тоже наблюдается на опыте [2].

В пользу механизма скачкообразного увеличения глубины внедрения индентора под действием неизменной нагрузки за счет локального плавления говорят экспериментальные данные о триксоотропном эффекте – появление в кристалле на

границе внедрения индентора бугорков аморфного вещества, по своей структуре, очень похожего на застывшее после плавления материал [11, 12].

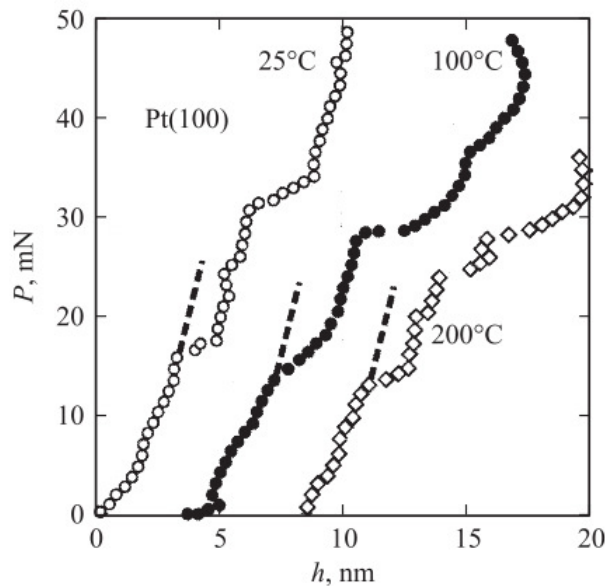


Рисунок 3. Температурная зависимость диаграммы $P-h$ (P – нагрузка на индентор, h – глубина проникновения индентора) для платины [2].

Для объяснения зависимости твердости от глубины индентирования рассмотрим как меняется сила химических связей в направлении от поверхности в объем. Крайние атомы на поверхности имеют ненасыщенные химические связи – лишние электроны, которые замыкаются на соседние боковые атомы. Происходит явление типа димеризации [13]. Эта избыточная плотность отрицательного заряда перетекает на химические связи атомов, расположенных в глубь от поверхности (**рисунок 4**), уменьшаясь с глубиной тем быстрее, чем меньше диэлектрическая проницаемость вещества [14].

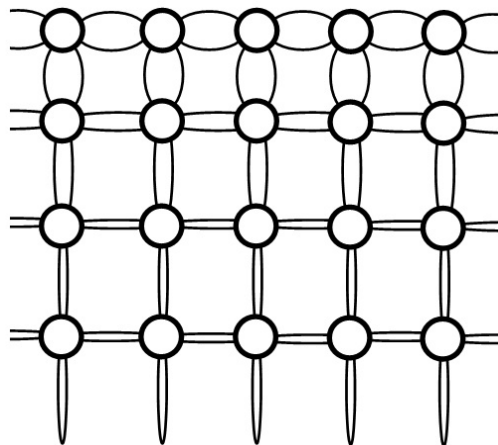


Рисунок 4. Схематическое изображение распределения избыточной плотности отрицательного заряда на химические связи атомов, расположенных в глубь от поверхности.

Таким образом, увеличение у поверхности плотности отрицательного заряда увеличивает силу химической связи и, следовательно, твердость, что и наблюдается на эксперименте (**рисунок 5**) [15].

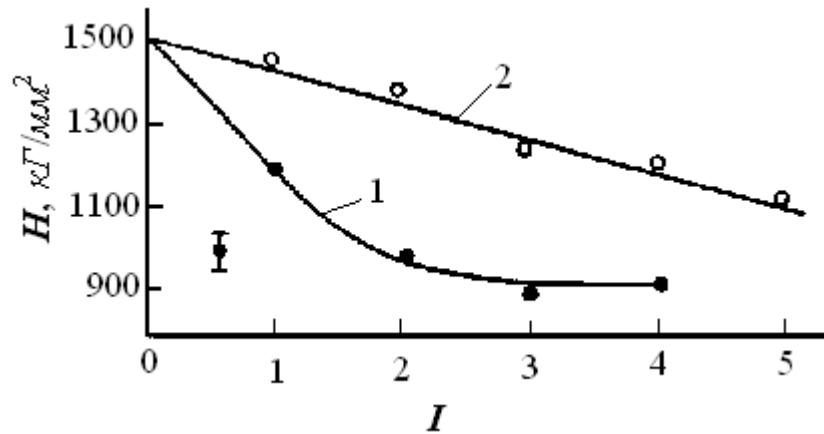


Рисунок 5. Зависимость микротвердости (H) кремния от интенсивности освещения, при воздействии квантами света: 1 – $h\nu > \Delta E_g$ и 2 – $h\nu < \Delta E_g$, (0 соответствует темноте, I – интенсивность в условных единицах источников света, а ΔE_g – ширина запрещенной зоны кремния).

В доказательство этого механизма, если на поверхности, каким-либо способом, увеличить концентрацию АКЧ и тем самым уменьшить силу химических связей, так что на поверхности образца концентрация АКЧ было бы максимальным и оно спадало-бы в глубь обраца, то твёрдость на поверхности должна быть меньше, чем в глубине. Нами был проведен такой эксперимент [15], результаты которого приведены на **рисунке 5**.

Поверхность исследуемого образца в процессе индентирования освещалась в одном случае сильно поглощаемым монохроматическим светом, а в другом – белым светом, проникающим на значительную глубину. Как видно из рисунка, в первом случае твердость на поверхности, где концентрация АКЧ максимальна, меньше чем в глубине, где АКЧ не генерируются светом. Зависимость увеличения твердости в глубь от поверхности совпадает с зависимостью уменьшения концентрации АКЧ, генерируемых светом. Во втором случае свет, проникая на всю исследуемую глубину образца, достаточно однородно генерирует АКЧ и уменьшение твердости происходит почти одинаково на всю исследуемую глубину образца. Эти данные, по нашему мнению, однозначно доказывает правоту предложенного механизма.

Ссылки

1. С. Н. Дуб. В сб.: Докл. 15-го Междунар. симп. "Тонкие пленки в электронике". 2003, Харьков: Изд. НИЦ ХТИ, 343.
2. Ю. И. Головин. ФТТ, 2008, 50, 2113.
3. А. Б. Герасимов. Основы низкотемпературной технологии создания полупроводниковых приборов. 2005, Тбилиси: Изд. ТГУ.
4. А. В. Gerasimov. In: Proc. 4th Int. Conf. Mater. Sci. Forum, 1990, 65-66, 47.
5. А. Б. Герасимов. В сб.: Междунар. конф. «Нанотехнологии» (Содержания). 2012, Тбилиси: Некери, 160.
6. Я. И. Френкель. Кинетическая теория жидкостей. 1975, Ленинград: Наука.

7. У. Харрисон. Электронная структура и свойства твердых тел: Физика химической связи, 1. 1983. Москва: Мир.
8. А. Л. Полякова. ФТТ, 1967, 9, 1164.
9. А. Л. Полякова. Акуст. журн., 1972, 18, 1.
10. Э. Г. Меликян, Ф. В. Арутюнян, М. Г. Акопян. ФТП, 1973, 7, 855.
11. Ю. И. Головин, А. И. Тюрин. ФТТ, 1995, 37, 5, 1562.
12. O. R. Fuente, J. A. Zimmerman, M. A. Gonzalez-Figuera, J. C. Hamilnon, J. M. Rojo. Phys. Rev. Lett., 2002, 88, 036101.
13. Ф. Бехштедт, Р. Эндерлайн. Поверхности и границы раздела полупроводников. 1990, Москва: Мир.
14. А. Милнс. Примеси с глубокими уровнями в полупроводниках. 1977, Москва: Мир.
15. А. Б. Герасимов, Г. Д. Чирадзе, Н. Г. Кутивадзе. ФТП, 2001, 35, 1, 70.

THE BEGINNINGS OF THE ALUMINUM INDUSTRY

F. Habashi

Laval University
Québec City, Canada
Fathi.Habashi@arul.ulaval.ca

Accepted December 24, 2012

Introduction

When Alessandro Volta in northern Italy discovered in 1800 that an electric current was generated when two metals were separated by an electrolyte, chemists in Europe immediately started to study this new phenomenon and tried to make use of it. Napoleon Bonaparte as First Consul invited Volta to Paris in 1801 to demonstrate to him at the French National Institute (the body that replaced the French Academy during the revolutionary period), the principle of his discovery. Napoleon was impressed by the demonstration. He gave Volta the Gold Medal of the Institute and ordered funds to the École Polytechnique to build a large battery for research.

The news of Volta's discovery reached England rapidly and a very large battery similar to the one constructed in Paris was built at the newly founded Royal Institution in London. Humphry Davy (1778 – 1829) at the Royal Institution succeeded in 1807 to isolate potassium and few days later, sodium using this battery. Once these two reactive metals were available they became the focus of intensive study. Their vigorous reaction with water and their spontaneous burning in air was very impressive. In 1808, Davy announced further his belief that the plentiful compound alumina was the earth (oxide) of an undiscovered metal. Since then, scientists had been making efforts to obtain this new metal. The naturally-occurring alum-stone used by alchemists to enhance the dyeing of textile fibers, was known to yield a white "earth" when heated at high temperature. This white earth was known as alumina and was an exceptionally stable material that it was considered a chemical element.

A discovery in Copenhagen

Davy never made any aluminum himself. It was the Danish scientist Hans Christian Oersted (1777 – 1851) (**Figure 1**) who succeeded in the early 1820s in producing a tiny sample of the metal in the laboratory by reducing the aluminum chloride with potassium amalgam. He had prepared aluminum chloride few years earlier for the first time by heating a mixture of alumina and charcoal in a stream of chlorine. Chlorine at that time was a laboratory curiosity isolated few years earlier by Carl Wilhelm Scheele.



Figure 1. Hans Christian Oersted
(1777 – 1851).



Figure 2. Friedrich Wöhler
(1800 – 1882).

Friedrich Wöhler (1800 – 1882) (**Figure 2**) on his return trip from Stockholm after finishing his studies there with Jöns Jacob Berzelius, stopped in Copenhagen in 1824 to visit the University. He met Oersted there and learned about his experiments to isolate aluminum. Now in his laboratory in Berlin he repeated successfully Oersted's experiment in 1827. In 1836 he moved to Göttingen to accept a professorship position at the University and in 1845 succeeded in making aluminum in slightly larger amounts from which he was able to show that aluminum was a light metal. Wöhler devoted his work later to organic chemistry and became known for his synthesis of urea from ammonium cyanate, a reaction that defeated the concept of “vital force”, that organic compounds could be produced only by living organism.

Aluminum production in France

French chemists were also active in research to produce aluminum. Henri Sainte–Claire Deville (1818 – 1881) (**Figure 3**) professor of chemistry at the École Normale in Paris produced aluminum in 1854 by electrolyzing molten aluminum chloride–sodium chloride mixture. However, this route was abandoned because, at that time, electric current needed for electrolysis was obtained only from batteries, which were tedious to construct, to operate, and to maintain. In addition, there was no material of a construction available that could withstand the molten chloride without being attacked. He, therefore, considered the chemical method devised by Oersted and Wöhler.



Figure 3. Henri Sainte–Claire Deville
(1818 – 1881).



Figure 4. Emperor Napoleon III
(1808 – 1873).

In 1854, he was able to prepare a small bar of the metal to show at the meeting of the French Academy of Sciences and at the Paris Exposition in 1855 under the title “The Silver of Clay” which attracted great attention. His friend the great chemist Jean–Baptiste Dumas got an audience with Emperor Napoleon III (**Figure 4**) and convinced him to subsidize the researches on aluminum.

Commercialization

Deville then went ahead to commercialize the process in a small plant at the Glacière District of Paris. He replaced potassium by sodium because he thought that sodium was easier to prepare by reduction of the carbonate with coal at high temperatures since there were no explosions associated with the reaction as was the case with potassium. This change resulted in a major improvement. He discovered that the reaction product, sodium chloride, formed a readily fusible double salt with excess aluminum chloride that acted as a protective layer allowing the globules of aluminum to coalesce, forming large lumps of the metal, which was not the case with Wöhler’s method.

Sainte–Claire Deville was interested more in the scientific aspects of the extraction of the metal than its commercial production. He, therefore, suggested to his friend Paul Morin, a mining engineer, to undertake the industrialization of the project. In 1856, Morin founded Paul Morin & Company to produce and market the new metal in the Glacière district of Paris. However, the inhabitants of the neighbourhood protested against the emissions from the plant which originated mainly from the production of alumina by thermal decomposition of alum. Morin had to move his factory to Nanterre, outside of Paris.

Sainte–Claire Deville was also looking for a substitute for alum. In the summer of 1856, he went to Greenland to evaluate the cryolite deposits there. He discovered that the deposit was of limited size and rightly considered that the French bauxite would be a more suitable raw material for an expanding aluminum industry. Sainte–Claire Deville proposed to his friend Louis Le Chatelier (1815 – 1873) (**Figure 5**) the Chief Inspector of Mines, to devise a method for producing alumina from bauxite, which he did in 1858 (**Figure 6**). In 1859, the Nanterre plant produced 500 kg of aluminum using Le Chatelier’s alumina. That same year, Sainte – Claire Deville wrote of his experiences in a book he published under the title *De l’aluminium, ses propriétés, sa fabrication, ses applications*. However, the price of the metal was quite high, nearly as high as silver; it sold for \$ 12 / pound while silver sold for \$ 15 / pound.

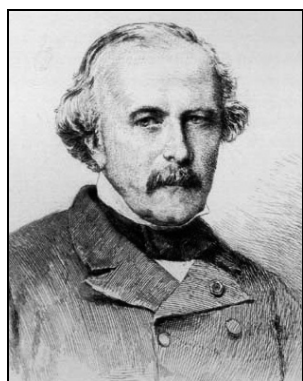


Figure 5. Louis Le Chatelier (1815 – 1873).

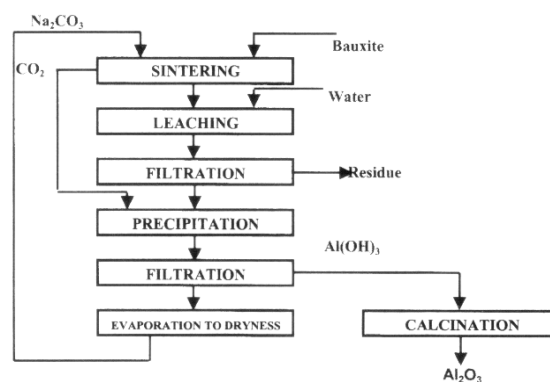


Figure 6. Le Chatelier process for the production of alumina from bauxite.

Salindres operations

Negotiations commenced with Henry Merle (1825 – 1877) (**Figure 7**) in Salindres in Southern France (Figure 8) who was near the bauxite deposits and who was, at that time, the major producer of inorganic chemicals in France, which included sodium carbonate needed for Le Chatelier's process to produce alumina. Dumas, who was on the Board of Directors of this company, welcomed the idea that the metal be produced in Salindre and that Paul Morin & Company would take charge of its marketing. Between 1860 and 1885, Merle was the only producer of aluminum in the world. When he died suddenly in 1877 at the age of 52, he was replaced by Alfred Pechiney (1833 – 1916) (**Figure 9**) whose name was given to the company in 1971 when it fused with other companies.

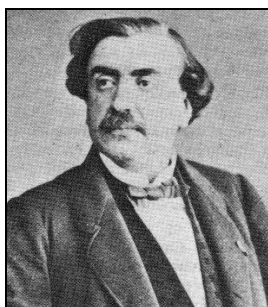


Figure 7. Henry Merle (1825 – 1877).



Figure 8. Location of Salindres in southern France.



Figure 9. Alfred Pechiney (1833 – 1916).

The process at Salindres involved the following steps:

- Preparation of alumina from bauxite by Le Chatelier's process;
- Production of aluminum chloride by reaction of chlorine with aluminum oxide and carbon (**Figure 10**);
- Production of metallic sodium by heating a mixture of calcined sodium carbonate, limestone, and coal in a retort (**Figure 11**);
- Production of metallic aluminum by reacting the double chloride with metallic sodium in a reverberatory furnace (**Figure 12**).

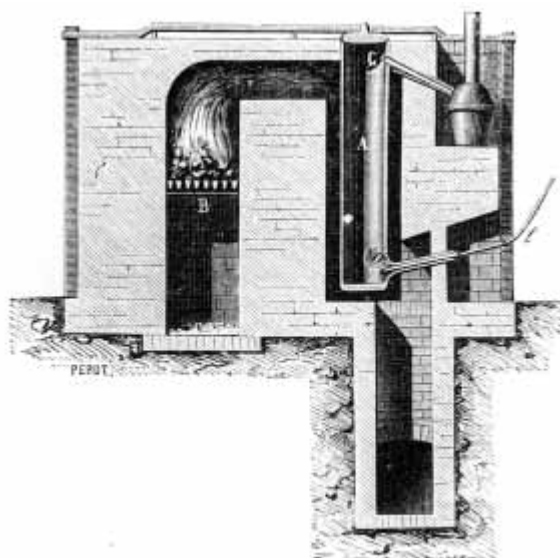


Figure 10. Production of aluminum chloride by chlorination of alumina.

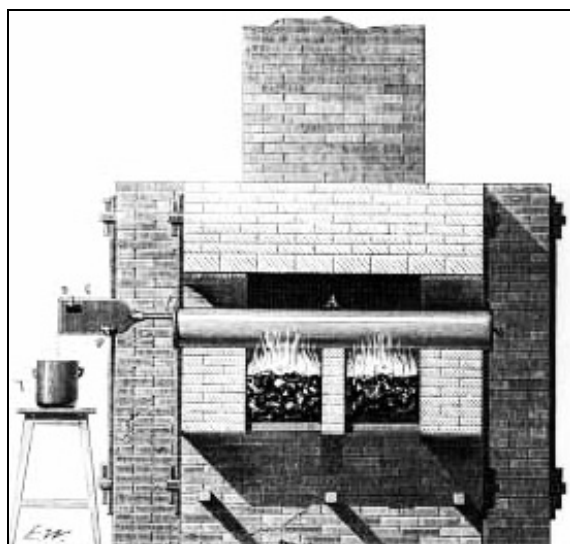


Figure 11. Production of metallic sodium.

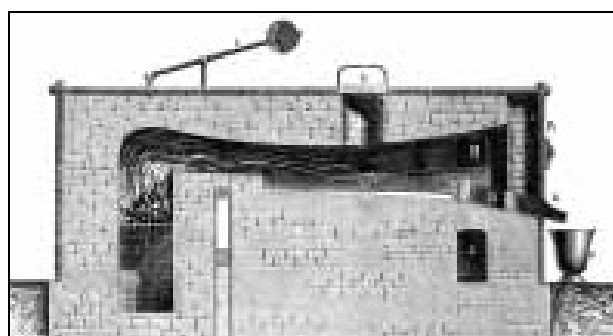


Figure 12. Reverberatory furnace for production of metallic aluminum.

It became evident that this chemical route was very expensive, not only due to the numerous steps involved, but also the large amount of sodium needed at least 2.6 kg to produce 1 kg of aluminum. Means to reduce the cost of production needed to be found.

Production of sodium

The production of sodium was a major cost item. The process used by Sainte–Claire Deville was very inefficient since only one third of the theoretical yield was obtained. In 1886, Hamilton Y. Castner (1859 – 1899) (**Figure 13**), a young graduate of Columbia University in New York, produced sodium by reduction of sodium hydroxide instead of sodium carbonate:



Figure 13. Hamilton Y. Castner (1859 – 1899).

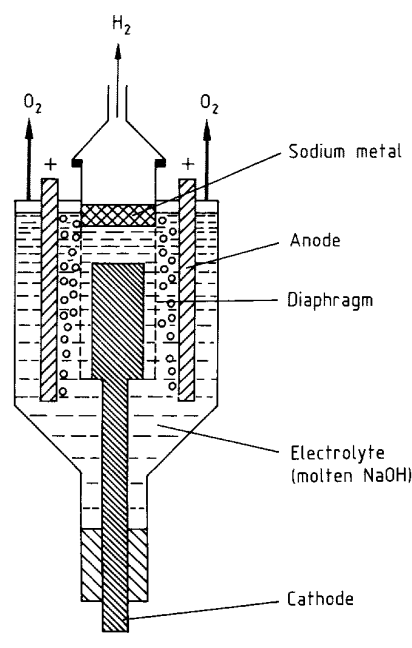


Figure 14. Castner's process for the electrolysis of molten NaOH for production of sodium.

The cost of production was reduced but not by enough. In 1891, he proposed the electrolysis of molten NaOH in a specially designed cell (**Figure 14**). The process was efficient and a pure product was obtained. Although the price of sodium produced by this method was less than that produced by Sainte–Claire Deville, it was still too high because NaOH must first be produced from sodium carbonate by reaction with calcium hydroxide. The solution must then be concentrated by evaporation and then melted.

Aluminum in USA

Aluminum alloys

Aluminum alloys, especially an aluminum-copper alloy known as aluminum bronze which had the appearance of gold and was used in ornaments and in making tableware, were produced in 1884 by the Cowles brothers who set up electric furnaces in Cleveland, Ohio, and a few years later, in Stoke-on-Trent. Current was supplied from a dynamo. Bauxite, charcoal, and the metal-forming alloy were placed in the furnace. When the current was turned on, resistance to the passage of the current offered by the charge generated heat which affected reduction of the alumina by the carbon. The liberated aluminum immediately combined with the molten metal present to form an alloy. This collected at the bottom of the furnace and was tapped out at the end of the operation, which lasted for about one hour.

Copper was commonly used and alloys containing 15 % to 40 % aluminum were usually produced (**Figure 15**). If no metals were present, alumina, on reduction with carbon, yields the carbide, hence, production of aluminum by this reaction is not feasible. For many years, the aluminum alloys made by the Cowles brothers' process were sold at \$ 5 / pound of contained aluminum, a price much lower than pure aluminum.

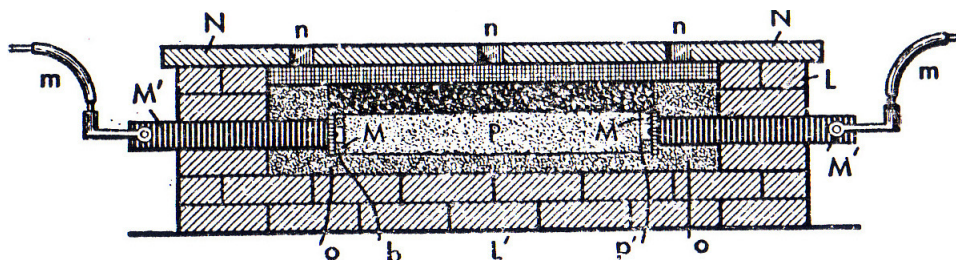


Figure 15. Cowles electric furnace for production of aluminum bronze.

A visitor from America

Frank Fanning Jewett (1844 – 1926) (**Figure 16**) who had received his undergraduate and graduate education in chemistry and mineralogy at Yale University spent two more years, 1873 to 1875, at the University of Göttingen with Wöhler. There he learned about the promise of the new metal. Jewett returned home to become an assistant at Harvard University. Soon he was nominated to teach at the Imperial University in Tokyo, Japan where from 1876 to 1880 he was one of the small groups of westerners who initiated the teaching of science at the university. In 1880, he became professor of chemistry and mineralogy at Oberlin College in Oberlin.



Figure 16. Frank Fanning Jewett
(1844 – 1926).

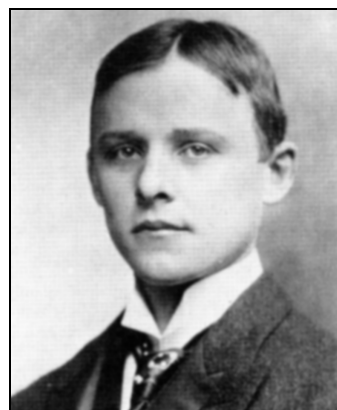


Figure 17. Charles Martin Hall
(1863 – 1914).

When Charles Martin Hall (1863 – 1914) (**Figure 17**) took his chemistry course at Oberlin, he heard Jewett lecture on aluminum, display his sample of the metal, and predict the fortune that awaited the person who could win this metal from its ore. Under Professor Jewett's guidance and encouragement, Hall worked on aluminum chemistry in Jewett's laboratory and at home until he succeeded in 1886 in producing the first ingot of aluminum by electrolyzing alumina dissolved in molten cryolite. **Figure 18** shows a pot line of early Hall cells in Pittsburgh in 1890.

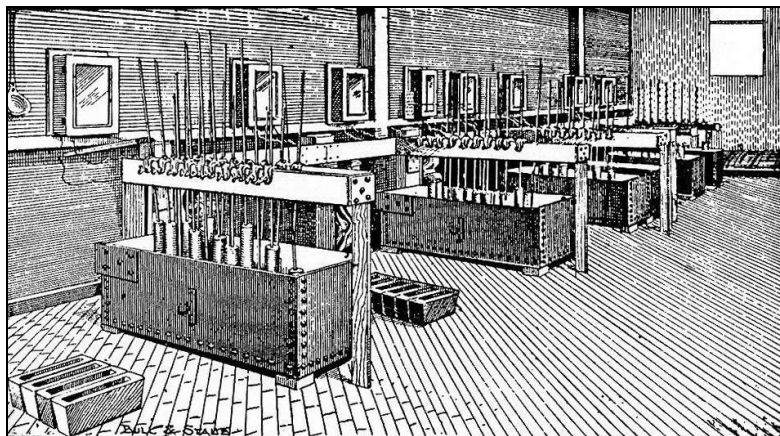


Figure 18. An early Hall cells in Pittsburgh in 1890.

The end of the chemical process

The same process was discovered simultaneously and independently by Paul Louis Heroult (1863 – 1914) (**Figure 19**) in France and is the same process used today. **Figure 20** shows Pot with six cylindrical anodes corresponding to the first type of pot installed by Hérault at the La Praz Plant in the district of Jura–Nord Vaudois in the canton of Vaud in Switzerland in 1893. The electrolytic process for the production of aluminum immediately displaced Sainte–Claire Deville’s process.



Figure 19. Paul Louis Hérault (1863 – 1914).

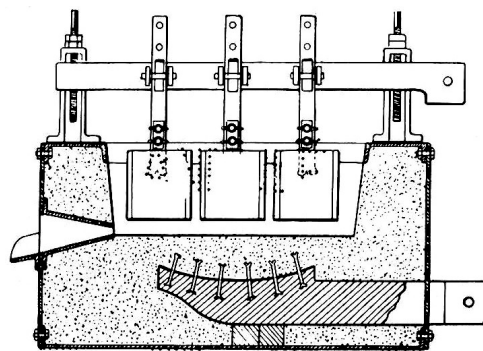


Figure 20. An early Hérault cell.

Production of alumina

Bayer process

Le Chatelier process did not survive for long time once Karl Josef Bayer (1847 – 1904) (**Figure 21**) invented a new hydrometallurgical process for producing alumina from bauxite (**Figures 22 and 23**). Bayer’s invention took place in two steps. In the first process invented in 1888 he used finely divided aluminum hydroxide as nuclei on which the hydroxide precipitates instead of using CO₂ gas. Later, in 1892 he used pressure leaching of bauxite with NaOH instead of sintering with sodium carbonate. This is now the process used world wide.

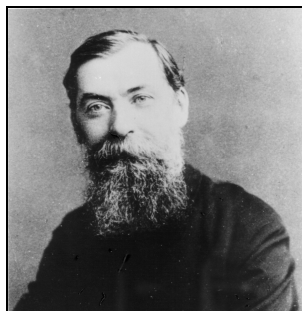


Figure 21. Karl Josef Bayer (1847 – 1904).

A problem of Bayer's process is the disposal of the leach residue known as red mud because of its color. For each ton of Al_2O_3 , about one ton of red mud is produced. Taking into consideration the large tonnage of bauxite processed, the amount of red mud produced annually worldwide is about 40 million tons. These are usually disposed of in ponds or in the sea.

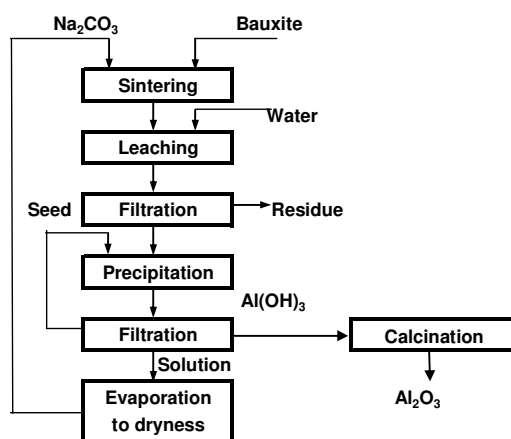


Figure 22. Bayer process 1888.

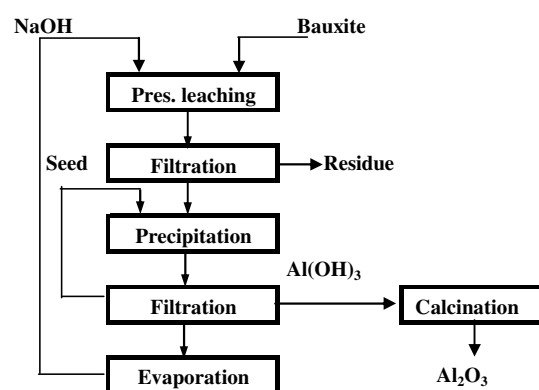


Figure 23. Bayer process 1892.

A new importance was given to the Bayer process when gallium was needed by the semiconducting industry and its recovery from process solution became desirable. Gallium was first discovered in zinc blend in 1875 and its first production was from this source. However, when it was discovered in bauxite in 1896 by the Irish chemist Walter N. Hartley (1846 – 1913) and Hugh Ramage (1865 – 1938), this new source became the major supplier although its average concentration is only less than 0.01 %. Alusuisse, a major aluminum manufacturer in Switzerland, commenced industrial production of gallium from bauxite in 1955. Gallium follows aluminum in the Bayer process and is recovered from the aluminate solution. The present world production of gallium is about 50 tons / year.

Alumina from cryolite

Before the utilization of bauxite for alumina manufacture, cryolite (Na_3AlF_6), which was discovered in Ivigtut, in south Greenland, by a Danish whaler who brought a piece of it to Copenhagen, was used. In 1854, one year before Le Chatelier invented his process, a process was developed by Julius Thomsen (1826 – 1909) (Figure 24), a professor at the Technical

The beginnings of the aluminum industry.

University of Copenhagen, which involved heating the cryolite with limestone, followed by water leaching, to extract sodium aluminate formed, leaving behind CaF_2 in the residue. Aluminum hydroxide was then precipitated from the aluminate solution by CO_2 leaving sodium carbonate in solution to be recovered as a by-product (Figure 25).



Figure 24. Julius Thomsen (1826 – 1909).

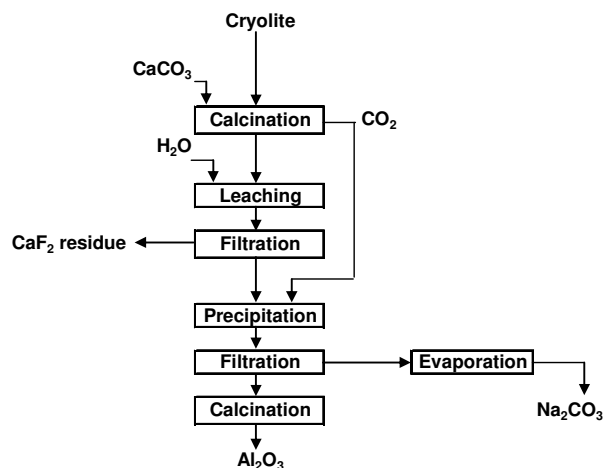


Figure 25. Thomsen process for the recovery of alumina from cryolite.

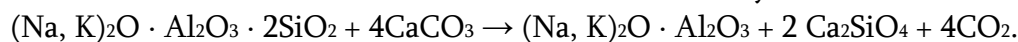
By the early 1860s, a large-scale soda and alumina production based on cryolite was in operation and was one of the largest industries in Denmark. The process was also implemented in other nearby countries as well as in the United States at the Pennsylvania Salt Company in Natrona, near Pittsburgh. However, in 1894 soda production from cryolite ceased in Copenhagen due to competition with the new Solvay process. In 1897, about 13 000 tons of the mineral were mined, the major part of which was delivered to the Pennsylvania company, but three years later, the process was also abandoned in the United States.

Thomsen is best known for developing the principle that the heat of formation is a measure of chemical affinity, and for a four-volume work, *Thermochemische Untersuchungen* he published between 1882 and 1886. Later, cryolite played an important role in the Hall–Héroult process when it was discovered by German chemist Martin Kiliiani (1858 – 1895) that a cryolite sample had an exceptionally low melting point, and when analyzed, it was found to contain a small amount of Al_2O_3 as an impurity. Thus, he concluded that Al_2O_3 decreases the melting point of cryolite. This information was immediately utilized by Héroult and Hall to propose cryolite as a molten salt solvent for Al_2O_3 . However, before this process was invented, German chemist Heinrich Rose, and, independently, British metallurgist Allan Dick devised a method for producing aluminum by reduction of cryolite with sodium. Henri Sainte–Claire Deville also considered using this method but abandoned the idea after a French expedition to Greenland in the summer of 1856 discovered that the cryolite deposit was of limited size. The French bauxite was considered to be a more suitable raw material for an expanding aluminum industry. In 1962, the Greenland operation was closed.

Alumina from other sources

The production of Al_2O_3 from nepheline is a unique process used only in Russia. The source material is the waste from the beneficiation of apatite–nepheline rock, which contains

enough Na₂O and K₂O to convert its alumina content into aluminates. The feed material is mixed with limestone and calcined at 1250 – 1300 °C in a rotary kiln:



The sintered product is then crushed, ground, then leached with recycle NaOH solution. The filtrate is processed by CO₂ to precipitate Al(OH)₃ while the residue is made to cement. Some sodium carbonate and potassium carbonate are also recovered by crystallization from the leach solution after precipitating Al(OH)₃.

Söderberg electrode

In the 1920s Carl Wilhelm Söderberg (1876 – 1955) (**Figure 26**) in Norway replaced the numerous pre-baked electrodes in the aluminum production cell by a single electrode to cut expenses of manipulation (**Figure 27**). Since the electrode is consumed gradually during production, a paste has to be continuously added on the top to compensate for the loss. The industry adopted this technology but later it was found to be highly polluting. As a result, the pre-baked electrodes came back into use in the 1970s although the Russian company Russal, the largest aluminum producer in the world, still uses the pre-baked system.

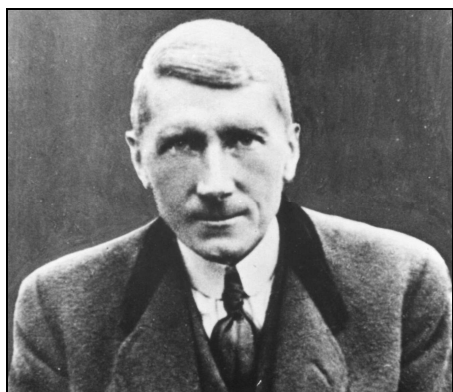


Figure 26. Carl Wilhelm Söderberg (1876 – 1955).

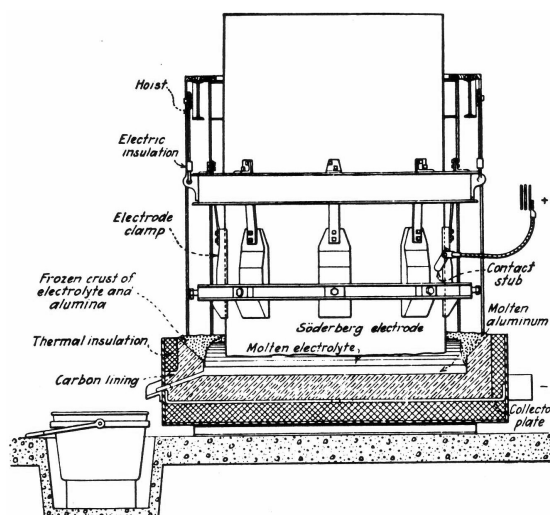


Figure 27. Söderberg electrode.

Epilogue

Although metallic aluminum was isolated for the first time in minute amount in Denmark by the Danish scientist Hans Christian Ørsted in 1825 and confirmed by the German chemist Friedrich Wöhler in 1827, the aluminum industry started in France by Henri Sainte-Claire Deville in 1854. France had large deposits of bauxite to supply the needed Al₂O₃ for the industry, but Denmark was unable to develop an aluminum industry because the cryolite from Greenland was not a competitive raw material. However, neither Le Chatelier's thermal process for treating bauxite developed in France nor Thomsen's process for treating cryolite developed in Denmark were able to compete with Bayer's hydrometallurgical route developed in Russia.

The beginnings of the aluminum industry.

Discoveries of bauxite were later reported in many parts of the world including Jamaica, Suriname, Guyana, Australia, the former USSR, USA, the former Yugoslavia, and Hungary. It now represents one of the largest tonnage mineral raw material treated chemically – about 90 million tons annually worldwide. Bayer's inventions in 1888 and 1892 to satisfy the need of the Russian textile manufacture soon turned out to become the most important invention for supplying the need of the growing electrolytic aluminum industry that was discovered four years earlier by Charles Hall and Paul Héroult.

In 1960 the production of aluminum surpassed that of copper and became the second largest metal produced after iron. The Industrial Revolution when started in England in the 18th century was based on coal and iron. After World War II the situation changed and the new civilization is now base on petroleum and aluminum.

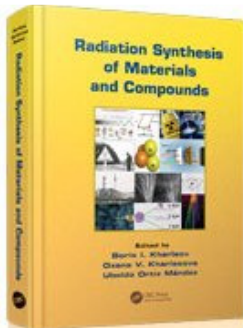
Suggested readings

1. F. Habashi. Aluminum. History & Metallurgy. 2008, Québec City: Métallurgie Extractive Québec – www.zone.ul.ca.
2. F. Habashi. Readings in Historical Metallurgy. Volume 1: Changing Technology in Extractive Metallurgy. 2006, Québec City: Métallurgie Extractive Québec. – Distributed by Laval University Bookstore, www.zone.ul.ca.

ნანომასალების რადიაციული სინთეზი

ამა წლის დასაწყისში სი-ერ-სი პრესმა ტეილორისა და ფრანციზის ჯგუფთან ერთად, ბ. ი. ხარისოვის, ო. ვ. ხარისოვასა და უ. ო. მენდესის რედაქციით, გამოსცა კოლექტიური მონოგრაფია “მასალებისა და ნაერთების რადიაციული სინთეზი”. ამ წიგნის დანიშნულება, თავად რედაქტორ-შემდგენლების მიერ, შემდგნაირად არის განსაზღვრული. ამჟამად ბირთვულ ლაბორატორიებში, ატომურ ელექტროსადგურებში და, საზოგადოდ, ნებისმიერ რადიოქიმიური დარგის საწარმოში მომუშავე მკვლევარებსა და ინჟინრებს ესაჭიროებათ ისეთი ცნობარი, სადაც მოცემული იქნება სრული ინფორმაცია გამოსხივებასა და მასალებს შორის ყველა შესაძლო რადიოქიმიური ურთიერთქმედების, სხვადასხვაგვარი დასხივებისას მასალების ფორმირების, დასხივებით მასალათა შესაძლო დაზიანების და ა.შ. თაობაზე. გარდა ამისა, რადიაციული ნანოტექნოლოგია ჯერ კიდევ რჩება პრატიკულად განუვითარებელ დარგად, თუ მხედველობაში არ მივიღებთ გარკვეულ მიღწევებს მაიონებელი ნაკადებით ლითონური ნანონაწილაკებისა მიღებაში. წიგნის მიზანია შეძლებისდაგვარად აღმოფხვრას ეს ხარვეზი. აქ გადმოცემულია მასალების (ნანომასალების ჩათვლით), კომპოზიტებისა და ქიმიური ნაერთების სხვადასხვა მაიონებელი გამოსხივების (რენტგენის, ალფა-, ბეტა- და გამა-სხივები, აგრეთვე, ნეიტრონული, პროტონული და იონური ნაკადები) მეშვეობით სინთეზირების თანამედროვე მეთოდები.

წიგნი გამოადგებათ არა მარტო წარმოებაში მოღვაწე პრაქტიკოსებს, არამედ – მკვლევარებს, უნივერსიტეტების პროფესურასა და დოქტორანტებსაც.



**Eds. B. I. Kharisov, O. V. Kharissova, U. O. Méndez.
Radiation Synthesis of Materials and Compounds.
2013, Boca Raton: CRC Press – Taylor & Francis Group**

წიგნი შედგება 24 თავისაგან, რომლებიც დაწერილია შესაბამისი სფეროს სპეციალისტების მიერ. სულ მონოგრაფიას 48 ავტორი ჰყავს მსოფლიოს 14 ქვეყნიდან (ამერიკის შეერთებული შტატები, ეგვიპტე, იაპონია, ინდოეთი, კანადა, კორეის რესპუბლიკა, ლატვია, მექსიკა, პოლონეთი, რუსეთი, საქართველო, უკრაინა, ჩეხეთის რესპუბლიკა და ხორვატია). 1-ლი თავი, რომელსაც ავტორებიც თავად რედაქტორები არიან, არსებითად შესავალს წარმოადგენს, რადგანაც აქ მოცემულია რადიაციის ძირითადი ტიპების ნივთიერებასთან ურთიერთქმედების ზოგადი დახასიათება. დანარჩენი თავები კი 3 ნაწილად არის დაჯგუფებული. ნაწილები I (თავები 2 – 9), II (თავები 10 – 16) და III (თავები 17 – 24) ეძღვნება, შესაბამისად, რადიაციის გამოყენებას არაორგანული და ორგანული მასალებისა და ნაერთების, და ნანომასალების მისაღებად. თავი 3: “ურთიერთქმედება ნეიტრონულ გამოსხივებასა და ბორშემცველ მასალებს შორის” (გვ. 43 – 80), დაწერილია ლევან ჩხარტიშვილის (საქართველო) მიერ.

მონოგრაფიის თემატიკასა და შინაარსზე თვალსაჩინო წარმოდგენას შეგვიქმნის მისი თავების დასათაურება:

- თავი 1 რადიაციის ძირითადი ტიპები და მათი ურთიერთქმედება ნივთიერებასთან
- თავი 2 ნეიტრონებითა და იონებით დასხივებისას დეფექტების წარმოქმნის სიჩქარის თეორია
- თავი 3 ურთიერთქმედება ნეიტრონულ გამოსხივებასა და ბორშემცველ მასალებს შორის
- თავი 4 ოქსიდური ნაერთების რადიაციული სინთეზი
- თავი 5 ფრენკელის დეფექტის წარმოქმნა სილიციუმის დიოქსიდში
- თავი 6 ZnO-ის ფუძეზე მომზადებული განზავების მოდიფიცირება დასხივებით
- თავი 7 Li-ის ფუძეზე შექმნილი ფოსფორები თერმოლუმინენსცენციური დოზიმეტრიისათვის
- თავი 8 ჩამკეტის მაღალი κ -ის მქონე HfO₂-ის დიელექტრული თხელი ფირების რადიაციული საიმედოობა
- თავი 9 ლითონის ოქსიდის მყარსხეულოვანი თხელი ფირების სტრუქტურისა და თვისებების მოდიფიცირება იონური იმპლანტაციით მათ გამოსაყენებლად გაზის სენსორში
- თავი 10 პოლიმერული მასალების ზედაპირის მოდიფიცირება და ფუნქციონალიზება γ -გამოსხივებით ბიოსამედიცინო გამოყენებებისათვის
- თავი 11 რადიაციული აღდგენის პროცესი: პოლიმერული დანაფარების მიღების მაღალმწარმოებლური და ეკოლოგიური ხერხი
- თავი 12 პოლიმერების რადიაციული მოდიფიცირება მაღალი ხარისხის პლასტიკური კარბიდების შესაქმნელად
- თავი 13 ელექტრული გამტარებლობის მეთოდი რადიაციული რეაქციების *in situ* მონიტორინგისათვის
- თავი 14 სპირტისა და ორგანული ხსნარების რადიოლიზი
- თავი 15 ჰიდროკარბონების ნიმუშების რადიაციით გამოწვეული სკდომა
- თავი 16 დაბალენერგეტიკული ელექტრონების მიერ ორგანულ მოლეკულებსა და პოლიმერებში დაზიანებათა წარმოქმნის მექანიზმი
- თავი 17 რადიაციის ურთიერთქმედება ნივთიერებასთან: ნანომეტრული მიდგომა
- თავი 18 რადიაციული მეთოდების გამოყენება ნანოტექნოლოგიაში
- თავი 19 რადიოიზოტოპური ლითონური ნანონაწილაკების რადიოლიზური სინთეზი
- თავი 20 მაიონებელი გამოსხივება, როგორც ვერცხლის ნანონაწილაკების ფორმირების საშუალება
- თავი 21 ნახშირბადის ნანოსტრუქტურების სტაბილურობა დასხივების მიმართ
- თავი 22 ნახშირბადის ნანომილაკებზე ლითონის ნანონაწილაკების ფორმირება გამა-გამოსხივებით
- თავი 23 ნახევრადგამტარული ნანომასალების სინთეზირების რადიაციულ-ქიმიური ხერხი
- თავი 24 იონური ბომბარდირების არეში მიღებული ნანოკრისტალური თხელფიროვანი სტრუქტურების თვისებები

თამარ ბერბერაშვილი

2013 წლის 16 სექტემბერი

შპს "ინტემი" – 2012

2012 წელს შესრულდა უკრაინის მეცნიერებათა ნაციონალური აკადემიის ი. ნ. ფრანცევიჩის სახელობის მასალათმცოდნეობის პრობლემათა ინსტიტუტის დაარსებიდან 60 წლისთავი. ამ თარიღს მიეძღვნა ქალაქ კიევში, უკრაინა, 2012 წლის 27 – 30 ნოემბერს გამართული საერთაშორისო სამეცნიერო კონფერენცია “ფხვნილური მეტალურგია: მისი დღევანდელი და ხვალისდელი დღეები” (ფმ – 2012). იუბილარ ინსტიტუტთან ერთად, ფმ – 2012-ის ორგანიზატორები იყვნენ უკრაინის მასალათმცოდნეთა საზოგადოება, ნაციონალური ტექნიკური უნივერსიტეტი “კიევის პოლიტექნიკური ინსტიტუტი” და შპს “ინტემი”.



უკრაინის მეცნიერებათა ნაციონალური აკადემიის ი. ნ. ფრანცევიჩის სახელობის მასალათმცოდნეობის პრობლემათა ინსტიტუტი

უკრაინის მასალათმცოდნეთა საზოგადოება

ნაციონალური ტექნიკური უნივერსიტეტი “კიევის პოლიტექნიკური ინსტიტუტი”

შპს “ინტემი”

კონფერენციის ორგანიზატორები

რამდენადაც ფხვნილური მეტალურგიის მიმართულებით განხორციელებული კვლევების მიხედვით კონფერენციის მასპინძელი უკრაინა ტრადიციულად ერთ-ერთი მოწინავე ქვეყანაა, მოხსენებათა უმრავლესობა სწორედ უკრაინის სამეცნიერო ცენტრებიდან იყო წარმოდგენილი. საერთოდ კი ამ საერთაშორისო სამეცნიერო ფორუმში 13 ქვეყნის (ავსტრია, აშშ, ბელარუსი, ბულგარეთი, იაპონია, პოლონეთი, რუსეთი, საფრანგეთი, საქართველო, სინგაპური, სლოვენია, სომხეთი და უკრაინა) მეცნიერები მონაწილეობდნენ.

კონფერენციის მუშაობა მიმდინარეობდა უკრაინის ეროვნულ ტექნიკურ უნივერსიტეტში “კიევის პოლიტექნიკური ინსტიტუტი”. გაიმართა 2 პლენარული სხდომა, რომლებიც დაეთმო, შესაბამისად, მისალმებებს იუბილარი ინსტიტუტისადმი და მოწვეულ მოხსენებებს.

საინტერესოა აღინიშნოს, რომ საიუბილეო სხდომაზე ი. ნ. ფრანცევიჩის სახელობის მასალათმცოდნეობის პრობლემათა ინსტიტუტის დირექტორს ვალერი სკოროხოვს ფ. თავაძის მეტალურგიისა და მასალათმცოდნეობის ინსტიტუტის დირექტორის მოადგილემ დავით სახვაძემ გადასცა ქართველი მეტალურგების სამახსოვრო საჩუქარი – საქართველოს ტერიტორიაზე აღმოჩენილი ანტიკური მეტალურგიული ნაკეთობის ასლი – ფ. თავაძის მეტალურგიისა და მასალათმცოდნეობის ინსტიტუტის თანამშრომლების მიერ ბულატის ფოლადისგან დამზადებული დანა.



ი. ნ. ფრანცევიჩის სახელობის
მასალათმცოდნეობის
პრობლემათა ინსტიტუტის
დირექტორს ვალერი სკოროხოვს
ინსტიტუტის იუბილეს ულოცავს
კიევის პოლიტექნიკური
ინსტიტუტის რექტორი
მიხაილო ზგუროვსკი

ი. ნ. ფრანცევიჩის სახელობის
მასალათმცოდნეობის
პრობლემათა ინსტიტუტის
დირექტორს ვალერი სკოროხოვს
საიუბილეო საჩუქარს გადასცემს
ფ. თავაძის მეტალურგიისა და
მასალათმცოდნეობის ინსტიტუტის
დირექტორის მოადგილე დავით სახვაძე



პლენარულ სხდომათა
შორის შესვენებაზე

მუშაობა სექციებში

გარდა ამისა, გაკეთდა თითქმის 200 ზეპირი და სასტენდო მოხსენება ფხვნილური მეტალურგიის აქტუალური პრობლემებისადმი მიძღვნილ სექციებში, მათ შორის, ფხვნილური მეტალურგიისა და მასალათმცოდნეობის ქართველი სპეციალისტების მიერ:

• ფხვნილების შესახებ მეცნიერების ფუნდამენტური პრობლემები. ფხვნილური მასალების მიღების ტექნოლოგიებისა და თვისებების მოდელირება.

გ. ფ. თავაძე, ჯ. ვ. ხანთაძე. ფხვნილების დისპერსულობის გავლენა თვითგავრცელებადი მაღალტემპერატურული სინთეზის პროცესზე.

• ფხვნილური მასალებისათვის ფორმის მიცემის ტექნოლოგიები (წნეხვა, გლინვა, შტამპვა, ლაზერული და იონოლაზერული ტექნოლოგიები, ფორმის მიცემა აფეთქებით).

• მყარ- და თხევადფაზურ შეცხოებათა გავლენა ფხვნილური ნაკეთობების თვისებებზე, შეცხოებისას თვითორგანიზების პრობლემები.

• ფხვნილური ნაკეთობების მიღების ტექნოლოგიები (ხახუნის, მაღალტემპერატურული, ფოროვანი, კონსტრუქციული და ა.შ. მასალები).

დ. ლ. გაბუნია, ო. ა. ცაგარეიშვილი, ლ. ს. ჩხარტიშვილი, ზ. მ. მირიჯანაშვილი. β-რომბოედრული ბორის ფხვნილების მიღება, სტრუქტურა და თვისებები.

ზ. მ. მირიჯანაშვილი, დ. ლ. გაბუნია, ვ. ი. ღარიბაშვილი, ა. ზ. კანდელაკი. ქლორიდ-ოქსიდური კაზმიდან კომპოზიტური მასალების მიღების კომბინირებული ტექნოლოგია.

გ. ფ. თავაძე, ბ. გ. მიქაბერიძე, ო. შ. ოქროსცვარიძე. მინერალური მადნების კონცენტრატებიდან ზოგიერთი ძნელდნობადი ნაერთის მიღება თვითგავრცელებადი მაღალტემპერატურული სინთეზით.

• ნანოტექნოლოგიები ფხვნილურ მეტალურგიაში.

• მაღალი წნევის ფაზები.

• ფხვნილური მასალების თვისებების ტესტირება.

ლ. ს. ჩხარტიშვილი, ო. ა. ცაგარეიშვილი, დ. ლ. გაბუნია, ბ. გ. მარგიევი, ა. ა. გაჩეჩილაძე, გ. ფ. თავაძე. ბორის ნიტრიდის ნანოფხვნილების კუთრი ზედაპირის განსაზღვრა ნაწილაკთა საშულო ზომის მიხედვით.

ი. ვ. მილმანი, ო. შ. ოქროსცვარიძე, ს. ი. ჩუგუნოვა, ვ. ა. გონჩარუკი, ა. ა. გოლუბენკო, ი. ვ. გონჩაროვა, ა. ი. იურკოვა, ა. ა. ვლასოვი, ა. ვ. ბიაკოვა. თვითგავრცელებადი მაღალტემპერატურული სინთეზისას კომპაქტირებით მიღებული მრავალფაზიანი კომპოზიტების სტრუქტურის კონტროლი.

ო. შ. ოქროსცვარიძე, ა. ა. გოლუბენკო, ს. ი. ჩუგუნოვა. თვითგავრცელებადი მაღალტემპერატურული სინთეზისას კომპაქტირებით მიღებული დანაფარების სისალის ტემპერატურული დამოკიდებულება.



არჩილ გაჩეჩილაძე ფმ – 2012-ზე



ლევან ჩხარტიშვილი ფმ – 2012-ზე



სასტენდო მოხსენებები



ფირმის Thermo Techno ბუკლეტი

კონფერენციის მონაწილეებს საშუალება ჰქონდათ დაეთვალიერებინათ უკრაინის მეცნიერებათა ეროვნული აკადემიის მთელი რიგი ინსტიტუტების სამეცნიერო-ტექნიკური ბაზები.

ისინი აგრეთვე გაეცნენ უკრაინაში Thermo Techno-ის წარმომადგენლობის ინფორმაციას იმ პროდუქციისა (რენტგენოფლუოროსენციური, ოპტიკური, აკუსტიკური და ელექტროაკუსტიკური სპექტრომეტრები; რენტგენული და ლაზერული დიფრაქტომეტრები; ნანონაწილაკების ზომებისა და ტრაექტორიების, ფორომეტრიისა და მეტა-პოტენციალის ანალიზატორები; კაპილარული პირომეტრები და ა.შ.) და სერვისის (მეთოდოლოგიური მხარდაჭერა ხელსაწყოთა შერჩევაში, მისი ინსტალაცია, საგარანტიო და პოსტ-საგარანტიო მომსახურება, სერტიფიკაცია და აკრედიტაცია, ტექნიკური დიაგნოსტიკა, კონსულტირება, დამკვეთის პერსონალის ტრენინგი და ა.შ.) შესახებ, რომელთაც ეს ფირმა თავაზობს 0.1 ნმ-დან 1 მმ-მდე ზომითი დიაპაზონის ნაწილაკებისაგან შედგენილი დისპერსიული სისტემების (ფხვნილების, სუსპენზიების, კოლოიდებისა და ფლოკული მასალების) ანალიზის თანამედროვე აპარატურით დაინტერესებულ სამეცნიერო-კვლევით ცენტრებს.

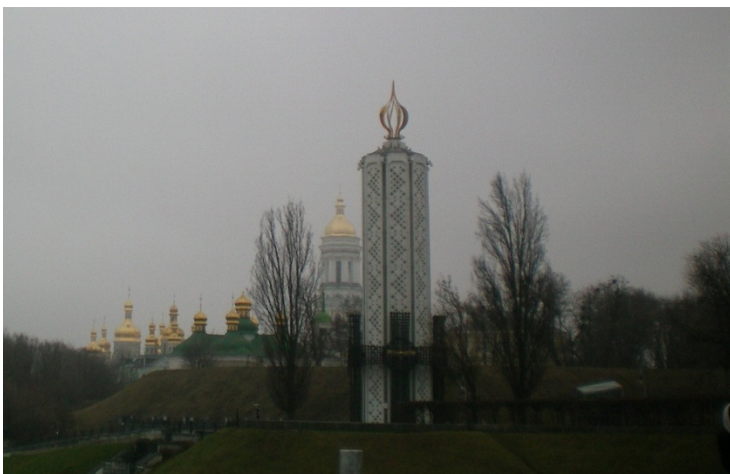
კონფერენციაზე გამომსვლელებს დამსწრეებმა მრავალი შეკითხვა დაუსვეს, გაიმართა ნაყოფიერი მეცნიერული დისკუსია.

ფმ – 2012-ში მონაწილეობამ ქართველ სპეციალისტებს საშუალება მისცა განევიტარებინათ თანამშრომლობა მეტალურგიის, მასალათმცოდნეობისა და ნანოტექნოლოგიების ისეთ მოწინავე სამეცნიერო ცენტრებთან უკრაინაში, როგორცაა ი. ნ. ფრანცევიჩის სახელობის მასალათმცოდნეობის პრობლემათა ინსტიტუტი, კიევის ეროვნული უნივერსიტეტი და ფ. დ. ოვჩარენკოს სახელობის ბიო-კოლოიდური ქიმიის ინსტიტუტი.



კონფერენციის წინასწარი პროგრამის გარეკანი და მოხსენებათა თეზისების სრული კრებულის სატიტულო გვერდი

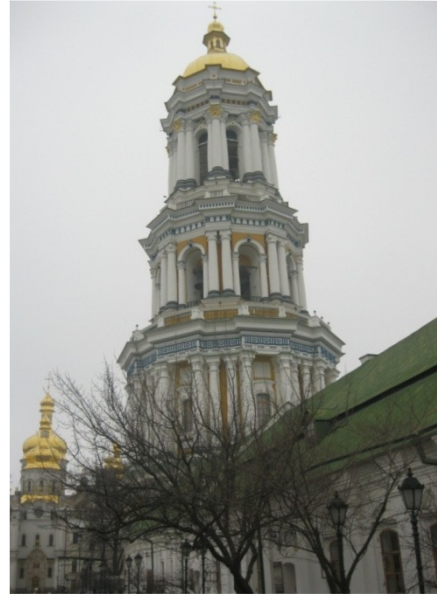
კონფერენციის “ფხვნილური მეტალურგია: მისი დღევანდელი და ხვალისდელი დღეები” (ფმ – 2012) პროგრამა დაიბეჭდა, ხოლო მოხსენებათა თეზისების სრული კრებული ელექტრონული ფორმით გამოქვეყნდა.



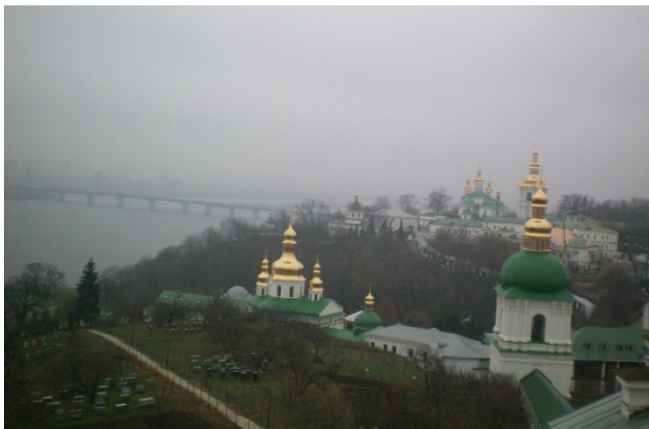
1932 – 1933 წლებში უკრაინაში მასობრივი შიმშილობის – გოლოდომორის – მსხვერპლთა მემორიალი კიევში



წმ. ღვთისმშობლის
მიძინების ტაძარი



სამრეკლო



ხედი მდ. დნეპრზე



კონფერენციის ქართველი
მონაწილეები მასპინძლებთან
ერთად კიევ-პეჩორის ლავრაში

გარდა დატვირთული სამეცნიერო პროგრამისა, ფმ – 2012-ის ორგანიზატორებმა დამსწრეთათვის საინტერესო სოციალური პროგრამაც მოამზადეს. უკრაინის მეცნიერებათა ნაციონალური აკადემიის ი. ნ. ფრანცევიჩის სახელობის მასალათმცოდნეობის პრობლემათა ინსტიტუტის დაარსებიდან 60 წლისთავისადმი მიძღვნილი ინსტიტუტის სამეცნიერო საბჭოს საზეიმო სხდომის შემდეგ გაიმართა მიღება ფურშეტით. კიევის პოლიტექნიკურ ინსტიტუტში კონფერენციის მონაწილეებს მოუწყვეს მეგობრული ვახშამი. შედგა ექსკურსია ქალაქ კიევის ღირსემანიშნობათა, კერძოდ, კიევ-პეჩორის ლავრის სამონასტრო კომპლექსის, დასათვალიერებლად.

არჩილ გაჩეჩილაძე

2012 წლის 10 დეკემბერი

მოწინავე და ნანო მასალების საერთაშორისო
კონფერენცია და გამოფენა 2013

მოწინავე და ნანო მასალების საერთაშორისო კონფერენცია და გამოფენა 2013 (მნმსკ 2013) მიმდინარეობდა ამა წლის 12 – 14 აგვისტოს ლავალის უნივერსიტეტში, კანადის ქალაქ კვებეკ-სიტიში – ფრანგულენოვანი პროვინციის კვებეკის (ე.წ. ახალი საფრანგეთის) ადმინისტრაციულ ცენტრში. კონფერენცია ჩატარდა ენერჯის, მინერალებისა და მასალების საერთაშორისო აკადემიის ეგიდით.



კონფერენციის ლოგო



National Science Foundation



კონფერენციის მედია-პარტნიორები

კონფერენციის სპონსორები

კონფერენცია მიზნად ისახავდა მთელი მსოფლიოდან მოეყარა თავი იმ მეცნიერების, ინჟინრების, მაღალტექნოლოგიური წარმოებისა და პოლიტიკის წარმომადგენლებისათვის, რომლებიც მოღვაწეობენ მოწინავე და ნანო მასალების უაღრესად სწრაფად განვითარებად სფეროში, რათა მათ მისცემოდათ საშუალება ერთმანეთისათვის გაეცნოთ თავიანთი უახლესი შედეგები და დაემყარებინათ ურთიერთსასარგებლო კონტაქტები, განვითარებინათ თანამშრომლობა.

საერთო ჯამში მნმსკ 2013-ზე წარმოდგენილი იყო 136 მოხსენება 26 ქვეყნიდან (ავსტრალია, ალჟირი, არაბეთის გაერთიანებული საემიროები, ამერიკის შეერთებული შტატები, ბელგია, ბრაზილია, დიდი ბრიტანეთი, ეგვიპტე, ერაყი, თურქეთი, იაპონია, ინდოეთი, ირანი, ისრაელი, კანადა, მალაიზია, მექსიკა, ომანი, პოლონეთი, საფრანგეთი, საქართველო, საუდის არაბეთი, სინგაპური, ტაივანი, შვეიცარია და ჩინეთი).

პლენარულ სხდომებზე გაკეთდა მოწვეული მოხსენებები ნანო და მოწინავე მასალათმცოდნეობის რიგი მნიშვნელოვანი და აქტუალური მიმართულებით:

- სუსპენზიასა და კოლოიდებში ნანოდან მიკრომდე ზომების ნაწილაკების განაწილების გაზომვა ინტერაქტიური ძალური აპარატით – ტოიშისა ფუჯიტა (ტოკიოს უნივერსიტეტი, ტოკიო, იაპონია)
- ნანოტექნოლოგია, მოწინავე მასალები და უჯრედები: სისხლძარღვთა ქსოვილის ინოვაციური ინჟინერიისა და შეცვლის სტრატეგიები – დიეგო მანტოვანი (ლავალის უნივერსიტეტი, კვებეკ-სიტი, კანადა)
- ნანო და მოწინავე მასალები: გამოწვევები და შესაძლებლობები – ჰოსსეინ ამინიანი (საერთაშორისო საკონსულტაციო ფირმა Fi Mat Con, ოტავა, კანადა)
- ბორის ნიტრიდის ნანოსისტემების გეომეტრია – ლევან ჩხარტიშვილი (საქართველოს ტექნიკური უნივერსიტეტი, თბილისი, საქართველო)
- ლანთანდით ლეგირებული ნანოკრისტალები – ანა რიჩი (ლავალის უნივერსიტეტი, კვებეკ-სიტი, კანადა)
- ფუნქციონალური ნანოდანაფარები – ჯას პალ ბადიალი (დურჰამის უნივერსიტეტი, დურჰამი, დიდი ბრიტანეთი)
- ინდუსტრიული რევოლუცია – ფათჰი ჰაბაში (ლავალის უნივერსიტეტი, კვებეკ-სიტი, კანადა)
- პოლიესტერსულფონებისა და პოლიესტერკეტონების ზუსტად კრისტალიზება – ჯოზი ბრისსონი (ლავალის უნივერსიტეტი, კვებეკ-სიტი, კანადა)



მოწინავე და ნანო მასალების საერთაშორისო კონფერენციისა და გამოფენის – 2013 პროგრამა

კონფერენციის თემატიკის მრავალფეროვნებაზე მეტყველებს, აგრეთვე, გამართული სექციების დასახელებებიც:

- მოწინავე და ნანომასალები: მიღება და გამოყენება
- ფუნქციონალური მოწინავე და ნანომასალები
- კომპოზიტები, პოლიმერული და ჰიბრიდული მასალები
- მასალების მოდელირება, სიმულირება და ოპტიმიზება
- ნანოელექტრონიკა, ნანოხელსაწყოები, ნანონახევრადგამტარები და ხელსაწყოები
- მოწინავე ტექნიკა მოწინავე და ნანომასალების დასახასიათებლად

- ნანომედიცინა, ნანიბიოტექნოლოგია, გარემო და ნანოტოქსიკოლოგია
- ნანოტექნოლოგია და ენერჯია
- ნახშირბადის ნანომილაკები და გრაფენი
- მოწინავე და ნანოსტრუქტურირებული მასალების მექანიკური მოქმედება

კონფერენციაზე წარმოდგენილი მოხსენებების სრული ტექსტების კრებული გამოქვეყნდება ელექტრონულად და CD-R-ზე ჩაწერილი დაეგზავნება მონაწილეებს. გარდა ამისა, კონფერენციის სარედაქციო ჯგუფის ექსპერტიზის შედეგად რეკომენდებული მოხსენებები სტატიების სახით ქვეყნდება წინამდებარე ჟურნალის Nano Studies 2013 წლის გამოშვებებში.

ამ ფორუმის სამუშაო პროგრამა ძალზე დატვირთული იყო: გაიმართა 3 პლენარული სხდომა, 14 სხდომა სექციებში, 2 პოსტერული სესია, კერამიკულ მასალებში პროფესიული დახელოვნების ვორქშოფის 5 სესია და, აგრეთვე, მოწინავე და ნანო მასალების მიღებისა და გამოკვლევის თანამედროვე მოწყობილობების გამოფენა.

ვორქშოფზე კერამიკული მასალების ახალგაზრდა მკვლევარებმა მოისმინეს შემდეგი ლექციები:

- ელექტრონული თვისებების ოქტაედრული მართვა ნახევრადგამტარულ პეროვსკიტულ ჰეტეროსტრუქტურებში – სტივენ მეი (დრექსელის უნივერსიტეტი, ფილადელფია, აშშ)
- ეკოლოგიური პიეზოელექტრიკული მასალების შექმნა მდგრადი სისტემებისათვის – ბრადი გიბზონსი (ორეგონის შტატის უნივერსიტეტი, კორვალისი, აშშ)
- Bi-ფაზურ კერამიკულ ნანოკომპოზიტებში ზედაპირთაშორის დაწყვილებასთან დაკავშირებული დამოკიდებულება სტრუქტურა-თვისება – ჯენიფერ ენდრიუ (ფლორიდას უნივერსიტეტი, გეინსვილი, აშშ)
- რადიაციის ურთიერთქმედება ნანოსტრუქტურირებულ კერამიკებთან – მაინტეგრებელი მასალები ბირთვულ განათლებაში – ჯიი ლიანი (რენსელარის პოლიტექნიკური ინსტიტუტი, ტროა, აშშ)
- გაძლიერებული პიროელექტრული და ელექტროკალორიული ეფექტები რთული ოქსიდების თხელფიროვან ჰეტეროსტრუქტურებში – ლან მარტინი (ილიონისის უნივერსიტეტი, ურბანა-ჩემპენი, აშშ)

თითოეული სალექციო სესიის ბოლოს გამოყოფილი იყო დრო დისკუსიისათვის, რომელიც, ჩვეულებრივ, გაცხოველებული, კითხვა-პასუხის რეჟიმში მიმდინარეობდა.

რაც შეეხება გამოფენას, იგი იძლეოდა საშუალებას შეგეტყოთ უახლესი მოწყობილობის, ტექნოლოგიის, საწარმოო პროცესებისა და მომსახურების შესახებ. აქ ერთმანეთს შეხვდნენ, ერთის მხრივ, სამეცნიერო კონფერენციის მონაწილეები და, მეორეს მხრივ, პროფესიონალები ნანოინდუსტრიიდან – მომწოდებლები, კონტრაქტორები და კონსულტანტები. გამოფენის პროფილი იყო:

- მოწყობილობა და ტექნოლოგიები მასალების მისაღებად
- ინოვაციური ტექნოლოგიები
- მოწინავე საწარმოო ტექნოლოგიები
- ნანოტექნოლოგია და მისი გამოყენებები
- ინჟინერია / ფორმირება
- მოწინავე მასალების გამოყენება
- ტექნოლოგიებისა და მომსახურების პროვაიდერები
- ტექნოლოგიების დამმუშავებელი უნივერსიტეტები და კვლევითი ცენტრები

საქართველოდან მნმსკ 2013-ის მუშაობაში მონაწილეობდა საქართველოს ტექნიკური უნივერსიტეტის საინჟინრო ფიზიკის დეპარტამენტის პროფესორი, ფერდინანდ თავაძის მეტალურგიისა და მასალათმცოდნეობის ინსტიტუტის ბორშემცველი და კომპოზიტური მასალების ლაბორატორიის მკვლევარი ლევან ჩხარტიშვილი (მისი გამგზავრება დააფინანსა ძირითადად საორგანიზაციო კომიტეტმა და ნაწილობრივ შოთა რუსთაველის ეროვნულმა სამეცნიერო ფონდმა). როგორც ითქვა, მან გააკეთა მიწვეული მოხსენება: “ბორის ნიტრიდის ნანოსისტემების გეომეტრია”, რომელმაც დიდი ინტერესი გამოიწვია. საკმარისია ითქვას, რომ კონფერენციის დასრულებიდან ერთ კვირაში ლ. ჩხარტიშვილმა მიიღო წინადადება მიკრო- და ნანომეცნიერების, ტექნოლოგიისა და მედიცინის საერთაშორისო გამომცემლობისაგან Pan Stanford Publishing, რომ მოხსენება გამოქვეყნდეს ცალკე მონოგრაფიის სახით.

გარდა ამისა, მისი თანაავტორობით წარმოდგენილი იყო ზეპირი მოხსენება სექციაში “მასალების მოდელირება, იმიტირება და ოპტიმიზება”:

- მუხტის გადამტანების ეფექტური ჰოლის ძვრადობა ნახევრადგამტარებში ნანოზომის “მეტალური” ჩანართებით: დასხივებული სილიციუმი – ლ. ჩხარტიშვილი, თ. ფაღავა.

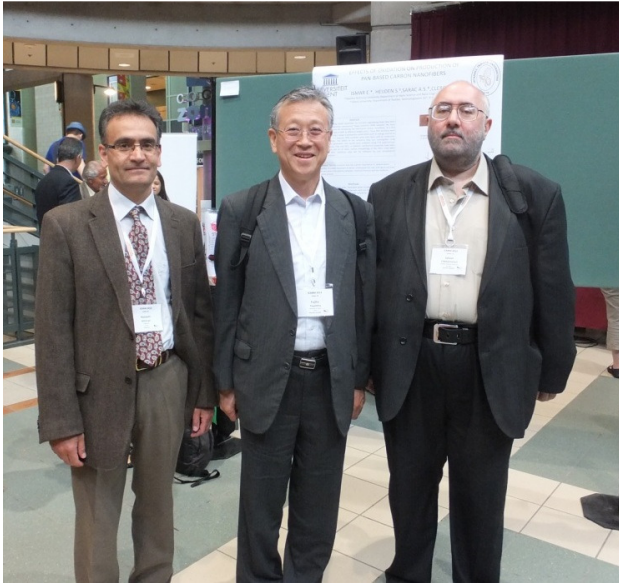
და კიდევ პოსტერული მოხსენებები:

- ნანოკრისტალური ბორის ნიტრიდის გავლენა თითბერში ცვეთის პროცესებზე – ლ. ჩხარტიშვილი, მ. დარჩიაშვილი, ა. გაჩეჩილაძე, ბ. მარგიევი, ლ. რუხაძე, ო. ცაგარეიშვილი
- გერმანიუმის და ინდიუმის ფუძეზე 1D ნანოსტრუქტურების თვითკატალიზური ზრდა – დ. ჯიშიაშვილი, ლ. ჩხარტიშვილი, ლ. ქირია, ზ. შიოლაშვილი, ნ. მახათაძე, ა. ჯიშიაშვილი, ვ. გობრონიძე



ლ. ჩხარტიშვილი ლავალის უნივერსიტეტის ბიბლიოთეკის დიდ გლობუსზე აჩვენებს თბილისს და კვებეკ-სიტის

იგი თავმჯდომარეობდა სექციების “ნანოელექტრონიკა, ნანოხელსაწყობები, ნანონახევრადგამტარები და ხელსაწყობები I”, “ნახშირბადის ნანომილაკები და გრაფენი” და “კომპოზიტები, პოლიმერული და ჰიბრიდული მასალები III” სხდომებს. კონფერენციის მიმდინარეობის პერიოდში პროფ. ლ. ჩხარტიშვილი შეხვდა და ნანომასალების კვლევებისა და გამოყენებების სფეროში თანამშრომლობის თაობაზე ესაუბრა დარგის მთელ რიგ საზღვარგარეთელ სპეციალისტებს. ესენია: პროფ. ფათჰი ჰაბაში (ლავალის უნივერსიტეტი, კვებეკ-სიტი, კანადა), პროფ. ტოიშისა ფუჯიტა (ტოკიოს უნივერსიტეტი, ტოკიო, იაპონია), დოქტ. ჰოსსეინ ამინიანი (საერთაშორისო საკონსულტაციო ფირმა Fi Mat Con, ოტავა, კანადა), დოქტ. ვოლფ ლემჩინსკი (მეტალების ფორმირების ინსტიტუტი, ვარშავა, პოლონეთი), მენეჯერი კიმიტაკა სატო (საერთაშორისო კორპორაცია Dowa, ნიუ-იორკი, აშშ), რიკ ბეკერი (ბორის კლასტერული მეტამასალები, იფსვიჩი, აშშ) და სხვ.



პროფ. ლ. ჩხარტიშვილი სტუმრად
პროფ. ფ. ჰაბაშის სამუშაო კაბინეტში

დოქტ. ჰ. ამინიანი (კანადა),
პროფ. ტ. ფუჯიტა (იაპონია) და
პროფ. ლ. ჩხარტიშვილი (საქართველო)

კონფერენცია და გამოფენა მიმდინარეობდა ლავალის უნივერსიტეტის კამპუსში, რომელიც კვებეკ-სიტის ერთ-ერთ ყველაზე შთამბეჭდავ ადგილას არის გაშენებული. თავად ქალაქი (ფრანგული კანადის – კვებეკის დედაქალაქი) – უძველესია ქვეყანაში – იგი 400 წლის წინათ დაარსდა. კვებეკ-სიტი ჩრდილო ამერიკის ისტორიის იმ ღირშესანიშნოობად ითვლება, სადაც ევროპული ატმოსფეროა შენარჩუნებული. კვებეკ-სიტი იუნესკოს მსოფლიო მემკვიდრეობის სიაშია შეტანილი. ქალაქის ძველი ნაწილია ე.წ. “დაუნ-თაუნი”, რაც შეეხება უნივერსიტეტს, იგი ახალ ნაწილშია.



სლაიდი პლენარულ სხდომაზე
პროფ. ფ. ჰაბაშის მოხსენებიდან:

ეპისკოპოსმა ფრანსუა დე ლავალმა დააარსა კვებეკში პირველი სასწავლებელი (სემინარია), რომელიც შემდგომში ლავალის უნივერსიტეტად გარდაიქმნა



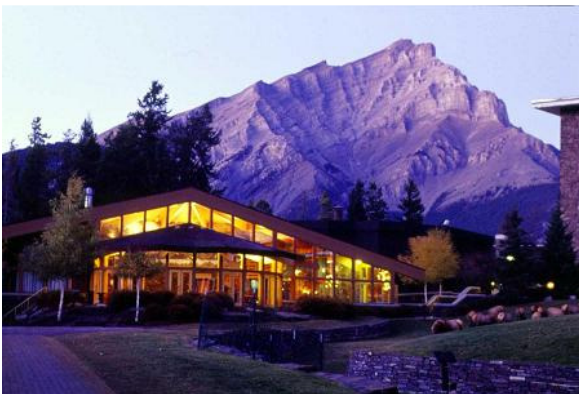
ლავალის უნივერსიტეტის კამპუსი

“დაუნ-თაუნის” ერთი კუთხე



კვებეკ-სიტის პანორამა წმ. ლოურენსის მდინარისა და სადამოს ცის ფონზე

მოწინავე და ნანო მასალების საერთაშორისო კონფერენცია და გამოფენა 2013 პირველი იყო ამ ტიპის ღონისძიებათა შორის. მისმა დიდმა წარმატებამ ორგანიზატორებს გადააწყვეტინა, რომ ასეთი ფორუმები კანადაში ყოველწლიურად ჩატარდეს.



მომავალ წელს გელით ბანფში –
კანადის კლდოვან მთიანეთში!

მინერალებისა და მასალების საერთაშორისო აკადემია მორიგ მოწინავე და ნანო მასალების საერთაშორისო კონფერენციას და გამოფენას მართავს 2014 წლის 11 – 13 აგვისტოს კანადის ქალაქ კალგარიში (ალბერტას პროვინცია), რომელიც მდებარეობს კანადის დიდი კლდოვანი მთიანეთის ბანფის აღმოსავლეთით.

ლევან ჩხარტიშვილი
2013 წლის 26 აგვისტო

ISSN 1987-8826